DISTORTIONAL BUCKLING OF COLD-FORMED STEEL MEMBERS IN BENDING

by

Cheng Yu and Benjamin W. Schafer

FINAL REPORT

American Iron and Steel Institute

Baltimore, Maryland

January 2005

Abstract

Laterally braced cold-formed steel beams generally fail due to local and/or distortional buckling in combination with yielding. For many cold-formed steel (CFS) studs, joists, purlins, or girts, distortional buckling may be the predominant buckling mode. However, distortional buckling of CFS beams remains a largely unaddressed problem in the current North American Specification for the Design of Cold-Formed Steel Structural Members (NAS). Further, adequate experimental data on unrestricted distortional buckling in bending is unavailable. Therefore, two series of bending tests on industry standard CFS C and Z-sections were performed and presented in this dissertation. The testing setup was carefully designed in the first series of tests (Phase 1) to allow local buckling failure to form while restricting distortional and lateral-torsional buckling. The second series of tests (Phase 2) used nominally identical specimens to Phase 1 tests, and a similar testing setup. However, the corrugated panel attached to the compression flange was removed in the constant moment region so that distortional buckling could occur. The experimental data was used to examine current specifications and new design methods. Finite element modeling in ABAQUS was developed and verified by the two series of bending tests and then applied to analyze more CFS beams.

An analytical method was derived to determine the elastic buckling stress of thin plates under longitidunal stress gradient. And finite element analysis was used to study the stress gradient effect on the ultimate strength of thin plates. It was found that the stress gradient increases the buckling stress of both stiffened and unstiffened elements, and current design methods can include the stress gradient effect if an appropriate elastic buckling cofficient is used.

The moment gradient effect on the distortional buckling of CFS beams was also studied by the finite element analysis. The results show that the moment gradient increases both the elastic buckling moment and ultimate strength of distortional buckling of CFS beams. A draft design provision was proposed to account for the moment gradient effect.

Research was conducted to explore the distortional buckling of CFS beams with partial restraint on the compression flange. A simple numerical model was proposed to calculate the elastic buckling moment of the CFS section-panel system. It was found that partial restraint has significant influence on distortional buckling, and that the influence could be considered by using a modified elastic buckling moment.

For design purposes, simplified closed-form solutions for the elastic buckling moment of CFS C and Z-sections were proposed and verified.

In the end, conclusions and recommendations for future research are presented.

Adviros: Professor Benjamin W. Schafer

Readers: Professor J. Hugh Ellis

Professor Sanjay R. Arwade

JHU Structures Lab Mascot

the every first test conducted by the author (January 2001)

Table of Contents

List of Figures

List of Tables

Chapter 1

Introduction

1.1 Cold-Formed Steel Structural Members

In steel construction, there are primarily two types of structural members: hot-rolled steel shapes and cold-formed steel shapes. Hot-rolled steel shapes are formed at elevated temperatures while cold-formed steel shapes are formed at room temperature, thus the name cold-formed steel. Cold-formed steel members are made from structural quality sheet steel and formed into shape, either through press-braking blanks sheared from sheets or coils Figure 1.1a, or more commonly, by roll forming the steel through a series of dies Figure 1.2b.

The idea behind cold-formed steel members is to use shape rather than thickness to support load. Due to the relatively easy method of manufacturing, a large number of different configurations can be produced to fit the demands of optimized design for both structural and economical purposes. Figure 1.2 shows typical cold-formed steel shapes. Besides the variety of shapes, cold-formed steel members offer many other advantages

including lightness, high strength and stiffness, mass production, fast and easy installation, and economy in transportation and handling.

The use of cold-formed steel members in building construction began in the 1850's (Yu 2001). Since the 1940's, cold-formed steel members have been widely used in both industrial and residential buildings. Cold-formed steel represents over 45 percent of today's steel construction market, and this share is increasing. For example, over 50% of housing starts in Hawaii are cold-formed steel homes (Elhajj 2001).

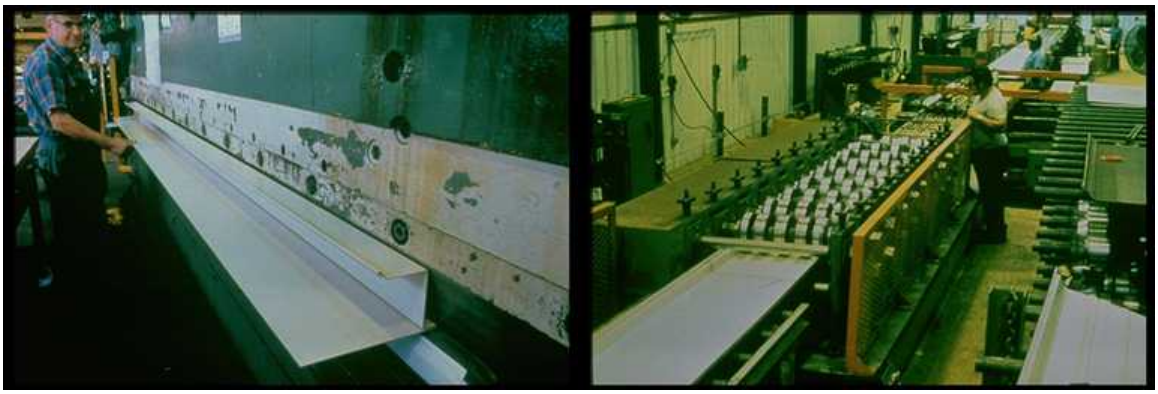

(a) Press braking (b) Roll forming

Figure 1.1 Forming methods for cold-formed steel members (www.steel.org)

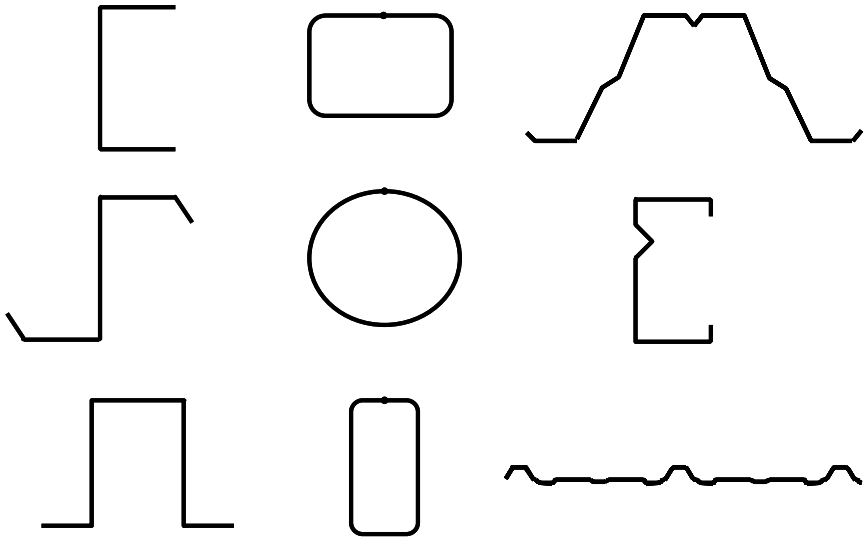

Figure 1.2 Common cold-formed steel shapes

1.2 Design Methods for Cold-Formed Steel Structural Members

1.2.1 Design Specifications for Cold-Formed Steel Structural Members

The first design specification for cold-formed steel structural members, "Specification for the Design of Light Gauge Steel Structural Members" was developed by the American Iron and Steel Institute (hereafter referred to as the AISI Specification) in 1946. The first edition of the AISI Specification was based primarily on the investigations conducted by Professor George Winter and his collaborators at Cornell University between 1939 and 1946. Subsequently, the AISI Specification (named "Specification for the Design of Cold-Formed Steel Structural Members") has been revised and updated by new research findings, but the main philosophy of the Specification remained unchanged until 1996 when the 50th anniversary edition was published. The 1996 AISI Specification is the first cold-formed steel design specification to combine allowable stress design (ASD) and load and resistance factor design (LRFD) and it also embraced modern effective width methods for all members according to the research done by Professor Teoman Peköz (Peköz 1986). The AISI Specification was a major source for the development of cold-formed steel specifications of many other countries including Canada ("S136 Standard for Cold Formed Steel Structural Members", hereafter referred to as the CSA S136 Specification), and Australia and New Zealand ("Australian/New Zealand Standard, Cold-Formed Steel Structures", hereafter referred to as the AS/NZS 4600 Specification).

In 2001, the first edition of the "North American Specification for the Design of Cold-formed Steel Structural Members" (hereafter referred to as the NAS Specification)

was published by a collaborative effort of the AISI Committee on Specifications, the Canadian Standard Association Committee on Specifications, and Camara Nacional de la Industria del Hiero y del Acero (CANACERO) in Mexico. NAS supercedes the previous editions of the AISI and CSA S136 Specifications, and incorporates recent research findings. NAS provides a unified document for cold-formed steel design in Canada, Mexico and the United States.

1.2.2 The Effective Width Concept

Since the thickness of individual plate elements of cold-formed steel (CFS) structural members are normally small compared to their width, buckling and postbuckling strength are two major concerns for strength prediction of CFS structural members. Unlike hot-rolled structural members, CFS members normally buckle prior to section yielding. Further, CFS compression elements do not collapse when the buckling stress is reached. Additional load can be carried by the element after buckling, by means of stress redistribution. This phenomenon, termed "postbuckling strength" is most pronounced for elements with high slenderness.

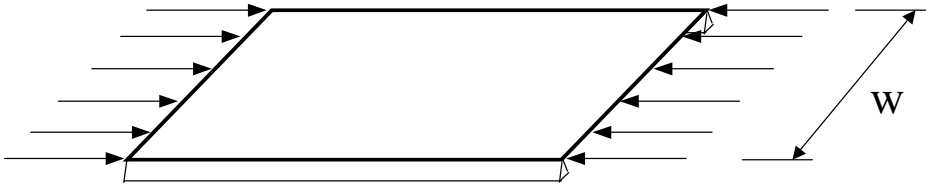

Figure 1.3 Stiffened compression element

For the stiffened compression element of Figure 1.3, Figure 1.4 shows an *idealization* of the longitudinal stress during consecutive stages of loading. The stress is uniformly distributed at the beginning load stage. As the applied stress approaches the

buckling stress, the stress distribution is no longer uniform and the maximum stress increases over the buckling stress until it reaches the yield stress, then the element fails. This idealization ignores longitudinal variations in the stress, but captures the mean, membrane stress behavior.

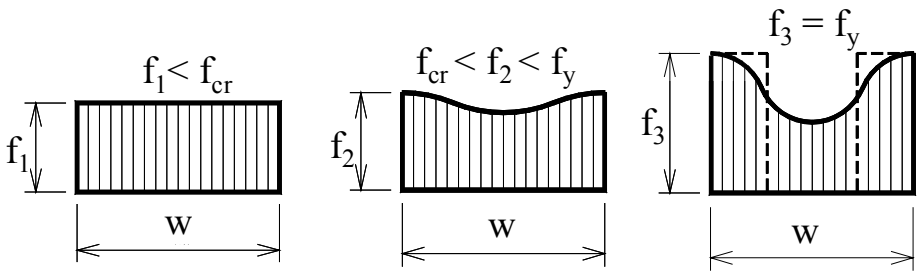

Figure 1.4 Development of stress distribution in stiffened compression elements

The elastic postbuckling behavior of a thin plate can be analyzed by using large deflection theory, but the result is generally too complex to be applied in practice. Therefore, the Effective Width Concept, introduced by von Karman et al. in 1932 (Von Karman, Sechler, and Donnell 1932) and subsequently modified by Winter (Winter 1947), became the key to the design of cold-formed steel members from the first AISI Specification in 1946 up to the latest 2001 NAS Specification.

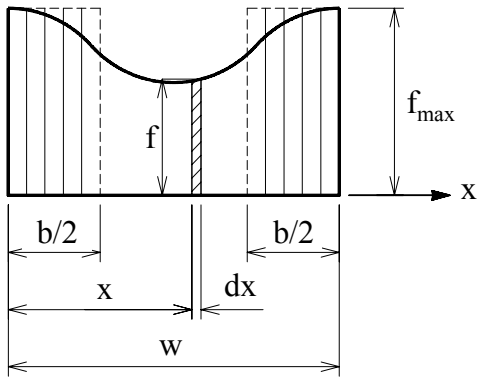

Figure 1.5 Effective width of stiffened compression element

In the Effective Width approach, instead of considering the non-uniform distribution of stress across the width of the element, it is assumed that the total load is carried by a fictitious width b, which is subjected to a uniformly distributed stress f_{max}. Where, f_{max} equals the edge stress, as shown in Figure 1.5. Calculating the postbuckling strength of a stiffened element is thus simplified to determining the effective width b. The basic formulas were developed under the leadership of Professor George Winter at Cornell University in the early 1940's, and is now known simply as "Winter's equation". These equations appeared in the first cold-formed specification (AISI 1946) and remain today.

$$b = w, \quad \text{for } \lambda \le 0.673 \tag{2.1}$$

$$b = \rho w, \quad \text{for } \lambda > 0.673 \tag{2.2}$$

where ρ = reduction factor

$$\rho = \left(1 - \frac{0.22}{\lambda}\right) \Big/ \lambda \le 1 \tag{2.3}$$

where λ = plate slenderness factor

$$\lambda = \sqrt{\frac{f}{f_{cr}}} = \frac{1.052}{\sqrt{k}} \left(\frac{w}{t}\right) \sqrt{\frac{f}{E}} \tag{2.4}$$

where k = plate buckling coefficient;

t = thickness of compression element;

E = modulus of elasticity;

f_{max} = maximum compressive edge stress in the element ($f_{max} = f_y$, the yield stress , for maximum capacity).

For more complicated configurations, such as the C-section of Figure 1.6, the effective width must be determined for each compression portion, and then the strength of the section can be obtained by assuming load is resisted only by the effective areas.

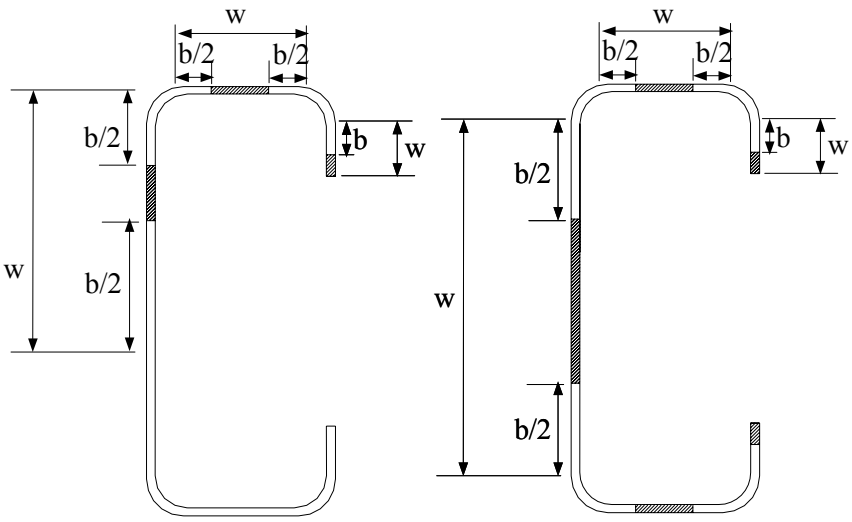

Figure 1.6 Effective width of a C-section in bending and compression (shading denotes ineffective regions)

1.2.3 New Design Method – Direct Strength Method

When sections become more complex and optimized, with additional edges and/or intermediate stiffeners, the computation of the effective widths (Figure 1.6) becomes extremely complicated and time consuming. Further, current design methods treat each element of the whole section independently, the interaction that exists between elements (e.g., the web and the flange) is generally ignored. To overcome these problems, a new method has been developed by Schafer and Peköz (1998a), called the Direct Strength Method (DSM). The new method avoids effective width/section calculations and instead uses strength curves for the entire member. Elastic buckling solutions for the entire member are employed rather than the traditional solutions for each individual element. The development of the Direct Strength Method is based on the same empirical assumption as the effective width method, which is that ultimate strength is a function of

elastic buckling loads (f_{cr} in Equation 2.4) and the yielding stress (f_y in Equation 2.4) of the material. Strength curves for DSM are calibrated by a large amount of experimental data. For example, for flexural members, the data was collected form 17 researchers for a total of 574 flexural members. The analyses show that DSM is accurate and reliable, and works as well as the AISI Specification with much greater ease (Schafer and Peköz 1998a).

The Direct Strength Method uses the entire cross-section in the elastic buckling determination and offers specific provisions for local, distortional and global buckling strength respectively for both compression and flexural CFS members. Below are the DSM provisions for the design of cold-formed steel beams.

The nominal flexural strength, M_{ne}, for lateral-torsional buckling is

for $M_{cre} < 0.56M_y$

$$M_{ne} = M_{cre} \tag{1.1}$$

for $2.78M_y \geq M_{cre} \geq 0.56M_y$

$$M_{ne} = \frac{10}{9} M_y \left(1 - \frac{10M_y}{36M_{cre}} \right) \tag{1.2}$$

for $M_{cre} > 2.78M_y$

$$M_{ne} = M_y \tag{1.3}$$

where M_y is yield moment, M_{cre} is critical elastic lateral-torsional buckling moment.

The nominal flexural strength, $M_{n\ell}$ for local buckling is

for $\lambda_\ell \leq 0.776$

$$M_{n\ell} = M_{ne} \tag{1.4}$$

for $\lambda_\ell > 0.776$

$$M_{n\ell} = \left(1 - 0.15 \left(\frac{M_{cr\ell}}{M_y} \right)^{0.4} \right) \left(\frac{M_{cr\ell}}{M_y} \right)^{0.4} M_y \tag{1.5}$$

where $\lambda_\ell = \sqrt{M_{ne} / M_{cr\ell}}$, $M_{cr\ell}$ critical elastic local buckling moment.

The nominal flexural strength, M_{nd}, for distortional buckling is

for $\lambda_d \leq 0.673$

$$M_{nd} = M_y \tag{1.7}$$

for $\lambda_d > 0.673$

$$M_{nd} = \left(1 - 0.22\left(\frac{M_{crd}}{M_y}\right)^{0.5}\right)\left(\frac{M_{crd}}{M_y}\right)^{0.5} M_y \tag{1.8}$$

where $\lambda_d = \sqrt{M_y / M_{crd}}$, M_{crd} critical elastic distortional buckling moment.

In 2004, the Direct Strength Method was approved by the AISI Committee on Specification and included in the "North American Specification for the Design of Cold-Formed Steel Structural Members" as an alternative design method for determination of the nominal axial (P_n) and flexural (M_n) strengths of cold-formed steel members (DSM 2004).

1.3 Motivation and Objectives

Determination of the ultimate bending capacity of cold-formed steel beams is complicated by potential failure mechanisms of material yielding, local bucking, distortional buckling, lateral-torsional buckling, and combinations thereof. Figure 1.7 illustrates a finite strip analysis of a Z-section in restrained flexure with web height 8.5 in., flange width 2.5 in., thickness 0.073 in., and material yield stress of 55 ksi. The results are shown in a plot of buckling half wavelength vs. critical buckling moment–to–yield moment ratio.

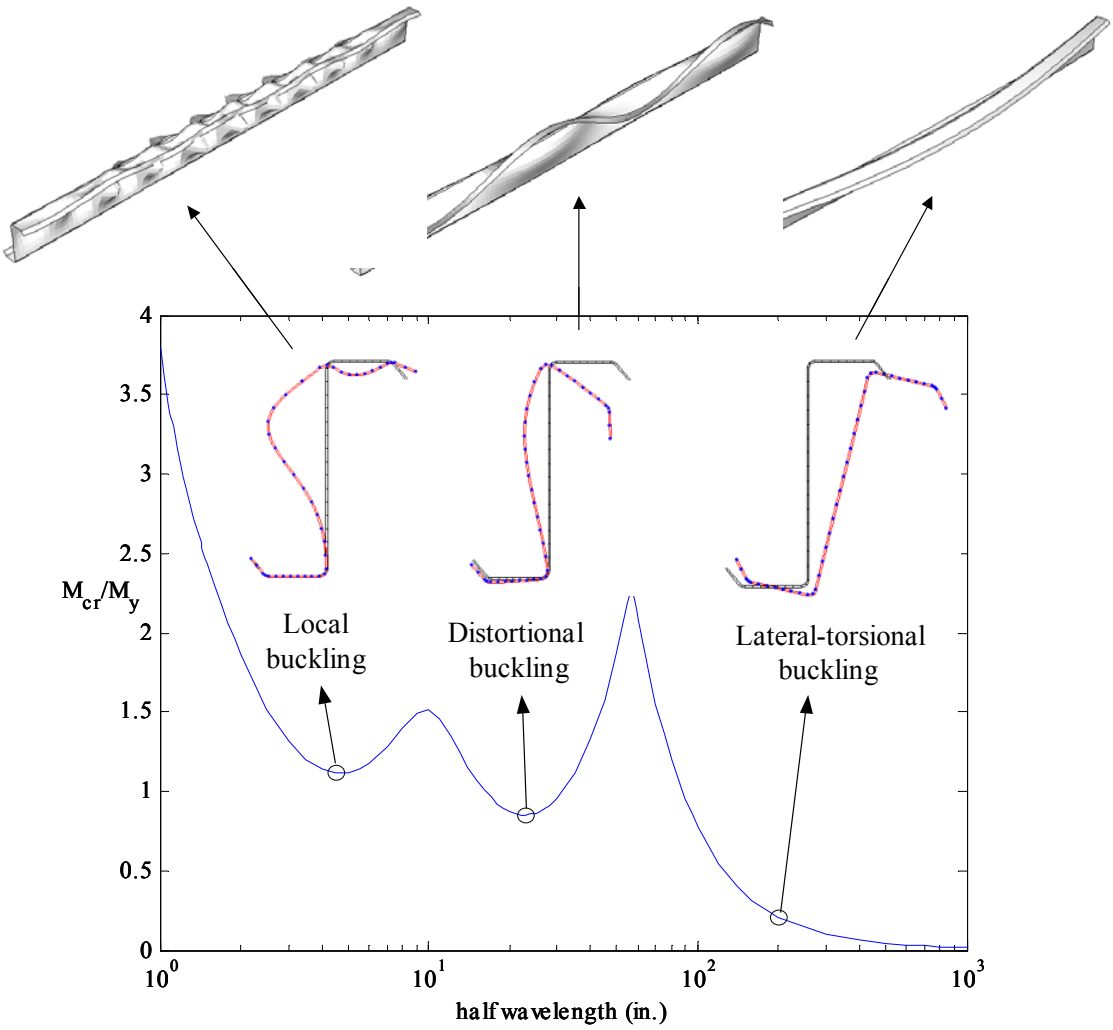

Figure 1.7 Buckling modes of a cold-formed steel Z-section in bending

Three different buckling modes are identified in the finite strip results. The first minimum, at a half-wavelength of 5 in., is the local buckling mode. In general, local buckling is particularly prevalent and is characterized by the relatively short and repeated wavelength buckling of individual plate elements (web, compression flange and lip stiffener) with no relative movement of the nodes at corners (e.g., web-flange, flange-stiffener). The distortional buckling mode occurs at the second minimum point of the half-wavelength curve (at approximately 20 in.). In the distortional mode, the section distorts and the compression flange-lip component rotates about the web-flange junction.

This phenomenon is commonly caused by buckling of the compression flange-lip component, but can also be driven by buckling of the web. Lateral-torsional buckling occurs at relatively long wavelengths. In the lateral-torsional mode, the section translates and rotates as a rigid-body without any change in the cross-sectional shape.

For the analyzed Z-section, lateral-torsional buckling will be the first (lowest) elastic buckling mode if the section is longer than approximately 100 in.. When the length is less than 10 in., local buckling becomes the lowest mode. For other cases, distortional buckling controls (final determination of the controlling mode requires examination of the post-buckling strength, but the elastic results do provide a helpful first indicator).

Distortional buckling most often occurs in sections where lateral deformations (i.e. lateral-torsional buckling) are prevented by intermittent bracing (Ellifritt et al. 1998). When the compression flange is not restrained by attachment to sheathing or paneling, such as in negative bending of continuous members (joist, purlins, etc.), members are prone to distortional failures. However, current design specifications (AISI 1996, CSA S136 1994, NAS 2001) do not have sufficient procedures for design against distortional buckling. The AISI Specification attempts to account for distortional buckling through an empirical reduction of the plate buckling coefficient (k) when calculating the effective width of the compression element (Schafer and Peköz 1998a). However, the experimental work (Desmond et al. 1981) carried out for determining the empirical k expressions concentrated on flange local bucking, as the test setup strongly restricted the bucking in web and partially restricted distortional buckling. The empirical k values do not agree with the actual elastic distortional buckling stress, and this oversight has been highlighted by experiments conducted by Willis and Wallace (1990), Schuster (1992), Moreyra

(1993), Ellifritt (1997), and Rogers and Schuster (1997). In those tests, cold-formed steel flexural members with edge stiffened flanges (C and Z-sections) and with lateral bracing were investigated. The results demonstrated unconservative strength predictions for currently used Specification methods.

Further, existing design procedures for the effective width (strength) of webs (AISI 1996, CSA S136 1994) were found to be theoretically inconsistent, discontinuous, and ignored the influence of the flange. Modifications adopted in the new North American Specification partially remove the web/flange interaction issue, but introduce a strength discontinuity at web width to flange width ratios (h/b) of 4 (Schafer and Trestain 2002).

Existing tests on C- and Z-sections (see summaries by Elhouar and Murray 1985, Schafer and Peköz 1999) generally focus on the performance of the compression flange and do not provide definitive evaluations of the design expressions for the web, due to: incomplete restriction of the distortional mode, arrangement of the specimens (back-to-back vs. toe-to-toe), and a general lack of information on bracing details. In many cases, existing data is not representative of sections currently used in practice. Therefore, new experiments are needed to develop and evaluate the design specifications as well as to examine the Direct Strength Method specifically for distortional buckling of CFS beams.

The first step of this study is to explore the post-buckling behavior and ultimate strength of cold-formed steel beams in local and distortional buckling failures. Two series of flexural tests on industry standard cold-formed steel sections were tested. Specific attention was paid to the restriction of the compression flange, in order to perform flexural experiments in local and distortional buckling mode, respectively. The first series of tests focused on the local buckling failure mode, also called “local buckling tests” or

"Phase 1 tests," in which the bracing was carefully considered to insure that distortional buckling and lateral-torsional buckling were restricted, but local buckling free to form. The second series, called "distortional buckling tests" or "Phase 2 tests," used nominally identical specimens as the local buckling tests, but allowed distortional buckling to occur while restricting lateral-torsional buckling. The two series of tests provide reliable upper and lower bounds for the bending capacity of laterally braced C and Z beams and the results can be used to examine the NAS 2001 Specification and the Direct Strength Method.

Finite element (FE) modeling was completed following the experimental investigations. The experimental data provide a calibration opportunity for the FE modeling and its many assumptions. The FE models also provide a supplementary tool to verify the design methods as well as to explore the buckling mechanism of CFS members with various configurations. In this research, the established FE modeling was verified by the two series of tests, and then was applied to study (1) the distortional buckling behavior and ultimate strength of a large number of Z or C-sections which are not examined directly by the tests, (2) the moment gradient influence on the elastic buckling and post-buckling behaviors of CFS beams in distortional buckling, and (3) the influence of partial flange restraints on the elastic buckling and post-buckling behavior of CFS beams in distortional buckling.

The moment gradient effect on the distortional buckling of CFS sections is of interest, in part because this topic has not been studied in detail. Further, since the wavelength of distortional buckling is relatively long compared to local buckling, the moment gradient may have significant influence on the distortional buckling capacity. When moment

gradient is applied to CFS sections, the compression flange (stiffened element or unstiffened element) of the section is under a longitudinal stress gradient. Therefore, the second step of the research includes a comprehensive study on the buckling and post-buckling behavior of thin plates under longitudinal stress gradients. Both stiffened elements and unstiffened elements are examined by analytical methods, as well as the finite element method.

The ultimate purpose of this study is to gain a better understanding of the distortional buckling behavior of CFS beams by means of both experiments and computational simulations, and then to include these findings into improved design procedures. Efforts are made to develop design provisions to account for moment gradient and partial restraint effects on the distortional buckling strength. Simplified hand solutions are also proposed for design purposes.

1.4 Outline of Thesis

This dissertation consists of a total of ten chapters and two appendices.

Chapter 1 presents the background, motivations, and objectives of this study. Brief summaries of current design specifications, the Effective Width Concept, and the Direct Strength Method are given.

Chapters 2, 3 and 4 contain the results of the first step of the research: experimental investigation of cold-formed steel beams. Chapter 1 and 2 detail the testing procedures and test results for the local buckling tests and the distortional buckling tests respectively.

Several existing design methods are used to analyze the experimental results. Chapter 4 includes the tensile test details and results.

Chapters 5, 6, 7, and 8 summarize the research efforts in the second step: finite element modeling and its applications including stress gradient effect on thin plates. Chapter 5 demonstrates the linear and nonlinear finite element modeling by ABAQUS (2001). Geometric imperfections and material nonlinearity are carefully considered in the FE modeling and discussed here. Chapter 5 also includes an extended FE analysis on CFS beams in bending, providing a wider coverage of beams. Chapter 6 details the studies on the stress gradient effect on the buckling of isolated thin plates. A numerical method is proposed to determine the elastic buckling stress of both stiffened elements and unstiffened elements under longitudinal stress gradients. Finite element analysis is utilized to explore the stress gradient influence on the post-buckling behavior. Chapter 7 presents research on the moment gradient effect on the distortional buckling of CFS beams. The partial restraint effect on distortional buckling is summarized in Chapter 8.

As a summary of the third step of research, Chapter 9 presents the proposed design provisions for determining the distortional buckling strengths of CFS beams. These include simplified hand solutions to calculate the elastic buckling moments.

Chapter 10 provides a summary of this study and presents recommendations for future research on the buckling behavior and design of cold-formed steel structures.

The data for the two series of conducted tests is included in detail in Appendix A.

A draft design ballot for distortional buckling of CFS beams is presented in Appendix B.

Chapter 2

Local Buckling Tests on Cold-Formed Steel Beams

2.1 Introduction

In the process of developing the new North American Specification for the Design of Cold-Formed Steel Structural Members (NAS 2001) and harmonizing the existing AISI (1996) and Canadian CSA S136 (1994) methods, one of the significant differences observed between the specifications was the calculation of the web effective width. The CSA S136 method systematically employed more conservative expression for the web effective width. Evaluation of existing data lead to the conclusion that web/flange interaction (driven by h/b) was of primary importance (Schafer and Trestain 2002). Interim rules were adopted for NAS (2001) which use AISI (1996) when $h/b \leq 4$ and CSA S136 (1994) when $h/b > 4$ (h is the out-to-out web height and b is the out-to-out flange width). However, at that time it was felt that the issue was not fully resolved, as existing data did not distinguish between local and distortional buckling failures and was

not considered to be generally representative of industry practice. Therefore, new testing and evaluation was initiated. A project was funded by the American Iron and Steel Institute (AISI) and Metal Building Manufacturers Association (MBMA) entitled "Test Verification of the Effect of Stress Gradient on Webs of Cee and Zee Sections." The project evolved in response to the inconclusive nature of existing test data on C and Z-sections in bending, and the need for a set of simple repeatable tests on industry standard sections that account for typical details in current practice and provide the actual bending capacity in local buckling.

2.2 Local Buckling Tests

2.2.1 Specimen Selection

A survey of industry standard members and tested member are summarized in Table 2.1.

Table 2.1 Range of geometry for industry members and available experimental data

		h/t		b/t		d/t		h/b		d/b	
		min	max	min	max	min	max	min	max	min	max
Available industry members	MBMA Z-sections	53	170	17	47	5	17	3.1	3.7	0.28	0.45
	SSMA members	25	318	11	132	1	33	1.0	10.9	0.12	0.33
	Rack members	23	136	16	45	6	15	1.0	3.2	0.27	0.38
Available experimental data	Elhouar & Murray (1985)	68	165	24	52	3	24	2.6	3.8	0.09	0.49
	Schafer & Peköz (1999)	43	270	15	75	3	34	1.5	13.7	0.14	0.70

Note: h – web height; b – flange width; t – thickness.

Available industry members

- CECO, Varco Pruden, and Butler each provided detailed cross-section information on their MBMA Z-sections for depths between 6.5 and 11.5 in. deep.

However, data provided by Light Gage Structural Institute (LGSI) for an earlier study indicates that in some cases Z-sections with h/b as high as 5.9 are used in current practice. Further, other common Z-sections (e.g. 10 in. × 2.5 in.) have h/b in excess of the collected MBMA Z members. While these sections do not appear to be in common use for the pre-engineered metal building industry, it is conceivable that Z-sections with high h/b ratios are used within the cold-formed steel industry.

- The geometric summaries attributed to the SSMA were compiled based on the geometry of C members submitted by Dietrich and Clark. Examination of the current SSMA profiles indicates a wide range of available products. Note, in particular the wide range of h/b ratios employed.
- The geometric summaries attributed to the Rack members were provided by Unarco. The rack members include C shapes with nearly square aspect ratio (h/b = 1.0) up to those that have aspect ratios common with the MBMA Z members, h/b ~ 3.

Available experimental data

- A compilation of industry tests on purlins was reported by Elhouar and Murray (1985). This database of tests covers member geometries consistent with those used as purlins for pre-engineered metal buildings. However, this database does not cover Z members reported by LGSI, nor does it cover the wider class of members reported in other industries.
- A large compilation of experimental data on C-sections in flexure was examined in Schafer and Peköz (1999). From this compilation the tests of: Cohen (1987),

LaBoube and Yu (1978), Moreyra (1993), Rogers (1995), Schardt and Schrade (1982), Schuster (1992), Shan et al. (1994), and Willis and Wallace (1990) are included. This database of members covers a broad range of geometric ratios, but does not include members with h/b near 1.0.

The AISI (1996) Specification calculates the effective width of a web as a function of the web slenderness (h/t) alone. The proposed tests are designed to provide systematic variation in h/t while also varying the other non-dimensional parameters: web height vs. flange width ratio, h/b, flange width vs. thickness ratio, b/t, edge stiffener length vs. thickness ratio, d/t. This is enough to determine the adequacy of existing and proposed design rules. The focus of the testing is on the web, therefore significant variation in stiffener length vs. flange width ratio, d/b, is not investigated.

Table 2.2 Summary of geometry of specimens for local buckling tests

Performed Tests	No	h/t		b/t		d/t		h/b		d/b	
		min	max	min	max	min	max	min	max	min	max
Group 1 Z: h, b, d fixed, t varied	10	71.3	144.1	21.8	42.5	8.1	13.2	3.1	3.5	0.31	0.38
Group 2 Z: h, b, d fixed, t varied	3	109.8	163.3	32.2	50.6	9.3	13.6	3.2	3.4	0.25	0.29
Group 3 C: h, b, d fixed, t varied	6	82.0	170.5	21.3	42.9	5.9	11.5	3.8	4.0	0.25	0.29
Group 4 C: b, d fixed, h, t varied	6	65.8	184.3	27.3	42.9	7.8	11.5	1.8	6.3	0.25	0.31
Total	25	65.8	184.3	21.3	50.6	5.9	13.6	1.8	6.7	0.25	0.38

Note: h – web height; b – flange width; t – thickness.

The primary consideration in investigating the web slenderness (h/t) is whether to achieve this variation by varying t, while holding h, b, d approximately constant or varying h while holding b, d and t approximately constant. Use of industry standard sections dictates that studies on the Z-sections vary t, while holding h, b, and d approximately constant. However, the wide variety of C specimens commonly produced by Steel Stud Manufacturers Association (SSMA – C studs, Table 2.1) allows both

methods of variation to be examined for C-sections. Table 2.2 presents the summary of the geometry of tested specimens, and typical sections are shown in Figure 2.1.

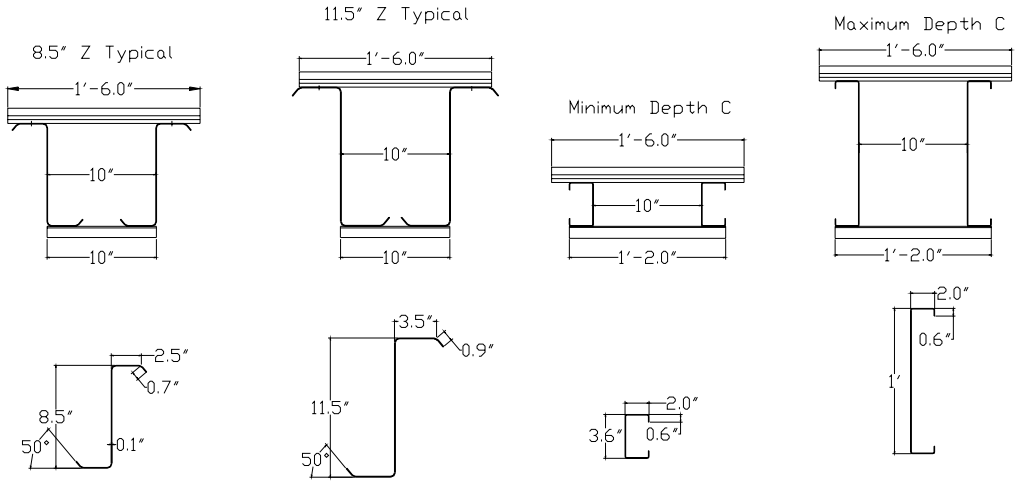

Figure 2.1 Range of tested specimens

2.2.2 Specimen Dimensions

The dimensions of the selected specimens were recorded at mid-length of the specimen and mid-distance between the center and loading points for a total of three measurement locations for each specimen. The mean specimen dimensions, as determined from the three sets of measurements within the constant moment region are given in Table 2.3. The notations used for the dimensions (shown in Figure 2.2) and metal properties are defined as follows:

- h out-to-out web depth
- b_c out-to-out compression flange width
- d_c out-to-out compression flange lip stiffener length
- θ_c compression flange stiffener angle from horizontal
- b_t out-to-out tension flange width
- d_t out-to-out compression flange lip stiffener length
- θ_t tension flange stiffener angle from horizontal
- r_{hc} outer radius between web and compression flange

r_{dc} outer radius between compression flange and lip

r_{ht} outer radius between web and tension flange

r_{dt} outer radius between tension flange and lip

t base metal thickness

f_y yield stress

E modulus of elasticity

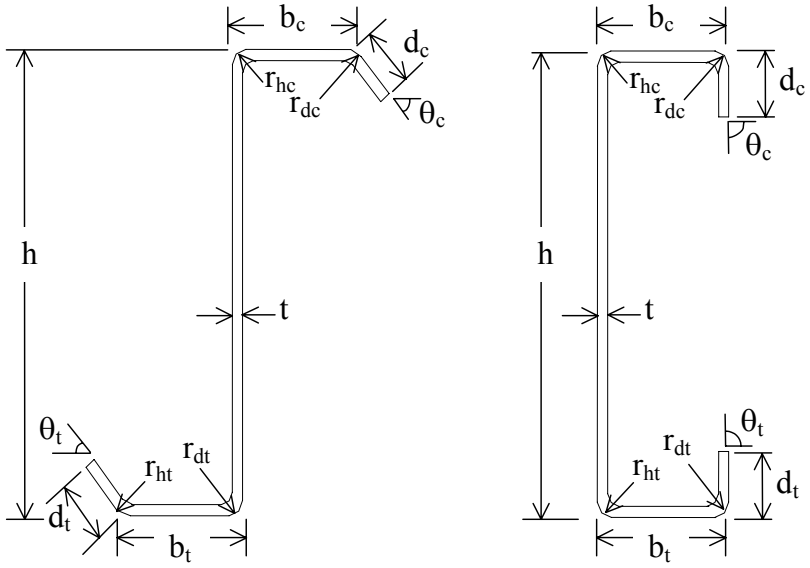

Figure 2.2 Definitions of specimen dimensions for C and Z-section

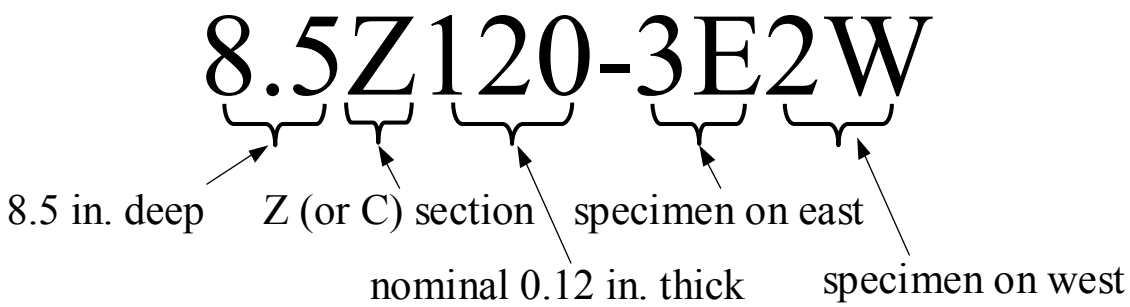

Figure 2.3 Label definition for local buckling tests

Figure 2.3 illustrates the definition of a typical local buckling test label. The test of 8.5Z120-3E2W means the two paired specimens (8.5Z120-3 and 8.5Z120-2) are Z-sections with 8.5 in. deep webs and the nominal thickness is 0.12 in., specimen 8.5Z120-3 is placed at the east side and specimen 8.5Z120-2 is at the west side.

Table 2.3 Measured geometry of specimens for local buckling tests

Group No	Test label	Specimen	h (in.)	b_c (in.)	d_c (in.)	θ_c (deg)	b_t (in.)	d_t (in.)	θ_t (deg)	r_{hc} (in.)	r_{dc} (in.)	r_{ht} (in.)	r_{dt} (in.)	t (in.)	f_y (ksi)
1	8.5Z120-3E2W	8.5Z120-3	8.44	2.58	0.96	47.2	2.46	0.99	48.9	0.36	0.36	0.35	0.35	0.1183	61.3
		8.5Z120-2	8.47	2.59	0.96	47.8	2.46	1.00	48.9	0.36	0.36	0.34	0.34	0.1180	60.1
	8.5Z105-2E1W	8.5Z105-2	8.48	2.66	0.95	50.5	2.36	0.95	48.7	0.32	0.32	0.34	0.34	0.1040	68.8
		8.5Z105-1	8.42	2.69	0.97	50.7	2.36	0.91	48.7	0.31	0.31	0.34	0.34	0.1050	66.8
	8.5Z092-4E2W	8.5Z092-4	8.41	2.61	0.93	53.0	2.41	0.96	50.8	0.29	0.29	0.31	0.31	0.0900	57.3
		8.5Z092-2	8.43	2.61	0.92	51.8	2.40	0.95	50.4	0.28	0.28	0.31	0.31	0.0887	57.0
	8.5Z082-1E2W	8.5Z082-1	8.46	2.50	0.95	49.0	2.36	0.97	50.3	0.28	0.28	0.30	0.30	0.0801	58.4
		8.5Z082-2	8.45	2.51	0.95	47.9	2.40	0.95	52.4	0.28	0.28	0.30	0.30	0.0804	58.1
	8.5Z073-6E5W	8.5Z073-6	8.50	2.52	0.92	49.6	2.40	0.94	50.9	0.28	0.28	0.30	0.30	0.0720	54.0
		8.5Z073-5	8.50	2.52	0.92	49.6	2.40	0.94	50.9	0.28	0.28	0.30	0.30	0.0727	55.6
	8.5Z073-4E3W	8.5Z073-4	8.51	2.53	0.93	49.6	2.41	0.92	50.3	0.28	0.28	0.29	0.29	0.0715	56.1
		8.5Z073-3	8.50	2.53	0.91	50.1	2.38	0.96	51.0	0.28	0.28	0.30	0.30	0.0720	55.6
	8.5Z073-1E2W	8.5Z073-2	8.50	2.54	0.93	50.2	2.41	0.92	51.0	0.28	0.28	0.30	0.30	0.0715	55.7
		8.5Z073-1	8.49	2.50	0.92	48.4	2.41	0.95	51.2	0.28	0.28	0.30	0.30	0.0720	54.8
	8.5Z065-3E1W	8.5Z065-3	8.47	2.42	0.83	47.3	2.43	0.79	47.3	0.27	0.27	0.28	0.28	0.0640	53.5
		8.5Z065-1	8.47	2.44	0.76	47.4	2.43	0.84	47.1	0.28	0.28	0.27	0.27	0.0640	53.1
	8.5Z059-4E3W	8.5Z059-4	8.50	2.50	0.77	50.9	2.35	0.72	48.9	0.28	0.28	0.28	0.28	0.0590	58.6
		8.5Z059-3	8.50	2.44	0.78	50.2	2.22	0.69	50.4	0.28	0.28	0.28	0.28	0.0595	58.5
	8.5Z059-2E1W	8.5Z059-2	8.49	2.51	0.78	50.6	2.33	0.70	50.2	0.28	0.28	0.28	0.28	0.0590	59.1
		8.5Z059-1	8.50	2.51	0.78	51.2	2.33	0.71	49.4	0.28	0.28	0.28	0.28	0.0590	58.9
2	8C097-2E3W	8C097-2	8.04	2.12	0.57	85.6	2.08	0.52	85.7	0.30	0.28	0.28	0.30	0.0980	59.9
		8C097-3	8.03	2.09	0.56	84.0	2.08	0.54	88.2	0.30	0.28	0.28	0.29	0.0940	59.6
	8C068-4E5W	8C068-5	8.03	2.03	0.52	83.2	2.04	0.53	87.0	0.28	0.25	0.24	0.24	0.0750	48.6
		8C068-4	8.01	2.05	0.52	84.0	2.04	0.54	87.6	0.27	0.26	0.24	0.27	0.0770	53.1
	8C068-1E2W	8C068-2	8.02	2.04	0.52	83.4	2.04	0.53	87.6	0.28	0.25	0.24	0.26	0.0758	51.7
		8C068-1	8.03	2.03	0.53	83.1	2.05	0.53	88.1	0.30	0.26	0.25	0.26	0.0754	51.4
	8C054-1E8W	8C054-1	8.00	2.04	0.52	88.9	2.07	0.50	84.7	0.22	0.23	0.23	0.23	0.0550	40.0
		8C054-8	8.08	2.02	0.58	88.1	1.96	0.48	82.3	0.22	0.20	0.22	0.23	0.0540	40.3
	8C043-5E6W	8C043-5	8.04	2.02	0.53	88.8	1.98	0.53	87.3	0.18	0.20	0.21	0.20	0.0496	44.9
		8C043-6	8.06	2.01	0.53	88.9	2.00	0.46	87.0	0.19	0.20	0.22	0.20	0.0490	45.0
	8C043-3E1W	8C043-3	8.04	2.02	0.54	89.3	2.01	0.53	87.5	0.19	0.19	0.19	0.19	0.0474	46.0
		8C043-1	8.03	2.02	0.54	89.0	1.98	0.54	85.8	0.19	0.19	0.29	0.19	0.0476	45.7
3	12C068-9E5W	12C068-9	12.02	1.92	0.53	82.0	2.00	0.55	85.3	0.28	0.27	0.30	0.28	0.0652	35.1
		12C068-5	12.00	1.79	0.55	85.9	2.06	0.53	94.8	0.27	0.27	0.22	0.27	0.0654	35.0
	12C068-3E4W	12C068-3	11.97	1.96	0.59	82.5	1.99	0.56	77.4	0.26	0.27	0.27	0.27	0.0671	56.6
		12C068-4	12.02	2.01	0.52	80.6	2.00	0.52	83.3	0.26	0.27	0.26	0.27	0.0670	57.3
	10C068-2E1W	10C068-2	10.08	1.93	0.50	83.2	1.98	0.52	83.3	0.27	0.25	0.27	0.25	0.0572	33.6
		10C068-1	10.03	2.04	0.55	80.7	1.97	0.54	81.9	0.27	0.26	0.28	0.25	0.0573	34.2
	6C054-2E1W	6C054-2	6.04	2.00	0.56	85.7	2.00	0.52	90.0	0.21	0.24	0.26	0.25	0.0616	36.1
		6C054-1	6.03	2.01	0.56	86.5	2.05	0.52	90.5	0.22	0.25	0.25	0.24	0.0616	37.0
	4C054-1E2W	4C054-1	3.95	1.99	0.55	79.2	2.02	0.55	77.4	0.24	0.24	0.23	0.24	0.0551	45.0
		4C054-2	3.96	1.95	0.50	74.2	1.96	0.55	74.8	0.22	0.27	0.25	0.25	0.0561	44.7
	3.62C054-1E2W	3.62C054-1	3.65	1.97	0.49	77.1	2.00	0.42	88.1	0.23	0.26	0.26	0.25	0.0555	32.8
		3.62C054-2	3.67	1.99	0.51	79.8	1.97	0.44	79.8	0.24	0.25	0.26	0.26	0.0554	32.0
4	11.5Z092-1E2W	11.5Z092-1	11.41	3.33	0.96	50.1	3.51	0.96	49.5	0.25	0.27	0.27	0.27	0.1027	61.0
		11.5Z092-2	11.34	3.33	0.98	48.3	3.54	0.89	48.1	0.28	0.27	0.28	0.28	0.1033	60.4
	11.5Z082-2E1W	11.5Z082-2	11.45	3.50	0.88	50.3	3.45	0.87	52.2	0.31	0.31	0.35	0.35	0.0837	61.5
		11.5Z082-1	11.47	3.49	0.90	50.6	3.43	0.88	51.0	0.32	0.32	0.35	0.35	0.0839	60.4
	11.5Z073-2E1W	11.5Z073-2	11.39	3.51	0.87	46.0	3.35	0.83	44.8	0.27	0.28	0.27	0.28	0.0709	65.4
		11.5Z073-1	11.35	3.52	0.95	45.4	3.40	0.90	44.2	0.27	0.11	0.27	0.07	0.0695	66.8

2.2.3 Testing Details

A series of four-point bending tests is proposed for the local buckling tests. As shown in Figure 2.4 and Figure 2.5, the 16 ft. span length, four-point bending test, consists of a pair of 18 ft. long C or Z-sections in parallel, loaded at the 1/3 points. The members are oriented in an opposed fashion; such that in-plane rotation of the C or Z-sections leads to tension in the panel, and thus provides additional restriction against distortional buckling of the compression flange.

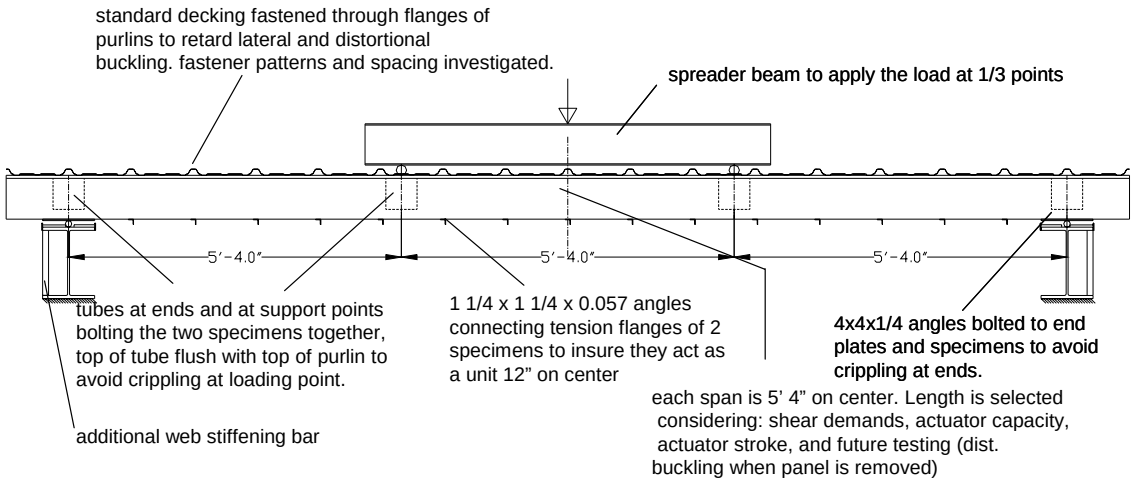

Figure 2.4 Elevation view of overall test arrangement for four point bending test

Small angles (1¼ × 1¼ × 0.057 in.), shown in Figure 2.7, are attached (screwed) to the tension flanges every 12 in., and a through-fastened standard steel decking (t = 0.019 in., 1.25 in. high ribs), shown in Figure 2.6, is attached (also screwed) to the compression flanges. Hot-rolled tube sections (10 × 7½ × 6 × ¼ in.), shown in Figure 2.7, bolt the pair of C or Z-sections together at the load points and the supports, and insure shear and web crippling problems are avoided at these locations. When testing the C-sections, the hot-

rolled angles detailed in Figure 2.8 connect to the tube and the end plate on the inside of the tube, instead of the outside of the tube, as detailed for the Z-sections.

Figure 2.5 Overall view of testing setup

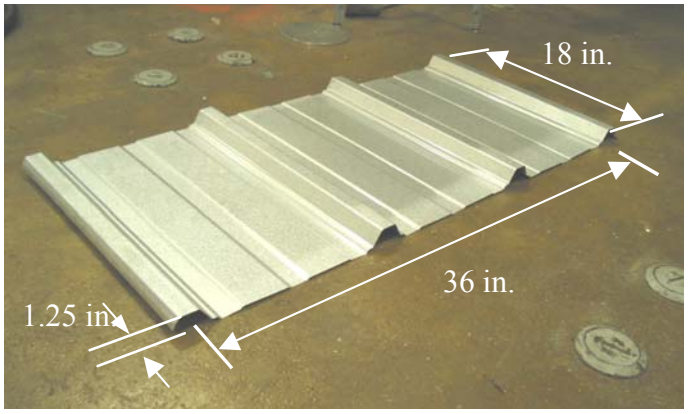

Figure 2.6 Standard steel panel

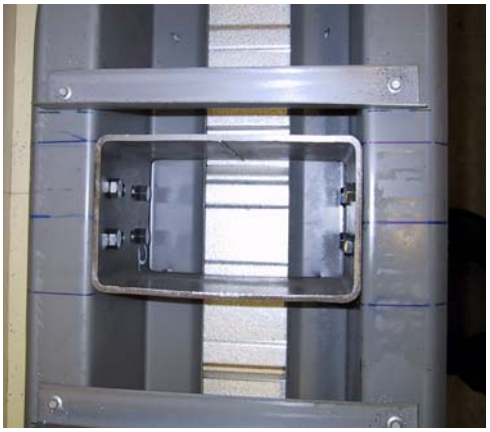

Figure 2.7 Hot-rolled tube section and angle screwed to tension flange (view from bottom)

(a) Z-sections (b) C-sections

Figure 2.8 End configurations for C and Z-sections

After initial testing the details were improved to insure pure bending was maintained, and to restrict distortional and lateral-torsional buckling. Major improvements were made on the panel-to-section fastener configuration (see detail in Section 2.2.4). The arrangement of rollers at the supports was modified to more closely model a pin-roller configuration (Figure 2.9). Additional web stiffening bars were added to the I-beams at the supports (Figure 2.8b) and load points. Machined, quarter-round aluminum blocks were placed as guides for the rollers at the loading points (Figure 2.9). Thin Teflon sheets

were added at the load points and support points to limit unwanted friction and help insure the boundary conditions were predictable (Figure 2.9 and Figure 2.10).

Figure 2.9 Support configuration

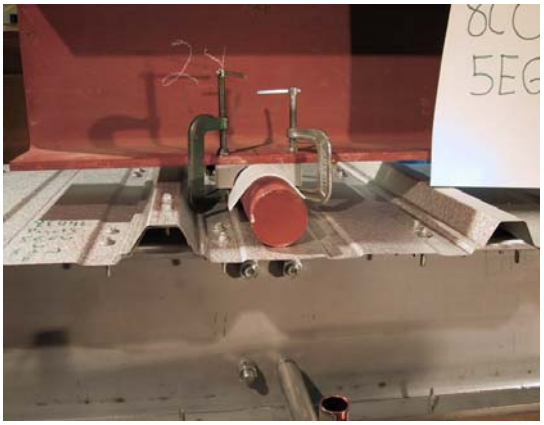

Figure 2.10 Loading point configuration

The loading system employs a 20 kip MTS actuator (Figure 2.11), which has a maximum 6 in. stroke. The test is performed in displacement control at a rate of 0.0015 in./sec. A MTS 407 controller and load cell (Figure 2.12) monitors the force and insures the desired displacement control is met. Meanwhile, deflections for one specimen at the 1/3 points were measured using two LVDTs. Later for the local buckling tests of 10 in. C-sections and 11.5 in. Z-sections, and all distortional buckling tests; the 2 LVDTs were replaced by 4 position transducers (Figure 2.13). For a limited number of tests, strain gages were placed at mid-span, on the lip and the top of the web, at the same vertical cross-section height, to monitor the longitudinal strain.

Figure 2.11 MTS actuator


Figure 2.12 Controlling system

(a) LVDTs

(b) Position transducers

Figure 2.13 Deflection measuring system

2.2.4 Panel-to-Section Fastener Configuration

Figure 2.14 shows a comparison of elastic buckling moments of Z-sections under bending moment. The figure indicates that elastic distortional buckling is lower than local buckling for all the Z-sections. Therefore, the panel-to-section fastener details need to be set carefully to restrict the distortional mode while allowing local bucking to occur and thus trigger the desired failure mode.

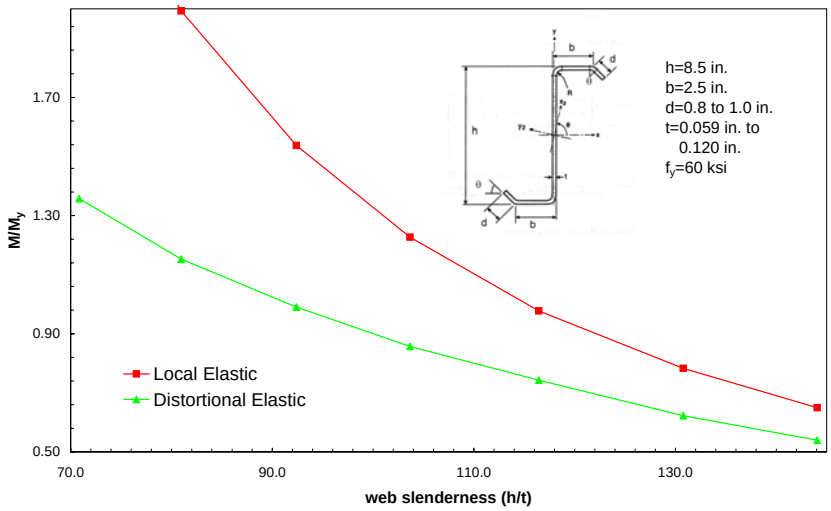

Figure 2.14 Comparison of elastic buckling moments of Z-sections

One way to restrict the distortional buckling mode is to limit the rotation of the compression flange. Figure 2.15 shows the result of a finite strip analysis (by CUFSM) of a Z-section. When a rotational spring (represented by a star in the figure) is added to the compression flange, the buckling curve moves from curve 1 to curve 2. The elastic distortional buckling moment is increased significantly, but local buckling does not change. In the tests, the standard panel screwed down to the compression flange is expected to work as a rotational spring to restrict the distortional buckling mode.

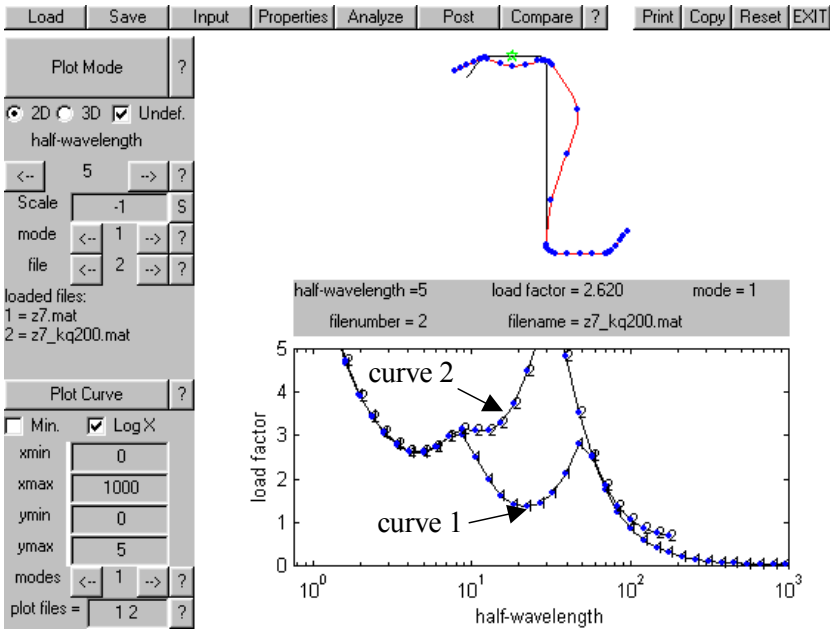

Figure 2.15 Finite strip analysis of a Z-section

In order to verify and determine the appropriate panel-to-section fastener detail for restricting the distortional mode, a series of tests on the 8.5 in. deep Z-sections with t = 0.073 in. and t = 0.059 in. was conducted. Investigated fastener (screw) locations are depicted in Figure 2.16. Initial testing using single panel-to-section fasteners placed through the center of the section flange and spaced at 12 in. o.c. (test 8.5Z073-6E5W, panel type A) failed at a capacity of 86% of the AISI (1996) prediction and visually

appeared to suffer from deformations consistent with distortional buckling. Elastic finite element analysis, shown in Figure 2.21, using the commercial finite element package ABAQUS (ABAQUS 2001) confirmed that the lowest elastic buckling mode for this fastener detail is distortional buckling (see Chapter 5 for more details on the ABAQUS modeling). Test of 8.5Z073-1E2W using fastener type B, one screw at each side of every panel rib, failed at 88% of the AISI (1996) prediction and with an observed distortional buckling mechanism. ABAQUS analysis (Figure 2.22) indicates that a pair of fasteners placed on either side of the raised ribs (panel type C) would force local buckling to be the lowest mode. Testing of 8.5Z073-4E3W confirmed this prediction, and paired fasteners as shown in Figure 2.19 provided a capacity 10% greater than single fasteners and 98% of the AISI (1996) prediction. Further, testing (8.5Z059-2E1W, Figure 2.20) with additional paired fasteners in the center of the pans (panel type D in Figure 2.16) did not improve the results over type C (compared with test 8.5Z059-4E3W). Additionally, the finite element modeling indicates that the paired fasteners do not change the local buckling mode; thus it can be safely assumed that panel type C restricts distortional buckling without artificially increasing the local buckling strength.

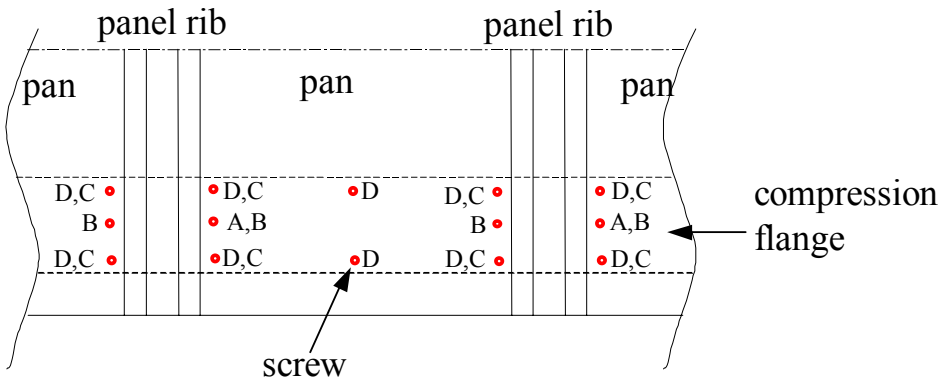

Figure 2.16 Plan view of screw locations for panel-to-section connection

Figure 2.17 Fastener configuration A for test 8.5Z073-6E5W

Figure 2.18 Fastener configuration B for test 8.5Z073-1E2W

Figure 2.19 Fastener configuration C for test 8.5Z073-4E3W

Figure 2.20 Fastener configuration D for test 8.5Z059-2E1W

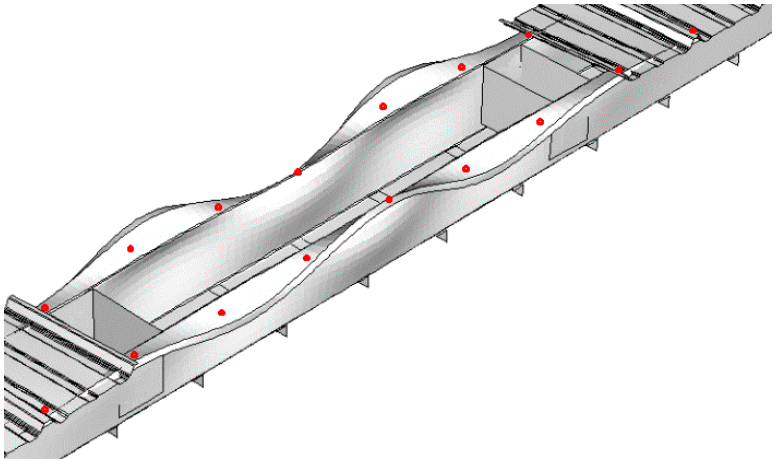

Figure 2.21 Lowest buckling mode predicted by FE model for single screw fastener configuration (note center panels removed for visual clarity only, the dots indicate fastener locations.)

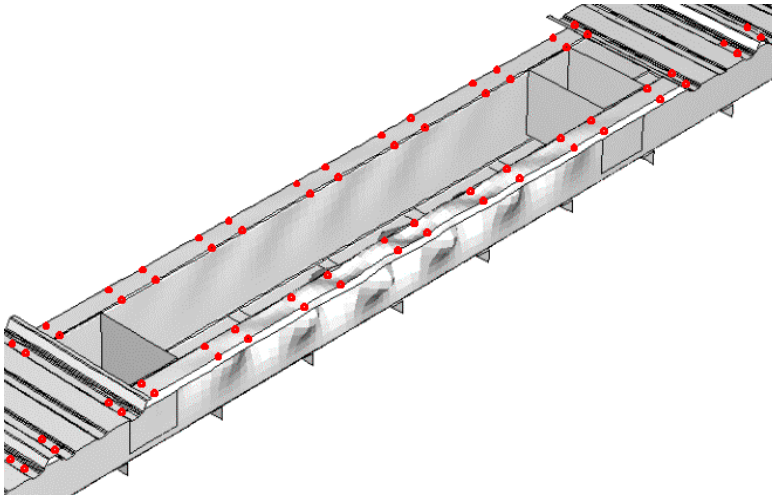

Figure 2.22 Lowest buckling mode predicted by FE model for paired screw fastener configuration (note center panels removed for visual clarity only, the dots indicate fastener locations.)

The selected standard panel-to-section fastener detail for the local buckling tests is fastener type C in Figure 2.16: a pair of screws placed 1.5 in. apart for C-sections, 2.5 in. apart for Z-sections, and spaced 8 in. away from a second pair in the pan of the deck, as shown in Figure 2.23 and Figure 2.24. The panels are connected to each other by four screws (two on each side). The paired fastener configuration is only maintained inside the constant moment region of the test. In the shear span, one screw is used instead of one pair, at the same location as that of the constant moment region.

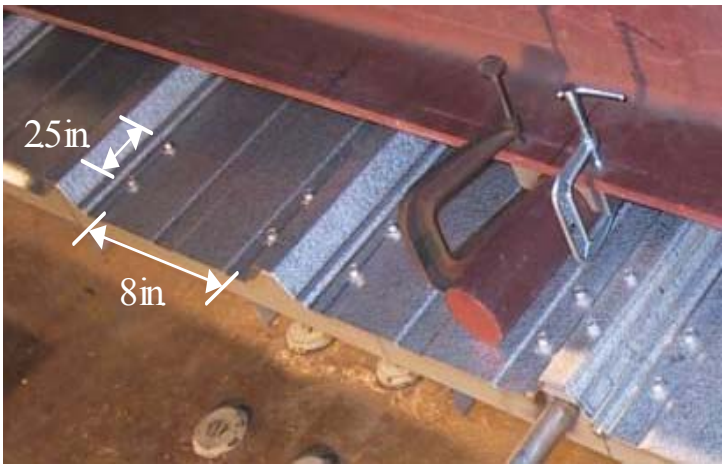

Figure 2.23 Selected standard panel-to-section and panel-to-panel fastener configuration (Z-section)

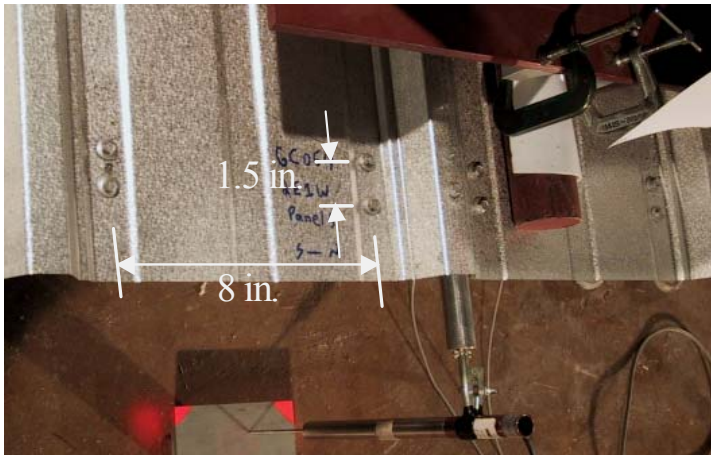

Figure 2.24 Selected standard panel-to-section and panel-to-panel fastener configuration (C-section)

2.3 Experimental Results

A summary of the local buckling test results is given in Table 2.4. Included for each test are the tested moments (M_{test}), yield moments (M_y), elastic buckling moments ($M_{cr\ell}$ for local buckling, M_{crd} for distortional buckling) as determined by the finite strip method using CUFSM (CUFSM 2001), and ratios of test-to-predicted capacities for different design methods including AISI 1996 (M_{AISI}), CSA S136 1994 (M_{S136}), NAS 2001 (M_{NAS}), AS/NZS 4600 (1996), EN1993 (2002) and DSM (Schafer and Peköz 1998a, DSM 2004) ($M_{DS\ell}$ for local buckling and M_{DSd} for distortional buckling). Further results are summarized in Appendix A.

2.3.1 Strains

Strain gages were placed at mid-span, on the lip and the top of the web, at the same vertical cross-section height, on 9 C-sections (denoted with a # in Table 2.4), to monitor the longitudinal strain. Typical output from the gages is given in Figure 2.25 and Figure 2.26. In the initial elastic range the gages read nearly identical and agree with simple beam theory predictions, indicating that the testing arrangement is achieving the desired loading about the geometric axis and no twisting is developing in the section. At an intermediate load level, before buckling deformations were visible, strain on either the lip or web began to reverse. In most, but not all tests, the strain on the lip began to reverse prior to the web. Once buckling initiates the strain distribution varies around the profile and along the length, and it becomes difficult to provide definitive conclusions from the limited strain data.

Table 2.4 Local buckling test results

Group No	Test label	Panel type†	Specimen	M_{test} (kip-in.)	M_y (kip-in.)	$M_{cr\ell}$ (kip-in.)	M_{crd} (kip-in.)	M_{test}/M_y	M_{test}/M_{AISI}	M_{test}/M_{S136}	M_{test}/M_{NAS}	$M_{test}/M_{AS/NZS}$	M_{test}/M_{EN1993}	$M_{test}/M_{DS\ell}$	M_{test}/M_{DSd}
1	8.5Z120-3E2W	C	8.5Z120-3	280	268	727	391	1.05	1.05	1.05	1.05	1.05	1.01	1.05	1.22
			8.5Z120-2 *	280	264	722	391	1.06	1.06	1.06	1.06	1.06	1.03	1.06	1.23
	8.5Z105-2E1W	C	8.5Z105-2	268	270	480	293	0.99	1.05	1.07	1.04	1.05	1.00	0.99	1.28
			8.5Z105-1 *	268	264	487	295	1.01	1.06	1.07	1.06	1.06	1.03	1.01	1.29
	8.5Z092-4E2W	C	8.5Z092-4	181	192	321	217	0.94	0.98	1.01	0.98	0.98	0.94	0.94	1.20
			8.5Z092-2 *	181	189	306	208	0.96	1.01	1.04	1.01	1.01	0.96	0.97	1.23
	8.5Z082-1E2W	C	8.5Z082-1 *	162	174	226	170	0.93	1.00	1.05	1.00	1.00	0.97	1.01	1.25
			8.5Z082-2	162	174	229	174	0.93	1.00	1.05	0.99	1.00	0.97	1.00	1.24
	8.5Z073-6E5W	A	8.5Z073-6 *	121	146	165	133	0.83	0.92	0.99	0.91	0.92	0.92	0.94	1.15
			8.5Z073-5	121	152	170	136	0.80	0.89	0.96	0.88	0.89	0.88	0.91	1.11
	8.5Z073-4E3W	C	8.5Z073-4	134	151	161	129	0.88	0.98	1.06	0.98	0.98	0.99	1.02	1.26
			8.5Z073-3 *	134	150	165	135	0.89	1.00	1.08	0.99	1.00	0.99	1.01	1.24
	8.5Z073-1E2W	B	8.5Z073-2 *	123	150	161	130	0.82	0.91	0.98	0.91	0.92	0.92	0.94	1.16
			8.5Z073-1	123	147	166	134	0.84	0.92	0.99	0.92	0.91	0.92	0.94	1.16
	8.5Z065-3E1W	C	8.5Z065-3	96	125	115	90	0.77	0.86	0.96	0.86	0.86	0.89	0.93	1.18
			8.5Z065-1 *	96	123	117	92	0.78	0.89	0.99	0.89	0.89	0.90	0.93	1.17
	8.5Z059-4E3W	C	8.5Z059-4 *	100	126	87	74	0.79	0.98	1.07	0.98	0.98	1.01	1.06	1.34
			8.5Z059-3	100	125	86	76	0.80	0.97	1.06	0.97	0.97	1.02	1.07	1.33
	8.5Z059-2E1W	D	8.5Z059-2	99	127	86	74	0.78	0.96	1.04	0.96	0.96	1.00	1.04	1.32
			8.5Z059-1 *	99	127	86	74	0.78	0.96	1.04	0.96	0.96	1.00	1.04	1.32
2	8C097-2E3W	C	8C097-2 #	172	166	334	241	1.04	1.07	1.08	1.07	1.07	0.97	1.04	1.21
			8C097-3 *	172	157	308	226	1.10	1.13	1.15	1.13	1.13	1.05	1.10	1.28
	8C068-4E5W	C	8C068-5 *	104	102	162	136	1.02	1.05	1.10	1.05	1.05	1.03	1.03	1.22
			8C068-4#	104	114	176	146	0.91	0.95	0.99	0.95	0.95	0.94	0.93	1.10
	8C068-1E2W	C	8C068-2 *	98	109	166	139	0.90	0.94	0.98	0.94	0.94	0.93	0.93	1.10
			8C068-1	98	108	165	137	0.91	0.94	0.98	0.94	0.94	0.94	0.94	1.11
	8C054-1E8W	C	8C054-1 *#	56	62	65	65	0.90	0.97	1.07	0.95	0.97	1.01	1.04	1.17
			8C054-8	56	63	59	61	0.89	0.93	1.02	0.93	0.93	0.99	1.07	1.20
	8C043-5E6W	C	8C043-5	51	64	47	51	0.80	0.95	1.04	0.95	0.95	0.96	1.05	1.17
			8C043-6 *	51	63	44	48	0.81	0.96	1.06	1.06	0.96	0.99	1.07	1.21
	8C043-3E1W	C	8C043-3	48	63	41	45	0.76	0.93	1.01	0.93	0.93	0.94	1.03	1.17
			8C043-1 *#	48	62	41	45	0.77	0.93	1.01	0.93	0.93	0.96	1.04	1.17
3	12C068-9E5W	C	12C068-9 *	104	113	88	115	0.92	0.95	1.08	1.08	0.95	1.13	1.18	1.32
			12C068-5 #	104	110	90	122	0.95	0.98	1.12	1.12	0.98	1.17	1.19	1.33
	12C068-3E4W	C	12C068-3	137	190	96	131	0.72	0.86	0.93	0.93	0.86	0.94	1.07	1.25
			12C068-4 *	137	192	94	121	0.71	0.90	0.97	0.95	0.90	0.93	1.07	1.28
	10C068-2E1W	C	10C068-2	70	73	65	121	0.96	0.98	1.11	1.11	0.98	1.13	1.18	1.28
			10C068-1 *	70	76	65	131	0.92	0.94	1.06	1.06	0.94	1.07	1.14	1.23
	6C054-2E1W	C	6C054-2 *#	45	42	101	87	1.06	1.09	1.09	1.09	1.09	0.96	1.06	1.16
			6C054-1	45	43	102	81	1.04	1.06	1.06	1.06	1.06	0.94	1.04	1.14
	4C054-1E2W	D	4C054-1	28	27	66	43	1.02	1.11	1.11	1.10	1.11	1.04	1.02	1.15
			4C054-2*#	28	27	73	45	1.03	1.13	1.13	1.11	1.13	1.03	1.03	1.15
	3.62C054-1E2W	D	3.62C054-1*#	20	17	64	38	1.16	1.20	1.20	1.20	1.20	1.10	1.16	1.24
			3.62C054-2	20	17	65	41	1.17	1.20	1.20	1.20	1.20	1.11	1.17	1.24
4	11.5Z092-1E2W!	C	11.5Z092-1	352	414	474	115	0.85	0.99	1.10	0.99	0.99	0.93	0.96	1.30
			11.5Z092-2*	352	409	477	122	0.86	1.00	1.10	1.00	1.00	0.94	0.96	1.34
	11.5Z082-2E1W	C	11.5Z082-2*	274	345	252	121	0.79	1.05	1.13	1.05	1.05	1.01	1.04	1.38
			11.5Z082-1	274	341	253	131	0.80	1.04	1.13	1.04	1.04	1.02	1.04	1.39
	11.5Z073-2E1W	C	11.5Z073-2*	194	311	150	115	0.62	0.96	1.01	0.96	0.96	0.92	0.94	1.31
			11.5Z073-1#	194	315	144	122	0.62	0.96	1.00	0.96	0.96	0.94	0.95	1.30

Note:!: Result is estimated due to peak load exceeding the recording range.

*: Controlling specimens

#: Strain gages were placed at mid-span, on the lip and the top of the web, at the same vertical cross-section height

†: Panel fastener type, see details in Figure 2.16.

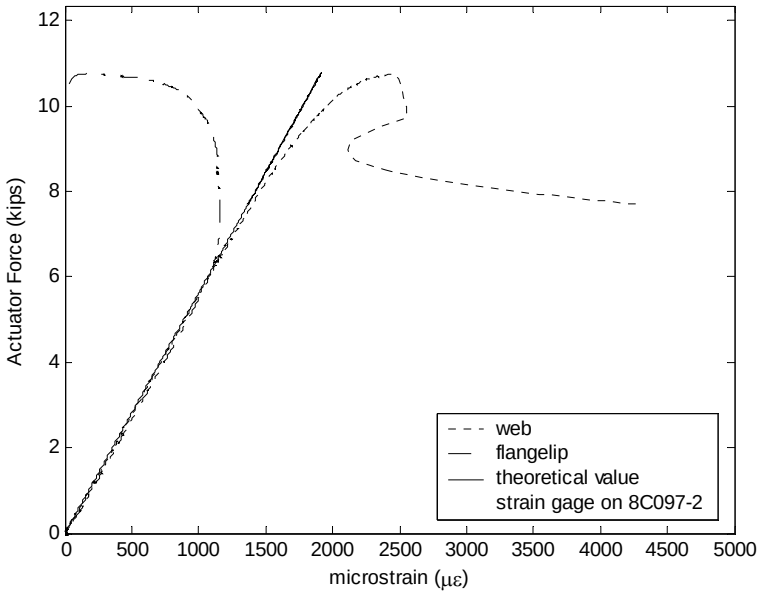

Figure 2.25 Strain gage output for test 8C097-2E3W, first failure occurred in this specimen near the strain gages

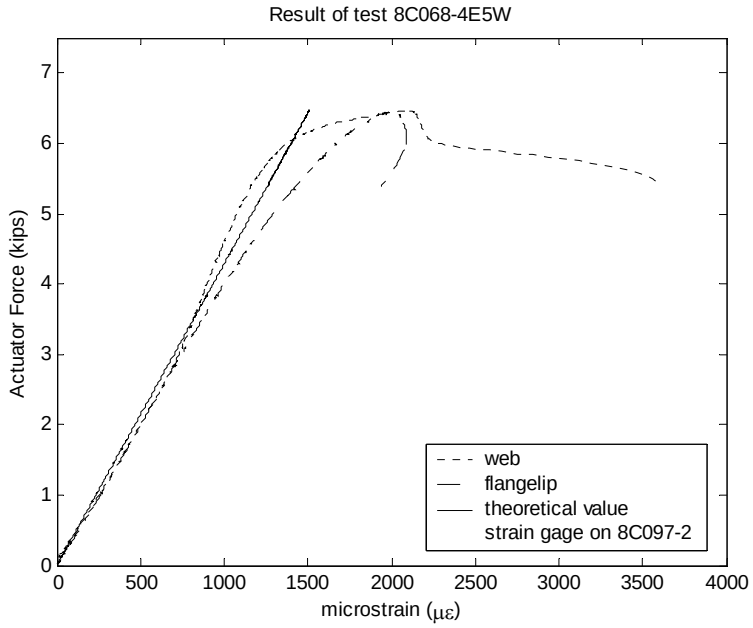

Figure 2.26 Strain gage output for test 8C068-4E5W, first failure occurred in the other beam of the pair

2.3.2 Load-to-Displacement

Actuator load-displacement response is given in Figure 2.27 through Figure 2.30. Little non-linear response is observed prior to formation of the failure mechanism. The specimens which have a tested capacity at or near the yield moment ($M_{test}/M_y \sim 1$, see Table 2.4) exhibit the most nonlinear deformation prior to failure; while the more slender specimens have essentially elastic response prior to formation of a sudden failure mechanism.

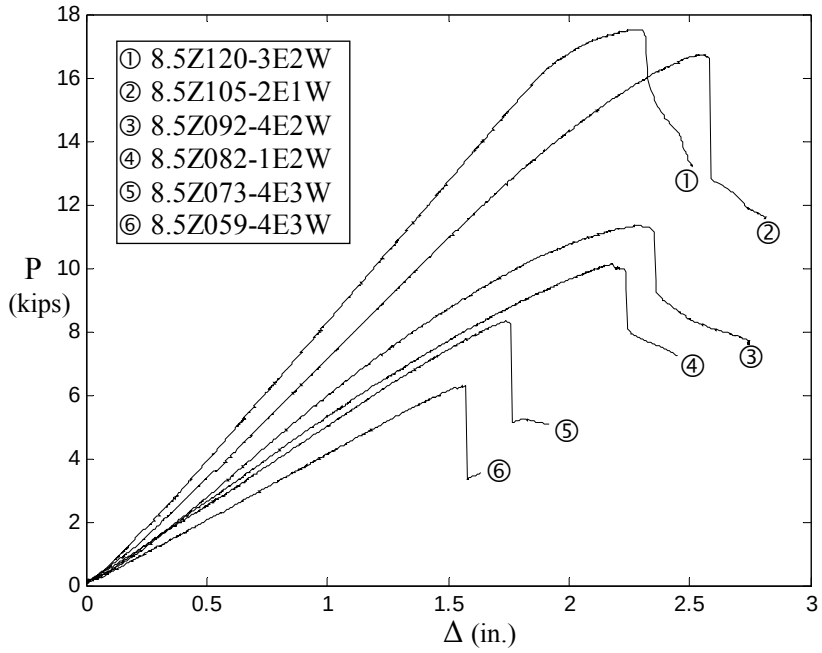

Figure 2.27 Actuator force-displacement response for tests of 8.5 in. nominal deep Z-sections

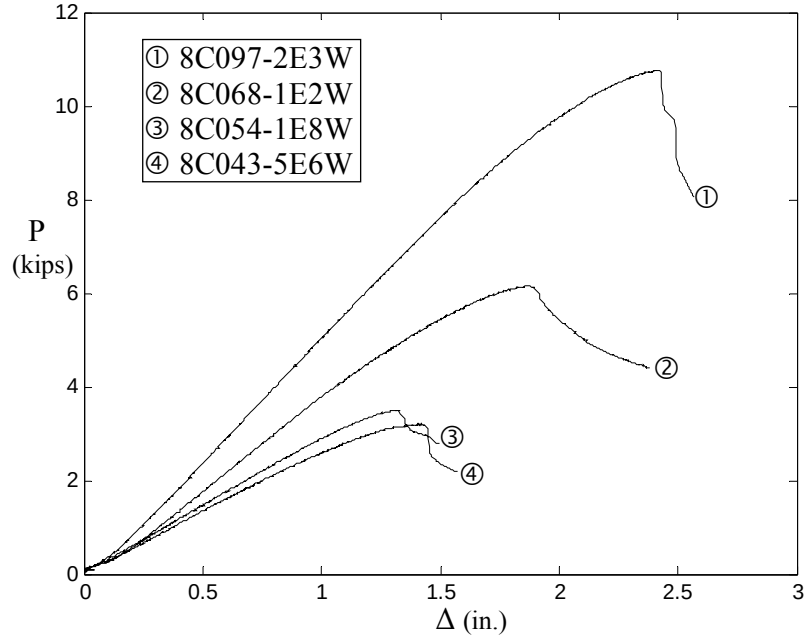

Figure 2.28 Actuator force-displacement response for tests of 8 in. nominal deep C-sections

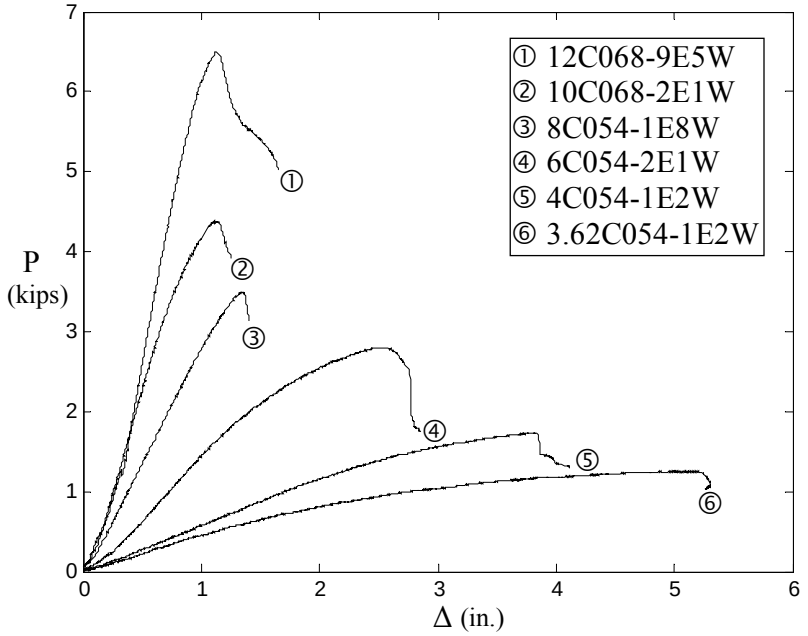

Figure 2.29 Actuator force-displacement response for tests of 92 to 3.62 to 12 in. nominal deep C-sections

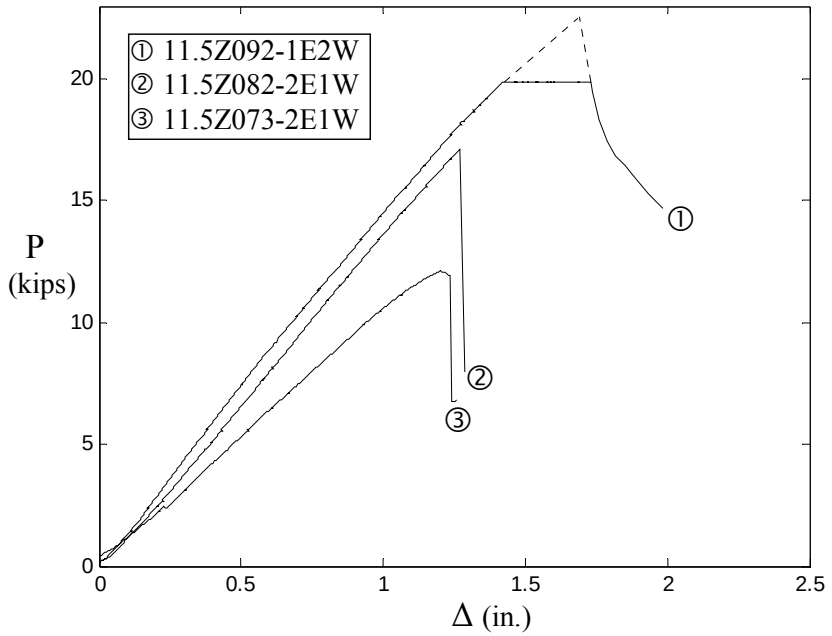

Figure 2.30 Actuator force-displacement response for tests of 11.5 in. nominal deep Z-sections (dash line is estimated)

As shown in the load-displacement plots, failure of the weaker specimen of the pair results in a significant loss in capacity. Redistribution of load into the second specimen of the pair causes complete failure soon thereafter. Failure of the second specimen can be recognized by the change in slope of the post-peak load-deformation response. In the studied members, the post-peak response of the C-sections was generally more gradual than comparable Z-sections (e.g. compare Figure 2.27 to Figure 2.28). In tests on the C-sections both specimens tend to fail at approximately the same time, as opposed to the progressive failure observed in most tests on Z-sections. The observed failure mechanisms for the C and Z-sections are shown in Figure 2.31 and Figure 2.32, respectively.

(a) t = 0.097 in. nominal (test 8C097-2E3W)

(b) t = 0.043 in. nominal (test 8C043-5E6W)

Figure 2.31 Observed failure mechanisms for tests on 8 in. nominal deep C-sections

(a) t = 0.073 in. nominal (test 8.5Z073-4E3W)

(b) t = 0.059 in. nominal (test 8.5Z059-4E3W)

Figure 2.32 Observed failure mechanisms of 8.5 in. nominal deep Z-sections

2.4 Comparison with Design Methods

Six existing design methods were considered for comparison: the American Specification (AISI 1996), the Canadian Standard (CSA S136 1994), the North American Specification (NAS 2001), the Australia/New Zealand Standard (AS/NZS 4600 1996), the European Standard (EN1993 2002) and the newly adopted Direct Strength Method (Schafer and Peköz 1998a; DSM 2004).

2.4.1 Test-to-Predicted Ratio

Test-to-predicted ratios for the considered design methods are provided for all specimens in Table 2.5 and depicted graphically as a function of web slenderness in Figure 2.33. The average (μ) and standard deviation (σ) of the test-to-predicted ratios indicate that overall, all considered methods provide an adequate prediction of the test data. The AISI and CSA S136 methods are identical except for the expressions for the effective width of the web. The CSA S136 method assumes the web is partially effective for $\lambda_{web} > 0.673$ while the AISI method does not. As shown in Table 2.5 and Figure 2.33 the AISI method either predicts the same strength as the CSA S136 method (in the case of fully effective sections) or systematically predicts higher strengths. The difference between the AISI and CSA S136 method is greatest for intermediate web slenderness values, $1.0 \leq \lambda_{web} \leq 1.5$. The average strength difference between the AISI and CSA S136 predictions is 7%, with AISI having a test-to-predicted ratio slightly less than 1.0 and that of CSA S136 greater than 1.0. For the majority of the tested members h/b is less than 4, therefore NAS and AISI are essentially the same; however for a few of the deeper C-

sections (10 in. deep and 12 in. deep) h/b is greater than 4 and thus NAS results match those of CSA S136.

Table 2.5 Summary of test-to-predicted ratios for existing and proposed design methods

		M_{test}/M_{AISI}		M_{test}/M_{S136}		M_{test}/M_{NAS}		$M_{test}/M_{AS/NZS}$		M_{test}/M_{EN1993}		$M_{test}/M_{DS\ell}$		M_{test}/M_{DSd}	
		μ	σ	μ	σ	μ	σ	μ	σ	μ	σ	μ	σ	μ	σ
Stocky N=6	Controlling	1.10	0.07	1.12	0.05	1.10	0.07	1.10	0.07	1.03	0.05	1.07	0.05	1.22	0.05
	Second	1.08	0.07	1.09	0.06	1.08	0.07	1.08	0.07	1.01	0.06	1.06	0.06	1.20	0.05
Slender N=17	Controlling	0.97	0.05	1.05	0.04	1.00	0.06	0.97	0.05	0.99	0.06	1.03	0.07	1.25	0.08
	Second	0.96	0.05	1.04	0.06	0.98	0.07	0.96	0.05	0.98	0.07	1.02	0.08	1.24	0.08
Overall	Controlling	101	0.08	1.07	0.06	1.02	0.07	1.01	0.08	1.00	0.06	1.04	0.07	1.24	0.07
	Second	0.99	0.08	1.05	0.06	1.00	0.08	0.99	0.08	0.99	0.07	1.03	0.08	1.23	0.08

Note: Note: μ – average; σ – standard deviation
Slender: the specimens with $M_{test}/M_y \leq 1.0$ (total N = 17 tests);
Stocky: the specimens with $M_{test}/M_y > 1.0$ (total N = 6 tests);
Controlling: the controlling specimen;
Second: the un-controlling specimen of the paired set;
M_{AISI}: AISI (1996) predicted flexural capacity;
M_{S136}: CSA S136 (1994) predicted flexural capacity;
M_{NAS}: NAS (2001) predicted flexural capacity;
$M_{AS/NZS}$: AS/NZS 4600 (1996) predicted flexural capacity;
M_{EN1993}: EN1993 (2002) predicted flexural capacity;
$M_{DS\ell}$: Direct Strength predication - local mode;
M_{DSd}: Direct Strength prediction - distortional mode.

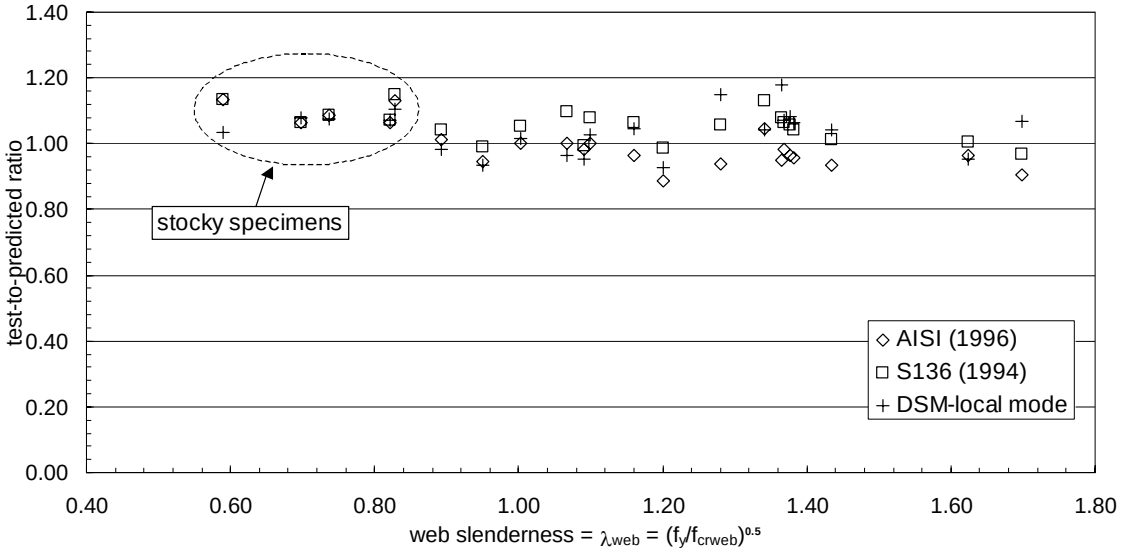

Figure 2.33 Test-to-predicted ratios vs. web slenderness for slender specimens

The Direct Strength Method provides separate strength predictions for local and distortional buckling. Since the beams are fully laterally braced, the maximum capacity due to long wavelength buckling $M_{ne} = M_y$. For local buckling the capacity is:

$$\lambda_\ell \le 0.776\,,\ M_{DS\ell} = M_y \tag{2.1}$$

$$\lambda_\ell > 0.776\,,\ M_{DS\ell} = \left(1 - 0.15\left(\frac{M_{cr\ell}}{M_y}\right)^{0.4}\right)\left(\frac{M_{cr\ell}}{M_y}\right)^{0.4} M_y \tag{2.2}$$

Where $\lambda_\ell = \sqrt{M_y / M_{cr\ell}}$, $M_{cr\ell}$ = critical elastic local buckling moment and M_y = moment at first yield.

Test-to-predicted ratios for distortional buckling (M_{test}/M_{DSd}) are included only to show that distortional buckling is successfully restricted with the testing details employed. However, the low strength predictions for M_{DSd} indicate that the if the beam DID NOT have a panel restricting the flange movement the observed capacity would be considerably less due to a tendency to fail in distortional buckling (As was observed in the initial panel tests described in Section 2.2.4). The overall agreement for $M_{DS\ell}$ is quite good, however, examination of Figure 2.33 shows that $M_{DS\ell}$ is a fundamentally different method than AISI, CSA S136 or NAS – and follows different trends as a function of web slenderness. For members with λ_{web}<1.1, $M_{DS\ell}$ generally provides higher strength predictions than AISI, CSA S136 or NAS, but as web slenderness increases to λ_{web}>1.3 this changes and $M_{DS\ell}$ generally provides lower strength predictions than the conventional methods.

2.5 Conclusions

Through computational and experimental means, the developed testing plan and details have been shown to adequately restrict distortional buckling and provide a simple repeatable test that generates the local buckling flexural capacity for C- and Z-sections. Overall the test results indicate that AISI (1996), CSA S136 (1994), NAS (2001), AS/NZS 4600 (1996), EN1993 (2002) and DSM (2004) design methods provide adequate strength predictions in local buckling failures. However, this overall agreement is primarily due to conservative predictions in stocky members that had observable inelastic reserve capacity ($M_{test}/M_y>1$). AISI 1996 provides either the same strength as the CSA S136 method (in the case of fully effective sections) or systematically higher strengths than CSA S136. Among the considered methods, the EN1993 Specification provides the best average test-to-predicted ratio for both slender and stocky specimens.

Chapter 3

Distortional Buckling Tests on Cold-Formed Steel Beams

3.1 Introduction

Existing experimental and analytical work indicates that the current North American Specification provisions (NAS 2001) are inadequate for predicting bending capacity of C and Z-sections when distortional buckling occurs (e.g., Hancock et al. 1996, Rogers and Schuster 1995, Schafer and Peköz 1999, Yu and Schafer 2002).

To investigate this problem, a two-phase joint MBMA-AISI project was undergone at Johns Hopkins University. The first phase, or local buckling tests, focused on the role of web slenderness in local buckling failures. A panel was through-fastened to the compression flange at a close fastener spacing to insure that distortional buckling and lateral-torsional buckling were restricted. The testing provided the upper-bound capacity for a bending member failing in the local mode, and is summarized in Chapter 2. The second phase, or distortional buckling tests, continued research on the same C and Z-

sections previously examined in Phase 1, but primarily investigated distortional buckling failures and are discussed here, in Chapter 3. In many flexural members, left unrestricted, distortional buckling is the expected failure mode. Although many C and Z-sections in bending have attachments (panel or otherwise) which stabilize the compression flange and help restrict distortional buckling, many do not. Negative bending of continuous members (joists, purlins, etc.) and wind suction on walls and panels (without interior sheathing) are common examples where no such beneficial attachments exist – these members are prone to distortional failures. Even when attachment to the compression flange exists, it may not fully restrict distortional buckling.

Flexural members are typically more prone to distortional failures than compression members, due to the dominance of local web buckling in standard compression members without intermediate web stiffeners. Further, geometry, unique to flexural members, such as the sloping lip stiffener used in Z-sections is inefficient in retarding distortional buckling. For example, a typical 8 in. deep Z-section with t = 0.120 in. has a distortional buckling stress that is 50% of the local buckling stress. The advent of higher strength steels also increases the potential for distortional failures (Schafer and Peköz 1999, Schafer 2002).

3.2 Distortional Buckling Tests

3.2.1 Specimen Selection and Dimensions

The distortional buckling tests were designed to employ nominally the same geometry as the previously conducted local buckling tests. Specimens were selected to

provide systematic variation in web slenderness (h/t) while also varying the other non-dimensional parameters that govern the problem such as flange slenderness (b/t), edge stiffener slenderness (d/t), and relevant interactions, such as the web height to flange width (h/b) ratio. However, as commercially available sections were used, the manner in which the h/t variation could be completed was restricted by the availability of sections (see discussion in Chapter 2, Section 2.2.1). A summary of the cross-sections selected for testing is given in Table 3.1.

Table 3.1 Summary of specimens selected for distortional buckling tests

Performed Tests	No	h/t		b/t		d/t		h/b		d/b	
		min	max	min	max	min	max	min	max	min	max
Group 1 Z: h, b ,d fixed, t varied	7	71.3	138.2	21.9	39.3	7.0	13.4	3.2	3.6	0.28	0.37
Group 2 Z: h, b, d fixed, t varied	2	126.6	140.4	38.6	42.0	10.1	11.5	3.2	3.3	0.26	0.28
Group 3 C: h, b d fixed, t varied	8	80.7	241.7	20.3	59.1	6.4	20.3	3.8	4.1	0.26	0.35
Group 4 C: b, d fixed, h, t varied	7	66.9	186.7	30.9	43.1	6.4	12.9	2.0	6.0	0.19	0.31
Total	24	66.9	241.7	20.3	59.1	6.4	20.3	2.0	6.0	0.19	0.37

Geometry of the C and Z-sections used in the distortional buckling tests is summarized in Table 3.1. The dimensions of the specimens were recorded at mid-length and mid-distance between the center and loading points, for a total of three measurement locations for each specimen. The mean dimensions, as determined from the three sets of measurements, are given in Table 3.2.

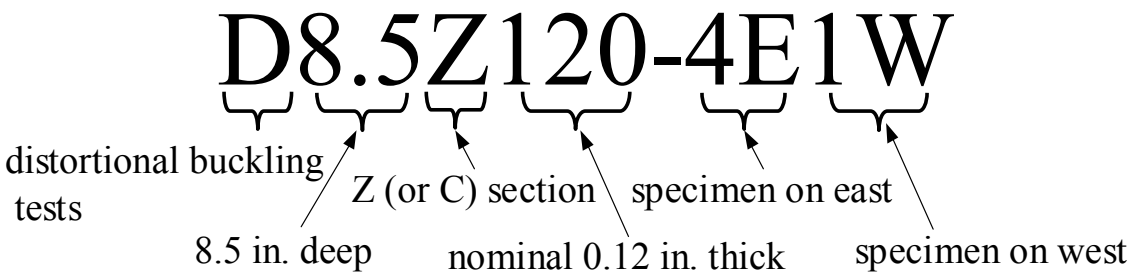

Figure 3.1 Label definition for distortional buckling tests

Figure 3.1 illustrates the definition of a typical distortional buckling test label. The test of D8.5Z120-4E1W means the two paired specimens (D8.5Z120-4 and D8.5Z120-1) are Z-sections with 8.5 in. deep webs and with a nominal thickness of 0.12 in., specimen D8.5Z120-4 is placed at the east side and specimen D8.5Z120-1 is at the west side.

Table 3.2 Measured geometry of specimens for distortional buckling tests

Group No.	Test label	Specimen	h (in.)	b_c (in.)	d_c (in.)	θ_c (deg)	b_t (in.)	d_t (in.)	θ_t (deg)	r_{hc} (in.)	r_{dc} (in.)	r_{ht} (in.)	r_{dt} (in.)	t (in.)	f_y (ksi)
1	D8.5Z120-4E1W	D8.5Z120-4	8.44	2.63	0.93	54.20	2.47	1.00	50.20	0.34	0.34	0.34	0.34	0.1181	61.4
		D8.5Z120-1	8.43	2.65	0.94	48.10	2.52	0.99	52.10	0.36	0.36	0.35	0.35	0.1181	61.9
	D8.5Z115-1E2W	D8.5Z115-2	8.54	2.56	0.91	49.00	2.40	0.89	48.30	0.35	0.35	0.37	0.37	0.1171	64.1
		D8.5Z115-1	8.50	2.66	0.82	48.33	2.47	0.87	48.30	0.37	0.37	0.39	0.39	0.1166	65.8
	D8.5Z092-3E1W	D8.5Z092-3	8.40	2.58	0.95	51.90	2.41	0.94	51.60	0.29	0.29	0.31	0.31	0.0893	57.6
		D8.5Z092-1	8.42	2.59	0.93	52.40	2.39	0.95	50.90	0.28	0.28	0.31	0.31	0.0897	57.8
	D8.5Z082-4E3W	D8.5Z082-4	8.48	2.52	0.94	48.50	2.39	0.97	51.30	0.28	0.28	0.30	0.30	0.0810	59.2
		D8.5Z082-3	8.50	2.53	0.94	49.90	2.37	0.96	49.50	0.28	0.28	0.30	0.30	0.0810	59.0
	D8.5Z065-7E6W	D8.5Z065-7	8.48	2.47	0.83	50.00	2.47	0.82	49.33	0.32	0.32	0.33	0.33	0.0642	62.4
		D8.5Z065-6	8.52	2.48	0.87	53.00	2.43	0.83	48.33	0.32	0.32	0.34	0.34	0.0645	63.3
	D8.5Z065-4E5W	D8.5Z065-5	8.50	2.36	0.67	51.33	2.52	0.90	47.17	0.27	0.27	0.28	0.28	0.0645	62.8
		D8.5Z065-4	8.40	2.40	0.81	47.33	2.25	0.65	51.17	0.30	0.30	0.27	0.27	0.0619	58.3
	D8.5Z059-6E5W	D8.5Z059-6	8.44	2.42	0.77	50.40	2.39	0.86	48.00	0.32	0.32	0.30	0.30	0.0618	58.5
		D8.5Z059-5	8.50	2.42	0.80	48.30	2.40	0.76	48.33	0.30	0.30	0.32	0.32	0.0615	59.1
2	D11.5Z092-3E4W	D11.5Z092-4	11.23	3.47	0.94	48.70	3.40	0.91	49.60	0.33	0.33	0.31	0.31	0.0887	69.9
		D11.5Z092-3	11.25	3.43	0.89	49.29	3.46	0.87	49.50	0.33	0.33	0.32	0.32	0.0889	70.1
	D11.5Z082-3E4W	D11.5Z082-4	11.40	3.41	0.88	48.40	3.40	0.86	49.90	0.30	0.30	0.32	0.32	0.0812	73.7
		D11.5Z082-3	11.33	3.41	0.94	50.20	3.42	0.93	50.97	0.31	0.31	0.31	0.31	0.0818	71.8
3	D8C097-7E6W	D8C097-7	8.13	2.15	0.65	80.75	2.13	0.62	80.00	0.27	0.29	0.27	0.30	0.1001	85.2
		D8C097-6	8.15	2.09	0.64	81.00	2.09	0.61	80.00	0.27	0.29	0.27	0.30	0.1005	85.3
	D8C097-5E4W	D8C097-5	8.06	2.00	0.66	86.70	1.99	0.67	83.00	0.28	0.30	0.28	0.28	0.0998	83.7
		D8C097-4	8.06	2.03	0.67	83.00	2.00	0.68	83.00	0.27	0.28	0.27	0.28	0.0998	84.2
	D8C085-2E1W	D8C085-2	8.06	1.98	0.63	86.00	1.96	0.68	86.60	0.22	0.22	0.23	0.22	0.0825	52.8
		D8C085-1	8.06	1.98	0.62	88.60	1.96	0.68	89.00	0.22	0.19	0.23	0.19	0.0848	51.9
	D8C068-6E7W	D8C068-6	7.94	1.91	0.66	80.00	1.97	0.64	77.80	0.16	0.16	0.16	0.16	0.0708	78.9
		D8C068-7	7.94	1.97	0.64	76.50	1.95	0.67	77.50	0.16	0.16	0.16	0.16	0.0708	79.9
	D8C054-7E6W	D8C054-7	8.01	2.04	0.53	83.40	2.03	0.57	88.70	0.24	0.23	0.21	0.23	0.0528	40.8
		D8C054-6	8.00	2.05	0.59	89.40	2.04	0.56	83.30	0.22	0.23	0.23	0.24	0.0520	40.7
	D8C045-1E2W	D8C045-1	8.18	1.95	0.67	89.00	1.92	0.66	87.60	0.28	0.19	0.22	0.20	0.0348	21.4
		D8C045-2	8.14	1.94	0.69	88.80	1.92	0.69	88.30	0.28	0.20	0.23	0.20	0.0348	21.0
	D8C043-4E2W	D8C043-4	8.02	2.01	0.53	87.30	2.01	0.53	88.80	0.17	0.18	0.17	0.20	0.0459	45.4
		D8C043-2	8.03	1.99	0.52	88.93	1.98	0.54	87.70	0.18	0.19	0.20	0.19	0.0472	45.5
	D8C033-1E2W	D8C033-2	8.15	1.99	0.68	87.10	1.91	0.63	85.80	0.17	0.30	0.20	0.30	0.0337	20.5
		D8C033-1	8.08	2.00	0.61	86.00	1.96	0.77	88.00	0.21	0.26	0.18	0.28	0.0339	20.4
4	D12C068-10E11W	D12C068-11	12.03	2.03	0.51	81.97	2.00	0.53	85.33	0.22	0.22	0.24	0.23	0.0645	32.9
		D12C068-10	12.05	2.02	0.54	85.87	1.98	0.51	94.80	0.24	0.24	0.27	0.23	0.0648	34.7
	D12C068-1E2W	D12C068-2	11.92	2.05	0.52	82.47	2.03	0.59	77.37	0.26	0.24	0.25	0.24	0.0664	56.3
		D12C068-1	11.97	2.12	0.52	80.60	2.00	0.56	83.30	0.25	0.25	0.26	0.26	0.0668	55.9
	D10C068-4E3W	D10C068-4	10.08	2.00	0.48	83.23	2.08	0.53	83.30	0.26	0.21	0.23	0.23	0.0626	22.0
		D10C068-3	10.10	2.07	0.53	80.70	2.08	0.52	81.85	0.24	0.23	0.23	0.22	0.0634	22.5
	D10C056-3E4W	D10C056-3	9.99	1.97	0.66	88.00	1.95	0.63	89.00	0.13	0.16	0.13	0.13	0.0569	77.3
		D10C056-4	10.00	1.94	0.72	88.60	1.92	0.66	87.70	0.13	0.16	0.13	0.18	0.0569	76.9
	D10C048-1E2W	D10C048-1	9.94	2.06	0.62	86.10	1.94	0.63	79.60	0.20	0.19	0.20	0.19	0.0478	51.1
		D10C048-2	9.94	2.02	0.63	85.70	1.95	0.63	83.70	0.18	0.19	0.19	0.20	0.0486	50.6
	D6C063-2E1W	D6C063-2	5.99	1.99	0.63	88.74	1.97	0.63	87.30	0.19	0.17	0.19	0.22	0.0578	55.9
		D6C063-1	5.99	1.99	0.62	87.03	1.97	0.63	86.13	0.22	0.17	0.22	0.17	0.0559	57.8
	D3.62C054-3E4W	D3.62C054-4	3.73	1.88	0.41	87.00	1.87	0.43	89.00	0.26	0.24	0.27	0.27	0.0555	32.1
		D3.62C054-3	3.72	1.89	0.35	88.00	1.86	0.36	88.00	0.24	0.28	0.26	0.26	0.0556	32.9

3.2.2 Testing Setup

The same testing setup and loading system as used in previous local buckling tests (Chapter 2) was employed except that the panel between the two loading points was removed, as shown in Figure 3.2 and Figure 3.3. The through-fastened panel is only attached to the compression flanges in the shear spans to restrict both the distortional and the lateral-torsional buckling in these regions. Full details of the testing setup are summarized in Chapter 2, Section 2.2.3.

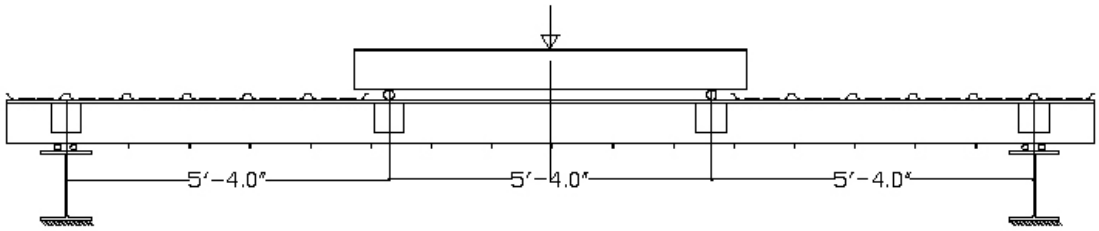

Figure 3.2 Elevation view of distortional buckling tests

Figure 3.3 Panel setup for distortional buckling tests

3.2.3 Panel-to-Section Fastener Configuration

The panel-to-section fastener configuration employed in the distortional buckling tests is the same as that used in the earlier local buckling tests, except the through-fastened panel in the constant moment region is removed. This setup is expected to restrict later-torsional buckling while allowing distortional and local buckling to occur. Examination of the ratio of the elastic distortional buckling moment (M_{crd}) to elastic local buckling moment ($M_{cr\ell}$) indicates that a large number of members, particularly the Z-sections, are anticipated to fail in a mechanism dominated by distortional buckling (because $M_{crd}/M_{cr\ell} \leq 1$). Even when $M_{crd}/M_{cr\ell} > 1$ distortional buckling may govern because of reduced post-buckling strength in distortional failures (Schafer and Peköz. 1999). Table 3.3 provides the elastic buckling loads of all performed tests, where $M_{cr\ell\text{-}CUFSM}$ and $M_{crd\text{-}CUFSM}$ respectively are the elastic local and distortional buckling moment calculated by the finite strip software CUFSM. $M_{cr\ell\text{-}ABAQUS}$, $M_{crd\text{-}ABAQUS}$ and $M_{crLTB\text{-}ABAQUS}$ respectively are elastic local, distortional and lateral-torsional buckling moment determined by a finite element model in ABAQUS considering the complete testing setup (see Chapter 5 for more details about the ABAQUS model).

As shown in Table 3.3, all tests except D8C097-5E4W have either elastic local buckling ($M_{cr\ell\text{-}ABAQUS}$) or elastic distortional buckling ($M_{crd\text{-}ABAQUS}$) as the lowest buckling mode, and lateral-torsional buckling ($M_{crLTB\text{-}ABAQUS}$) is successfully restricted. The test setup does not change the local and distortional buckling moments significantly, as can be observed by comparing the elastic buckling moments calculated by CUFSM, which only includes the pure member under constant moment CUFSM, with the more

detailed ABAQUS model, as given in Table 3.3. Based on these elastic results, distortional buckling is expected to be the failure mechanism for all Z-sections and most C-sections. Figure 3.4, 3.5 and 3.6 show the typical elastic buckling modes generated by ABAQUS for lateral-torsional, distortional, and local buckling, respectively.

Table 3.3 Elastic buckling moments of performed tests

Test label	$M_{cr\ell\text{-CUFSM}}$ (kip-in.)	$M_{crd\text{-CUFSM}}$ (kip-in.)	$M_{cr\ell\text{-ABAQUS}}$ (kip-in.)	$M_{crd\text{-ABAQUS}}$ (kip-in.)	$M_{crLTB\text{-ABAQUS}}$ (kip-in.)
D8.5Z120-4E1W	1474	753	1521	772	1219
D8.5Z115-1E2W	1405	696	>1451	720	1174
D8.5Z092-3E1W	653	418	684	450	747
D8.5Z082-4E3W	480	328	501	352	>566
D8.5Z065-7E6W	239	197	253	211	>302
D8.5Z065-4E5W	216	171	206	174	>230
D8.5Z059-6E5W	206	168	218	183	>255
D11.5Z092-3E4W	609	418	634	464	>760
D11.5Z082-3E4W	468	352	500	385	>608
D8C097-5E4W	761	593	796	610	534
D8C085-2E1W	447	394	451	397	>468
D8C068-6E7W	278	273	294	280	>338
D8C054-7E6W	113	129	117	129	>144
D8C045-1E2W	34	69	36	>43	>43
D8C043-4E2W	78	97	86	>107	>107
D8C033-1E2W	31	61	33	>42	>42
D12C068-1E2W	198	199	202	208	>256
D12C068-10E11W	170	184	183	189	>232
D10C068-4E3W	171	181	184	186	>227
D10C056-3E4W	132	186	140	>166	>166
D10C048-1E2W	81	121	89	>89	>88
D6C063-2E1W	186	149	181	163	>190
D3.62C054-3E4W	139	65	>120	66	94

Note: lower bounds, indicated by ">", are given to those modes which are not included in the first 30 eigenmodes calculated by ABAQUS.

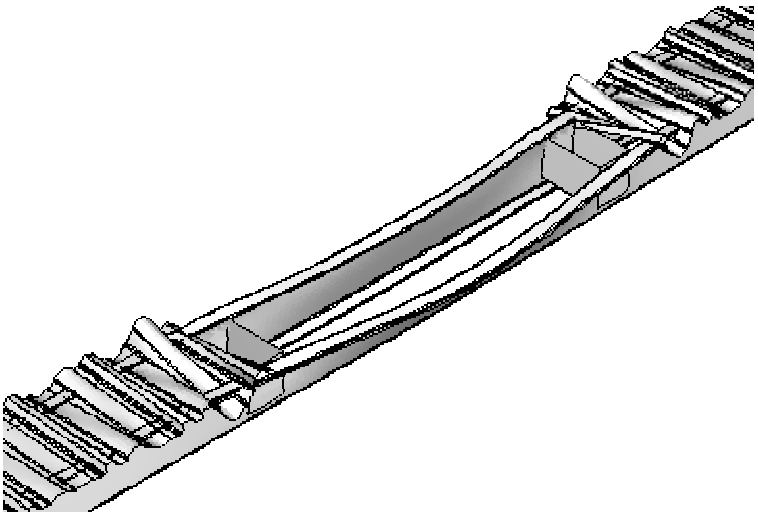

Figure 3.4 Lateral-torsional buckling mode of beam D8C097-5E4W

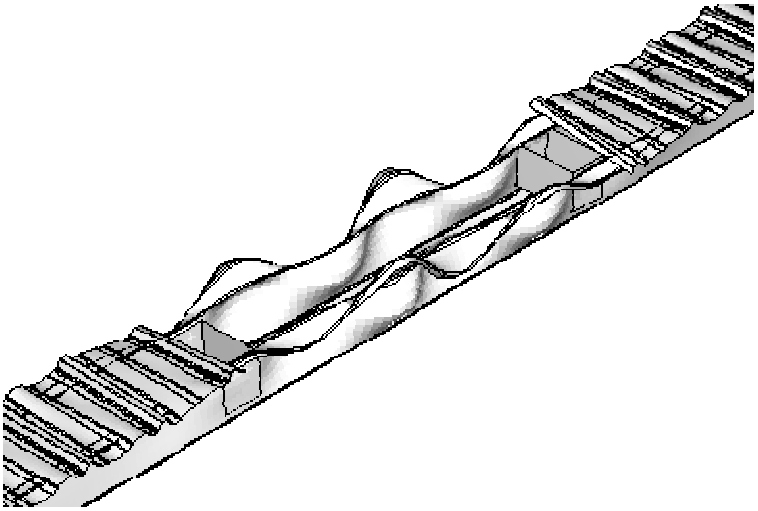

Figure 3.5 Distortional buckling mode of beam D8C097-5E4W

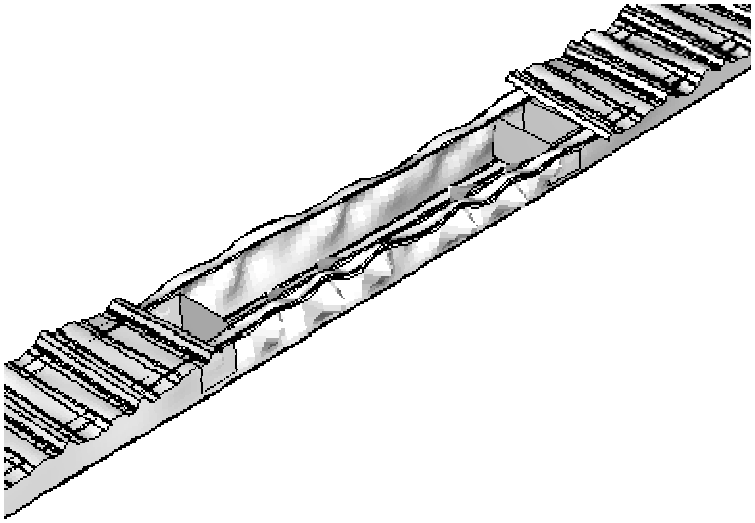

Figure 3.6 Local buckling mode of beam D8C097-5E4W

3.3 Experimental Results

Summaries of the distortional buckling test results are given in Table 3.4. Included for each test are the elastic buckling moments ($M_{cr\ell}$, M_{crd}) as determined by the finite strip method using CUFSM (2001) and the ratios of test-to-predicted capacities for several design methods including the existing American Specification, M_{AISI} (AISI 1996), the existing Canadian Standard, M_{S136} (CSA S136 1994), the newly adopted North American Specification, M_{NAS} (NAS 2001), the existing Australia/New Zealand Standard, $M_{AS/NZS}$ (AS/NZS 4600 1996), the existing European Standard EN1993, M_{EN1993} (EN1993 2002) and the Direct Strength Method (Schafer and Peköz 1998a; DSM 2004 – $M_{DS\ell}$ for local failure, M_{DSd} for distortional failure).

The actuator load-displacement response of all distortional buckling tests are given in Figure 3.7 to Figure 3.10. Compared with the local buckling tests (Chapter 2), more non-linear response is observed prior to formation of the failure mechanism. The specimens which have a capacity at or near the yield moment ($M_{test}/M_y \sim 1$, see Table 3.4) exhibit the most nonlinear deformation prior to failure; while the more slender specimens have essentially elastic response prior to formation of a sudden failure mechanism.

Table 3.4 Distortional buckling test results

Group No.	Test label	Specimen	M_{test} (kip-in)	M_y (kip-in)	$M_{cr\ell}$ (kip-in)	M_{crd} (kip-in)	M_{test}/M_y	M_{test}/M_{AISI}	M_{test}/M_{S136}	M_{test}/M_{NAS}	$M_{test}/M_{AS/NZS}$	M_{test}/M_{EN1993}	$M_{test}/M_{DS\ell}$	M_{test}/M_{DSd}
1	D8.5Z120-4E1W	D8.5Z120-4*	254	265	734	391	0.96	0.95	0.95	0.95	1.08	1.00	0.96	1.08
		D8.5Z120-1	254	269	740	362	0.94	0.93	0.93	0.93	1.09	1.00	0.94	1.09
	D8.5Z115-1E2W	D8.5Z115-2	237	271	712	363	0.88	0.86	0.86	0.86	1.02	0.92	0.88	1.02
		D8.5Z115-1*	237	278	693	332	0.85	0.88	0.88	0.88	1.03	0.93	0.85	1.03
	D8.5Z092-3E1W	D8.5Z092-3*	153	186	325	209	0.82	0.83	0.85	0.82	1.01	0.88	0.82	1.01
		D8.5Z092-1	153	188	328	210	0.82	0.83	0.85	0.83	1.00	0.87	0.82	1.00
	D8.5Z082-4E3W	D8.5Z082-4*	127	176	240	163	0.72	0.77	0.81	0.76	0.95	0.83	0.77	0.95
		D8.5Z082-3	127	176	240	166	0.72	0.77	0.81	0.76	0.94	0.83	0.77	0.94
	D8.5Z065-7E6W	D8.5Z065-7*	93	146	118	95	0.64	0.75	0.82	0.75	0.96	0.93	0.81	0.96
		D8.5Z065-6	93	149	121	103	0.63	0.72	0.79	0.72	0.92	0.88	0.79	0.92
	D8.5Z065-4E5W	D8.5Z065-5	80	144	109	88	0.56	0.70	0.75	0.70	0.86	0.83	0.72	0.86
		D8.5Z065-4*	80	122	107	83	0.65	0.72	0.80	0.72	0.97	0.90	0.80	0.97
	D8.5Z059-6E5W	D8.5Z059-6*	71	129	103	85	0.55	0.65	0.71	0.65	0.83	0.80	0.70	0.83
		D8.5Z059-5	71	130	103	83	0.55	0.64	0.70	0.64	0.83	0.79	0.69	0.83
2	D11.5Z092-3E4W	D11.5Z092-4	262	402	306	210	0.65	0.85	0.92	0.85	1.07	1.15	0.84	1.07
		D11.5Z092-3*	262	404	303	208	0.65	0.86	0.93	0.86	1.07	1.07	0.84	1.07
	D11.5Z082-3E4W	D11.5Z082-4*	233	393	230	169	0.59	0.86	0.91	0.86	1.06	1.03	0.84	1.06
		D11.5Z082-3	233	387	238	183	0.60	0.84	0.89	0.84	1.03	1.02	0.84	1.03
3	D8C097-7E6W	D8C097-7	204	251	394	287	0.81	0.85	0.88	0.85	0.99	0.90	0.83	0.99
		D8C097-6*	204	250	392	290	0.82	0.85	0.89	0.85	0.99	0.91	0.83	0.99
	D8C097-5E4W	D8C097-5*	166	234	377	296	0.71	0.73	0.76	0.76	0.84	0.77	0.71	0.84
		D8C097-4	166	238	384	297	0.69	0.72	0.74	0.72	0.83	0.75	0.70	0.83
	D8C085-2E1W	D8C085-2*	122	124	215	191	0.99	0.99	1.02	1.02	1.09	1.03	0.99	1.10
		D8C085-1	122	124	232	203	0.98	0.98	1.01	1.01	1.07	1.02	0.98	1.07
	D8C068-6E7W	D8C068-6	105	158	138	139	0.67	0.76	0.85	0.83	0.89	0.84	0.82	0.89
		D8C068-7*	105	161	140	134	0.65	0.77	0.86	0.84	0.89	0.85	0.80	0.89
	D8C054-7E6W	D8C054-7	49	61	58	62	0.79	0.86	0.96	0.85	1.01	0.98	0.95	1.01
		D8C054-6*	49	60	56	67	0.80	0.86	0.95	0.85	1.00	0.98	0.97	0.99
	D8C045-1E2W	D8C045-1	17	22	17	34	0.75	0.76	0.84	0.83	0.83	0.90	0.96	0.84
		D8C045-2*	17	21	17	35	0.77	0.77	0.86	0.85	0.85	0.91	0.98	0.84
	D8C043-4E2W	D8C043-4*	43	60	38	47	0.72	0.90	0.97	0.90	1.00	1.03	0.99	1.01
		D8C043-2	43	61	40	49	0.70	0.86	0.94	0.94	0.98	0.98	0.95	0.97
	D8C033-1E2W	D8C033-2	16	20	15	32	0.82	0.82	0.91	0.90	0.90	0.97	1.05	0.89
		D8C033-1*	16	20	15	29	0.81	0.82	0.91	0.91	0.93	1.00	1.04	0.92
4	D12C068-10E11W	D12C068-11*	95	107	84	90	0.88	0.92	1.05	1.05	1.21	1.13	1.12	1.21
		D12C068-10	95	112	86	94	0.84	0.88	1.00	1.00	1.15	1.07	1.08	1.15
	D12C068-1E2W	D12C068-2*	99	188	92	98	0.52	0.67	0.72	0.70	0.86	0.79	0.79	0.86
		D12C068-1	99	188	96	101	0.52	0.67	0.72	0.70	0.85	0.78	0.77	0.85
	D10C068-4E3W	D10C068-4*	51	53	82	85	0.95	0.95	1.01	1.01	1.05	1.01	0.98	1.05
		D10C068-3	51	57	89	96	0.90	0.90	0.94	0.95	0.96	0.94	0.91	0.97
	D10C056-3E4W	D10C056-3*	85	174	66	90	0.49	0.71	0.74	0.74	0.81	0.79	0.80	0.81
		D10C056-4	85	172	66	96	0.49	0.69	0.72	0.72	0.79	0.76	0.80	0.79
	D10C048-1E2W	D10C048-1*	62	96	40	59	0.65	0.86	0.90	0.90	1.00	1.00	1.03	1.00
		D10C048-2	62	96	41	62	0.64	0.85	0.89	0.89	0.98	0.97	1.01	0.98
	D6C063-2E1W	D6C063-2	52	62	87	78	0.85	0.94	0.99	0.92	1.00	0.85	0.89	1.00
		D6C063-1*	52	62	79	71	0.85	0.95	1.01	0.94	1.03	0.85	0.92	1.03
	D3.62C054-3E4W	D3.62C054-4	17	16	70	35	1.04	1.08	1.08	1.08	1.07	1.08	1.04	1.05
		D3.62C054-3*	17	16	69	30	1.04	1.14	1.14	1.11	1.12	1.10	1.04	1.09

Note: *--- Controlling specimen, weaker capacity by AISI (1996)

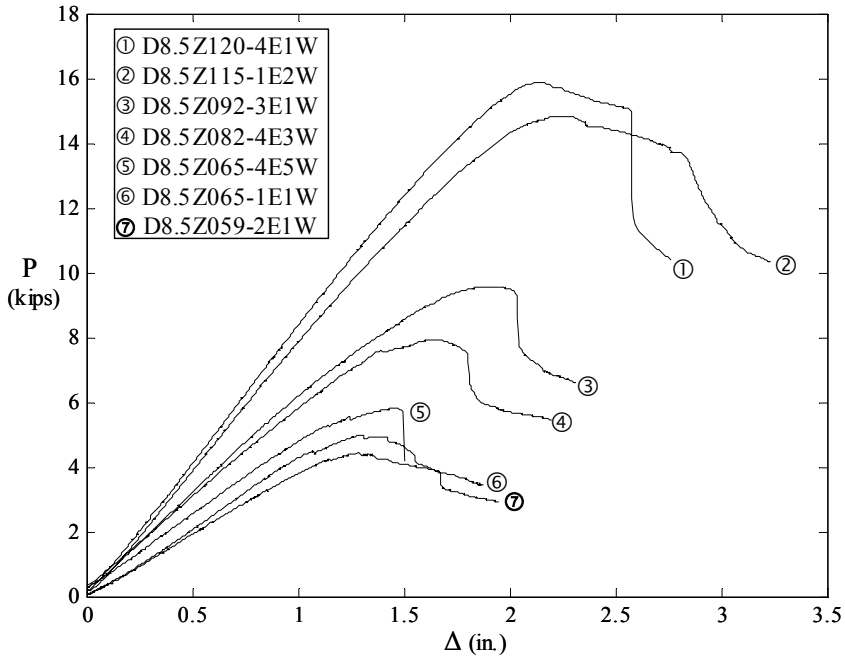

Figure 3.7 Actuator load-displacement response of Group 1 distortional buckling tests

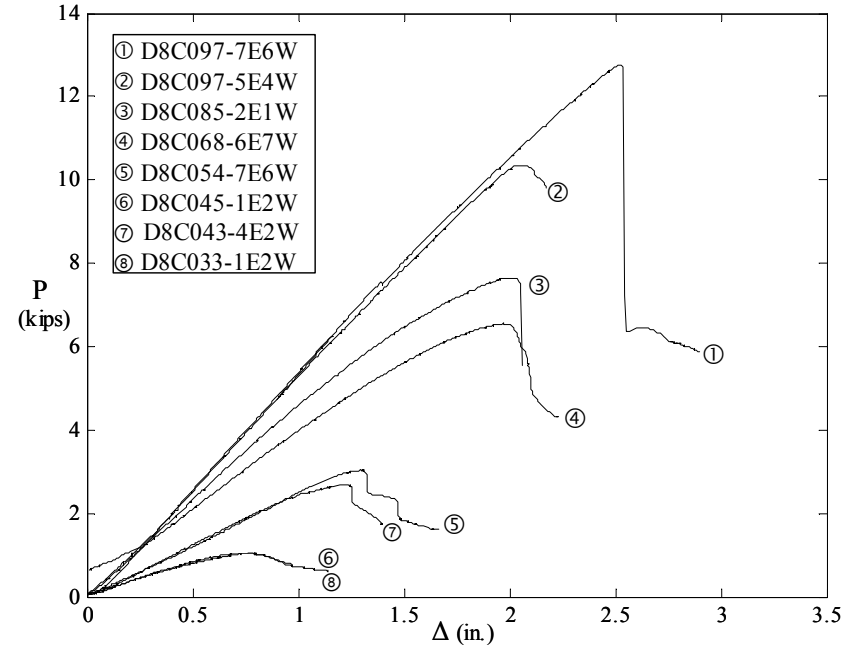

Figure 3.8 Actuator load-displacement response of Group 2 distortional buckling tests

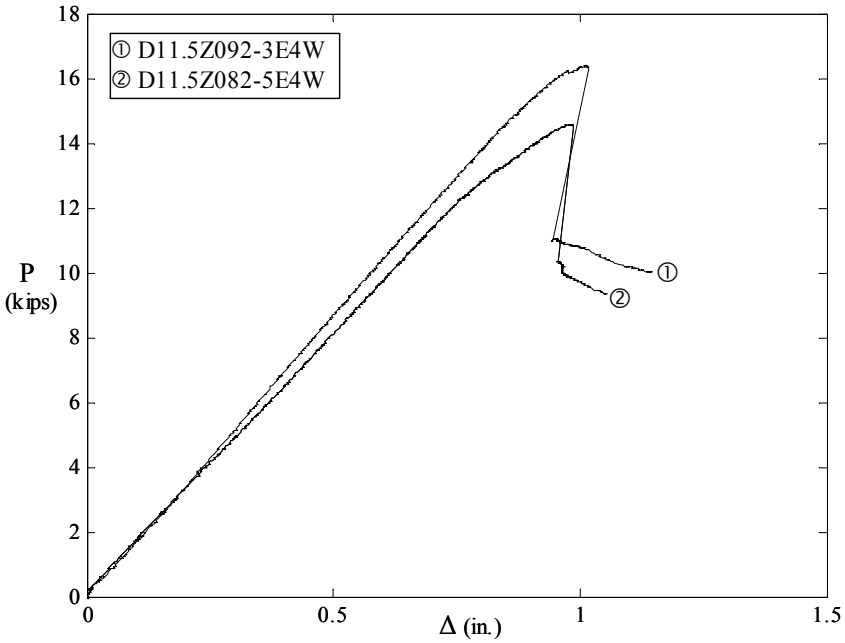

Figure 3.9 Actuator load-displacement response of Group 3 distortional buckling tests

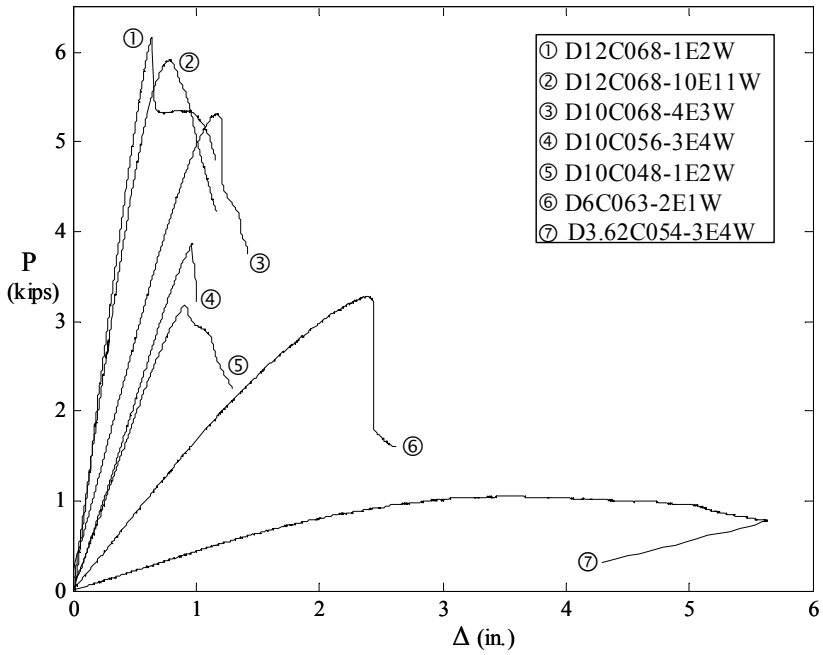

Figure 3.10 Actuator force-displacement responses of Group 4 distortional buckling tests

3.4 Comparison with Local Buckling Tests

For the Z beams, Figure 3.11 provides a typical comparison between the local buckling and distortional buckling tests. The buckling wavelength is visibly longer in the distortional buckling test and the compression flange rotates about the web/compression flange junction. This is expected as the Z beams have an elastic distortional buckling moment (M_{crd}) which is lower than local buckling for all the tests.

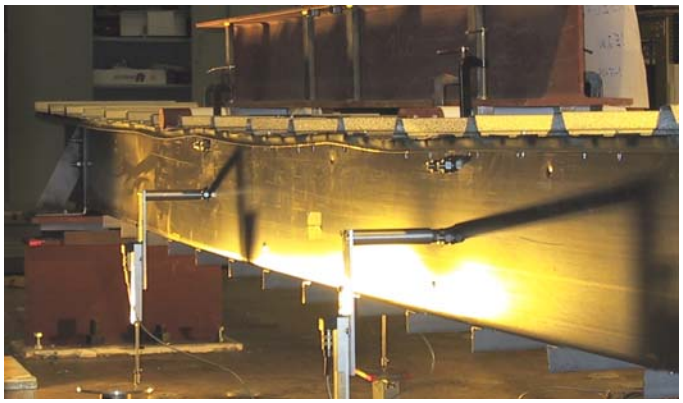

(a) Local buckling test of 11.5Z092-1E2W

(b) Distortional buckling test of D11.5Z092-3E4W

Figure 3.11 Comparison of tests on 11.5Z092

Local buckling failures and more complicated local-distortional buckling combined modes were observed in some C beam tests. Due to the right angle (not sloped) lip stiffeners for C-sections compared with that of the Z-sections, the distortional buckling

strength of C beams is significantly higher than the Z beams. However, distortional buckling is still the most likely failure mode for the C beams, even those beams with lower elastic local buckling moment, as shown in Figure 3.12.

(a) Test D8C054-7E6W

(b) Test D8C043-4E2W

Figure 3.12 Distortional buckling failures of beams observed even when elastic local buckling moment is lower than elastic distortional buckling moment

Typically, the compression flanges of the C beams did not exhibit the same large rotations as observed in the Z beams. In the post-buckling range the majority of the tested C beams include some rotation of the compression flange, but in many cases translation and rotation of the cross-section as well. This observation indicates a more complicated collapse response and the possible interaction of distortional buckling with local/lateral-torsional buckling in the C beams.

Among 25 local buckling and 24 distortional buckling tests, 9 pairs of tests use beams with nominally identical geometry and material. The test comparison for these specimens is summarized in Table 3.5. The notations of P_y, P_{crL}, P_{crD} are respectively the actuator load, P, that causes yielding, elastic local buckling, and elastic distortional buckling in the beam (where M (kip-in.) = 32 (in.) × P (kips)). On average, the beam bending strength will lose 17% when the through-fastened panel is removed from the compression flanges.

Table 3.5 Comparison of 9 pairs of tests having the same nominal geometry and material property

Pair No.	Local buckling test label	Distortional buckling test label	Actuator peak load of local test P_L (kips)	Actuator peak load of distortional test P_D (kips)	P_D/P_L
1	8.5Z120-3E2W	D8.5Z120-4E1W	17.52	15.87	91%
2	8.5Z092-4E2W	D8.5Z092-3E1W	11.33	9.57	84%
3	8.5Z082-1E2W	D8.5Z082-4E3W	10.13	7.92	78%
4	8.5Z059-2E1W	D8.5Z059-4E3W	6.18	4.44	72%
5	8C054-1E8W	D8C054-7E6W	3.49	3.03	87%
6	8C043-5E6W	D8C043-4E2W	3.19	2.68	84%
7	12C068-3E4W	D12C068-1E2W	8.54	6.16	72%
8	12C068-9E5W	D12C068-10E11W	6.51	5.91	91%
9	3.62C054-1E2W	D3.62C054-3E4W	1.26	1.07	85%
				Average	83%

The actuator load-displacement curves and failure modes for these pairs of tests are provided in Figure 3.13 through Figure 3.30. It is shown that the two tests in each pair have the same elastic stiffness, but different peak loads, buckling, and post-buckling behavior. The distortional buckling tests present more nonlinear behavior before failure than the local buckling tests, while significant deformations in the web were observed in the local buckling tests. For the distortional buckling tests, the failure in the compression flange is dominant. At the same time, lateral-torsional buckling is also involved in post-

buckling region for some distortional buckling tests. It can be seen that with the through-fastened panel removed, the cold-formed steel C and Z beams have lower bending strength and less flexibility (less out-of-plane deflection before buckling) as expected.

While the initial buckling deformations are observably different between the two test types (local and distortional), and the strength is clearly different, the final failure mechanisms, deep in the post-peak range, often share striking similarities, as depicted in the figures. These similarities in collapse mechanisms make it difficult to visually identify a failed specimen as local or distortional. Instead, observation of the entire test, as well as direct comparisons and supplementary analysis are often required.

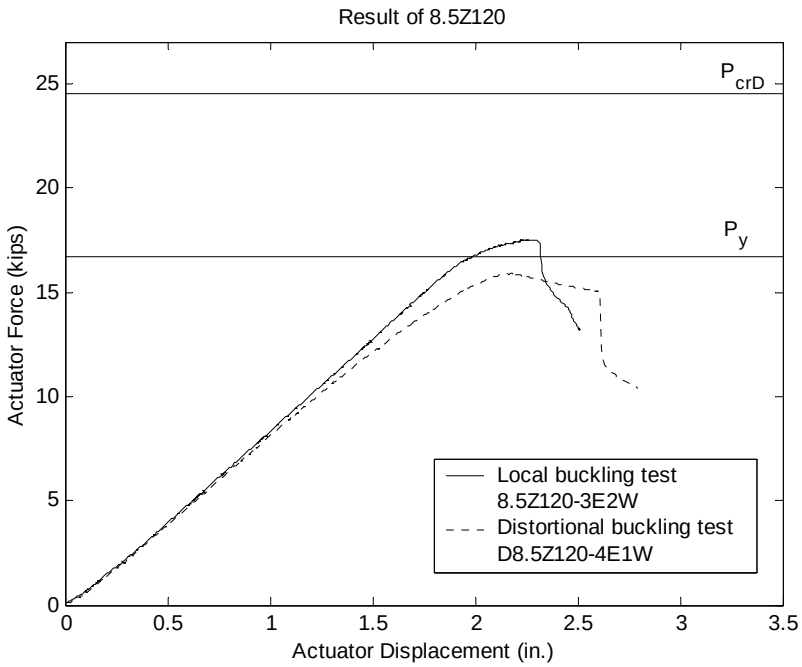

Figure 3.13 Comparison of tests on 8.5Z120

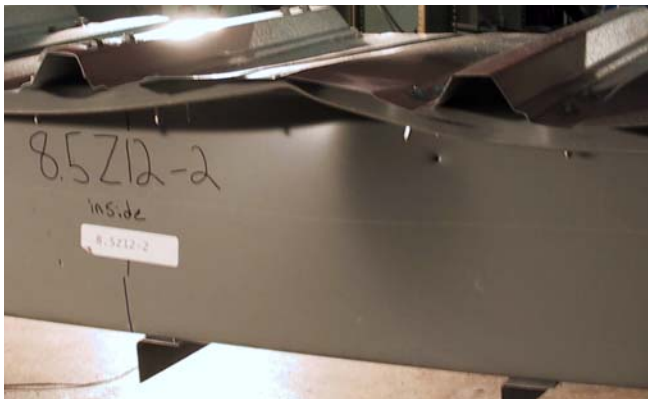

(a) Local buckling test

(b) Distortional buckling test

Figure 3.14 Comparison of tests on 8.5Z120

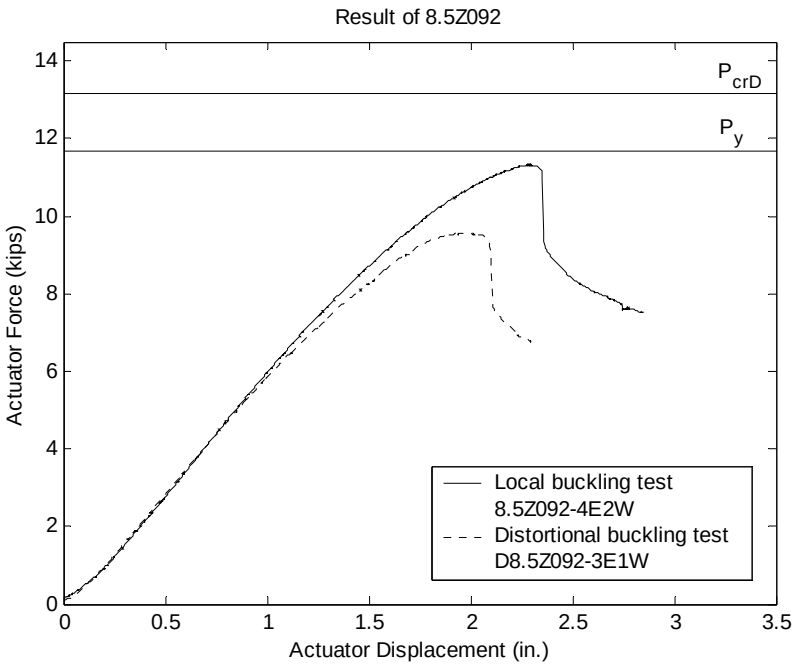

Figure 3.15 Comparison of tests on 8.5Z092

(a) Local buckling test

(b) Distortional buckling test

Figure 3.16 Comparison of tests on 8.5Z092

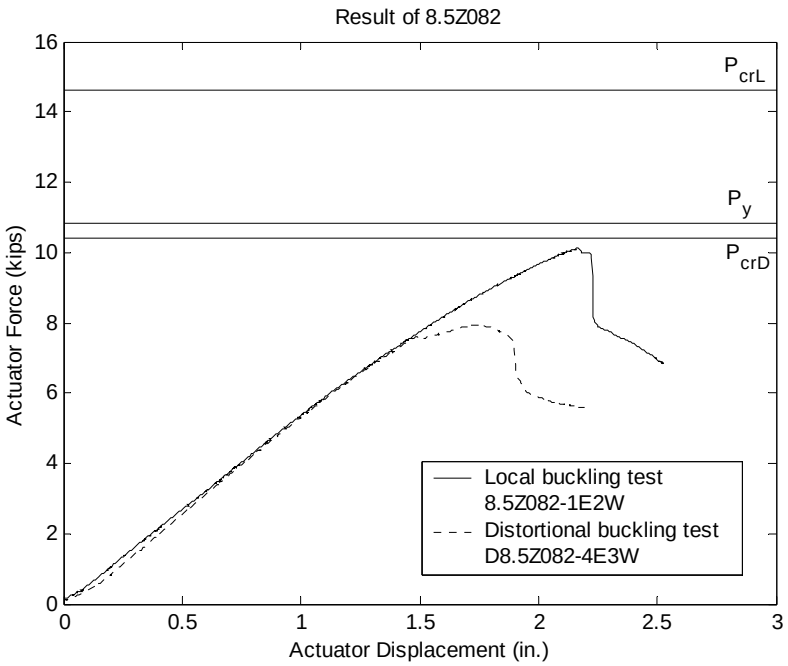

Figure 3.17 Comparison of tests on 8.5Z082

(a) Local buckling test

(b) Distortional buckling test

Figure 3.18 Comparison of tests on 8.5Z082

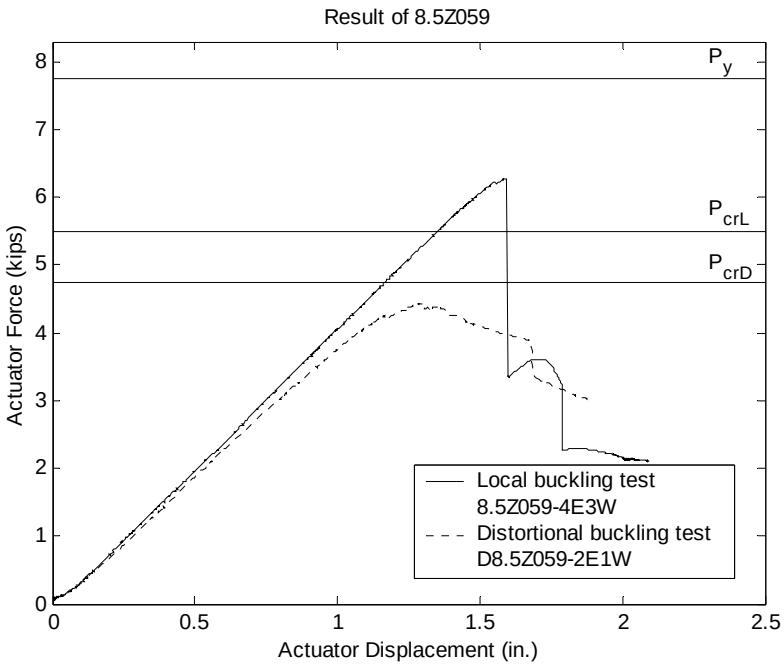

Figure 3.19 Comparison of tests on 8.5Z059

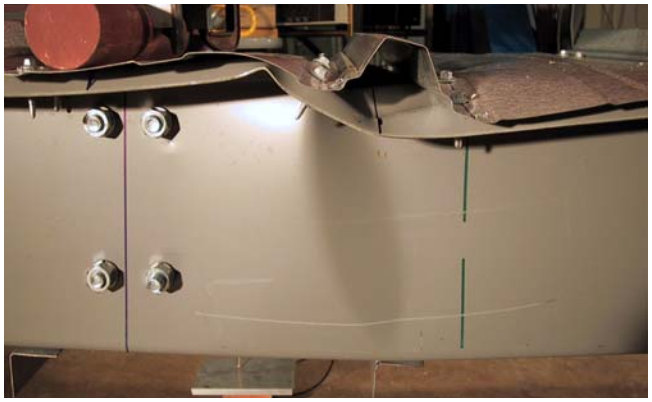

(a) Local buckling test

(b) Distortional buckling test

Figure 3.20 Comparison of tests on 8.5Z059

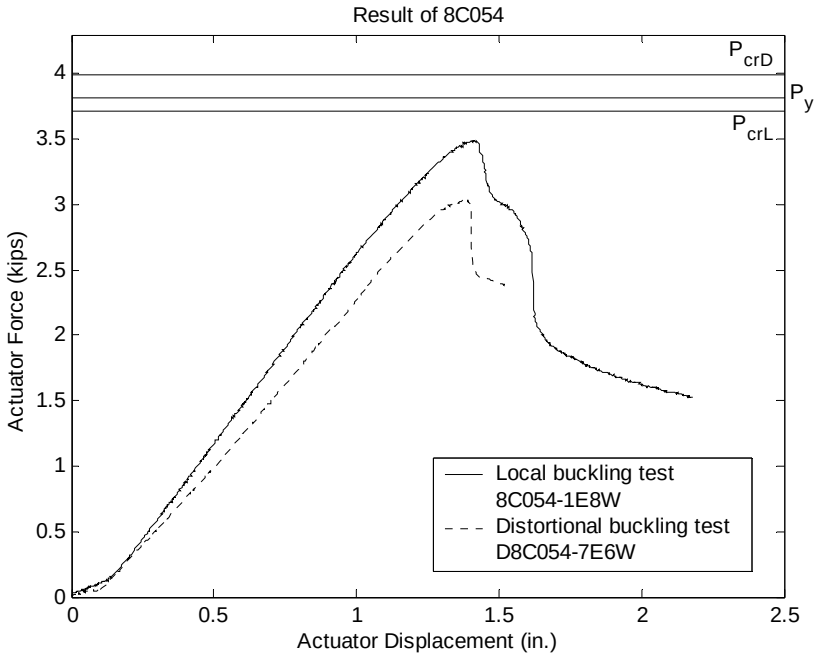

Figure 3.21 Comparison of tests on 8.5Z054

(a) Local buckling test

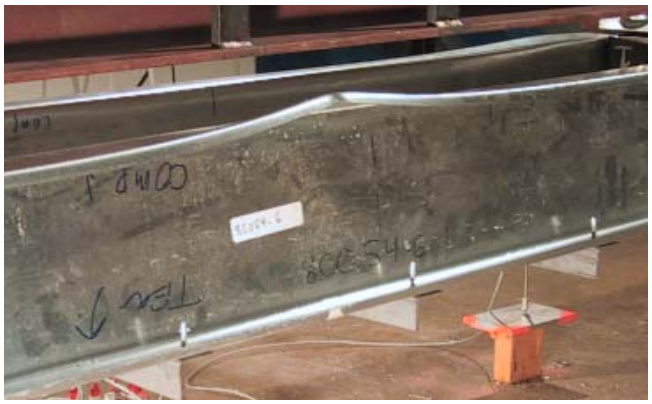

(b) Distortional buckling test

Figure 3.22 Comparison of tests on 8.5Z054

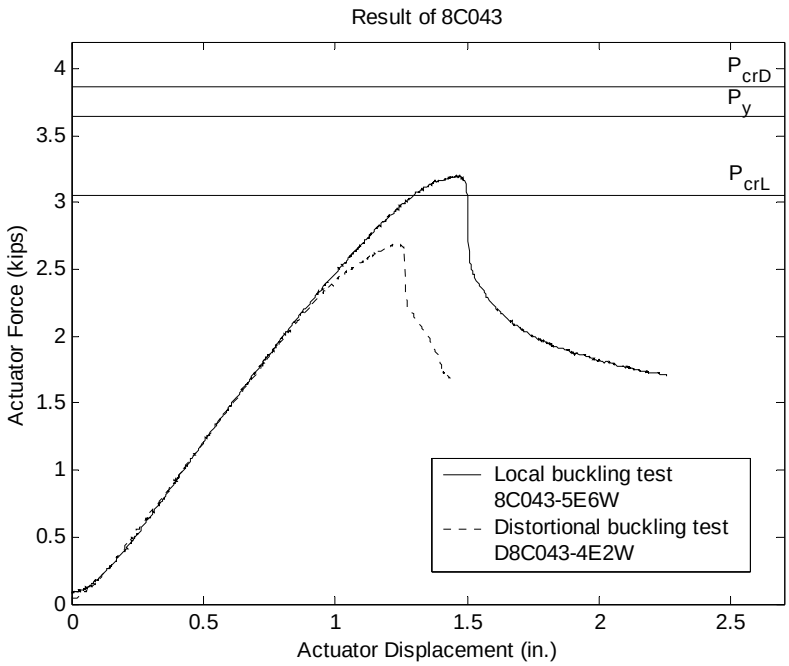

Figure 3.23 Comparison of tests on 8C043

(a) Local buckling test

(b) Distortional buckling test

Figure 3.24 Comparison of tests on 8C043

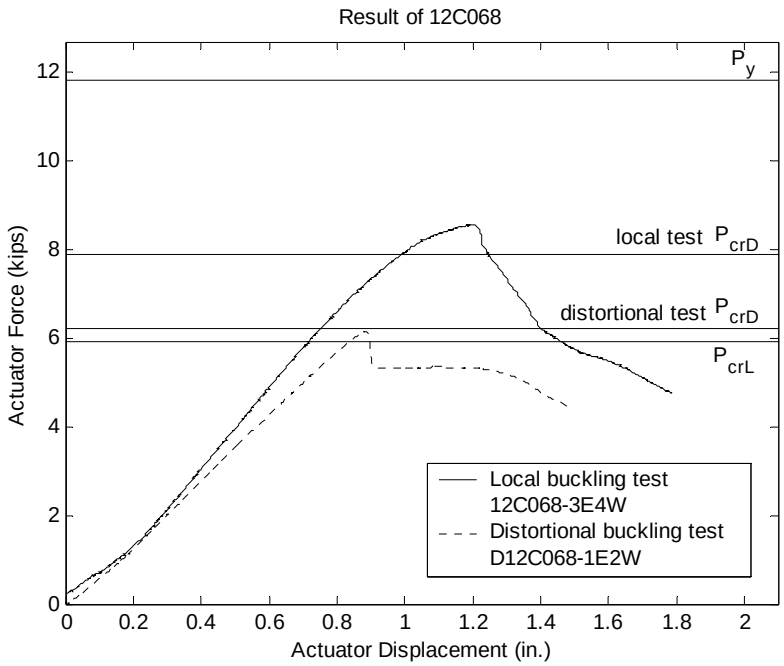

Figure 3.25 Comparison of tests on 12C068 with higher strength material

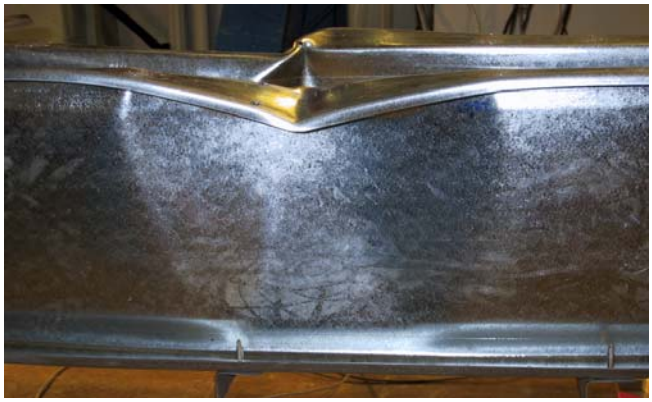

(a) Local buckling test

(b) Distortional buckling test

Figure 3.26 Comparison of tests on 12C068 with higher strength material

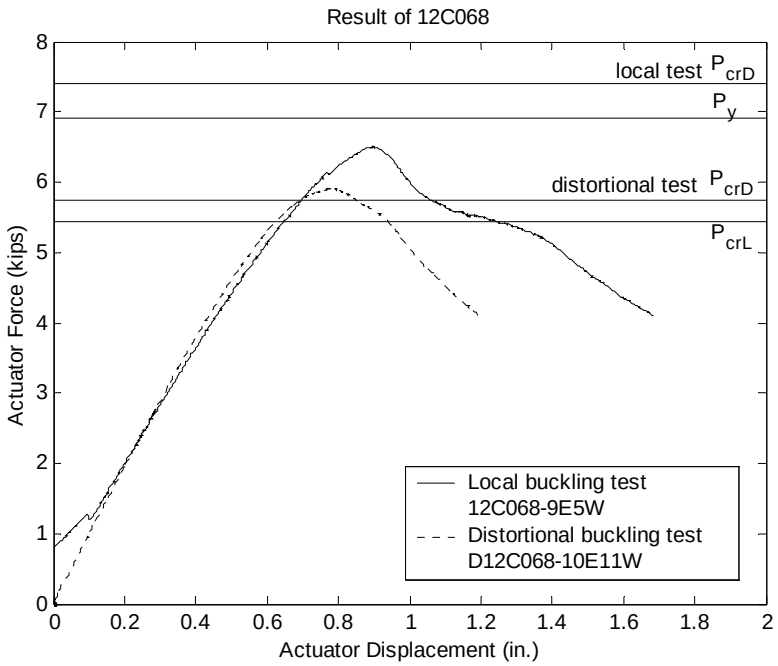

Figure 3.27 Comparison of tests on 12C068 with lower strength material

(a) Local buckling test

(b) Distortional buckling test

Figure 3.28 Comparison of tests on 12C068 with lower strength material

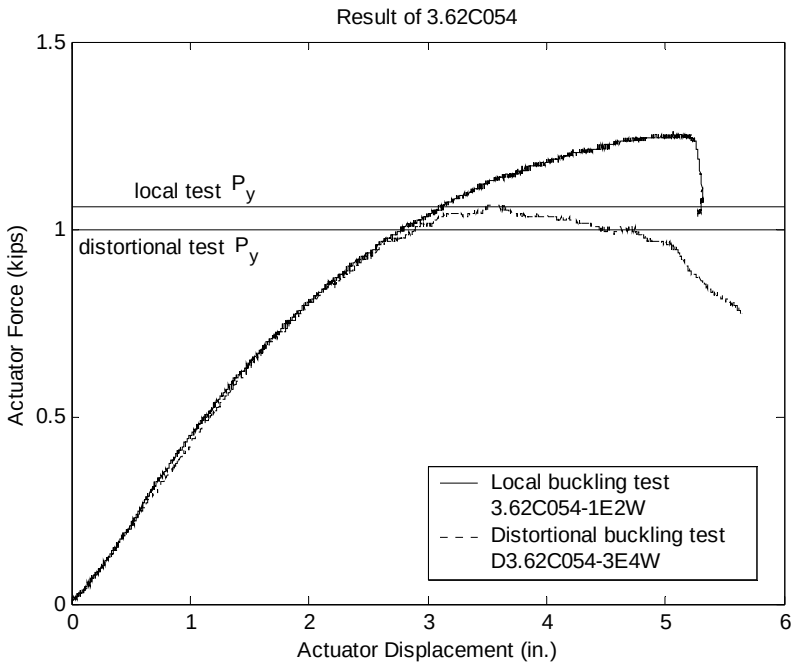

Figure 3.29 Comparison of tests on 3.62C054

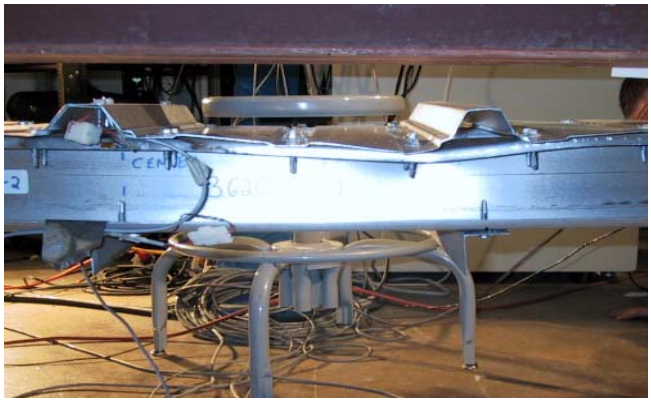

(a) Local buckling test

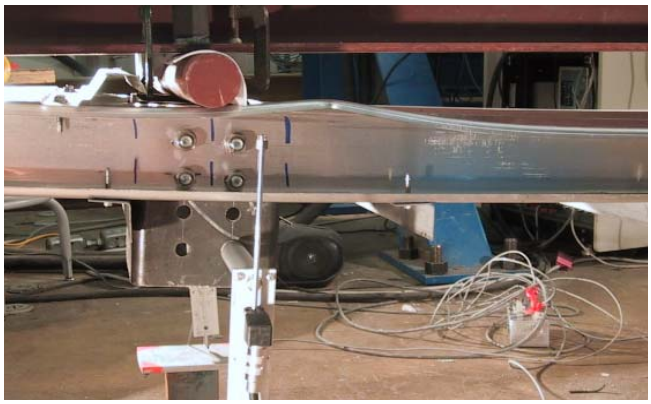

(b) Distortional buckling test

Figure 3.30 Comparison of tests on 3.62C054

3.5 Examination of Several Tests of Note

In the distortional buckling tests, the compression flange restraint was removed from the maximum loaded region so that distortional buckling was free to form. Elastic buckling analysis by ABAQUS indicated that distortional buckling is likely to control the failures for all Z-sections and most C-sections. However, not all the tests failed in distortional buckling. Here, the tests which exhibited other behavior are presented in detail.

3.5.1 Test Failed in Lateral-Torsional Buckling Mode: Re-Test of D8C097

As shown in Table 3.3, D8C097-5E4W is the only test, which has a lower elastic lateral-torsional buckling moment than that of local or distortional buckling (Figure 3.4, 3.6 and 3.7). Lateral-torsional buckling failure was observed in the test, as shown in Figure 3.31. The beam rotated and large flexural deflection was observed at the same time. The test passed the peak load point gradually and no local collapse or sharp loss of bending capacity occurred. Therefore, a re-test of D8C097-7E6W with proper modifications was performed. In the new test, an additional angle was used to connect the two sections at mid-span, in order to restrict later-torsional buckling (Figure 3.32) while at the same time not to boost the distortional buckling moment.

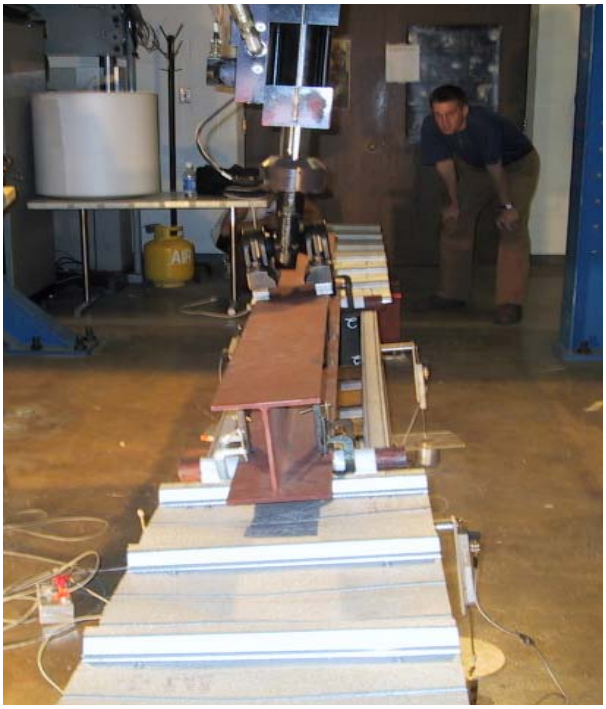

Figure 3.31 Test D8C097-5E4W with standard setup

Figure 3.32 Test D8C097-7E6W with angle added

Elastic finite element analysis was performed to examine the new testing setup. After the angle is added to the compression flange the lateral-torsional buckling moment of

D8C097-7E6W is increased from 589.5 kip-in., to 618.7 kip-in. Distortional buckling remains at the value of 602 kip-in. Without the benefit of a nonlinear finite element analysis it was decided to conduct the experiment with the angle attached. Figure 3.32 shows the failure mode of the new test (D8C097-7E6W) and Figure 3.33 shows the comparison of actuator load-displacement curves. During the new test, the rotation and lateral movement observed in the previous test did not occur. Distortional buckling initiated at the compression flange which rotated against the web-flange junction. Deflection was also observed in the compression portion of web, but it did not trigger the failure. Figure 3.34 shows a comparison of the rotation of the beams at the south loading point, the rotation angle is calculated according to the deflection data from two position transducers. Figure 3.34 indicates the new test (D8C097-7E6W) had little rotation. The new test yielded an increased strength and featured a distortional buckling failure mechanism. Further, the ratio of test-to-DSM prediction is increased from 84% for the old test D8C097-5E4W to 99% for new test D8C097-7E6W. Test D8C097-7E6W is believed to fail in distortional buckling, and its data is included in subsequent analyses. D8C097-5E4W which provides an examination of the role of lateral-torsional buckling is not considered as a distortional buckling test.

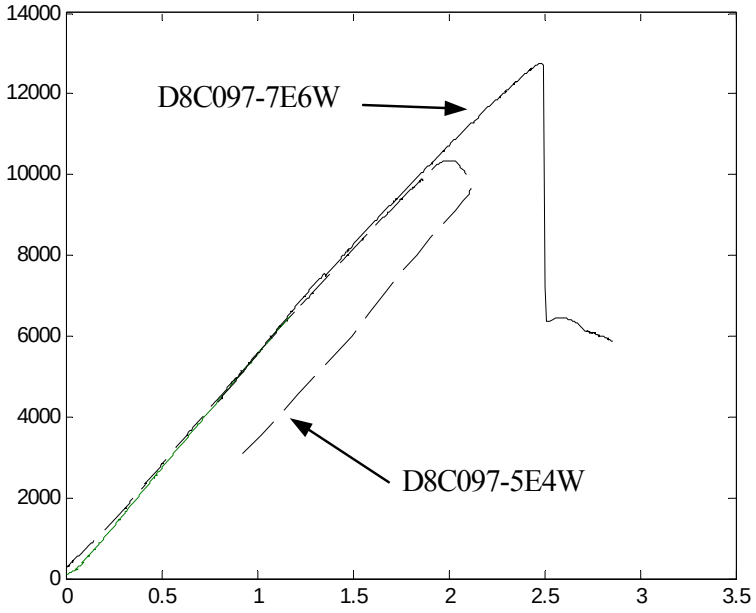

Figure 3.33 Actuator load-displacement curves

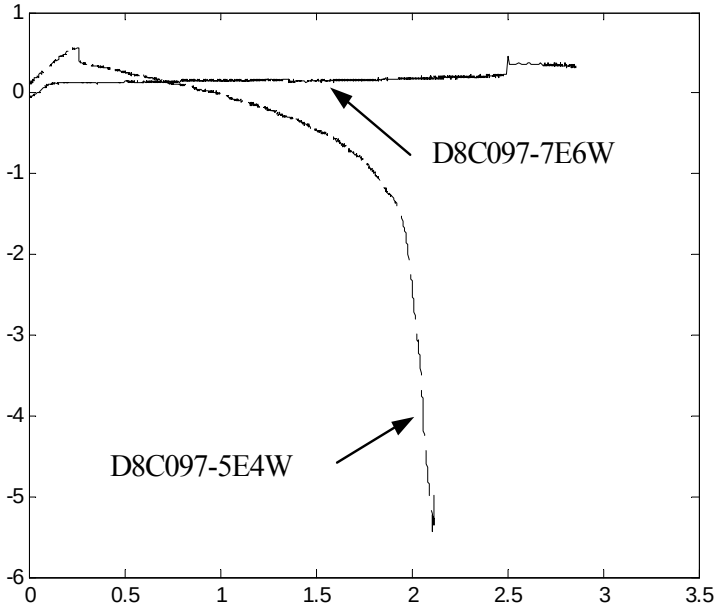

Figure 3.34 Beam rotation at the south loading point

3.5.2 Test Failed by Material Yielding: D3.62C054-3E4W

Test D3.62C054-3E4W is believed to fail primarily by material yielding, based on both the experimental data and observation during the test. The beam's calculated yield moment is 34.3 kip-in. which is much lower than the first elastic buckling (distortional buckling) moment of 65.9 kip-in. The test result is 34.2 kip-in. and this beam showed significant non-linearity, but no sharp strength loss, during the loading process.

Figure 3.35 Test D3.62C054-3E4W

3.5.3 Tests Failed in Local Buckling Mode

Since the distortional buckling test setup allows both local buckling and distortional buckling failures, beams with lower local buckling strength are expected to show a local failure mechanism. Local buckling failures were observed at compression flanges, and in the web, during 3 tests: D8C045-1E2W; D8C033-1E2W; D10C056-3E4W. According to the Direct Strength Method predictions, these tests have lower (or similar) local buckling strength than that of distortional buckling. Therefore, these tests are believed to fail in the local buckling mode and the results are sorted into the local buckling tests.

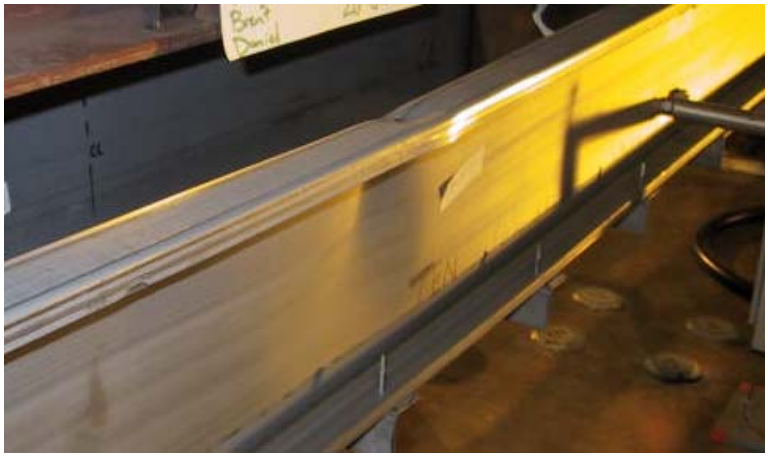

Figure 3.36 Failure of test D8C045-1E2W

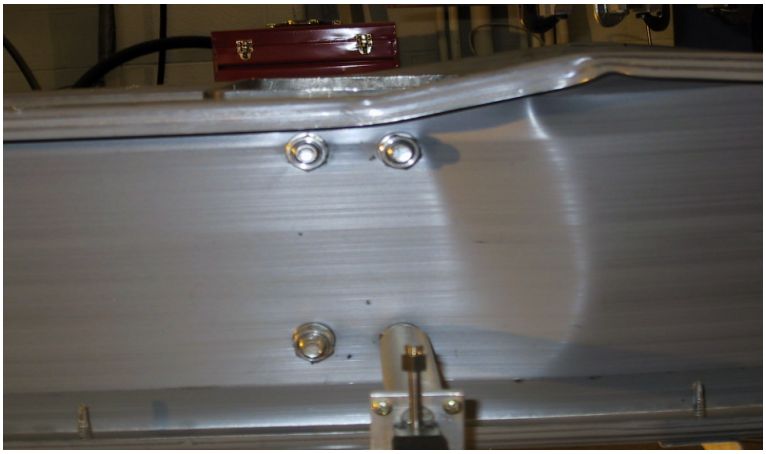

Figure 3.37 Failure of test D8C033-1E2W

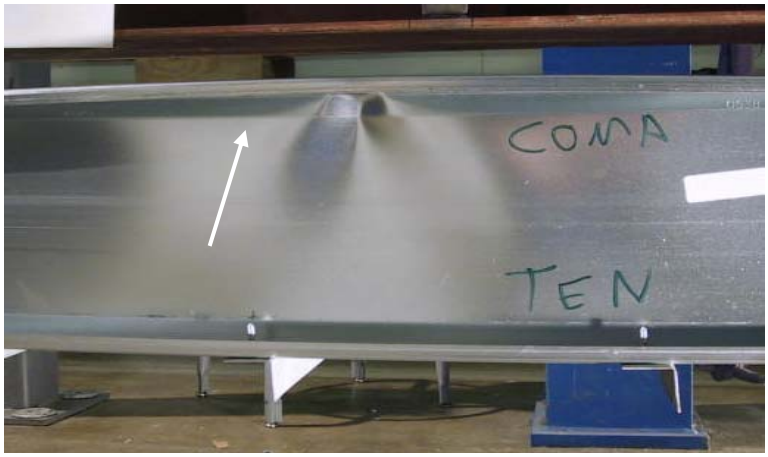

Figure 3.38 Failure of test D10C056-3E4W

It is perhaps noteworthy that the web of the sections in test D10C056-3E4W has an additional small fold line, as pointed out in Figure 3.38 and Figure 3.39. This fold line was identified before the test. The observed local buckling failure occurred on the fold line and the test yielded lower bending capacity, 70% of AISI (1996) prediction and 80% of DSM prediction for distortional buckling failure, than anticipated. Assuming such imperfections to be a normal part of the forming process, this data was kept in the testing database for distortional buckling tests, and not discarded.

Figure 3.39 Initial damage of test D10C056-3E4W

3.5.4 Tests Failed in Unexpected Mode

3.5.4.1 Imperfection Influence

Test D12C068-1E2W had a dent (initial imperfection) in the compression flange, which initiated the failure during testing. Figure 3.40 shows the dent and deformation at the point in the test when the beam buckled. As a result of the dent, the test provided a low bending capacity, about 23% off the distortional buckling prediction by the Direct Strength Method and 30% off the section strength by NAS (2001).

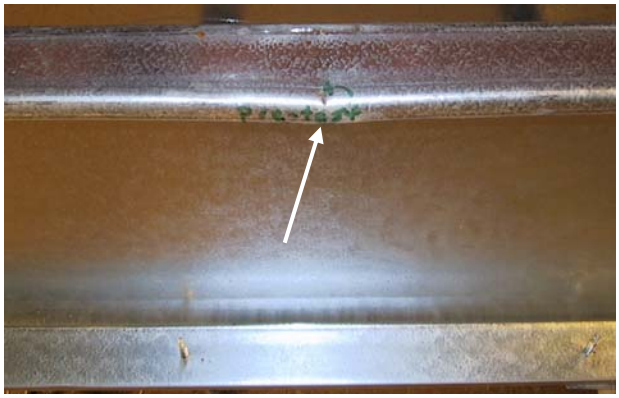

(a) Pre-test damage

(b) Beam buckled

Figure 3.40 Test D12C068-1E2W

While numerical analysis often indicates extreme sensitivity to imperfections (see for example Chapter 5 in this thesis) practicing engineers may assume the sensitivity is an artifact of the analysis method and not real behavior. Tests such as this one indicate that dents and imperfections can have an important and deleterious influence on cold-formed steel section strength. A focused study on the impact of dents on cold-formed steel member capacity and concomitant Quality Assurance/Quality Control (QA/QC) guidelines for handling these dents is overdue in the industry.

3.5.4.2 Shear-Bending Influence

Figure 3.41 shows the failure of test D8.5Z059-6E5E, which occurred outside of the constant moment region. Initial geometric imperfections, uneven specimen setup, and shear-bending interaction are possible reasons for the unexpected failure mode. The test provided an unanticipated low bending capacity, about 17% off the Direct Strength distortional mode prediction and 35% off the section strength by NAS (2001). Test data for these specimens is not included in the subsequent analyses of the distortional buckling tests.

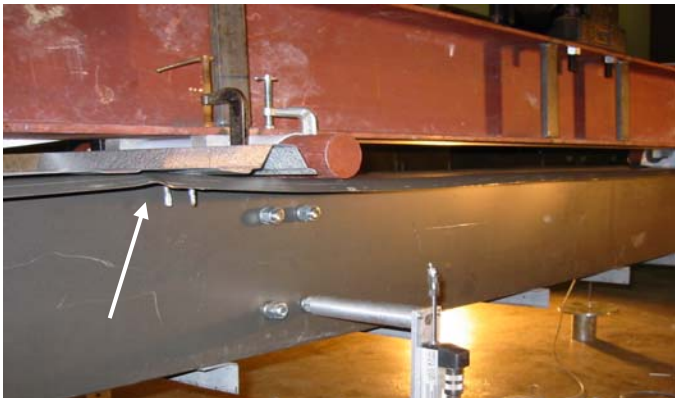

(a) Local failure begins

(b) Deformation continues

Figure 3.41 Failure of test D8.5Z059-6E5W

In design, a check on shear-bending interaction is performed, and would control the strength in this case. If a pure distortional buckling result was desired for this individual

specimen additional supplemental bracing (thicker panel, extra stiffeners, etc.) would be required at this location. The existence of this failure mode makes general procedures to test only for distortional buckling difficult. In our case, the loss of one data point was considered acceptable and this test was not included as a distortional buckling failure.

3.6 Comparison with Design Methods

Six design methods are considered for comparison: AISI (1996), CSA S136 (1994), AS/NZS 4600 (1996), NAS (2001), EN1993 (2002) and DSM (2004). Specific specification predictions of the tested beams are listed in Table 3.4. On average, all six methods give good strength predictions for the local buckling tests. The Direct Strength Method (DSM) uses a single strength curve, while the other five methods apply effective width concepts in the calculation of bending strength. For distortional buckling, only AS/NZS 4600, EN1993 and DSM have specific methodologies. AS/NZS 4600 and DSM employ the minimum of separate local and distortional buckling strength predictions, while EN1993 assumes distortional buckling is an additional reduction on top of local buckling.

Table 3.6 shows that AS/NZS 4600, EN1993, and DSM provide reasonable strength predictions for the distortional buckling failures, though Eurocode (EN1993) still remains about 4% unconservative on average. The Australian/New Zealand code and Direct Strength Method's employ the same basic procedure for distortional buckling, and thus provide the same prediction for the distortional buckling tests. DSM and AS/NZS 4600 statistically give the best results for any of the distortional buckling methods. While, AISI, CSA S136 and NAS provide systematically unconservative predictions for the

distortional buckling strength, with an average error between 10~15%. AISI (1996), CSA S136 (1994) and NAS (2001) are only applicable to local buckling failures.

Table 3.6 Summary of test-to-predicted ratios for existing design methods

			M_{test}/M_{AISI}	M_{test}/M_{S136}	M_{test}/M_{NAS}	$M_{test}/M_{AS/NZS}$	M_{test}/M_{EN1993}	M_{test}/M_{DSM}
Local buckling tests	Controlling specimens	μ	1.01	1.07	1.02	1.01	1.00	1.04
		σ	0.08	0.06	0.07	0.08	0.06	0.07
	Second specimens	μ	0.99	1.05	1.00	0.99	0.99	1.03
		σ	0.08	0.06	0.08	0.08	0.07	0.08
Distortional buckling tests	Controlling specimens	μ	0.86	0.92	0.88	1.02	0.96	1.01
		σ	0.08	0.08	0.09	0.07	0.09	0.07
	Second specimens	μ	0.85	0.90	0.87	1.00	0.94	1.00
		σ	0.08	0.07	0.09	0.07	0.09	0.07

Note: μ – average; σ – standard deviation

Direct Strength Method

The Direct Strength Method (DSM) provides specific strength predictions for both local and distortional buckling of cold-formed steel beams. The provisions for local buckling are presented in Chapter 2, Section 2.4.1. The following equations provide the DSM predictions for the distortional buckling failure of beams:

$$\lambda_d \le 0.673,\ M_{nd} = M_y \tag{3.1}$$

$$\lambda_d > 0.673,\ M_{nd} = \left(1 - 0.22\left(\frac{M_{crd}}{M_y}\right)^{0.5}\right)\left(\frac{M_{crd}}{M_y}\right)^{0.5} M_y \tag{3.2}$$

where $\lambda_d = \sqrt{M_y / M_{crd}}$, M_y = moment at first yield, M_{crd} = critical elastic distortional buckling moment.

Figure 3.42 provides a graphical representation of DSM predictions (Equations 2.1-2.3 for the local mode and Equations 3.1-3.2 for the distortional mode) with the experimental results for both the local and distortional buckling tests. In the figure, M_{cr} represents $M_{cr\ell}$ for the local buckling tests and M_{crd} for the distortional buckling tests. It

is shown that the strength predictions of the Direct Strength Method have good agreement with the results of both local and distortional buckling tests. Local buckling test data are relatively more concentrated along the corresponding design curve than that of distortional buckling tests. The distortional buckling data shows greater deviation as the slenderness $(M_y/M_{cr})^{0.5}$ increases. The overall agreement for M_{DSM} in the distortional buckling tests indicates that distortional buckling dominated the failure mechanism when the compression flanges were unrestrained and validates the general expression used for distortional buckling in the DSM method (which was calibrated to other data).

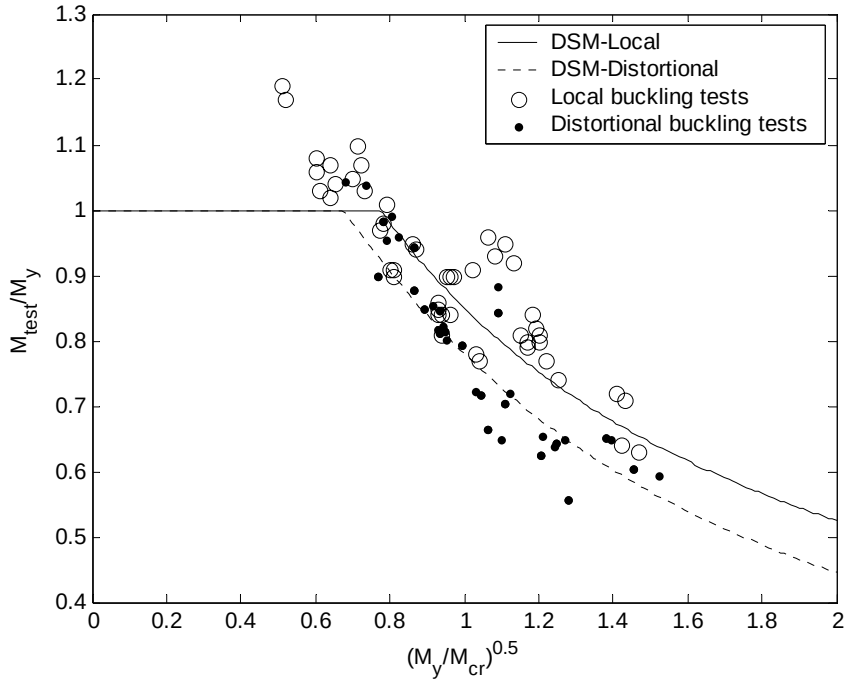

Figure 3.42 Direct Strength Method predictions vs. results of both series of tests

3.6 Conclusions

Experiments on a wide variety of industry standard laterally braced C and Z beams where the compression flange is unrestrained over a distance of 64 in. indicate that distortional buckling is the most likely failure mode. Distortional failures occur even

when local buckling is at a lower critical elastic moment than distortional buckling. Previous testing (local buckling tests, Chapter 2) demonstrated that if additional rotational restraint can be provided to the compression flange, such as by engagement of a through-fastened deck, the distortional mode can be avoided and a local mode triggered instead. While in nearly all of the sections distortional buckling dominated the failure, other limit states are possible, even at unbraced lengths of 64 in. For example, in one test on an 8 in. deep C beam with a nominal t = 0.097 in. and a 64 in. unbraced length lateral-torsional buckling initiated the failure. The thicker specimens have high local and distortional buckling stresses and can thus be controlled by lateral-torsional buckling. The thinnest specimens may also be controlled by other limit states, one member was observed to fail in local buckling, and another in shear-bending interaction. While these failure modes were uncommon, they serve to demonstrate the variety of behavior that may occur at even modest unbraced lengths.

Comparison of the experimental results with existing and proposed design specifications indicates that the previously employed AISI Specification and CSA S136 Specification, as well as the newly adopted NAS, provide a poor prediction of the strength for members failing in the distortional mode. Errors are, on average, 10 – 15 % unconservative for these design specifications. The Eurocode EN1993 which provides some measures for distortional buckling is, on average, 4% unconservative. Two methods which include explicit procedures for distortional buckling AS/NZS 4600 and DSM (recently adopted as Appendix 1 of the NAS) provide better (and simpler) predictions in distortional failures with conservative errors of, on average, 2% and 1% for the respective methods.

Chapter 4

Tensile Tests

4.1 Introduction

The material property (yield stress, ultimate strength and stress-to-strain behavior) of each specimen in both series of tests (Chapters 2 and 3) was obtained by tensile tests following each bending test. The data is used in the calculation of bending strength by the various design methods, and is also employed in the finite element modeling (Chapter 5).

4.2 Testing Setup

The tension tests were carried out following "E8-00, Standard test methods for tension testing of metallic material" (ASTM 2000). The dimensions of a typical tensile coupon are shown in Figure 4.1. A total of three tensile coupons were taken from the end of each specimen: one from the web flat, one from the compression flange flat, and one from the tension flange flat. A screw-driven ATS 900 (Figure 4.2); with a maximum capacity of 10 kips was used for the loading. An MTS 634.11E-54 extensometer was

employed to monitor the deformation (Figure 4.3). Strain gages were installed on selected tensile coupons at the center, and on both sides, to verify the modulus of elasticity E in a few cases.

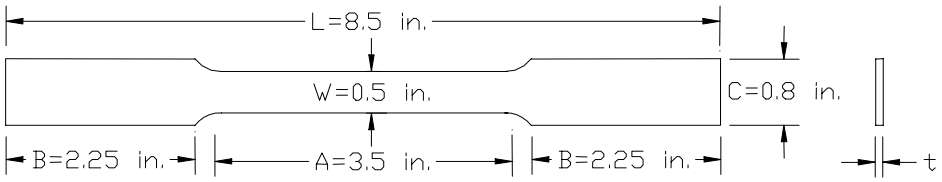

Figure 4.1 Dimensions of tensile coupon

Figure 4.2 Overall view of tension test setup

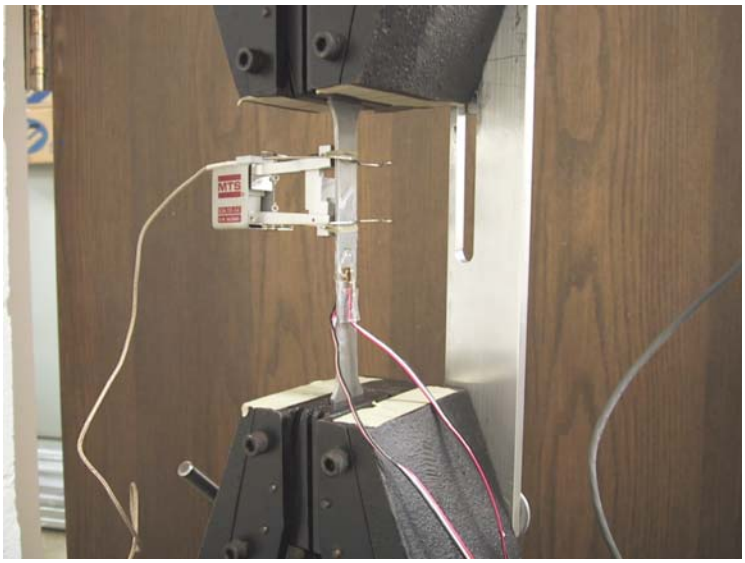

Figure 4.3 Details of tensile coupon with extensometer and strain gages

Two methods for yield strength determination were employed as permitted by ASTM E8: 1) 0.2% Offset Method for the continuous yielding materials (Figure 4.4); and 2) Auto Graphic Diagram Method for the materials exhibiting discontinuous yielding (Figure 4.5).

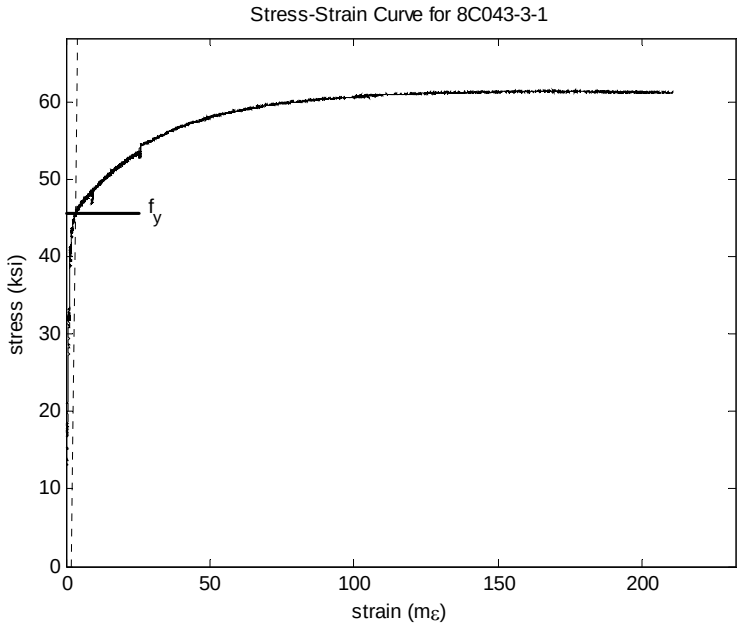

Figure 4.4 Typical tension test result of continuous yielding material

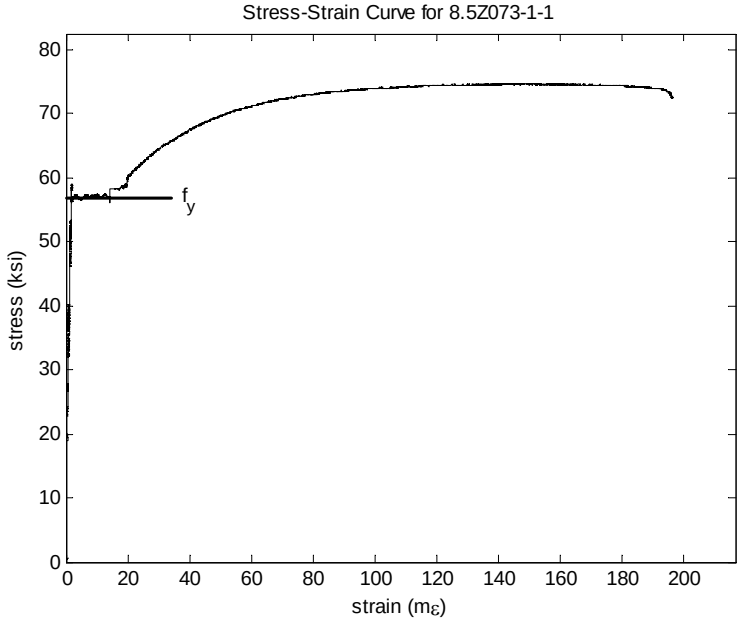

Figure 4.5 Typical tension test result of discontinuous yielding material

4.3 Experimental Results

Tension test results are summarized in Table 4.1 for local buckling tests and Table 4.2 for distortional buckling tests. The yield stress (f_y) varies from thickness to thickness. The Z beams have similar material properties; the yield stresses are between 60 to 70 ksi and for most Z-sections the f_u/f_y ratios are around 130%. On the contrary, the C-sections have greatly varying material properties, the yield stresses are measured from 20 to 85 ksi, and the range of f_u/f_y ratios is from the lowest 101% (for a high strength material) to the highest 207% (for a low strength material). In all cases the tested yield stresses are employed to calculate the beam strength.

In both Table 4.1 and Table 4.2, the specimens with the last sample label number "1" or "2" were cut from the flat area of flanges, the specimens with last sample number "3" were cut from the flat area of the web. Figure 4.6 shows a comparison of the yield stresses of the tensile coupons cut from flanges and webs of the beams. No trends are observed in the data, so it is concluded that the f_y in the web and flange flat are nominally the same. Testing of the tensile properties in the corner regions was not conducted.

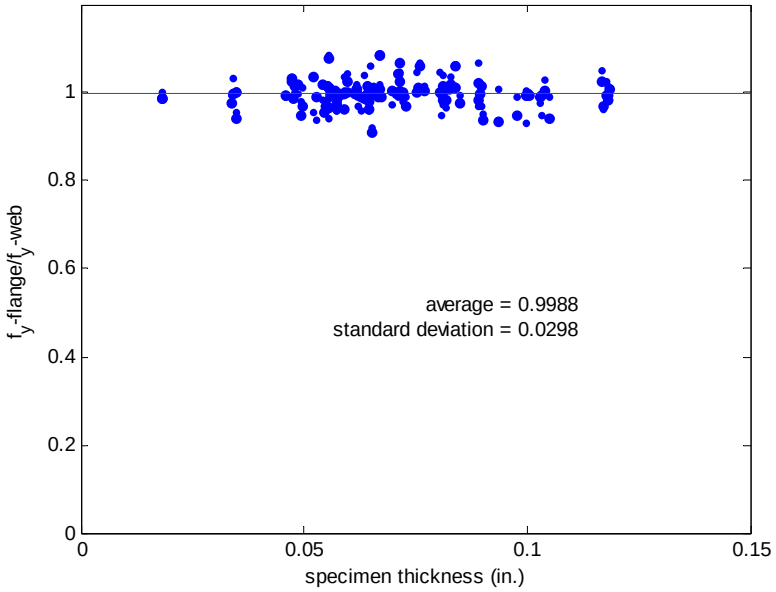

Figure 4.6 Comparison of yield stresses of flange and web

Strain gages were applied for 6 tensile tests to obtain a more accurate value of the elastic modulus, E. Each side of the tensile coupon has one strain gage installed at its center. This setup is selected to help avoid error due to initial bending of the coupon. Table 4.3 gives the test results from the strain gages and the average tested E is 29330 ksi. For design of cold-formed steel, NAS (2001) specifies an E of 29500 ksi. This small series of tests supports this value, therefore the elastic modulus E of the cold-formed steel beams is assumed to be 29500 ksi throughout this research.

Table 4.1 Tension test results of specimens of local buckling tests

Specimen label	Sample label	t (in.)	f_y (ksi)	f_u (ksi)		t (in.)	f_y (ksi)	f_u (ksi)	f_u/f_y
8.5Z073-6	8.5Z073-6-1	0.0723	53.48	72.80	MEAN	0.0720	54.02	72.63	134.5%
	8.5Z073-6-2	0.0721	54.10	72.59	STDEV	0.0003	0.51	0.15	
	8.5Z073-6-3	0.0716	54.48	72.51					
8.5Z073-1	8.5Z073-1-1	0.0713	56.16	74.69	MEAN	0.0715	55.66	74.07	133.1%
	8.5Z073-1-2	0.0719	57.24	74.44	STDEV	0.0003	1.88	0.87	
	8.5Z073-1-3	0.0713	53.58	73.08					
8.5Z073-2	8.5Z073-2-1	0.0718	54.69	73.27	MEAN	0.0720	54.78	73.15	133.5%
	8.5Z073-2-2	0.0725	54.76	72.89	STDEV	0.0005	0.10	0.22	
	8.5Z073-2-3	0.0716	54.88	73.29					
8.5Z073-3	8.5Z073-3-1	0.0725	55.24	73.87	MEAN	0.0720	55.55	74.33	133.8%
	8.5Z073-3-2	0.0717	55.79	74.97	STDEV	0.0004	0.28	0.57	
	8.5Z073-3-3	0.0718	55.63	74.15					
8.5Z073-4	8.5Z073-4-1	0.0718	55.94	74.38	MEAN	0.0715	56.15	74.68	133.0%
	8.5Z073-4-2	0.0713	56.97	75.04	STDEV	0.0003	0.74	0.33	
	8.5Z073-4-3	0.0712	55.53	74.63					
8.5Z073-5	8.5Z073-5-1	0.0729	55.88	73.87	MEAN	0.0727	55.58	73.62	132.5%
	8.5Z073-5-2	0.0727	54.57	72.69	STDEV	0.0002	0.90	0.83	
	8.5Z073-5-3	0.0725	56.29	74.29					
Deck1	Deck-1-1	0.0180	101.76	105.66	MEAN	0.0182	101.24	104.21	102.9%
	Deck-1-2	0.0181	100.44	104.06	STDEV	0.0002	0.71	1.38	
	Deck-1-3	0.0184	101.54	102.91					
8.5Z059-2	8.5Z059-2-1	0.0591	60.54	81.21	MEAN	0.0590	59.10	80.83	136.8%
	8.5Z059-2-2	0.0592	58.31	80.13	STDEV	0.0002	1.25	0.56	
	8.5Z059-2-3	0.0588	58.44	80.95					
8.5Z059-1	8.5Z059-1-1	0.0592	59.87	81.04	MEAN	0.0590	58.90	80.58	136.8%
	8.5Z059-1-2	0.0594	57.33	79.59	STDEV	0.0005	1.37	0.86	
	8.5Z059-1-3	0.0584	59.49	81.12					
8.5Z059-3	8.5Z059-3-1	0.0597	59.60	81.39	MEAN	0.0595	58.46	81.03	138.6%
	8.5Z059-3-2	0.0594	58.66	81.86	STDEV	0.0001	1.25	1.07	
	8.5Z059-3-3	0.0596	57.12	79.83					
8.5Z082-2	8.5Z082-2-1	0.0810	59.87	75.21	MEAN	0.0804	58.10	74.04	127.4%
	8.5Z082-2-2	0.0804	57.28	74.11	STDEV	0.0007	1.53	1.20	
	8.5Z082-2-3	0.0797	57.16	72.81					
8.5Z082-1	8.5Z082-1-1	0.0801	56.34	72.81	MEAN	0.0806	58.37	74.01	126.8%
	8.5Z082-1-2	0.0804	59.37	74.08	STDEV	0.0007	1.76	1.16	
	8.5Z082-1-3	0.0814	59.39	75.13					
8.5Z120-3	8.5Z120-3-1	0.1188	60.99	83.53	MEAN	0.1183	61.34	84.27	137.4%
	8.5Z120-3-2	0.1186	61.75	84.56	STDEV	0.0007	0.38	0.65	
	8.5Z120-3-3	0.1176	61.29	84.73					
8.5Z120-2	8.5Z120-2-1	0.1164	61.18	83.26	MEAN	0.1176	60.05	82.56	137.5%
	8.5Z120-2-2	0.1176	59.30	82.48	STDEV	0.0012	0.99	0.66	
	8.5Z120-2-3	0.1188	59.68	81.95					
8.5Z059-4	8.5Z059-4-1	0.0596	58.72	80.65	MEAN	0.0595	58.63	80.89	138.0%
	8.5Z059-4-2	0.0590	58.65	81.79	STDEV	0.0004	0.09	0.81	
	8.5Z059-4-3	0.0598	58.54	80.23					
8.5Z105-1	8.5Z105-1-1	0.1050	67.77	89.53	MEAN	0.1048	66.85	89.13	133.3%
	8.5Z105-1-2	0.1051	64.43	87.81	STDEV	0.0005	2.11	1.17	
	8.5Z105-1-3	0.1042	68.35	90.06					
8.5Z105-2	8.5Z105-2-1	0.1033	70.09	91.99	MEAN	0.1038	68.84	91.30	132.6%
	8.5Z105-2-2	0.1039	68.40	91.15	STDEV	0.0004	1.10	0.63	
	8.5Z105-2-3	0.1040	68.02	90.75					
8.5Z092-4	8.5Z092-4-1	0.0886	56.77	71.45	MEAN	0.0901	57.36	72.30	126.1%
	8.5Z092-4-2	0.0907	55.79	72.31	STDEV	0.0012	1.93	0.84	
	8.5Z092-4-3	0.0908	59.51	73.13					
8.5Z065-3	8.5Z065-3-1	0.0648	52.76	68.91	MEAN	0.0644	53.52	68.86	128.7%
	8.5Z065-3-2	0.0645	53.86	68.59	STDEV	0.0005	0.66	0.25	
	8.5Z065-3-3	0.0638	53.95	69.08					

Table 4.1 (Continued)

Specimen label	Sample label	t (in.)	f_y (ksi)	f_u (ksi)		t (in.)	f_y (ksi)	f_u (ksi)	f_u/f_y
8C068-1	8C068-1-1	0.0759	53.01	66.57	MEAN	0.0757	51.75	65.34	126.3%
	8C068-1-2	0.0756	52.68	65.62	STDEV	0.0002	1.90	1.40	
	8C068-1-3	0.0756	49.56	63.82					
8C068-2	8C068-2-1	0.0754	52.97	66.96	MEAN	0.0753	51.43	65.95	128.2%
	8C068-2-2	0.0758	50.71	65.87	STDEV	0.0005	1.34	0.98	
	8C068-2-3	0.0749	50.60	65.01					
8.5Z092-2	8.5Z092-2-1	0.0908	59.11	72.66	MEAN	0.0891	56.99	71.91	126.2%
	8.5Z092-2-2	0.0888	56.51	71.80	STDEV	0.0016	1.93	0.71	
	8.5Z092-2-3	0.0877	55.34	71.25					
8C043-1	8C043-1-1	0.0474	46.11	61.24	MEAN	0.0475	46.08	61.33	133.1%
	8C043-1-2	0.0475	45.75	61.07	STDEV	0.0001	0.31	0.31	
	8C043-1-3	0.0476	46.36	61.68					
8.5Z065-1	8.5Z065-1-1	0.0642	53.48	68.92	MEAN	0.0642	53.07	68.58	129.2%
	8.5Z065-1-2	0.0650	52.86	68.44	STDEV	0.0008	0.35	0.30	
	8.5Z065-1-3	0.0634	52.88	68.37					
8C043-3	8C043-3-1	0.0472	46.76	61.48	MEAN	0.0472	47.63	61.48	129.1%
	8C043-3-2	0.0470	48.84	61.73	STDEV	0.0002	1.08	0.25	
	8C043-3-3	0.0474	47.31	61.22					
8C043-5	8C043-5-1	0.0496	46.66	60.76	MEAN	0.0496	45.83	60.97	133.0%
	8C043-5-2	0.0496	44.69	61.27	STDEV	0.0000	1.02	0.27	
	8C043-5-3	0.0496	46.13	60.87					
8C043-6	8C043-6-1	0.0489	45.31	60.31	MEAN	0.0491	45.11	60.78	134.7%
	8C043-6-2	0.0492	43.87	61.15	STDEV	0.0002	1.16	0.43	
	8C043-6-3	0.0494	46.16	60.89					
8C097-2	8C097-2-1	0.0976	60.51	76.36	MEAN	0.0978	59.89	76.69	128.0%
	8C097-2-2	0.0974	58.07	76.33	STDEV	0.0006	1.61	0.59	
	8C097-2-3	0.0984	61.11	77.37					
Deck2	Deck-2-1	0.0185	100.18	101.81	MEAN	0.0183	100.72	101.54	100.8%
	Deck-2-2	0.0183	100.40	100.40	STDEV	0.0002	0.74	1.02	
	Deck-2-3	0.0181	101.56	102.40					
8C068-4	8C068-4-1	0.0770	53.50	66.87	MEAN	0.0768	53.05	66.25	124.9%
	8C068-4-2	0.0765	52.95	65.78	STDEV	0.0003	0.40	0.56	
	8C068-4-3	0.0769	52.71	66.10					
8C054-8	8C054-8-1	0.0542	39.69	53.02	MEAN	0.0540	40.35	52.75	130.7%
	8C054-8-2	0.0540	41.04	52.84	STDEV	0.0002	0.68	0.32	
	8C054-8-3	0.0538	40.31	52.40					
8C097-3	8C097-3-1	0.0971	61.31	77.99	MEAN	0.0936	59.64	76.12	127.6%
	8C097-3-2*	0.0862	56.83	72.62	STDEV	0.0064	2.45	3.03	
	8C097-3-3	0.0976	60.77	77.74					
8C054-1	8C054-1-1	0.0543	39.84	52.19	MEAN	0.0545	40.04	52.05	130.0%
	8C054-1-2	0.0556	39.21	51.11	STDEV	0.0010	0.94	0.88	
	8C054-1-3	0.0537	41.06	52.85					
8C068-5	8C068-5-1	0.0749	48.84	65.01	MEAN	0.0755	48.58	64.58	132.9%
	8C068-5-2	0.0755	48.71	64.41	STDEV	0.0005	0.34	0.38	
	8C068-5-3	0.0760	48.19	64.31					
4C054-1	4C054-1-1	0.0557	44.25	54.86	MEAN	0.0551	44.97	55.49	123.4%
	4C054-1-2	0.0545	45.69	56.11	STDEV	0.0006	0.72	0.63	
	4C054-1-2	0.0551	44.97	55.49					
4C054-2	4C054-2-1	0.0559	44.45	54.38	MEAN	0.0561	44.71	54.54	122.0%
	4C054-2-2	0.0562	44.98	54.69	STDEV	0.0001	0.26	0.15	
	4C054-2-3	0.0561	44.71	54.54					
3.62C054-1	3.62C054-1-1	0.0553	32.43	53.93	MEAN	0.0555	32.77	53.91	164.5%
	3.62C054-1-2	0.0557	33.12	53.90	STDEV	0.0002	0.35	0.02	
	3.62C054-1-3	0.0555	32.77	53.91					
4C054-1	4C054-1-1	0.0557	44.25	54.86	MEAN	0.0551	44.97	55.49	123.4%
	4C054-1-2	0.0545	45.69	56.11	STDEV	0.0006	0.72	0.63	
	4C054-1-2	0.0551	44.97	55.49					

Table 4.1 (Continued)

Specimen label	Sample label	t (in.)	f_y (ksi)	f_u (ksi)		t (in.)	f_y (ksi)	f_u (ksi)	f_u/f_y
3.62C054-2	3.62C054-2-1	0.0550	31.57	54.40	MEAN	0.0554	31.98	54.11	169.2%
	3.62C054-2-2	0.0557	32.40	53.82	STDEV	0.0003	0.42	0.29	
	3.62C054-2-3	0.0554	31.98	54.11					
6C054-1	6C054-1-1**	0.0618	36.96	49.87	MEAN	0.0616	36.96	50.01	135.3%
	6C054-1-2	0.0615	37.11	50.15	STDEV	0.0002	0.15	0.14	
	6C054-1-3	0.0616	36.81	50.01					
6C054-2	6C054-2-1	0.0614	35.93	50.38	MEAN	0.0616	36.10	50.22	139.1%
	6C054-2-2	0.0618	36.27	50.28	STDEV	0.0002	0.17	0.19	
	6C054-2-3	0.0616	36.10	50.01					
12C068-9	12C068-9-1	0.0652	34.26	57.85	MEAN	0.0652	35.08	58.50	166.8%
	12C068-9-2	0.0655	33.84	58.15	STDEV	0.0002	1.79	0.88	
	12C068-9-3	0.0650	37.13	59.51					
12C068-3	12C068-3-1	0.0675	56.47	75.19	MEAN	0.0671	56.64	74.90	132.3%
	12C068-3-2	0.0670	56.44	75.10	STDEV	0.0003	0.32	0.42	
	12C068-3-3	0.0668	57.00	74.42					
12C068-5	12C068-5-1	0.0658	35.21	58.22	MEAN	0.0654	34.86	58.63	168.2%
	12C068-5-2	0.0650	34.64	59.30	STDEV	0.0004	0.31	0.59	
	12C068-5-3	0.0656	34.72	58.36					
10C068-2	10C068-2-1	0.0571	33.53	56.76	MEAN	0.0572	33.56	57.32	170.8%
	10C068-2-2	0.0572	33.32	57.50	STDEV	0.0002	0.26	0.49	
	10C068-2-3	0.0574	33.84	57.69					
12C068-4	12C068-4-1	0.0671	56.07	74.24	MEAN	0.0670	57.28	75.93	132.6%
	12C068-4-2	0.0654	60.31	79.85	STDEV	0.0015	2.64	3.41	
	12C068-4-3	0.0684	55.46	73.71					
10C068-1	10C068-1-1	0.0576	33.55	56.28	MEAN	0.0573	34.19	56.93	166.5%
	10C068-1-2	0.0571	34.06	57.52	STDEV	0.0003	0.71	0.62	
	10C068-1-3	0.0572	34.96	56.99					
10C068-2	10C068-2-1	0.0571	33.53	56.76	MEAN	0.0572	33.56	57.32	170.8%
	10C068-2-2	0.0572	33.32	57.50	STDEV	0.0002	0.26	0.49	
	10C068-2-3	0.0574	33.84	57.69					
12C068-4	12C068-4-1	0.0671	56.07	74.24	MEAN	0.0670	57.28	75.93	132.6%
	12C068-4-2	0.0654	60.31	79.85	STDEV	0.0015	2.64	3.41	
	12C068-4-3	0.0684	55.46	73.71					
10C068-1	10C068-1-1	0.0576	33.55	56.28	MEAN	0.0573	34.19	56.93	166.5%
	10C068-1-2	0.0571	34.06	57.52	STDEV	0.0003	0.71	0.62	
	10C068-1-3	0.0572	34.96	56.99					
11.5Z073-1	11.5Z073-1-1	0.0691	65.46	82.82	MEAN	0.0695	66.82	84.55	126.5%
	11.5Z073-1-2	0.0697	67.67	85.43	STDEV	0.0004	1.19	1.49	
	11.5Z073-1-3	0.0698	67.32	85.39					
11.5Z073-2	11.5Z073-2-1	0.0708	64.18	80.89	MEAN	0.0709	65.40	82.82	126.6%
	11.5Z073-2-2	0.0698	67.38	85.32	STDEV	0.0011	1.73	2.27	
	11.5Z073-2-3	0.0719	64.64	82.26					
11.5Z082-1	11.5Z082-1-1	0.0842	61.73	80.36	MEAN	0.0838	60.43	79.92	132.3%
	11.5Z082-1-2	0.0841	61.52	80.66	STDEV	0.0005	2.07	1.03	
	11.5Z082-1-3	0.0833	58.04	78.75					
11.5Z082-2	11.5Z082-2-1	0.0842	61.91	82.33	MEAN	0.0837	61.49	81.00	131.7%
	11.5Z082-2-2	0.0830	61.64	80.22	STDEV	0.0006	0.51	1.16	
	11.5Z082-2-3	0.0839	60.92	80.45					
11.5Z092-1	11.5Z092-1-1	0.1022	60.29	78.62	MEAN	0.1027	61.02	78.54	128.7%
	11.5Z092-1-2	0.1025	61.09	78.83	STDEV	0.0006	0.70	0.35	
	11.5Z092-1-3	0.1034	61.68	78.16					
11.5Z092-2	11.5Z092-2-1	0.1029	58.46	76.90	MEAN	0.1033	60.42	78.00	129.1%
	11.5Z092-2-2	0.1036	61.19	78.18	STDEV	0.0004	1.71	1.02	
	11.5Z092-2-3	0.1035	61.60	78.92					

Note: MEAN --- mean value; STDEV --- standard deviation

Table 4.2 Tension test results of specimens of distortional buckling tests

Specimen label	Sample label	t (in.)	f_y (ksi)	f_u (ksi)		t (in.)	f_y (ksi)	f_u (ksi)	f_u/f_y
D11.5Z092-2	D11.5Z092-2-1	0.0902	64.85	82.00	MEAN	0.0889	65.86	84.25	127.9%
	D11.5Z092-2-2	0.0889	65.86	84.25	STDEV	0.0013	1.00	2.25	
	D11.5Z092-2-3	0.0876	66.86	86.51					
D11.5Z092-3	D11.5Z092-3-1	0.0818	71.16	90.15	MEAN	0.0827	69.89	89.91	128.6%
	D11.5Z092-3-2	0.0827	69.89	89.91	STDEV	0.0009	1.27	0.24	
	D11.5Z092-3-3	0.0836	68.63	89.67					
D11.5Z082-5	D11.5Z082-5-1	0.0812	70.58	91.82	MEAN	0.8180	71.80	92.02	128.2%
	D11.5Z082-5-2	0.0818	71.80	92.02	STDEV	0.0006	1.23	0.20	
	D11.5Z082-5-3	0.0824	73.03	92.21					
D11.5Z082-4	D11.5Z082-4-1	0.0800	73.80	95.36	MEAN	0.0812	73.65	93.21	126.6%
	D11.5Z082-4-2	0.0812	73.65	93.21	STDEV	0.0012	0.16	2.14	
	D11.5Z082-4-3	0.0824	73.49	91.07					
D12C068-2	D12C068-2-1	0.0663	56.31	73.79	MEAN	0.0664	56.31	73.69	130.9%
	D12C068-2-2	0.0664	56.05	73.69	STDEV	0.0002	0.27	0.10	
	D12C068-2-3	0.0666	56.58	73.60					
D12C068-10	D12C068-10-1	0.0646	36.05	55.85	MEAN	0.0648	34.70	56.75	163.5%
	D12C068-10-2	0.0646	34.06	57.33	STDEV	0.0004	1.16	0.79	
	D12C068-10-3	0.0653	34.01	57.07					
D12C068-11	D12C068-11-1	0.0632	32.28	56.41	MEAN	0.0645	32.90	56.92	173.0%
	D12C068-11-2	0.0649	32.90	57.29	STDEV	0.0011	0.62	0.46	
	D12C068-11-3	0.0653	33.52	57.08					
D10C068-4	D10C068-4-1	0.0627	21.50	39.92	MEAN	0.0626	22.01	40.26	182.9%
	D10C068-4-2	0.0626	22.16	40.38	STDEV	0.0001	0.45	0.29	
	D10C068-4-3	0.0624	22.38	40.47					
D10C068-3	D10C068-3-1	0.0644	23.23	41.17	MEAN	0.0634	22.54	40.87	181.3%
	D10C068-3-2	0.0631	22.05	40.52	STDEV	0.0009	0.61	0.32	
	D10C068-3-3	0.0626	22.34	40.91					
D12C068-1	D12C068-1-1	0.0665	56.45	73.83	MEAN	0.0668	55.86	73.61	131.8%
	D12C068-1-2	0.0669	55.82	74.13	STDEV	0.0003	0.57	0.65	
	D12C068-1-3	0.0671	55.32	72.88					
D8.5Z082-4	D8.5Z082-4-1	0.0820	60.53	75.00	MEAN	0.0810	59.21	74.02	125.0%
	D8.5Z082-4-2	0.0810	58.98	73.92	STDEV	0.0010	1.22	0.93	
	D8.5Z082-4-3	0.0801	58.12	73.15					
D8.5Z120-1	D8.5Z120-1-1	0.1175	62.91	84.19	MEAN	0.1181	61.89	83.26	134.5%
	D8.5Z120-1-2	0.1180	60.89	82.55	STDEV	0.0007	1.01	0.84	
	D8.5Z120-1-3	0.1189	61.87	83.04					
D8.5Z120-4	D8.5Z120-4-1	0.1170	61.50	83.87	MEAN	0.1181	61.35	83.10	135.5%
	D8.5Z120-4-2	0.1184	60.82	82.57	STDEV	0.0010	0.47	0.68	
	D8.5Z120-4-3	0.1189	61.73	82.85					
D8.5Z082-3	D8.5Z082-3-1	0.0802	58.26	72.84	MEAN	0.0810	58.99	73.85	125.2%
	D8.5Z082-3-2	0.0808	58.93	74.12	STDEV	0.0009	0.76	0.91	
	D8.5Z082-3-3	0.0819	59.78	74.59					
D8.5Z092-1	D8.5Z092-1-1	0.0880	56.30	71.18	MEAN	0.0897	57.75	72.59	125.7%
	D8.5Z092-1-2	0.0906	58.95	74.13	STDEV	0.0014	1.35	1.48	
	D8.5Z092-1-3	0.0904	58.01	72.46					
D8.5Z092-3	D8.5Z092-3-1	0.0907	58.54	72.94	MEAN	0.0893	57.59	72.14	125.3%
	D8.5Z092-3-2	0.0891	57.09	71.90	STDEV	0.0013	0.82	0.71	
	D8.5Z092-3-3	0.0882	57.15	71.58					
D8C043-4	D8C043-4-1	0.0463	45.27	60.91	MEAN	0.0459	45.44	61.04	134.3%
	D8C043-4-2	0.0455	45.44	61.13	STDEV	0.0004	0.17	0.11	
	D8C043-4-3	0.0459	45.61	61.07					
D8C043-2	D8C043-2-1	0.0471	45.81	61.66	MEAN	0.0472	45.47	61.01	134.2%
	D8C043-2-2	0.0468	45.87	61.16	STDEV	0.0005	0.64	0.74	
	D8C043-2-3	0.0477	44.73	60.21					
D8C054-7	D8C054-7-1	0.0533	39.25	51.61	MEAN	0.0528	40.81	52.52	128.7%
	D8C054-7-2	0.0527	41.44	52.56	STDEV	0.0005	1.36	0.90	
	D8C054-7-3	0.0523	41.74	53.40					

Table 4.2 (Continued)

Specimen label	Sample label	t (in.)	f_y (ksi)	f_u (ksi)		t (in.)	f_y (ksi)	f_u (ksi)	f_u/f_y
D8.5Z065-2	D8.5Z065-2-1	0.0651	62.11	82.43	MEAN	0.0645	62.79	83.24	132.6%
	D8.5Z065-2-2	0.0644	62.90	83.48	STDEV	0.0006	0.63	0.72	115.1%
	D8.5Z065-2-3	0.0639	63.35	83.82					
D8.5Z065-3	D8.5Z065-3-1	0.0638	62.38	83.28	MEAN	0.0645	63.34	83.36	131.6%
	D8.5Z065-3-2	0.0649	62.61	83.19	STDEV	0.0006	1.48	0.23	15.3%
	D8.5Z065-3-3	0.0647	65.05	83.62					
D8.5Z065-4	D8.5Z065-4-1	0.0638	62.53	83.87	MEAN	0.0642	62.36	83.47	133.9%
	D8.5Z065-4-2	0.0641	62.77	83.54	STDEV	0.0005	0.53	0.44	83.4%
	D8.5Z065-4-3	0.0648	61.76	83.00					
D8.5Z065-1	D8.5Z065-1-1	0.0614	57.18	77.77	MEAN	0.0619	58.26	78.44	134.6%
	D8.5Z065-1-2	0.0619	58.62	78.84	STDEV	0.0004	0.95	0.58	
	D8.5Z065-1-3	0.0623	58.97	78.71					
D8.5Z059-1	D8.5Z059-1-1	0.0612	59.15	80.04	MEAN	0.0615	59.05	79.41	134.5%
	D8.5Z059-1-2	0.0608	58.92	79.19	STDEV	0.0009	0.12	0.55	
	D8.5Z059-1-3	0.0625	59.07	79.00					
D8.5Z115-1	D8.5Z115-1-1	0.1172	67.38	85.47	MEAN	0.1166	65.79	84.67	128.7%
	D8.5Z115-1-2	0.1166	65.79	84.67	STDEV	0.0006	1.59	0.80	
	D8.5Z115-1-3	0.1160	64.21	83.87					
D8.5Z115-2	D8.5Z115-2-1	0.1168	63.13	83.09	MEAN	0.1171	64.14	83.88	130.8%
	D8.5Z115-2-2	0.1169	63.68	83.88	STDEV	0.0004	1.29	0.80	
	D8.5Z115-2-3	0.1176	65.60	84.68					
D8.5Z059-2	D8.5Z059-2-1	0.0624	59.12	79.53	MEAN	0.0618	58.54	79.11	135.1%
	D8.5Z059-2-2	0.0618	58.50	79.29	STDEV	0.0005	0.56	0.53	
	D8.5Z059-2-3	0.0613	58.00	78.51					
D3.62C054-3	D3.62C050-3-1	0.0557	33.85	53.54	MEAN	0.0556	32.91	53.32	162.0%
	D3.62C050-3-2	0.0558	33.68	53.72	STDEV	0.0003	1.48	0.55	
	D3.62C050-3-3	0.0553	31.21	52.69					
D3.62C054-4	D3.62C050-4-1	0.0555	31.21	53.67	MEAN	0.0555	32.11	53.56	166.8%
	D3.62C050-4-2	0.0554	31.99	53.37	STDEV	0.0001	0.97	0.16	
	D3.62C050-4-3	0.0556	33.14	53.63					
D8C054-6	D8C054-6-1	0.0505	38.96	49.16	MEAN	0.0520	40.68	50.85	125.0%
	D8C054-6-2	0.0527	42.27	51.78	STDEV	0.0013	1.66	1.47	
	D8C054-6-3	0.0527	40.81	51.62					
D8C097-5	D8C097-5-1	0.0996	79.96	88.24	MEAN	0.0998	83.73	90.74	108.4%
	D8C097-5-2	0.0999	85.35	92.17	STDEV	0.0002	3.28	2.17	
	D8c097-5-3	0.0999	85.90	91.82					
D8C033-2	D8C033-2-1	0.0334	20.53	41.36	MEAN	0.0337	20.47	41.95	205.0%
	D8C033-2-2	0.0339	20.22	41.70	STDEV	0.0003	0.23	0.75	
	D8C033-2-3	0.0338	20.66	42.80					
D8C033-1	D8C033-1-1	0.0342	20.83	42.55	MEAN	0.0339	20.35	42.19	207.3%
	D8C033-1-2	0.0337	20.08	41.80	STDEV	0.0002	0.42	0.37	
	D8C033-1-3	0.0338	20.14	42.22					
D8C097-4	D8C097-4-1	0.0998	84.74	91.46	MEAN	0.0998	84.16	91.08	108.2%
	D8C097-4-2	0.0997	83.57	90.69	STDEV	0.0001	0.58	0.39	
	D8C097-4-3	0.0998	84.16	91.08					
D8C068-6	D8C068-6-1	0.0709	78.90	80.81	MEAN	0.0708	78.94	80.75	102.3%
	D8C068-6-2	0.0708	78.98	80.68	STDEV	0.0000	0.04	0.06	
	D8C068-6-3	0.0709	78.94	80.75					
D8C068-7	D8C068-7-1	0.0707	79.90	81.05	MEAN	0.0708	79.87	80.87	101.3%
	D8C068-7-2	0.0708	79.83	80.69	STDEV	0.0001	0.04	0.18	
	D8C068-7-3	0.0709	79.87	80.87					
D8C097-6	D8C097-6-1	0.1005	85.27	91.82	MEAN	0.1005	85.27	91.82	107.7%
	D8C097-6-2	0.1002	85.07	91.69	STDEV	0.0003	0.20	0.13	
	D8C087-6-3	0.1007	85.47	91.96					
D8C097-7	D8C097-7-1	0.0997	85.00	90.00	MEAN	0.1001	85.18	90.77	106.6%
	D8C097-7-2	0.1006	85.18	90.73	STDEV	0.0004	0.18	0.79	
	D8C087-7-3	0.1001	85.36	91.58					

Table 4.2 (Continued)

Specimen label	Sample label	t (in.)	f_y (ksi)	f_u (ksi)		t (in.)	f_y (ksi)	f_u (ksi)	f_u/f_y
D10C048-1	D10C048-1-1	0.0479	50.93	58.29	MEAN	0.0478	51.08	58.54	114.6%
	D10C048-1-2	0.0476	51.52	58.66	STDEV	0.0001	0.39	0.22	
	D10C048-1-3	0.0479	50.78	58.67					
D10C048-2	D10C048-2-1	0.0486	50.19	57.96	MEAN	0.0486	50.62	57.77	114.1%
	D10C048-2-2	0.0486	51.34	57.72	STDEV	0.0000	0.63	0.17	
	D10C048-2-3	0.0486	50.34	57.64					
D10C056-3	D10C056-3-1	0.0566	77.08	81.68	MEAN	0.0569	77.28	80.38	104.0%
	D10C056-3-2	0.0569	77.58	78.32	STDEV	0.0004	0.26	1.80	
	D10C056-3-3	0.0573	77.18	81.12					
D10C056-4	D10C056-4-1	0.0564	77.07	81.97	MEAN	0.0569	76.93	81.60	106.1%
	D10C056-4-2	0.0570	76.85	81.45	STDEV	0.0005	0.12	0.31	
	D10C056-4-3	0.0574	76.86	81.40					
D8C085-1	D8C085-1-1	0.0847	52.03	64.05	MEAN	0.0848	51.85	64.17	123.8%
	D8C085-1-2	0.0848	51.15	64.05	STDEV	0.0000	0.62	0.20	
	D8C085-1-3	0.0848	52.35	64.39					
D8C085-2	D8C085-2-1	0.0824	53.29	66.00	MEAN	0.0825	52.80	65.85	124.7%
	D8C085-2-2	0.0823	52.81	66.14	STDEV	0.0002	0.49	0.39	
	D8C085-2-3	0.0827	52.31	65.41					
D6C063-2	D6C063-2-1	0.0577	56.09	67.13	MEAN	0.0578	55.94	66.77	119.4%
	D6C063-2-2	0.0581	55.72	66.26	STDEV	0.0002	0.20	0.46	
	D6C063-2-3	0.0576	56.01	66.93					
D6C063-1	D6C063-1-1	0.0558	58.36	69.81	MEAN	0.0559	57.82	69.46	120.1%
	D6C063-1-2	0.0562	57.53	69.09	STDEV	0.0002	0.47	0.36	
	D6C063-1-3	0.0558	57.56	69.47					
D8C045-1	D8C045-1-1	0.0343	21.44	42.59	MEAN	0.0348	21.38	42.67	199.6%
	D8C045-1-2	0.0354	21.36	42.16	STDEV	0.0005	0.05	0.56	
	D8C045-1-3	0.0346	21.34	43.27					
D8C045-2	D8C045-2-1	0.0348	20.81	42.47	MEAN	0.0348	21.04	42.64	202.7%
	D8C045-2-2	0.0348	20.52	42.48	STDEV	0.0000	0.66	0.29	
	D8C045-2-3	0.0348	21.77	42.97					

Table 4.3 Elastic moduli data from strain gages

Specimen label	E1 (10^3 ksi)	E2 (10^3 ksi)	Average (10^3 ksi)
8.5Z059-3-1	29.36	29.61	29.49
8.5Z059-3-3	29.91	29.04	29.48
8.5Z082-2-1	30.42	28.55	29.45
8.5Z082-2-3	31.03	27.41	29.14
8C043-3-3	29.14	29.57	29.35
8C043-6-1	29.51	28.65	29.08
mean			29.33

Note: E1 --- elastic moduli from strain gage 1
E2 --- elastic moduli from strain gage 2

Chapter 5

Finite Element Modeling of Cold-Formed Steel Beams

5.1 Introduction

The finite element method (FEM) is a numerical procedure for analyzing structures and continua. Basically, FEM is used to solve partial differential equations by replacing continuous functions by piecewise approximations defined on polygons, which are referred to as elements. Usually polynomial approximations are used. The finite element method reduces the problem of finding the solution at the vertices of the polygons to that of solving a set of linear equations. FEM originated in structural engineering, and has been used in the fields of heat transfer, fluid flow, electric and magnetic fields and many others. The finite element method has been proven as an efficient and powerful approach to calculate the elastic buckling load and ultimate strength of cold-formed steel (CFS) structural members. A successful static analysis of the unstable collapse and postbuckling behavior of CFS members requires the nonlinear solution method consider geometric nonlinearity, material nonlinearity, boundary nonlinearity and residual stresses of the

physical objects, as well as have the capability to deal with convergence, locking and other difficulties related to implementing the numerical algorithm.

The commercial finite element package ABAQUS 6.2 (ABAQUS 2001) is used for both elastic buckling and postbuckling analysis of cold-formed steel beams in this research. The finite strip method (FSM) software CUFSM is also employed to calculate the elastic buckling moments of cold-formed steel sections. The finite element model is verified by two completed series of buckling tests (Chapters 2 and 3) and is then applied to analyze other cold-formed steel sections, which are not examined in the physical tests conducted for this research.

5.2 Elastic Buckling Solution Methods

5.2.1 Finite Element Method

Consider a linear elastic structure in an equilibrium state at a reference level of loading $\{R\}_{ref}$, in general the load and displacement relation can be described by the finite element method as:

$$([K]+[K_\sigma])\{D\}=\{R\} \tag{5.1}$$

where, [K] is the initial stiffness matrix, $[K_\sigma]$ is the geometric stiffness matrix, $\{D\}$ is the nodal displacements and $\{R\}$ is the nodal loads.

Now, introducing the reference level of loading, equation 5.1 is revised as:

$$([K]+\lambda[K_\sigma]_{ref})\{D\}=\lambda\{R\}_{ref} \tag{5.2}$$

where λ is a scalar multiplier, and $[K_\sigma]=\lambda[K_\sigma]_{ref}$ when $\{R\}=\lambda\{R\}_{ref}$.

When buckling is reached, the structure can move from an equilibrium configuration to another by a infinitesimal displacement increment dD without changing the load $\{R\}$, therefore equation 5.3 can be obtained.

$$([K]+\lambda[K_\sigma]_{ref})\{D\}=([K]+\lambda[K_\sigma]_{ref})\{D+dD\}=\lambda\{R\}_{ref} \tag{5.3}$$

The equation can be simplified as:

$$([K]+\lambda[K_\sigma]_{ref})\{dD\}=0 \tag{5.4}$$

Equation 5.4 is an eigenvalue problem, the eigenvalue λ is associated with the critical buckling load, and the eigenvector $\{dD\}$ defines the buckling mode shape. The elastic buckling solution of cold-formed steel members is an eigenvalue problem, ABAQUS offers the Lanczos and the subspace iteration method for eigenvalue extraction. The Lanczos methods is generally faster when a large number of eigenmodes is required, while the subspace iteration method is suitable when only a few eigenmodes are required (less than 20). In this research, the Lanczos method is selected because normally more than 30 modes are needed to capture all three typical buckling modes (local, distortional and lateral-torsional) of cold-formed steel beams, also the Lanczos method has more useful options in ABAQUS, as it allows the user to specify the minimum and/or maximum eigenvalues of interest. Subspace iteration only allows the user to set the maximum eigenvalue.

5.2.2 Finite Strip Method

The finite strip method was originally introduced by Y. K. Cheung and the details of this method are well presented in his book (Cheung 1997). The use of the finite strip method for cold-formed steel members has been greatly extended by G. Hancock.

(Hancock 1977, 1978, 1994) and the finite strip method has been shown to be an efficient tool for analyzing structures with regular geometric section and simple boundary conditions. The finite strip method is, in fact, a variation of the finite element method. Both methods use the same basic methodology and theory. Piecewise shape functions are utilized to approximate the continuous curves (functions) in terms of nodal degrees of freedom. The only difference between the finite element and finite strip methods is the discretization. The finite strip method employs a single element (strip) to model the longitudinal direction instead of a series of full elements, as shown in Figure 5.1. As a result, by using the finite strip method, the total number of elements or equations needed for the solution are greatly reduced compared with that of a typical finite element solution.

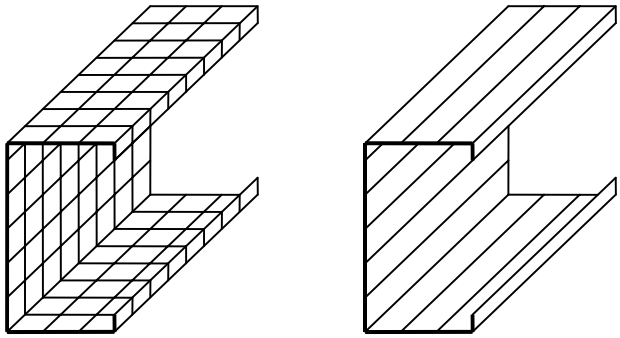

Figure 5.1 Finite element and finite strip mesh

A software for finite strip analysis, CUFSM (http://www.ce.jhu.edu/bschafer/cufsm/), developed by Professor Ben Schafer was intensively used throughout this research. CUFSM employs a polynomial in the transverse direction and a harmonic function in the longitudinal direction. The longitudinal direction is assumed to take the form of a half sine wave. This is consistent with the boundary condition of **simply supported ends**.

This assumptions makes the integrals used in forming the stiffness matrix decouple, and simplifies the solution.

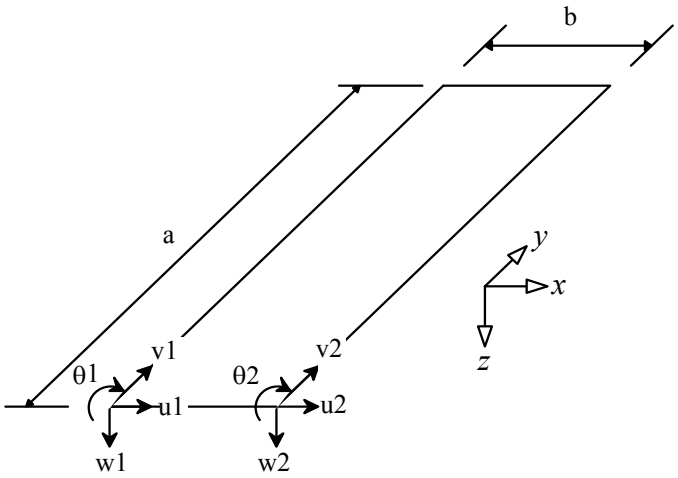

Figure 5.2 Degree of freedom of a strip

Figure 5.2 shows one strip (element) and its degrees of freedom. The initial stiffness matrix [K] consists of two stiffness submatrices: $[K_{uv}]$ (plane stress) and $[K_{w\theta}]$ (bending), Equation 5.5.

$$[K]=\begin{bmatrix} [K_{uv}] & \begin{matrix}0&0&0&0\\0&0&0&0\\0&0&0&0\\0&0&0&0\end{matrix} \\ \begin{matrix}0&0&0&0\\0&0&0&0\\0&0&0&0\\0&0&0&0\end{matrix} & [K_{w\theta}] \end{bmatrix} \tag{5.5}$$

The initial stiffness matrix can be obtained by Equation 5.6.

$$[K]=\int [B]^T [E][B]dV \text{ or } \int [N']^T [E][N']dV \tag{5.6}$$

Where: [B] or [N'] is the appropriate derivatives of the shape functions [N] which is defined from $(u\ v\ w)^T = [N]\{d\}$. Where, $(u\ v\ w)^T$ is the displacement field and {d} is a vector of the nodal degrees of freedom.

The shape functions employed by CUFSM are listed below.

$$u = \left[\left(1-\frac{x}{b}\right) \quad \left(\frac{x}{b}\right)\right]\begin{Bmatrix} u_1 \\ u_2 \end{Bmatrix} Y_m \tag{5.7}$$

$$v = \left[\left(1-\frac{x}{b}\right) \quad \left(\frac{x}{b}\right)\right]\begin{Bmatrix} v_1 \\ v_2 \end{Bmatrix} \frac{a}{m\pi} Y_m' \tag{5.8}$$

$$w = Y_m\left[\left(1-\frac{3x^2}{b^2}+\frac{2x^3}{b^3}\right) \quad x\left(1-\frac{2x}{b}+\frac{x^2}{b^2}\right) \quad \left(\frac{3x^2}{b^2}-\frac{2x^3}{b^3}\right) \quad x\left(\frac{x^2}{b^2}-\frac{x}{b}\right)\right]\begin{Bmatrix} w_1 \\ \theta_1 \\ w_2 \\ \theta_2 \end{Bmatrix} \tag{5.9}$$

$$Y_m = \sin\left(\frac{m\pi y}{a}\right) \tag{5.10}$$

The geometric stiffness matrix for a plate strip subjected to linearly varying edge traction can be determined by constructing the potential energy due to in-plane forces.

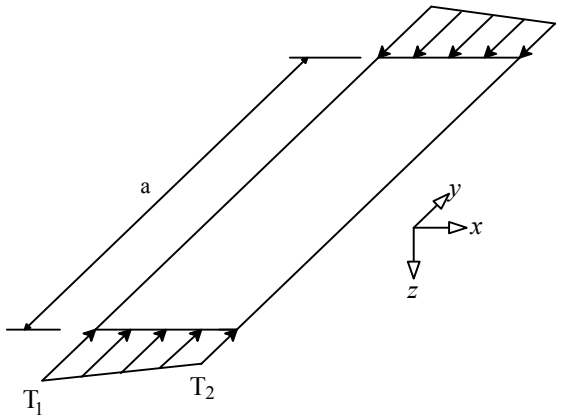

Figure 5.3 Strip with Edge Traction

Consider a strip with linear edge traction as shown in Figure 5.3. The tractions correspond to linear edge stresses f_1 and f_2 via $T_1 = f_1 t$ and $T_2 = f_2 t$. The expression for the potential energy (U) due to the in-plane forces can be expressed as below:

$$U = \frac{1}{2}\int_0^a\int_0^b \left(T_1 - (T_1 - T_2)\frac{x}{b} \right) \left(\begin{bmatrix} \frac{\partial u}{\partial y} & \frac{\partial v}{\partial y} & \frac{\partial w}{\partial y} \end{bmatrix} \begin{Bmatrix} \frac{\partial u}{\partial y} & \frac{\partial v}{\partial y} & \frac{\partial w}{\partial y} \end{Bmatrix}^T \right) dxdy \qquad (5.11)$$

The potential energy may now be expressed in terms of of the nodal degrees of freedom {d} and the geometric stiffness $[K_g]$.

$$U = \frac{1}{2}\{d\}^T [K_g] \{d\} \qquad (5.12)$$

$$[K_g] = \int_0^a\int_0^b \left(T_1 - (T_1 - T_2)\frac{x}{b} \right) [G]^T [G] dxdy \qquad (5.13)$$

where

$$\begin{Bmatrix} \frac{\partial u}{\partial y} & \frac{\partial v}{\partial y} & \frac{\partial w}{\partial y} \end{Bmatrix}^T = [G]\{d\} \qquad (5.14)$$

Similar to the finite element method, the global initial stiffness matrix [K] and the global geometric matrix stiffness $[K_\sigma]$ in the finite strip method are formed by properly assembling the initial stiffness matrix and geometric stiffness matrix of each strip. The elastic buckling problem is a standard eigenvalue problem of the following form:

$$[K]\{d\} = \lambda [K_g] \{d\} \qquad (5.15)$$

Where the eigenvalues λ, are the buckling load, and the eigenvectors the buckling modes. Since [K] and $[K_g]$ are a function of the length a, the elastic buckling stress and the corresponding buckling modes are also a function of *a*, the problem can be solved for several lengths, *a*, and thus a complete figure of buckling load vs. length a can be obtained. The minima of such a curve can be considered as the critical buckling loads and modes for the member.

5.3 Ultimate Strength Solution Method/Post-buckling Strength Analysis

The analysis of the ultimate strength of cold-formed steel members involves obtaining the nonlinear static equilibrium solution of an unstable problem. For such a problem, the generalized load-displacement response can exhibit the type of behavior shown in Figure 5.4. During a given portion of the response, the incremental load and/or displacement may be non-monotonic as the solution evolves.

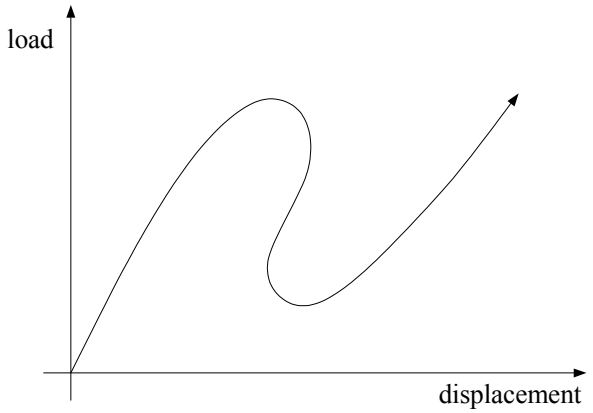

Figure 5.4 Typical unstable static response

Several methods have been applied for such unstable problems, for example the Newton-Raphson method, Modified New-Raphson method, Incremental methods, and Quasi-Newton method, etc. Among them, the modified Riks method has been proven efficient and accurate (Crisfield 1981, Ramm 1981, and Powell and Simons 1981). This method is used for cases where the loading is proportional, in other words; the load magnitude is governed by a single scalar parameter. The two series of four point bending tests are such a case, therefore the modified Riks method is considered in the ABAQUS modeling of this research. Besides the modified Riks method, an alternative approach is to use added "damping" to stabilize the structure during a static analysis. ABAQUS

offers an automated version of this approach by using the STABILIZE parameter. This method is suitable for unstable problems having localized instability, and it is also used in this research.

5.3.1 Modified Riks Method

The Riks method can be considered as a more refined version of incremental load, or displacement control, algorithms. Simple load or displacement increments will fail to reproduce the non-monotonic equilibrium path of Figure 5.4. The Riks method, takes step which combine load and displacements, and in essence can be considered as an incremental work method.

The modified Riks method assumes that the loading is proportional: all load magnitudes vary with a single scalar parameter. The essence of the method is to find the solution of a single equilibrium path in a space defined by the nodal variables and the loading parameter.

$$\text{Load} = \lambda P \tag{5.16}$$

Figure 5.6 shows the basic algorithm. Assume a converged solution exists at point A_0. The tangent stiffness ($K+K_g$) is K_0, and we solve:

$$K_0 v_0 = \lambda_1 P \tag{5.17}$$

Move from point A_0 to A_1 along the direction of v_0, the increment size is determined from a specified path length, Δl in the solution space. The value Δl is initially chosen by the user and is adjusted by the ABAQUS automatic load increment algorithm for static problems, based on the convergence rate. The direction of Δl is determined by checking

the sign of the dot product of the previous increment (v_{-1} in Figure 5.5) to point A_0 and current increment (v_0 in Figure 5.5) being positive.

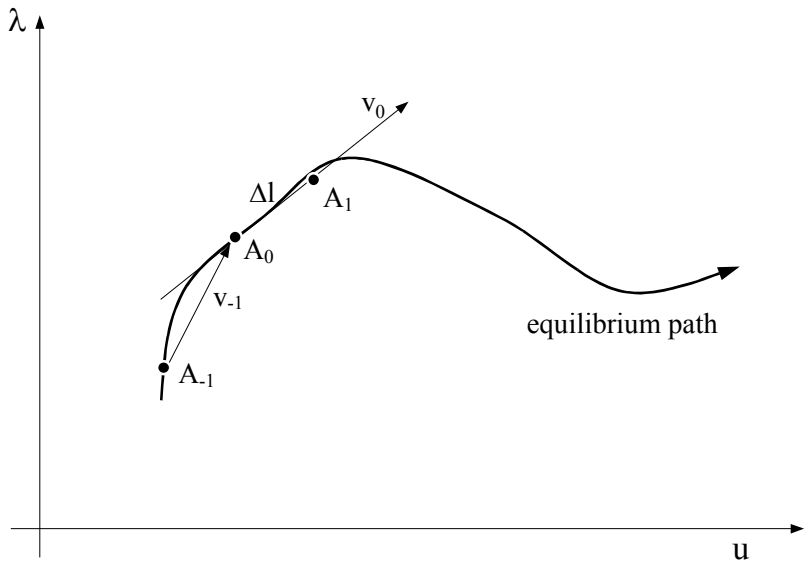

Figure 5.5 Choice of sign for increment

Next, check equilibrium at point A_1:

$$R_1 = \lambda_1 P - I_1 \tag{5.18}$$

where I_1 is the internal force at point 1. If the imbalance R_1 is sufficiently small, the increment has converged, and we accept the solution. If not, proceed to the next point. Compute the tangent stiffness K_1 at point 1, and solve:

$$K_1 v_1 = \lambda_1 P \tag{5.19}$$

Move from point 1 to A_2 along the tangent stiffness K_1, A_2 should be located in the plane orthogonal to v_0. Check the force imbalance at point A_2, if convergence is not reached, proceed to the next iteration.

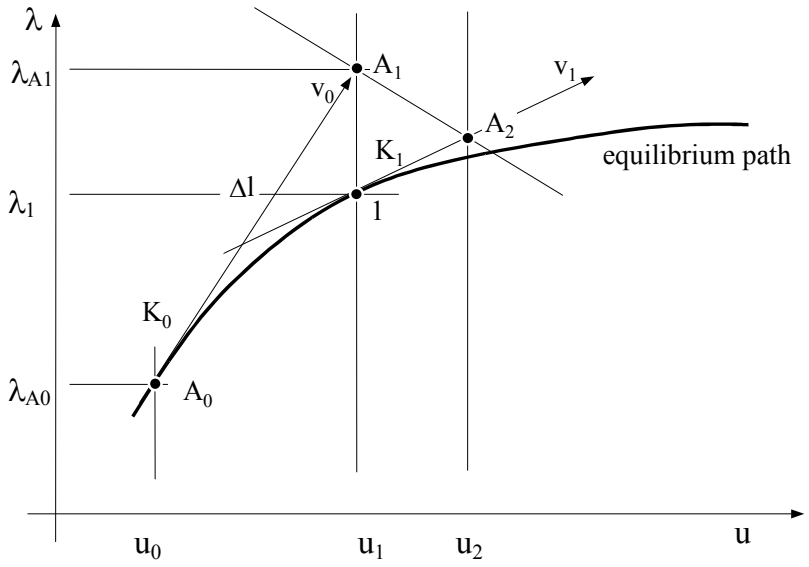

Figure 5.6 Modified Riks algorithm

5.3.2 STABILIZATION Method in ABAQUS

Nonlinear static problems can be unstable. Such instabilities may be of a geometrical nature, such as buckling, or of a material nature, such as material softening. If the instability manifests itself in a global load-displacement response with a negative stiffness, the problem can be solved by global solution methods such as the modified Riks method. However, if the instability is localized, the large local transfer of strain energy from one part of the model to neighboring parts, can cause global solution methods to fail. This class of problems has to be solved either dynamically or with the aid of artificial damping.

ABAQUS offers the option to stabilize this class of problems by adding fictitious linear damping/viscous forces, of the form $F_v = cM^* v$ to the global equilibrium equations $P - I - F_v = 0$, where P is external forces, I is internal (nodal) forces, M^* is an artificial mass matrix calculated with unity density, c is a damping factor, $v = \Delta u/\Delta t$ is the vector of nodal velocities and Δt is the increment of time. Unlike the definition of time in

dynamics problems, the time in the nonlinear static analysis refers to the total arc-length (ABAQUS 2001). Ideally, the damping is applied in such a way that the viscous forces are sufficiently large to prevent instantaneous buckling or collapse, but small enough not to affect the behavior significantly. ABAQUS generates an artificial damping matrix by forming a mass matrix with a unit density from the mesh, and assuming mass-proportional damping. The damping factor is chosen such that, based on extrapolation of the results obtained during the first increment, the dissipated energy during the step is a small fraction of the change in strain energy during the step. This dissipated energy fraction is controlled by the user and has a default value of 2×10^{-4}. If the problem is either unstable or contains rigid body motions during the first increment, an alternative method is used to determine the damping factor; this method is based on constructing an averaged damping stiffness equal to the dissipated energy fraction times an averaged material stiffness. In our model, the first method was used.

5.4 Finite Element Modeling

5.4.1 Shell Element

Since the material thickness of cold-formed steel members is thin compared to the element's width, the shell element is an appropriate choice. For cold-formed steel flexural members, the in-plane stress and deformation are of primary importance, therefore the beam elements commonly used in structural engineering do not work well for such analysis. Beam elements only calculate the bending stress, no membrane stresses, and do not allow cross-section distortion.

ABAQUS provides a full library of shell elements that allow the modeling of curved, intersecting shells, which can exhibit nonlinear material response and undergo large overall motions. The library is divided into three categories consisting of general-purpose, thin, and thick shell elements. The general-purpose element is appropriate for static analysis, and includes:

STRI3 (3 node triangular facet thin shell);

S3 (3-node triangular general-purpose shell);

S3R (3-node triangular general-purpose shell);

STRI65 (6-node triangular thin shell, using five degrees of freedom per node);

S4 (4-node doubly curved general-purpose shell);

S4R (4-node doubly curved general-purpose shell, reduced integration with hourglass control);

S4R5 (4-node doubly curved thin shell, reduced integration with hourglass control, using five degrees of freedom per node);

S8R (8-node doubly curved thick shell, reduced integration);

S8R5 (8-node doubly curved thin shell, reduced integration, using five degrees of freedom per node); and

S9R5 (9-node doubly curved thin shell, reduced integration, using five degrees of freedom per node).

Figure 5.7 shows the shell elements used for stress/displacement analysis in ABAQUS, the ‘x’ in the figure represents an integration point.

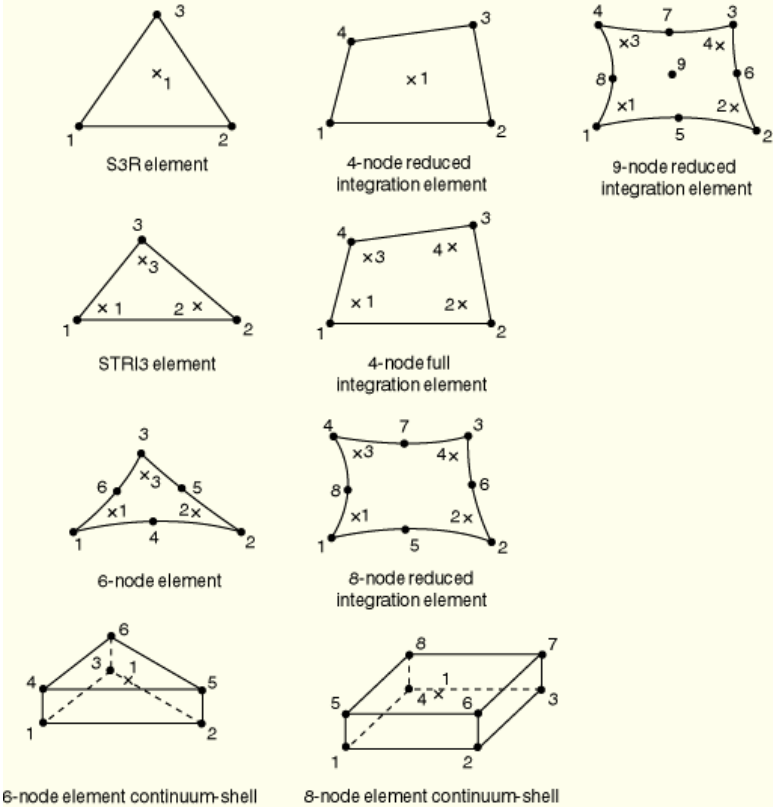

Figure 5.7 Shell elements in ABAQUS (from ABAQUS/Standard 6.2 User's Manual)

For the purpose of easy mesh generation by the author's MATLAB program, a 4-node shell element was adopted for the ABAQUS model. ABAQUS provides three types of 4-node shell elements: S4, S4R ("R" stands for reduced integration), and S4R5. The differences among these three element types are (1) the number of integration points, S4 employs 4 integration points and the elements with reduced integration use 1; (2) the number of degrees of freedom, S4 and S4R elements have 6 degrees of freedom, S4R5 has 5 degrees of freedom (the rotation about the axis normal to the shell mid-surface is removed).

The shell element type and mesh size were determined through a series of elastic buckling calculations on a simply supported cold-formed steel C-section subjected to end moments. The cross-section dimensions are h = 8 in., $b_c = b_t = 2.5$ in., $d_c = d_t = 0.8$ in., t =

0.05 in., $\theta_c = \theta_t = 90$ degrees, $r_{hc} = r_{dc} = r_{ht} = r_{dt} = 0.2$ in. (the notations refer to Figure 2.2), and the section length is 174 in. (3 times the distortional buckling wavelength). In the transverse direction, 3 nodes are adopted for the lip stiffener, 3 nodes for the corner, 5 nodes for the flange, and 9 nodes for the web. The elastic buckling moment calculated by the finite strip method (CUFSM) is 58.3 kip-in. for local buckling, and 75.7 kip-in. for distortional buckling. A convergence study was performed with a concentration on the longitudinal mesh size and element type. The results for local buckling are summarized in Table 5.1. Figure 5.8 shows the ratio of ABAQUS to CUFSM vs. the FEM mesh aspect ratio, where the aspect ratio refers to the longitudinal size of the web element divided by the transverse size. The results indicate that for local buckling, ABAQUS is slightly, but systematically higher than CUFSM The S4R and S4R5 elements provide close and converged results in the examined range of mesh sizes. The result for the S4 element varies dramatically and has not converged for the given mesh range (although it appears to be approaching the finite strip results in the limit).

Table 5.1 Elastic local buckling moments by finite element model

Web element aspect ratio	Buckling moments (kip-in.)		
	S4 element	S4R element	S4R5 element
2	63.17	60.05	59.75
1.5	61.36	59.92	59.71
1	59.98	59.74	59.61
0.5	59.11	59.57	59.51
0.2	58.88	59.53	59.47

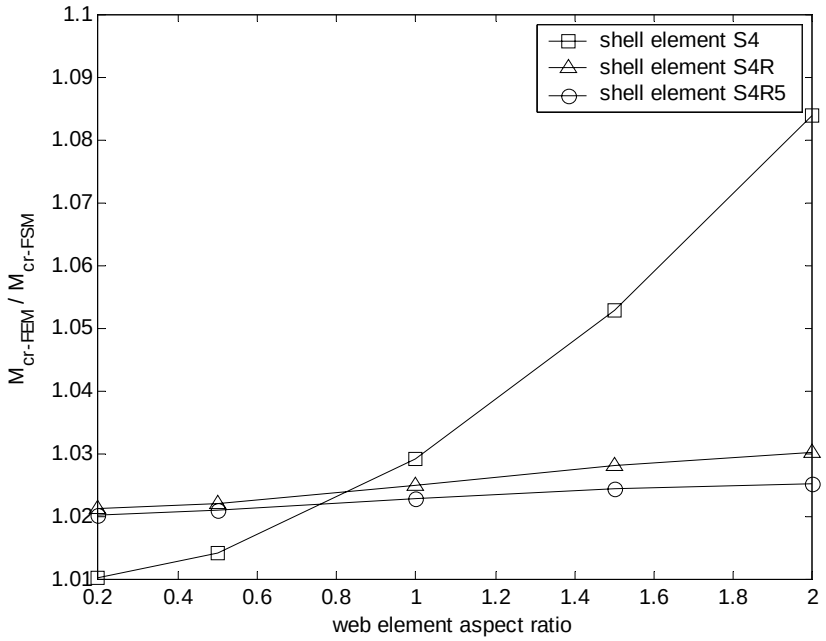

Figure 5.8 Convergence study for local buckling

The results of the convergence study for distortional buckling are summarized in Table 5.2, and Figure 5.9 presents the ratio of ABAQUS results to CUFSM results vs. the mesh aspect ratio. All three element types give better results for distortional buckling, than for local buckling. Results for S4R and S4R5 are closer to the CUFSM results than S4, but are slightly below (< 1%) the expected result.

Table 5.2 Elastic distortional buckling moments by finite element mode

Web element aspect ratio	Buckling moments (kip-in.)		
	S4 element	S4R element	S4R5 element
2	77.01	75.60	75.28
1.5	76.853	75.47	75.21
1	76.74	75.36	75.16
0.5	76.65	75.26	75.14
0.2	76.62	75.22	75.13

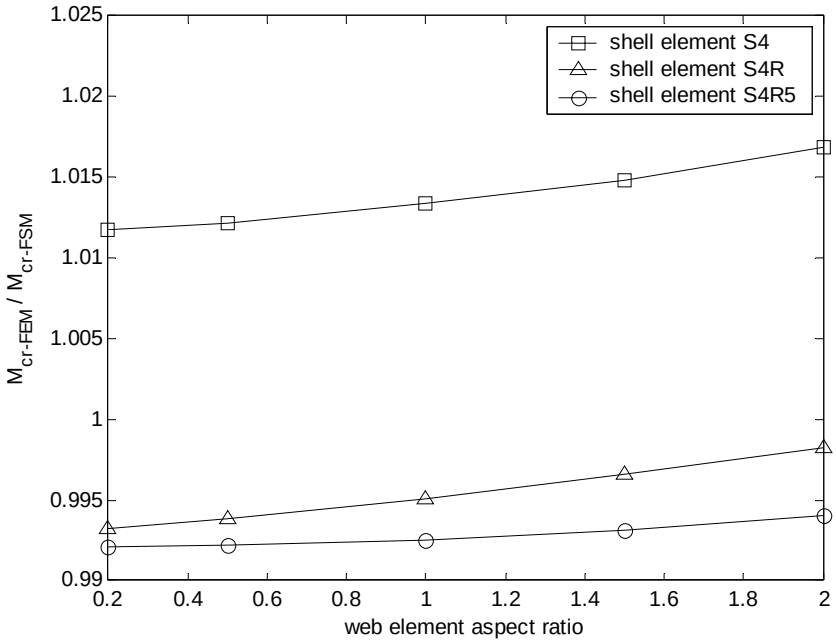

Figure 5.9 Convergence study for distortional buckling

Based on the convergence study, and the consideration of computational efficiency as well ease of generating the mesh, the S4R (4-node, quadrilateral, stress/displacement shell element with reduced integration) shell element was finally selected for the ABAQUS model of cold-formed steel members in this research. The element mesh is set as 1 in. for the longitudinal element size (or a web element aspect ratio equal to 1 approximately), and in the transverse direction, 3 nodes are adopted for the lip stiffener, 3 nodes for the corner, 5 nodes for the flange, and 9 nodes for the web. Figure 5.10 shows the selected mesh for the ABAQUS model of cold-formed steel members.

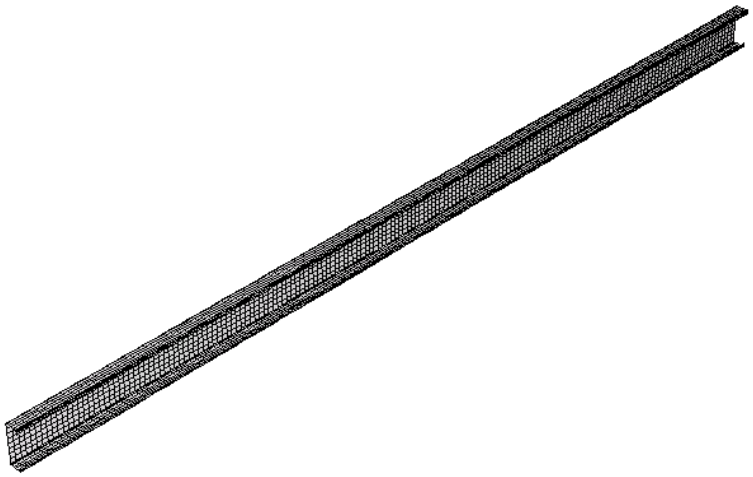

Figure 5.10 Selected mesh for ABAQUS model

5.4.2 Modeling Details and Loading/Boundary Conditions

An overall view of the finite element model for the tests (Chapters 2 and 3) is shown in Figure 5.11. The cold-formed steel sections, panel, and hot-rolled tubes are modeled using S4R shell elements. The loading beam employs an 8-node linear solid element (C3D8) and is simplified to be a rigid rectangular section by employing a high modulus of elasticity (10 times the E used for the sections).

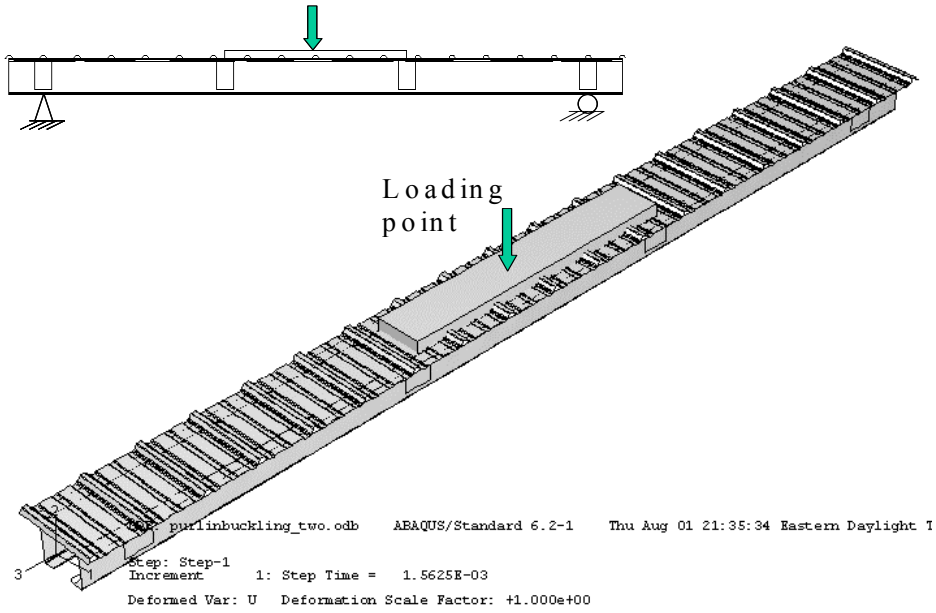

Figure 5.11 Finite element modeling of beams in local buckling tests.

The beam is simply supported at the bottom flanges under the two end tubes. The tube and section are connected by tieing 4 nodes of the section to the surface of the tube (to simulate the four bolts). ABAQUS provides a Multi-Point Constraint (*MPC in ABAQUS) library for different connection/contact modeling. The "*Tie" option is used for the tube-to-section connection (Figure 5.12), that is to make the global displacements and rotations equal at the two nodes, thus, simulating a "perfect" no-slip bolt. The contact and potential friction between the tube and section are ignored in the model since the forces are mainly transferred from the tube to section via the bolts, the contact at other areas between the tube and section will not affect the failure mechanism of the section. This assumption is also applied to the panel-to-section connector. The panel and section are connected only at the fastener locations via the "*Tie" constraint between the corresponding nodes (Figure 5.13). The loading beam is simply connected to the tubes (Figure 5.12) using "*Pin" option in ABAQUS, this ties the global displacements but leaves the rotations free. The steel angle bolted at the bottom flanges of the paired sections is simulated by the use of "*Link" restraints on these two nodes (Figure 5.14). The "*Link" option in ABAQUS enforces a fixed distance between two nodes, and thus ignores any rotational restraint provided by the fasteners attaching the angle to the bottom flange, also this assumes the angles are axially rigid. Since the bottom flanges are subjected to tension stresses in the tests, local or distortional buckling will not form on the flanges; therefore, ignoring the rotational restraint and bending of the angles is assumed reasonable.

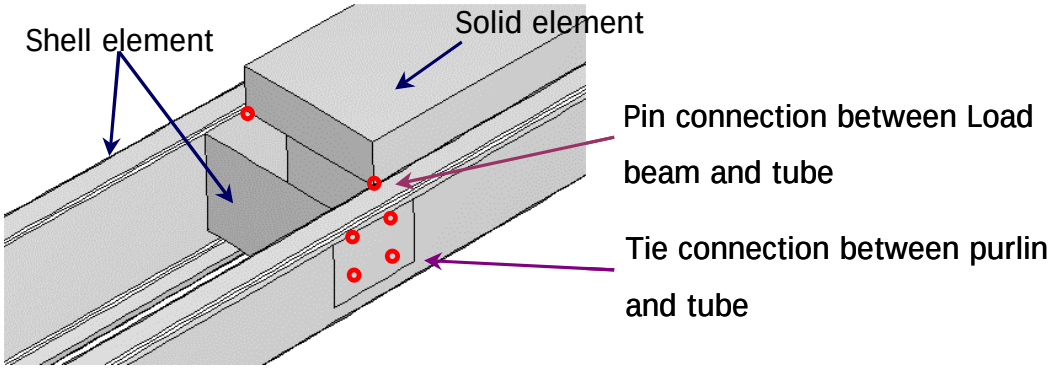

Figure 5.12 Connections at the 1/3 point of beams

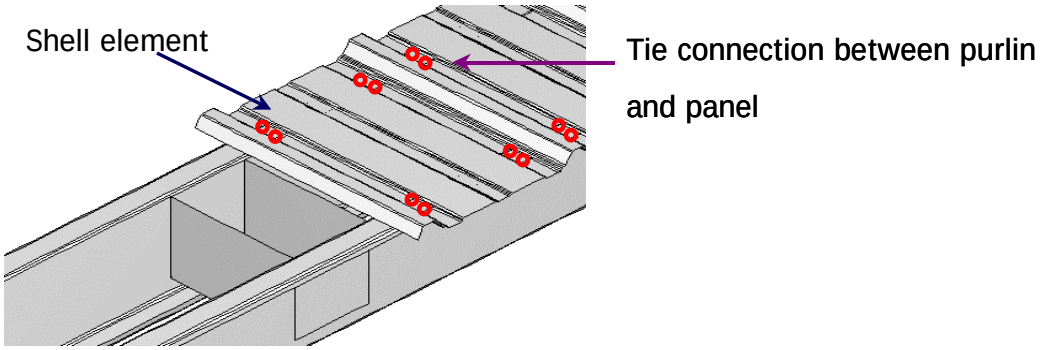

Figure 5.13 Panel-to-section connection

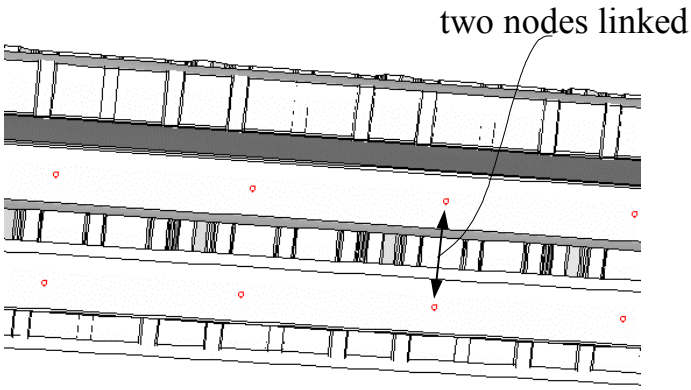

Figure 5.14 Modeling of angles at the tension flanges (view from under the beam)

5.4.3 Geometric Imperfection

Geometric imperfections include bowing, warping, twisting and local deviations and exist in every real cold-formed steel member. Geometric imperfections have a significant

effect on the strength and post-buckling behavior of many C and Z-sections. Therefore, it is necessary and important to consider geometric imperfections in the finite element model.

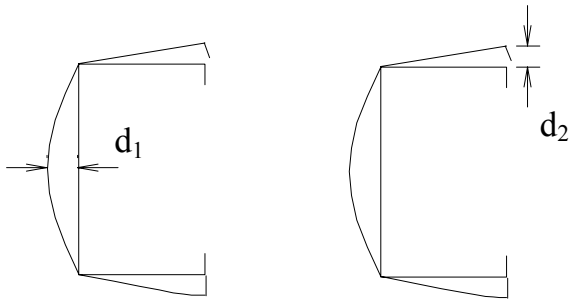

type1 type2

Figure 5.15 Definition of geometric imperfections

Table 5.3 CDF values for maximum imperfection (Schafer and Peköz, 1998b)

	Type 1	Type 2
P(Δ<d)	d_1/t	d_2/t
0.25	0.14	0.64
0.50	0.34	0.94
0.75	0.66	1.55
0.95	1.35	3.44
0.99	3.87	4.47
mean	0.50	1.29
standard deviation	0.66	1.07

Geometric imperfections of cold-formed steel members have been measured by many researchers, and the data was sorted in two categories: type 1, maximum local imperfection in a stiffened element and type 2, maximum deviation from straightness for a lip stiffened or unstiffened flange, as shown in Figure 5.15 (Schafer and Peköz 1998b). The histogram (Figure 5.16 and Figure 5.17) and cumulative distribution function (CDF) values (Table 5.3) of the maximum imperfection for the two types are available. A CDF

value is written as **P**($\Delta <$ d) and indicates the probability that a randomly selected imperfection value, Δ, is less than a deterministic imperfection, d.

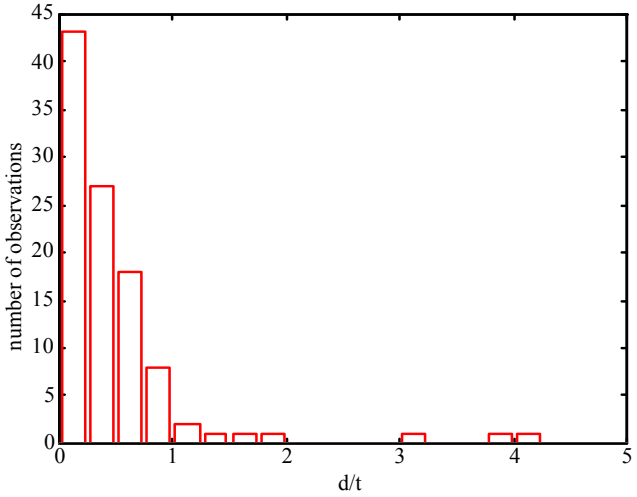

Figure 5.16 Histogram of type 1 imperfection (Schafer and Peköz 1998b)

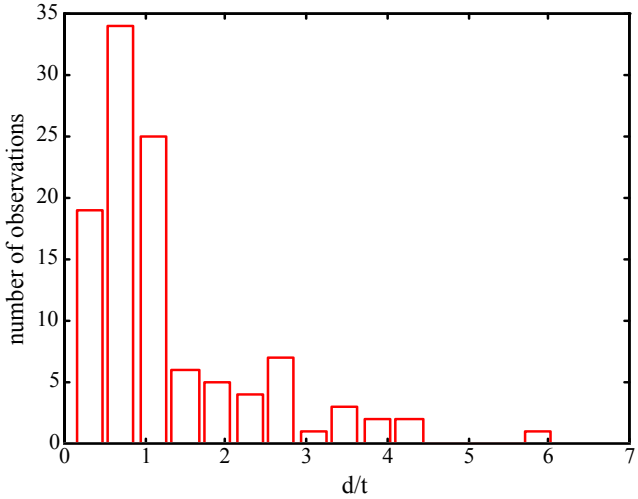

Figure 5.17 Histogram of type 2 imperfection (Schafer and Peköz 1998b)

The geometric imperfections of the tested cold-formed steel C and Z-sections in this research were not measured in part due to the lack of appropriate and efficient measuring devices. Therefore, the imperfections used in the finite element modeling were based on the CDF values summarized in Table 5.3. Knowing the amplitude of imperfections in the lowest eigenmodes is often sufficient to characterize the most influential imperfections.

We conservatively assume that the type 1 imperfection may be applied to the local buckling mode and the type 2 imperfection applied to the distortional buckling mode.

For each test, two FEM simulations were performed. One simulation used a larger initial geometric imperfection with a 75% CDF magnitude ($d_1/t = 0.66$ for local buckling; $d_2/t = 1.55$ for distortional buckling), the other used a smaller magnitude with 25% CDF magnitude ($d_1/t = 0.14$ for local buckling; $d_2/t = 0.64$ for distortional buckling), thus covering the middle 50% of anticipated imperfection magnitudes. According to the AISI Standard for Cold-Formed Steel Framing (AISI 2001), the manufacturing tolerances for the stud web crown (type 1 imperfection) are 0.0625 in. for structural members and 0.125 in. for non-structural members. The maximum magnitudes of type 1 geometric imperfection selected in the FEM are for the thickest specimen D8C097-6 (t = 0.1005 in.): 0.066 in. corresponding to the 25% CDF and 0.014 in. corresponding to the 75% CDF. Both values are possible in practice. The imperfection shape is a superposition of the local and distortional buckling mode, scaled to the appropriate CDF value. For numerical efficiency the imperfection shape is obtained by using the finite strip software CUFSM and the resulting coordinates used to offset the geometry of the ABAQUS model appropriately.

5.4.4 Material Modeling

Material nonlinearity is a consideration for postbuckling analysis of cold-formed steel members. Since study of the C and Z-sections are the primary research objective, only the Z or C-section is modeled as inelastic, all other components are modeled as linear elastic. (Note, typical yield stress for the panel is quite high, about 100 ksi, and

failures were observed to initiate in the members, not the panels, for all local and distortional buckling tests).

All the components of the tests are made of steel, the Poisson's ratio μ is set to 0.3 and the elastic moduli E is set to 29500 ksi for both the section and panel (as verified by tensile tests in Chapter 4). Since the tubes and loading beam are of little interest for this research, they are approximated as rigid bodies by setting an artificially high elastic modulus $E = 10E_{steel}$.

Tension test results are used for the material stress-strain properties of the sections. The true stress-strain (σ_t, ε_t) is employed in ABAQUS, thus the tensile test results (engineering stress-strain) (σ_e, ε_e) need to be converted:

$$\sigma_t = \sigma_e(1+\varepsilon_e) \tag{5.20}$$

$$\varepsilon_t = \ln(1+\varepsilon_e) \tag{5.21}$$

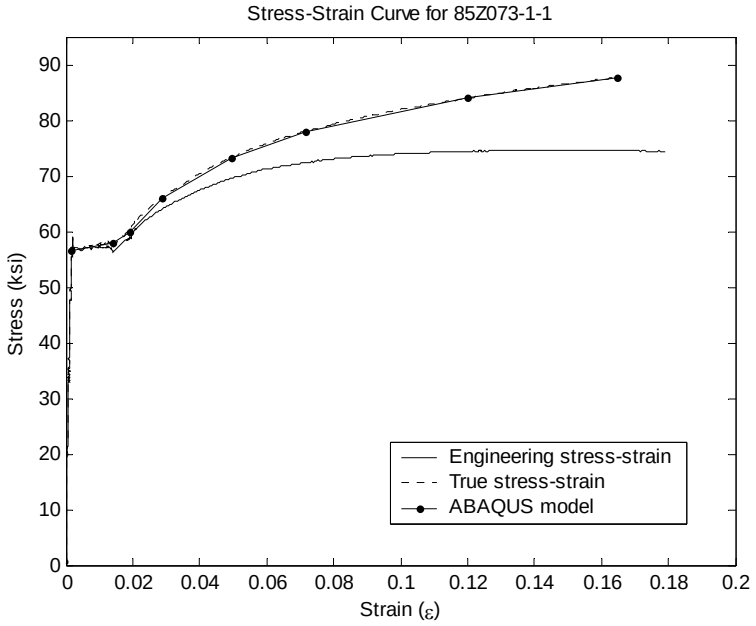

Figure 5.18 Comparison of stress-strain cures

Figure 5.18 shows a comparison of a typical test/engineering stress-strain curve vs. the true stress-strain used in the finite element model.

5.4.5 Residual Stress

Residual stresses in cold-formed steel members do not play the dominating role that they do in hot-rolled steel members. In hot-rolled steel members, membrane residual stress developed during the cooling process can be as high as 1/3 of the yield stress, or greater, and can occur in important regions such as the flange tips of I and C-sections. Prediction of the compression strength of hot-rolled steel members generally requires inclusion of residual stresses.

In cold-formed steel, residual stresses also develop in the forming process-both in the coil and during the roll-forming operation. While the largest residual stresses are likely in the transverse direction due to the bending (forming) of the section, of interest for strength is the resulting longitudinal residual stresses. Measurement of cold-formed steel longitudinal residual stresses generally rely on a sectioning technique, and values are only available at the faces of the thin steel plate. Thus, cold-formed steel residual stresses are generally categorized into a membrane and a flexural (through-thickness) component as shown in Figure 5.19, which from Schafer and Peköz (1998b) summarizes the expected state of residual stresses in cold-formed steel members.

Membrane residual stresses are the most important, as they have a net impact on the strength of the steel under applied stress. In the flat regions of cold-formed steel members membrane residual stresses are generally found to be close to zero. In the corner regions membrane residual stresses can be high, but here one also finds elevated yield stresses

due to cold-work of forming. In the modeling conducted here it has been decided to ignore the beneficial effect of elevated yield stress in the corners and ignore the detrimental effect of membrane residual stresses in the corner-as these two phenomena are expected to generally offset one another. Thus, the stress-strain properties measured in the flat regions without membrane residual stresses are used for the entire C- or Z-section.

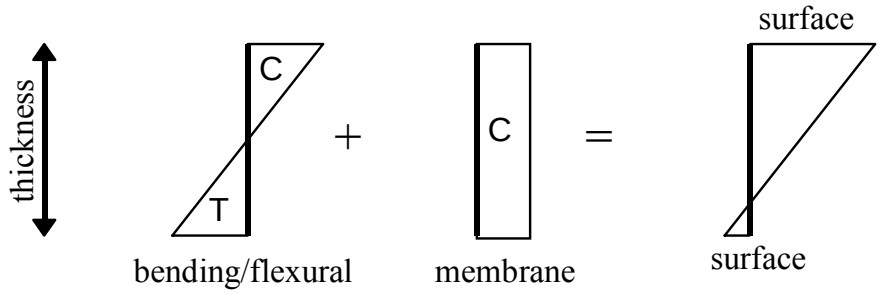

Figure 5.19 Definition of flexural and membrane residual stress

Flexural residual stresses have little net effect on the section strength. The primary impact of flexural residual stresses is to influence the distribution of the yielding pattern on the face of plates of the section undergoing local bending. It is possible, but not likely, that this change in the yielding pattern could initiate subtly different failure mechanisms (and thus post-perk response).

Including residual stresses increases the model complexity, little is known about residual stresses distributions, and measured magnitudes are highly variable. As a result, it was decided to ignore residual stresses (both membrane and flexural) in the developed models.

5.5 Finite Element Analysis

5.5.2 Elastic Buckling Results

Eigenvalue buckling analysis as described in Section 5.2 using ABAQUS has been used intensively in the pre-test panel-to-section configuration study (Chapter 2), and in examining the expected buckling mode for the distortional buckling tests (Chapter 3). Elastic buckling via the finite strip method (CUFSM) is also used intensively for basic section strength calculations. For elastic buckling, ABAQUS has good agreement with that of CUFSM (refer to Section 5.4.1). ABAQUS is appropriate for the beams when the full test setup (panel, tube, etc) is needed while CUFSM is most efficient for pure section calculations. Elastic buckling analysis has additional application for the study of the effect of moment gradient and modeling partial restraint - details on these models will be presented in Chapter 6 and Chapter 7 respectively.

5.5.3 Ultimate Strengths/Postbuckling Results

5.5.3.1 Comparison of Nonlinear Solution Methods

The "load" in the nonlinear finite element analysis was applied as incremental displacement, mimicking the loading method of the testing itself. The automatic stabilization technique (*stabilize in ABAQUS) was adopted for the nonlinear static analysis. The arc-length based modified Riks method was also considered; however analyses by this method typically stopped when calculation was close to the peak load due to convergence problems. As discussed earlier in this chapter, the modified Riks method does not work well on problems which involve strong local instability and

redistribution. The model developed for the buckling tests in this research appear to be such a case. The automatic stabilization method provided good simulation of the actual tests and less convergence problems near the peak loads than modified Riks method.

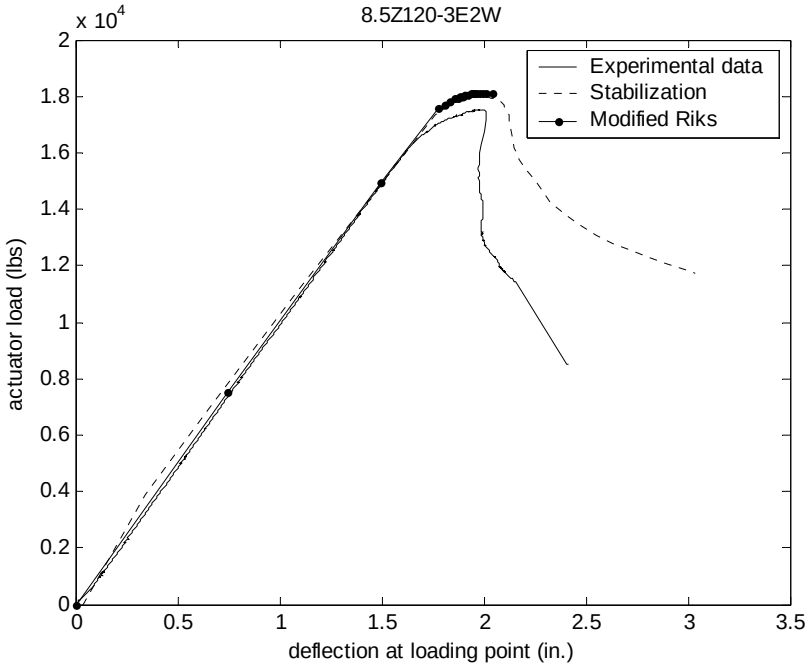

Figure 5.20 Comparison of nonlinear algorithms

Figure 5.20 shows a comparison of the results for both methods on a test of an 8.5 in. deep Z-section. The automatic stabilization method passed through the peak load and had fairly good simulation of the postbuckling behavior and collapse, the analysis terminated when the displacement of the loading point reached the desired limit (3 in.). The modified Riks method ended earlier due to convergence problems. Therefore, the automatic stabilization method was chosen for the postbuckling analyses of the two series of tests of cold-formed steel beams.

5.5.3.2 Comparison with Experimental Results

For each test, two nonlinear finite element analyses are performed, one FEM model uses an geometric imperfection magnitude with a 25% probability of exceedance (25% CDF) and the second analysis uses an imperfection magnitude with 75% probability of exceedance (75% CDF) thus covering the middle 50% of anticipated imperfection magnitudes. The imperfection shape is obtained by superposing the local and distortional buckling mode, scaled to the appropriate CDF value. For numerical efficiency, the finite strip analysis by CUFSM is used to generate the buckling shapes.

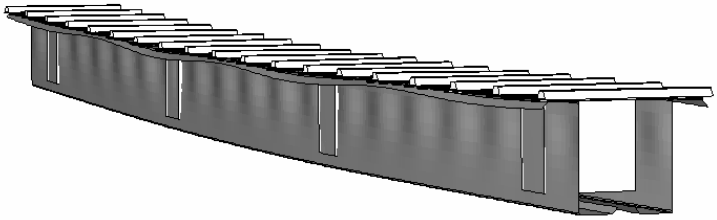

(a) FEM result (loading beam removed for better view, displacement scale =1)

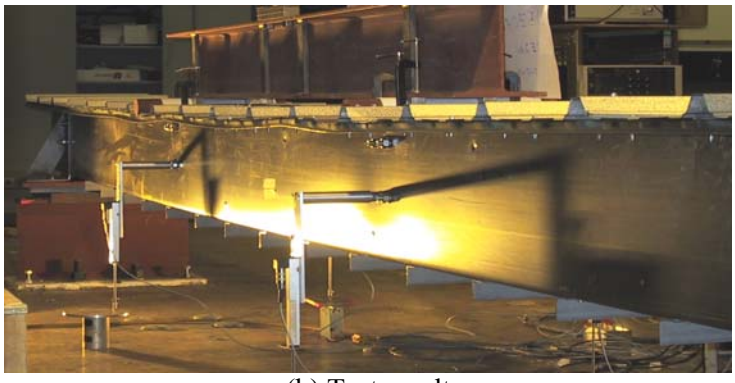

(b) Test result

Figure 5.21 Local buckling test of 11.5Z092-1E2W

Figure 5.21 shows a comparison of the local buckling test result for 11.5Z092-1E2W with the result of a finite element model with 25% CDF imperfection. Figure 5.22 shows a comparison of the distortional buckling test result of D11.5Z092-3E4W with the result of a finite element model with 25% CDF imperfection. ABAQUS provides a good

prediction of the buckling shapes for both tests: the local buckling test is characterized by short and repeated buckling waves in the compression flange and top portion of the web; the distortional buckling test which removes the restraint provided by the panel fails in a typical distortional buckling mode, with the compression flange rotating, and with a longer buckling wavelength than in the local mode.

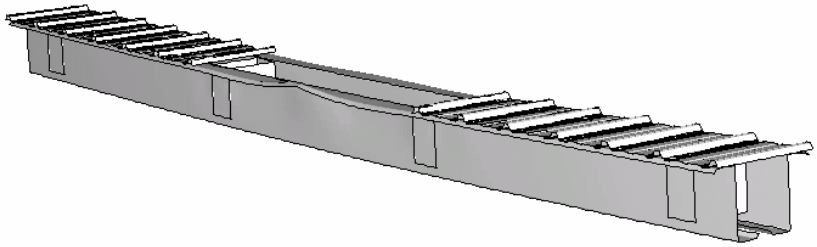

(a) FEM result (loading beam removed for better view, displacement scale=1)

(b) Test result

Figure 5.22 Distortional buckling test of D11.5Z092-3E4W

The results of the finite element analyses are summarized in Table 5.4 for the local buckling tests and Table 5.5 for the distortional buckling tests, where P_{test} is the peak actuator load, and $P_{25\%}$ and $P_{75\%}$ are the peak load of the simulation with 25%, and 75% CDF of maximum imperfection respectively. On average, the peak load of the tests are bounded by the results of the two finite element simulations. The pair of simulations show that the middle 50% of expected imperfection magnitudes result in a range of 13% of the bending capacity for local buckling and a range of 15% for distortional buckling,

thus providing a measure of the imperfection sensitivity. The finite element analysis for the distortional buckling tests shows slightly greater scatter (greater imperfection sensitivity). The mean response of the FEM simulations has a good agreement with the average tested strength. Taken as a whole, the mean prediction of the 25% CDF and 75% CDF FEM simulations predicts 100% of the local buckling capacity results and 101% of the distortional buckling capacity.

Table 5.4 Summary of finite element analysis results for local buckling tests

Test label	P_{test} (lbs)	$P_{25\%\sigma}$ (lbs)	$P_{25\%\sigma}/P_{test}$	$P_{75\%\sigma}$ (lbs)	$P_{75\%\sigma}/P_{test}$	P_{mean}/P_{test}
8.5Z120-3E2W	17520	17968	103%	16484	94%	98%
8.5Z105-2E1W	16720	17294	103%	15806	95%	99%
8.5Z092-4E2W	11330	11901	105%	11170	99%	102%
8.5Z082-1E2W	10130	11446	113%	10749	106%	110%
8.5Z073-4E3W	8341	8770	105%	7309	88%	97%
8.5Z065-3E1W	5969	6771	113%	5886	99%	106%
8.5Z059-2E1W	6180	6749	109%	5748	93%	101%
11.5Z073-2E1W	12120	13956	115%	12396	102%	109%
11.5Z082-2E1W	17123	17294	101%	15806	92%	97%
11.5Z092-1E2W	22000	23417	106%	19790	90%	98%
8.5Z059-4E3W	6275	6855	109%	5763	92%	101%
8C097-2E3W	10770	11175	104%	10200	95%	99%
8C068-4E5W	6476	6762	104%	5614	87%	96%
8C054-1E8W	3492	3849	110%	3233	93%	101%
8C043-5E6W	3195	3574	112%	3082	96%	104%
6C054-2E1W	2803	2882	103%	2240	80%	91%
4C054-1E2W	1731	1720	99%	1365	79%	89%
12C068-9E5W	6505	6697	103%	5968	92%	97%
3.62C054-1E2W	1263	1170	93%	987	78%	86%
12C068-3E4W	8542	9458	111%	8655	101%	106%
10C068-2E1W	4381	4233	97%	3937	90%	93%
8C068-1E2W	6141	6854	112%	5557	90%	101%
8C043-3E1W	2985	3482	117%	3026	101%	109%
mean			106%		93%	100%
standard deviation			6%		7%	6%

Note: P_{test}: Peak tested actuator load;
$P_{25\%\sigma}$: Peak load of simulation with 25% CDF of maximum imperfection;
$P_{75\%\sigma}$: Peak load of simulation with 75% CDF of maximum imperfection;
P_{mean}: Average value of $P_{25\%\sigma}$: and $P_{75\%\sigma}$.

Table 5.5 Summary of finite element analysis results for distortional buckling tests

Test label	P_{test} (lbs)	$P_{25\%\sigma}$ (lbs)	$P_{25\%\sigma}/P_{test}$	$P_{75\%\sigma}$ (lbs)	$P_{75\%\sigma}/P_{test}$	P_{mean}/P_{test}
D8.5Z120-4E1W	15870	16283	103%	14839	94%	99%
D8.5Z115-1E2W	14837	16402	111%	13028	88%	100%
D8.5Z092-3E1W	9566	10740	112%	8779	92%	102%
D8.5Z082-4E3W	7921	9160	116%	7775	98%	107%
D8.5Z065-7E6W	5826	6891	118%	6053	104%	111%
D8.5Z059-6E5W#	4430	5738	130%	5294	120%	113%
D11.5Z092-3E4W	16377	16817	103%	14443	88%	96%
D8.5Z065-4E5W	4993	5876	118%	5155	103%	111%
D11.5Z082-4E3W	14578	15172	104%	14473	99%	102%
D12C068-1E2W#	6160	8157	132%	7566	123%	128%
D8C043-4E2W	2678	3051	114%	2751	103%	109%
D12C068-10E11W	5912	5497	93%	4930	83%	88%
D8C033-1E2W	1024	1089	106%	950.8	93%	100%
D8C054-7E6W	3032	3363	111%	2919	96%	104%
D10C068-4E3W	3185	3235	102%	2746	86%	94%
D8C097-5E4W	10350	12353	119%	9985	96%	108%
D3.62C054-3E4W	1071	1027	96%	838	78%	87%
D8C097-7E6W	12751	13690	107%	10771	84%	96%
D10C048-1E2W	3874	4228	109%	3806	98%	104%
D8C045-1E2W	1033	1134	110%	1023	99%	105%
D6C063-2E1W	3271	3470	106%	2834	87%	97%
D8C085-2E1W	7646	7723	106%	7264	95%	101%
D10C056-3E4W#	5309	6775	128%	6003	113%	120%
D8C068-6E7W	6553	6829	104%	6211	95%	100%
mean*			108%		93%	101%
standard deviation*			7%		7%	6%

Note: P_{test}: Peak tested actuator load;
$P_{25\%\sigma}$: Peak load of simulation with 25% CDF of maximum imperfection;
$P_{75\%\sigma}$: Peak load of simulation with 75% CDF of maximum imperfection;
P_{mean}: Average value of $P_{25\%\sigma}$ and $P_{75\%\sigma}$;
#: tests failed in unexpected mode;
*: tests with unexpected failure mode are excluded.

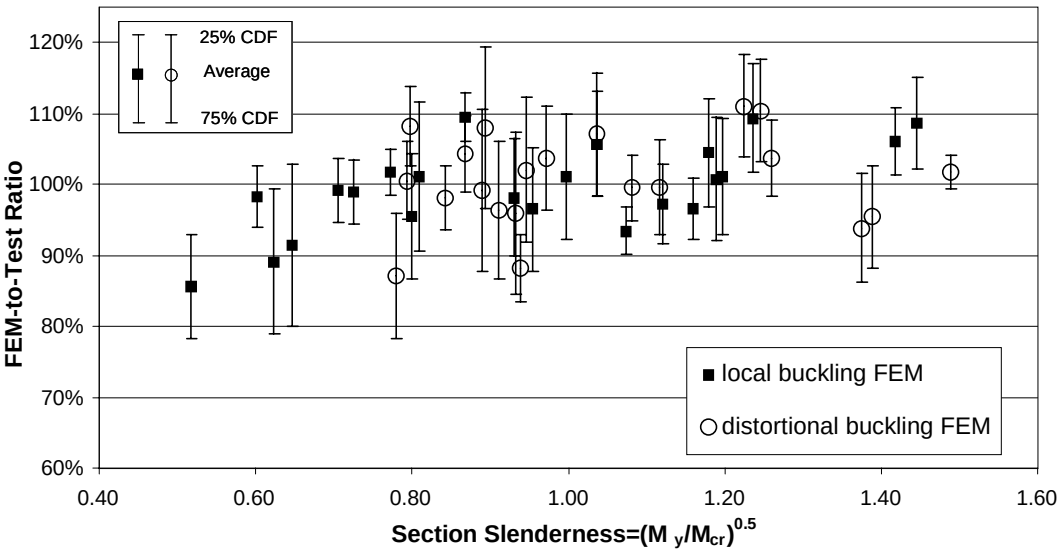

Figure 5.23 Comparison of finite element results with tests

Figure 5.23 shows the FEM accuracy vs. section slenderness, and indicates a slight tendency for the finite element analysis to over-predict the observed strength for very slender sections, and under-predict for stockier sections.

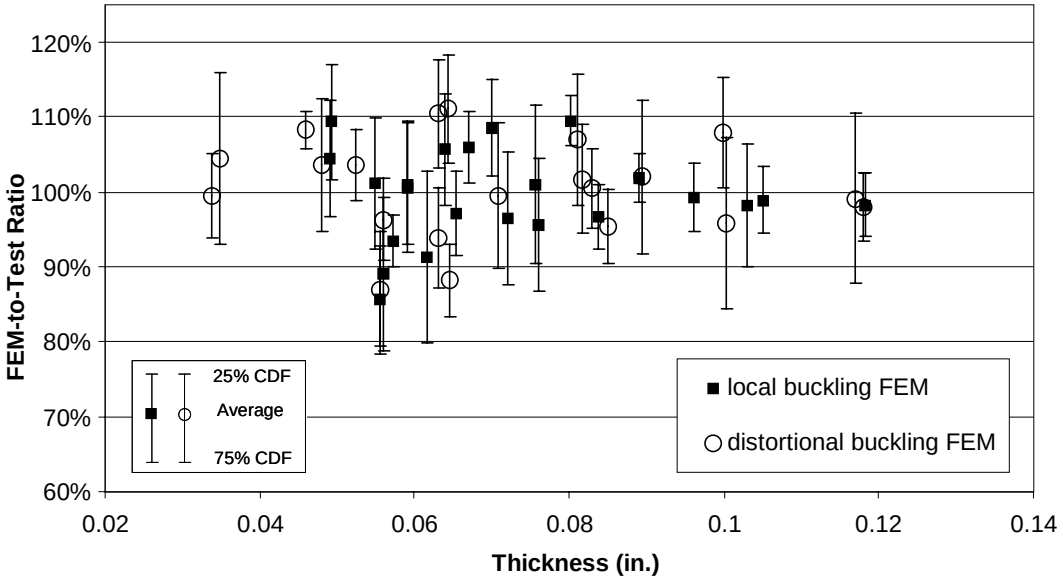

Figure 5.24 Comparison of finite element results with tests

Figure 5.24 illustrates the FEM accuracy vs. specimen thickness. No tendency is observed with respect to the thickness. This may be partially driven by two opposing effects: (1) the strength of thinner elements is more sensitive to the geometric imperfection, thus bigger imperfections leads to more scattered FEM results; (2) the choice of a constant d/t imperfection size – thus leading to smaller imperfection sizes for the thinner material.

In total, it is concluded that the elastic behavior and post-buckling strengths for both local buckling and distortional buckling of cold-formed steel beams are well simulated by this finite element model. However, the post-collapse behavior and final mechanism formation is only approximated by the model. Lack of agreement in the large deflection post-collapse range could be a function of the solution scheme (e.g., use of artificial damping via the *stabilize option) or more basic modeling assumptions, such as ignoring any plasticity in the panels and the contact between components of the beam.

Select load-to-deflection response of FEM simulations are shown with comparison to the test results in Figure 5.25 to Figure 5.54. one measure of imperfection sensitivity is the difference between the 25% and 75% CDF values in the figures. Sensitivity to the peak strength is depicted by the vertical difference between the two curves at peak load, sensitivity to the final failure mechanism is also shown. For example, Figure 5.31 shows a case where the peak load is sensitive to imperfection, but the failure mechanism itself in the post-peak range appears nearly identical. Figure 5.32 presents a case where post-peak mechanism response is clearly quick different for the two models. Many cases exist where the post-peak slop predicted by the models is in qualitative agreement between the tests. This is even true for some cases with striking nonlinearity such as Figure 5.42,

Figure 5.45, Figure 5.48 and others. In particular, the progressive nature of the collapse in the distortional buckling tests (Figure 5.38 to Figure 5.54) appears well approximated by the model. While the selected ABAQUS model clearly has limitations it does appear to quantitatively and qualitatively capture the essential nonlinearities observed in the testing.

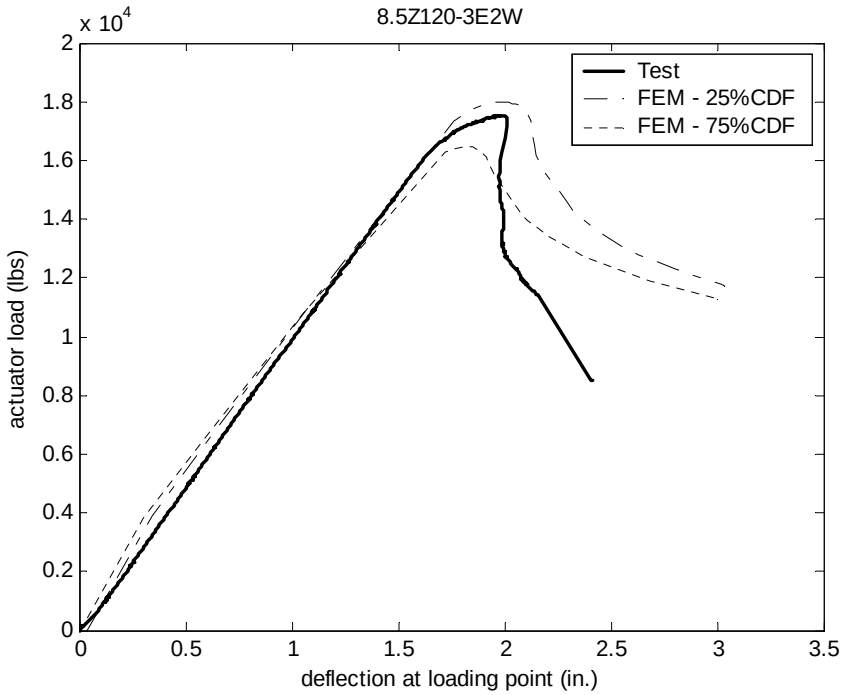

Figure 5.25 Comparison of FEM results with test 8.5Z120-3E2W

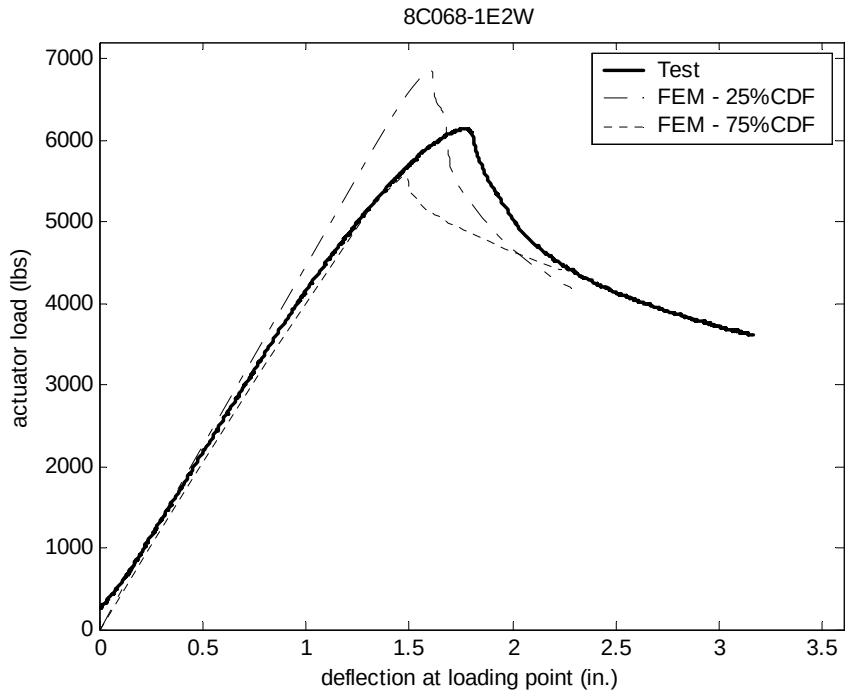

Figure 5.26 Comparison of FEM results with test 8C068-1E2W

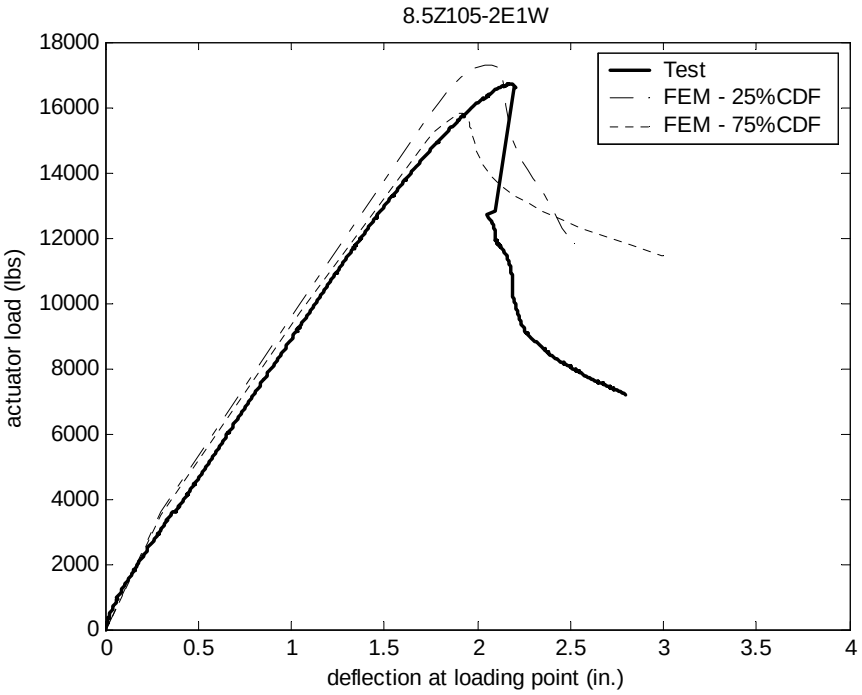

Figure 5.27 Comparison of FEM results with test 8.5Z105-2E1W

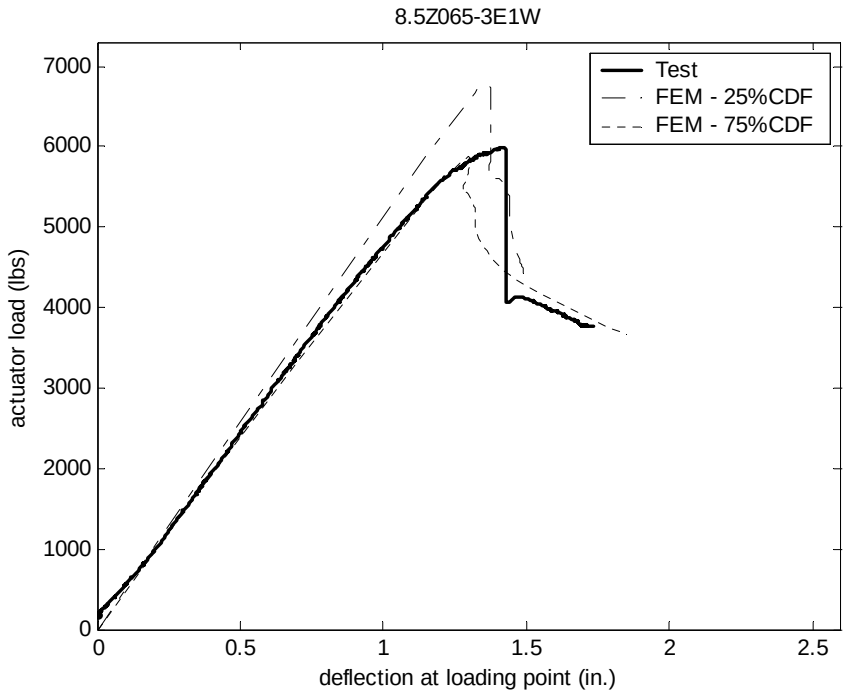

Figure 5.28 Comparison of FEM results with test 8.5Z065-3E1W

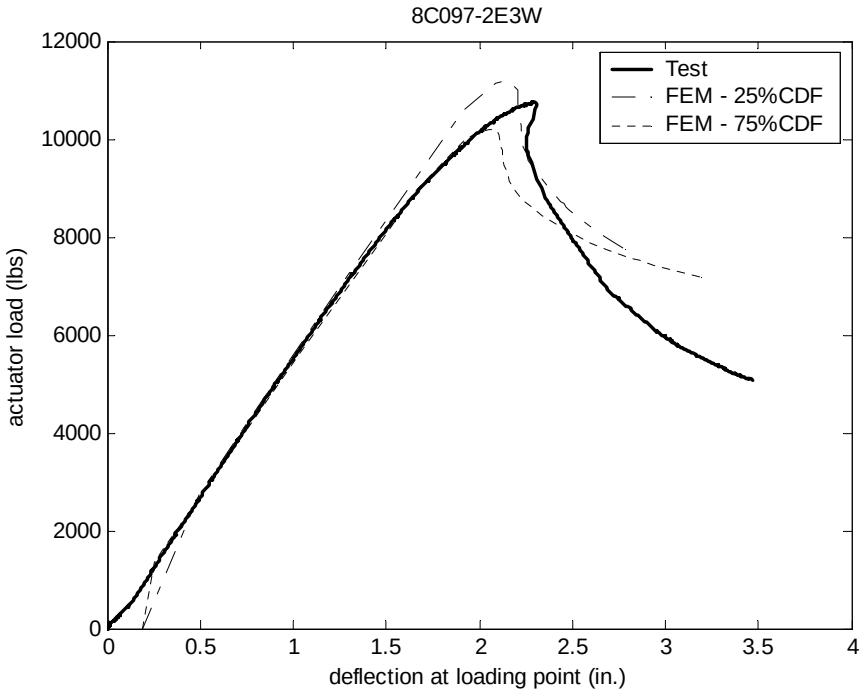

Figure 5.29 Comparison of FEM results with test 8C097-2E3W

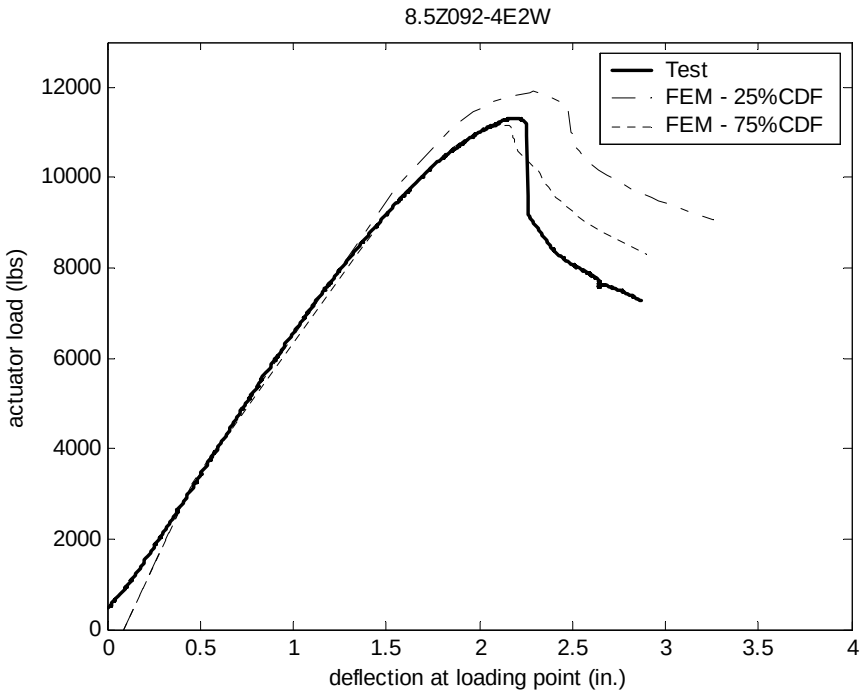

Figure 5.30 Comparison of FEM results with test 8.5Z092-4E2W

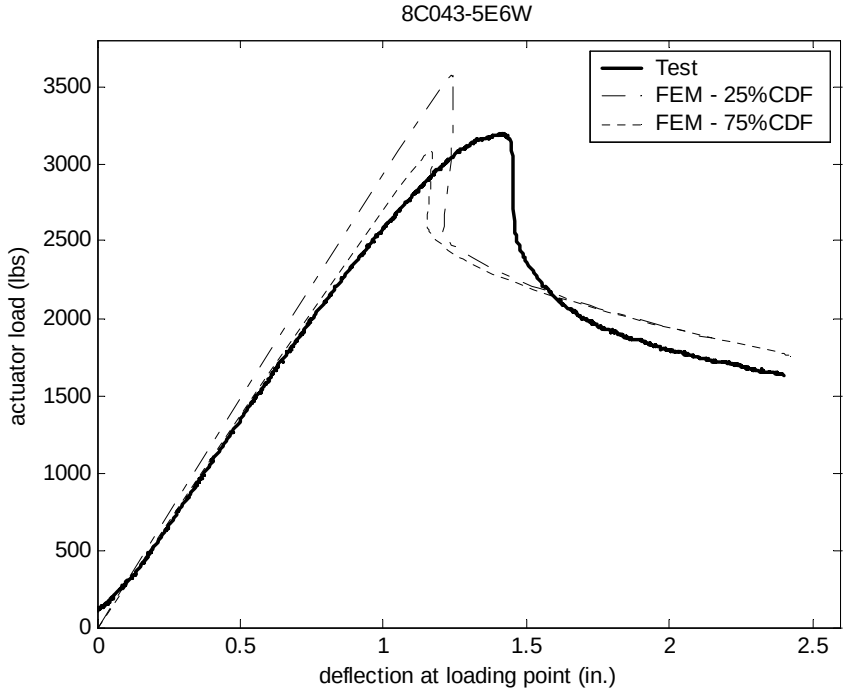

Figure 5.31 Comparison of FEM results with test 8C043-5E6W

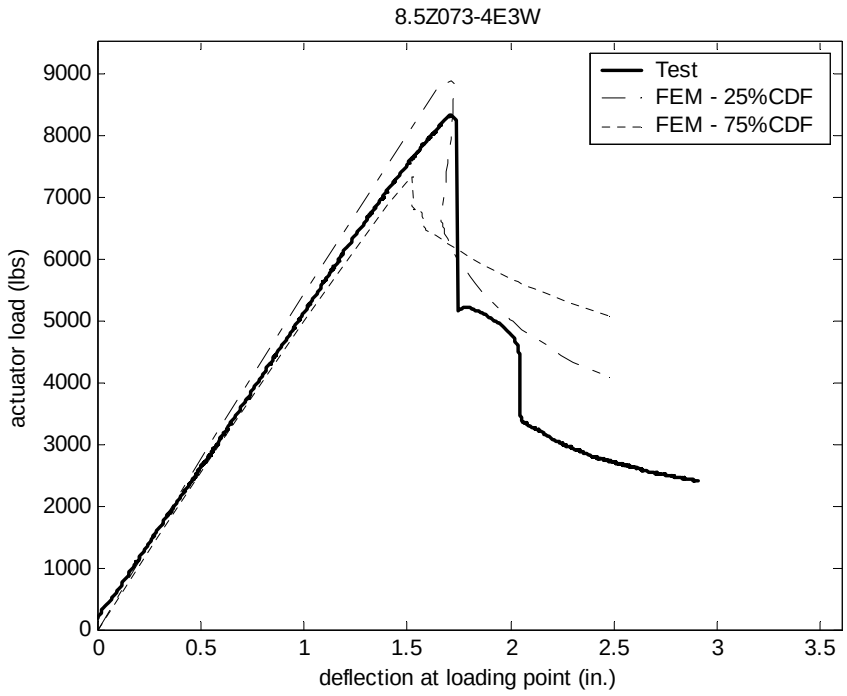

Figure 5.32 Comparison of FEM results with test 8.5Z073-4E3W

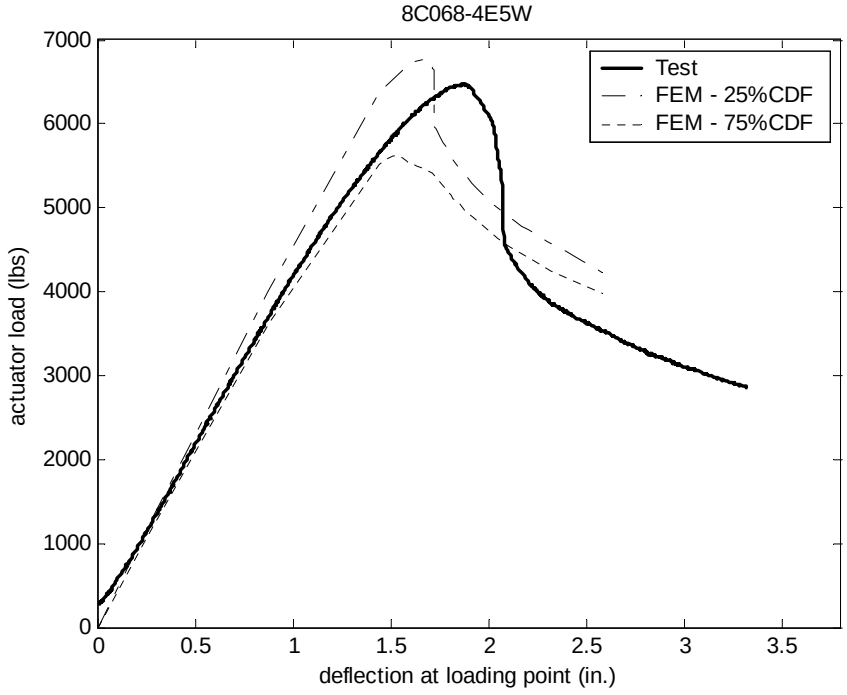

Figure 5.33 Comparison of FEM results with test 8C068-4E5W

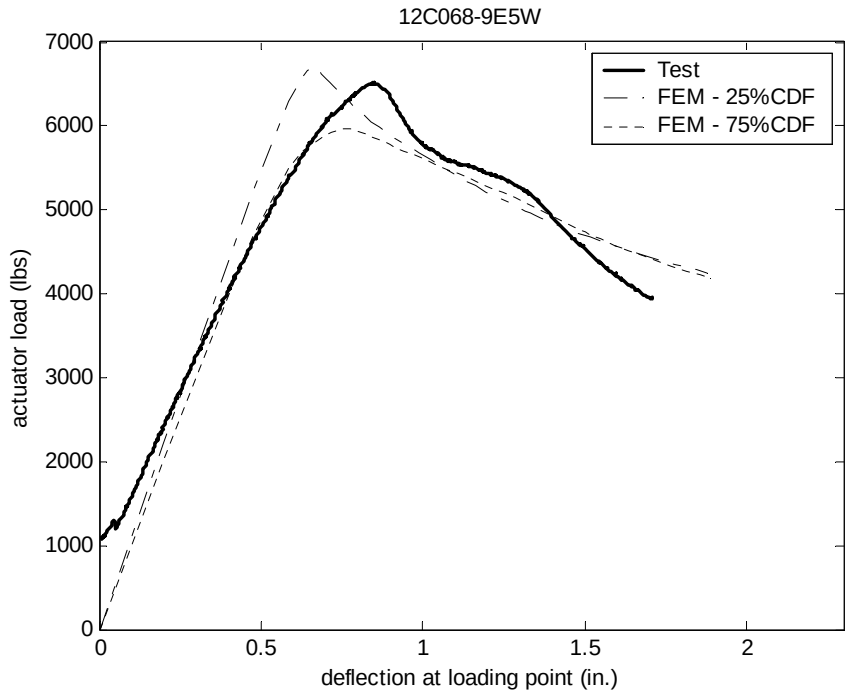

Figure 5.34 Comparison of FEM results with test 12C068-9E5W

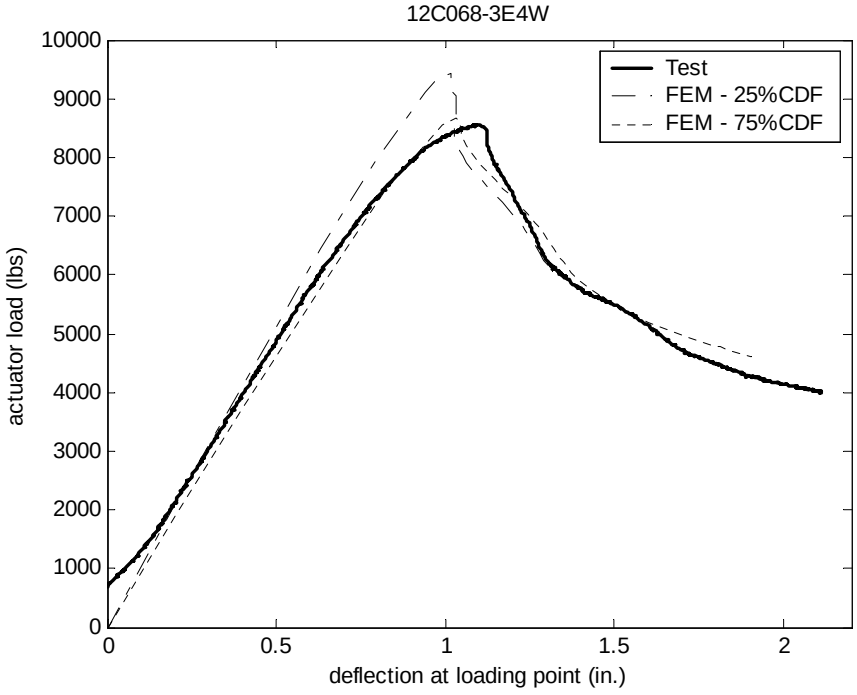

Figure 5.35 Comparison of FEM results with test 12C097-3E4W

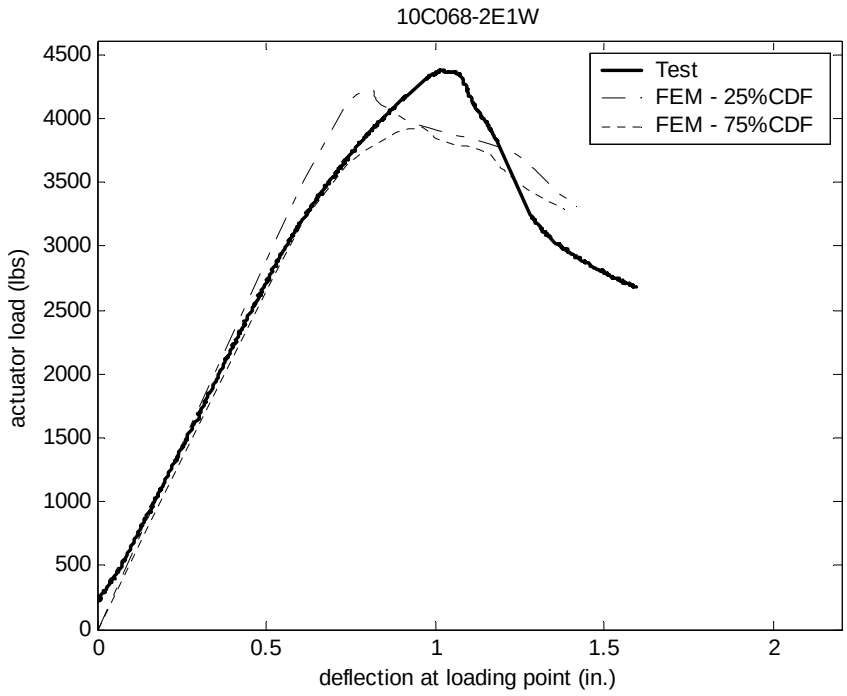

Figure 5.36 Comparison of FEM results with test 10C068-2E1W

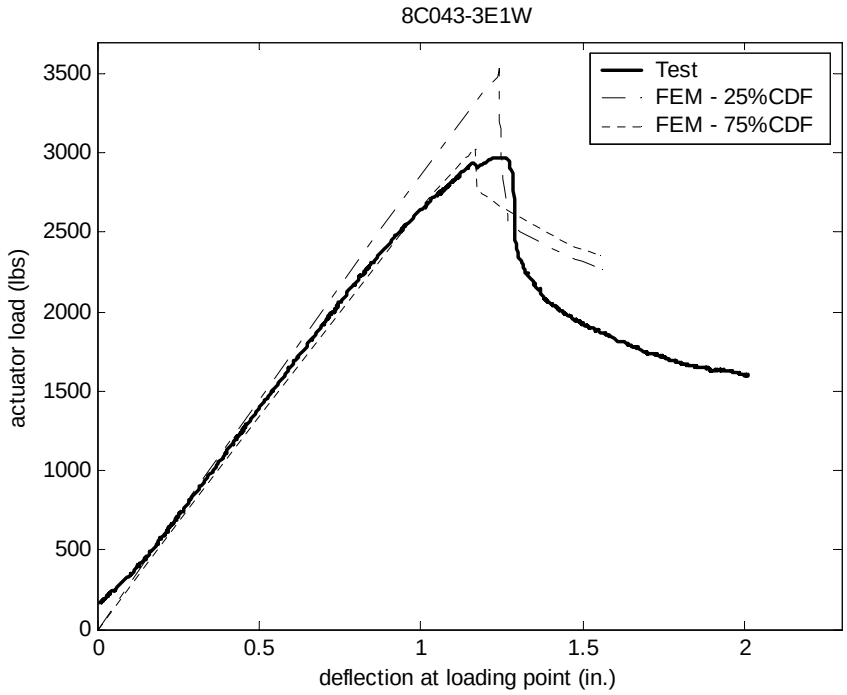

Figure 5.37 Comparison of FEM results with test 8C043-3E1W

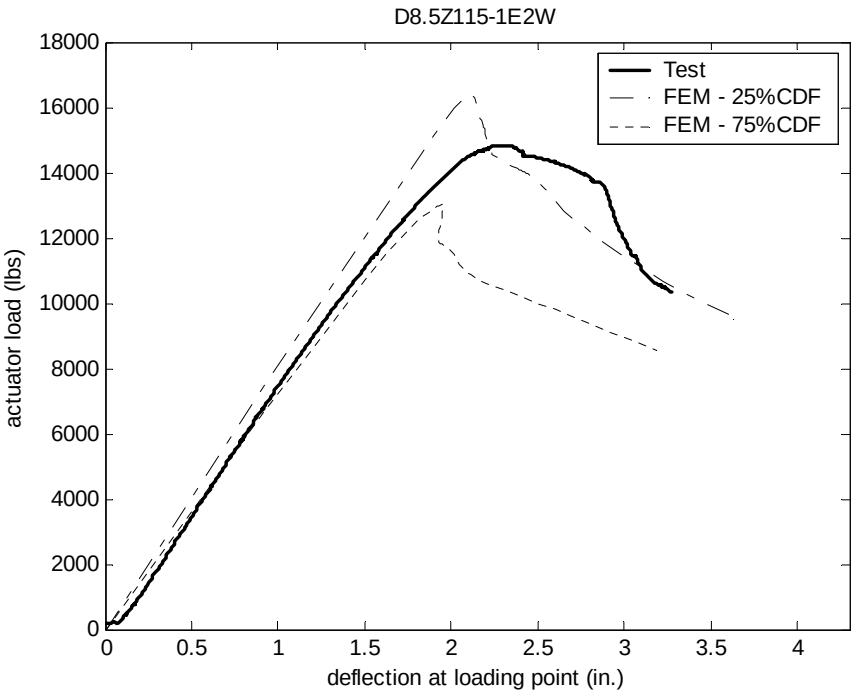

Figure 5.38 Comparison of FEM results with test D8.5Z115-1E2W

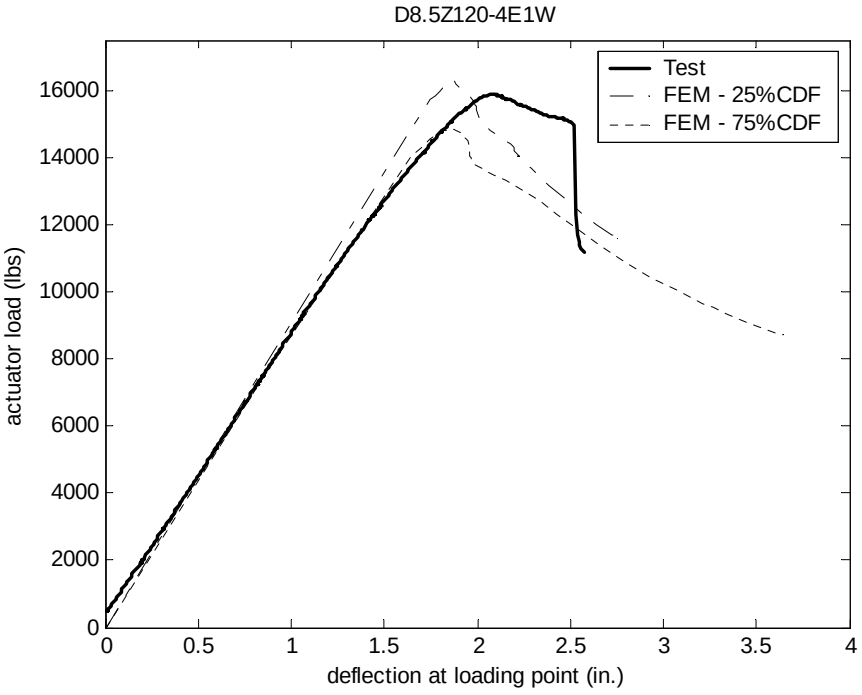

Figure 5.39 Comparison of FEM results with test D8.5Z120-4E1W

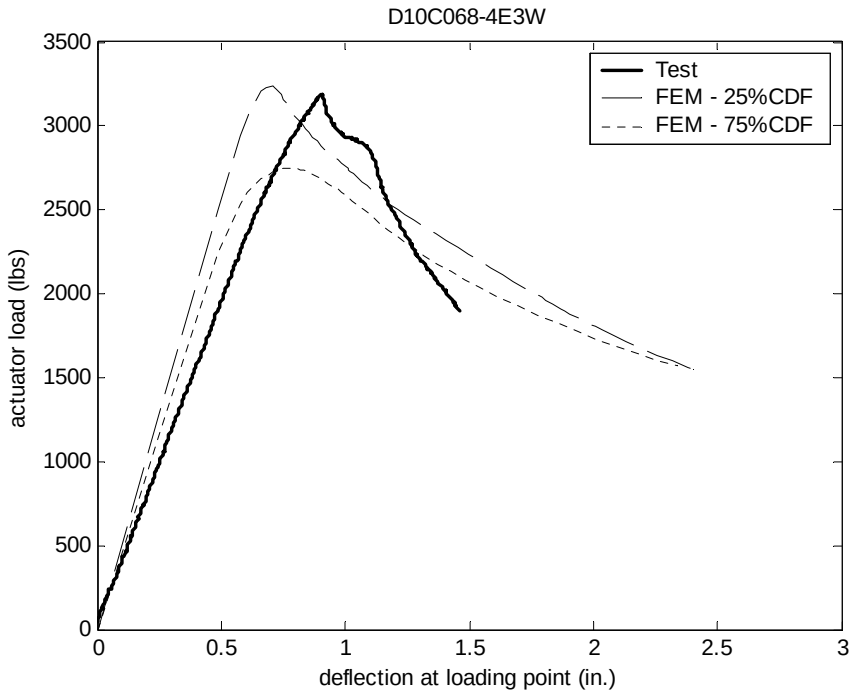

Figure 5.40 Comparison of FEM results with test D10C068-4E3W

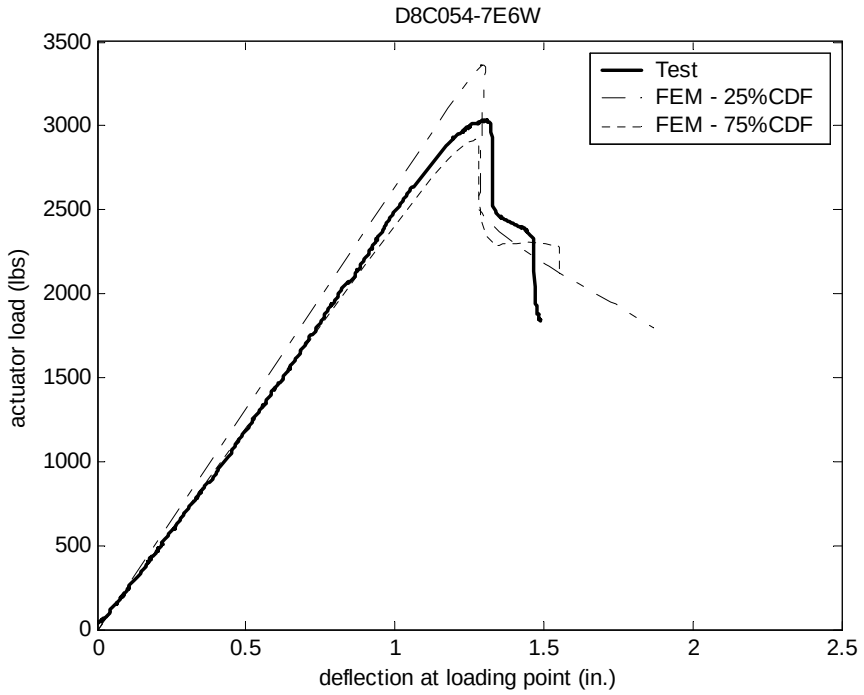

Figure 5.41 Comparison of FEM results with test D8C054-7E6W

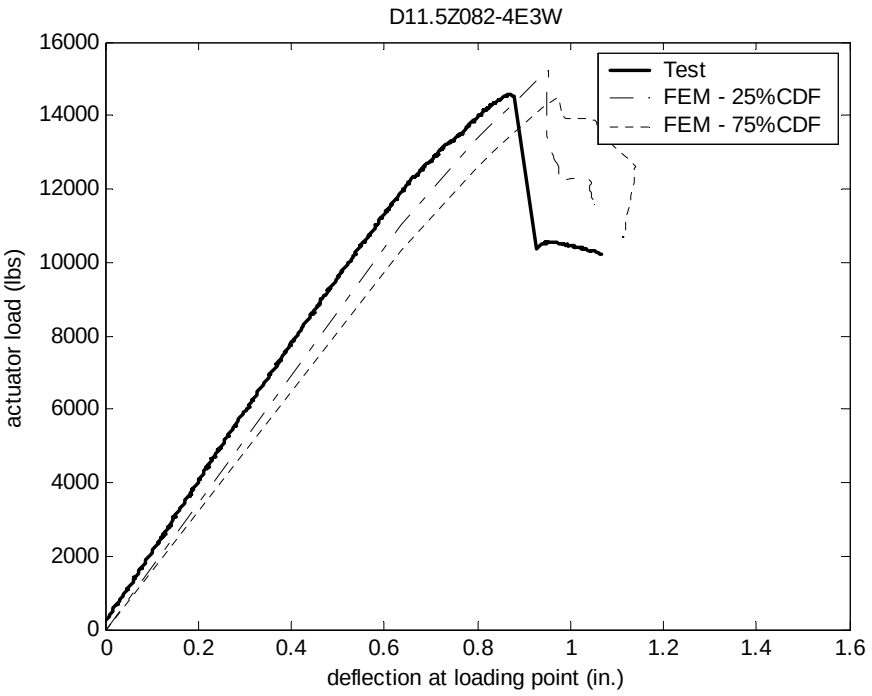

Figure 5.42 Comparison of FEM results with test D11.5Z082-4E3W

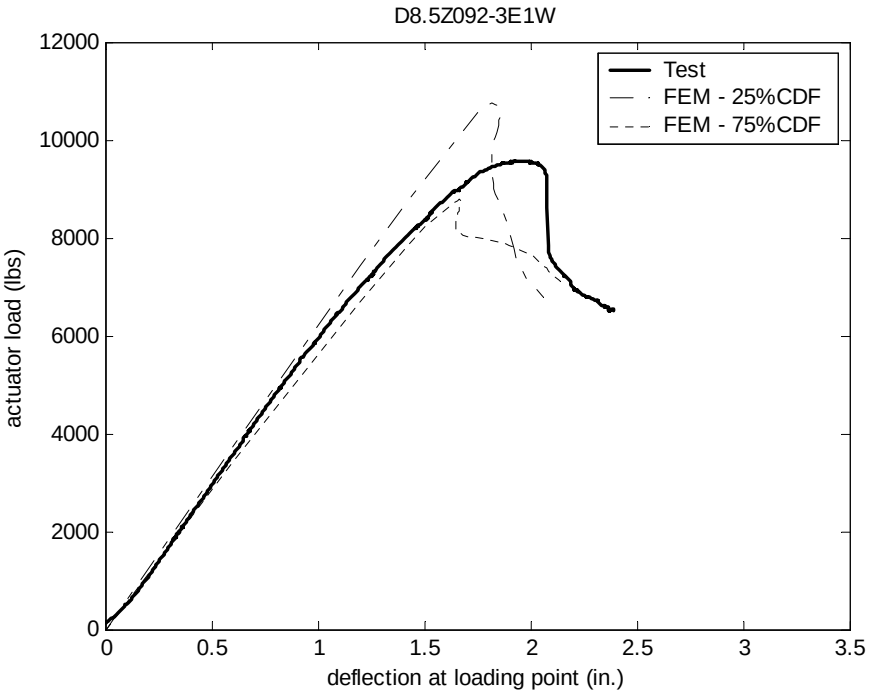

Figure 5.43 Comparison of FEM results with test D8.5Z092-3E1W

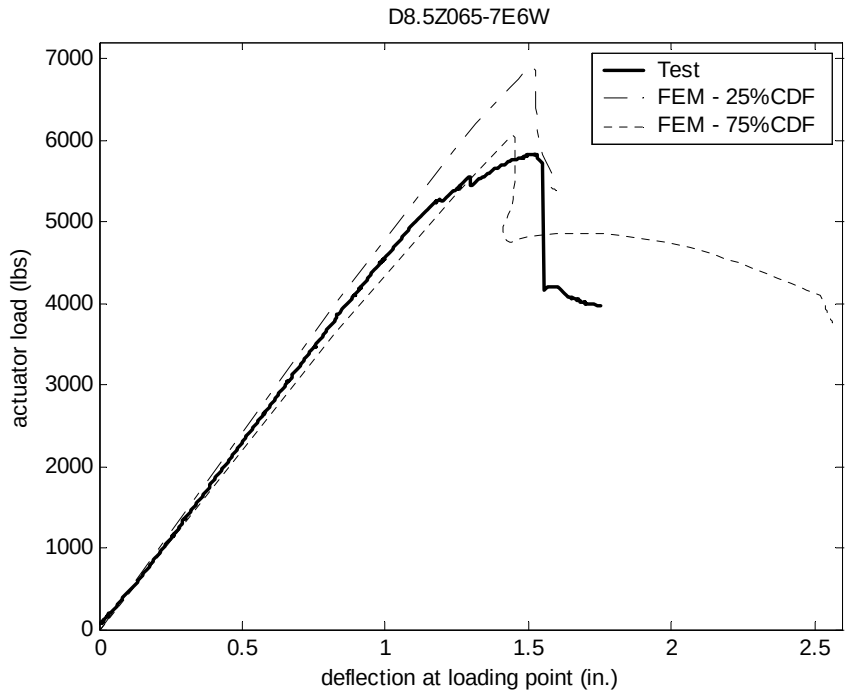

Figure 5.44 Comparison of FEM results with test D8.5Z065-7E6W

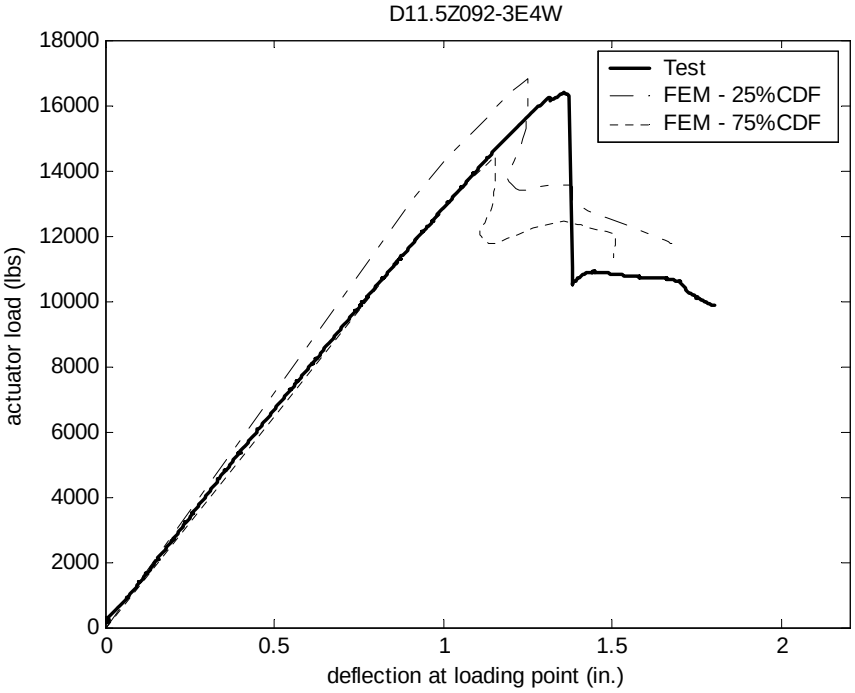

Figure 5.45 Comparison of FEM results with test D11.5Z092-3E4W

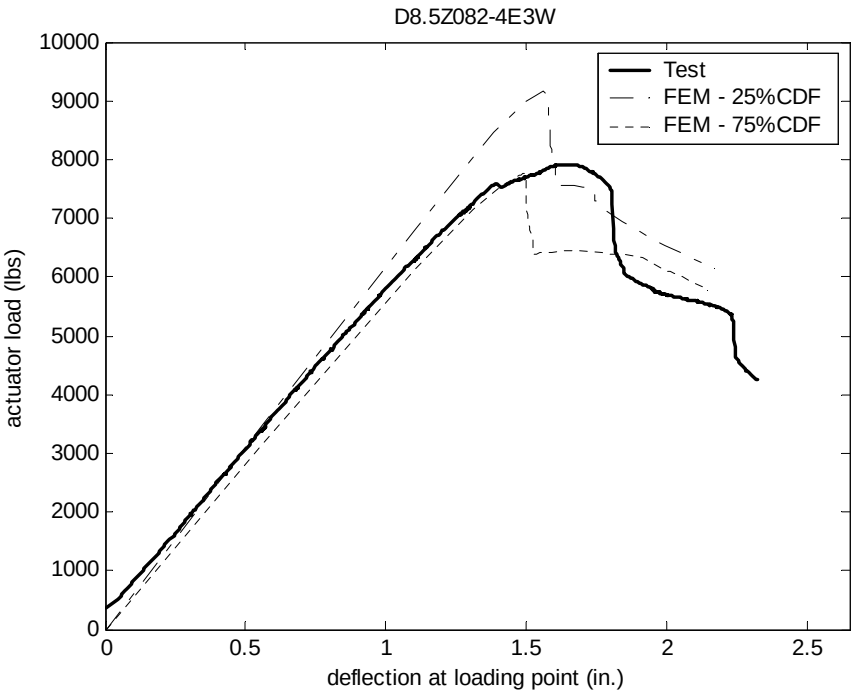

Figure 5.46 Comparison of FEM results with test D8.5Z082-4E3W

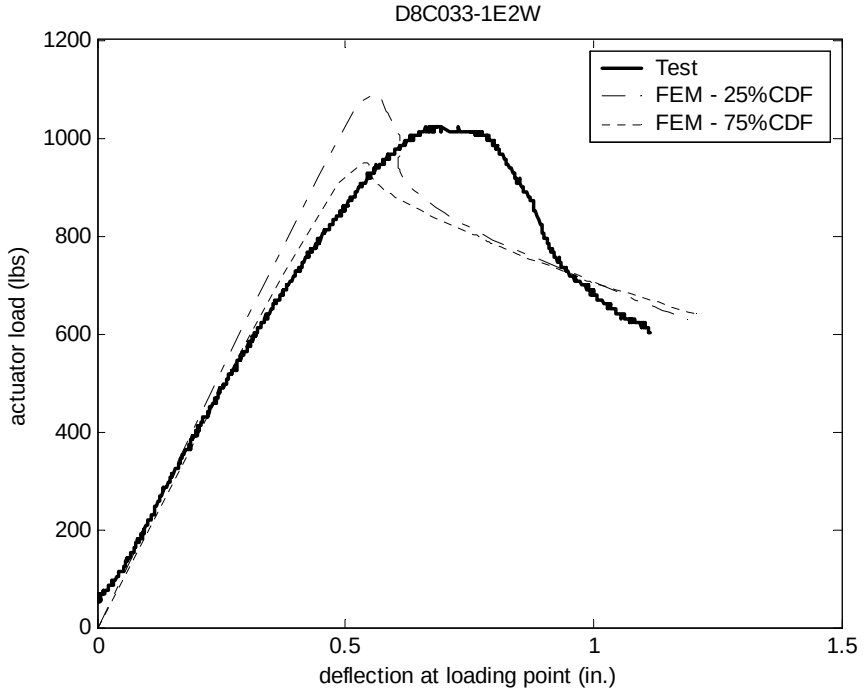

Figure 5.47 Comparison of FEM results with test 8C033-1E2W

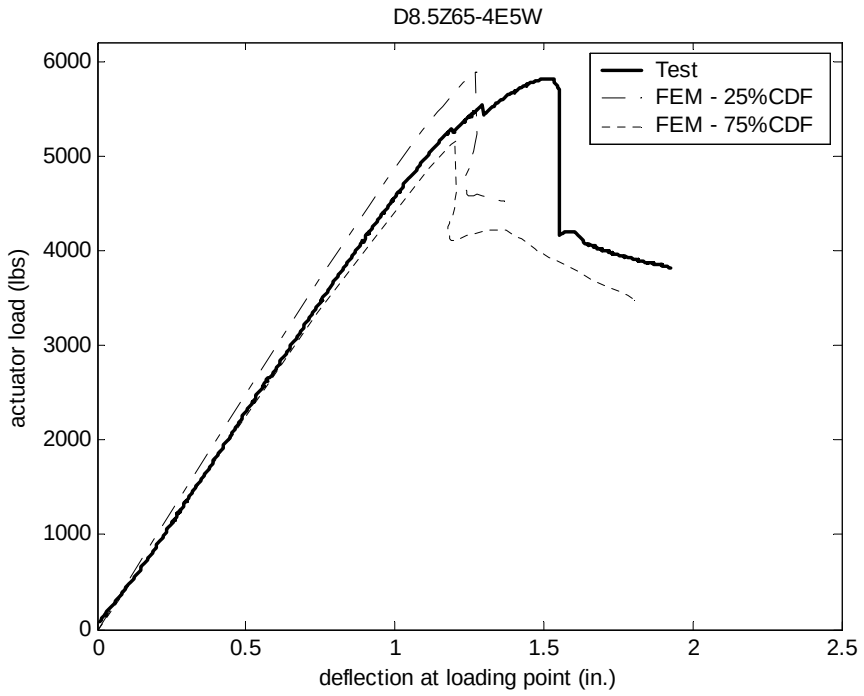

Figure 5.48 Comparison of FEM result with test D8.5Z065-4E5W

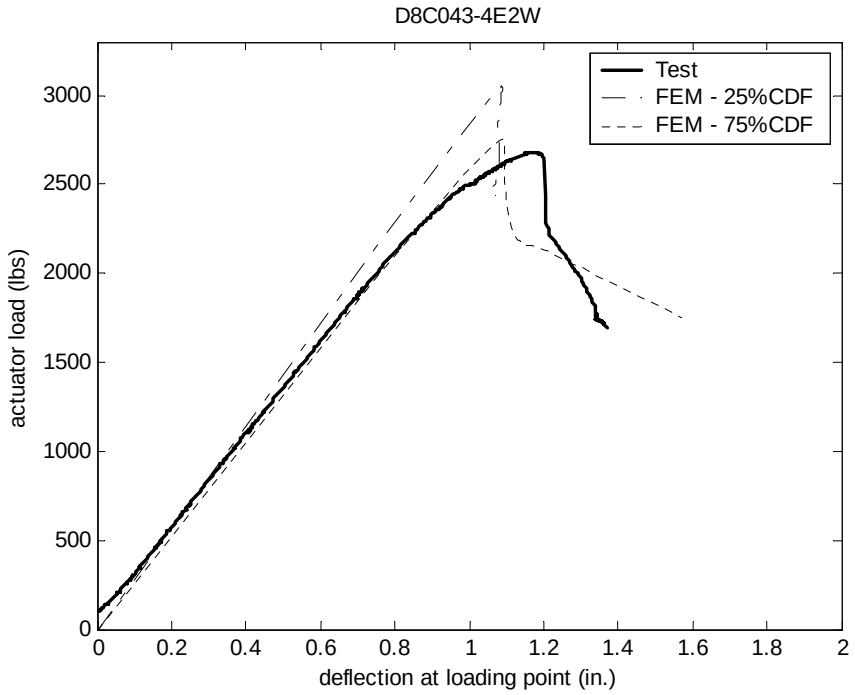

Figure 5.49 Comparison of FEM results with test D8C043-4E2W

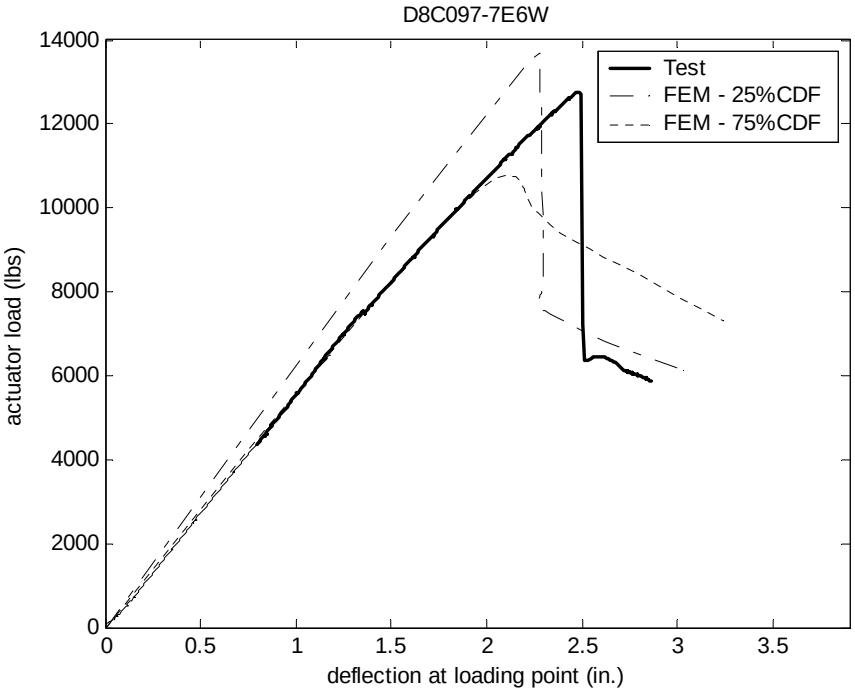

Figure 5.50 Comparison of FEM results with test D8C097-7E6W

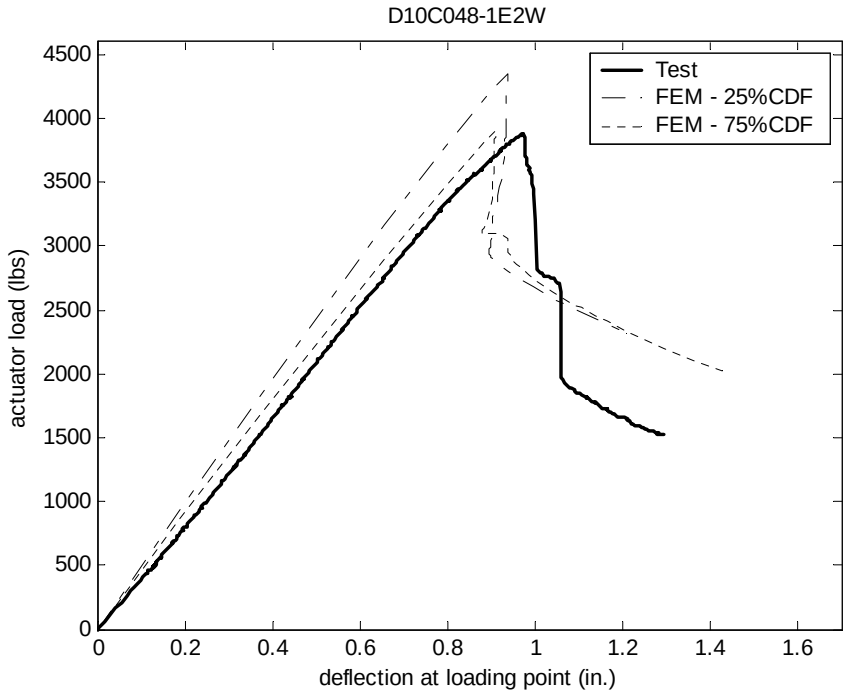

Figure 5.51 Comparison of FEM results with test D10C048-1E2W

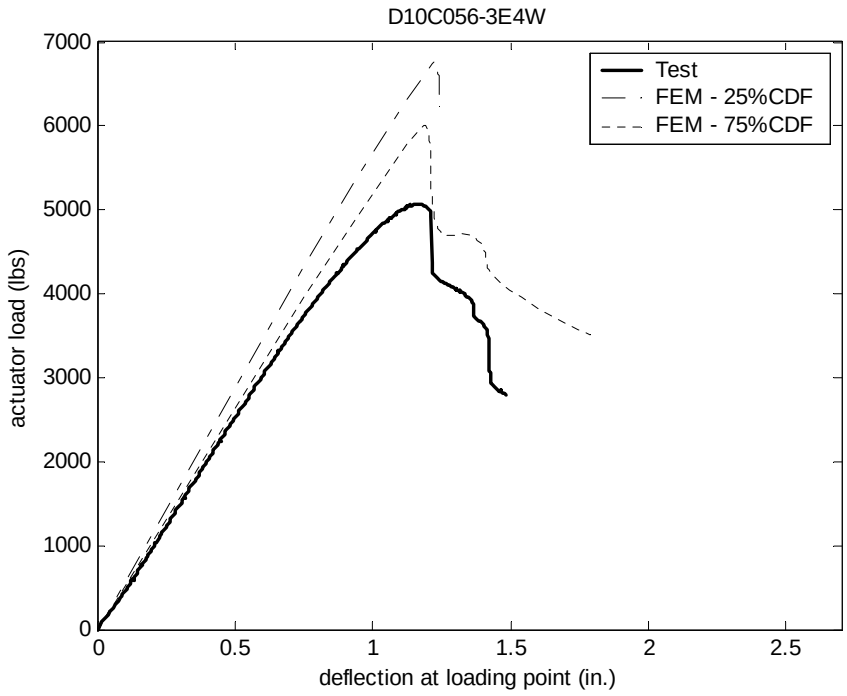

Figure 5.52 Comparison of FEM result with test D10C056-3E4W

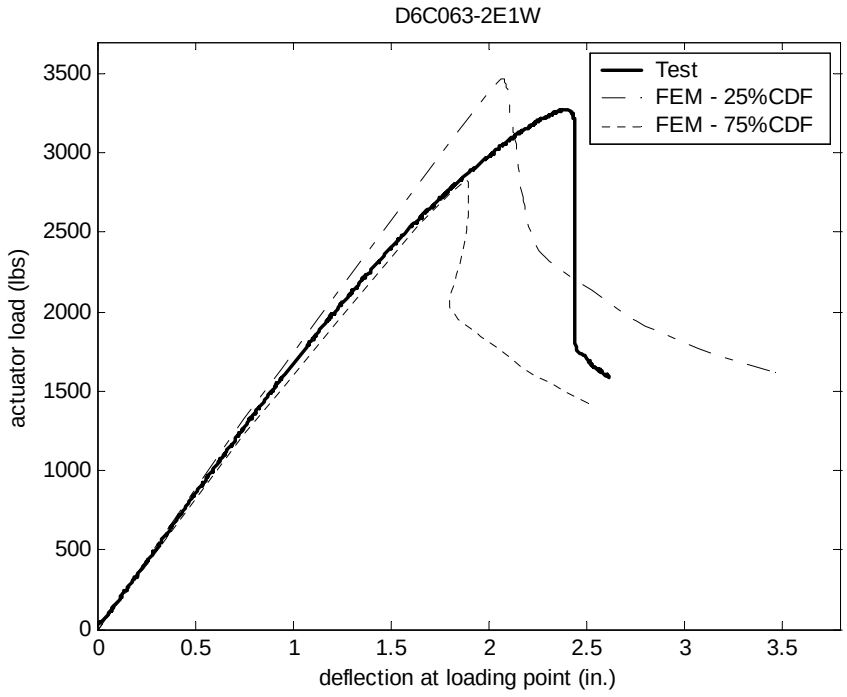

Figure 5.53 Comparison of FEM result with test D6C063-2E1W

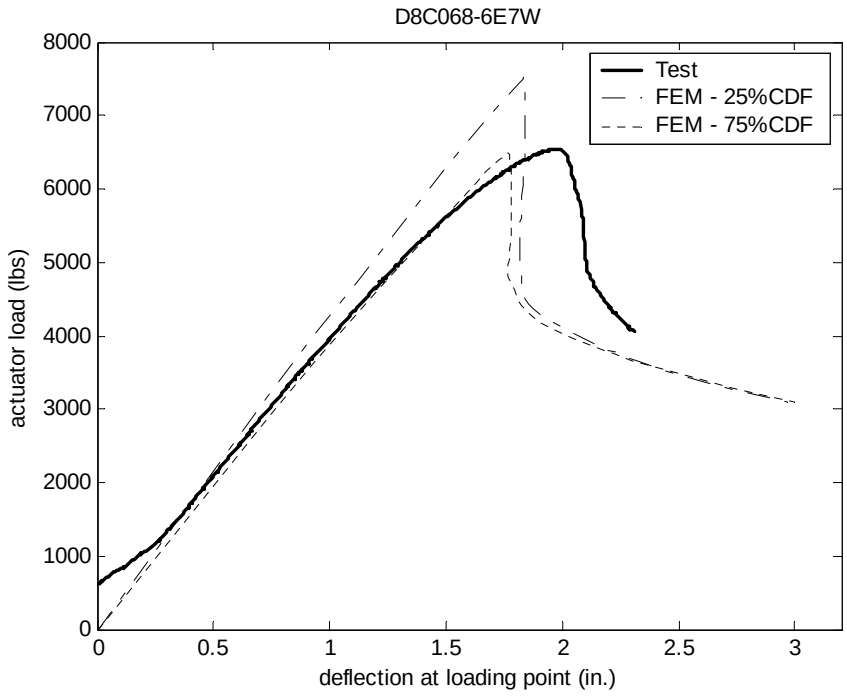

Figure 5.54 Comparison of FEM results with test D8C068-6E7W

5.6 Extended Finite Element Analysis on Cold-Formed Steel Beams

Given the successful verification of the developed finite element model, extension to a greater variety of cold-formed steel sections (not examined experimentally) is possible. The data obtained from both the tests and the extended finite element analysis is helpful for studying the Direct Strength Method, the effective width method, and post-buckling reserve on a broad range of cold-formed steel beams.

The geometry for the extended FE modeling was chosen to cover the full-range of expected industry standard cold-formed steel sections, as discussed in Section 2.2.1, and summarized in Table 5.6. Seven stress-strain curves, obtained from the tension tests, were used for the material model. The method of generating geometric imperfections described in Section 5.4.3 was again employed. The maximum imperfection magnitude was

selected to correspond to a 50% probability of exceedance (50% CDF: $d_1/t = 0.34$ for local buckling mode; $d_2/t = 0.94$ for distortional buckling mode). Based on the results of Table 5.4 and Table 5.5, an FEM model with an imperfection from the 50% CDF value will, on average, provide strength predictions less than 7% offset from the tested strength. The section geometry, material yield stress, and FEM results, are detailed in Table 5.7.

Table 5.6 Summary of geometry and yield stress of analyzed sections

	h/t	b/t	d/t	f_y (ksi)
Max	176	46	18	73.4
Min	72	21	6	33.0

Table 5.7 Section dements and results of extended finite element analyses

Specimen	h (in.)	b_c (in.)	d_c (in.)	θ_c (deg)	b_t (in.)	d_t (in.)	θ_t (deg)	r_{hc} (in.)	r_{dc} (in.)	r_{ht} (in.)	r_{dt} (in.)	t (in.)	f_y (ksi)	M_y (kip-in.)	M_{crL} (kip-in.)	M_{crD} (kip-in.)	M_{FEL} (kip-in.)	M_{FED} (kip-in.)	M_{DSL} (kip-in.)	M_{DSD} (kip-in.)
8Z2.25x050	8.0	2.3	0.9	50	2.3	0.9	50	0.24	0.24	0.24	0.24	0.0500	33.0	54.7	56.1	58.5	52.8	48.2	46.9	43.7
8Z2.25x050	8.0	2.3	0.9	50	2.3	0.9	50	0.24	0.24	0.24	0.24	0.0500	44.0	72.9	56.1	58.5	65.9	58.6	56.8	52.4
8Z2.25x050	8.0	2.3	0.9	50	2.3	0.9	50	0.24	0.24	0.24	0.24	0.0500	56.1	93.0	56.1	58.5	79.1	67.6	66.7	60.9
8Z2.25x050	8.0	2.3	0.9	50	2.3	0.9	50	0.24	0.24	0.24	0.24	0.0500	62.2	103.2	56.1	58.5	83.5	70.6	71.4	64.8
8Z2.25x050	8.0	2.3	0.9	50	2.3	0.9	50	0.24	0.24	0.24	0.24	0.0500	73.4	121.7	56.1	58.5	89.6	76.0	79.5	71.5
8Z2.25x100	8.0	2.3	0.9	50	2.3	0.9	50	0.24	0.24	0.24	0.24	0.0500	33.0	106.2	438.0	261.5	114.2	114.2	106.2	106.2
8Z2.25x100	8.0	2.3	0.9	50	2.3	0.9	50	0.24	0.24	0.24	0.24	0.0500	44.0	141.6	438.0	261.5	145.6	136.4	141.6	134.9
8Z2.25x100	8.0	2.3	0.9	50	2.3	0.9	50	0.24	0.24	0.24	0.24	0.0500	56.1	180.6	438.0	261.5	180.3	165.5	180.6	159.8
8Z2.25x100	8.0	2.3	0.9	50	2.3	0.9	50	0.24	0.24	0.24	0.24	0.0500	62.2	200.3	438.0	261.5	189.1	173.3	200.3	171.3
8Z2.25x100	8.0	2.3	0.9	50	2.3	0.9	50	0.24	0.24	0.24	0.24	0.0500	73.4	236.3	438.0	261.5	214.1	196.0	236.3	191.0
8.5Z2.5x70	8.5	2.5	0.9	50	2.5	0.9	50	0.25	0.25	0.25	0.25	0.0700	73.4	193.2	152.3	119.4	157.1	136.3	151.7	125.6
8.5Z2.5x70	8.5	2.5	0.9	50	2.5	0.9	50	0.25	0.25	0.25	0.25	0.0700	62.2	163.8	152.3	119.4	142.6	124.2	135.9	113.6
8.5Z2.5x70	8.5	2.5	0.9	50	2.5	0.9	50	0.25	0.25	0.25	0.25	0.0700	56.1	147.6	152.3	119.4	135.5	119.0	126.8	106.5
8.5Z2.5x70	8.5	2.5	0.9	50	2.5	0.9	50	0.25	0.25	0.25	0.25	0.0700	44.0	115.8	152.3	119.4	111.2	100.1	107.6	91.3
8.5Z2.5x70	8.5	2.5	0.9	50	2.5	0.9	50	0.25	0.25	0.25	0.25	0.0700	33.0	86.8	152.3	119.4	87.9	81.7	86.8	75.6
11.5Z3.5x80	11.5	3.5	0.9	50	3.5	0.9	50	0.30	0.30	0.30	0.30	0.0800	33.0	179.5	221.9	169.9	171.3	152.4	163.5	137.3
11.5Z3.5x80	11.5	3.5	0.9	50	3.5	0.9	50	0.30	0.30	0.30	0.30	0.0800	44.0	239.4	221.9	169.9	212.7	182.6	198.4	164.3
11.5Z3.5x80	11.5	3.5	0.9	50	3.5	0.9	50	0.30	0.30	0.30	0.30	0.0800	56.1	305.3	221.9	169.9	255.5	213.0	233.2	190.4
11.5Z3.5x80	11.5	3.5	0.9	50	3.5	0.9	50	0.30	0.30	0.30	0.30	0.0800	62.2	338.6	221.9	169.9	267.6	224.3	249.7	202.5
11.5Z3.5x80	11.5	3.5	0.9	50	3.5	0.9	50	0.30	0.30	0.30	0.30	0.0800	73.4	399.5	221.9	169.9	292.7	242.5	278.3	223.1
8C068	7.9	1.9	0.7	80	2.0	0.6	77.8	0.16	0.16	0.16	0.16	0.0700	33.0	65.2	134.3	136.3	69.4	63.7	65.2	64.3
8C068	7.9	1.9	0.7	80	2.0	0.6	77.8	0.16	0.16	0.16	0.16	0.0700	44.0	86.9	134.3	136.3	87.5	79.4	85.0	78.9
8C068	7.9	1.9	0.7	80	2.0	0.6	77.8	0.16	0.16	0.16	0.16	0.0700	56.1	110.8	134.3	136.3	107.2	97.1	100.3	92.9
8C068	7.9	1.9	0.7	80	2.0	0.6	77.8	0.16	0.16	0.16	0.16	0.0700	62.2	122.9	134.3	136.3	112.5	101.8	107.5	99.4
8C068	7.9	1.9	0.7	80	2.0	0.6	77.8	0.16	0.16	0.16	0.16	0.0700	73.4	145.0	134.3	136.3	115.1	115.1	120.2	110.6
8.5Z092	8.4	2.6	0.9	51.8	2.4	1.0	50.4	0.28	0.28	0.31	0.31	0.0900	33.0	108.0	332.7	208.9	117.2	109.5	108.0	104.3
8.5Z092	8.4	2.6	0.9	51.8	2.4	1.0	50.4	0.28	0.28	0.31	0.31	0.0900	44.0	144.1	332.7	208.9	149.3	136.6	144.1	127.5
8.5Z092	8.4	2.6	0.9	51.8	2.4	1.0	50.4	0.28	0.28	0.31	0.31	0.0900	56.1	183.7	332.7	208.9	185.4	165.9	183.7	149.9
8.5Z092	8.4	2.6	0.9	51.8	2.4	1.0	50.4	0.28	0.28	0.31	0.31	0.0900	62.2	203.7	332.7	208.9	194.0	172.8	202.6	160.3
8.5Z092	8.4	2.6	0.9	51.8	2.4	1.0	50.4	0.28	0.28	0.31	0.31	0.0900	73.4	240.3	332.7	208.9	221.1	193.2	227.0	178.1
8.5Z120	8.5	2.6	1.0	47.8	2.5	1.0	48.9	0.36	0.36	0.34	0.34	0.1176	33.0	142.6	728.9	365.5	155.6	149.7	142.6	142.6
8.5Z120	8.5	2.6	1.0	47.8	2.5	1.0	48.9	0.36	0.36	0.34	0.34	0.1176	44.0	190.2	728.9	365.5	198.2	190.3	190.2	183.2
8.5Z120	8.5	2.6	1.0	47.8	2.5	1.0	48.9	0.36	0.36	0.34	0.34	0.1176	56.1	242.5	728.9	365.5	245.7	236.2	242.5	217.3
8.5Z120	8.5	2.6	1.0	47.8	2.5	1.0	48.9	0.36	0.36	0.34	0.34	0.1176	62.2	268.9	728.9	365.5	258.3	248.1	268.9	233.1
8.5Z120	8.5	2.6	1.0	47.8	2.5	1.0	48.9	0.36	0.36	0.34	0.34	0.1176	73.4	317.3	728.9	365.5	293.0	283.3	317.3	260.1

Table 5.7 (continued)

Specimen	h (in.)	b_c (in.)	d_c (in.)	θ_c (deg)	b_t (in.)	d_t (in.)	θ_t (deg)	r_{hc} (in.)	r_{dc} (in.)	r_{ht} (in.)	r_{dt} (in.)	t (in.)	f_y (ksi)	M_y (kip-in.)	M_{crL} (kip-in.)	M_{crD} (kip-in.)	M_{FEL} (kip-in.)	M_{FED} (kip-in.)	M_{DSL} (kip-in.)	M_{DSD} (kip-in.)
8.5Z082	8.46	2.50	0.95	49.0	2.36	0.97	50.3	0.28	0.28	0.30	0.30	0.0806	33.0	97.0	236.1	164.0	103.2	94.8	97.0	91.2
8.5Z082	8.46	2.50	0.95	49.0	2.36	0.97	50.3	0.28	0.28	0.30	0.30	0.0806	44.0	129.3	236.1	164.0	130.6	116.9	129.3	113.2
8.5Z082	8.46	2.50	0.95	49.0	2.36	0.97	50.3	0.28	0.28	0.30	0.30	0.0806	56.1	164.9	236.1	164.0	161.2	141.3	164.9	136.0
8.5Z082	8.46	2.50	0.95	49.0	2.36	0.97	50.3	0.28	0.28	0.30	0.30	0.0806	62.2	182.8	236.1	164.0	169.6	147.3	179.8	147.2
8.5Z082	8.46	2.50	0.95	49.0	2.36	0.97	50.3	0.28	0.28	0.30	0.30	0.0806	73.4	215.7	236.1	164.0	204.2	164.4	205.6	167.6
8C097	8.04	2.09	0.58	85.1	2.07	0.53	86.3	0.28	0.28	0.29	0.28	0.0980	33.0	90.1	361.0	258.0	98.1	92.3	90.1	90.1
8C097	8.04	2.09	0.58	85.1	2.07	0.53	86.3	0.28	0.28	0.29	0.28	0.0980	44.0	120.1	361.0	258.0	124.6	118.0	120.1	120.1
8C097	8.04	2.09	0.58	85.1	2.07	0.53	86.3	0.28	0.28	0.29	0.28	0.0980	56.1	153.1	361.0	258.0	154.6	140.6	153.1	148.0
8C097	8.04	2.09	0.58	85.1	2.07	0.53	86.3	0.28	0.28	0.29	0.28	0.0980	62.2	169.8	361.0	258.0	162.9	148.3	169.8	160.7
8C097	8.04	2.09	0.58	85.1	2.07	0.53	86.3	0.28	0.28	0.29	0.28	0.0980	73.4	200.3	361.0	258.0	184.9	162.8	200.3	183.8
12C068	12.00	2.00	0.60	85.0	2.00	0.60	85.0	0.26	0.27	0.26	0.26	0.0680	33.0	113.4	99.6	110.7	94.0	93.2	97.2	92.7
12C068	12.00	2.00	0.60	85.0	2.00	0.60	85.0	0.26	0.27	0.26	0.26	0.0680	44.0	151.2	99.6	110.7	114.9	114.1	122.0	115.8
12C068	12.00	2.00	0.60	85.0	2.00	0.60	85.0	0.26	0.27	0.26	0.26	0.0680	56.6	194.5	99.6	110.7	146.9	132.7	151.0	142.8
12C068	12.00	2.00	0.60	85.0	2.00	0.60	85.0	0.26	0.27	0.26	0.26	0.0680	62.2	213.7	99.6	110.7	155.4	139.2	164.4	155.3
12C068	12.00	2.00	0.60	85.0	2.00	0.60	85.0	0.26	0.27	0.26	0.26	0.0680	73.4	252.2	99.6	110.7	168.6	148.2	192.9	182.1

Note: M_{crL} --- elastic local buckling moment;
M_{crD} --- elastic distortional buckling moment;
M_{FEL} --- local buckling strength by finite element model;
M_{FED} --- distortional buckling strength by finite element model;
M_{DSL} --- local buckling strength prediction by Direct Strength Method;
M_{DSD} --- distortional buckling strength prediction by Direct Strength Method.

5.6.1 The Performance of the Direct Strength Method

Figure 5.55 shows a comparison of the local buckling strength of cold-formed steel beams calculated by the Direct Strength Method with data from both the tests and the extended FEM simulations. The figure provides the normalized bending capacity (M_n/M_y) as a function of the section slenderness ratio. A similar comparison for distortional buckling is provided in Figure 5.56. The Direct Strength Method provides a good agreement with the combined data for both local and distortional buckling strength. The local buckling strength predictions are more scattered than those of distortional buckling. Though slender sections, $(M_y/M_{crd})^{0.5} > 1.0$, in distortional buckling demonstrate noticeable scatter.

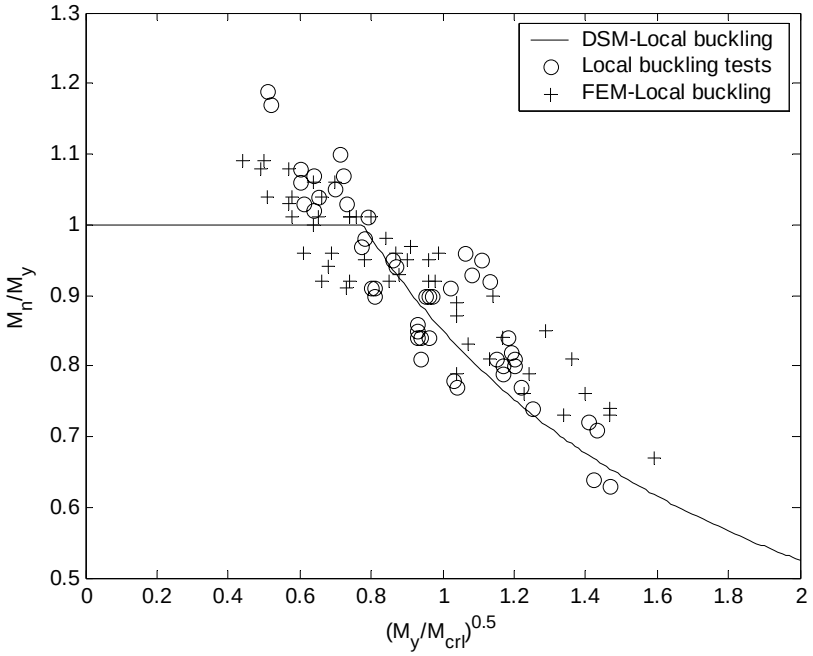

Figure 5.55 Performance of the DSM prediction of local buckling strengths

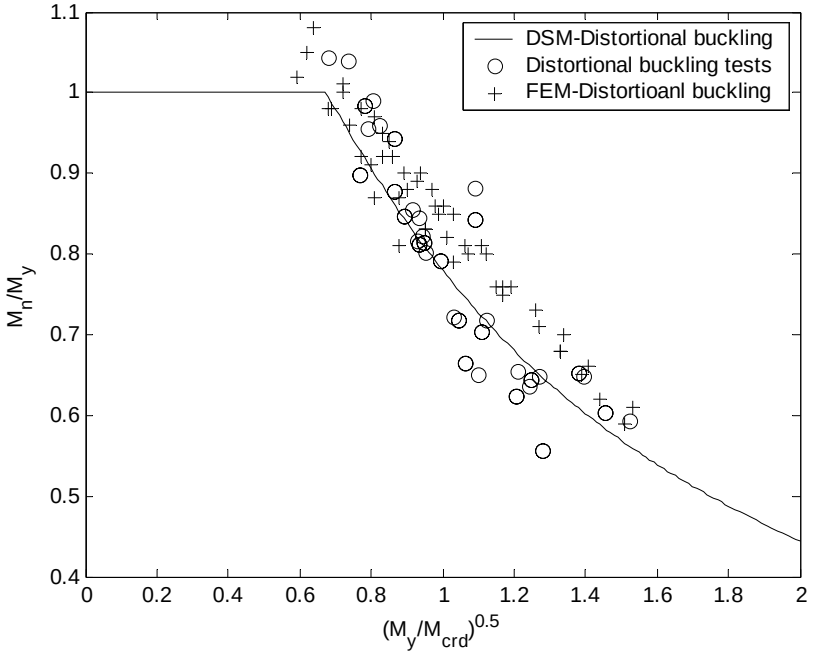

Figure 5.56 Performance of the DSM prediction of distortional buckling strengths

Table 5.8 Summary of DSM predictions vs. test and FEM results

		Local buckling		Distortional buckling	
		M_n/M_{DSM}	Number	M_n/M_{DSM}	Number
Tests	μ	1.03	23	1.01	18
	σ	0.06	23	0.07	18
FEM	μ	1.02	50	1.04	50
	σ	0.07	50	0.07	50
Overall	μ	1.03	73	1.03	68
	σ	0.07	73	0.07	68

Note: μ – average;
σ – standard deviation;
M_n – bending capacity of beams;
M_{DSM} – predictions of Direct Strength Method;
Number – the number of analyzed sections.

Table 5.8 summarizes the comparison of DSM predictions with both the tested and extended FEM model bending capacities. In general, DSM provides reliable and conservative predictions for the bending strength of cold-formed steel beams. On average, the tested strength is 3% greater than the predicted strength with a standard deviation of 7%, for both local and distortional buckling failures.

5.6.2 The Web Effective Width

The results of both series of tests and the extended finite element analyses have indicated that current specifications AISI (1996), CSA S136 (1994), NAS (2001) AS/NZS (1996), and, EN1993 (2002) have good predictions for the local buckling strength of cold-formed steel beams. However the effective width equations for web elements in flexure are significantly different between AISI (1996), CSA S136 (1994) and EN1993 (2002) Specification (AS/NZS adopts the same method as AISI). A consistent effective width approach for web elements was also proposed by Schafer (1997). In the process of harmonization of the AISI (1996) and CSA S136 (1994) for the North American Specification (NAS 2001), an interim solution was adopted by using the AISI approach when $h_0/b_0 \leq 4$ and the CSA S136 approach when $h_0/b_0 > 4$ (h_0 is the out-to-out width of the web and b_0 is the out-to-out width of the compression flange). Four existing procedures are presented for calculations of b_1 and b_2 (as shown in Figure 5.57). The four selected procedures are: AISI Specification (1996), Canadian CSA S136 Specification (1996), Eurocode EN1993 (2002), and a proposed approach by Schafer (1997). In each method, the procedure follows the same steps:

- Based on ψ ($\psi = f_1/f_2$) the plate buckling coefficient, k, is estimated.
- An effective width, b_e, is determined using Winter's equation, at stress f_1 and k of previous step.
- Based on ψ empirical expressions are used to determine b_1 and b_2

AISI Specification (1996)

Determine effective width b_e

$$k = 4 + 2(1-\psi)^3 + 2(1-\psi)$$

$$\lambda = \frac{1.052}{\sqrt{k}}\left(\frac{w}{t}\right)\sqrt{\frac{f_1}{E}}$$

$\lambda \le 0.673$

$$b_e = w$$

$\lambda > 0.673$

$$b_e = \rho w$$

$$\rho = (1 - 0.22/\lambda)/\lambda$$

Determine b_1 and b_2

$$b_1 = b_e/(3-\psi)$$

$\psi \le -0.236$

$$b_2 = b_e/2$$

$b_1 + b_2$ shall not exceed the compression portion of the web.

$\psi > -0.236$

$$b_2 = b_e - b_1$$

CSA S136 Specification (1994)

Determine effective width b_e

$-1 \le \psi \le 1$

$$k = 4 + 2(1-\psi)^3 + 2(1-\psi)$$

$-3 \le \psi \le -1$

$$k = 6(1-\psi)^2$$

$$\lambda = \frac{1.052}{\sqrt{k}}\left(\frac{w}{t}\right)\sqrt{\frac{f_1}{E}}$$

$\lambda \le 0.673$

$$b_e = w$$

$\lambda > 0.673$

$$b_e = \rho w$$

$$\rho = (1 - 0.22/\lambda)/\lambda$$

Determine b_1 and b_2

$$b_1 = b_e/(3-\psi)$$

$\psi < 0$

$$b_2 = (b_e/(1-\psi)) - b_1$$

$\psi \ge 0$

$$b_2 = b_e - b_1$$

EN1993 Specification (2002)

Determine effective width b_e

$1 > \psi > 0$

$$k = \frac{8.2}{1.05 + \psi}$$

$0 > \psi > -1$

$$k = 7.81 - 6.29\psi + 9.78\psi^2$$

$-1 > \psi > -3$

$$k = 5.98(1-\psi)^2$$

$$\lambda = \frac{1.052}{\sqrt{k}}\left(\frac{w}{t}\right)\sqrt{\frac{f_1}{E}}$$

$\lambda \le 0.673$

$$b_e = w$$

$\lambda > 0.673$

$$b_e = \rho w$$

$$\rho = (1 - 0.22/\lambda)/\lambda$$

Determine b_1 and b_2

$\psi < 0$

$$b_1 = 0.4(b_e/(1-\psi))$$

$$b_2 = 0.6(b_e/(1-\psi))$$

$\psi \ge 0$

$$b_1 = 2b_e/(5-\psi)$$

$$b_2 = b_e - b_1$$

Schafer Method (1997)

$k = \frac{1}{2}(1-\psi)^3 + 4(1-\psi)^2 + 4$

$\lambda = \frac{1.052}{\sqrt{k}}\left(\frac{w}{t}\right)\sqrt{\frac{f_1}{E}}$

$\lambda \le 0.673$

$\rho = 1$ element is fully effective.

$\lambda > 0.673$

$\rho = (1 - 0.22/\lambda)/\lambda$

$0 \le \rho < 0.77 \quad \omega = 0.33\rho$

$0.77 \le \rho < 0.95 \quad \omega = 0.23$

$0.95 \le \rho \le 1.00 \quad \omega = -4.6\rho + 4.6$

$\psi < 0$

$b_1 = b\omega/(1-\psi)$

$b_2 = (b/(1-\psi))\sqrt{\omega^2 - 2\omega + \rho}$

$\psi \ge 0$

$b_1 = b[\omega - (\omega - \frac{1}{2}\rho)\psi]$

$b_2 = b\left[\sqrt{\omega^2 - 2\omega + \rho} - \left(\sqrt{\omega^2 - 2\omega + \rho} - \frac{1}{2}\rho\right)\psi\right]$

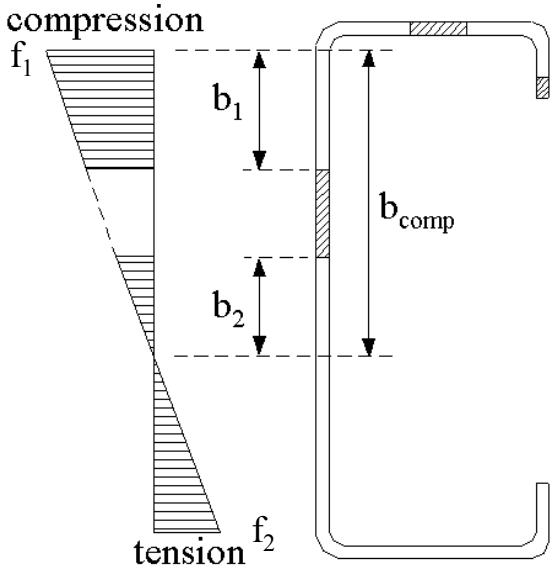

Figure 5.57 Web under a stress gradient

Assuming that the effective flange expressions of AISI (1996) are accurate, then we can use the experimentally observed capacity (as well as the FEM results) back-calculate the correct effective width for the web, expressed as $\rho=(b_1+b_2)/b_{comp}$, where b_1 and b_2 are the effective width of the compressive portions of the web, and b_{comp} is the depth of the full compression portion of the web, as shown in Figure 5.57. The results of this

calculation are given in Table 5.9 for the tested specimens (only controlling specimens in valid local buckling tests are included) and Table 5.10 for the sections analyzed by the extended finite element analysis (local buckling simulations), where $\lambda_{web} = \frac{1.052}{\sqrt{k}}\left(\frac{w}{t}\right)\sqrt{\frac{f_1}{E}} = \sqrt{f_y / f_{crweb}}$ (denoted as λ in the given Specification procedures).

Table 5.9 Web effectiveness for tested specimens

Specimen	AISI			S136			EN1993			Schafer		
	λ_{web}	ρ_{test}	ρ_{AISI}	λ_{web}	ρ_{test}	ρ_{S136}	λ_{web}	ρ_{test}	ρ_{EN1993}	λ_{web}	ρ_{test}	$\rho_{Schafer}$
8.5Z120-2	0.60	1.00	1.00	0.60	1.00	1.00	0.61	1.00	1.00	0.61	1.00	1.00
8.5Z105-1	0.73	1.00	1.00	0.73	1.00	0.96	0.73	1.00	0.96	0.73	1.00	0.98
8.5Z092-2	0.81	1.00	1.00	0.81	1.00	0.90	0.82	1.00	0.89	0.81	1.00	0.93
8.5Z082-1	0.92	0.96	1.00	0.92	0.94	0.83	0.92	0.95	0.83	0.92	0.97	0.88
8.5Z073-3	1.04	1.00	1.00	1.04	1.00	0.76	1.04	1.00	0.76	1.03	1.00	0.82
8.5Z065-1	1.16	0.71	1.00	1.16	0.62	0.70	1.16	0.68	0.70	1.15	0.73	0.77
8.5Z059-4	1.31	0.83	0.91	1.31	0.77	0.63	1.32	0.81	0.63	1.30	0.86	0.72
8.5Z059-1	1.31	0.78	0.92	1.31	0.70	0.63	1.32	0.75	0.63	1.30	0.80	0.72
8C097-3	0.74	1.00	1.00	0.74	1.00	0.95	0.74	1.00	0.95	0.74	1.00	0.97
8C068-5	0.87	0.87	1.00	0.87	0.81	0.86	0.87	0.85	0.86	0.87	0.89	0.90
8C068-2	1.09	0.92	1.00	1.09	0.89	0.73	1.09	0.91	0.73	1.09	0.94	0.80
8C054-1	1.33	0.78	0.91	1.33	0.70	0.63	1.34	0.75	0.62	1.33	0.81	0.71
8C043-6	1.37	0.65	0.88	1.37	0.54	0.61	1.38	0.61	0.61	1.36	0.68	0.70
8C043-1	1.28	0.85	0.96	1.28	0.78	0.65	1.29	0.83	0.64	1.28	0.87	0.73
12C068-9	1.63	0.51	0.78	1.63	0.40	0.53	1.63	0.47	0.53	1.62	0.56	0.64
12C068-4	1.19	0.87	1.00	1.19	0.82	0.69	1.19	0.86	0.68	1.19	0.90	0.76
10C068-1	0.66	1.00	1.00	0.66	1.00	1.00	0.66	1.00	1.00	0.66	1.00	1.00
6C054-2	0.52	1.00	1.00	0.52	1.00	1.00	0.52	1.00	1.00	0.52	1.00	1.00
4C054-2	0.39	1.00	1.00	0.39	1.00	1.00	0.39	1.00	1.00	0.38	1.00	1.00
3.62C054-1	1.06	1.00	1.00	1.06	1.00	0.75	1.07	1.00	0.74	1.05	1.00	0.81
11.5Z092-2	1.33	0.92	0.88	1.33	0.89	0.63	1.33	0.91	0.63	1.31	0.94	0.72
11.5Z082-2	1.65	0.57	0.73	1.65	0.47	0.52	1.66	0.53	0.52	1.63	0.61	0.63
11.5Z073-2	0.60	1.00	1.00	0.60	1.00	1.00	0.61	1.00	1.00	0.61	1.00	1.00

Table 5.10 Web effectiveness for analyzed specimens by FEM

Section	f_y	AISI			S136			EN1993			Schafer		
		λ_{web}	ρ_{test}	ρ_{AISI}	λ_{web}	ρ_{test}	ρ_{S136}	λ_{web}	ρ_{test}	ρ_{EN1993}	λ_{web}	ρ_{test}	$\rho_{Schafer}$
8Z2.25x050	33.0	1.07	1.00	1.00	1.07	1.00	0.74	1.07	1.00	0.74	1.07	1.00	0.80
8Z2.25x050	44.0	1.26	0.98	0.95	1.26	0.97	0.66	1.26	0.98	0.65	1.25	0.99	0.74
8Z2.25x050	56.1	1.44	0.93	0.84	1.44	0.89	0.59	1.45	0.91	0.59	1.43	0.94	0.68
8Z2.25x050	62.2	1.53	0.84	0.80	1.53	0.78	0.56	1.54	0.82	0.56	1.52	0.87	0.66
8Z2.25x050	73.4	1.68	0.69	0.73	1.68	0.60	0.52	1.68	0.65	0.52	1.66	0.71	0.63
8Z2.25x100	33.0	0.51	1.00	1.00	0.51	1.00	1.00	1.53	1.00	0.56	0.51	1.00	1.00
8Z2.25x100	44.0	0.59	1.00	1.00	0.59	1.00	1.00	1.77	1.00	0.50	0.59	1.00	1.00
8Z2.25x100	56.1	0.67	1.00	1.00	0.67	0.99	1.00	1.99	1.00	0.45	0.67	1.00	1.00
8Z2.25x100	62.2	0.70	0.83	1.00	0.70	0.75	0.98	2.10	0.80	0.43	0.70	0.85	0.99
8Z2.25x100	73.4	0.76	0.70	1.00	0.76	0.60	0.93	2.28	0.67	0.40	0.76	0.72	0.96
8.5Z2.5x70	73.4	1.27	0.90	0.92	1.27	0.86	0.65	1.28	0.89	0.65	1.26	0.92	0.73
8.5Z2.5x70	62.2	1.16	0.99	1.00	1.16	0.98	0.70	1.16	0.98	0.70	1.15	0.99	0.77
8.5Z2.5x70	56.1	1.09	1.00	1.00	1.09	1.00	0.73	1.09	1.00	0.73	1.08	1.00	0.80
8.5Z2.5x70	44.0	0.93	0.99	1.00	0.93	0.98	0.82	0.94	0.99	0.82	0.93	0.99	0.87
8.5Z2.5x70	33.0	0.80	1.00	1.00	0.80	1.00	0.91	2.20	1.00	0.41	0.80	1.00	0.94
11.5Z3.5x80	33.0	1.00	1.00	1.00	1.00	1.00	0.78	1.01	1.00	0.78	1.00	1.00	0.84
11.5Z3.5x80	44.0	1.17	1.00	0.99	1.17	1.00	0.69	1.18	1.00	0.69	1.16	1.00	0.77
11.5Z3.5x80	56.1	1.34	1.00	0.88	1.34	1.00	0.62	1.35	1.00	0.62	1.33	1.00	0.71
11.5Z3.5x80	62.2	1.42	0.95	0.83	1.42	0.92	0.59	1.43	0.94	0.59	1.41	0.96	0.69
11.5Z3.5x80	73.4	1.56	0.85	0.77	1.56	0.79	0.55	1.57	0.83	0.55	1.54	0.87	0.66
8C068	33.0	0.77	1.00	1.00	0.77	1.00	0.93	0.77	1.00	0.93	0.77	1.00	0.95
8C068	44.0	0.89	1.00	1.00	0.89	1.00	0.85	0.89	1.00	0.85	0.89	1.00	0.89
8C068	56.1	1.01	0.94	1.00	1.01	0.91	0.78	1.01	0.93	0.77	1.01	0.95	0.84
8C068	62.2	1.07	0.86	1.00	1.07	0.80	0.74	1.07	0.84	0.74	1.07	0.88	0.80
8C068	73.4	1.19	0.69	1.00	1.19	0.59	0.69	1.19	0.65	0.68	1.18	0.71	0.76
8.5Z092	33.0	0.60	1.00	1.00	0.60	1.00	1.00	0.60	1.00	1.00	0.60	1.00	1.00
8.5Z092	44.0	0.69	1.00	1.00	0.69	1.00	0.99	0.69	1.00	0.99	0.69	1.00	0.99
8.5Z092	56.1	0.79	1.00	1.00	0.79	1.00	0.91	0.80	1.00	0.91	0.79	1.00	0.94
8.5Z092	62.2	0.85	1.00	1.00	0.85	1.00	0.87	0.85	1.00	0.87	0.85	1.00	0.91
8.5Z092	73.4	0.95	1.00	1.00	0.95	1.00	0.81	0.95	1.00	0.81	0.94	1.00	0.87
8.5Z120	33.0	0.45	1.00	1.00	0.45	1.00	1.00	0.45	1.00	1.00	0.45	1.00	1.00
8.5Z120	44.0	0.52	1.00	1.00	0.52	1.00	1.00	0.52	1.00	1.00	0.52	1.00	1.00
8.5Z120	56.1	0.59	1.00	1.00	0.59	1.00	1.00	0.59	1.00	1.00	0.59	1.00	1.00
8.5Z120	62.2	0.62	0.84	1.00	0.62	0.77	1.00	0.62	0.81	1.00	0.62	0.86	1.00
8.5Z120	73.4	0.68	0.79	1.00	0.68	0.70	1.00	0.68	0.76	1.00	0.68	0.81	1.00
8.5Z082	33.0	0.67	1.00	1.00	0.67	1.00	1.00	0.67	1.00	1.00	0.67	1.00	1.00
8.5Z082	44.0	0.78	0.97	1.00	0.78	0.96	0.92	0.78	0.97	0.92	0.78	0.99	0.95
8.5Z082	56.1	0.90	1.00	1.00	0.90	1.00	0.84	0.90	1.00	0.84	0.90	1.00	0.89
8.5Z082	62.2	0.96	1.00	1.00	0.96	1.00	0.80	0.97	1.00	0.80	0.96	1.00	0.86
8.5Z082	73.4	1.07	1.00	1.00	1.07	1.00	0.74	1.07	1.00	0.74	1.06	1.00	0.81
8C097	33.0	0.53	1.00	1.00	0.53	1.00	1.00	0.53	1.00	1.00	0.53	1.00	1.00
8C097	44.0	0.61	1.00	1.00	0.61	1.00	1.00	0.61	1.00	1.00	0.61	1.00	1.00
8C097	56.1	0.69	1.00	1.00	0.69	1.00	0.99	0.69	1.00	0.99	0.69	1.00	0.99
8C097	62.2	0.73	0.94	1.00	0.73	0.91	0.96	0.73	0.93	0.96	0.73	0.95	0.97
8C097	73.4	0.80	0.88	1.00	0.80	0.83	0.91	0.80	0.86	0.91	0.80	0.90	0.94
12C068	33.0	1.19	0.63	1.00	1.19	0.51	0.69	1.19	0.58	0.69	1.19	0.66	0.76
12C068	44.0	1.38	0.50	0.91	1.38	0.38	0.61	1.38	0.45	0.61	1.38	0.55	0.70

The comparison of the back-calculated web effective width ratio ρ_{test} with the predications for the four analyzed methods AISI (1996), CSA S136 (1994), EN1993 (2002), and Schafer (1997) is illustrated in Figure 5.58 to Figure 5.61. Figure 5.62 shows a comparison of the predicted web effective width ratio for the four methods. AISI (1996) and CSA S136 (1994) have significantly different predictions for the sections with intermediate web slenderness, $1.0 < \lambda_{web} < 1.6$. For example, the AISI prediction for 8C054-1, $\lambda_{web} = 1.33$, $\rho_{AISI} = 91\%$, CSA S136 prediction is $\rho_{S136} = 63\%$ - a 28% difference, the back-calculated experimental web effectiveness is 78% for AISI and 70% for CSA S136. Schafer' method provides an intermediate prediction between AISI and CSA S136, and Schafer's prediction follows a similar tendency, as CSA S136, with respect to web slenderness, λ_{web}. Predictions by Eurocode EN1993 have a good agreement with CSA S136, however the back-calculated results of both methods are slightly different due to the different procedures for buckling coefficient, k. In general, CSA S136, EN1993 and Schafer's method provide more conservative predictions of the web effective width than AISI. However, it should be noted that the majority of the bending strength is derived from the flange. Therefore, large changes are required in the web effective width in order to make a small change in the predicted bending capacity. For example, the AISI prediction for 8.5Z059-1, $\lambda_{web} = 1.31$, $M_{test}/M_{AISI} = 96\%$, the predicted web effectiveness by AISI is 92% and the back-calculated experimental web effectiveness is 78% – a 14% difference! For the CSA S136 prediction on the same section, $M_{test}/M_{S136} = 104\%$, the predicted web effectiveness by CSA S136 is 63% and the back-calculated experimental web effectiveness is 70% – a 7% difference. And the difference of the predicted web effectiveness is 29% for the two Specifications, although

the difference of predicted bending capacity is only 8%. Therefore, the large differences between the two methods tend to get overstated when examining the web effective width in isolation.

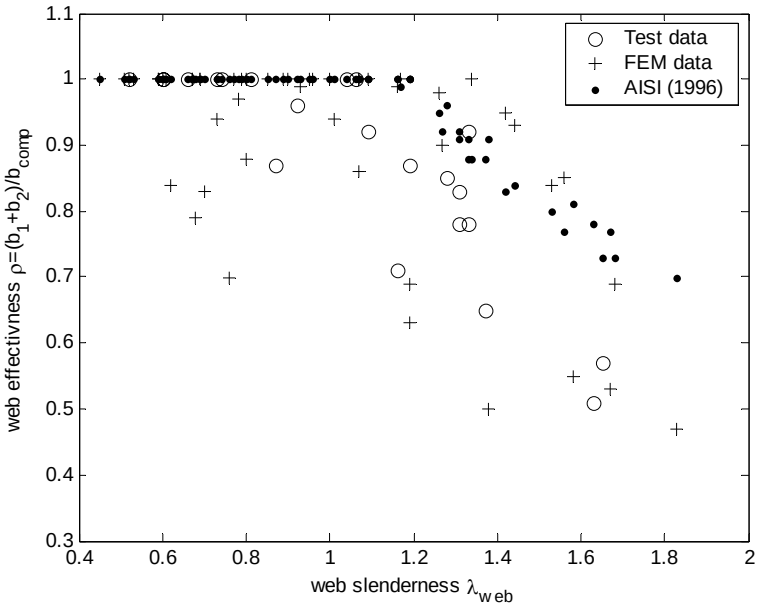

Figure 5.58 Back-calculated web effective width vs. AISI prediction

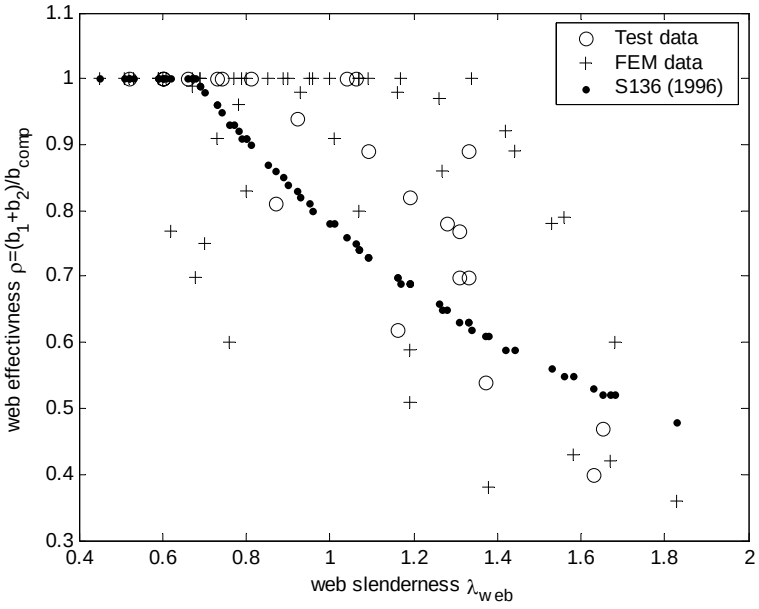

Figure 5.59 Back-calculated web effective width vs. CSA S136 prediction

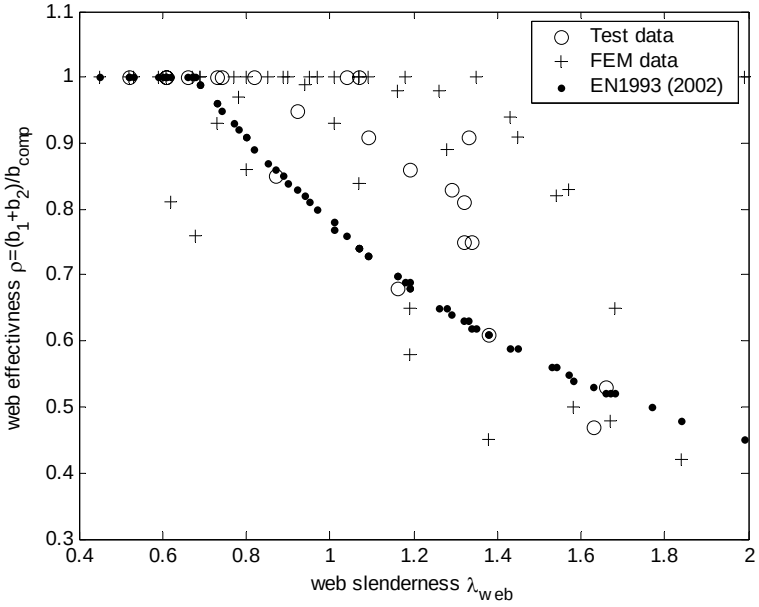

Figure 5.60 Back-calculated web effective width vs. EN1993 prediction

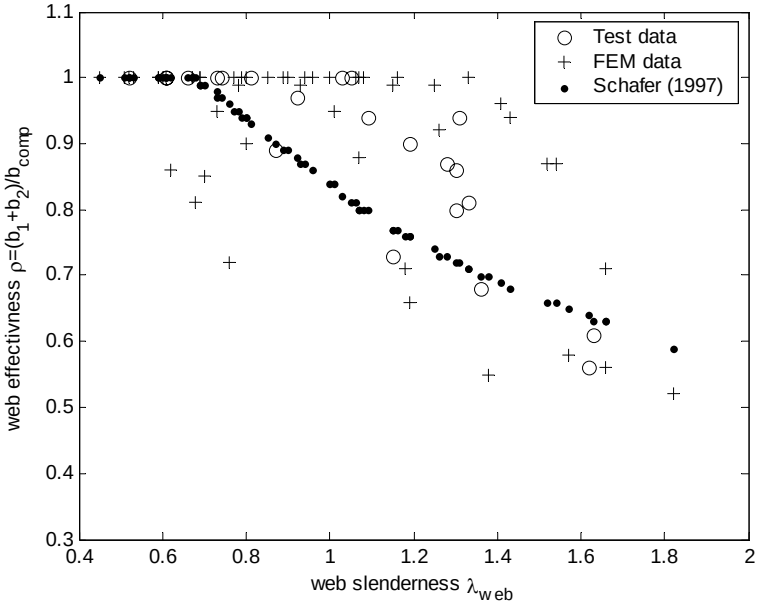

Figure 5.61 Back-calculated web effective width vs. Schafer prediction

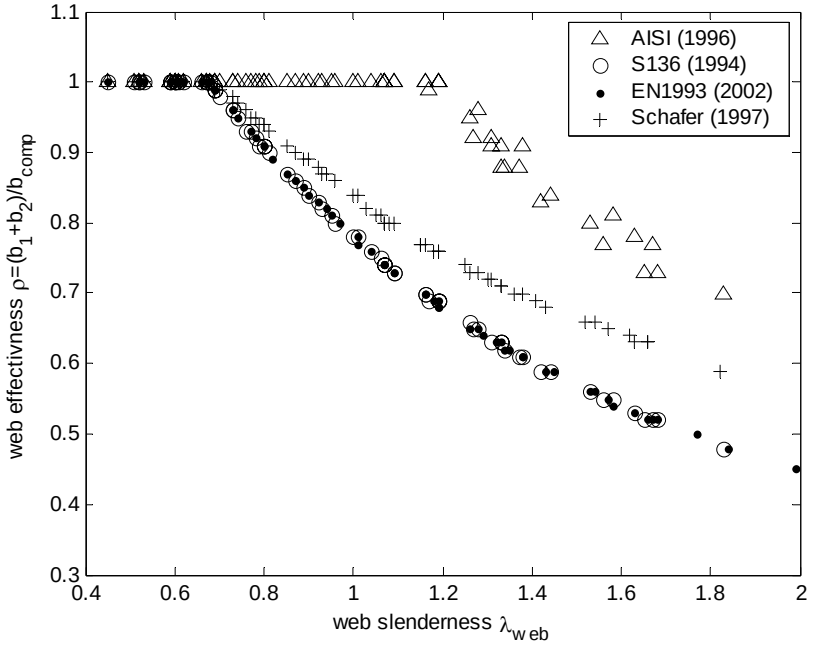

Figure 5.62 Comparison of predicted effective width of web

5.6.3 Postbuckling Strength Reserve

As introduced in Chapter 1, stiffened compression elements will not collapse when their elastic buckling stress is reached. This phenomenon of undertaking extra load over the elastic buckling stress is known as postbuckling strength. Postbuckling strength has also been observed for full cold-formed steel sections under compression or bending loads, here called postbuckling strength reserve, in which the CFS section has higher capacity than its elastic buckling load. Figure 5.63 presents a comparison of the bending capacities of C and Z-sections with the elastic buckling moments for local buckling failures. Both test results and extended finite element analysis results are included in the figure, as well as the DSM local buckling strength curve. Slender sections ($(M_y/M_{cr\ell})^{0.5} >$ 1.1) demonstrate postbuckling strength reserve in bending (data points are above the elastic buckling curve).

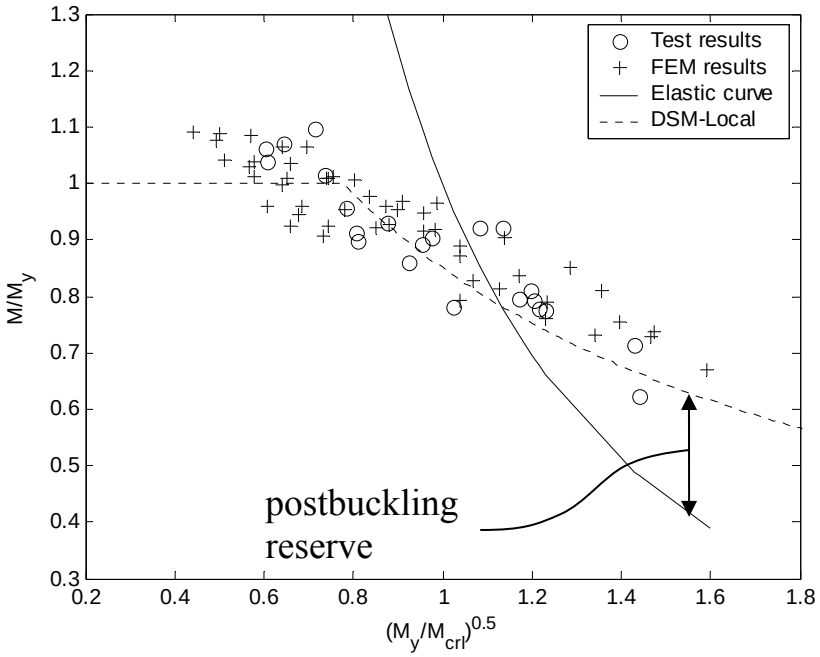

Figure 5.63 Postbuckling reserve for local buckling of beams

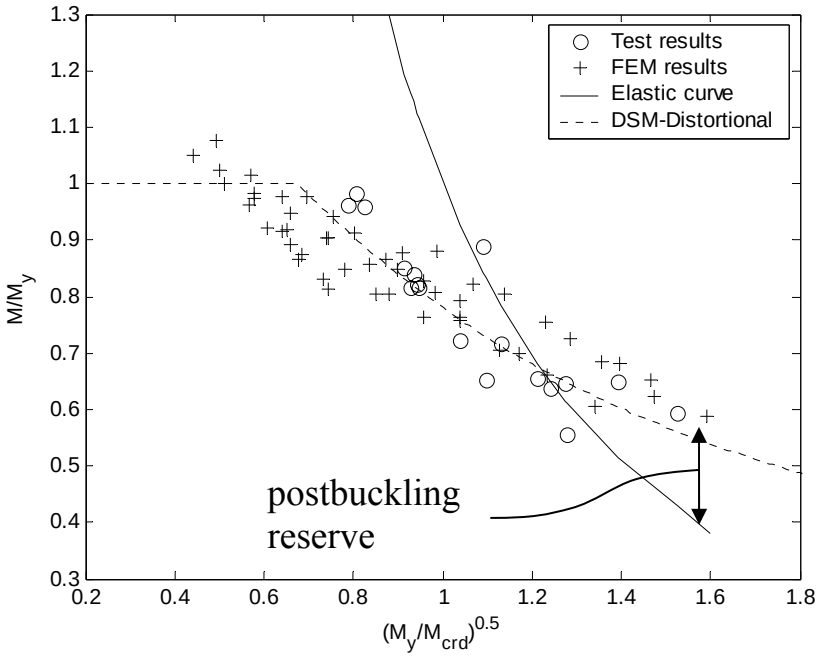

Figure 5.64 Postbuckling reserve for distortional buckling of beams

Figure 5.64 illustrates a similar comparison of bending strength with the elastic buckling moment for distortional buckling. Two tested and several simulated beams are

identified as having postbuckling strength reserve in distortional buckling. However, compared with local buckling, the distortional buckling failures tend to have less postbuckling strength reserve, and the reserve occurs only on more slender sections. In general, sections with slender geometry (high h/t, low M_{cr}, etc.) and high yield strength exhibit greater postbuckling strength reserve.

5.7 Conclusions

A finite element model of the testing of Chapters 2 and 3 was developed. Geometric imperfections were considered and introduced in the ABAQUS model by combining both the local and distortional buckling mode for the final imperfection shape and selecting the magnitude based on the statistical summary of Schafer and Peköz (1998b). Material nonlinearity was included. The connections (bolts, fasteners, etc.) were simulated by using constraints; surface contact, such as the contact between panel and section or between tube and section, was ignored. The automatic Stabilization technique (*stabilize in ABAQUS) was adopted for the nonlinear analysis.

The finite element model was verified by tests and was extended to simulate the laboratory experiments on a wide geometric range of cold-formed steel beams. The FEM data together with the test data was used to examine the Direct Strength Method. The results showed that DSM provides reliable and conservative predictions for both local and distortional buckling failures of cold-formed steel beams. The combined data was also used to study the effective width equations for webs, and the postbuckling strength reserve. Postbuckling reserve exists in both local and distortional buckling of cold-formed steel beams, though distortional buckling has less postbuckling reserve than local

buckling. The verified finite element model provides a useful tool to investigate additional issues in cold-formed steel structures. As demonstrated further in Chapters 7 and 8.

Chapter 6

Stress Gradient Effect on Thin Plates

6.1 Introduction

The design of thin-walled beams traditionally involves the consideration of both plate stability (local buckling) and member stability (lateral-torsional buckling). Plate stability is considered by examining the slenderness of the individual elements that make up the member and the potential for local buckling of those elements. Member stability is considered by examining the slenderness of the cross-section, and the potential for lateral-torsional buckling. Member stability modes, such as lateral-torsional buckling, occur over the unbraced length of the beam, which is typically much greater than the depth of the member ($L/d >> 1$). Classic stability equations for lateral-torsional buckling are derived for a constant moment demand over the unbraced length. For beams with unequal end moments, or transverse loads, the moment is not constant and the moment gradient on the beam must be accounted for. In design, this influence is typically captured in the form of an empirical moment gradient factor (C_b) which is multiplied times the lateral-torsional buckling moment under a constant demand.

The moment gradient, which so greatly influences the member as a whole, also creates a stress gradient on the plates which make up the member. In this chapter, the influence of stress gradients on plate stability is investigated.

For plate local buckling, the influence of the stress gradient (or moment gradient) is typically ignored in design. Figure 6.1 provides a variety of classical plate buckling solutions that are intended to help indicate why moment gradient has been traditionally ignored for local buckling. The results are presented in terms of the plate buckling coefficient k, as a function of the plate aspect ratio β = a/b for different numbers of longitudinal half sine waves, m. where: $\sigma_{cr} = k\pi^2 D/(b^2 t)$ and the plate of length a, and width b, is simply supported at the loaded edges and either simply supported (ss), fixed (fix) or free at the unloaded edges.

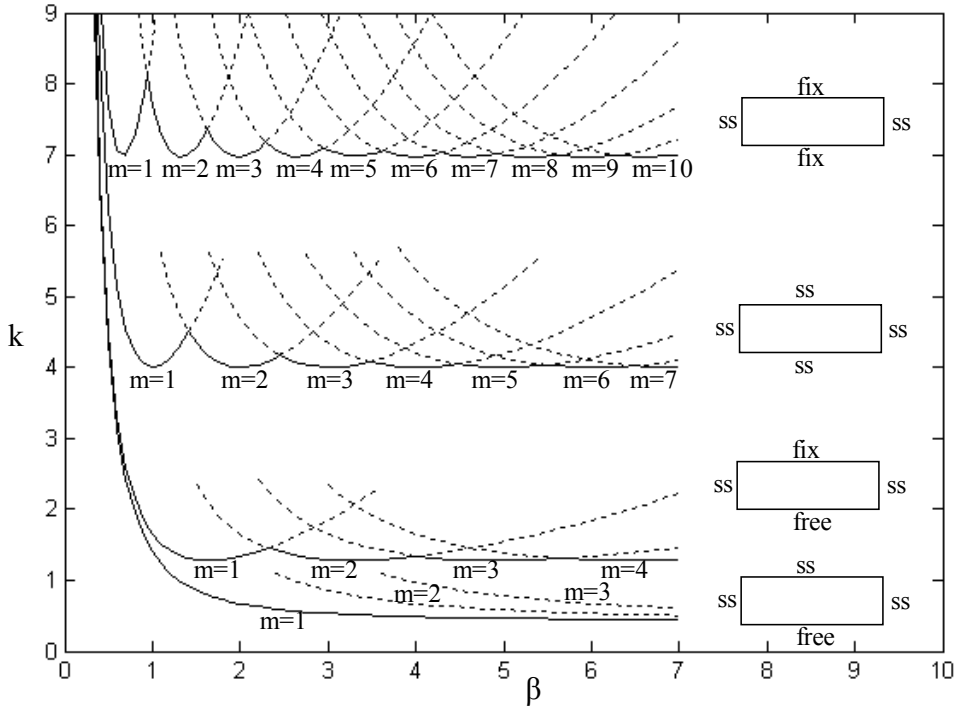

Figure 6.1 Buckling of uniformly compressed rectangular plates

Figure 6.1 indicates that when the unloaded edges are supported, the length of the buckled wave is quite short and many buckled waves (high m) can form in even relatively short lengths. When one of the unloaded edges is unsupported (e.g. fix-free) the behavior is modified from the supported case, and now even at relatively large β values the number of expected half-waves (m) are small. The behavior of the ss-free case is particularly interesting. Instead of the distinct garland curves of the earlier cases, now for higher β, the single half-wave case (m = 1) asymptotes to k = 0.425 instead of increasing for large β. For the ss-free case multiple wavelengths (m) all yield similar solutions for large β.

To connect the plate solutions of Figure 6.1 to actual beams, consider the top flange of the beams of Figure 6.2. Local buckling of the compression flange of the hat of Figure 6.2(a) is somewhere between the ss-ss and fix-fix case of Figure 6.1. What would be the influence of moment gradient on the local buckling of the compression flange in this solution? One anticipates that even a sharply varying moment gradient is unlikely to change the stress demands on the flange significantly. Therefore, traditional local buckling of a stiffened element – such as the compression flange of the hat – is assumed to not require modification due to the moment gradient. However, now consider the channel of Figure 6.2(b). As the compression flange buckles the web/flange juncture provides support somewhere between the fix-free and ss-free case of Figure 6.1. The potential that moment gradient may have influence on the buckling results is real. Further, and somewhat counter-intuitively, the weaker the support on the unloaded edge, the greater the potential for an increase in the buckling load due to the moment gradient.

(a) hat section (b) channel section

Figure 6.2 Section shapes

Channel sections with unstiffened flanges such as that of Figure 6.2(b) are widely used in practice. Finite strip analysis (FSA) provides a means to examine the plate stability and member stability within one solution. Figure 6.3 gives a typical FSA result for a 9 in. deep, 4 in. wide C-section (with t = 0.04 in.) subjected to bending moment. The y-axis of Figure 6.3 is a multiplier times the applied moment (load factor) which indicates the magnitude of the elastic buckling moment, and the x-axis is the half wavelength in inches.

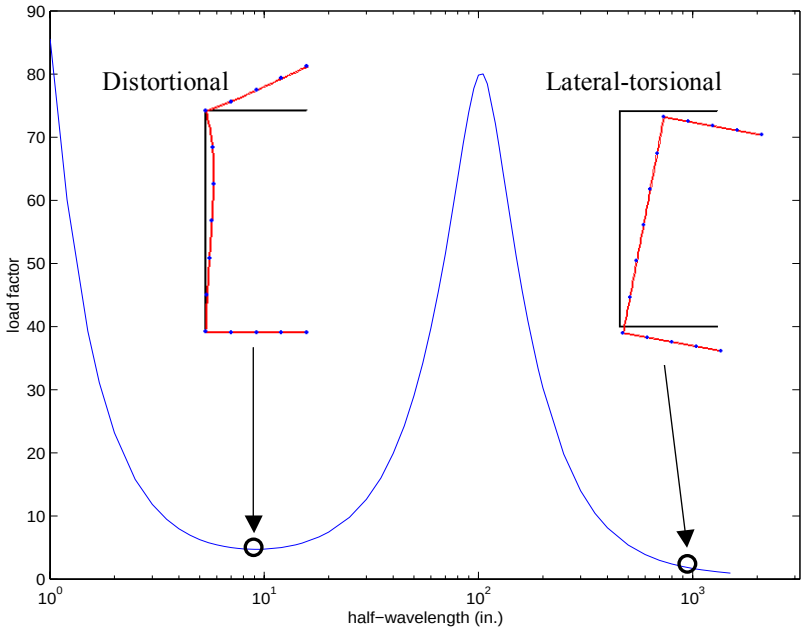

Figure 6.3 Finite strip result of the buckling of C-section in bending

The finite strip analysis results show that distortional buckling involves rotation of the compression flange about the web-flange juncture, while lateral-torsional buckling

involves translation and rotation of the entire section, without any distortion of the cross-section itself. Distortional buckling occurs at about a 10 in. half-wavelength, which is relatively long compared to the flange width. Therefore, the influence of moment gradient on the buckling of this section may be of practical interest.

6.2 Stress Gradient Effect on the Elastic Buckling of Thin Plates

6.2.1 Analytic Solution (Energy Method) for Elastic Buckling

The elastic buckling of both stiffened and unstiffened plates under stress gradient is studied here by the Rayleigh-Ritz method. As shown in Figure 6.4 and Figure 6.5, the thin rectangular plate is simply supported under uneven compressive stresses applied at the two loaded edges. The difference in stress is equilibrated by uniform shear forces along the other two edges (for the stiffened element) or one edge (for the unstiffened element). Elastic rotational restraints are applied at the longitudinal edge, which has shear forces applied as well.

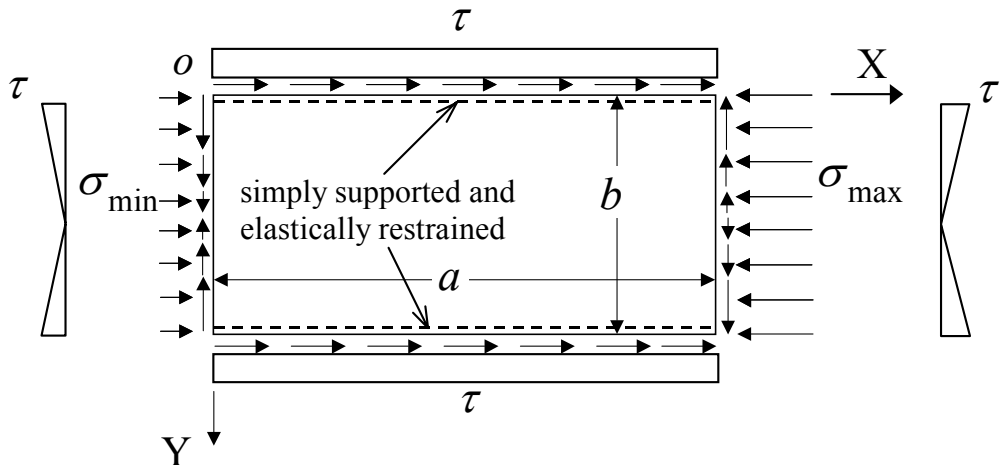

Figure 6.4 Stiffened element subjected to a stress gradient

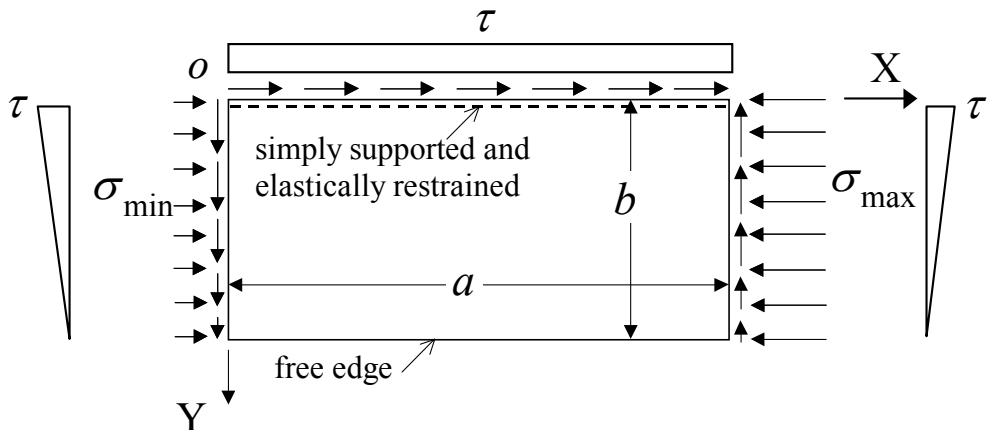

Figure 6.5 Unstiffened element subjected to a stress gradient

The Rayleigh-Ritz method has been widely applied to determine the buckling stress of plates. In this method, an assumed deflection function $w(x,y)$ satisfying the boundary conditions is used in the expression for the total potential energy, Π. The total potential energy is the summation of internal strain energy of the plate due to bending, U_1, the strain energy due to the elastic restraint, U_2, and the work done by the external forces, T. Classical solutions from thin plate theory (e.g. Timoshenko and Gere 1961) result in Equation (6.1) to (6.4).

$$\Pi = U_1 + U_2 + T \tag{6.1}$$

$$U_1 = \frac{D}{2}\int_0^b\int_0^a \left\{\left(\frac{\partial^2 w}{\partial x^2}+\frac{\partial^2 w}{\partial y^2}\right)^2 - 2(1-\mu)\left[\frac{\partial^2 w}{\partial x^2}\frac{\partial^2 w}{\partial y^2}-\left(\frac{\partial^2 w}{\partial x \partial y}\right)^2\right]\right\} dxdy \tag{6.2}$$

$$U_2 = \frac{S}{2}\int_0^a \left[\left(\frac{\partial w}{\partial y}\right)^2_{y=0}\right] dx + \frac{S}{2}\int_0^a \left[\left(\frac{\partial w}{\partial y}\right)^2_{y=b}\right] dx \quad \text{(for stiffened elements)} \tag{6.3a}$$

$$U_2 = \frac{S}{2}\int_0^a \left[\left(\frac{\partial w}{\partial y}\right)^2_{y=0}\right] dx \qquad \text{(for unstiffened elements)} \tag{6.3b}$$

$$T = -\frac{t}{2}\int_0^b\int_0^a\left[\sigma_x\left(\frac{\partial w}{\partial x}\right)^2 + \sigma_y\left(\frac{\partial w}{\partial y}\right)^2 + 2\tau_{xy}\frac{\partial w}{\partial x}\frac{\partial w}{\partial y}\right]dxdy \tag{6.4}$$

where D is the plate flexural rigidity $D = \frac{Et^3}{12(1-\mu^2)}$, and S is the stiffness of the elastic rotational restraint.

Using the principle of minimum total potential energy, the equilibrium configuration of the plate is identified:

$$\frac{\partial \Pi}{\partial w_i} = 0 \qquad (i = 1,\ \ 2\ldots\ \ N) \tag{6.5}$$

Equation (6.5) represents a system of N simultaneous homogeneous equations with w_i and load σ (σ_{max} is used in the present work) as unknowns. For nontrivial solution of w_i's, the determinant of the coefficient matrix of the system of equations must vanish. The lowest value of σ_{max} that leaves the determinant of the coefficient matrix zero is the critical load of the plate. Thus, the eigenvalues of system (6.5) are the buckling stress of the thin plates, and the eigenvectors represent the buckling shapes. The lowest eigenvalue is the first elastic buckling stress, and is of the most interest in this work. The accuracy of the Rayleigh-Ritz method depends on how closely the assumed deflection functions describe the true deflection surface of the plates.

6.2.2 Stress Gradient Effect on the Elastic Buckling of Stiffened Elements

6.2.2.1 Stress Distribution

Since the applied compression difference is equilibrated by the uniform shear forces along two edges in the longitudinal direction, the shear forces can be found as Equation (6.6).

$$\tau_{xy|y=0,b} = \frac{(\sigma_{max} - \sigma_{min})b}{2a} \tag{6.6}$$

The distribution of internal stress σ_x is assumed to be linear along the plate length, and uniform in the x direction, Equation (6.7). σ_y is assumed zero in the plate, Equation (6.8).

$$\sigma_x = \sigma_{max}\left[\frac{(1-r)x}{a} + r\right] \tag{6.7}$$

$$\sigma_y = 0 \tag{6.8}$$

Equilibrium is enforced by insuring $\sum F_x = 0$, $\sum F_y = 0$, $\sum M_0 = 0$ (about the origin). Assuming plane stress conditions, then equilibrium can be found:

$$\frac{\partial \sigma_x}{\partial x} + \frac{\partial \tau_{xy}}{\partial y} = 0 \tag{6.9}$$

$$\frac{\partial \sigma_y}{\partial y} + \frac{\partial \tau_{xy}}{\partial x} = 0 \tag{6.10}$$

where the body force has been neglected. By substituting Equation (6.7) into Equations (6.9) and (6.10) along with the fact that $\sigma_{x|x=0} = \sigma_{min} = r\sigma_{max}$, the internal shear stresses can be obtained in functional form as:

$$\tau_{xy} = \sigma_{max} \frac{(1-r)}{2}\left(\frac{b}{2} - y\right) \tag{6.11}$$

Equations (6.8), (6.9), and (6.11) satisfy the equilibrium conditions as well as compatibility, and therefore represent a physically possible set of stresses for the plate.

6.2.2.2 Boundary Conditions

Six boundary conditions are observed for the stiffened element. Simple support at the transverse and longitudinal edges (two conditions):

$$(w)_{x=0} = 0 \tag{6.12}$$

$$(w)_{x=a} = 0 \tag{6.13}$$

Elastic restraint against rotation along both longitudinal edges (four conditions):

$$(w)_{y=0,b} = 0 \tag{6.14}$$

$$D\left(\frac{\partial^2 w}{\partial y^2} + \mu\frac{\partial^2 w}{\partial x^2}\right)_{y=0,b} = S\left(\frac{\partial w}{\partial y}\right)_{y=0,b} \tag{6.15}$$

The linearity of the differential Equations of (6.15) implies that the deflection function $w(x,y)$ can be formed as $\sum_{i=1}^{N} A_i(y)B_i(x)$, where A_i is a function of *y* alone and B_i is a function of x alone. If, for every i, $A_i(y)B_i(x)$ is compatible with all the

boundary conditions, then the linear summation of each term $A_i(y)B_i(x)$ will satisfy the boundary conditions.

6.2.2.3 Trial Deflection Function 1 --- Early Work

Early work of Libove, Ferdman and Reusch (1949) considered the influence of stress gradient on a simply supported rectangular plate (ss-ss) of uniform thickness. The plate is shown in Figure 6.6. No elastic restraint was considered.

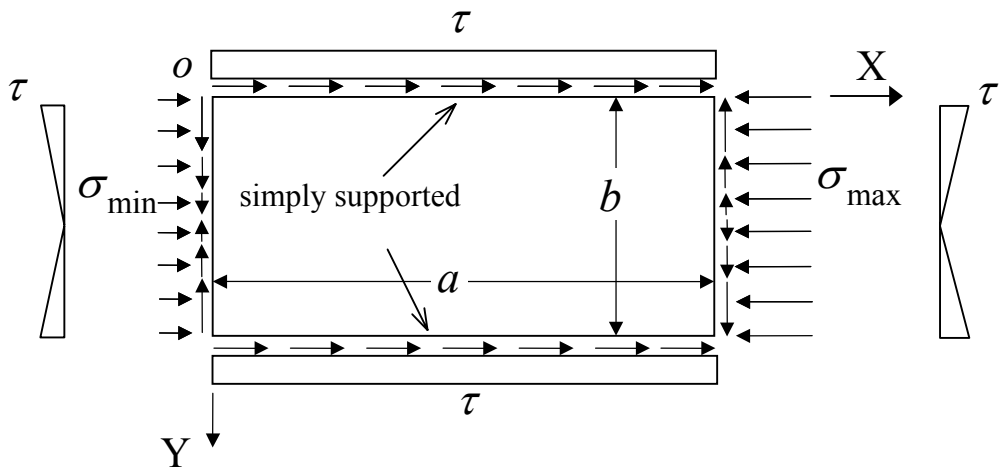

Figure 6.6 Stiffened elements under a stress gradient

A double Fourier sine series is employed as the assumed deflection function:

$$w = \sum_{i=1}^{M}\sum_{j=1}^{N} w_{ij} \sin\frac{i\pi x}{a}\sin\frac{j\pi y}{b} \tag{6.16}$$

Via (6.5) the equilibrium equations are derived as Equation (6.17) (same as Equation A11 of Libove, et al 1949) and it is used to write a stability determinant. The maximum value of $1/k_{av}$ corresponds to the minimum value of k_{av} which is the lowest average buckling stress. And the buckling coefficient at the maximum loaded edge, k_{max}, can be

obtained by the equation $k_{max} = \frac{2}{1+r} k_{av}$. The size of the stability determinant matrix is determined by the number of w_{ij} terms included in the deflection function. Due to the limit of computational tools at that time, the work done by Libove, et al (1949) only considered the deflection function with up to $M = 7$ and $N = 5$. Present work recalculated the buckling stress after a complete study of convergence.

$$w_{ij}\frac{\pi^2}{8}\left[\frac{1}{k_{av}}\left(\frac{i^2}{\beta}+\beta j^2\right)^2 - i^2\right] + \left(\frac{1-r}{1+r}\right)\sum_{\substack{p=1 \\ p\pm i=odd}}^{M} w_{pj}\frac{ip\left(i^2+p^2\right)}{\left(i^2-p^2\right)^2}$$

$$-4\left(\frac{1-r}{1+r}\right)\sum_{p=1}^{M}\sum_{\substack{q=1,3,5,\ldots \\ p\pm i=odd \\ q\neq j}}^{N} w_{pq}\frac{ijpq}{\left(q^2-j^2\right)\left(i^2-p^2\right)} = 0 \qquad (6.17)$$

$$i = 1,\quad 2,\quad 3,\quad \ldots\quad M;\quad j = 1,\quad 3,\quad 5,\quad \ldots\quad N$$

$$\text{where } r = \frac{\sigma_{min}}{\sigma_{max}} \qquad (6.18)$$

6.2.2.4 Trial Deflection Function 2 (Eq. 6.19)

Libove's model does not consider the case with elastic rotational restraints applied at the longitudinal edges. The deflection function proposed here works for both cases of stiffened plates: with or without elastic rotational restraint on the unloaded edges. The deflection function is assumed as a linear combination of polynomial and trigonometric functions as given in Equation (6.19). In each term, a fourth order polynomial is assumed for the transverse deflection and a sine function is selected for the longitudinal deflection.

$$w = \sum_{i=1}^{N} w_i \left(p_i y(y-b) + q_i y^2 (y-b)^2 \right) \sin\left(\frac{i\pi x}{a} \right) \tag{6.19}$$

The deflection function must satisfy all the boundary conditions. Therefore, the parameters p_i , q_i are determined by substituting Equation (6.19) into the boundary conditions (Equations 6.12 to 6.15) term by term and the results are given below.

For plates with two longitudinal edges fixed and the two loaded edges simply supported,

$$p_i = 0 \tag{6.20}$$

$$q_i = 1 \tag{6.21}$$

For plates with four edges simply supported and no rotational restraint:

$$p_i = -b^2 \tag{6.22}$$

$$q_i = 1 \tag{6.23}$$

For plates with four edges simply supported and rotational restraint applied at the two unloaded longitudinal edges:

$$p_i = -\frac{b^2}{2D + Sb} \tag{6.24}$$

$$q_i = 1 \tag{6.25}$$

Equilibrium equations can be constructed via Equations (6.5), the buckling stress $(\sigma_{max})_{cr}$ is the minimum eigenvalue of the resulting $N \times N$ matrix of equilibrium expressions.

6.2.2.5 Trial Deflection Function 3 (Eq. 6.26)

The final trial deflection function is based on the same principle as deflection function 2 (Equation 6.19). In each term, a sine function is used for the longitudinal deflection. Unlike the previous deflection function, a sine function plus a second order polynomial are chosen for the transverse direction, as given in Equation (6.26), this idea is motivated by Lundquist and Stowell (1942a).

$$w = \sum_{i=1}^{N} w_i \left(p_i y(y-b) + q_i \sin(\frac{\pi y}{b}) \right) \sin\left(\frac{i\pi x}{a} \right) \tag{6.26}$$

The parameters p_i, q_i are determined by substituting Equation (6.26) into the boundary conditions of Equations (6.12) to (6.15), resulting in:

For plates with two longitudinal edges fixed, two loaded edges simply supported:

$$p_i = \frac{\pi}{b^2} \tag{6.27}$$

$$q_i = 1 \tag{6.28}$$

For plates with four edges simply supported and no rotational restraint:

$$p_i = 0 \tag{6.28}$$

$$q_i = 1 \tag{6.29}$$

For plates with four-edge simply supported and rotational restraint applied at two unloaded longitudinal edges,

$$p_i = -\frac{S\pi}{b(2D + Sb)} \tag{6.30}$$

$$q_i = 1 \tag{6.31}$$

6.2.2.6 Verification by Finite Element Analysis

Finite element analysis using ABAQUS was employed to examine the analytical results by the three different trial deflection functions. The plate properties are E = 29500 ksi and μ = 0.3. The S4R5 shell element was used for the finite element model. The element size is 0.1 in. × 0.1 in. Plate length was varied from 10 in. to 12 in. in the analysis, and plate width was varied from 2.5 in. to 4 in. The plate is simply supported on all four edges. Uneven compression loads are applied to the two ends, and the difference is equilibrated by shear forces, acting along the two longitudinal edges, as shown in Figure 6.7.

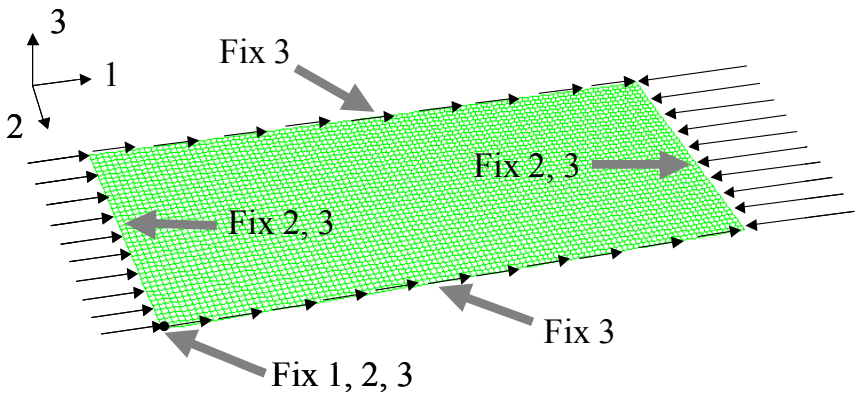

Figure 6.7 Finite element model for ss-ss stiffened elements under a stress gradient

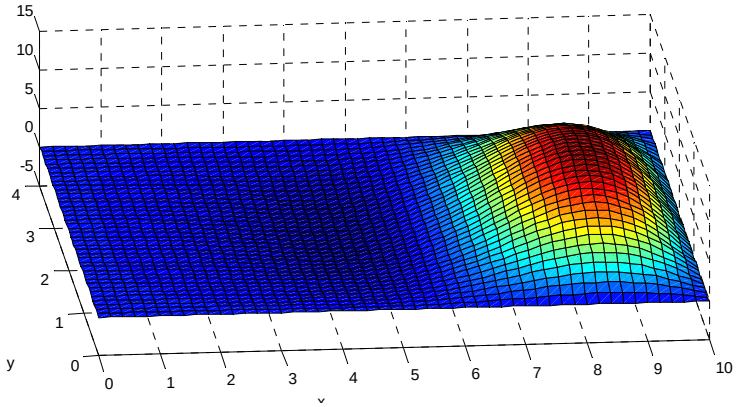

Figure 6.8 Buckling shape of a ss-ss stiffened element under a stress gradient r = 0 by analytical solution

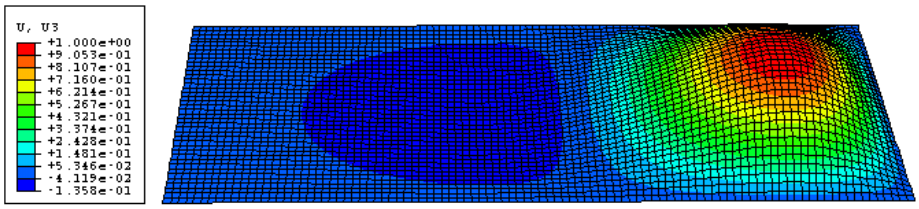

Figure 6.9 Buckling shape of a ss-ss stiffened element under a stress gradient r = 0 by FE solution

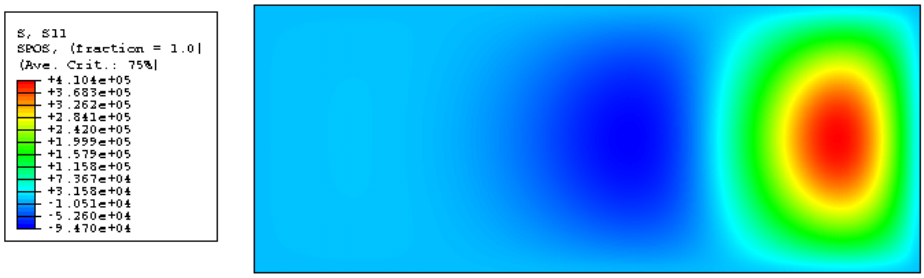

Figure 6.10 Stress σ_x distribution on top surface of a ss-ss stiffened element under a stress gradient r = 0 by elastic FE solution

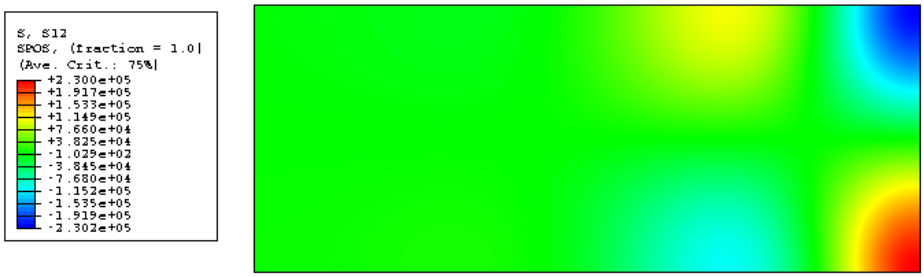

Figure 6.11 Stress τ_{xy} distribution on top surface of a ss-ss stiffened element under a stress gradient r = 0 by elastic FE solution

Figure 6.8 and Figure 6.9 show a comparison of the buckled shape of a thin plate under stress gradient with r = 0 (compression at one end only) using trial defection function 3 (Equation. 6.26). The dimensions of the plate are: a = 10 in., b = 4 in., t = 0.025 in., and S = 0 kip-in./in. Figure 6.10 shows the stress distribution of σ_x on the top surface of the plate, negative values represent compression in ABAQUS. Figure 6.11

shows the stress distribution of τ_{xy}. The internal stresses are calculated based on the buckled shape by the elastic analysis of ABAQUS, and there is no stress on the mid-surface (membrane), the stresses on the bottom surface are the opposite values of top surface. Table 6.1 provides the buckling stresses calculated by ABAQUS, $(\sigma_{max})_{cr}$ (FEM), and the ratio of the analytical solutions (DF1 stands for result by trial deflection function 1, DF2 for deflection function 2 and DF3 for deflection function 3) to the ABAQUS solution (presented as FEM in Table 6.1). In general, trial deflection functions 1 and 2 give fair agreement with the finite element results. Error grows when the stress gradient effect is large or the stiffness of the rotational restraint S is large. Trial deflection function 3 has the best results, and is therefore chosen for the study of stress gradient effect on stiffened elements. A convergence study was performed on a thin plate with thickness t = 0.01 in. and varying aspect ratio β. The plate is subjected to pure compression and fixed at two unloaded edges. Figure 6.12 through Figure 6.14 show the analytical solution-to-theoretical result ratio (k_a/k_t) vs. the number of selected terms of deflection function (N) for plates with aspect ratio β equal to 10, 20, and 40 respectively. This study indicates that for plates with β = 10, the analytical solution converges when N is larger than 20; for β = 20, the required N = 30; and for β = 40, the required N = 60. Plates with β over 40 are not included in this study.

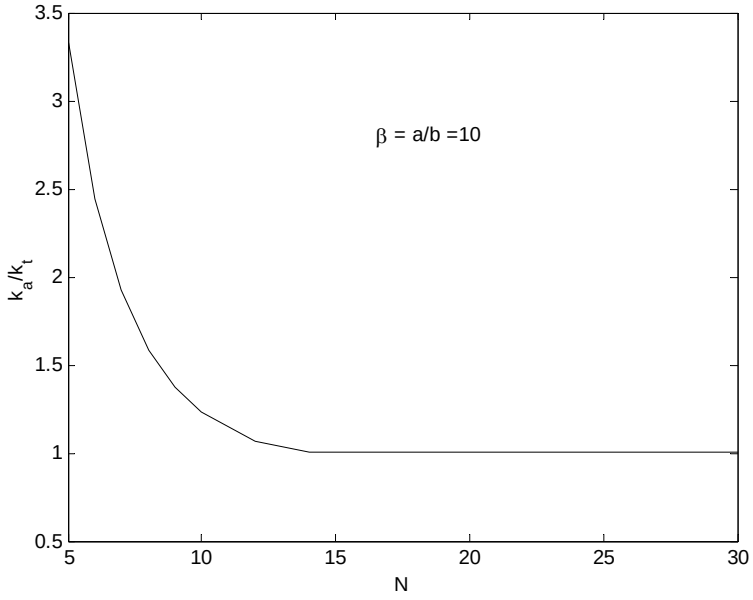

Figure 6.12 Convergence study on a fix-ss plate with β = 10

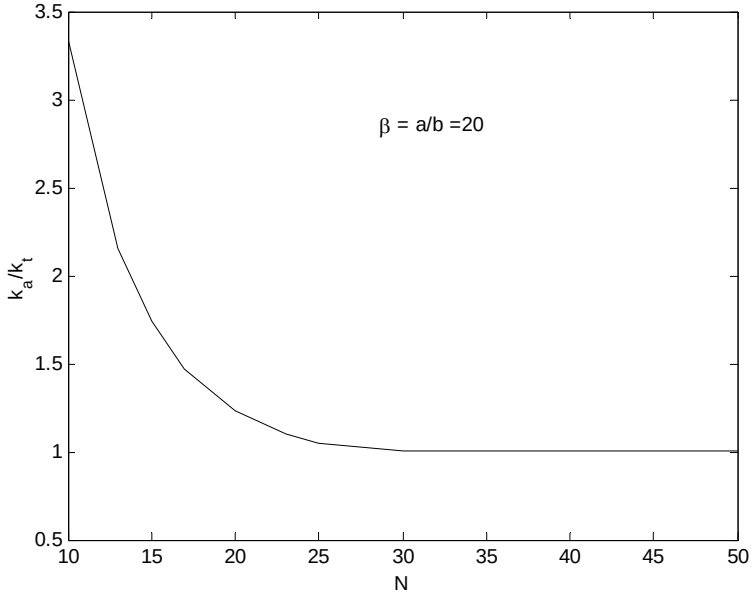

Figure 6.13 Convergence study on a fix-ss plate with β = 20

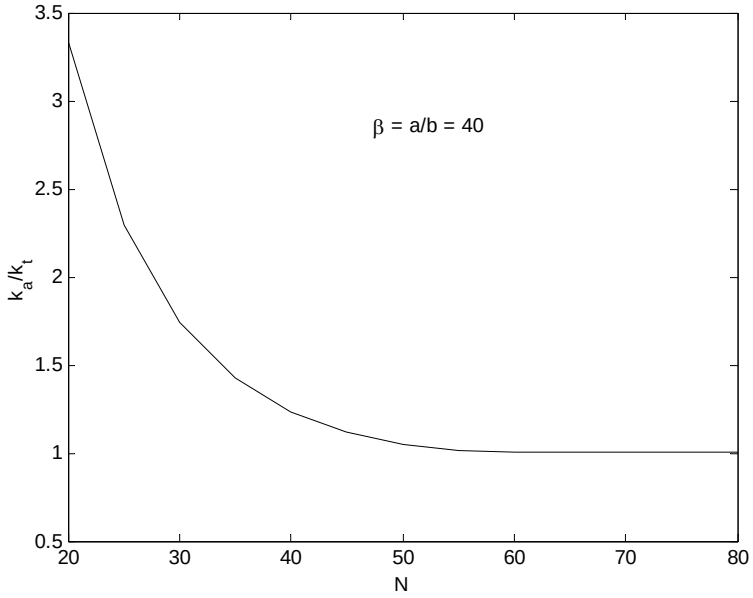

Figure 6.14 Convergence study on a fix-ss plate with β = 40

According to the convergence study, the number of terms of the deflection function (N) to be kept in the expansions (and thus the size of the N×N matrix to be solved) is selected via the following algorithm:

For a/b <= 10, N = 20;
For a/b > 10 and a/b <= 20, N = 40;
For a/b > 20 and a/b <= 40, N = 60;

This selection is conservative, which ensures accurate results, and the computation cost is felt to be reasonable.

Table 6.1 Comparison of analytical solutions with the FE results for stiffened elements

	r	a (in.)	b (in.)	t (in.)	S(kip-in./in.)	$(\sigma_{\max})_{cr}$ (FEM) (ksi)	DF1/FEM	DF2/FEM	DF3/FEM
Case 1	1	10	2.5	0.04	0	27.469	99.38%	71.66%	99.39%
	0.9	10	2.5	0.04	0	28.480	99.82%	72.63%	99.66%
	0.7	10	2.5	0.04	0	29.706	100.82%	76.56%	100.04%
	0.5	10	2.5	0.04	0	30.725	101.74%	80.65%	100.13%
	0.3	10	2.5	0.04	0	31.668	102.72%	84.42%	100.13%
	0.1	10	2.5	0.04	0	32.567	103.79%	87.84%	100.09%
	0	10	2.5	0.04	0	33.006	104.34%	89.44%	100.05%
	-0.1	10	2.5	0.04	0	33.438	104.94%	90.99%	100.01%
	-0.3	10	2.5	0.04	0	34.288	106.19%	93.96%	99.91%
	-0.5	10	2.5	0.04	0	35.124	107.56%	96.83%	99.80%
	-0.7	10	2.5	0.04	0	35.948	109.05%	99.63%	99.69%
	-0.9	10	2.5	0.04	0	36.764	110.68%	97.41%	99.56%
	-1	10	2.5	0.04	0	37.170	N/A	96.35%	99.50%
Case 2	1	12	3	0.05	0	29.657	99.89%	72.01%	99.89%
	0.9	12	3	0.05	0	31.074	99.26%	72.24%	99.11%
	0.7	12	3	0.05	0	32.046	101.42%	76.99%	100.62%
	0.5	12	3	0.05	0	33.125	102.40%	81.16%	100.78%
	0.3	12	3	0.05	0	34.121	103.44%	85.02%	100.84%
	0.1	12	3	0.05	0	35.071	104.56%	88.51%	100.85%
	0	12	3	0.05	0	35.532	105.16%	90.15%	100.84%
	-0.1	12	3	0.05	0	35.987	105.79%	91.75%	100.83%
	-0.3	12	3	0.05	0	36.881	107.13%	94.79%	100.79%
	-0.5	12	3	0.05	0	37.759	108.58%	97.73%	100.74%
	-0.7	12	3	0.05	0	38.623	110.14%	100.62%	100.67%
	-0.9	12	3	0.05	0	39.478	111.84%	98.43%	100.61%
	-1	12	3	0.05	0	3.9902	N/A	97.39%	100.57%
Case 3	1	10	4	0.025	0	4.2700	100.84%	72.79%	100.84%
	0.9	10	4	0.025	0	4.4130	101.40%	74.08%	100.99%
	0.7	10	4	0.025	0	4.6316	102.91%	78.25%	101.30%
	0.5	10	4	0.025	0	4.8340	104.74%	83.20%	101.55%
	0.3	10	4	0.025	0	5.0266	106.90%	88.59%	101.76%
	0.1	10	4	0.025	0	5.2122	109.37%	94.18%	101.92%
	0	10	4	0.025	0	5.3030	110.73%	97.00%	101.99%
	-0.1	10	4	0.025	0	5.3925	112.17%	99.79%	102.06%
	-0.3	10	4	0.025	0	5.5685	115.32%	96.63%	102.18%
	-0.5	10	4	0.025	0	5.7414	118.83%	93.72%	102.29%
	-0.7	10	4	0.025	0	5.9102	122.76%	91.05%	102.42%
	-0.9	10	4	0.025	0	6.0809	127.02%	88.49%	102.49%
	-1	10	4	0.025	0	6.1649	N/A	87.28%	102.55%
Case 4	1	10	4	0.025	Inf	7.1904	N/A	105.80%	101.98%
	0.9	10	4	0.025	Inf	7.4519	N/A	105.47%	102.49%
	0.7	10	4	0.025	Inf	7.7781	N/A	106.53%	103.36%
	0.5	10	4	0.025	Inf	8.0511	N/A	107.85%	103.87%
	0.3	10	4	0.025	Inf	8.3043	N/A	109.11%	104.24%
	0.1	10	4	0.025	Inf	8.5453	N/A	110.28%	104.55%
	0	10	4	0.025	Inf	8.6627	N/A	110.84%	104.68%
	-0.1	10	4	0.025	Inf	8.7780	N/A	111.39%	104.81%
	-0.3	10	4	0.025	Inf	9.0042	N/A	112.47%	105.05%
	-0.5	10	4	0.025	Inf	9.2253	N/A	113.51%	105.28%
	-0.7	10	4	0.025	Inf	9.4425	N/A	114.53%	105.49%
	-0.9	10	4	0.025	Inf	9.6563	N/A	115.54%	105.71%
	-1	10	4	0.025	Inf	9.7621	N/A	116.05%	105.81%
Mean							106.77%	93.65%	101.67%
Standard deviation							6.3%	12.9%	1.9%

6.2.2.7 The Elastic Buckling Stress of Stiffened Elements Under Stress Gradients

Figure 6.15 and Table 6.2 quantitatively demonstrate the influence of stress gradient on ss-ss stiffened elements. The stress gradient increases the buckling stress at the maximum loaded edge, and the increase becomes significant when the stress gradient is large and the plate is short (small aspect ratio, β). The stress gradient influence vanishes when the aspect ratio of the plate (β) becomes larger.

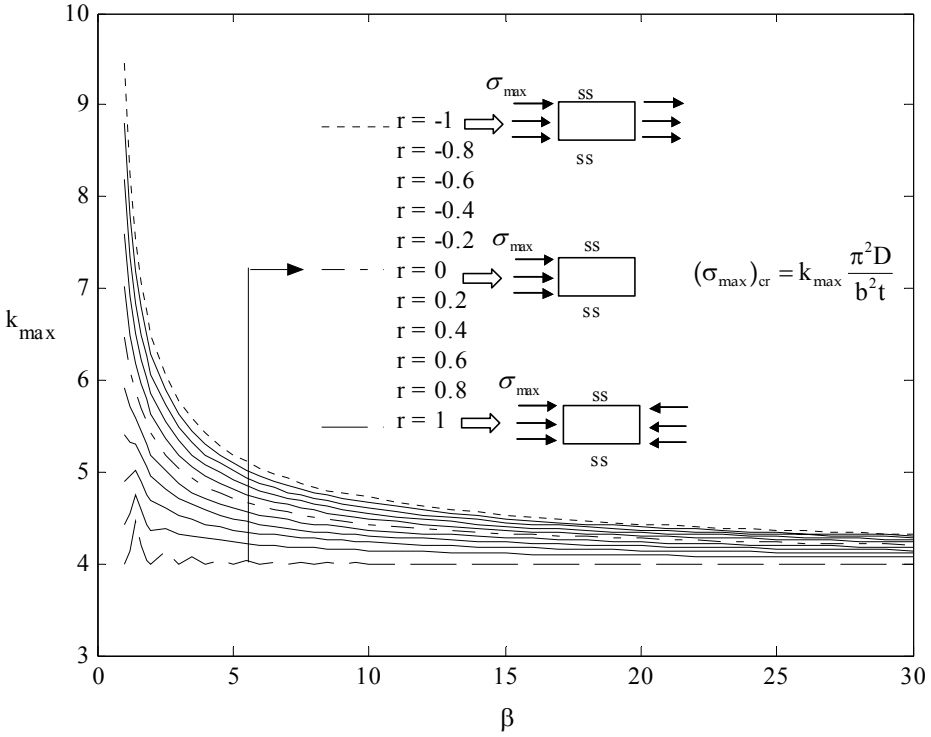

Figure 6.15 k_{max} vs. plate aspect ratio (β) for ss-ss stiffened element

Table 6.2 Numerical results of k_{max} values for ss-ss stiffened elements

r / β	-1	-0.8	-0.6	-0.4	-0.2	0	0.2	0.4	0.6	0.8	1
1.0	9.451	8.806	8.188	7.593	7.019	6.463	5.922	5.397	4.894	4.425	4.000
1.2	8.248	7.786	7.341	6.913	6.501	6.103	5.716	5.334	4.949	4.549	4.134
1.4	7.537	7.181	6.838	6.507	6.188	5.879	5.582	5.295	5.019	4.752	4.470
1.6	7.074	6.786	6.505	6.231	5.963	5.700	5.439	5.175	4.899	4.587	4.203
1.8	6.748	6.502	6.261	6.023	5.786	5.548	5.304	5.047	4.763	4.431	4.045
2.0	6.501	6.285	6.070	5.856	5.641	5.421	5.194	4.953	4.687	4.375	4.000
2.5	6.070	5.898	5.726	5.551	5.374	5.193	5.007	4.814	4.611	4.395	4.134
3.0	5.783	5.638	5.492	5.344	5.193	5.039	4.879	4.712	4.530	4.315	4.000
3.5	5.576	5.450	5.323	5.193	5.061	4.925	4.785	4.636	4.476	4.297	4.072
4.0	5.418	5.307	5.193	5.078	4.960	4.838	4.712	4.578	4.433	4.265	4.000
4.5	5.294	5.193	5.091	4.986	4.879	4.768	4.653	4.531	4.399	4.247	4.045
5.0	5.193	5.101	5.007	4.912	4.813	4.712	4.605	4.493	4.370	4.229	4.000
5.5	5.110	5.025	4.938	4.849	4.758	4.664	4.565	4.461	4.347	4.215	4.030
6.0	5.039	4.960	4.879	4.797	4.712	4.624	4.531	4.433	4.326	4.202	4.000
6.5	4.978	4.904	4.829	4.751	4.671	4.589	4.502	4.410	4.309	4.191	4.022
7.0	4.926	4.856	4.785	4.712	4.636	4.558	4.476	4.389	4.293	4.182	4.000
7.5	4.880	4.814	4.746	4.677	4.606	4.531	4.453	4.370	4.279	4.174	4.017
8.0	4.839	4.776	4.712	4.646	4.578	4.508	4.433	4.354	4.267	4.166	4.000
8.5	4.803	4.743	4.682	4.619	4.554	4.486	4.415	4.339	4.256	4.159	4.013
9.0	4.771	4.713	4.654	4.594	4.532	4.467	4.399	4.326	4.246	4.153	4.000
9.5	4.742	4.687	4.630	4.572	4.512	4.450	4.384	4.314	4.237	4.148	4.011
10.0	4.717	4.663	4.608	4.552	4.494	4.434	4.371	4.303	4.229	4.143	4.000
11.0	4.664	4.615	4.565	4.514	4.461	4.405	4.347	4.284	4.215	4.134	4.000
12.0	4.624	4.578	4.531	4.483	4.433	4.381	4.326	4.267	4.202	4.126	4.000
13.0	4.589	4.546	4.502	4.457	4.410	4.360	4.309	4.253	4.191	4.119	4.000
14.0	4.558	4.518	4.476	4.433	4.389	4.342	4.293	4.240	4.182	4.114	4.000
15.0	4.531	4.493	4.454	4.413	4.370	4.326	4.279	4.229	4.174	4.108	4.000
16.0	4.508	4.471	4.433	4.395	4.354	4.312	4.267	4.219	4.166	4.104	4.000
17.0	4.486	4.451	4.415	4.378	4.340	4.299	4.256	4.210	4.159	4.100	4.000
18.0	4.467	4.434	4.399	4.363	4.326	4.287	4.246	4.202	4.153	4.096	4.000
19.0	4.450	4.417	4.384	4.350	4.314	4.277	4.237	4.195	4.148	4.092	4.000
20.0	4.434	4.403	4.371	4.338	4.303	4.267	4.229	4.188	4.143	4.089	4.000
21.0	4.419	4.389	4.358	4.326	4.293	4.258	4.222	4.182	4.138	4.086	4.000
22.0	4.405	4.376	4.347	4.316	4.284	4.250	4.215	4.176	4.134	4.084	4.000
23.0	4.393	4.365	4.336	4.306	4.275	4.243	4.208	4.171	4.130	4.081	4.000
24.0	4.381	4.354	4.326	4.297	4.267	4.236	4.202	4.166	4.126	4.079	4.000
25.0	4.371	4.344	4.317	4.289	4.260	4.229	4.197	4.162	4.123	4.077	4.000
26.0	4.361	4.335	4.309	4.281	4.253	4.223	4.191	4.157	4.119	4.075	4.000
27.0	4.351	4.326	4.301	4.274	4.246	4.217	4.187	4.153	4.116	4.073	4.000
28.0	4.342	4.318	4.293	4.267	4.240	4.212	4.182	4.150	4.114	4.071	4.000
29.0	4.334	4.311	4.286	4.261	4.235	4.207	4.178	4.146	4.111	4.069	4.000
30.0	4.326	4.303	4.280	4.255	4.229	4.202	4.174	4.143	4.108	4.068	4.000

Figure 6.16 and Table 6.2 provide quantitative demonstration of the influence of stress gradient on fix-fix stiffened elements. Similar to the ss-ss stiffened elements case, the buckling stress at the maximum loaded edge increases when the stress gradient is applied to the plate. The influence of stress gradient becomes significant for the short plates (low β values).

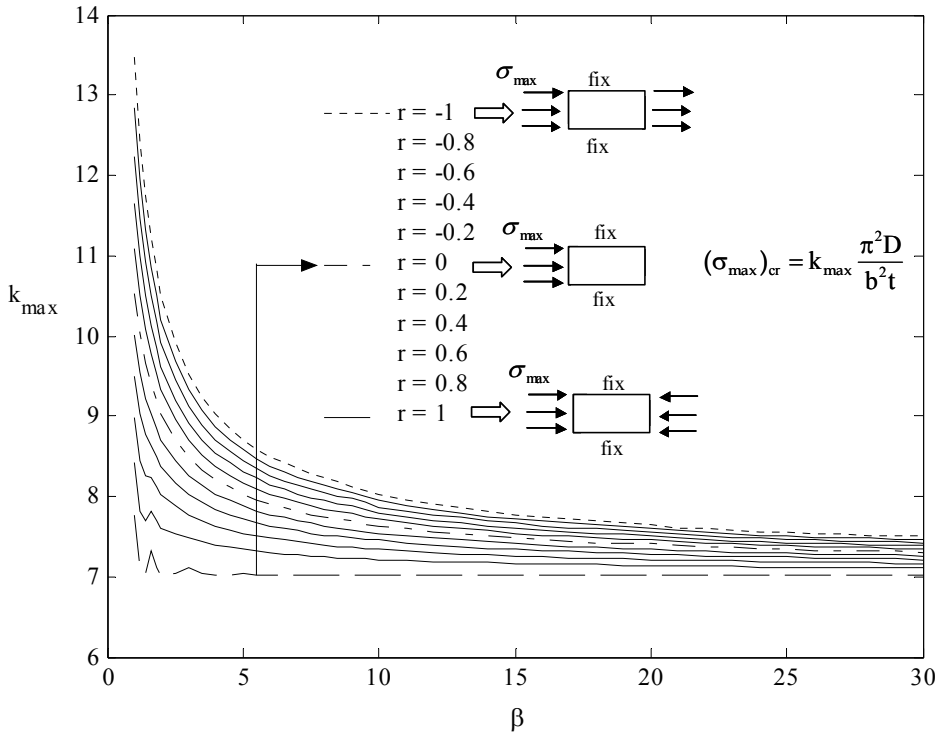

Figure 6.16 k_{max} vs. plate aspect ratio (β) for fix-fix stiffened element

Table 6.3 Numerical results of k_{max} values for fix-fix stiffened elements

r / β	-1	-0.8	-0.6	-0.4	-0.2	0	0.2	0.4	0.6	0.8	1
1.0	13.475	12.843	12.234	11.647	11.082	10.536	10.007	9.490	8.976	8.432	7.758
1.2	12.431	11.942	11.461	10.987	10.514	10.038	9.546	9.025	8.450	7.803	7.101
1.4	11.735	11.324	10.914	10.503	10.088	9.665	9.227	8.766	8.266	7.697	7.033
1.6	11.221	10.861	10.501	10.138	9.771	9.398	9.018	8.628	8.225	7.808	7.326
1.8	10.820	10.500	10.178	9.853	9.525	9.191	8.850	8.496	8.120	7.690	7.101
2.0	10.499	10.210	9.918	9.624	9.325	9.021	8.707	8.379	8.021	7.597	7.008
2.5	9.918	9.683	9.445	9.204	8.959	8.707	8.446	8.173	7.879	7.543	7.041
3.0	9.525	9.325	9.123	8.917	8.707	8.491	8.266	8.029	7.773	7.482	7.101
3.5	9.239	9.065	8.888	8.707	8.522	8.331	8.132	7.922	7.694	7.431	7.033
4.0	9.021	8.865	8.707	8.546	8.380	8.208	8.029	7.839	7.632	7.394	7.008
4.5	8.848	8.707	8.564	8.417	8.266	8.110	7.946	7.772	7.583	7.364	7.017
5.0	8.708	8.579	8.447	8.312	8.173	8.029	7.878	7.718	7.542	7.339	7.041
5.5	8.591	8.472	8.350	8.224	8.095	7.962	7.821	7.672	7.508	7.318	7.018
6.0	8.493	8.381	8.267	8.150	8.029	7.904	7.773	7.632	7.479	7.300	7.008
6.5	8.410	8.305	8.197	8.087	7.973	7.855	7.731	7.598	7.453	7.285	7.012
7.0	8.340	8.239	8.137	8.032	7.924	7.812	7.694	7.569	7.431	7.271	7.024
7.5	8.282	8.184	8.086	7.985	7.881	7.774	7.662	7.543	7.412	7.259	7.014
8.0	8.236	8.140	8.043	7.945	7.845	7.742	7.634	7.520	7.394	7.248	7.008
8.5	8.183	8.093	8.011	7.914	7.816	7.715	7.610	7.499	7.379	7.239	7.010
9.0	8.125	8.047	7.970	7.873	7.784	7.693	7.590	7.482	7.365	7.230	7.017
9.5	8.071	7.995	7.921	7.831	7.746	7.660	7.563	7.468	7.353	7.222	7.012
10.0	8.019	7.947	7.871	7.789	7.709	7.626	7.535	7.459	7.344	7.215	7.008
11.0	7.962	7.892	7.821	7.748	7.672	7.592	7.508	7.418	7.318	7.201	7.014
12.0	7.904	7.839	7.773	7.704	7.632	7.558	7.479	7.394	7.300	7.190	7.008
13.0	7.855	7.794	7.731	7.666	7.599	7.528	7.453	7.373	7.285	7.181	7.012
14.0	7.812	7.754	7.694	7.633	7.569	7.502	7.431	7.355	7.271	7.172	7.008
15.0	7.775	7.719	7.662	7.604	7.543	7.479	7.412	7.339	7.259	7.165	7.010
16.0	7.743	7.689	7.635	7.578	7.520	7.459	7.394	7.325	7.248	7.158	7.008
17.0	7.717	7.664	7.611	7.556	7.500	7.441	7.379	7.312	7.239	7.152	7.010
18.0	7.697	7.645	7.592	7.538	7.483	7.426	7.365	7.301	7.230	7.147	7.008
19.0	7.676	7.623	7.580	7.526	7.470	7.413	7.354	7.291	7.222	7.142	7.009
20.0	7.646	7.592	7.556	7.520	7.464	7.406	7.346	7.283	7.215	7.137	7.008
21.0	7.612	7.569	7.525	7.479	7.431	7.381	7.328	7.271	7.208	7.133	7.009
22.0	7.593	7.551	7.508	7.464	7.418	7.370	7.318	7.263	7.201	7.129	7.008
23.0	7.575	7.535	7.493	7.450	7.406	7.359	7.309	7.255	7.196	7.125	7.009
24.0	7.559	7.520	7.479	7.438	7.394	7.349	7.300	7.248	7.190	7.122	7.008
25.0	7.545	7.506	7.467	7.426	7.384	7.339	7.292	7.242	7.185	7.119	7.008
26.0	7.532	7.494	7.455	7.415	7.374	7.331	7.285	7.236	7.181	7.116	7.008
27.0	7.521	7.483	7.445	7.406	7.365	7.323	7.278	7.230	7.176	7.113	7.008
28.0	7.512	7.475	7.437	7.398	7.358	7.316	7.272	7.225	7.172	7.111	7.008
29.0	7.506	7.468	7.430	7.391	7.351	7.310	7.266	7.220	7.169	7.108	7.008
30.0	7.504	7.465	7.426	7.387	7.347	7.305	7.262	7.216	7.165	7.106	7.008

Consistent with the intuition from Figure 6.1, it can be concluded that the influence of stress gradient diminishes quickly for local buckling of a stiffened element, but perhaps not as quickly as is generally assumed in design. For example, for a simply supported plate with length-to-width ratio 5, when a stress gradient r = 0 (loaded on only one edge) is applied, the buckling coefficient k_{max} will equal 4.712 - still an 18% increase in buckling stress compared with the pure compression case. The k_{max} values of Table 6.2 may be used to predict the increased local buckling stress due to the influence of a stress gradient, and for continuous beams where sharp moment gradients are more likely to persist, the boost may be significant.

6.2.3 Stress Gradient Effect on the Elastic Buckling of Unstiffened Elements

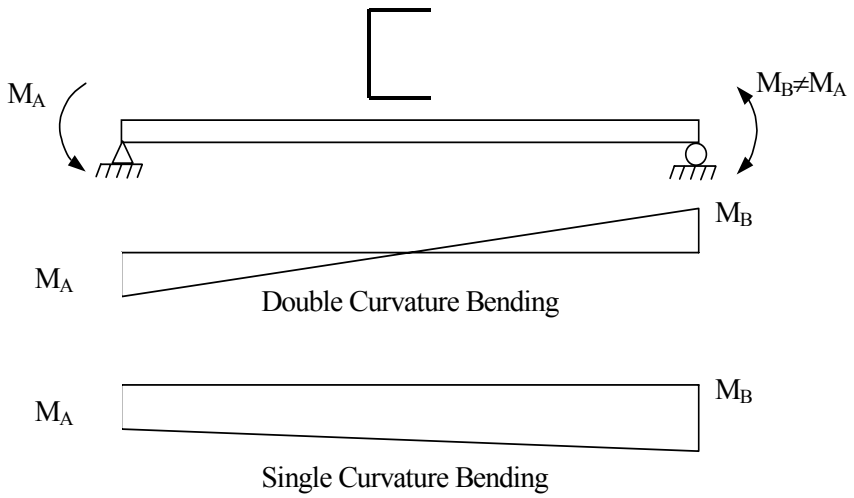

Figure 6.17 Channel subjected to moment gradient

Consider a channel under moment gradient as shown in Figure 6.17. Distortional buckling ("local buckling" of the unstiffened element) of this channel may be considered by isolating the compression flange and modeling the flange as a thin plate supported on one unloaded edge, free on the opposite edge and loaded with unequal axial stresses, as

shown in Figure 6.5. The web's contribution to the stability of the flange may be treated as a rotational spring along the supported edge. As discussed in Schafer and Peköz (1999) this rotational support is stress dependent and may have a net positive or negative contribution to the stiffness depending on whether the buckling is triggered by buckling of the web first (net negative stiffness) or buckling of the flange (net positive stiffness). The analysis here will focus on the case where the flange buckles before the web. The specific thin plate model examined here is shown in detail in Figure 6.5. The difference between the compressive stresses is equilibrated by uniform shear stresses acting along the longitudinal supported edge. Shear stresses along the two compressive loaded edges are linearly distributed. Elastic rotational restraint from the web is also applied along the longitudinal supported edge.

6.2.3.1 Stress Distribution

The uniform shear stress at the edge y = 0 can be determined by force equilibrium in the x direction, Equation (6.32) is the result. In addition, along the free edge no stress exists, Equation (6.33).

$$\tau_{xy|y=0} = \frac{(\sigma_{max} - \sigma_{min})b}{a} \tag{6.32}$$

$$\tau_{xy|y=b} = 0 \tag{6.33}$$

Equilibrium is enforced by insuring $\sum F_x = 0$, $\sum F_y = 0$, $\sum M_0 = 0$ (about the origin). The internal shear stress distribution is assumed to be linear along the plate width and uniform in the x direction:

$$\tau_{xy} = \sigma_{max} \frac{b(1-r)}{a}\left(1 - \frac{y}{b}\right) \tag{6.34}$$

By assuming plane stress conditions and ignoring the body force the compressive stresses can be obtained in functional form as:

$$\sigma_x = \sigma_{max}\left[\frac{(1-r)x}{a} + r\right] \tag{6.35}$$

$$\sigma_y = 0 \tag{6.36}$$

6.2.3.2 Boundary Conditions

The numerical model of unstiffened elements is shown in Figure 6.5, a total of six boundary conditions are observed and stated below.

Simply supported at the transverse, loaded edges:

$$(w)_{x=0} = 0 \tag{6.37}$$

$$(w)_{x=a} = 0 \tag{6.38}$$

Elastic restraint against rotation along one supported longitudinal edge:

$$(w)_{y=0} = 0 \tag{6.39}$$

$$D\left(\frac{\partial^2 w}{\partial y^2} + \mu\frac{\partial^2 w}{\partial x^2}\right)_{y=0} = S\left(\frac{\partial w}{\partial y}\right)_{y=0} \tag{6.40}$$

One free longitudinal edge:

$$D\left(\frac{\partial^2 w}{\partial y^2} + \mu\frac{\partial^2 w}{\partial x^2}\right)_{y=b} = 0 \tag{6.41}$$

$$D\left[\frac{\partial^3 w}{\partial y^3}+(2-\mu)\frac{\partial^3 w}{\partial x^2 \partial y}\right]_{y=b}=0 \tag{6.42}$$

Similar to the structure of deflection functions for stiffened elements, the deflection functions $w(x,y)$ for unstiffened elements is $\sum_{i=1}^{N} A_i(y)B_i(x)$, where A_i is a function of y alone and B_i is a function of x alone. Each term should satisfy all six boundary conditions, then the linear summation will also satisfy all the boundary conditions. In this work, three different functions were proposed and analyzed.

6.2.3.2 Trial Deflection Function 1 (Eq. 6.43)

The first proposed deflection function, Equation (6.43), is motivated by the work of Lundquist and Stowell (1942b) who explored the buckling of unstiffened elements subjected to uniform compressive stresses. Lundquist and Stowell employed a trigonometric term in the longitudinal direction and a polynomial term in the transverse direction to establish the deflection function, as below:

$$w=\left\{A\frac{y}{b}+B\left[\left(\frac{y}{b}\right)^5+a_1\left(\frac{y}{b}\right)^4+a_2\left(\frac{y}{b}\right)^3+a_3\left(\frac{y}{b}\right)^2\right]\right\}\sin\left(\frac{\pi x}{a}\right) \tag{6.43}$$

In Equation (6.43) A and B are arbitrary deflection amplitudes and $a_1=-4.963$, $a_2=9.852$, and $a_3=-9.778$. The deflection curve across the width of the plate is taken as the sum of a straight line and a cantilever-deflection curve. The values of a_1, a_2 and a_3 were determined by taking the proportion of two deflection curves that gave the lowest buckling stress for a fixed-edge flange with $\mu=0.3$.

For the unstiffened element under a stress gradient, the single trigonometric term in the loading direction is no longer appropriate. Therefore, a summation of trigonometric terms is selected in the longitudinal direction and polynomial terms in the transverse direction for the deflection function, Equation (6.44). The values of a_1, a_2 and a_3 in Equation (6.44) are the same as Equation (6.43).

$$w = \sum_{i=1}^{N} \left\{ A\frac{y}{b} + B\left[\left(\frac{y}{b}\right)^5 + a_1\left(\frac{y}{b}\right)^4 + a_2\left(\frac{y}{b}\right)^3 + a_3\left(\frac{y}{b}\right)^2 \right] \right\} \sin\left(\frac{i\pi x}{a}\right) \tag{6.44}$$

The arbitrary amplitudes A and B are actually related to each other; the relationship can be obtained by substituting Equation (6.44) into boundary conditions, resulting in

$$B = \frac{Sb}{2a_3 D} A \tag{6.45}$$

Therefore, the deflection function, Equation (6.44), may be simplified as:

$$w = \sum_{i=1}^{N} w_i \left\{ \frac{y}{b} + \frac{Sb}{2a_3 D}\left[\left(\frac{y}{b}\right)^5 + a_1\left(\frac{y}{b}\right)^4 + a_2\left(\frac{y}{b}\right)^3 + a_3\left(\frac{y}{b}\right)^2 \right] \right\} \sin\left(\frac{i\pi x}{a}\right) \tag{6.46}$$

The equilibrium equations can be constructed by substituting the deflection function into the total potential energy expression Equation (6.1) and taking the derivative of the function as Equation (6.5). The buckling stress σ_{max} is the minimum eigenvalue of the resulting matrix of equilibrium expressions. The size of the matrix is $N \times N$.

It should be noted that trial deflection function 1 (Equation 6.43) is not compatible with the boundary conditions, Equations (6.41) and (6.42). However, it was found to give reasonable results in the research done by Lundquist and Stowell (1942b) and was thus considered here.

6.2.3.3 Trial Deflection Function 2 (Eq. 6.47)

Unlike the first trial deflection function which is based on a physical representation of the expected shape, the second trial deflection function (Equation 6.47) is a more general combination of polynomials and trigonometric functions. A fourth order polynomial is assumed for the transverse deflection and a sine function for the longitudinal deflection:

$$w = \sum_{i=1}^{N} w_i \left(c_{i1} y + c_{i2} y^2 + c_{i3} y^3 + c_{i4} y^4\right) \sin\left(\frac{i\pi x}{a}\right) \tag{6.47}$$

The deflection function must satisfy all the boundary conditions. Therefore, the parameters c_{i1}, c_{i2}, c_{i3}, c_{i4} are determined by substituting Equation (6.47) into the boundary conditions of Equations (6.37) to (6.42), resulting in:

$$c_{i1} = 1 \tag{6.48}$$

$$c_{i2} = \frac{S}{2D} \tag{6.49}$$

$$\begin{aligned} c_{i3} = &\left(\mu\frac{i^2\pi^2 b}{a^2 k_1^2 k_3} + \mu\frac{i^2\pi^2 b^2 S}{2a^2 k_1^2 k_3 D} - (2-\mu)\frac{i^2\pi^2}{a^2 k_1 k_2 k_3} - (2-\mu)\frac{i^2\pi^2 bS}{a^2 k_1 k_2 k_3 D} - \frac{S}{k_1^2 k_3 D}\right) \\ &\times\left(\mu\frac{i^2\pi^2 b^4}{a^2} - 12b^2\right) + \frac{S}{2k_1 D}\left(\mu\frac{i^2\pi^2 b^2}{a^2} - 2\right) \end{aligned} \tag{6.50}$$

$$c_{i4} = \mu\frac{i^2\pi^2 b}{a^2 k_1 k_3} + \mu\frac{i^2\pi^2 b^2 S}{2a^2 k_1 k_3 D} - (2-\mu)\frac{i^2\pi^2}{a^2 k_2 k_3} - (2-\mu)\frac{i^2\pi^2 bS}{a^2 k_2 k_3 D} - \frac{S}{k_1 k_3 D} \tag{6.51}$$

$$i = 1, \quad 2, \quad \ldots \quad N$$

where

$$k_1 = 6b - \mu\frac{i^2\pi^2 b^3}{a^2} \tag{6.52}$$

$$k_2 = 6 - (2-\mu)\frac{3i^2\pi^2 b^2}{a^2} \tag{6.53}$$

$$k_3 = \frac{12b^2}{k_1} - \mu\frac{i^2\pi^2 b^4}{a^2 k_1} - \frac{24b}{k_2} + (2-\mu)\frac{4i^2\pi^2 b^3}{a^2 k_2} \tag{6.54}$$

The equilibrium equations can be constructed by the same method as described for the deflection function 1. The size of the resulting matrix of equilibrium expressions is $N \times N$.

6.2.3.4 Trial Deflection Function 3 (Eq. 6.55)

As an extension of the second deflection function, a third deflection function using a 5th order polynomial in the transverse direction was also considered:

$$w = \sum_{i=1}^{N}\left[w_{i1}\left(p_{i1}y + p_{i2}y^2 + p_{i3}y^3 + p_{i4}y^4\right) + w_{i2}\left(q_{i1}y^3 + q_{i2}y^4 + q_{i3}y^5\right)\right]\sin\left(\frac{i\pi x}{a}\right) \tag{6.55}$$

where w_{i1}, w_{i2} are arbitrary deflection amplitudes. The parameters p and q were determined by the boundary conditions.

$$p_{i1} = 1 \tag{6.56}$$

$$p_{i2} = \frac{S}{2D} \tag{6.57}$$

$$p_{i3} = \mu\frac{i^2\pi^2 b}{a^2 k_1} + \frac{S}{2k_1 D}\left(\mu\frac{i^2\pi^2 b^2}{a^2} - 2\right) + \mu\frac{i^2\pi^2 b^4 M_1}{a^2 k_1} \tag{6.58}$$

$$p_{i4} = M_1 \tag{6.59}$$

$$q_{i1} = \mu \frac{i^2 \pi^2 b^5}{a^2 k_1} - 20 \frac{b^3}{k_1} + \mu \frac{i^2 \pi^2 b^4 M_2}{a^2 k_1} - \frac{12 b^2 M_2}{k_1} \tag{6.60}$$

$$q_{i2} = M_2 \tag{6.61}$$

$$q_{i3} = 1 \tag{6.62}$$

where

$$k_1 = 6b - \mu \frac{i^2 \pi^2 b^3}{a^2} \tag{6.63}$$

$$k_2 = 6 - (2 - \mu) \frac{3 i^2 \pi^2 b^2}{a^2} \tag{6.64}$$

$$k_3 = \left(\mu \frac{i^2 \pi^2 b^4}{a^2} - 12 b^2 \right) \frac{1}{k_1} - \left((2 - v) \frac{4 i^2 \pi^2 b^3}{a^2} - 24 b \right) \frac{1}{k_2} \tag{6.65}$$

$$M_1 = (2 - \mu) \frac{i^2 \pi^2}{a^2 k_2 k_3} + (2 - \mu) \frac{i^2 \pi^2 b S}{k_2 k_3 D} - \mu \frac{i^2 \pi^2 b}{a^2 k_1 k_3} - \mu \frac{i^2 \pi^2 b^2 S}{2 k_1 k_3 D} + \frac{S}{D k_1 k_3} \tag{6.66}$$

$$M_2 = (2 - \mu) \frac{5 i^2 \pi^2 b^4}{a^2 k_2 k_3} - \frac{60 b^2}{k_2 k_3} - \mu \frac{i^2 \pi^2 b^5}{a^2 k_1 k_3} + \frac{20 b^3}{k_1 k_3} \tag{6.67}$$

The size of the resulting matrix of equilibrium expressions is $2N \times 2N$.

6.2.3.5 Verification by Finite Element Analysis

Finite element analysis using ABAQUS was employed to examine the results of the analytical solutions for unstiffened elements. The S4R5 shell element was used for the thin plate with E = 29500 ksi and $\mu = 0.3$. The element size is 0.1 in. × 0.1 in. Plate width was varied in the analysis, but plate length was generally 10 in. The plate is simply supported along three edges, and free along one unloaded edge. The uneven applied load

is equilibrated by shear forces acting along one simply supported edge, as shown in Figure 6.18.

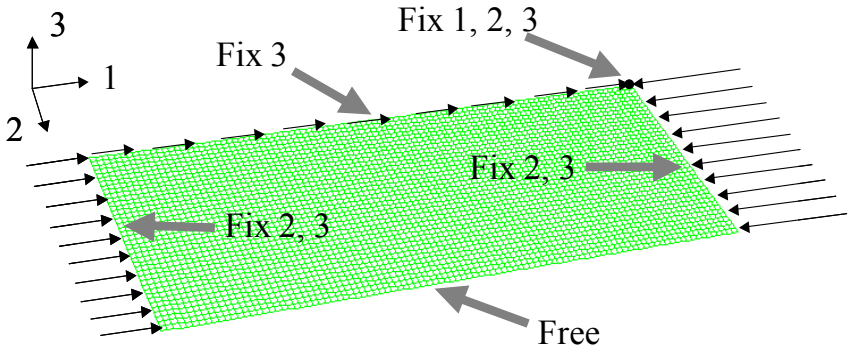

Figure 6.18 Finite element model for ss-free unstiffened elements under a stress gradient

Figure 6.19 and Figure 6.20 show the buckled shape for the plate with a = 10 in., b = 3 in., t = 0.0333 in., S = 0 kip-in./in. and the stress gradient factor r = 0. Figure 6.21 and Figure 6.22 illustrate the stress distribution of σ_x and τ_{xy} on the top surface of the plate respectively. The results are obtained by the elastic analysis of ABAQUS based on the buckled shape. The stress distributions on top surface are not uniform and stress concentration forms at those areas close to the maximum loaded edge where large deformations form. Since the reported stress is based on the buckled shape, the stresses on the bottom surface are the opposite of values on the top surface, and no stress exists on the mid-surface (membrane). Table 6.4 provides the buckling stresses calculated by ABAQUS, $(\sigma_{max})_{cr}$ (FEM), and the ratio of the analytical solutions (DF1 stands for result by trial deflection function 1, similar definition for DF2 and DF3) to the ABAQUS solution (presented as FEM). In general, all three trial deflection functions give good agreement with the finite element results. The trial deflection function 2 (Equation 6.47) and the trial deflection 3 (Equation 6.55) have closer results to FEM, with average error

less than 1%. The trial deflection function 1 (Equation 6.43) provides systematically higher buckling stress than the FEM results as well as the other two deflection functions, and the error grows when the stress gradient effect is large or S is large. Since trial deflection function 2 (Equation 6.47) provides both accuracy and reasonable computational efficiency, it is selected for further analyses.

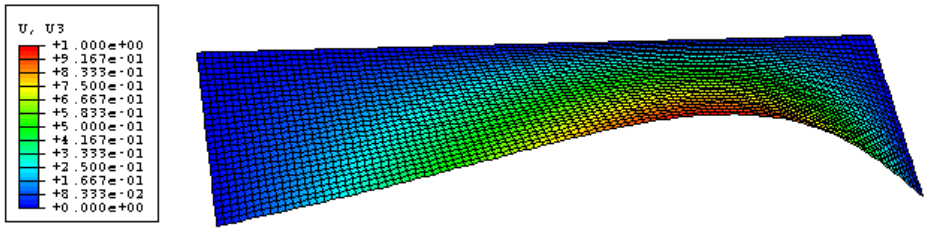

Figure 6.19 Buckling shape of a unstiffened plate by FE solution

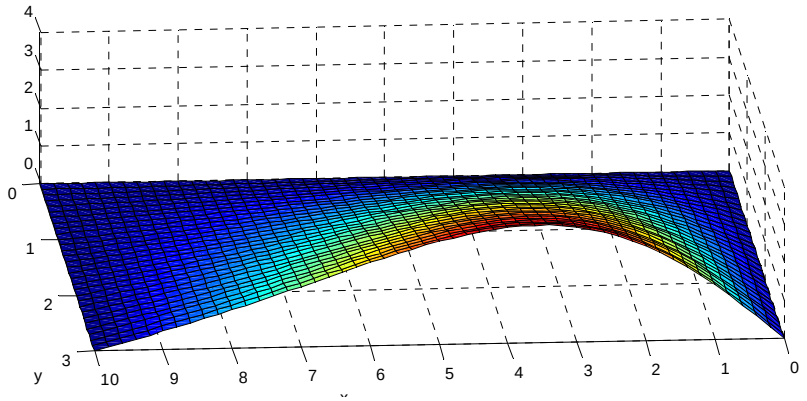

Figure 6.20 Buckling shape of an unstiffened element by analytical solution

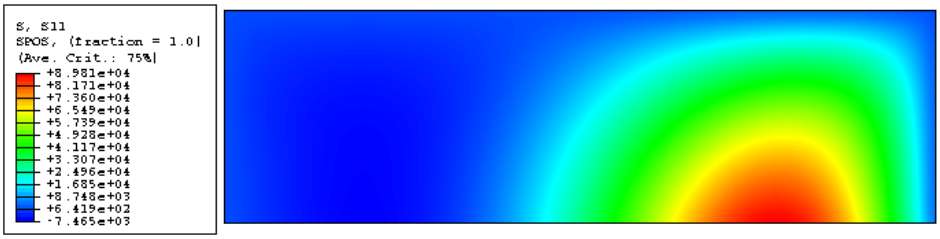

Figure 6.21 Stress σ_x distribution on top surface of a ss-free plate subjected to a stress gradient r = 0 by elastic FE solution

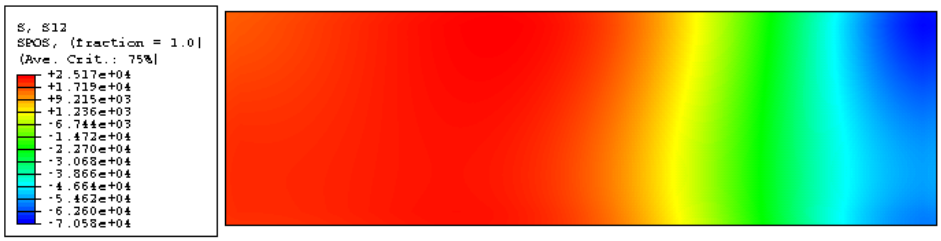

Figure 6.22 Stress τ_{xy} distribution on top surface of a ss-free plate subjected to a stress gradient r = 0 by elastic FE solution

A convergence study for trial deflection function 2 was conducted on a fix-free unstiffened element with t = 0.01, and aspect ratio β varied from 10 to 40. Figure 6.23 through Figure 6.25 provides the results, which indicate that for the fix-free unstiffened element with β = 10, the analytical solution converges if the number of selected terms of the deflection function is greater than 10; for plates with β = 20, the reasonable value of N is 15; and for plates with β = 40, N should be larger than 30.

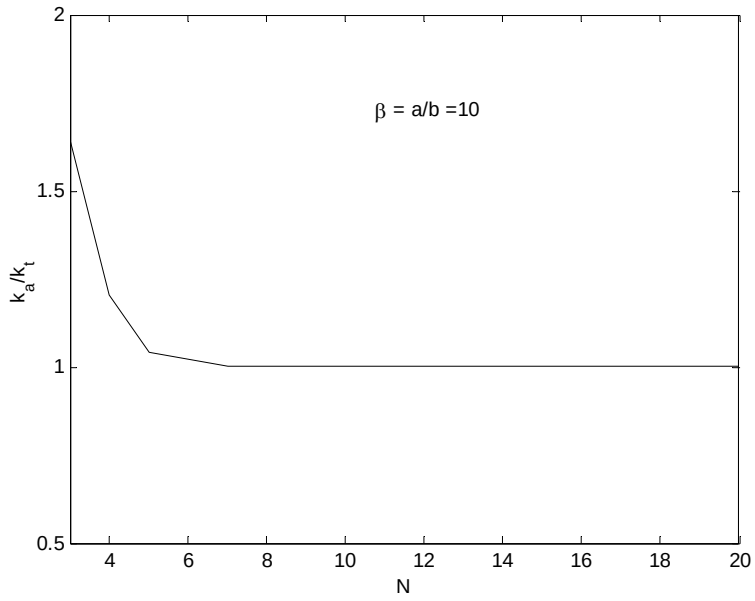

Figure 6.23 Convergence study on a fix-free plate with β = 10

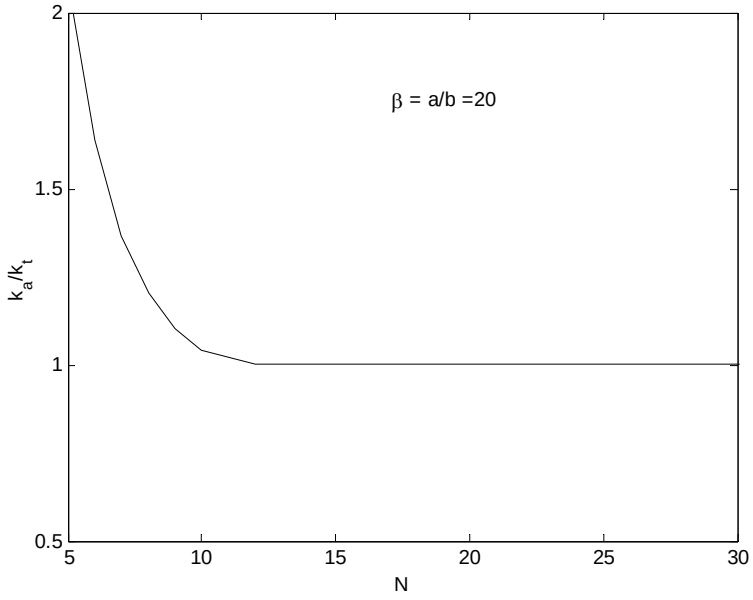

Figure 6.24 Convergence study on a fix-free plate with β = 20

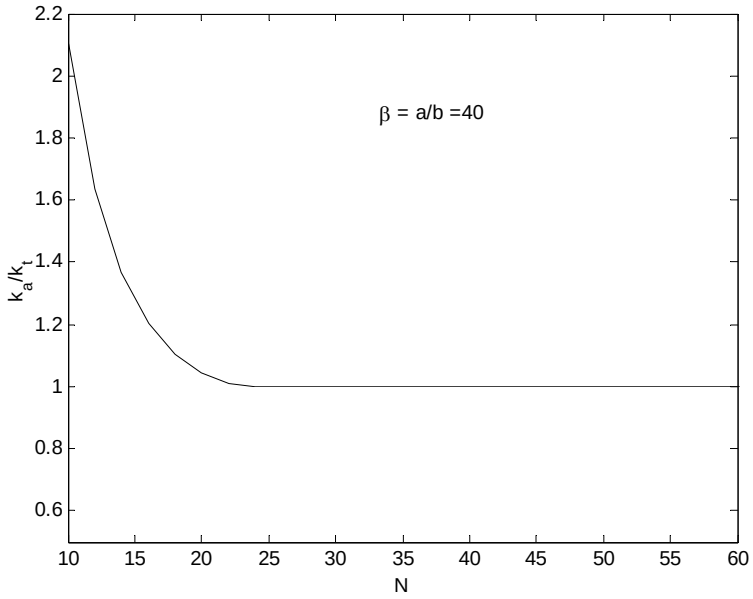

Figure 6.25 Convergence study on a fix-free plate with β = 40

According to a convergence study of trial deflection function 2, the number of terms to be kept in the expansions (and thus the size of the N×N matrix to be solved) is selected via the following rule:

For a/b <= 10, N = 20;

For a/b > 10 and a/b <= 20, N = 40;

For a/b > 20 and a/b <= 40, N = 60.

Table 6.4 Results of numerical models with different deflection functions

	r	a (in.)	b (in.)	t (in.)	S(kip-in./in.)	$(\sigma_{\max})_{cr}$ (FEM) (ksi)	DF1/FEM	DF2/FEM	DF3/FEM
	1	10	2.5	0.04	0	3.3277	100.11%	99.90%	99.79%
	0.9	10	2.5	0.04	0	3.4976	100.11%	99.89%	99.79%
	0.7	10	2.5	0.04	0	3.8523	100.15%	99.88%	99.77%
	0.5	10	2.5	0.04	0	4.2131	100.23%	99.85%	99.73%
	0.3	10	2.5	0.04	0	4.5697	100.35%	99.81%	99.68%
	0.1	10	2.5	0.04	0	4.9198	100.50%	99.76%	99.62%
Case 1	0	10	2.5	0.04	0	5.093	100.58%	99.73%	99.59%
	-0.1	10	2.5	0.04	0	5.2654	100.66%	99.71%	99.57%
	-0.3	10	2.5	0.04	0	5.6091	100.85%	99.68%	99.51%
	-0.5	10	2.5	0.04	0	5.9528	101.07%	99.65%	99.47%
	-0.7	10	2.5	0.04	0	6.2979	101.32%	99.63%	99.43%
	-0.9	10	2.5	0.04	0	6.645	101.60%	99.63%	99.40%
	-1	10	2.5	0.04	0	6.8194	101.96%	99.64%	99.36%
	1	10	2	0.05	0	7.7316	100.34%	100.19%	100.09%
	0.9	10	2	0.05	0	8.1205	100.35%	100.19%	100.09%
	0.7	10	2	0.05	0	8.8898	100.38%	100.16%	100.06%
	0.5	10	2	0.05	0	9.618	100.44%	100.11%	100.00%
	0.3	10	2	0.05	0	10.305	100.52%	100.06%	99.93%
	0.1	10	2	0.05	0	10.966	100.60%	99.99%	99.85%
Case 2	0	10	2	0.05	0	11.29	100.65%	99.96%	99.82%
	-0.1	10	2	0.05	0	11.612	100.69%	99.92%	99.78%
	-0.3	10	2	0.05	0	12.249	100.81%	99.87%	99.71%
	-0.5	10	2	0.05	0	12.884	100.93%	99.82%	99.64%
	-0.7	10	2	0.05	0	13.517	101.08%	99.78%	99.59%
	-0.9	10	2	0.05	0	14.152	101.25%	99.74%	99.53%
	-1	10	2	0.05	0	14.471	101.33%	99.72%	99.50%
	1	10	3	0.0333	0	1.6963	100.04%	99.79%	99.68%
	0.9	10	3	0.0333	0	1.7836	100.05%	99.78%	99.67%
	0.7	10	3	0.0333	0	1.9715	100.09%	99.78%	99.66%
	0.5	10	3	0.0333	0	2.1721	100.19%	99.77%	99.65%
	0.3	10	3	0.0333	0	2.3793	100.35%	99.74%	99.62%
	0.1	10	3	0.0333	0	2.5884	100.56%	99.72%	99.58%
Case 3	0	10	3	0.0333	0	2.6931	100.68%	99.71%	99.57%
	-0.1	10	3	0.0333	0	2.7979	100.81%	99.70%	99.55%
	-0.3	10	3	0.0333	0	3.0078	101.10%	99.69%	99.52%
	-0.5	10	3	0.0333	0	3.2185	101.43%	99.70%	99.51%
	-0.7	10	3	0.0333	0	3.4307	101.81%	99.74%	99.52%
	-0.9	10	3	0.0333	0	3.6446	102.24%	99.79%	99.54%
	-1	10	3	0.0333	0	3.7522	99.31%	99.83%	99.55%
	1	10	3	0.0333	Inf	4.2469	99.81%	99.79%	99.75%
	0.9	10	3	0.0333	Inf	4.4542	99.91%	99.78%	99.74%
	0.7	10	3	0.0333	Inf	4.8233	100.73%	99.69%	99.64%
	0.5	10	3	0.0333	Inf	5.1333	102.05%	99.56%	99.51%
	0.3	10	3	0.0333	Inf	5.4055	103.63%	99.44%	99.38%
	0.1	10	3	0.0333	Inf	5.6546	105.40%	99.33%	99.27%
Case 4	0	10	3	0.0333	Inf	5.7731	106.36%	99.29%	99.22%
	-0.1	10	3	0.0333	Inf	5.8887	107.35%	99.26%	99.18%
	-0.3	10	3	0.0333	Inf	6.1131	109.47%	99.20%	99.11%
	-0.5	10	3	0.0333	Inf	6.3309	111.76%	99.17%	99.07%
	-0.7	10	3	0.0333	Inf	6.5442	114.21%	99.17%	99.05%
	-0.9	10	3	0.0333	Inf	6.7545	116.84%	99.18%	99.04%
	-1	10	3	0.0333	Inf	6.8587	118.22%	99.20%	99.05%
Mean							102.37%	99.71%	99.58%
Standard deviation							4.27%	0.26%	0.26%

6.2.3.6 Elastic Buckling Stress of Unstiffened Elements under Stress Gradients

Two unstiffened elements are investigated here, one where the supported longitudinal edge has no rotational restraint (ss-free) and one where the supported edge has infinite rotational restraint (fix-free). The plate buckling coefficient k_{max} for the elements subjected to a variety of stress gradients is summarized in Table 6.5 for the ss-free case and Table 6.6 for the fix-free case. Figure 6.26 and Figure 6.27 give a graphic representation of the stress gradient effect on these two different unstiffened elements. For the ss-free unstiffened plate under uniform compression, the plate buckling coefficient k asymptotes to 0.425. It is shown in Figure 9 that the stress gradient boosts the buckling stress at the maximum loaded edge greatly, especially when the plate aspect ratio (β) is less than 10. Similar results are observed for the fix-free unstiffened element, the buckling coefficient k_{max} converges to 1.287 (buckling coefficient for uniform compression) gradually.

Table 6.5 Numerical results of k_{max} values of ss-free unstiffened element

r / β	-1	-0.8	-0.6	-0.4	-0.2	0	0.2	0.4	0.6	0.8	1
1.0	4.765	4.298	3.841	3.402	2.992	2.621	2.299	2.025	1.796	1.606	1.447
1.2	3.605	3.263	2.930	2.609	2.306	2.029	1.785	1.576	1.399	1.252	1.128
1.4	2.894	2.631	2.375	2.127	1.891	1.673	1.477	1.307	1.163	1.041	0.938
1.6	2.423	2.214	2.009	1.810	1.619	1.440	1.278	1.134	1.010	0.905	0.816
1.8	2.093	1.921	1.752	1.588	1.430	1.279	1.140	1.016	0.906	0.813	0.733
2.0	1.852	1.707	1.565	1.426	1.291	1.162	1.041	0.930	0.832	0.747	0.674
2.5	1.465	1.363	1.264	1.166	1.070	0.976	0.885	0.798	0.718	0.647	0.584
3.0	1.241	1.164	1.088	1.013	0.939	0.866	0.794	0.723	0.655	0.592	0.535
3.5	1.096	1.035	0.974	0.914	0.854	0.795	0.735	0.676	0.616	0.559	0.506
4.0	0.996	0.945	0.894	0.844	0.794	0.744	0.694	0.642	0.590	0.538	0.487
4.5	0.922	0.879	0.836	0.793	0.750	0.707	0.663	0.618	0.571	0.523	0.474
5.0	0.866	0.828	0.791	0.753	0.715	0.677	0.639	0.599	0.556	0.512	0.465
5.5	0.822	0.789	0.755	0.722	0.688	0.654	0.619	0.583	0.545	0.503	0.458
6.0	0.786	0.756	0.726	0.696	0.666	0.635	0.603	0.571	0.536	0.497	0.453
6.5	0.757	0.730	0.703	0.675	0.647	0.619	0.590	0.560	0.528	0.491	0.449
7.0	0.733	0.708	0.683	0.657	0.632	0.606	0.579	0.551	0.521	0.487	0.446
7.5	0.712	0.689	0.665	0.642	0.618	0.594	0.569	0.543	0.515	0.483	0.443
8.0	0.694	0.672	0.651	0.629	0.607	0.584	0.561	0.537	0.510	0.480	0.441
8.5	0.678	0.658	0.638	0.617	0.597	0.576	0.554	0.531	0.506	0.477	0.439
9.0	0.664	0.645	0.627	0.607	0.588	0.568	0.547	0.525	0.502	0.474	0.438
9.5	0.652	0.634	0.617	0.598	0.580	0.561	0.541	0.521	0.498	0.472	0.436
10.0	0.641	0.624	0.608	0.590	0.573	0.555	0.536	0.516	0.495	0.470	0.435
11.0	0.623	0.607	0.592	0.577	0.561	0.544	0.527	0.509	0.489	0.467	0.434
12.0	0.607	0.593	0.579	0.565	0.551	0.535	0.520	0.503	0.485	0.464	0.432
13.0	0.594	0.582	0.569	0.556	0.542	0.528	0.513	0.498	0.481	0.461	0.431
14.0	0.583	0.572	0.560	0.547	0.535	0.522	0.508	0.494	0.478	0.459	0.431
15.0	0.574	0.563	0.552	0.540	0.528	0.516	0.503	0.490	0.475	0.457	0.430
16.0	0.566	0.555	0.545	0.534	0.523	0.511	0.499	0.486	0.472	0.456	0.429
17.0	0.558	0.549	0.539	0.528	0.518	0.507	0.496	0.483	0.470	0.454	0.429
18.0	0.552	0.543	0.533	0.524	0.514	0.503	0.492	0.481	0.468	0.453	0.429
19.0	0.546	0.537	0.528	0.519	0.510	0.500	0.489	0.478	0.466	0.452	0.428
20.0	0.541	0.533	0.524	0.515	0.506	0.497	0.487	0.476	0.464	0.451	0.428
21.0	0.536	0.528	0.520	0.512	0.503	0.494	0.484	0.474	0.463	0.450	0.428
22.0	0.532	0.524	0.516	0.508	0.500	0.491	0.482	0.472	0.461	0.449	0.428
23.0	0.528	0.521	0.513	0.505	0.497	0.489	0.480	0.471	0.460	0.448	0.427
24.0	0.524	0.517	0.510	0.503	0.495	0.487	0.478	0.469	0.459	0.447	0.427
25.0	0.521	0.514	0.507	0.500	0.493	0.485	0.477	0.468	0.458	0.446	0.427
26.0	0.518	0.511	0.505	0.498	0.490	0.483	0.475	0.466	0.457	0.446	0.427
27.0	0.515	0.509	0.502	0.496	0.489	0.481	0.474	0.465	0.456	0.445	0.427
28.0	0.513	0.506	0.500	0.493	0.487	0.480	0.472	0.464	0.455	0.445	0.427
29.0	0.510	0.504	0.498	0.492	0.485	0.478	0.471	0.463	0.454	0.444	0.427
30.0	0.508	0.502	0.496	0.490	0.483	0.477	0.470	0.462	0.454	0.444	0.427

Table 6.6 Numerical results of k_{max} values for fix-free unstiffened element

r / β	-1	-0.8	-0.6	-0.4	-0.2	0	0.2	0.4	0.6	0.8	1
1.0	5.073	4.626	4.187	3.760	3.351	2.971	2.628	2.327	2.071	1.854	1.672
1.2	4.024	3.702	3.386	3.077	2.776	2.490	2.223	1.982	1.770	1.587	1.432
1.4	3.404	3.161	2.922	2.687	2.457	2.233	2.017	1.815	1.630	1.466	1.323
1.6	3.012	2.820	2.632	2.448	2.268	2.089	1.914	1.742	1.578	1.425	1.288
1.8	2.749	2.594	2.442	2.294	2.148	2.005	1.863	1.720	1.577	1.434	1.299
2.0	2.566	2.437	2.311	2.187	2.067	1.950	1.834	1.719	1.601	1.476	1.343
2.5	2.291	2.201	2.112	2.025	1.939	1.855	1.772	1.689	1.605	1.514	1.396
3.0	2.139	2.067	1.996	1.925	1.854	1.781	1.705	1.623	1.532	1.424	1.299
3.5	2.037	1.976	1.915	1.853	1.790	1.725	1.656	1.583	1.503	1.410	1.293
4.0	1.961	1.907	1.853	1.797	1.741	1.682	1.622	1.558	1.492	1.421	1.343
4.5	1.901	1.853	1.804	1.753	1.702	1.649	1.594	1.537	1.474	1.402	1.299
5.0	1.853	1.809	1.763	1.718	1.670	1.622	1.571	1.518	1.459	1.390	1.287
5.5	1.813	1.772	1.730	1.688	1.644	1.599	1.552	1.503	1.449	1.387	1.304
6.0	1.779	1.741	1.702	1.662	1.622	1.580	1.536	1.490	1.439	1.382	1.299
6.5	1.749	1.714	1.678	1.641	1.603	1.563	1.522	1.478	1.431	1.375	1.287
7.0	1.724	1.691	1.657	1.622	1.586	1.549	1.510	1.469	1.424	1.371	1.293
7.5	1.702	1.670	1.638	1.605	1.571	1.536	1.499	1.460	1.417	1.368	1.299
8.0	1.682	1.652	1.622	1.591	1.558	1.525	1.490	1.452	1.412	1.364	1.288
8.5	1.665	1.636	1.607	1.577	1.547	1.515	1.481	1.445	1.406	1.361	1.289
9.0	1.649	1.622	1.594	1.566	1.536	1.506	1.473	1.439	1.402	1.358	1.299
9.5	1.635	1.609	1.582	1.555	1.527	1.497	1.466	1.434	1.398	1.356	1.289
10.0	1.622	1.597	1.571	1.545	1.518	1.490	1.460	1.428	1.394	1.353	1.287
11.0	1.599	1.576	1.552	1.528	1.503	1.476	1.449	1.419	1.387	1.349	1.290
12.0	1.580	1.558	1.536	1.513	1.490	1.465	1.439	1.412	1.381	1.346	1.290
13.0	1.563	1.543	1.522	1.501	1.478	1.455	1.431	1.405	1.376	1.342	1.287
14.0	1.549	1.530	1.510	1.490	1.469	1.447	1.424	1.399	1.372	1.340	1.291
15.0	1.536	1.518	1.499	1.480	1.460	1.439	1.417	1.394	1.368	1.337	1.287
16.0	1.525	1.507	1.490	1.471	1.452	1.432	1.412	1.389	1.364	1.335	1.288
17.0	1.515	1.498	1.481	1.464	1.445	1.426	1.406	1.385	1.361	1.333	1.289
18.0	1.506	1.490	1.473	1.457	1.439	1.421	1.402	1.381	1.358	1.332	1.287
19.0	1.497	1.482	1.466	1.450	1.434	1.416	1.398	1.378	1.356	1.330	1.289
20.0	1.490	1.475	1.460	1.445	1.428	1.412	1.394	1.375	1.353	1.328	1.287
21.0	1.483	1.469	1.454	1.439	1.424	1.407	1.390	1.372	1.351	1.327	1.288
22.0	1.476	1.463	1.449	1.434	1.419	1.404	1.387	1.369	1.349	1.326	1.288
23.0	1.471	1.457	1.444	1.430	1.415	1.400	1.384	1.367	1.347	1.325	1.287
24.0	1.465	1.452	1.439	1.426	1.412	1.397	1.381	1.364	1.346	1.324	1.288
25.0	1.460	1.448	1.435	1.422	1.408	1.394	1.378	1.362	1.344	1.323	1.287
26.0	1.455	1.443	1.431	1.418	1.405	1.391	1.376	1.360	1.342	1.322	1.287
27.0	1.451	1.439	1.427	1.415	1.402	1.388	1.374	1.358	1.341	1.321	1.288
28.0	1.447	1.435	1.424	1.412	1.399	1.386	1.372	1.357	1.340	1.320	1.287
29.0	1.443	1.432	1.420	1.409	1.396	1.383	1.370	1.355	1.339	1.319	1.288
30.0	1.439	1.428	1.417	1.406	1.394	1.381	1.368	1.353	1.337	1.319	1.287

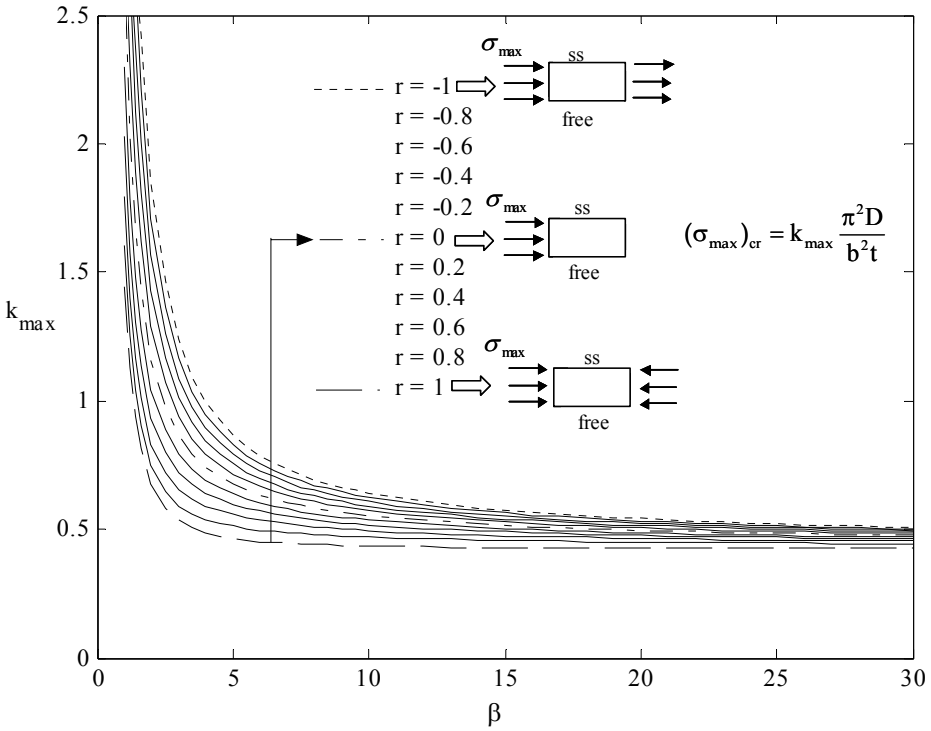

Figure 6.26 k_{max} vs. plate aspect ratio (β) for ss-free unstiffened element

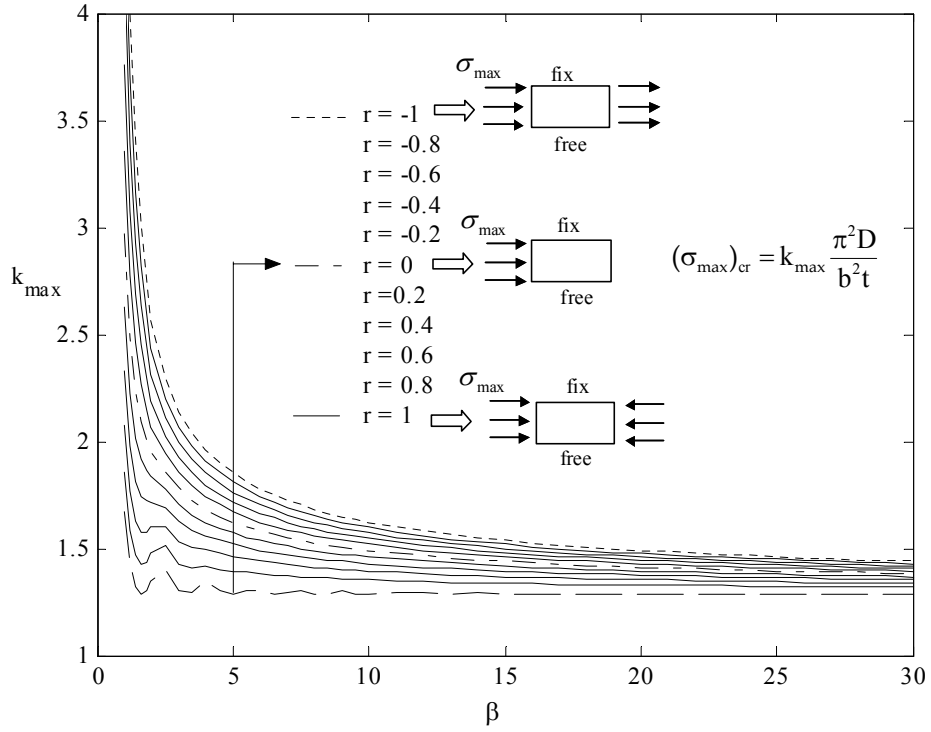

Figure 6.27 k_{max} vs. plate aspect ratio (β) for fix-free unstiffened element

6.2.3 Discussion

Figure 6.28 shows a comparison of the four different elements subject to a stress gradient with r = 0 (compressive stress acting only on one edge). The y-axis is the stress gradient solutions derived here, normalized to k_0 which is the solution for elements under uniform stress (i.e., no stress gradient, r = 1).

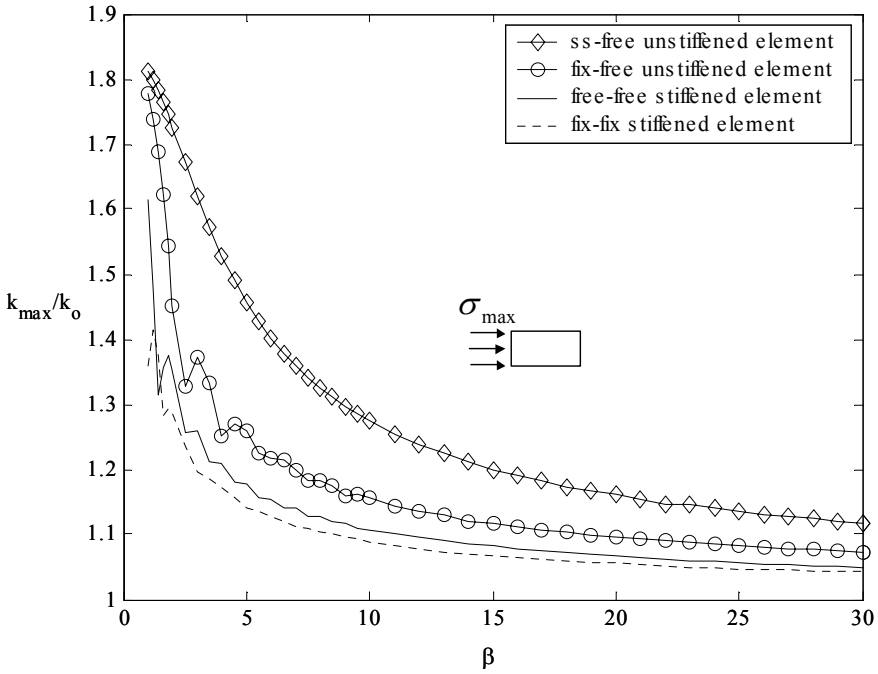

Figure 6.28 Comparison of stiffened and unstiffened elements subjected to stress gradient r = 0

As shown in Figure 6.28, the buckling stresses of the elements are increased by the stress gradient ($k_{max} / k_o > 1$). Under the same magnitude of stress gradient, unstiffened elements have a higher increase in the buckling stress than stiffened elements. The ss-free unstiffened element is most influenced by the stress gradient, even for a plate with length/width (β) of 10, the buckling stress increases about 30%. The plate buckling coefficient for the stiffened element k_{max} converges rapidly to approximately $1.1k_0$, and

then more slowly to $1.0k_0$. For the ss-free unstiffened element, $k_{max}>1.1k_0$ even for β as large as 30.

The moment gradient influence on members with flanges composed of unstiffened elements (Figure 6.2b) can be expected to fall between the curves of the ss-free and fix-free unstiffened elements. Comparing to the channel section of Figure 6.3, if a moment gradient changes from a maximum to an inflection point (M = 0, r = 0) over a length of 20 in. (which equals β of 5) then one would expect a boost in the plate buckling coefficient of as much as 25%. If the moment gradient is sharper, the boost would be greater. The significant influence on the unstiffened element, particularly in the case where the web provides little restraint, can make the moment gradient a considerable factor when one analyzes the buckling strength. These solutions suggest a reserve is currently ignored in design, particularly with regard to unstiffened elements.

6.3 Stress Gradient Effect on the Ultimate Strength of Thin Plates

The study in the previous sections demonstrates that stress gradient appreciably increases the elastic local buckling stress of thin plates, which implies a potential reserve when one calculates the strength of cold-formed steel members under a moment gradient. In this section, the research is extended to explore the stress gradient influence on the ultimate strength of a thin plate undergoing local buckling, and to develop design methods to account for this influence.

6.3.1 Stress Gradient Effect on the Ultimate Strength of Stiffened Elements

6.3.1.1 Verification of Winter's Equation

Current design methods adopt the Effective Width concept to obtain the ultimate strength of cold-formed steel members. The AISI Specification uses Winter's equation (6.68) to calculate the effective width for both stiffened and unstiffened elements. Therefore, the first step of the research is to explore Winter's equation by nonlinear inelastic finite element analysis, and then extend to the longitudinal stress gradient case of interest. Winter's reduction in the actual width of the plate is encompassed by:

$$\rho = \left(1 - \frac{0.22}{\lambda}\right) \Big/ \lambda \le 1 \tag{6.68}$$

where

ρ = reduction factor for effective width;

λ = plate slenderness factor $\lambda = \sqrt{\frac{f_{max}}{f_{cr}}} = \frac{1.052}{\sqrt{k}}\left(\frac{w}{t}\right)\sqrt{\frac{f_{max}}{E}}$;

k = plate buckling coefficient;

t = thickness of compression element;

E = modulus of elasticity;

f_{cr} = elastic buckling stress;

f_{max} = maximum compressive edge stress in the element.

ABAQUS is employed for the nonlinear finite element modeling. Both geometric imperfections and nonlinear material properties are considered. The shell element S4R5 is chosen for the plate. The element size is set to 0.1 in. × 0.1 in. The shape of the initial geometric imperfection is assumed to be the first buckling mode, and the maximum amplitude is scaled to a value equal to the 50% CDF for the local buckling shape, d/t = 0.34 (Chapter 5, Section 5.4.3). The material stress-strain curves are chosen from the

tensile tests of the two series of buckling tests of cold-formed steel beams (Chapter 4). Five different yield strength levels are selected: 33 ksi, 44 ksi, 56.1 ksi, 62.2 ksi, and 73.4 ksi. The loading and boundary conditions are shown in Figure 6.29. The Modified Riks method in ABAQUS is employed for the nonlinear analysis.

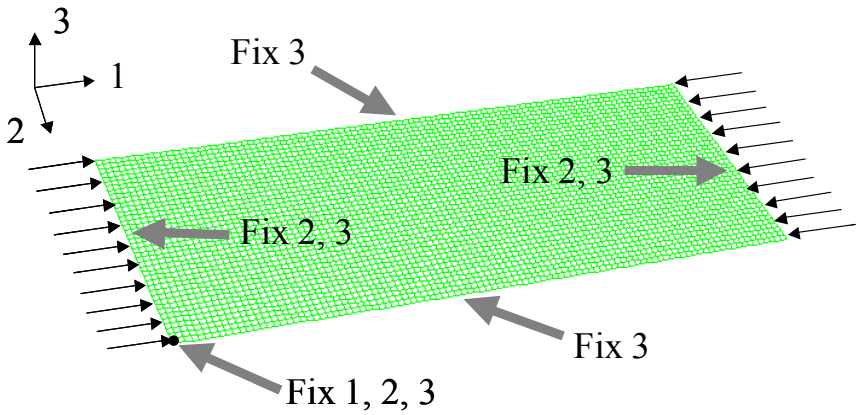

Figure 6.29 Finite element models of ss-ss stiffened elements under uniform stresses

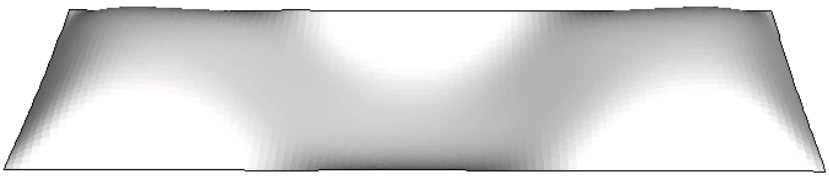

Figure 6.30 Buckled shape (at peak load) of a ss-ss stiffened element under pure compression by nonlinear FE analysis

Figure 6.30 shows the buckled shape obtained by nonlinear finite element analysis on a ss-ss stiffened element with a = 10 in., b = 4 in., t = 0.03 in., and f_y = 62.2 ksi. The thin plate is subjected to pure compression. Figure 6.31 and Figure 6.32 respectively illustrate the stress distribution of σ_x and τ_{xy} on the mid-surface (membrane) of the thin plate when the plate reaches its maximum compression capacity. Negative values of σ_x in the ABAQUS plots mean compression. The stress distributions inside the plate are not uniform, the highest stress (σ_x) exists along the two longitudinal edges and tension stress

is observed at the center of plate when the peak load occurs. Large shear stress τ_{xy} is observed at the area close to the four corners, and it vanishes at the center part of the plate.

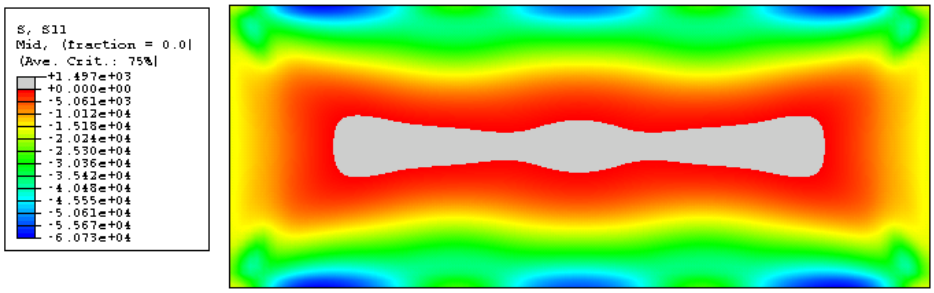

Figure 6.31 Stress σ_x distribution (at peak load, on mid-surface) of a ss-ss stiffened element under pure compression by nonlinear FE analysis

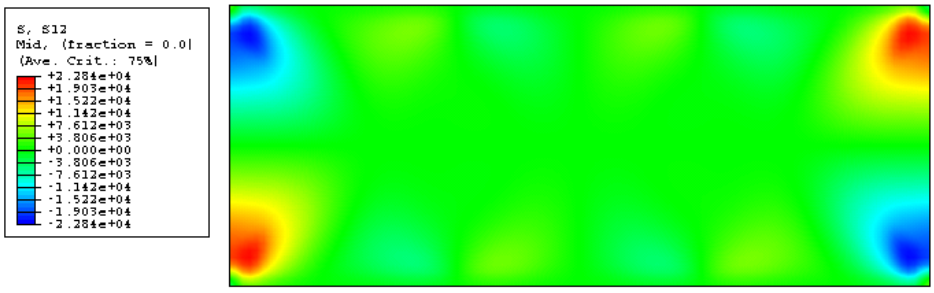

Figure 6.32 Stress τ_{xy} distribution (at peak load, on mid-surface) of a ss-ss stiffened element under pure compression by nonlinear FE analysis

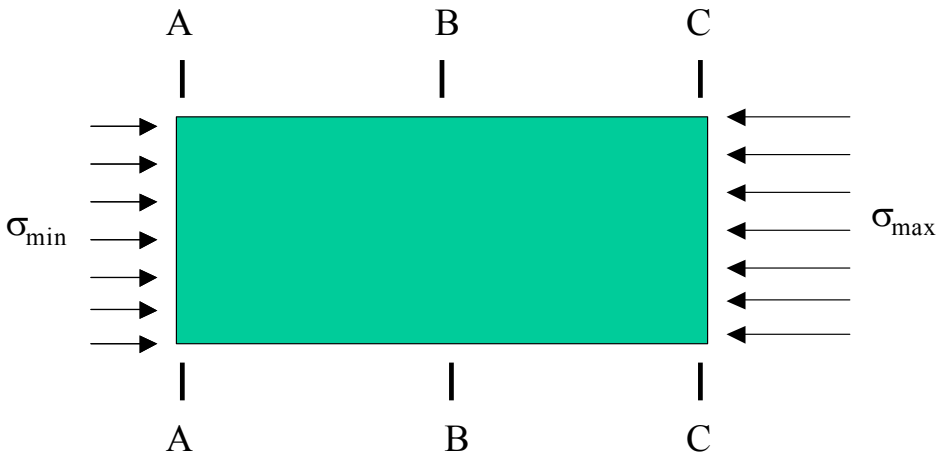

Figure 6.33 Location of analyzed cross-sections

Figure 6.34 through Figure 6.37 illustrate the development of the stress distribution of σ_x on the mid-surface along the center cross-section (section B in Figure 6.33) of the analyzed ss-ss stiffened element with a = 10 in., b = 4 in., t = 0.03 in., and f_y = 62.2 ksi. Each figure contains a plot of edge load vs. displacement, and a plot of the σ_x distribution across the cross-section (in Y direction as shown in Figure 6.4), where positive stress represents compression (opposite sign convention from ABAQUS plots). The edge load vs. displacement plot is used to identify the analyzed point for the stress distribution. The plots show that the stress is not uniformly distributed in the transverse direction; high σ_x stress is observed along the two longitudinal edges and stress is low in the middle of the plate. At the point of peak load (Figure 6.36), the stress σ_x reaches its highest at the two edges (but does not reach f_y) and also reaches its minimum value (approximately zero) in the middle of the cross-section. The middle part of the cross-section undergoes no load, therefore it could be treated as "un-effective width", and the "effective width" exists at the region close to the edges. The result is basically consistent with the assumption of the Effective Width Concept that when the stiffened element buckles, the load is undertaken by only a portion of the section.

The elastic local buckling stress of this plate is 6 ksi, which is obtained by the classic equation of critical buckling stress depicted in Figure 6.10. The yield stress is 62.2 ksi, and the plate demonstrates a compression capacity of 16.8 ksi. The additional load over the elastic buckling stress (postbuckling strength) is carried by means of stress redistribution.

The analysis of Figure 6.34 – Figure 6.37 provides only an idealization of the membrane longitudinal stress (σ_x) at the mid-length value. As Figure 6.31 shows,

significant variation occurs in the longitudinal stress along the length. At the maximum deformation location consistent with a buckled wave, the stress follows the patterns of Figure 6.34 – 6.37 which are essentially consistent with the effective width model. However, at locations between the buckled waves the σ_x stress is uniform and larger than shown in these figures. If the stress is averaged over the length of the plate, a somewhat different idealization emerges. Finally, the classic effective width explanation suggests that deviation from uniform stress begins when the applied stress equals the critical buckling stress of the plate (6 ksi); however due to imperfections, the stress becomes non-uniform earlier than this (Figure 6.34). Further, the effective width model suggests that final capacity is reached when the edge stress reaches the yield stress, but in a realistic multi-axial stress state the reality (as shown in the figures) is somewhat more complicated.

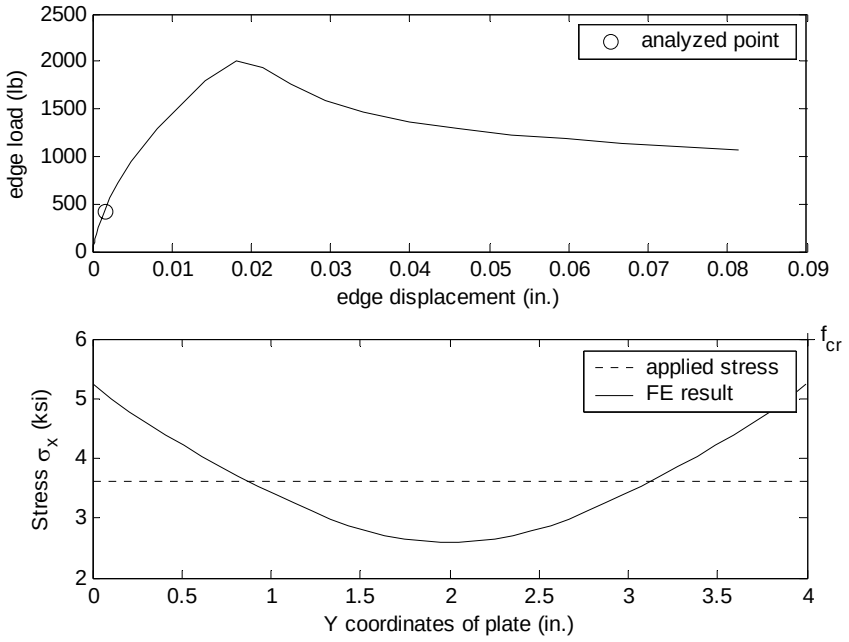

Figure 6.34 Stress distribution σ_x along the transverse-section of a ss-ss stiffened element under pure compression

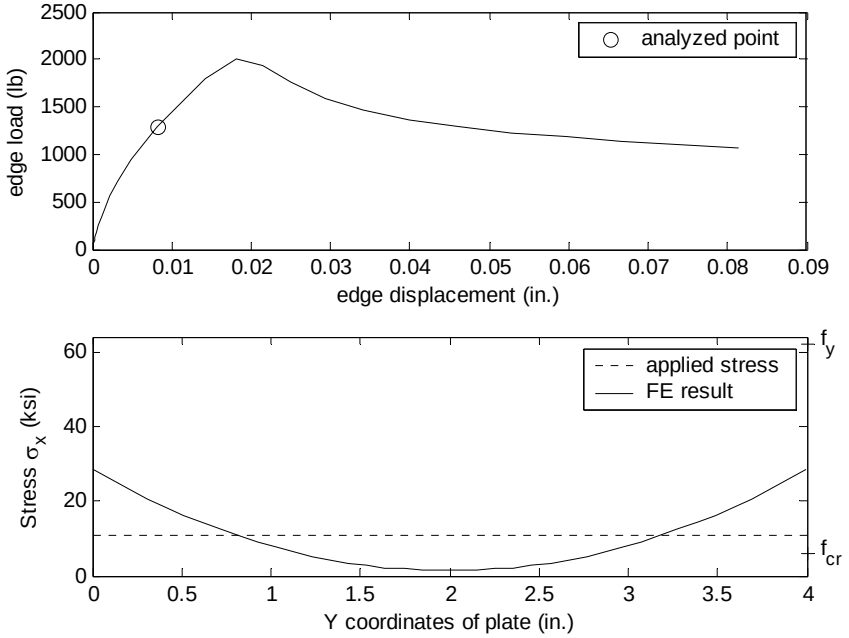

Figure 6.35 Stress distribution σ_x along the transverse-section of a ss-ss stiffened element under pure compression

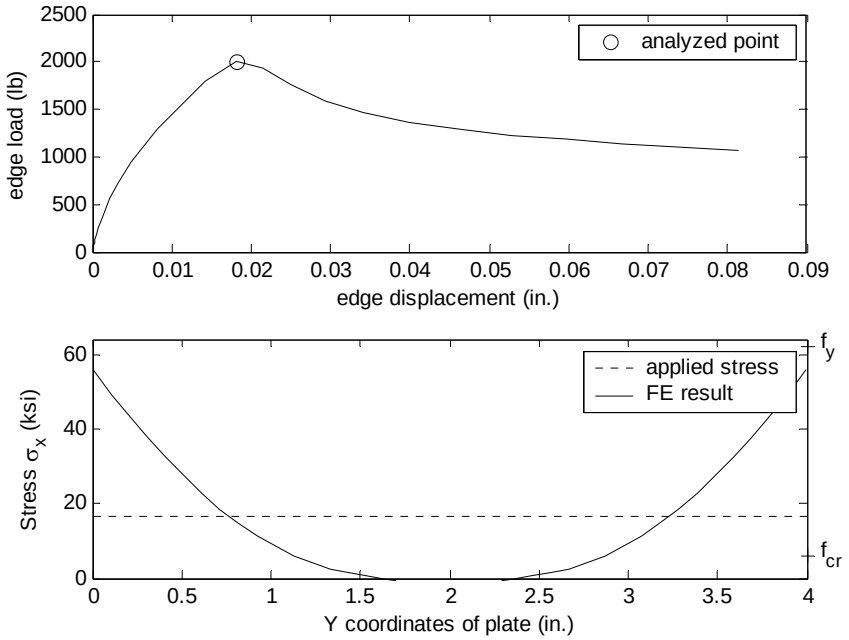

Figure 6.36 Stress distribution σ_x along the transverse-section of a ss-ss stiffened element under pure compression

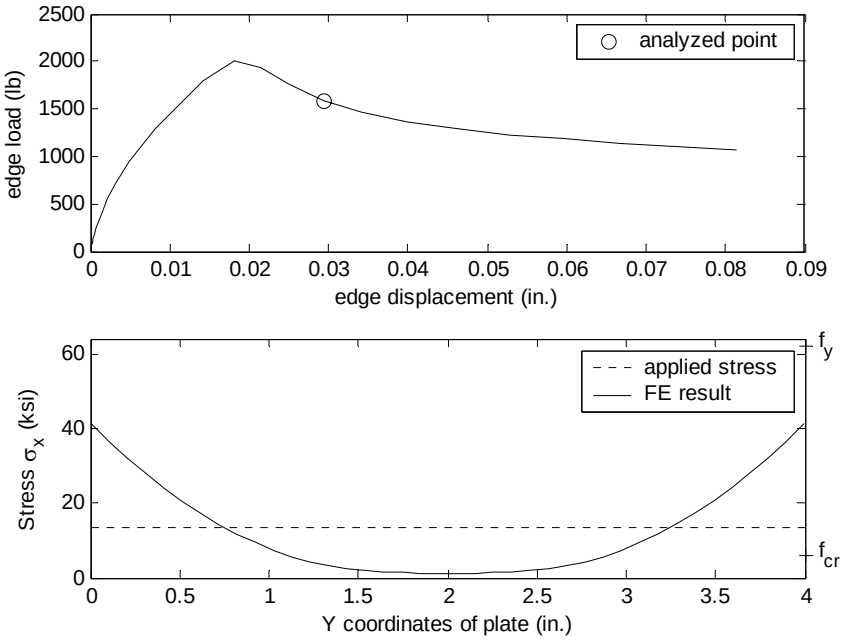

Figure 6.37 Stress distribution σ_x along the transverse-section of a ss-ss stiffened element under pure compression

Table 6.7 summarizes the results of the finite element analyses on a total of 25 ss-ss stiffened elements. The strength predictions by Winter's equation have a good agreement with the finite element results. However, the average ABAQUS results are systematically lower than Winter's predictions. The average ratio is 94%. Winter tested hat sections to originally derive the expressions; perhaps the web provides a small amount of beneficial restraint to the flange in this case. Further, only one imperfection was investigated. We conclude that the ABQUS model is a conservative predictor of the strength, and Winter's equation captures the basic behavior.

Table 6.7 Result of stiffened element under uniform compression stresses

b (in.)	a (in.)	t (in.)	f_y (ksi)	σ_u (ksi)	ρ_{ABAQUS}	k_{winter}	ρ_{winter}	ABAQUS /Winter
2.5	10	0.04	33	22.3	0.675	4	0.728	92.8%
2.5	10	0.04	44	26.8	0.610	4	0.651	93.6%
2.5	10	0.04	56.1	31.6	0.564	4	0.590	95.5%
2.5	10	0.04	62.2	33.1	0.532	4	0.566	94.1%
2.5	10	0.04	73.4	36.6	0.498	4	0.528	94.4%
4	10	0.03	33	12.0	0.365	4	0.386	94.5%
4	10	0.03	44	14.1	0.320	4	0.339	94.2%
4	10	0.03	56.1	16.2	0.289	4	0.303	95.4%
4	10	0.03	62.2	16.8	0.270	4	0.289	93.4%
4	10	0.03	73.4	18.3	0.250	4	0.268	93.2%
3	6	0.05	33	22.8	0.691	4	0.750	92.2%
3	6	0.05	44	27.4	0.623	4	0.672	92.6%
3	6	0.05	56.1	32.5	0.579	4	0.610	94.9%
3	6	0.05	62.2	33.7	0.541	4	0.585	92.5%
3	6	0.05	73.4	37.3	0.508	4	0.546	93.0%
4	12	0.05	33	18.6	0.563	4	0.599	94.0%
4	12	0.05	44	22.0	0.501	4	0.532	94.1%
4	12	0.05	56.1	25.7	0.459	4	0.480	95.7%
4	12	0.05	62.2	26.9	0.432	4	0.459	94.2%
4	12	0.05	73.4	29.3	0.399	4	0.426	93.7%
2.5	10	0.05	33	25.4	0.770	4	0.853	90.3%
2.5	10	0.05	44	31.0	0.704	4	0.771	91.2%
2.5	10	0.05	56.1	37.0	0.660	4	0.705	93.7%
2.5	10	0.05	62.2	39.1	0.629	4	0.677	92.9%
2.5	10	0.05	73.4	43.4	0.592	4	0.634	93.3%
							average	93.7%

Note: f_y --- yield stress;
σ_u --- ultimate stress obtained by ABAQUS analyses;
ρ_{ABAQUS} --- effective width ratio obtained by ABAQUS analyses;
ρ_{winter} --- effective width ratio by Winter's equation;
k_{winter} --- the buckling coefficient used in Winter's equation.

6.3.1.2 Stress Gradient Effect on the Ultimate Strength

The same ABAQUS finite element model, and plate dimensions used in the examination of Winter's equation, are employed to study the stress gradient effect on the ultimate strength of thin plates. The stress gradient is achieved by applying compression stresses at the two end edges, and shear forces along the two longitudinal edges, which equilibrate the difference of compression loads, as shown in Figure 6.38 (this is the case with r = 0).

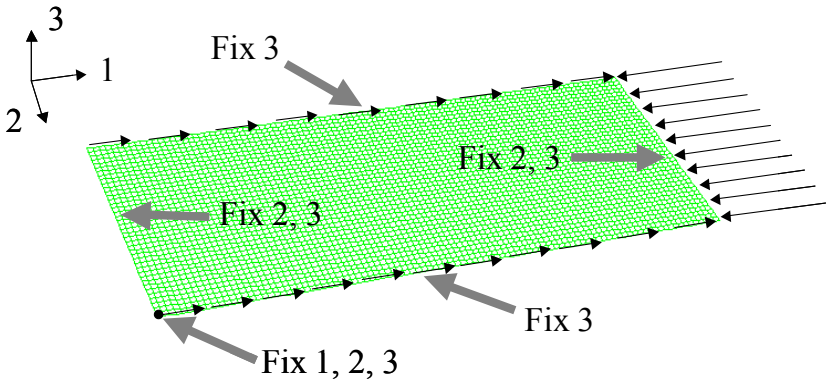

Figure 6.38 Finite element model for ss-ss stiffened elements under a stress gradient with r = 0

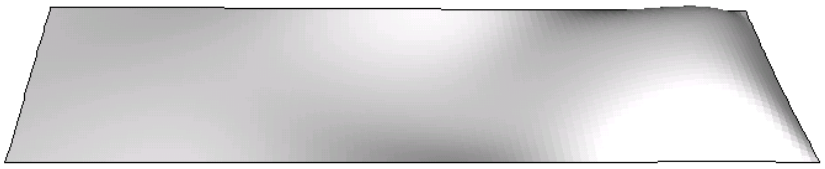

Figure 6.39 Buckled shape of a ss-ss stiffened element under a stress gradient r = 0

Figure 6.39 shows the buckled shape of a ss-ss stiffened element under a stress gradient r = 0 by nonlinear finite element analysis. The dimensions of the plate are: a = 12 in., b = 4 in., t = 0.05 in., and the yield stress is f_y = 62.2 ksi. Large deformation is

observed at the region close to the maximum loaded edge. Figure 6.40 shows the stress σ_x distribution on the mid-surface when the plate is in the elastic region. The stress varies gradually from the highest value on the loaded edge to zero on the other end; the distribution is close to the assumed linear distribution in the analytical model. Figure 6.41 shows the shear stress τ_{xy} distribution on the mid-surface when the plate is in the same elastic region, the result (except for the area near the loaded edge) is similar to the stress distribution used in the analytical model which assumes the shear stress varies from its highest values at the two unloaded edge to zero at the center of the plate.

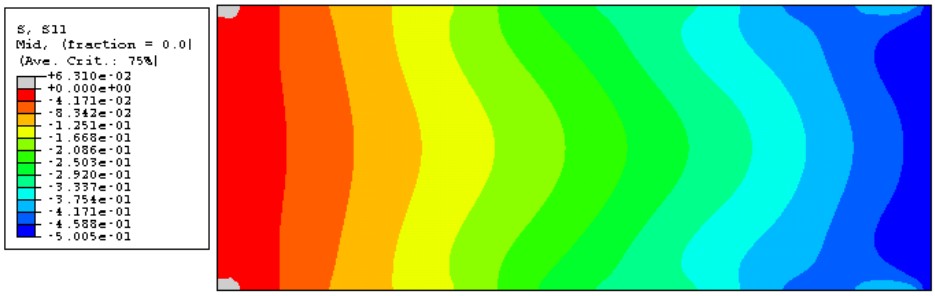

Figure 6.40 Stress σ_x distribution on mid-surface of a ss-ss stiffened element in elastic region under a stress gradient r = 0

Figure 6.41 Stress τ_{xy} distribution on mid-surface of a ss-ss stiffened element in elastic region under a stress gradient r = 0

Figure 6.42 illustrates the stress distribution of σ_x on the three different surfaces (top, mid, and bottom) at the cross-section B, when the plate reaches its maximum compression capacity. Compared with the pure compression case (Figure 6.31), σ_x

concentrates at the maximum loaded region and vanishes at the unloaded edge for the plate under a stress gradient r = 0. Tension is observed on the mid-surface at the center of buckled region. At the region close to the loaded edge, the top surface is subjected to tension and bottom surface is in compression. Figure 6.43 illustrates the shear stress distribution of $\tau_{xy,}$ when the plate is subjected to the maximum load, shear stress only exists at the two corners on the loaded side, and no shear stress is observed at other areas.

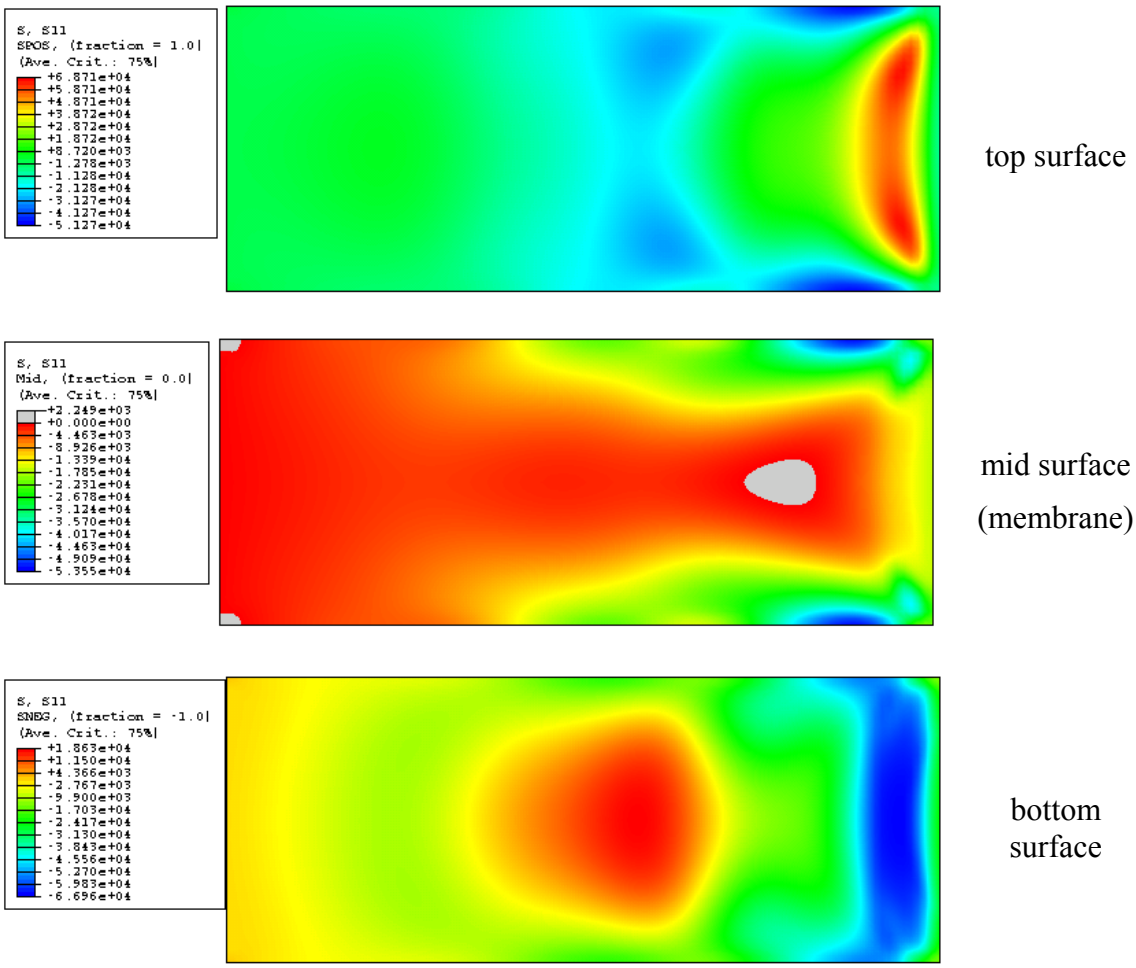

Figure 6.42 Stress σ_x distribution (at peak load) of a ss-ss stiffened element under a stress gradient r = 0

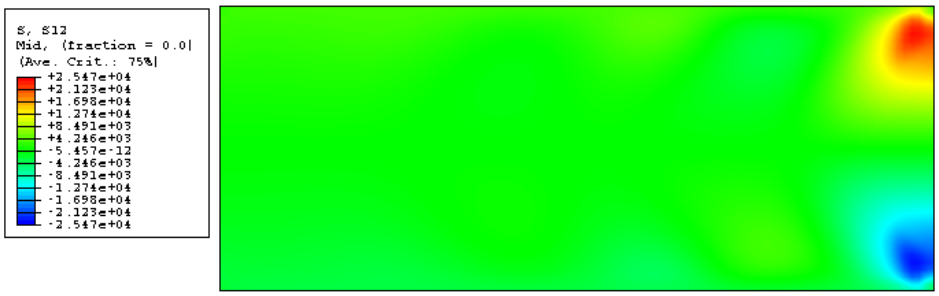

Figure 6.43 Stress τ_{xy} distribution (at peak load, on mid-surface) of a ss-ss stiffened element under a stress gradient r = 0

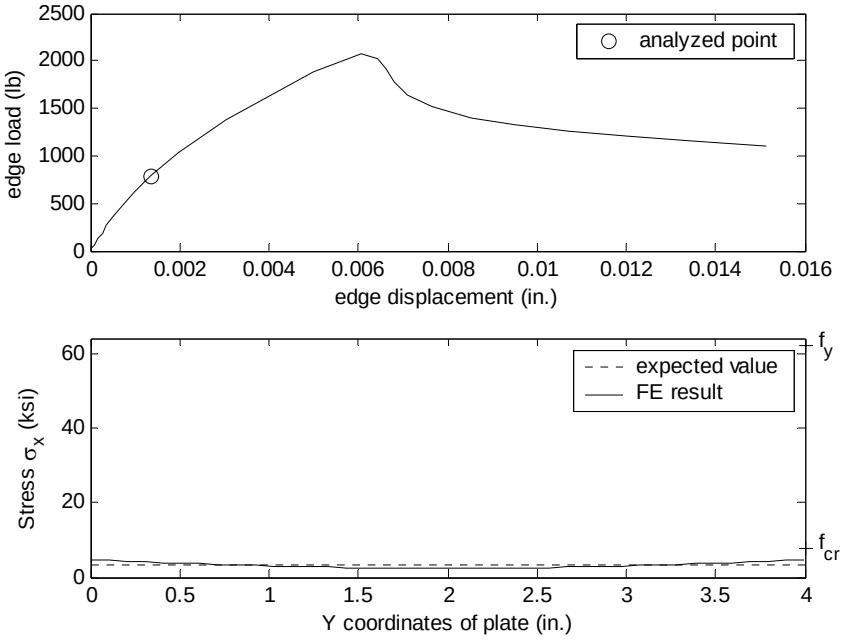

Figure 6.44 Stress σ_x distribution on mid-surface along the cross-section B of a ss-ss stiffened element under a stress gradient r = 0

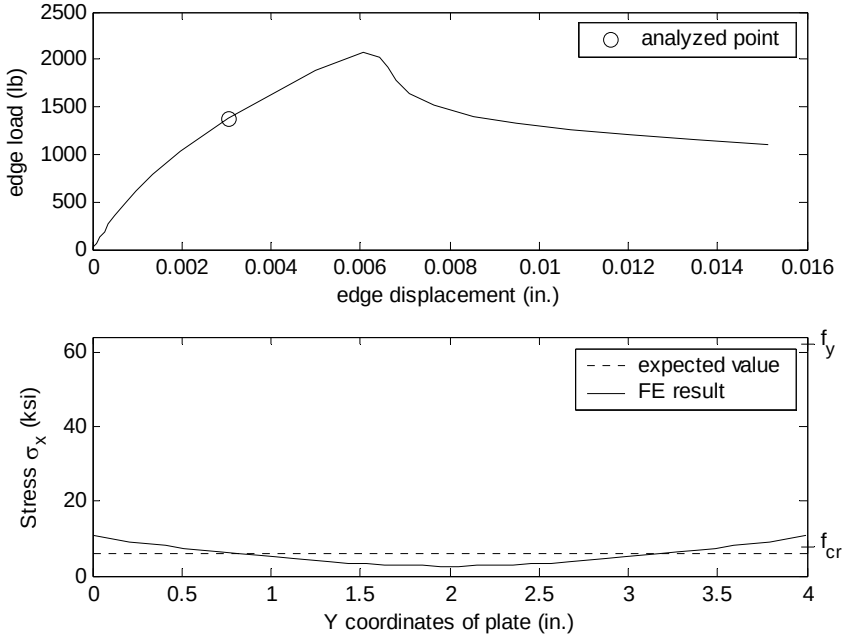

Figure 6.45 Stress σ_x distribution on mid-surface along the cross-section B of a ss-ss stiffened element under a stress gradient r = 0

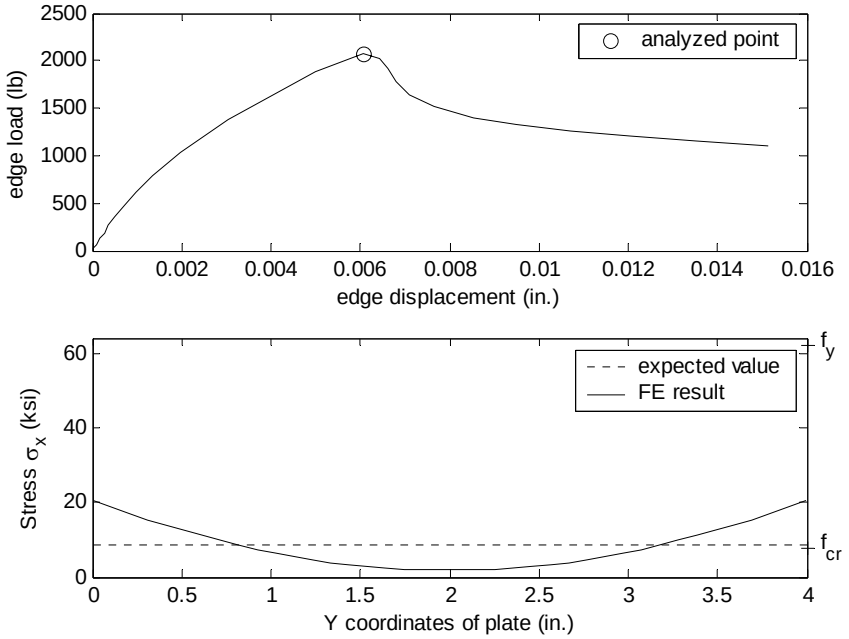

Figure 6.46 Stress σ_x distribution on mid-surface along the cross-section B of a ss-ss stiffened element under a stress gradient r = 0

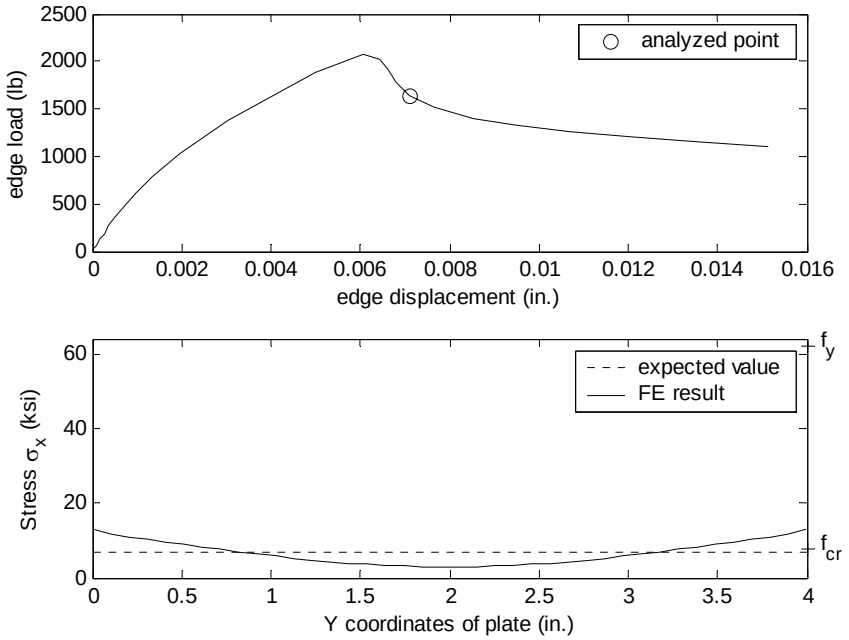

Figure 6.47 Stress σ_x distribution on mid-surface along the cross-section B of a ss-ss stiffened element under a stress gradient r = 0

Figure 6.44 through Figure 6.47 show the development of internal stress σ_x on the mid-surface along the cross-section B which is located in the middle of the plate. Each figure includes a plot of the external load vs. edge displacement, and a plot of stress distribution along the cross-section in the Y direction where the expected value is calculated by assuming σ_x is linearly distributed in the longitudinal direction (X) and positive stress represents compression. Similar to the result for the pure compression case, the stress σ_x is non-uniformly distributed across the section for the plate subjected to a stress gradient, and the external load is mainly undertaken by the "effective width" close to the two longitudinal edges. Figure 6.48 presents the stress distribution of σ_x on the mid-surface at cross-sections A, B, and C (refers to Figure 6.33) respectively, at the point when the plate reaches its maximum compression capacity. The width next to the maximum loaded edge (cross-section C) is essentially fully effective; the cross-section B

(in the middle of plate) is partially effective; and at the minimum loaded edge (no load for this case), the section is fully effective, but bears no load.

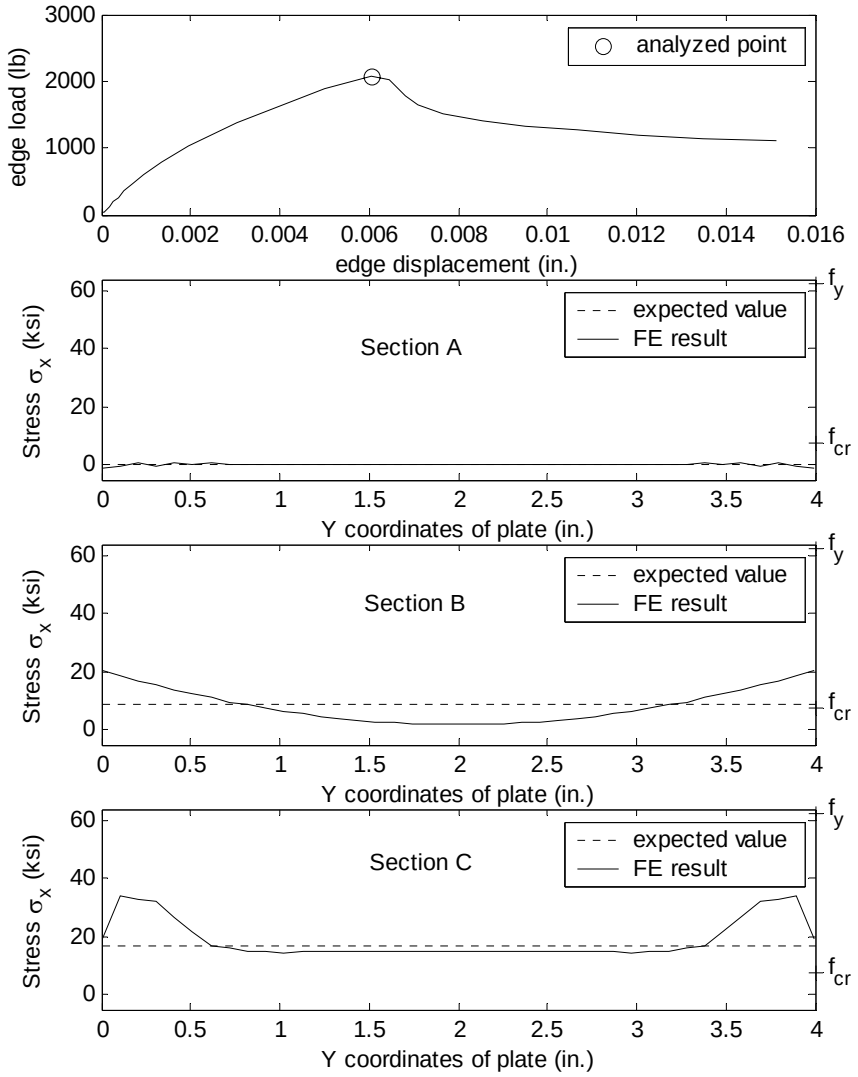

Figure 6.48 σ_x distribution on mid-surface along three cross-sections of the plate under a stress gradient r = 0

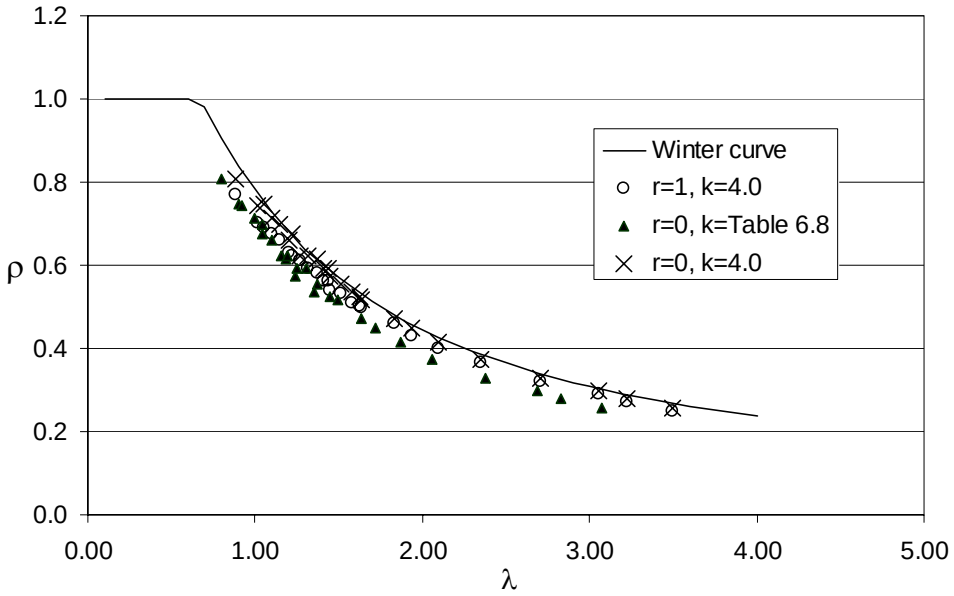

Figure 6.49 ABAQUS results vs. Winter's curve

A total of 25 ss-ss stiffened elements were analyzed by the ABAQUS model and the results are summarized in Table 6.8. Figure 6.49 shows a comparison of finite element results vs. Winter's equation, where the x-axis is the plate slenderness λ, and the y-axis is the reduction factor for effective width, ρ. The "o" in the plot represents the FEA results of the stiffened element under uniform compression stress. As discussed in Section 6.5.1, Winter's equation provides a reasonable prediction to stiffened elements with no stress gradient. The "x" represents the result of the plates under stress gradient. It shows that the strength of stiffened plates is increased after the stress gradient is applied. The increase is not significant; the average is 105% (column "r = 0/r = 1" in Table 6.8). The "▲" in the plot represents the plates with stress gradient, but with the correct buckling coefficients k_{max} (calculated by the analytical method summarized in Section 6.4) used in the Winter's equation. It is concluded that stress gradient has little effect on the ultimate strength of stiffened elements, but Winter's equation can be used to calculate the ultimate strength of plates under stress gradients with the corresponding buckling coefficient, k.

Table 6.8 Result of stiffened element under stress gradient r = 0

b (in.)	a (in.)	t (in.)	f_y (ksi)	σ_u (ksi)	ρ_{ABAQUS}	k_{winter}	ρ_{winter}	ABAQUS /Winter	r=0 /r=1
2.5	10	0.04	33	23.6	0.714	4.84	0.780	91.5%	105.7%
2.5	10	0.04	44	27.4	0.623	4.84	0.701	88.8%	102.2%
2.5	10	0.04	56.1	33.2	0.592	4.84	0.638	92.8%	105.0%
2.5	10	0.04	62.2	34.4	0.553	4.84	0.612	90.4%	103.8%
2.5	10	0.04	73.4	38.0	0.517	4.84	0.572	90.5%	103.8%
4	10	0.03	33	12.4	0.374	5.19	0.434	86.3%	102.6%
4	10	0.03	44	14.5	0.329	5.19	0.382	86.1%	102.9%
4	10	0.03	56.1	16.7	0.298	5.19	0.342	87.1%	102.9%
4	10	0.03	62.2	17.3	0.277	5.19	0.326	85.1%	102.7%
4	10	0.03	73.4	18.8	0.256	5.19	0.302	84.6%	102.4%
3	6	0.05	33	24.7	0.748	5.42	0.835	89.6%	108.3%
3	6	0.05	44	29.7	0.676	5.42	0.754	89.6%	108.6%
3	6	0.05	56.1	34.6	0.616	5.42	0.688	89.5%	106.3%
3	6	0.05	62.2	35.6	0.572	5.42	0.661	86.6%	105.8%
3	6	0.05	73.4	39.3	0.536	5.42	0.619	86.5%	105.4%
4	12	0.05	33	19.6	0.592	5.04	0.658	90.1%	105.2%
4	12	0.05	44	23.0	0.523	5.04	0.586	89.3%	104.5%
4	12	0.05	56.1	26.5	0.472	5.04	0.529	89.1%	102.8%
4	12	0.05	62.2	27.9	0.448	5.04	0.507	88.5%	103.8%
4	12	0.05	73.4	30.4	0.414	5.04	0.472	87.8%	103.8%
2.5	10	0.05	33	26.7	0.809	4.84	0.906	89.2%	105.1%
2.5	10	0.05	44	32.6	0.742	4.84	0.825	89.9%	105.5%
2.5	10	0.05	56.1	39.2	0.699	4.84	0.757	92.4%	105.9%
2.5	10	0.05	62.2	41.2	0.662	4.84	0.728	90.9%	105.2%
2.5	10	0.05	73.4	45.6	0.621	4.84	0.684	90.8%	105.0%
							average	88.9%	104.6%

Note: f_y --- yield stress;
σ_u --- ultimate stress obtained by ABAQUS analyses;
ρ_{ABAQUS} --- effective width ratio obtained by ABAQUS analyses;
ρ_{winter} --- effective width ratio by Winter's equation;
k_{winter} --- the buckling coefficient used in Winter's equation.

6.3.2 Stress Gradient Effect on the Ultimate Strength of Unstiffened Elements

6.3.2.1 Verification of Winter's Equation

Intensive experiments and analytical investigations on the post-buckling strength of unstiffened compression elements have been conducted by Kalyanaraman, Peköz and Winter (1972, 1977, 1978), and Bambach and Rasmussen (2002). Those studies show that the Winter's equation gives reasonable, but conservative predictions. Bambach and Rasmussen proposed new effective width equations for unstiffened elements.

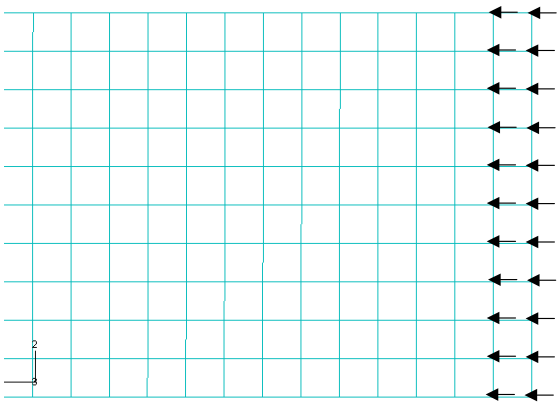

Figure 6.50 Loading configuration at one edge for unstiffened elements

A similar finite element model as that used for the stiffened elements was employed again for the unstiffened elements. The S4R5 shell element is chosen for the plate. The element size is set to 0.1 in. × 0.1 in. The shape of the initial geometric imperfection is assumed to be the first buckling mode of the ss-free unstiffened element, and the maximum amplitude is scaled to be the 50% CDF for type 1 imperfection, d/t = 0.34 (Chapter 5, Section 5.4.3). Instead of using the type 2 maximum imperfection values, the analysis on the unstiffened element employs the same maximum imperfection value as

used for the stiffened element, so that a direct comparison of the same plate with different boundary conditions can be given. The plate is simply supported at the two loaded edges and along one longitudinal edge. To avoid the stress concentration near the loaded edge, the loading strategy at each end is shown in Figure 6.50. The loads are applied at two rows of nodes on one edge.

Figure 6.51 Buckled shape of a ss-free unstiffened element under pure compression

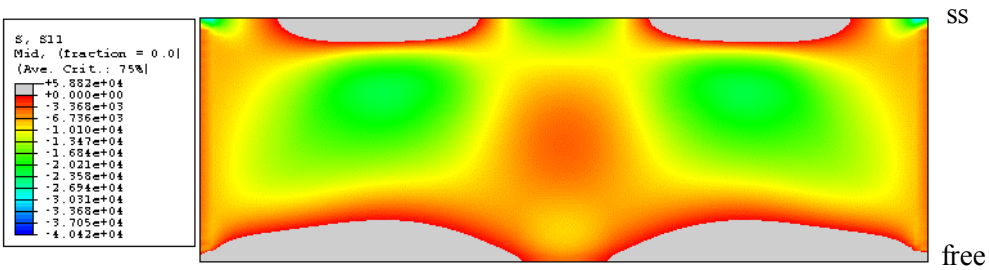

Figure 6.52 Stress σ_x distribution on the mid-surface of a ss-free unstiffened element under pure compression at the peak load

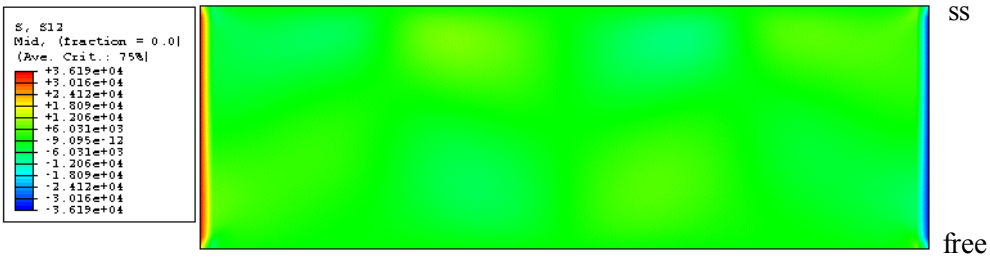

Figure 6.53 Shear stress τ_{xy} distribution on the mid-surface of a ss-free unstiffened element under pure compression at the peak load

Figure 6.51 shows the buckled shape of a ss-free unstiffened element subjected to pure compression. The dimensions of the plate are: a = 12 in., b= 4 in., t = 0.05 in., and

the yield stress is f_y = 62.2 ksi. Figure 6.52 and Figure 6.53 respectively show the stress distribution of σ_x and τ_{xy} on the mid-surface when the peak load occurs. It is shown that the distribution of stress σ_x is non-uniform and complicated, including tension stress along part of the two longitudinal edges. No shear stress τ_{xy} is observed on the mid-surface inside the plate, while large shear stress exists along the two loaded edges.

Figure 6.54 through Figure 6.57 present the σ_x stress distribution on the middle surface, across the mid-length (cross-section B of Figure 6.33). Each figure includes a plot of the external load vs. edge displacement, and a plot of stress distribution along the cross-section in the Y direction, positive stress represents compression. The stress distribution in the transverse direction is not uniform, high compression stress exists at regions close to the simply supported edge (thus more effective), and less stress is observed close to the free edge (thus less effective in load bearing). This finding for the mid-length section is consistent with the assumption of the Effective Width method for unstiffened elements (obtained from tests on cold-formed steel channel sections) which assumes the effective width is next to the supported longitudinal edge. However, Figure 6.52 indicates that tension exists at both the longitudinal edges in region between mid-length to the end, therefore the "effective width" is not always close to the simply supported edge for the unstiffened element, it could be in the center portion of one cross-section. Further, compared with the stiffened element, the stress for the unstiffened element is relatively low, and the maximum stress σ_x on the mid-surface is only 51% of the yield stress when the plate reaches its maximum compression capacity.

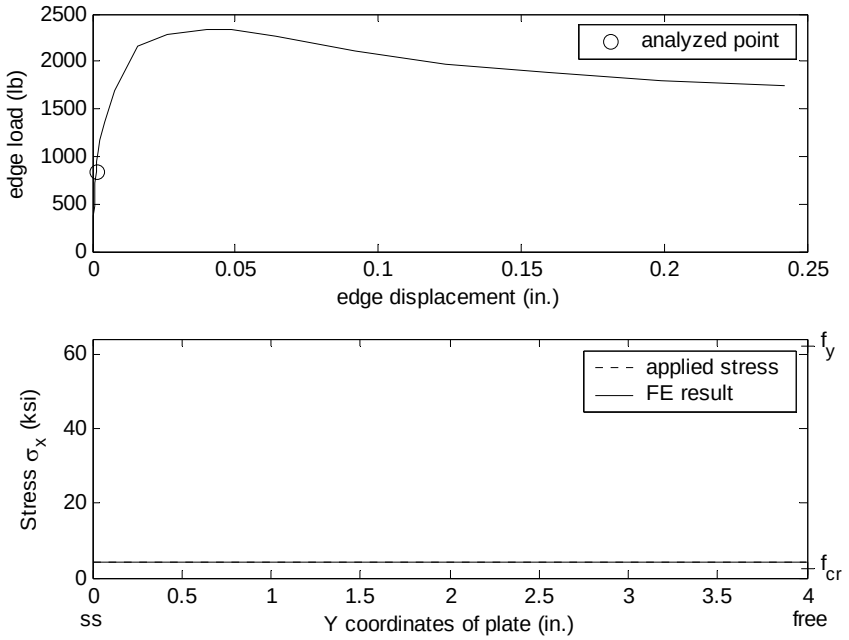

Figure 6.54 σ_x distribution on mid-surface along cross-section B of a ss-free unstiffened element under pure compression

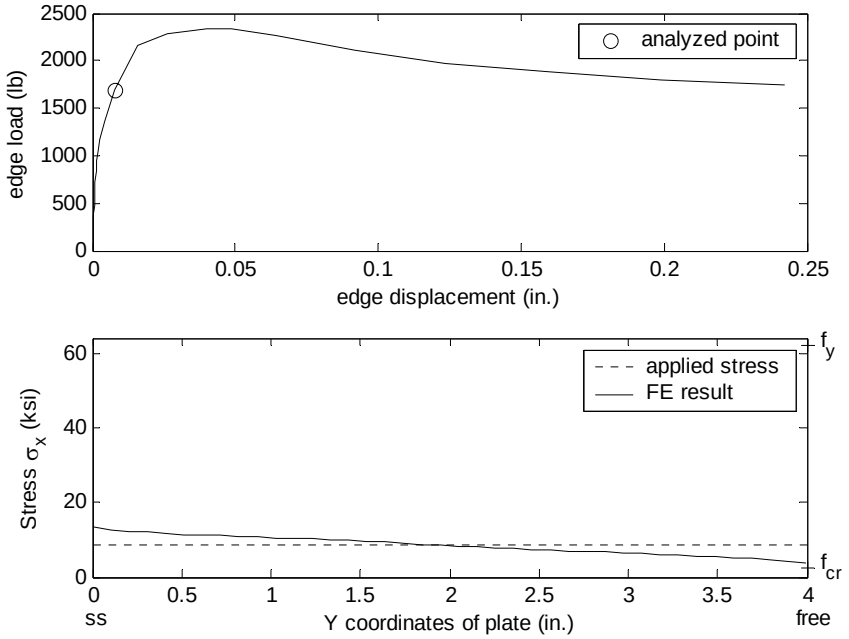

Figure 6.55 σ_x distribution on mid-surface along cross-section B of a ss-free unstiffened element under pure compression

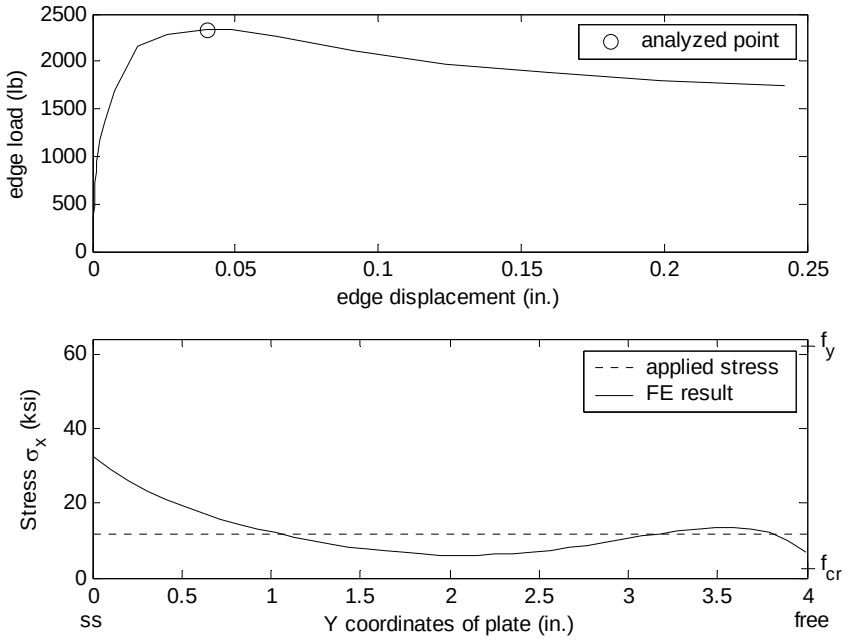

Figure 6.56 σ_x distribution on mid-surface along cross-section B of a ss-free unstiffened element under pure compression

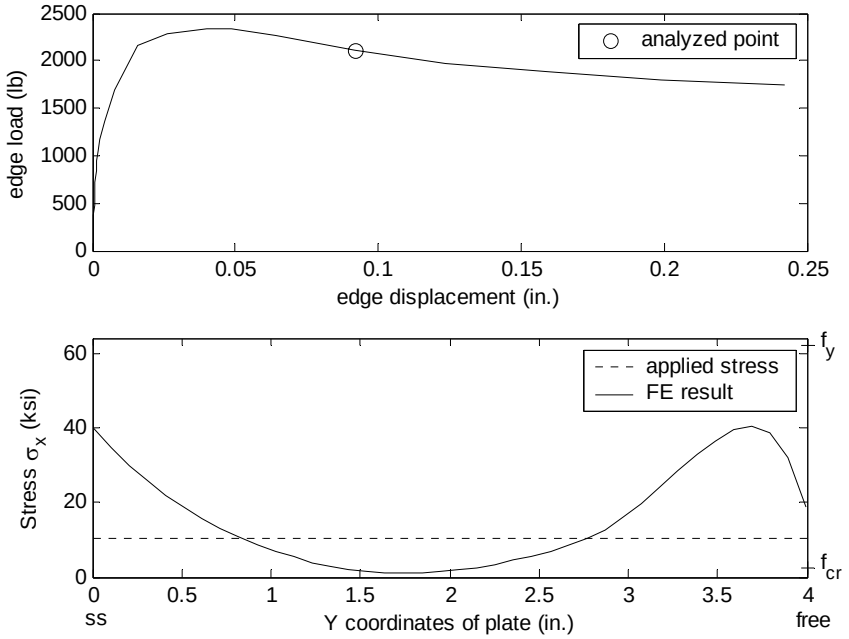

Figure 6.57 σ_x distribution on mid-surface along cross-section B of a ss-free unstiffened element under pure compression

A total of 25 ss-free unstiffened elements subjected to pure compression were analyzed by ABAQUS. The results are summarized in Table 6.9. The k_{winter} column in Table 6.9 is the buckling coefficient value used in the Winter's equation, as calculated by the analytical method of Section 6.4. The results show that the strength predictions by Winter's equation have a good agreement with results by the finite element analysis. The average ratio of ABAQUS vs. Winter is 106%, which indicates that Winter's predictions are conservative for the unstiffened elements; but in general fine.

Table 6.9 Result of unstiffened element under uniform compression stresses

b (in.)	a (in.)	t (in.)	f_y (ksi)	σ_u (ksi)	ρ_{ABAQUS}	k_{winter}	ρ_{winter}	ABAQUS /Winter
3	6	0.04	33	11.3	0.343	0.674	0.290	118.2%
3	6	0.04	44	13.1	0.298	0.674	0.253	117.4%
3	6	0.04	56.6	14.5	0.257	0.674	0.225	114.1%
3	6	0.04	62.2	15.2	0.245	0.674	0.215	113.7%
3	6	0.04	73.4	16.3	0.221	0.674	0.199	111.2%
4	12	0.05	33	8.8	0.266	0.5352	0.245	108.7%
4	12	0.05	44	10.0	0.228	0.5352	0.214	106.5%
4	12	0.05	56.6	11.3	0.199	0.5352	0.190	104.7%
4	12	0.05	62.2	11.7	0.188	0.5352	0.181	103.9%
4	12	0.05	73.4	12.7	0.173	0.5352	0.168	103.0%
2.5	10	0.05	33	13.1	0.397	0.487	0.362	109.6%
2.5	10	0.05	44	15.0	0.342	0.487	0.318	107.7%
2.5	10	0.05	56.6	17.3	0.306	0.487	0.283	108.3%
2.5	10	0.05	62.2	17.9	0.288	0.487	0.271	106.6%
2.5	10	0.05	73.4	19.4	0.264	0.487	0.250	105.6%
3	12	0.1	33	19.8	0.600	0.487	0.565	106.3%
3	12	0.1	44	22.7	0.515	0.487	0.500	102.9%
3	12	0.1	56.6	27.0	0.477	0.487	0.449	106.4%
3	12	0.1	62.2	28.7	0.462	0.487	0.431	107.3%
3	12	0.1	73.4	31.4	0.428	0.487	0.400	107.0%
3	20	0.1	33	17.8	0.540	0.4476	0.545	99.0%
3	20	0.1	44	20.5	0.465	0.4476	0.483	96.3%
3	20	0.1	56.6	23.0	0.406	0.4476	0.432	93.9%
3	20	0.1	62.2	23.8	0.383	0.4476	0.415	92.3%
3	20	0.1	73.4	25.7	0.351	0.4476	0.385	91.0%
							average	105.7%

Note: f_y --- yield stress;
σ_u --- ultimate stress obtained by ABAQUS analyses;
ρ_{ABAQUS} --- effective width ratio obtained by ABAQUS analyses;
ρ_{winter} --- effective width ratio by Winter's equation;
k_{winter} --- the buckling coefficient used in Winter's equation.

6.3.2.2 Stress Gradient Effect on the Ultimate Strength

Figure 6.58 shows the finite element model for the ss-free unstiffened elements under a stress gradient r = 0 (compression at one loaded edge only). Compression load is applied at one end, and shear forces are applied along one longitudinal edge to achieve the desired stress gradient in the plate.

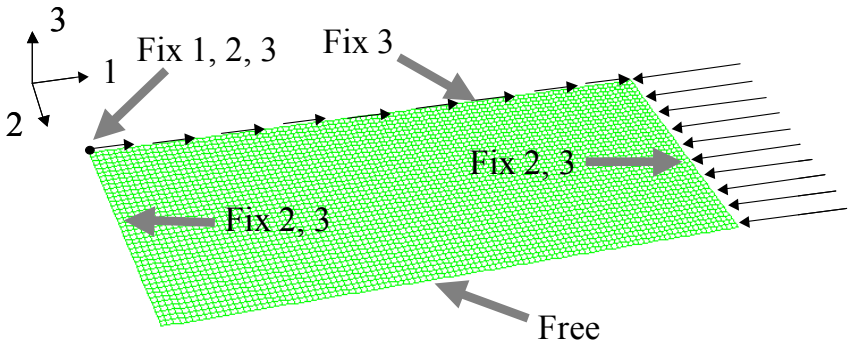

Figure 6.58 Finite element model for ss-free unstiffened element under a stress gradient with r = 0

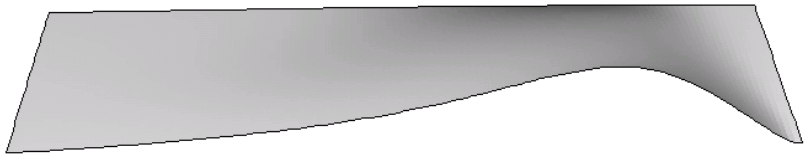

Figure 6.59 Buckled shape of a ss-free unstiffened element under a stress gradient r = 0

Figure 6.59 shows the buckled shape of a ss-free unstiffened element under a stress gradient r = 0 analyzed by the nonlinear FE model. The dimensions of the plate are: a = 12 in., b = 4 in., t = 0.05 in., and the yield stress is 62.2 ksi. Unlike the pure compression case, the plate buckled near the maximum loaded edge. Figure 6.60 and Figure 6.61 respectively show the stress σ_x and τ_{xy} on the mid-surface when the plate is still in the elastic region. It shows the stress distributions determined by ABAQUS are close to the

assumptions of the analytical model in Section 6.2.3.1 in which σ_x varies linearly from maximum loaded edge to the minimum loaded edge, and τ_{xy} varies from highest value at the simply supported edge to zero at the free edge. Finite element analysis also indicates that tension stress σ_x exists at the corner of the simply supported edge and the minimum loaded edge for this plate.

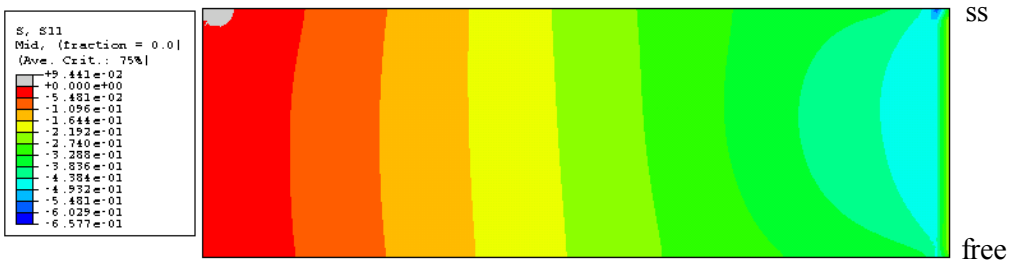

Figure 6.60 Stress σ_x distribution on mid-surface of a ss-free unstiffened element in elastic region under a stress gradient r = 0

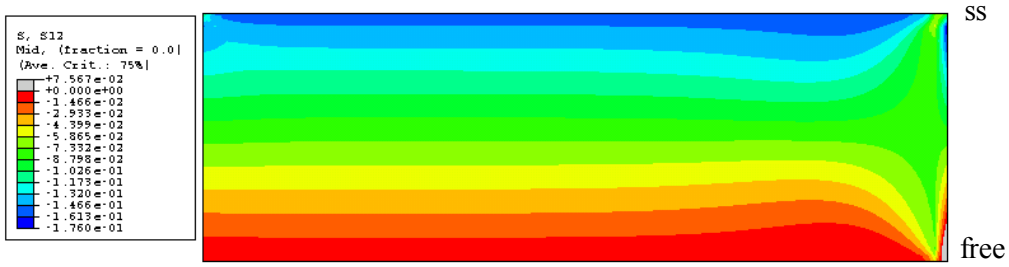

Figure 6.61 Stress τ_{xy} distribution on mid-surface of a ss-free unstiffened element in elastic region under a stress gradient r = 0

Figure 6.62 illustrates distribution of stress σ_x on the top, mid, and bottom surfaces at the mid-length (cross-section B in Figure 6.33) when the unstiffened plate reaches its maximum compression capacity. The distribution is complicated, large stress exists at the area close to the maximum loaded edge and tension is observed along both longitudinal edges. Figure 6.63 shows the distribution of τ_{xy}, large shear stress is observed at the region close to the corner of simply supported edge and maximum loaded edge, a large

part of plate has no shear stress. The distributions of both stresses are much more complicated compared with the result of the plate in the elastic region (Figure 6.60, Figure 6.61).

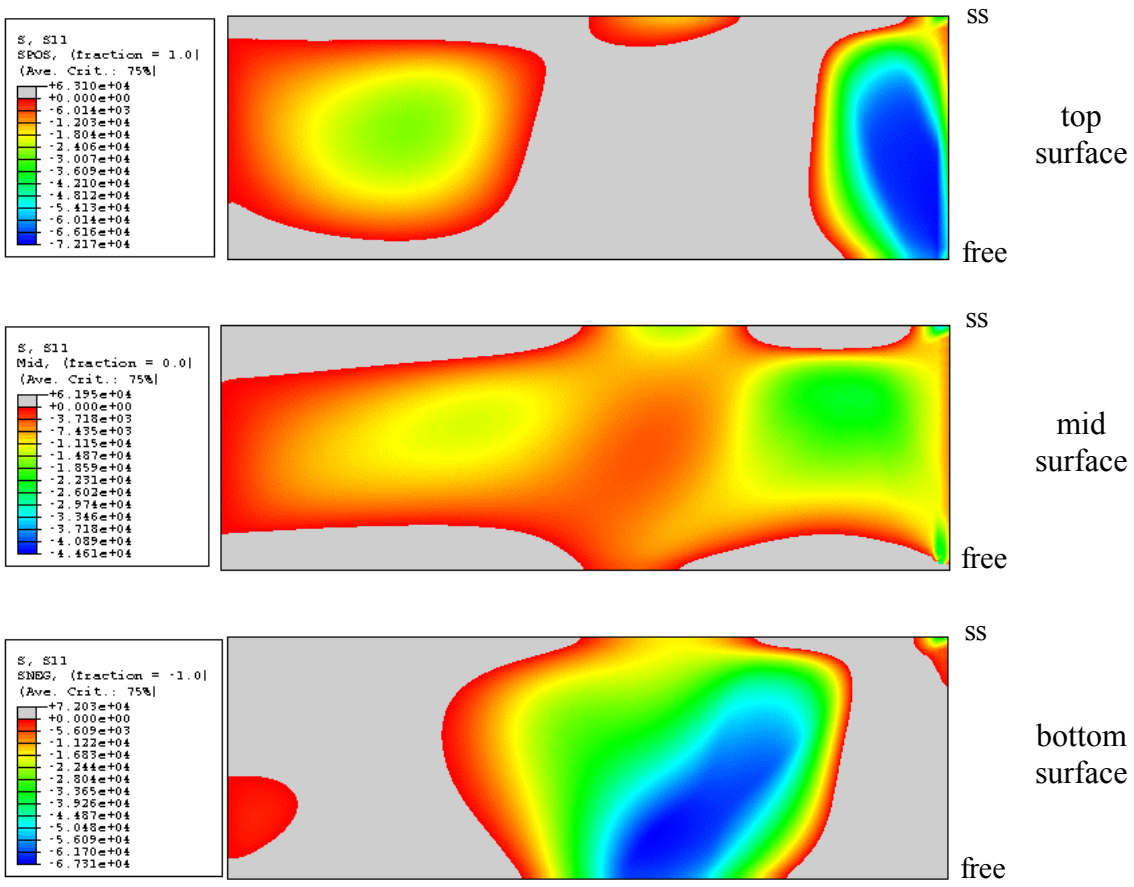

Figure 6.62 Stress σ_x distribution on mid-surface of a ss-free unstiffened element under a stress gradient r = 0

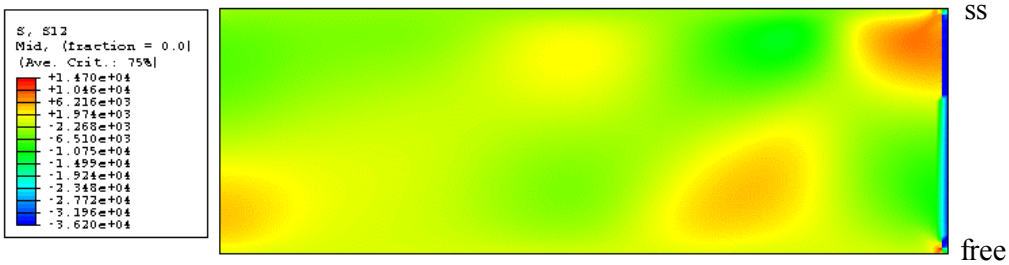

Figure 6.63 Stress τ_{xy} distribution on mid-surface of a ss-free unstiffened element under a stress gradient r = 0

Figure 6.64 through Figure 6.67 show the development of longitudinal stress σ_x on the mid-surface at the mid-length (cross-section B of Figure 6.33). Each figure includes a plot of the external load vs. edge displacement and a plot of stress distribution where the expected value is calculated by assuming the stress is linearly distributed in the longitudinal direction. Positive stress represents compression. High compression stress σ_x occurs close to the simply supported edge when the plate is in the elastic region. For the region of peak load and postbuckling, high compression stress is observed at the middle part of the cross-section; at the same time, tension stress occurs along both edges, and the magnitude increases significantly in the postbuckling region.

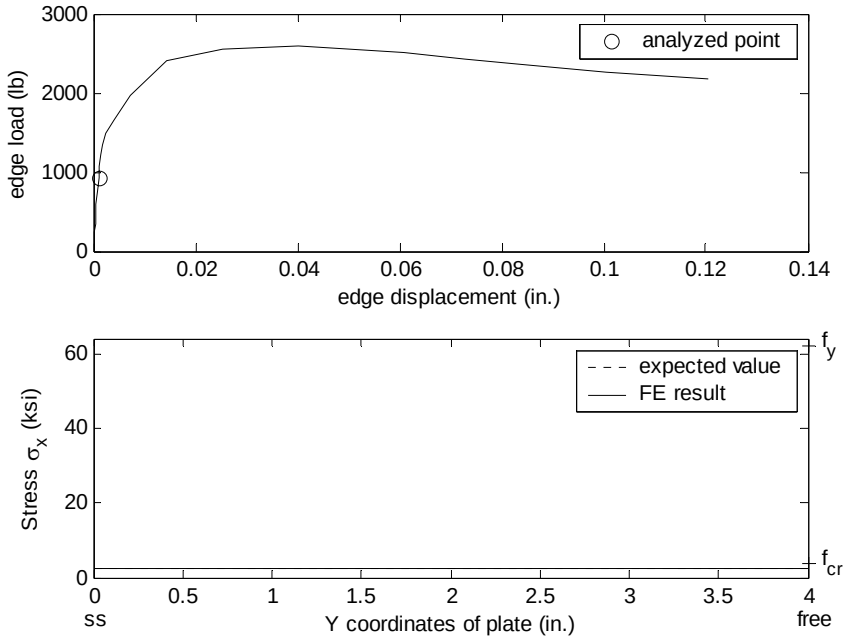

Figure 6.64 σ_x distribution on mid-surface along cross-section B of a ss-free unstiffened element under a stress gradient r = 0

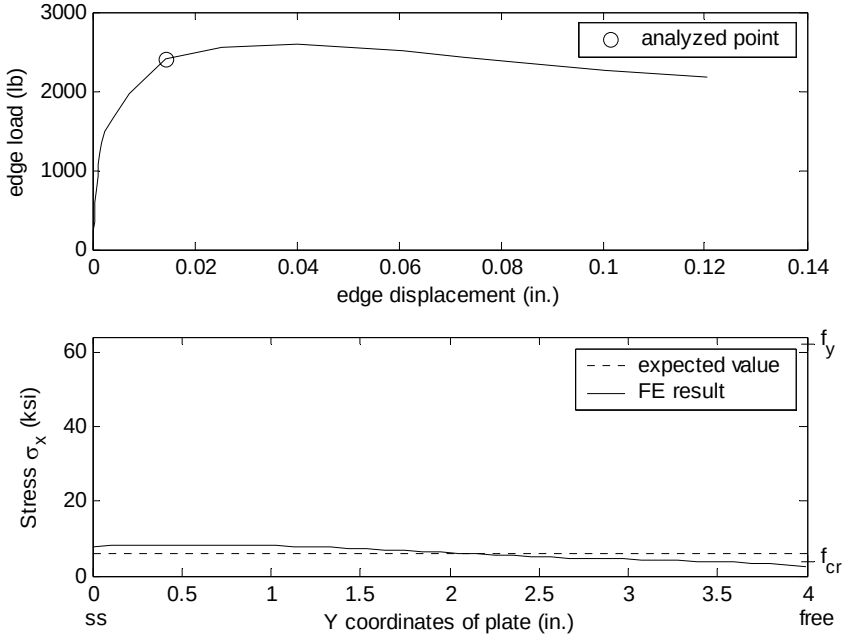

Figure 6.65 σ_x distribution on mid-surface along cross-section B of a ss-free unstiffened element under a stress gradient r = 0

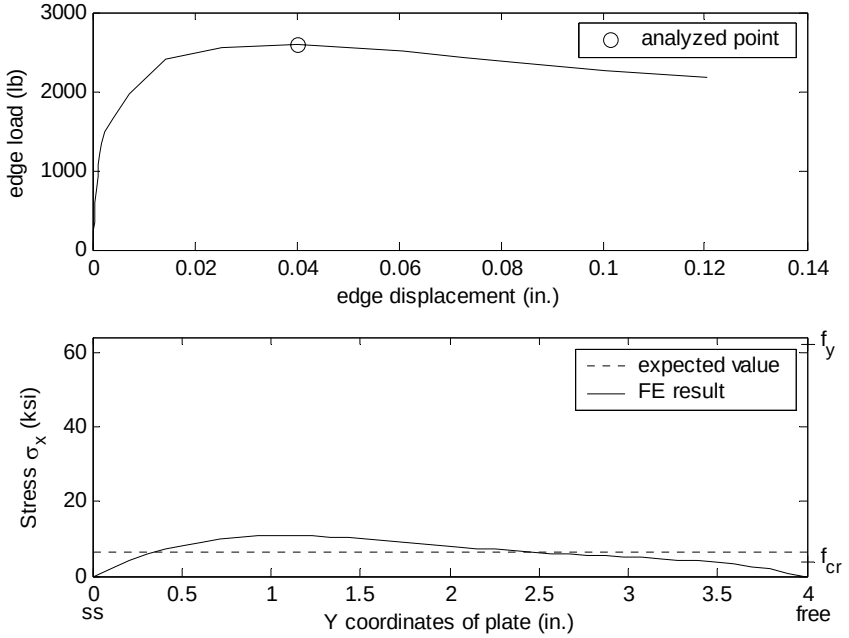

Figure 6.66 σ_x distribution on mid-surface along cross-section B of a ss-free unstiffened element under a stress gradient r = 0

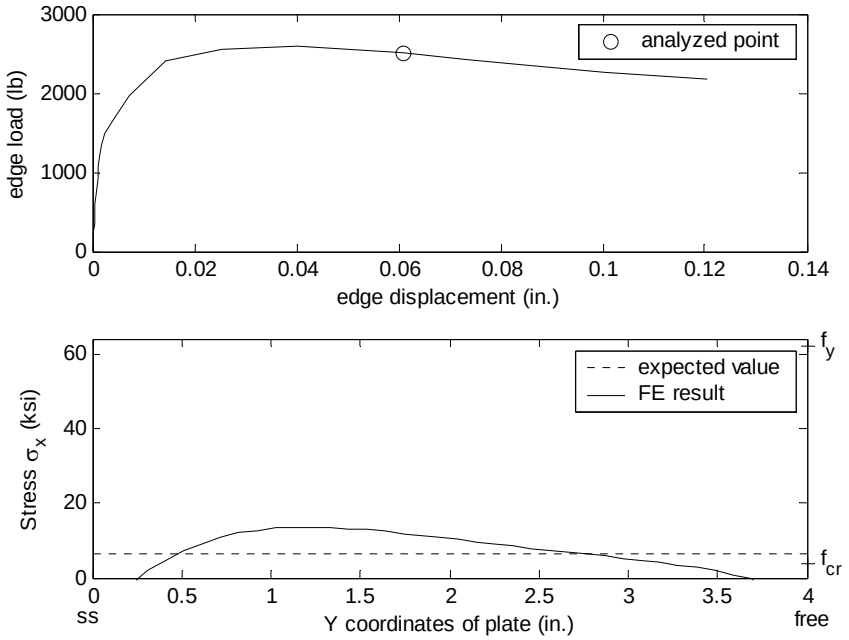

Figure 6.67 σ_x distribution on mid-surface along cross-section B of a ss-free unstiffened element under a stress gradient r = 0

Figure 6.68 shows the stress development on the mid-surface along three cross-sections A, B, and C (as shown in Figure 6.33) at the point when the plate reaches its maximum capacity. Cross-section C is almost fully effective, except the free edge, and the stress is close to the uniform value. High compression stress at section B occurs in the middle, while both edges are essentially un-effective. Cross-section A is at the unloaded edge so the small amount of load is expected. None of the distributions are perfectly consistent with traditional effective width assumptions for such elements.

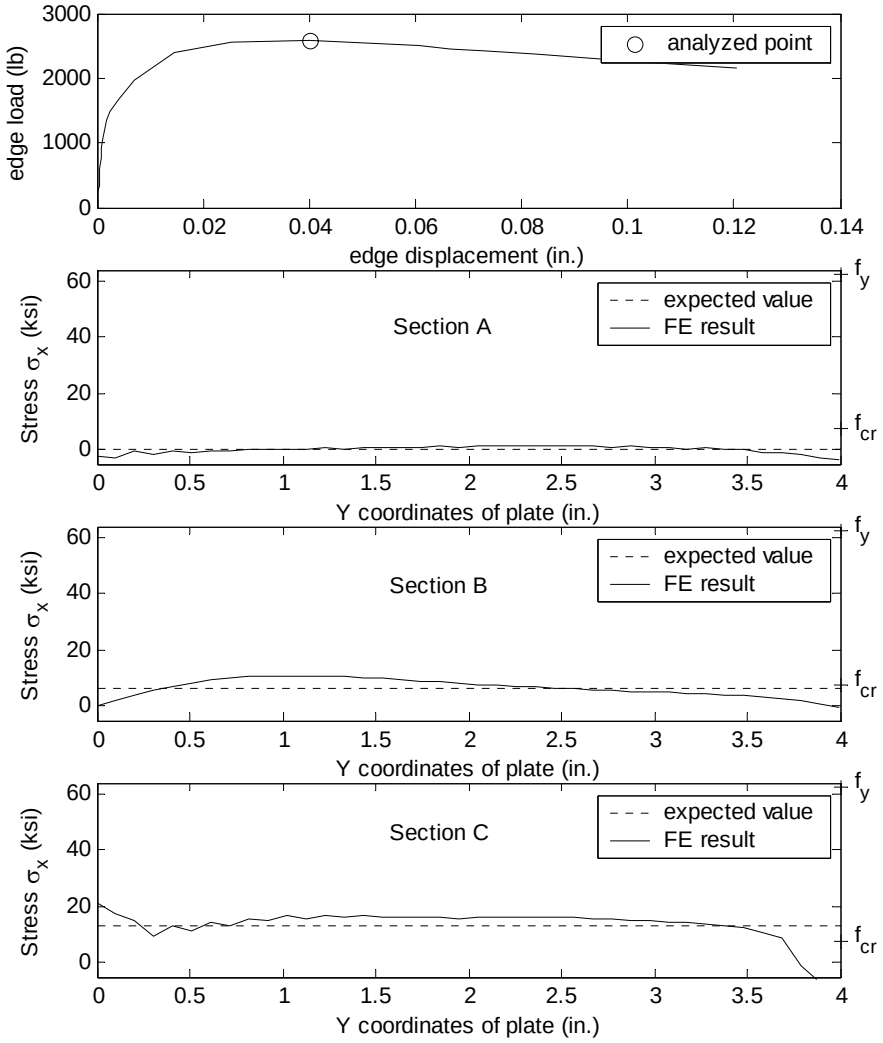

Figure 6.68 σ_x distribution on mid-surface of a ss-free unstiffened element under a stress gradient r = 0

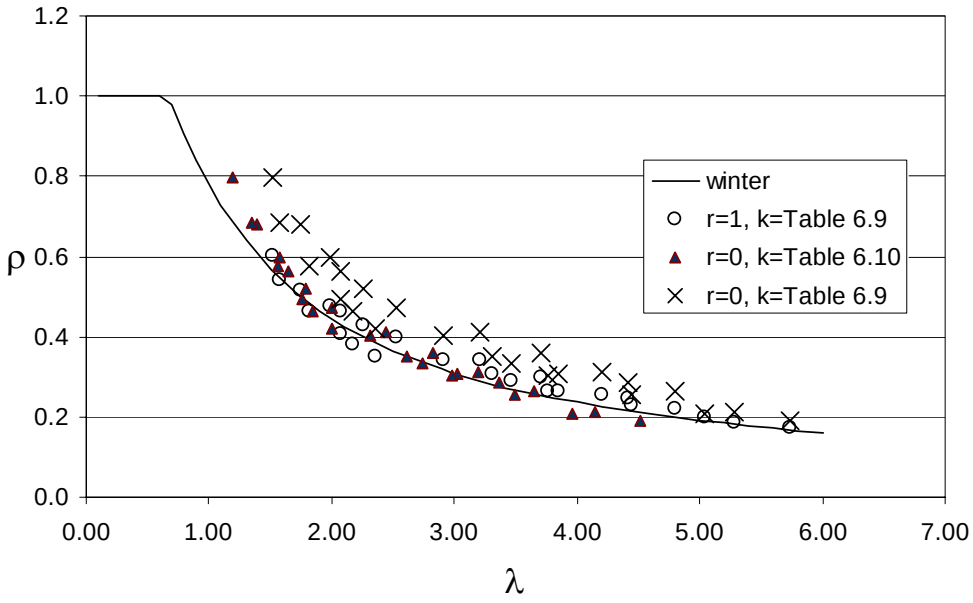

Figure 6.69 ABAQUS results vs. Winter's curve

A total of 25 ss-free unstiffened elements under a stress gradient r = 0 were studied, and the results are summarized in Table 6.10. Figure 6.69 shows the comparison of finite element results with Winter's predictions. The strength of the unstiffened elements is increased significantly when the stress gradient is applied, "x" in Figure 6.69. The average increase is 119%. If the appropriate buckling coefficient k (accounting for the stress gradient) is used, Winter's equation works well. Therefore, in the design of unstiffened elements, the stress gradient effect can be accounted for by using an improved buckling coefficient, k (Table 6.5), otherwise Winter's equation will give overly conservative predictions.

Table 6.10 Results of unstiffened elements under stress gradient r = 0

b (in.)	a (in.)	t (in.)	f_y (ksi)	σ_u (ksi)	ρ_{ABAQUS}	k_{winter}	ρ_{winter}	ABAQUS /Winter	r=0 /r=1
3	6	0.04	33	13.6	0.413	1.162	0.372	111.1%	120.5%
3	6	0.04	44	15.8	0.359	1.162	0.326	109.9%	120.5%
3	6	0.04	56.6	17.6	0.313	1.162	0.292	107.3%	120.8%
3	6	0.04	62.2	17.8	0.287	1.162	0.278	103.2%	117.2%
3	6	0.04	73.4	19.5	0.266	1.162	0.257	103.2%	120.0%
4	12	0.05	33	10.2	0.308	0.8664	0.307	100.6%	115.8%
4	12	0.05	44	11.3	0.257	0.8664	0.268	95.8%	112.9%
4	12	0.05	56.6	11.8	0.208	0.8664	0.238	87.1%	104.5%
4	12	0.05	62.2	13.1	0.211	0.8664	0.228	92.4%	111.9%
4	12	0.05	73.4	14.1	0.191	0.8664	0.211	90.8%	110.9%
2.5	10	0.05	33	15.5	0.471	0.7742	0.445	105.7%	118.6%
2.5	10	0.05	44	17.7	0.401	0.7742	0.392	102.4%	117.3%
2.5	10	0.05	56.6	19.7	0.352	0.7742	0.351	100.1%	113.8%
2.5	10	0.05	62.2	20.6	0.331	0.7742	0.335	98.9%	114.9%
2.5	10	0.05	73.4	22.3	0.304	0.7742	0.311	97.8%	115.0%
3	12	0.1	33	26.2	0.795	0.7742	0.681	116.8%	132.4%
3	12	0.1	44	30.0	0.682	0.7742	0.607	112.3%	132.4%
3	12	0.1	56.6	33.8	0.597	0.7742	0.547	109.0%	125.1%
3	12	0.1	62.2	35.1	0.565	0.7742	0.526	107.4%	122.3%
3	12	0.1	73.4	38.1	0.519	0.7742	0.490	105.8%	121.2%
3	20	0.1	33	22.7	0.686	0.6144	0.621	110.5%	127.2%
3	20	0.1	44	25.4	0.578	0.6144	0.552	104.7%	124.3%
3	20	0.1	56.6	27.9	0.493	0.6144	0.496	99.3%	121.3%
3	20	0.1	62.2	28.9	0.464	0.6144	0.477	97.5%	121.4%
3	20	0.1	73.4	30.7	0.418	0.6144	0.443	94.3%	119.3%
							average	102.6%	119.3%

Note: f_y --- yield stress;
σ_u --- ultimate stress obtained by ABAQUS analyses;
ρ_{ABAQUS} --- effective width ratio obtained by ABAQUS analyses;
ρ_{winter} --- effective width ratio by Winter's equation;
k_{winter} --- the buckling coefficient used in Winter's equation.

6.4 Conclusions

An analytical method to determine the elastic buckling stress of thin plates subjected to a stress gradient is derived and verified by finite element analysis. The results show that under a longitudinal stress gradient, the elastic buckling stress at the maximum loaded end is higher than for the same plate under uniform compressive stress. The influence of stress gradient on both stiffened and unstiffened elements is derived and

quantified. Compared with the stiffened element, the unstiffened element exhibits a stronger dependency on the applied stress gradient, and the dependency decreases more slowly as the plate aspect ratio becomes large (the plate becomes longer).

Nonlinear finite element analysis is performed to study the ultimate strength of thin plates under uniform stresses and stress gradients. Winter's equation is verified by the FE modeling for both stiffened and unstiffened elements. Similar to the finding in the elastic buckling research, the stress gradient increases the strength of both stiffened and unstiffened elements. However, the influence on the stiffened element is limited, and can likely be ignored in design; while the strength of unstiffened elements is boosted greatly, and the effect could be considered in design. It is also found that plate width is not fully engaged to provide the compression capacity. For the stiffened element, high longitudinal compressive stress is observed near the two unloaded edges, conceptually similar to the traditional effective width idealization. For the unstiffened element, the stress distribution is more complicated and tension is observed at both unloaded edges which is contrary to traditionally assumed effective width distributions. Nonetheless, the finite element analysis shows that Winter's equation can provide accurate predictions for the stress gradient effect when the plate buckling coefficient k is calculated including the effect of the stress gradient. Plate buckling coefficients (k values) under different stress gradients are summarized in this chapter and can be used for design.

Chapter 7

Moment Gradient Effect on the Distortional Buckling of Cold-Formed Steel Beams

7.1 Introduction

In practical situations, beams are subjected to a wide variety of loading and support conditions, thus producing non-uniform moment along the length. For distortional buckling, one of the most common cases of concern is the negative bending region (bottom flanges under compression) near the supports (columns) of a continuous beam, as shown in Figure 7.1. Significant moment gradients exist at this region, and distortional buckling is prone to control the failure since little restraint is placed on the bottom flanges in practice.

The moment gradient effect on local buckling of cold-formed steel beams is generally ignored in design because the buckling wavelength is relatively short, thus each buckled wave is subjected to only a limited moment gradient. On the other hand, the wavelength in lateral-torsional buckling is quite long; and the moment gradient has

significant influence on the critical moment. Therefore, current design methods consider such influence by employing an equivalent moment factor, C_b, in calculation. The moment gradient effect on distortional buckling of cold-formed steel beams has not been studied in detail, however, since the wavelength of distortional buckling is consistently longer than that of local buckling, the critical distortional buckling moment may be influenced by moment gradient.

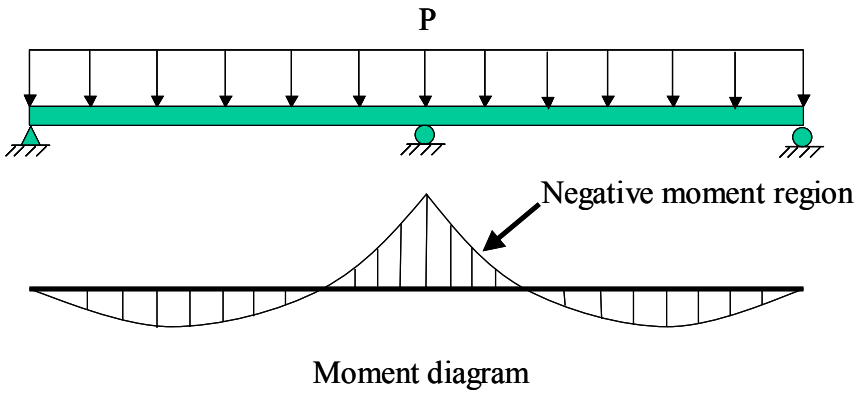

Figure 7.1 A continuous beam under uniform distributed loads.

Moment gradient on beams create stress gradients on plates. Research summarized in Chapter 6 indicates that stress gradient has significant influence on unstiffened elements; and increases in strength due to longitudinal stress gradient should be accounted for in design. Compression flange behavior generally characterizes the distortional buckling of cold-formed steel sections. Buckling of unstiffened elements is behaviorally similar to distortional buckling, both in terms of cross-section deflection and buckling wavelength. Therefore, it is expected that the results of Chapter 6 for unstiffened elements are relevant to distortional buckling of beams.

Traditional design methods for cold-formed steel members, and the newer Direct Strength Method, were both initiated from Winter's equation on plates. The results

addressed in Chapter 6 also indicate a potential solution for moment gradient effect on cold-formed steel beams in both local and distortional buckling. That is, to include the moment gradient effect in the calculation of the elastic buckling moments, and then employ the original strength prediction method for beams under constant moment.

In this chapter, the moment gradient effect on both the elastic and the ultimate strength of distortional buckling of cold-formed beams is analyzed by finite element analysis. The results lead to the development of additional provisions for the Direct Strength Method to account for the moment gradient effect.

7.2 Moment Gradient Effect on the Elastic Distortional Buckling of Cold-Formed Steel Beams

Elastic buckling moment has been found as one of the controlling factors for the ultimate strength of cold-formed steel beams. In the Direct Strength Method, the elastic buckling moment, along with the yield moment, determines the ultimate strength of sections in both local and distortional buckling failures. Therefore, the first step of this research is to examine the moment gradient effect on the elastic distortional buckling of cold-formed steel beams.

7.2.1 Finite Element Modeling of Cold-Formed Beams under Moment Gradients

Finite element modeling (ABAQUS) is utilized to determine the elastic distortional buckling of cold-formed steel beams under a moment gradient, r (where $r = M_1/M_2$, M_1 and M_2 are the end moments, $|M_2| > |M_1|$). The ABAQUS model is shown in Figure 7.2.

ABAQUS shell element S4R is employed. The displacements in direction 1 and 2 are fixed at the two ends of the beam; one corner node at the minimum loaded end is fixed in all three directions 1, 2, and 3. Concentrated loads are applied at each node at the two ends in a distribution to simulate the moments, as shown in Figure 7.3.

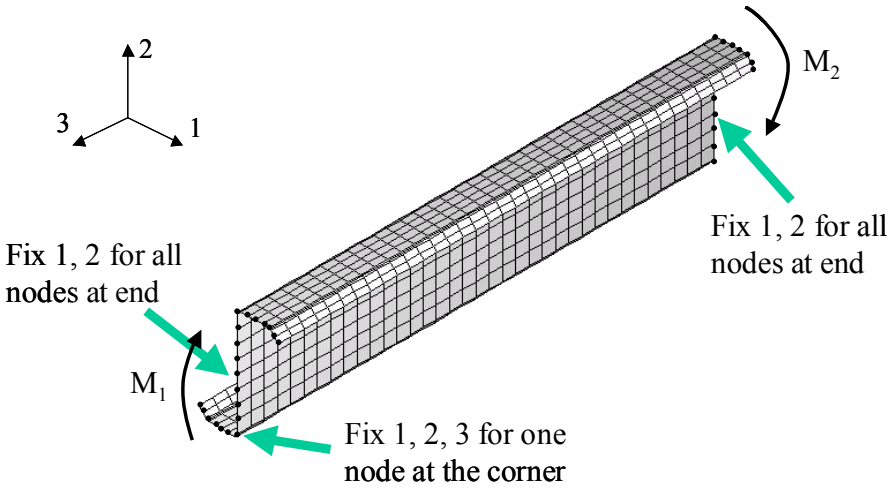

Figure 7.2 Finite element model of cold-formed beams under moment gradients

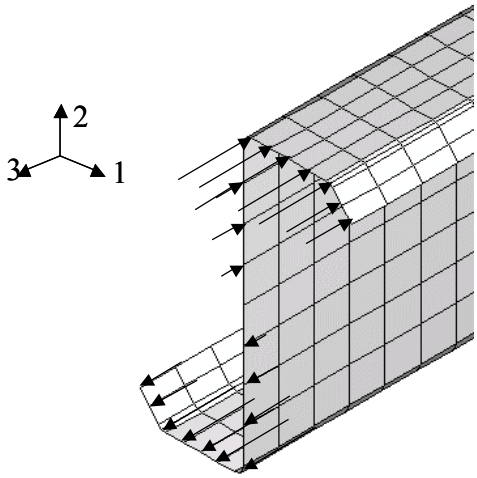

Figure 7.3 Loading configurations at the end

Figure 7.4, Figure 7.5, and Figure 7.6 illustrate the distortional buckling modes of an 8.5 in. deep, 0.082 in. thick, 63 in. long Z-section beam under moment gradients r = 1, r =

0, and r = -1 respectively. When the beam is loaded by even end moments (r = 1, no moment gradient exists along the beam length), repeated buckling waves are observed, Figure 7.4. If a moment gradient (-1 < r < 1) is applied to the beam, only one half-wave is observed at the region near the maximum loaded end. For the case with equal and opposite end moments r = -1, the beam buckles at the compression flanges near either end.

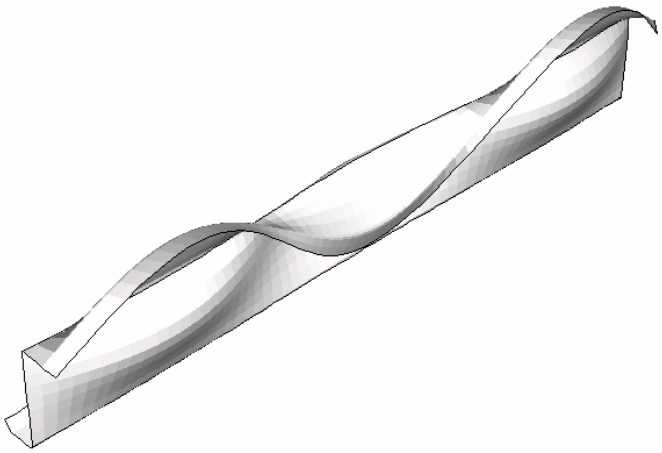

Figure 7.4 Distortional buckling shape of a 8.5 in. deep Z-section under constant moment r = 1 (single curvature)

Figure 7.5 Distortional buckling shape of a 8.5 in. deep Z-section under moment gradient r = 0 (moment on one end only)

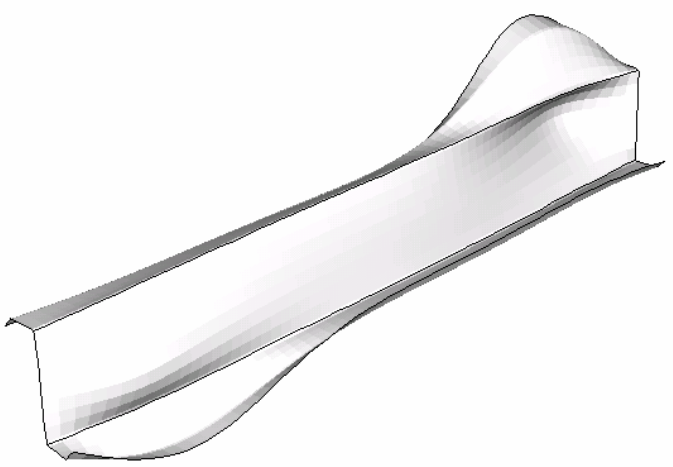

Figure 7.6 Distortional buckling shape of a 8.5 in. deep Z-section under moment gradient r = -1 (double curvature)

7.2.2 Results of the Finite Element Analyses

Twelve typical cold-formed steel C and Z-sections are chosen for detailed elastic distortional buckling finite element analysis. The geometry of the selected sections is summarized in Table 7.1. To avoid the influence of other buckling modes, most of the selected sections have lower elastic distortional buckling moment than local buckling moment and lateral-torsional buckling. Distortional buckling is expected to be the first mode when the length of section is not relatively long (for long unbraced lengths lateral-torsional buckling always controls).

The influence of the moment gradient on the elastic bucking moment as a function of the moment gradient magnitude r, is summarized in Table 7.2. L_{crd} is the half-wavelength and M_{crd} is the elastic buckling moment for distortional buckling under constant moment ($r = 1$), and M_d is the distortional buckling moment under a moment gradient ($r \neq 1$). For these analyses, the length of each section is set to three times the half-wavelength L_{crd}.

Table 7.1 Geometry of selected sections

Section type	Section label	h (in.)	b_c (in.)	d_c (in.)	θ_c (deg)	b_t (in.)	d_t (in.)	θ_t (deg)	r_{hc} (in.)	r_{dc} (in.)	r_{ht} (in.)	r_{dt} (in.)	t (in.)
Z sections	8Z50	8.00	2.25	0.93	50.0	2.25	0.93	50.0	0.24	0.24	0.24	0.24	0.0500
	8Z100	8.00	2.25	0.93	50.0	2.25	0.93	50.0	0.24	0.24	0.24	0.24	0.1000
	11.5Z100	11.50	3.50	0.90	50.0	3.50	0.90	50.0	0.30	0.30	0.30	0.30	0.1000
	8.5Z070	8.50	2.50	0.90	50.0	2.50	0.90	50.0	0.25	0.25	0.25	0.25	0.0700
	8.5Z082	8.46	2.50	0.95	49.0	2.36	0.97	50.3	0.28	0.28	0.30	0.30	0.0806
	8.5Z120	8.47	2.59	0.96	47.8	2.46	1.00	48.9	0.36	0.36	0.34	0.34	0.1176
	8.5Z092	8.43	2.61	0.92	51.8	2.40	0.95	50.4	0.28	0.28	0.31	0.31	0.0900
	11.5Z080	11.50	3.50	0.90	50.0	3.50	0.90	50.0	0.30	0.30	0.30	0.30	0.0800
C sections	8C097	8.04	2.09	0.58	85.1	2.07	0.53	86.3	0.28	0.28	0.29	0.28	0.0980
	8C054	8.00	2.05	0.59	89.4	2.04	0.56	83.3	0.22	0.23	0.23	0.24	0.0520
	10C068	10.10	2.07	0.53	80.7	2.08	0.52	81.9	0.24	0.23	0.23	0.22	0.0634
	3.62C054	3.73	1.88	0.41	87.0	1.87	0.43	89.0	0.26	0.24	0.27	0.27	0.0555

Table 7.2 Distortional buckling of beams under moment gradient r = 0

Section label	L_{crd} (in.)	M_{crd} (kip-in.)	M_d/M_{crd}			
			r = 0.5	r = 0	r = -0.5	r = -1
8Z50	25	58.41	1.15	1.26	1.33	1.39
8Z100	17	260.54	1.14	1.24	1.31	1.33
11.5Z100	25	270.28	1.16	1.27	1.35	1.40
8.5Z070	22	120.02	1.14	1.25	1.33	1.36
8.5Z082	21	162.92	1.15	1.26	1.34	1.39
8.5Z120	18	365.54	1.13	1.24	1.32	1.38
8.5Z092	21	206.26	1.14	1.25	1.33	1.35
11.5Z080	30	170.27	1.15	1.26	1.33	1.38
8C097	13	257.08	1.17	1.24	1.25	1.32
8C054	19	66.93	1.15	1.21	1.26	1.32
10C068	16	95.89	1.14	1.21	1.25	1.33
3.62C054	12	35.15	1.18	1.30	1.41	1.50

Figure 7.7 is a graphic representation of the influence of moment gradient on elastic distortional buckling. The elastic distortional buckling moment is increased when a moment gradient is applied along the section. The buckling moment of the beams is greatest when the moment gradient is sharpest. For the case with r = -1, the beams demonstrates the highest elastic buckling moments. The selected sections show a 30% to 50% increase in the distortional buckling moment (with r = -1) compared with the

situation with no moment gradients (r = 1). Thus, the equal and even end moments loading case (r = -1) represents the most severe loading condition for the beam in distortional buckling.

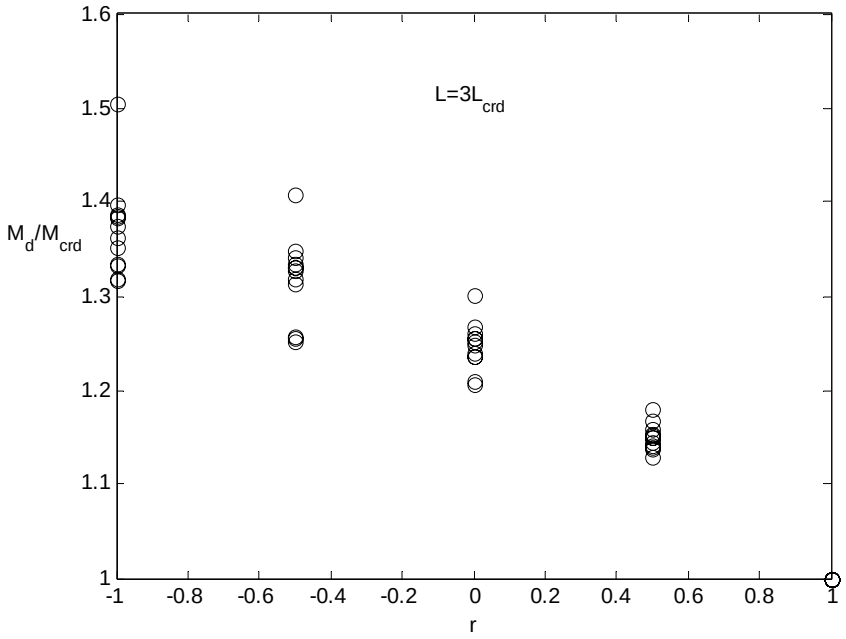

Figure 7.7 Moment gradient influence with respect to r

Table 7.3 and Figure 7.8 provide the moment gradient influence with respect to the section length. In this parametric study, the moment gradient factor r is kept the same (r = 0), in which the moment is only applied at one end of the simply supported beam, and decreases linearly to zero at the far end (a triangular bending moment diagram). The length of each section is changed from the original distortional buckling half-wavelength under no moment gradient (L_{crd}) to ten times this value. Under the same moment gradient magnitude, longer sections have less increase in the distortional buckling moments. Theoretically, as $L \rightarrow \infty$, the buckling moment will converge to the value of the case with no moment gradient (independent of r), but the finite element analysis indicates convergence to these limiting values is slow. For sections with a length of $10L_{crd}$, at least

a 10% increase in the distortional buckling moment is still observed. The lower bound of the moment gradient (r = 0) effects can be approximated by a simple function:

$$M_d / M_{crd} = 1.0 \le 1.0 + 0.4\left(\frac{L_{crd}}{L}\right)^{0.7} \le 1.3 \tag{7.1}$$

Table 7.3 Distortional buckling of beams under moment gradient r = 0

Section label	L_{crd} (in.)	M_{crd} (kip-in.)	M_d/M_{crd}				
			L= $1L_{crd}$	L= $3L_{crd}$	L= $5L_{crd}$	L= $7L_{crd}$	L= $10L_{crd}$
8Z50	25	58.41	1.36	1.26	1.18	1.13	1.10
8Z100	17	260.54	1.37	1.24	1.17	1.12	1.09
11.5Z100	25	270.28	1.39	1.27	1.18	1.14	1.11
8.5Z070	22	120.02	1.30	1.25	1.16	1.13	1.09
8.5Z082	21	162.92	1.40	1.26	1.17	1.13	1.10
8.5Z120	18	365.54	1.45	1.24	1.13	1.11	1.08
8.5Z092	21	206.26	1.42	1.25	1.13	1.13	1.09
11.5Z080	30	170.27	1.36	1.26	1.17	1.14	1.10
8C097	13	257.08	1.29	1.24	1.20	1.16	1.12
8C054	19	66.93	1.34	1.21	1.19	1.15	1.10
10C068	16	95.89	1.41	1.21	1.14	1.14	1.12
3.62C054	12	35.15	1.60	1.30	1.21	1.16	1.13

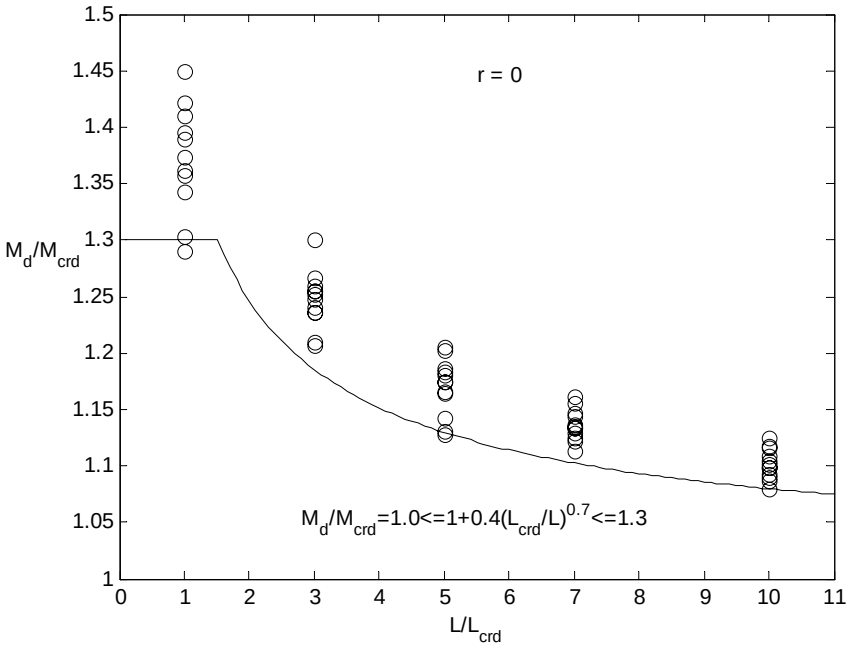

Figure 7.8 Moment gradient influence with respect to the section length ratio

7.2.3 Equivalent Moment Concept

The moment gradient factor r, and section length ratio L_{crd}/L, are two essential parameters to represent the moment gradient magnitude. The Equivalent Moment Concept proposed here is an approximate method to simplify the possible loading configurations (different r and L_{crd}/L) to a single case. The idea is shown schematically in Figure 7.9 for a single curvature moment gradient, and in Figure 7.10 for a double curvature moment gradient. When a single curvature moment gradient ($0 < r < 1$, $r = M_1/M_2$) is applied to a simply supported beam with length L, the moment diagram is a trapezoid, the long side is L_e. The Equivalent Moment Concept presumes that the elastic distortional buckling moment of a beam with length L and moment gradient $r = M_1/M_2$ is equal to the elastic distortional buckling moment of the same section with a length L_e and under a moment gradient r = 0, as shown in Figure 7.9.

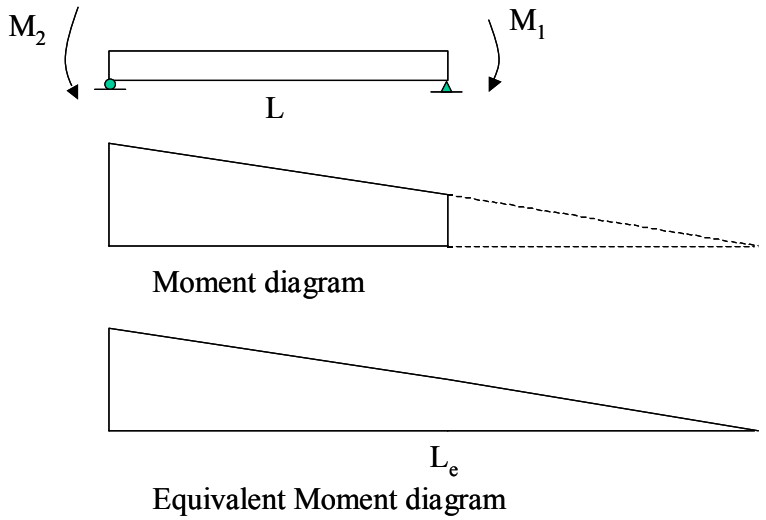

Figure 7.9 Equivalent Moment Concept applied to a single curvature moment gradient

For beams under the double curvature moment gradients ($-1 < r < 0$), the moment diagram will be as shown in Figure 7.10. The equivalent moment diagram (r = 0) will be

the triangle at the maximum loaded side and the equivalent beam length, L_e, is less than the original length, L.

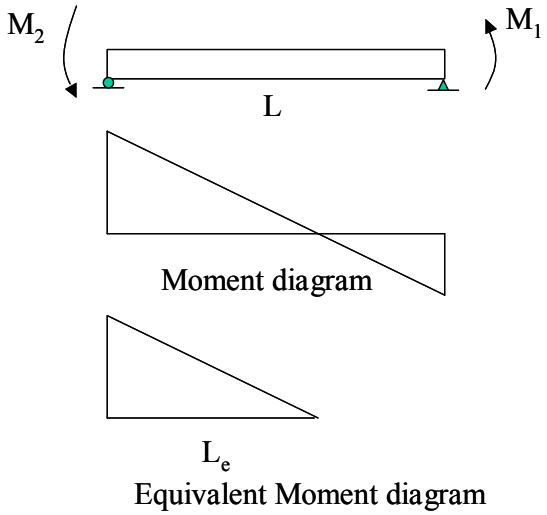

Figure 7.10 Equivalent Moment Concept applied to a double curvature moment gradient

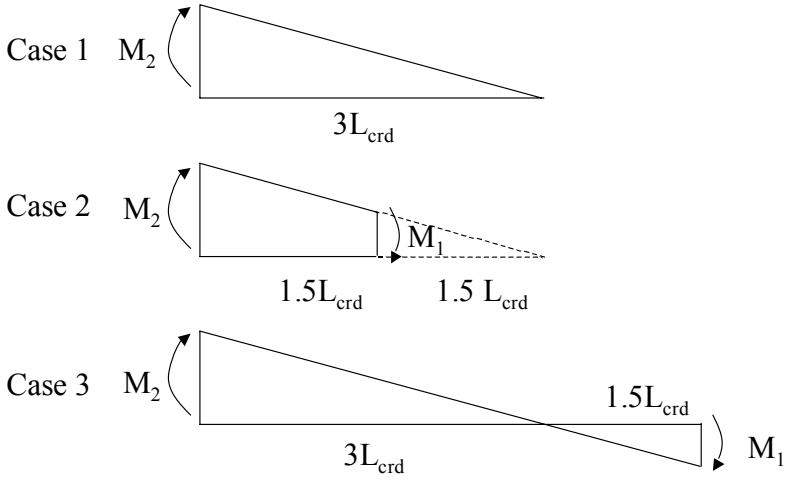

Figure 7.11 Three analyzed cases for Equivalent Moment Concept

A series of finite element analyses were performed to examine the Equivalent Moment Concept. Three cases of each section were studied: (1) $L = 3L_{crd}$, r = 0; (2) $L = 1.5L_{crd}$, r = 0.5; (3) $L = 4.5L_{crd}$, r = -0.5, the L_{crd} is the distortional buckling half-wavelength of beams with constant moment. As shown in Figure 7.11, the Equivalent Moment Concept presumes that these three cases of each section should yield the same

distortional buckling moment. The FEA results are summarized in Table 7.4, and it is shown that the distortional buckling moment of these three cases, for each section, are indeed quite close; the offset is below 3% on average. The Equivalent Moment Concept is a simplification with validity, at least for the studied sections.

Table 7.4 Finite element results for Equivalent Moment Concept

Section label	M_{crd-1} (kip-in.) ($r = 0$, $L = 3L_{crd}$)	M_{crd-2}/M_{crd-1} ($r = 0.5$, $L = 1.5L_{crd}$)	M_{crd-3}/M_{crd-1} ($r = -0.5$, $L = 4.5L_{crd}$)
8Z50	73.33	1.02	0.99
8Z100	323.13	1.03	0.99
11.5Z100	342.36	1.03	1.00
8.5Z070	150.34	1.04	1.00
8.5Z082	205.23	1.03	0.99
8.5Z120	451.59	1.03	1.00
8.5Z092	257.51	1.03	0.99
11.5Z080	213.73	1.02	1.00
8C097	317.85	1.04	0.94
8C054	80.78	1.03	0.99
10C068	115.94	0.97	0.95
3.62C054	45.74	1.03	1.00
	mean	1.03	0.99

Note: M_{crd-1} --- elastic distortional buckling moment of case 1 in Figure 7.11;
M_{crd-2} --- elastic distortional buckling moment of case 2 in Figure 7.11;
M_{crd-3} --- elastic distortional buckling moment of case 3 in Figure 7.11.

By the Equivalent Moment Concept, all moment gradient effects can be projected to the same case in which a moment gradient r = 0 is applied to the beam with the equivalent length L_e. Then, the elastic distortional buckling moment under moment gradients, M_d, can be obtained by substituting the length ratio of L_{crd}/L, the end moment ratio of M_1/M_2, and the elastic distortional buckling moment, M_{crd}, for constant moment into Equation (7.2).

$$M_d/M_{crd} = 1.0 \le 1 + 0.4\left(L_{crd}/L\right)^{0.7}\left(1 - M_1/M_2\right)^{0.7} \le 1.3 \qquad (7.2)$$

where M_2 and M_1 are the end moments on a beam of length L;

$|M_2| > |M_1|$, single curvature is positive;

L_{crd} is the half wavelength of distortional buckling under constant moment ($M_1=M_2$);

M_{crd} is the distortional buckling moment under constant moment ($M_1=M_2$);

M_d is the distortional buckling moment under a moment gradient $r=M_1/M_2$ ($M_1 \neq M_2$).

7.3 Moment Gradient Effect on the Distortional Buckling Strength of Cold-Formed Steel Beams

The previous sections explored the effect of moment gradient on elastic distortional buckling. Of course, moment gradient effect on the post-buckling/ultimate strength is of the most importance for design. In this section, the previously verified nonlinear finite element model in ABAQUS (Chapter 5) and an extended ABAQUS model are employed to investigate ultimate strength in distortional buckling under a moment gradient.

7.3.1 Nonlinear Finite Element Modeling

Two nonlinear finite element models were used to investigate the moment gradient influence on the ultimate strength of cold-formed steel beams. The first model was detailed in Chapter 5, as shown in Figure 7.12. Each beam consists of two 18 ft. long C or Z-sections which are oriented opposed. The two sections are connected together by four tubes: two at the ends and two at the 1/3 points, the tubes are placed 64 in. apart. The ABAQUS shell element S4R is used for the sections. A steel panel is attached to the top flanges outside the two 1/3 points, so that the buckling is expected to occur inside the two 1/3 points where no flange restraint exists. Nonlinear material properties and geometric imperfections are considered in the FE model. Geometric imperfection is introduced by

the same method as detailed in Chapter 5: a local and distortional buckling combined shape is selected, and the magnitude corresponds to a 50% probability of exceedance (50% CDF). Five typical stress vs. strain curves obtained from the tensile tests (Chapter 4) are used for the material model, the yield stresses are 33 ksi, 44 ksi, 57 ksi, 62 ksi, and 73 ksi respectively.

In order to apply moment gradients to the region in the middle third points, a single load P is applied at the first 1/3 point, as depicted in Figure 7.12, then the unrestrained part of beam is subjected to a moment gradient r = 0.5.

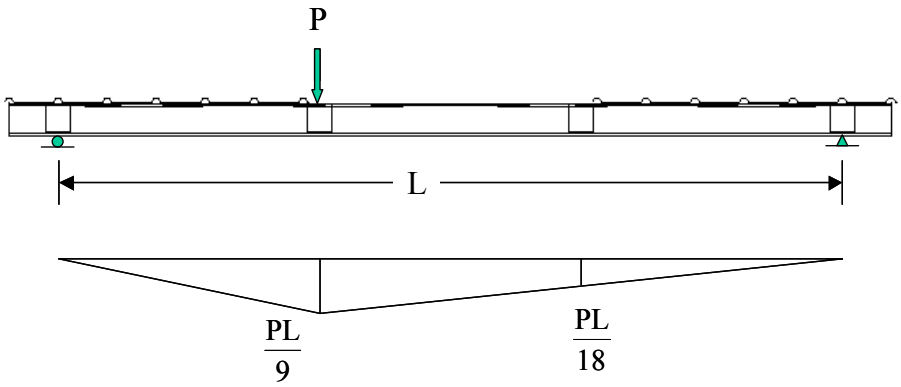

Figure 7.12 Finite element modeling strategy for moment gradient (r = 0.5)

The second finite element model is similar to the first model. As shown in Figure 7.13, two 152 in. long C or Z-sections are bolted together by three tubes, the tubes are 64 in. apart. A steel panel is installed on the compression flange covering only half of the beam length. The same methods used in the first model are chosen to introduce the geometric imperfection, as well as the material nonlinearity. A concentrated load P is applied at the middle point to generate a moment gradient r = 0 on both sides of the beam, as depicted in Figure 7.13. A steel panel is only attached on one side in order to restrict

lateral-torsional buckling, and distortional buckling failure is expected to occur in the area without flange restraint.

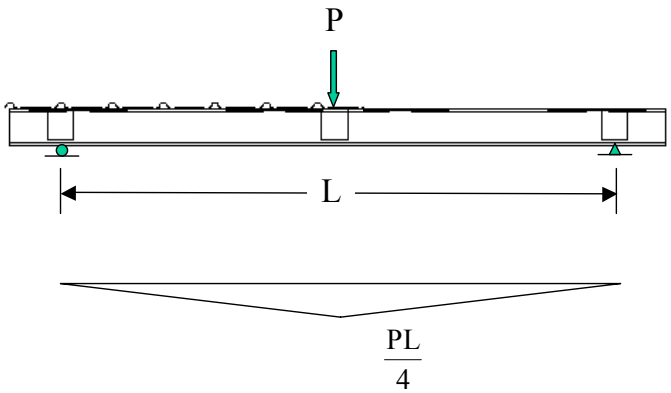

Figure 7.13 Finite element modeling strategy for moment gradient (r = 0)

7.3.2 The Finite Element Results

In Chapter 5 extended finite element analyses were carried out on a number of standard C and Z-sections, where the center part of the beams is under constant moment. The same sections are chosen here for the moment gradient analyses. Two moment gradients r = 0.5 and r = 0 were applied as described in the previous section, and depicted in Figure 7.12 and Figure 7.13.

Figure 7.14 shows the deformed shape of beam 11.5Z080 subjected to a moment gradient, r = 0.5, analyzed by the first finite element model, the material yield stress is 62 ksi. A distortional buckling wave is observed close to the load point where maximum bending moment exists. The finite element analysis shows the bending capacity of this beam is increased 15% when the moment gradient r = 0.5 is applied.

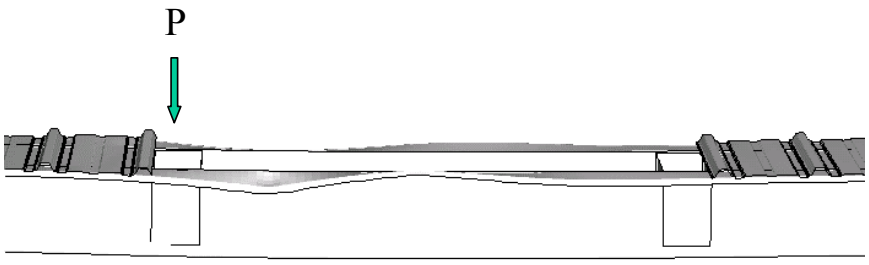

Figure 7.14 Deformed shape of 11.5Z080 beam subjected to moment gradient r = 0.5

Figure 7.15 illustrates the deformed shape of beam 8.5Z070 subjected to a moment gradient r = 0, analyzed by the second finite element model. It can be seen that a distortional buckling half-wave formed next to the load point. The finite element analysis indicates the strength of the beam is boosted 22.5% compared with the same beam under constant moment.

Figure 7.15 Deformed shape of 8.5Z070 beam subjected to moment gradient r = 0

Table 7.5 provides the geometry of analyzed C and Z-sections. Table 7.6 and Table 7.7 summarize the results by finite element model 1 (moment gradient r = 0.5) and model 2 (moment gradient r = 0) respectively. In both Table 7.6 and Table 7.7, M_{crd} is the elastic distortional buckling moment of beams under a constant moments; $M_{crd\text{-}MG}$ is the elastic distortional buckling moment of beams under the a moment gradient r, which is calculated by Equation (7.2); $M^*_{crd\text{-}MG}$ is the elastic distortional buckling moment of

beams under the a moment gradient r, determined by finite element analysis; M_{FEd} is the distortional buckling strength of beams under constant moment by the finite element analysis described in Chapter 5; $M_{FED\text{-}MG}$ is the distortional buckling strength of beams under a moment gradient r, by the finite element analysis in this chapter; M_{DSd} is the distortional buckling strength prediction by Direct Strength Method using M_{crd}; $M_{DSd\text{-}MG}$ is the distortional buckling strength prediction by Direct Strength Method using $M_{crd\text{-}MG}$, and $M^*_{DSd\text{-}MG}$ is the distortional buckling strength prediction by Direct Strength Method using $M^*_{crd\text{-}MG}$.

Table 7.5 Geometry of analyzed C and Z-sections

Specimen	h (in.)	b_c (in.)	d_c (in.)	θ_c (deg)	b_t (in.)	d_t (in.)	θ_t (deg)	r_{hc} (in.)	r_{dc} (in.)	r_{ht} (in.)	r_{dt} (in.)	t (in.)
8.5Z082	8.46	2.50	0.95	49.0	2.36	0.97	50.3	0.28	0.28	0.30	0.30	0.0806
8.5Z120	8.47	2.59	0.96	47.8	2.46	1.00	48.9	0.36	0.36	0.34	0.34	0.1176
11.5Z080	11.50	3.50	0.90	50.0	3.50	0.90	50.0	0.30	0.30	0.30	0.30	0.0800
8C097	8.04	2.09	0.58	85.1	2.07	0.53	86.3	0.28	0.28	0.29	0.28	0.0980
8.5Z070	8.50	2.50	0.90	50.0	2.50	0.90	50.0	0.25	0.25	0.25	0.25	0.0700
8Z100	8.00	2.25	0.93	50.0	2.25	0.93	50.0	0.24	0.24	0.24	0.24	0.1000
11.5Z100	11.50	3.50	0.90	50.0	3.50	0.90	50.0	0.30	0.30	0.30	0.30	0.1000
8Z050	8.00	2.25	0.93	50.0	2.25	0.93	50.0	0.24	0.24	0.24	0.24	0.0500

Note: notations refer to Figure 2.2.

Comparing M_{FEd} with $M_{FEd\text{-}MG}$ in both Table 7.6 and Table 7.7 indicates that when the beams are loaded with a moment gradient, the ultimate strength is boosted significantly. The average strength increase is 18.5% for the beams under a moment gradient r = 0.5 and 24.5% for cases with a moment gradient r = 0, compared with the beams under constant moment.

Table 7.6 Results by FE model with a moment gradient r = 0.5

Specimen	f_y (ksi)	M_y (kip-in.)	M_{crd} (kip-in.)	M_{crd-MG} (kip-in.)	M^*_{crd-MG} (kip-in.)	M_{FEd} (kip-in.)	M_{FEd-MG} (kip-in)	M_{DSd} (kip-in)	M_{DSd-MG} (kip-in)	M^*_{DSd-MG} (kip-in)
8.5Z082	33.0	97.0	164.0	181.8	187.1	94.8	107.0	90.0	92.8	93.5
8.5Z082	44.0	129.3	164.0	181.8	187.1	116.9	132.3	109.5	113.3	114.4
8.5Z082	56.6	164.9	164.0	181.8	187.1	141.3	157.9	128.3	133.1	134.5
8.5Z082	62.2	182.8	164.0	181.8	187.1	147.3	168.4	137.0	142.3	143.8
8.5Z082	73.4	215.7	164.0	181.8	187.1	164.4	186.8	152.0	158.0	159.7
8.5Z120	33.0	142.6	365.5	475.2	476.2	149.7	163.5	147.9	155.8	155.9
8.5Z120	44.0	190.2	365.5	475.2	476.2	190.3	207.9	183.2	196.1	196.2
8.5Z120	56.6	242.5	365.5	475.2	476.2	236.2	260.7	217.3	234.9	235.1
8.5Z120	62.2	268.9	365.5	475.2	476.2	248.1	273.3	233.1	252.9	253.1
8.5Z120	73.4	317.3	365.5	475.2	476.2	283.3	305.6	260.1	283.7	283.9
8.5Z092	33.0	108.0	208.9	271.6	275.1	109.5	121.0	104.3	111.6	111.9
8.5Z092	44.0	144.1	208.9	271.6	275.1	136.6	152.7	127.5	138.1	138.6
8.5Z092	56.6	183.7	208.9	271.6	275.1	165.9	183.7	149.9	163.6	164.3
8.5Z092	62.2	203.7	208.9	271.6	275.1	172.8	194.5	160.3	175.4	176.2
8.5Z092	73.4	240.3	208.9	271.6	275.1	193.2	221.1	178.1	195.7	196.6
11.5Z080	33.0	179.5	169.9	220.9	223.7	152.4	172.7	137.3	150.5	151.2
11.5Z080	44.0	239.4	169.9	220.9	223.7	182.6	210.0	164.3	181.4	182.2
11.5Z080	56.6	305.3	169.9	220.9	223.7	213.0	243.9	190.4	211.1	212.1
11.5Z080	62.2	338.6	169.9	220.9	223.7	224.3	258.0	202.5	224.9	226.0
11.5Z080	73.4	399.5	169.9	220.9	223.7	242.5	284.8	223.1	248.4	249.7
8C097	33.0	90.1	258.0	279.4	289.3	92.3	103.0	95.7	97.2	97.8
8C097	44.0	120.1	258.0	279.4	289.3	118.0	131.4	119.3	121.7	122.7
8C097	56.6	153.1	258.0	279.4	289.3	140.6	158.9	142.0	145.4	146.8
8C097	62.2	169.8	258.0	279.4	289.3	148.3	171.1	152.5	156.3	158.0
8C097	73.4	200.3	258.0	279.4	289.3	162.8	193.5	170.6	175.1	177.1
8.5Z070	33.0	86.8	119.4	133.8	137.9	81.7	92.2	75.6	78.3	79.1
8.5Z070	44.0	115.8	119.4	133.8	137.9	100.1	114.6	91.3	95.0	96.0
8.5Z070	56.6	147.6	119.4	133.8	137.9	119.0	134.9	106.5	111.1	112.4
8.5Z070	62.2	163.8	119.4	133.8	137.9	124.2	142.3	113.6	118.6	119.9
8.5Z070	73.4	193.2	119.4	133.8	137.9	136.3	155.3	125.6	131.3	132.9
8Z100	33.0	106.2	261.5	286.9	290.1	114.2	120.2	109.1	111.4	111.7
8Z100	44.0	141.6	261.5	286.9	290.1	136.4	154.0	134.9	138.4	138.9
8Z100	56.6	180.6	261.5	286.9	290.1	165.5	185.0	159.8	164.5	165.1
8Z100	62.2	200.3	261.5	286.9	290.1	173.3	201.2	171.3	176.6	177.2
8Z100	73.4	236.3	261.5	286.9	290.1	196.0	224.7	191.0	197.3	198.0
11.5Z100	33.0	223.0	270.3	304.7	319.9	205.2	227.8	186.1	193.7	196.7
11.5Z100	44.0	297.4	270.3	304.7	319.9	250	280.3	224.0	234.0	238.1
11.5Z100	56.6	382.5	270.3	304.7	319.9	293.0	331.0	262.1	274.4	279.4
11.5Z100	62.2	420.6	270.3	304.7	319.9	310.7	351.9	277.7	291.0	296.5
11.5Z100	73.42	496.2	270.3	304.7	319.9	342.4	392.4	306.8	321.8	328.0
8Z050	33.0	54.7	58.5	65.9	68.7	48.2	54.9	43.7	45.6	46.2
8Z050	44.0	72.9	58.5	65.9	68.7	58.6	67.1	52.4	54.8	55.7
8Z050	56.6	93.0	58.5	65.9	68.7	67.7	76.6	60.9	63.8	64.8
8Z050	62.2	103.2	58.5	65.9	68.7	70.6	80.1	64.8	68.0	69.1
8Z050	73.4	121.7	58.5	65.9	68.7	76.0	86.2	71.5	75.1	76.3

Note: f_y --- yield stress; M_y --- yield moment;
M_{crd} --- elastic distortional buckling moment under constant moment;
M_{crd-MG} --- elastic distortional buckling moment under a moment gradient r by Equation 7.2;
M^*_{crd-MG} --- elastic distortional buckling moment under a moment gradient r by FE model;
M_{FEd} --- distortional buckling strength under constant moment by finite element analysis;
M_{FEd-MG} --- distortional buckling strength under moment gradient r by finite element analysis;
M_{DSd} --- distortional buckling strength prediction by Direct Strength Method using M_{crd};
M_{DSd-MG} --- distortional buckling strength prediction by Direct Strength Method using M_{crd-MG};
M^*_{DSd-MG} --- distortional buckling strength prediction by Direct Strength Method using M^*_{crd-MG}.

Table 7.7 Results by FE model with a moment gradient r = 0

Specimen	f_y (ksi)	M_y (kip-in.)	M_{crd} (kip-in.)	M_{crd-MG} (kip-in.)	M^*_{crd-MG} (kip-in.)	M_{FEd} (kip-in.)	M_{FEd-MG} (kip-in)	M_{DSd} (kip-in)	M_{DSd-MG} (kip-in)	M^*_{DSd-MG} (kip-in)
8.5Z070	33.0	86.8	119.4	142.7	151.1	81.7	95.7	75.6	79.9	81.3
8.5Z070	44.0	115.8	119.4	142.7	151.1	100.1	119.3	91.3	97.1	99.0
8.5Z070	56.6	147.6	119.4	142.7	151.1	119.0	138.8	106.5	113.8	116.1
8.5Z070	62.2	163.8	119.4	142.7	151.1	124.2	146.9	113.6	121.5	124.1
8.5Z070	73.4	193.2	119.4	142.7	151.1	136.3	159.3	125.6	134.7	137.6
8C097	33.0	90.1	258.0	292.7	310.3	92.3	108.8	95.7	98.0	98.9
8C097	44.0	120.1	258.0	292.7	310.3	118.0	140.3	119.3	123.1	124.8
8C097	56.6	153.1	258.0	292.7	310.3	140.6	169.6	142.0	147.3	149.7
8C097	62.2	169.8	258.0	292.7	310.3	148.3	182.6	152.5	158.5	161.2
8C097	73.4	200.3	258.0	292.7	310.3	162.8	207.6	170.6	177.8	181.1

Note: f_y --- yield stress; M_y --- yield moment;
M_{crd} --- elastic distortional buckling moment under constant moment;
M_{crd-MG} --- elastic distortional buckling moment under a moment gradient r by Equation 7.2;
M^*_{crd-MG} --- elastic distortional buckling moment under a moment gradient r by FE model;
M_{FEd} --- distortional buckling strength under constant moment by finite element analysis;
M_{FEd-MG} --- distortional buckling strength under moment gradient r by finite element analysis;
M_{DSd} --- distortional buckling strength prediction by Direct Strength Method using M_{crd};
M_{DSd-MG} --- distortional buckling strength prediction by Direct Strength Method using M_{crd-MG};
M^*_{DSd-MG} --- distortional buckling strength prediction by Direct Strength Method using M^*_{crd-MG}.

Figure 7.16 shows a comparison of the distortional buckling prediction by the Direct Strength Method for the finite element modeling with and without moment gradient. Figure 7.16(a) illustrates the no moment gradient case, it indicates that the Direct Strength Method provides reasonable and conservative predictions for the distortional buckling failure of beams under constant moment. Figure 7.16(b) demonstrates moment gradient effect on the same beams as analyzed in Figure 7.16(a), the distortional buckling strength is increased significantly by the moment gradient, and the current design method will give overly conservative predictions (an average 1.22 FE-to-predicted ratio).

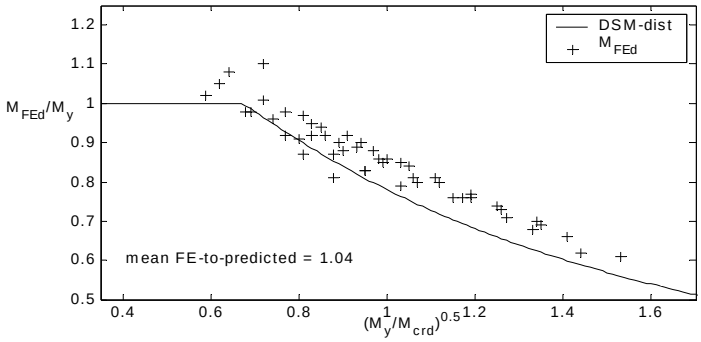

(a) no moment gradient

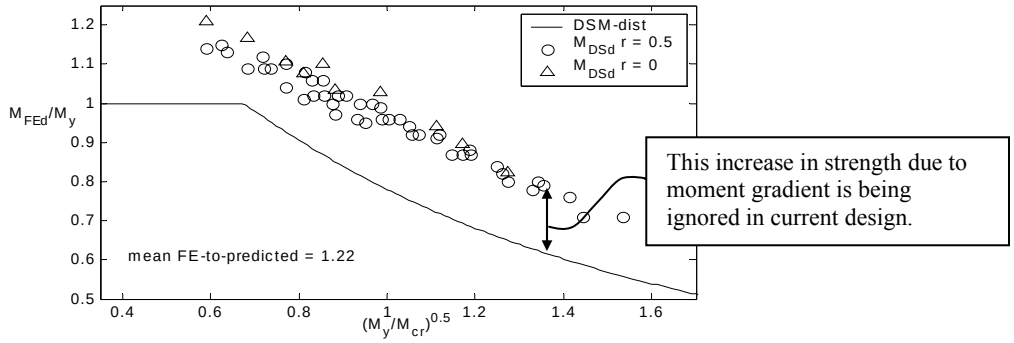

(b) observed increase due to moment gradient but no inclusion of moment gradient in strength prediction

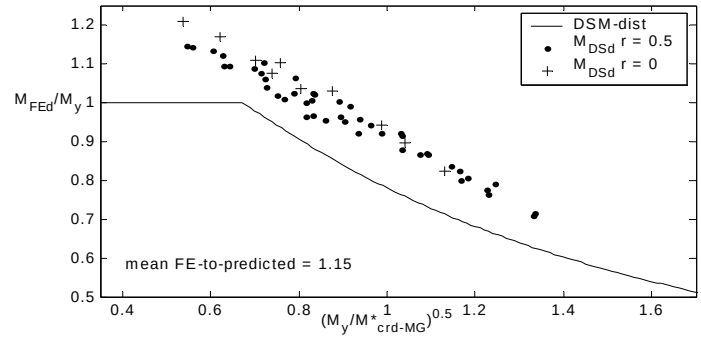

(c) moment gradient included in elastic buckling prediction and used in DSM prediction

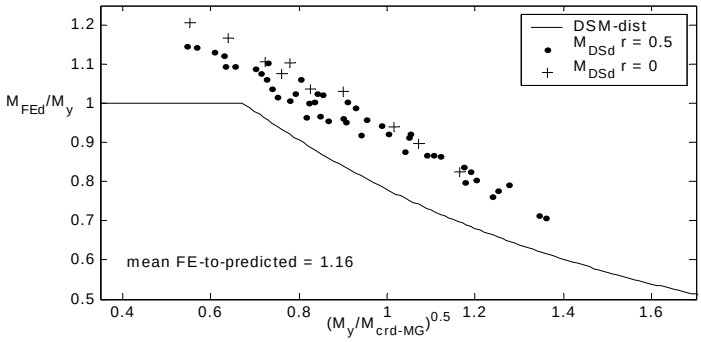

(d) simplified method (Eq. 7.2) included in elastic buckling prediction and used in DSM prediction

Figure 7.16 Comparison of the Direct Strength Method distortional buckling prediction with finite element modeling with and without moment gradient

Instead, the moment gradient effect can be included in the Direct Strength Method by using a modified (or an appropriate) elastic distortional buckling moment. Figure 7.16(c) shows the comparison of FE results with DSM using a modified elastic distortional buckling $M^*_{crd\text{-}MG}$ which is calculated by the finite element model described in Section 7.2.1 to consider the moment gradient effect. The average FE-to-DSM predicted ratio is improved to 1.15. The simplified method (Equation 7.2) can also be used to obtain the appropriate elastic distortional buckling moment, $M_{crd\text{-}MG}$, and the result is expected to be more conservative than the finite element modeling, $M^*_{crd\text{-}MG}$. Figure 7.16(d) shows a comparison of FE results with DSM using $M_{crd\text{-}MG}$, the average FE-to-predicted ratio is 1.16. The Direct Strength Method is conservative for the distortional buckling of beams subjected to a moment gradient.

Table 7.8 Comparisons of DSM predictions with FE results

		$M_{FEd\text{-}MG}/M_{FEd}$	$M^*_{DSd\text{-}MG}/M_{DSd}$	$M_{FEd\text{-}MG}/M_{DSd}$	$M_{FEd\text{-}MG}/M_{DSd\text{-}MG}$	$M_{FEd\text{-}MG}/M^*_{DSd\text{-}MG}$
FE model with r = 0.5	μ	1.13	1.06	1.21	1.15	1.14
	σ	0.02	0.03	0.06	0.05	0.05
FE model with r = 0	μ	1.25	1.07	1.29	1.22	1.20
	σ	0.04	0.02	0.06	0.04	0.04
Overall	μ	1.15	1.06	1.22	1.16	1.15
	σ	0.05	0.03	0.07	0.06	0.05

Note: μ - average; σ - standard deviation

Table 7.8 summarizes the comparisons of finite element results with the predictions of the Direct Strength Method. On average, for the analyzed cases, the bending capacity of beams is increased 15% due to the moment gradient ($M_{FEd\text{-}MG}/M_{FEd}$ in Table 7.8). The test-to-predicted ratio for the moment gradient case is 1.22 if the conventional Direct Strength Method is used ($M_{FEd\text{-}MG}/M_{DSd}$ in Table 7.8). By using the appropriate elastic distortional buckling moment (e.g. through Equation 7.2), the ratio is decreased to 1.16. Since Equation 7.2 is an approximate lower bound of the moment gradient curve (Figure

7.8), it gives conservative results of the elastic buckling moment. If the exact value of the elastic distortional buckling moment is used in the Direct Strength Method, the test-to-predicted is lowered to 1.15 and the results have the minimum standard deviation. The comparisons indicate that moment gradient effect is significant for most cold-formed steel beams if distortional buckling controls the failure. The Direct Strength Method works well, but is perhaps a bit conservative, for the distortional buckling strength of beams under moment gradient, if the moment gradient is considered in the determination of the elastic buckling moment.

7.4 Conclusions

The moment gradient effect on distortional buckling of cold-formed steel beams has been investigated by finite element analysis. The results show that moment gradient significantly increases both the elastic distortional buckling moment and the ultimate strength of the studied C and Z beams, and the effect could be considered in design.

The Equivalent Moment Concept was proposed and used to obtain an empirical equation for the calculation of elastic distortional buckling moment of a beam under a moment gradient. The method is verified by finite element analyses.

The previously verified nonlinear finite element model (detailed in Chapter 5) was utilized to study the distortional post-buckling behavior of cold-formed steel beams under moment gradient. The moment gradients were achieved by applying uneven loads at the two 1/3 points of the beams as originally tested (Chapters 2 and 3). The finite element results show that overly conservative predictions will be made if the moment gradient effect is ignored. It is also shown that with the appropriate elastic buckling moments, the

Direct Strength Method is a conservative predictor of the increased strength due to moment gradient in distortional buckling. The elastic distortional buckling moment under a moment gradient can be determined by finite element analysis, or by the empirical equation proposed in this chapter, Equation 7.2.

Chapter 8

Partial Restraint Effect on the Distortional Buckling of Cold-Formed Steel Beams

8.1 Introduction

Cold-formed steel structural members such as C and Z-sections are often used in roof and wall systems where the member supports a steel panel. In a traditional through-fastened roof system, the steel panel is directly fastened to the flanges of a C or Z-section by screws, and therefore significant lateral (diaphragm) bracing is supplied to the section by the panel. However, the standing seam roof system, unlike the traditional through-fastened roof system, uses clips placed intermediately between the sections and the panel. The introduction of the clips does not allow the steel panel to provide full bracing, thus the standing seam roof system acts somewhere between fully braced and unbraced conditions (Brooks and Murray 1990).

The series of tests conduced for finding the appropriate panel fastener configuration to restrict distortional buckling (Phase 1 tests, Chapter 2, Section 2.2.4) indicate that the

screw pattern significantly influenced the bracing stiffness provided by the panel. In the test setup, a through-fastened panel with single screws spaced every 12 in. did not give sufficient restraint to the beams to preclude distortional buckling. The experiments showed that the cold-formed steel sections would gain as much as 14% bending capacity if the through-fastened panel was fully engaged and distortional buckling was restricted. Pairs of fasteners spaced 8 in. apart and on each side of the raised ribs of the panel were needed to fully engage the panel. The results are dependent on the details of the tested configuration (Chapter 2). In particular, since the load is applied at discrete points instead of directly through the panels, friction between the panel and section is not engaged. Nevertheless, the tests serve to illustrate the sensitivity of the section strength to restraint of the compression flange, a topic of much interest in this chapter.

The effect of partial restraint on distortional buckling is ignored in current design methods, including: DSM, AS/NZS 4600, and EN1993 which otherwise provide specific provisions for distortional buckling. Current design options: assuming the restraint provides full bracing regardless of its magnitude, or ignoring the restraint in all cases is not viable as the first assumption is unconservative and unsafe, and the second is uneconomical. A general provision considering the effect of partial restraint on distortional bucking is needed for design.

The first step of this research is to characterize the partial restraint effect on the elastic distortional buckling moment of cold-formed steel C or Z-sections. A simple numerical model is proposed to replace the more complicated finite element modeling. The second step is to study the post-buckling strength of partially restrained sections with nonlinear finite element analysis. Finally, design provisions accounting for partial

restraint of the compression flange in distortional bucking will be proposed as an addition to the Direct Strength Method for cold-formed steel beams.

8.2 Partial Restraint Effect on the Elastic Buckling of Sections

8.2.1 Computational Model for the Section-Panel System

8.2.1.1 Detailed Finite Element Model

The elastic buckling moment of a cold-formed steel section restrained by a fastened panel can be approximated from an eigenvalue buckling analysis by finite element (FE) packages such as ABAQUS (or ANSYS, etc.) which can include essential details of the section-panel system. A complete finite element model in ABAQUS, based on the conducted tests, was proposed and described in Chapter 5, and the model is employed here to determine the elastic buckling moment of the section-panel system.

Table 8.1 Geometry of analyzed sections

Section	h (in.)	b_c (in.)	d_c (in.)	θ_c (deg)	b_t (in.)	d_t (in.)	θ_t (deg)	r_{hc} (in.)	r_{dc} (in.)	r_{ht} (in.)	r_{dt} (in.)	t (in.)
8.5Z070	8.50	2.50	0.90	50.0	2.50	0.90	50.0	0.25	0.25	0.25	0.25	0.0700
8.5Z092	8.42	2.59	0.93	52.4	2.39	0.95	50.9	0.28	0.28	0.31	0.31	0.0897
8.5Z120	8.47	2.59	0.96	47.8	2.46	1.00	48.9	0.36	0.36	0.34	0.34	0.1176
6C054	6.03	2.05	0.55	80.7	2.04	0.54	81.9	0.27	0.26	0.28	0.25	0.0616
8C068	8.01	2.05	0.52	84.0	2.04	0.54	87.6	0.27	0.26	0.24	0.27	0.0768
8C097	8.04	2.09	0.58	85.1	2.07	0.53	86.3	0.28	0.28	0.29	0.28	0.0980

A series of FE analyses on cold-formed steel C and Z-sections with standard panel fastener configuration was performed. Table 8.1 summarizes the geometry of the analyzed C and Z-sections. The standard panel is 0.019 in. thick and 1.25 in. high at the rib; the rib repeats every 12 in., as shown in Figure 8.1. A pair of screws is placed at each

side of the panel rib, and the distance between the two screws in one pair depends on the width of the section flange. The two screws are spaced apart approximately 2.5 in. for Z-sections (Figure 8.2a) and 1.5 in. for C-sections (Figure 8.2b).

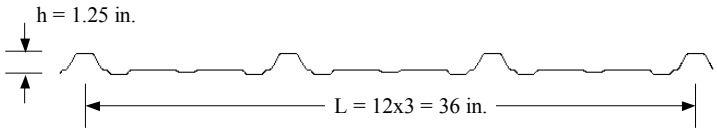

Figure 8.1 Geometry of standard steel panel

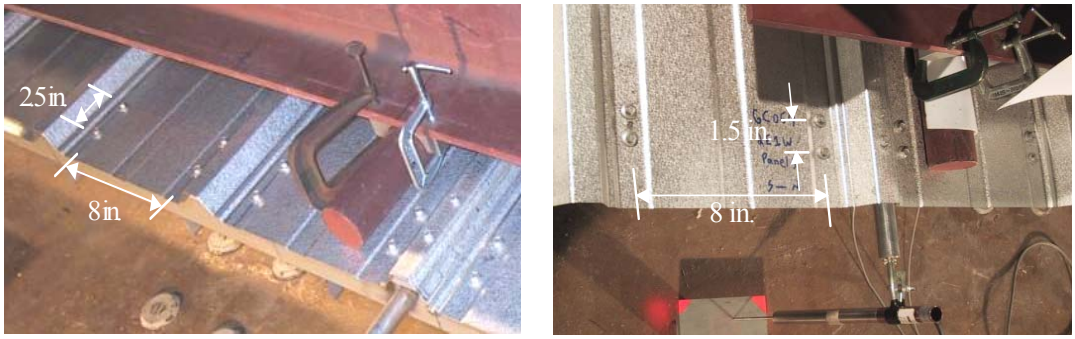

(a) Z-section (b) C-section

Figure 8.2 Selected standard panel-to-section and panel-to-panel fastener configurations

Table 8.2 Elastic buckling moments of selected section-panel systems by ABAQUS

	Section label	L_{crd} (in.)	Panel dimensions	ABAQUS		k (kip-in./rad/in.)	k* (kip-in./rad/in.)
				$M_{cr\ell}$ (kip-in.)	M_{crd} (kip-in.)		
Z section	8.5Z070	22	t = 0.019 in. h = 1.25 in.	165.3	185.4	0.70	0.71
	8.5Z092	21	t = 0.019 in. h = 1.25 in.	354.3	283.1	0.79	0.76
	8.5Z120	18	t = 0.019 in. h=1.25 in.	779.8	423.8	0.75	0.73
C section	6C054	16	t = 0.019 in. h = 1.25 in.	113.4	103.7	0.36	0.38
	8C068	15	t = 0.019 in. h = 1.25 in.	187.1	166.3	0.37	0.37
	8C097	13	t = 0.019 in. h = 1.25 in.	384.0	287.9	0.37	0.38

Note: k --- rotational stiffness obtained by comparing elastic buckling moment of ABAQUS and CUFSM;
k* --- rotational stiffness obtained by static analysis.

The elastic buckling moments of selected C and Z-sections obtained by the ABAQUS model are summarized in Table 8.2 where $M_{cr\ell}$ is the elastic local buckling moment and M_{crd} is the elastic distortional buckling moment, and include the influence of the partial restraint.

8.2.1.2 Simpler Numerical Model

A complete finite element model can include all the details of the section-panel system; however, the work required for the modeling is typically too much for everyday design. Therefore, a simpler computational model is proposed and illustrated in Figure 8.3.

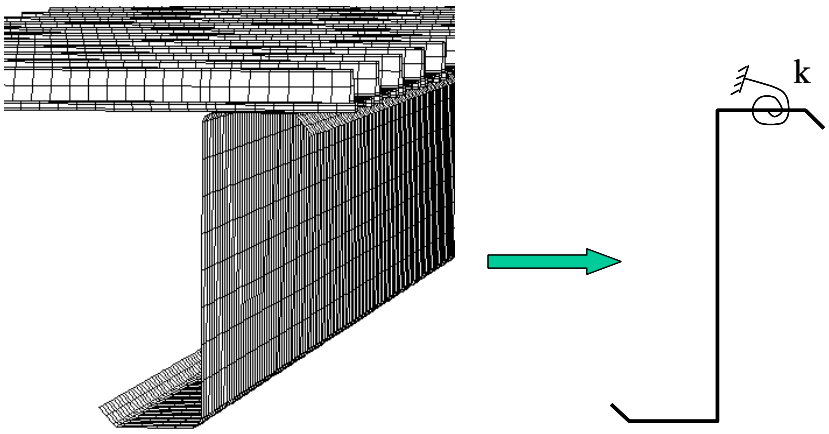

Figure 8.3 Simple computational model of section-panel system

In the simple model, the through-fastened panel is simulated by a uniform rotational spring, distributed along the length of the section, and placed on the center of the compression flange (even the panel is actually discretely fastened). For our tests, the stiffness of the rotational spring, k, should be determined according to the panel stiffness and fastener configuration. The displacement restraint provided by the panel is ignored, and only rotational restraint is selected, in part, because of the important role of the

web/flange rotational stiffness in determining the stability of the flange in distortional buckling. The model is applicable only for a section braced against lateral-torsional buckling, as here the focus is on the effect of partial restraint on the compression flange in distortional buckling.

The problem of calculating the elastic buckling moment of the section-panel system is thus simplified to one of determining the buckling moment of a section with a uniform rotational spring at the flange. The finite strip method has been shown to be efficient and accurate in analyzing such sections. The finite strip software CUFSM is employed to calculate the elastic buckling moment of cold-formed steel sections with partial restraint. Figure 8.4 shows the finite strip model in CUFSM. The section is subjected to constant moment, and a rotational spring with a foundation stiffness acts at the center of the flange, the spring is assumed grounded.

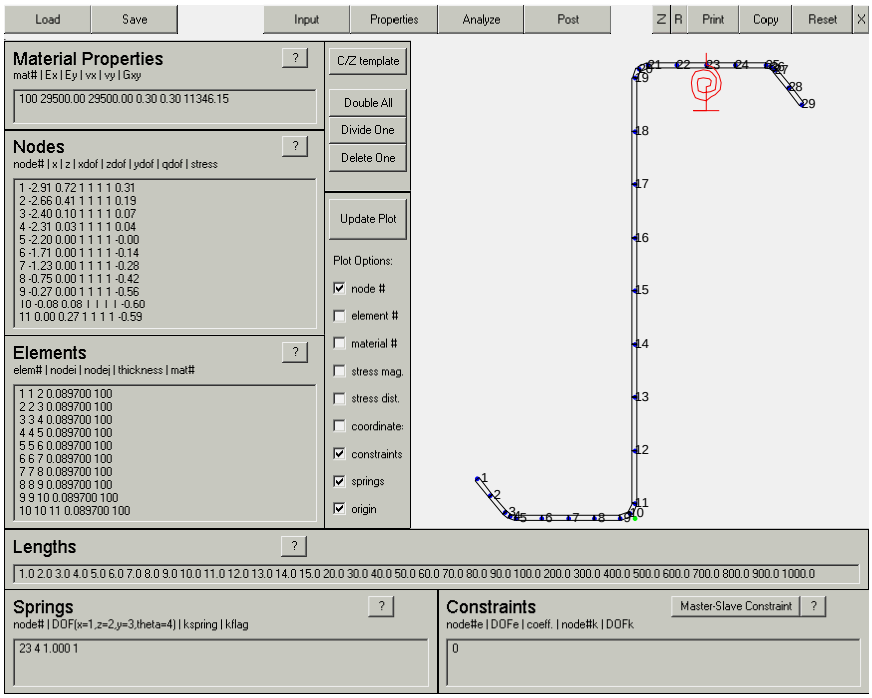

Figure 8.4 Finite strip model by CUFSM

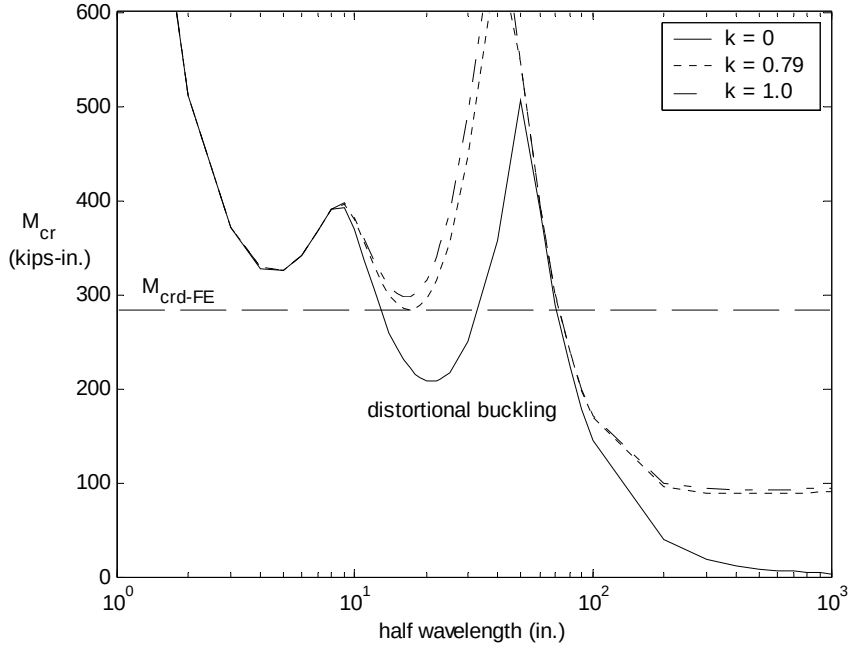

Figure 8.5 Method to determine the spring stiffness k

The rotational spring stiffness, k, in the simplified numerical model is determined by ensuring the finite strip model generates the same elastic distortional buckling moment as the complete finite element model. Figure 8.5 illustrates a series of finite strip analyses on the 8.5Z092 section with different k values. The elastic distortional buckling moment of this section is 283.1 kip-in. calculated by the complete finite element model in ABAQUS (Table 8.2, "$M_{crd\text{-}FE}$" in Figure 8.5). As shown in Figure 8.5, the finite strip model with k = 0.79 kip-in./rad/in. yields the same elastic distortional buckling moment as the finite element model, therefore 0.79 kip-in./rad/in. is the appropriate value for the simplified numerical model. The same procedure was completed on the entire analyzed C and Z-sections and the k values are included in Table 8.2. The results indicate that within this limited study for a given fastener pattern, and panel geometry, a single elastic rotational spring, with constant stiffness k, may be employed in the finite strip model to simulate the panel restraint. For the section-panel fastener configuration of the analyzed Z-sections

(Figure 8.2a), the k value is about 0.75 kip-in./rad/in. The k of section 8.5Z070 is relatively small perhaps in part due to the width of flange being less than the other Z-sections. For the fastener configuration of the C-sections (Figure 8.2b), the panel functions as a uniformly distributed rotational spring with stiffness k = 0.37 kip-in./rad/in. The developed approximate spring stiffness, k, values are not completely general, but indicate that simplified values are possible for different classes of section-panel configurations.

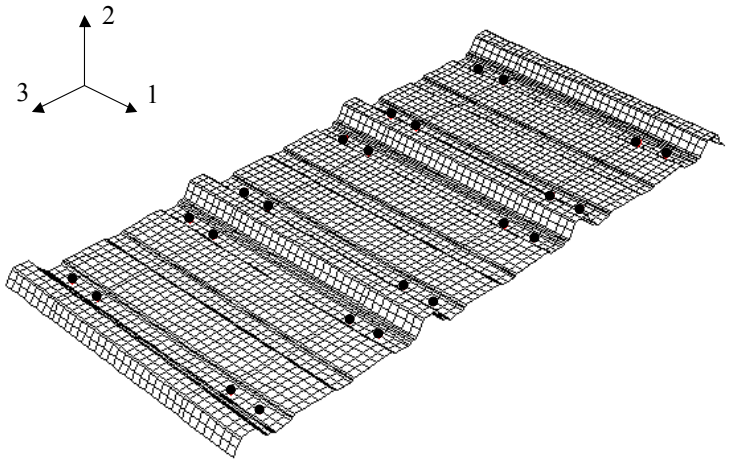

(a) Finite element mesh ("•" indicates screw locations)

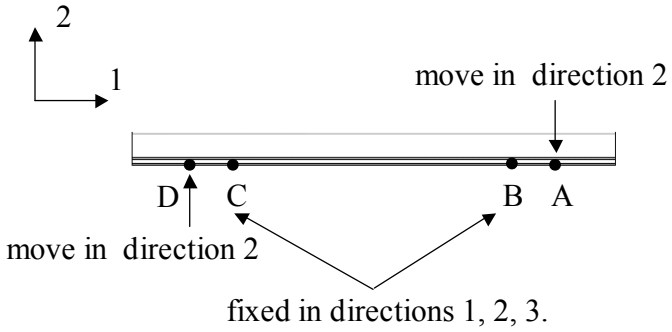

(b) Static analysis model

Figure 8.6 Panel model by ABAQUS

Instead of back-calculating the panel stiffness, a direct method is also explored. The isolated panel rotational stiffness is investigated by static analysis in ABAQUS. Figure

8.6(a) shows the finite element mesh of the model, the dots represent the nodes (screws) used to connect the panel to the section. The panel is assumed elastic with an elastic modulus of 29500 ksi and a Poisson's ratio of 0.3. In this panel model, the screws are divided into four groups: A, B, C, and D as shown in Figure 8.6(b). The screws in each group have the same coordinate in direction 1. The panel is simply supported at the nodes of group B and C. And nodes of group A and D are forced to move in direction 2 in a way similar to the actual behavior of the panel when the section buckles. As shown in Figure 8.7, the panel deforms along the buckling waves of the section, and the two sides of the panel move in an opposite way. The displacement of nodes in group A follow: $d_2 = \sin(\frac{\pi x}{L_{crd}})$ and the displacement of nodes in group D follows $d_2 = -\sin(\frac{\pi x}{L_{crd}})$, where d_2 is the nodal displacement in direction 2, x is the coordinate in direction 3, and L_{crd} is the elastic distortional buckling half-wavelength of the sections.

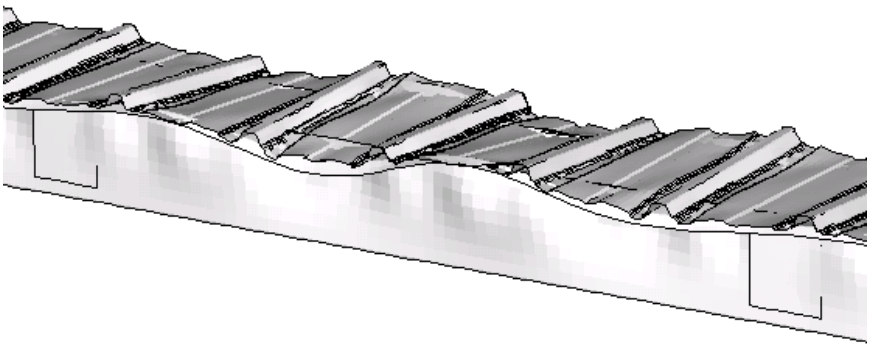

Figure 8.7 Buckled shape of a section-panel system

Figure 8.8 illustrates a typical deformed shape of the panel obtained by ABAQUS. The panel rotational stiffness obtained by the static analysis is summarized in Table 8.2 (denoted as k*). The static analysis generates close results with the analytical method

which compares the elastic distortional buckling of the complete finite section-panel model in ABAQUS with simple numerical model by CUFSM. The static analysis is an alternative method for determining the panel rotational stiffness in the section-panel systems.

Figure 8.8 Deformed shape of a panel by the static analysis

8.2.2 Partial Restraint Effect on the Elastic Buckling of Sections

A parametric study using the finite strip method (CUFSM) is conducted on the simplified spring model to demonstrate the influence of the panel rotational stiffness on the elastic buckling of C and Z-sections. The stiffness, k, is varied from 0.01 kip-in./rad/in. to 1 kip-in./rad/in., this selection is expected to fall into the range of practical panel conditions.

The elastic distortional buckling of the section-panel system can also be approximated by a closed-form solution. Schafer and Peköz (1999) developed closed-form formulae for the distortional buckling stress, f_d, of cold-formed steel C and Z-sections (Equation 8.1):

$$f_d = \frac{k_{\phi fe} + k_{\phi we}}{\tilde{k}_{\phi fg} + \tilde{k}_{\phi wg}} \tag{8.1}$$

where $k_{\phi fe}$ and $k_{\phi we}$ are the elastic rotational stiffness of the flange and web, respectively and $\tilde{k}_{\phi fg}$ add $\tilde{k}_{\phi wg}$ are the stress dependent geometric stiffness of the flange and web, (divided by stress f_d) respectively. Complete details of this expression are given in Chapter 9. The distortional buckling moment (M_{crd}) is determined by multiplying f_d times the gross section modulus (referenced to the extreme compression fiber).

Based on Equation 8.1, a closed-form formula for the distortional buckling moment f_{d-pp} of a section-panel system can be derived and expressed as Equation 8.2.

$$f_{d-pp} = \frac{k_{\phi fe} + k_{\phi we} + k_p}{\tilde{k}_{\phi fg} + \tilde{k}_{\phi wg}} = f_d + \frac{k_p}{\tilde{k}_{\phi fg} + \tilde{k}_{\phi wg}} \tag{8.2}$$

where k_p is elastic rotational stiffness of the panel. It is assumed that the panel suffers no reduction in stiffness under load (i.e. $\tilde{k}_{pg}$ is ignored).

Table 8.3 includes the elastic buckling moments for Z-sections determined by the finite strip analysis (M_{crd}) as well as the distortional buckling moments by the closed-form solution (M^*_{crd}, Equation 8.2). Figure 8.9 to Figure 8.11 provide a graphic representation of the relation between elastic buckling moment and the rotational restraint stiffness. Table 8.4 and Figure 8.12 to Figure 8.14 provide similar results for the studied C-sections. The rotational spring has essentially no influence on the elastic local buckling of both C and Z-sections, because at the center of the flange, no rotation occurs for the local buckling mode, therefore the rotational spring is not engaged. For distortional buckling, significant influence of the rotational restraint is observed, because distortional

buckling is characterized by rotation of the flange-lip component about the web-flange junction. The spring limits such rotation, and thus boosts the buckling moment of this mode. The closed-form solution (Equation 8.2) provides a good agreement with the finite strip results, particularly when the distortional buckling moment is less than the local buckling moment. For the cases when the rotational stiffness, k, is large enough to increase the distortional buckling moment above local buckling, the closed-form solution provides systematically higher results than the finite strip method. Web buckling is more involved in determining the critical moment of the section when stiffer restraint is placed on the flange, and the closed-form solution is unconservative when distortional buckling is driven by the web. The finite strip analysis is able to capture the buckling behavior of sections involving complicated interaction between the web and the flange-lip component.

Table 8.3 Elastic buckling moments of selected Z section-panel systems

k (kip-in./rad/in.)	8.5Z070			8.5Z092			8.5Z120		
	$M_{cr\ell}$ (kip-in.)	M_{crd} (kip-in.)	M^*_{crd} (kip-in.)	$M_{cr\ell}$ (kip-in.)	M_{crd} (kip-in.)	M^*_{crd} (kip-in.)	$M_{cr\ell}$ (kip-in.)	M_{crd} (kip-in.)	M^*_{crd} (kip-in.)
0.01	151.0	121.2	111.9	325.0	209.3	193.2	740.3	363.1	340.5
0.05	151.0	127.4	117.5	325.0	214.6	198.7	740.3	367.1	343.8
0.1	151.0	134.4	124.5	325.5	220.7	204.3	740.3	372.0	347.8
0.2	151.0	146.6	138.4	325.1	232.4	215.5	740.3	380.7	356.0
0.3	151.0	156.7	152.3	325.1	242.6	226.6	740.3	389.3	364.2
0.4	151.6	165.4	166.3	325.1	252.3	237.8	740.3	397.7	372.3
0.5	151.6	173.1	180.2	325.2	261.0	248.9	740.4	405.8	380.5
0.6	151.7	179.6	194.1	325.2	269.4	260.0	740.4	413.1	388.7
0.7	151.7	185.7	208.1	325.2	276.8	271.2	740.4	420.3	396.8
0.8	151.7	190.7	222.0	325.2	283.8	282.3	740.4	427.4	405.0
0.9	151.8	195.5	235.9	325.3	290.7	293.5	740.4	434.4	413.1
1	151.8	199.6	249.9	325.3	297.1	304.6	740.4	441.2	421.3

Note: $M_{cr\ell}$ --- elastic local buckling moment determined by finite strip method (CUFSM)
M_{crd} --- elastic distortional buckling moment determined by finite strip method (CUFSM)
M^*_{crd} --- elastic distortional buckling moment determined by closed-form solution (Eq. 8.2)

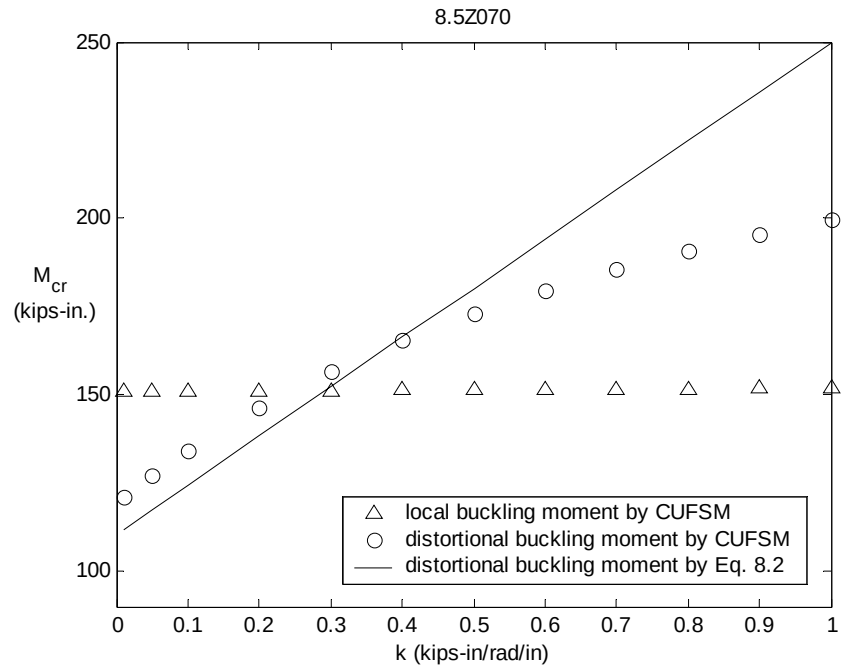

Figure 8.9 Buckling moments vs. spring stiffness for 8.5Z070 section

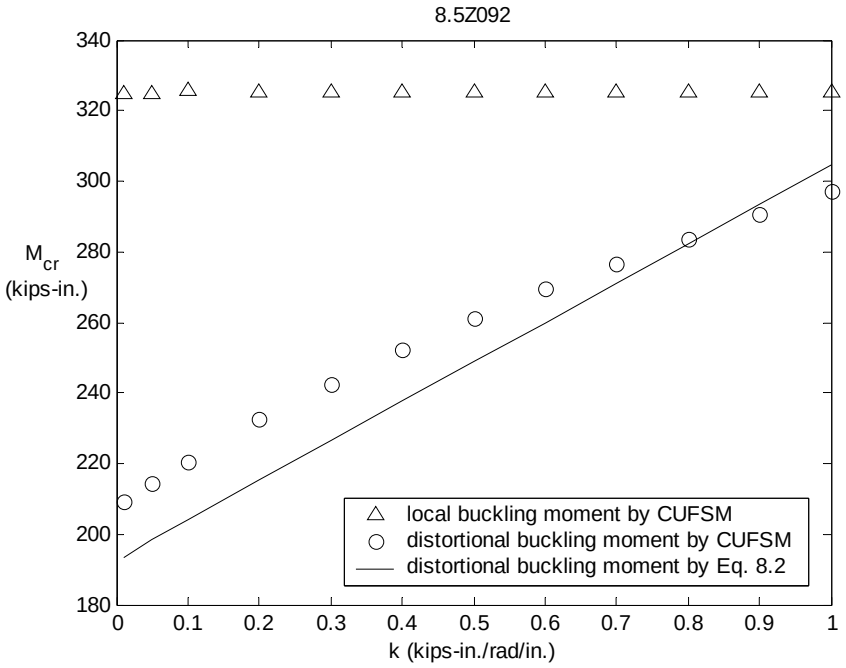

Figure 8.10 Buckling moments vs. spring stiffness for 8.5Z092 section

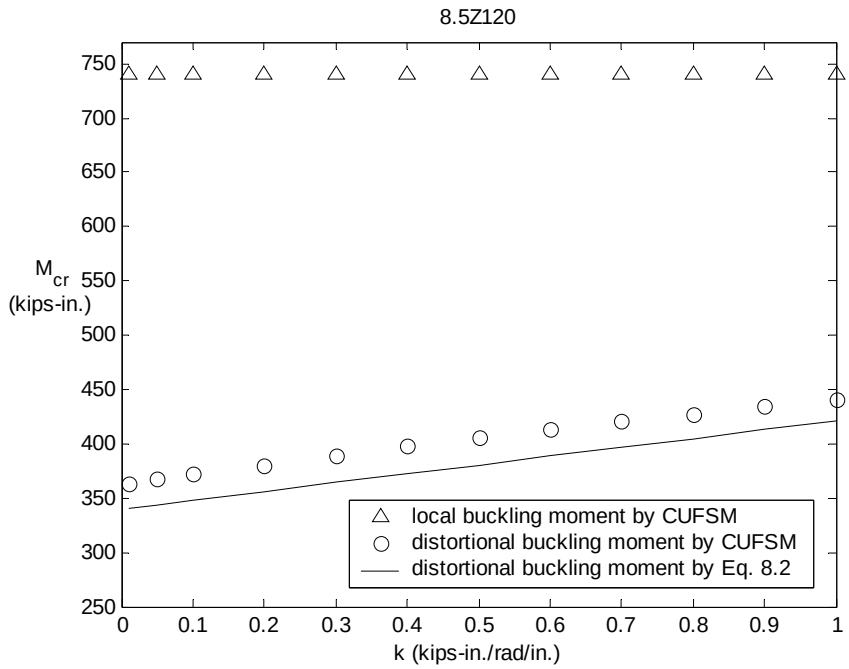

Figure 8.11 Buckling moments vs. spring stiffness for 8.5Z120 section

Table 8.4 Elastic buckling moments of selected C section-panel systems

k (kip-in./rad/in.)	6C054			8C068			8C097		
	$M_{cr\ell}$ (kip-in.)	M_{crd} (kip-in.)	M^*_{crd} (kip-in.)	$M_{cr\ell}$ (kip-in.)	M_{crd} (kip-in.)	M^*_{crd} (kip-in.)	$M_{cr\ell}$ (kip-in.)	M_{crd} (kip-in.)	M^*_{crd} (kip-in.)
0.01	106.8	77.3	68.7	171.5	139.6	128.2	362.0	259.4	237.5
0.05	106.8	81.4	72.2	171.5	143.7	132.2	362.0	262.9	241.0
0.1	106.8	86.2	76.6	171.5	148.1	137.3	362.0	267.2	245.4
0.2	106.8	94.0	85.4	171.5	156.2	147.4	362.0	274.1	254.1
0.3	106.9	100.5	94.3	171.5	162.5	157.4	362.0	282.9	262.9
0.4	106.9	106.3	103.1	171.5	168.3	167.5	362.0	289.6	271.7
0.5	106.9	110.8	111.9	171.5	172.7	177.6	362.1	296.2	280.4
0.6	106.9	115.1	120.7	171.5	176.9	187.7	362.1	302.6	289.2
0.7	106.9	118.8	129.6	171.5	180.0	197.8	362.1	307.7	298.0
0.8	107.0	121.8	138.4	171.5	182.7	207.9	362.1	312.6	306.8
0.9	107.0	124.7	147.2	171.5	184.8	218.0	362.1	317.4	315.5
1	107.0	127.5	156.0	171.5	187.8	228.0	362.1	322.1	324.3

Note: $M_{cr\ell}$ --- elastic local buckling moment determined by finite strip method (CUFSM)
M_{crd} --- elastic distortional buckling moment determined by finite strip method (CUFSM)
M^*_{crd} --- elastic distortional buckling moment determined by closed-form solution (Eq. 8.2)

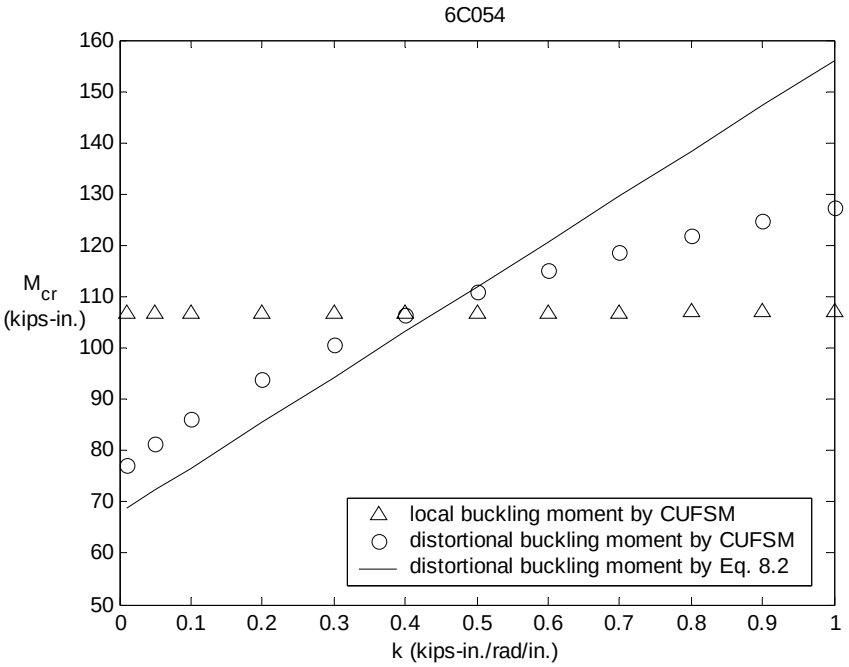

Figure 8.12 Buckling moments vs. spring stiffness for 6C054 section

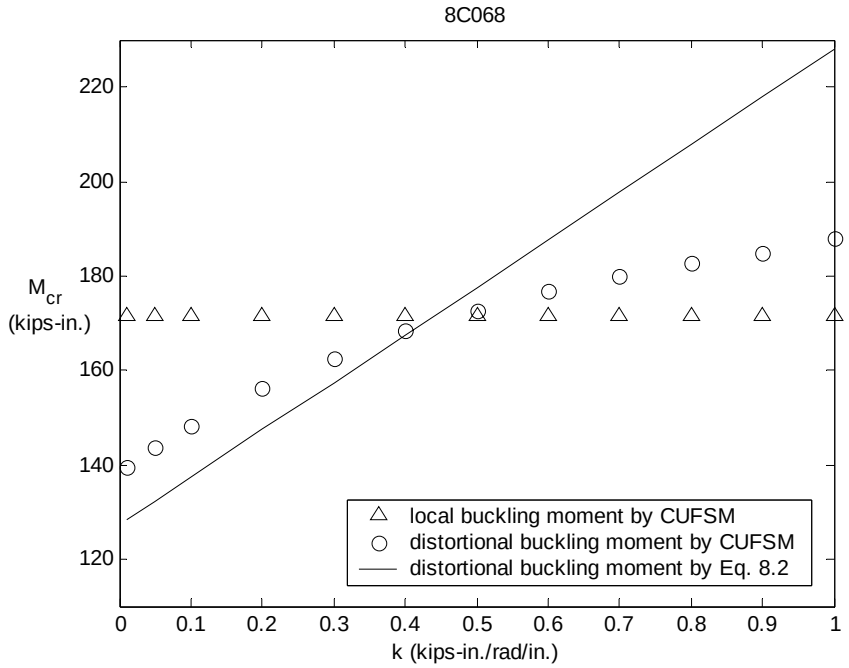

Figure 8.13 Buckling moments vs. spring stiffness for 8C068 section

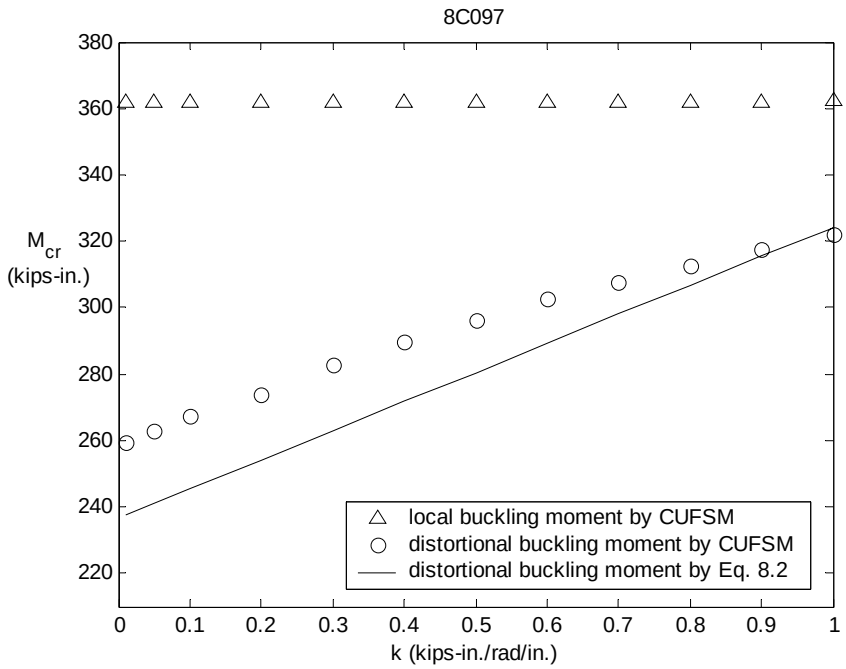

Figure 8.14 Buckling moments vs. spring stiffness for 8C097 section

8.3 Partial Restraint Effect on the Ultimate Strength of Sections

The verified finite element modeling methods of Chapter 5 were utilized to obtain the postbuckling/ultimate strength of the section-panel system. The paired sections have through-fastened steel panels on the compression flanges. Concentrated loads are applied at the 1/3 points of the beam, thus maximum moment occurs in the center 1/3 of the beam. The applied panel stiffness is varied in the analysis by changing the panel thickness and rib height. Geometric imperfections and nonlinear material behavior of the sections is considered. The section strength is compared with a modified version of the Direct Strength Method.

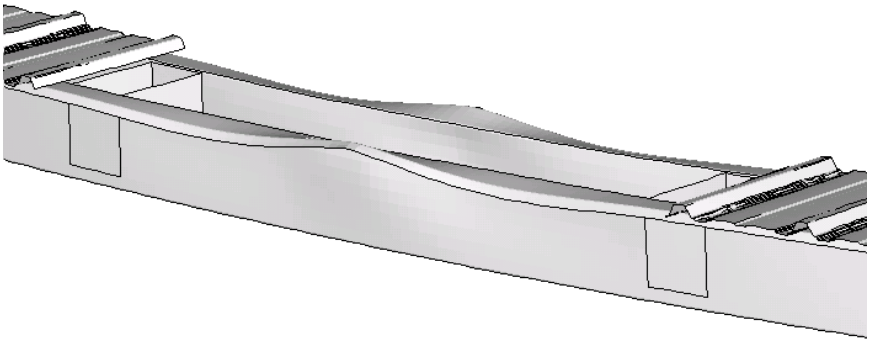

Figure 8.15 Deformed shape of 8.5Z070 with no panel in the center 1/3 region

The finite element analyses were performed on an 8.5Z070 Z-section beam and a 8C097 C-section beam. The geometry of both sections is summarized in Table 8.1. Figure 8.15 shows the deformed shape of the 8.5Z070 beam with no panel attached in the center 1/3 region, distortional buckling failure is observed, and the obtained bending capacity is 119 kip-in.

Figure 8.16 shows the deformed shape of the 8.5Z070 beam with a panel attached along the whole length. The dimensions of the panel in the center 1/3 region are 0.25 in. high and 0.019 in. thick. The distortional buckling mode is identified, however compared with the deformed shape of the beam without the panel (Figure 8.15), larger and local buckling type deformation on the web is observed for this beam with the panel. Web local buckling and flange distortional buckling combine to control the failure mechanism. The failure of the flange caused the collapse, and the obtained bending capacity is 131.1 kip-in. - a 10% increase compared with the no panel case.

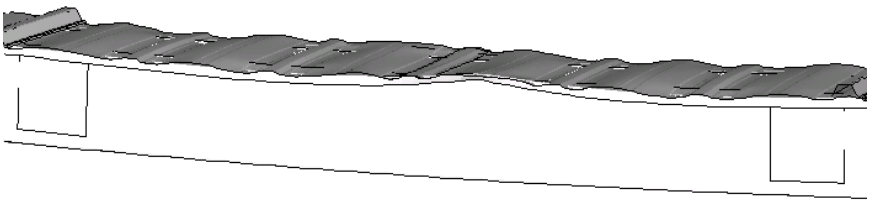

(a) Overall view

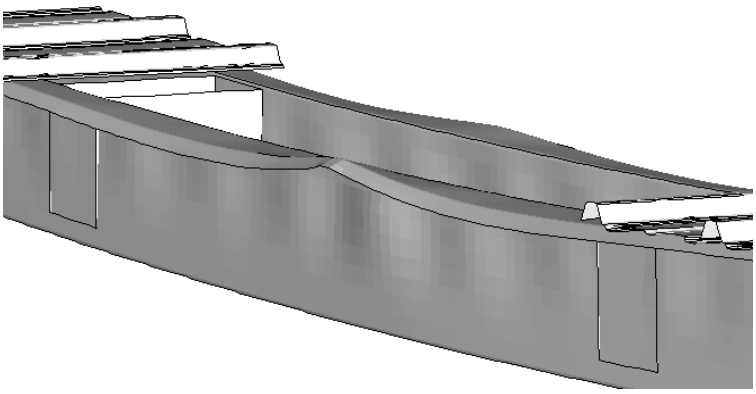

(b) Close-up view with panel removed

Figure 8.16 Deformed shape of 8.5Z070 with panel h = 0.25 in., t = 0.019 in.

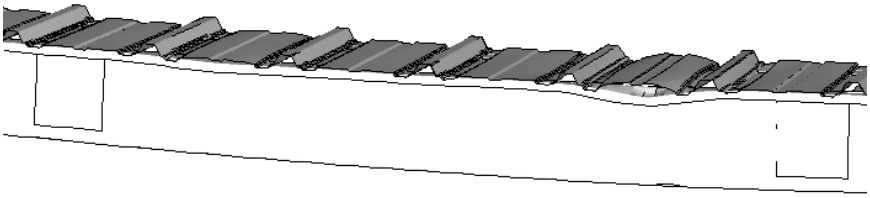

(a) Overall view

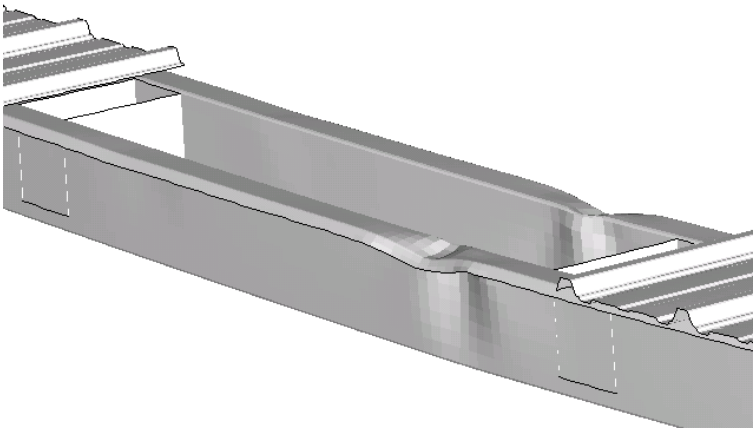

(b) Close-up view with panel removed

Figure 8.17 Deformed shape of 8.5Z070 with panel h = 1.25 in., t = 0.019 in.

Figure 8.17 illustrates the deformed shape of the 8.5Z070 beam with a standard panel (h = 1.25 in., t = 0.019 in.). Local buckling failure can be observed, and the obtained bending capacity is 134.3 kip-in. The panel restraint has significant influence on the buckling mode and the ultimate strength of cold-formed steel beams.

Table 8.5 Finite element results of the strengths of section-panel systems

Section	Panel type		k	f_y	M_y	$M_{cr\ell}$	M_{crd}	M_{FE}/M_y	$M_{DS\ell}/M_y$	M_{DSd}/M_y	M_{DSM}/M_y
	t (in.)	h (in.)	(kip-in./rad/in.)	(ksi)	(kip-in.)	(kip-in.)	(kip-in.)				
8C097	N/A	N/A	0	56.6	153.1	384.4	268.0	0.894	1.00	0.938	0.938
	0.01	0.25	0.141	56.6	153.1	385.4	270.1	0.907	1.00	0.940	0.940
	0.01	0.625	0.218	56.6	153.1	384.3	275.7	0.961	1.00	0.946	0.946
	0.019	0.625	0.372	56.6	153.1	385.4	285.7	0.981	1.00	0.955	0.955
	0.019	1.25	0.375	56.6	153.1	384.0	287.9	0.983	1.00	0.958	0.958
	0.025	1.25	0.651	56.6	153.1	386.5	305.2	0.995	1.00	0.973	0.973
	0.03	0.625	0.829	56.6	153.1	388.2	314.0	1.006	1.00	0.981	0.981
	0.03	1.25	1.368	56.6	153.1	389.3	328.8	1.004	1.00	0.993	0.993
8.5Z070	N/A	N/A	0	56.6	147.6	163.8	135.2	0.807	0.879	0.755	0.755
	0.015	0.125	0.222	56.6	147.6	164.5	148.9	0.852	0.881	0.782	0.782
	0.015	0.25	0.349	56.6	147.6	165.0	161.0	0.860	0.882	0.804	0.804
	0.019	0.25	0.460	56.6	147.6	166.0	170.0	0.888	0.883	0.820	0.820
	0.019	0.875	0.656	56.6	147.6	165.5	183.0	0.902	0.882	0.841	0.841
	0.019	1.25	0.695	56.6	147.6	165.3	185.4	0.910	0.882	0.844	0.844
	0.021	1.25	0.858	56.6	147.6	165.5	193.5	0.908	0.882	0.857	0.857

Note: M_{DSM} = minimum of $M_{DS\ell}$ and M_{DSd}.

The results of finite element analyses are summarized in Table 8.5, where $M_{cr\ell}$ and M_{crd} are the elastic local and distortional buckling moment respectively. The elastic buckling moments ($M_{cr\ell}$ and M_{crd}) are calculated by the finite element model and thus include the influence of the flange restraint. The rotational stiffness, k, is the equivalent rotational stiffness in a simple finite strip model such that the ABAQUS and CUFSM models give the same M_{crd}. M_{FE} is the ultimate strength of the section-panel system obtained by the nonlinear FE analysis of ABAQUS. The Direct Strength Method

predictions for both local buckling ($M_{DS\ell}$) and distortional buckling (M_{DSd}) failures are included in Table 8.5.

The elastic buckling results of the finite element model ($M_{cr\ell}$, M_{crd} in Table 8.5) demonstrate again that the rotational stiffness has almost no influence on the elastic local buckling moment, but great influence on the elastic distortional buckling moment.

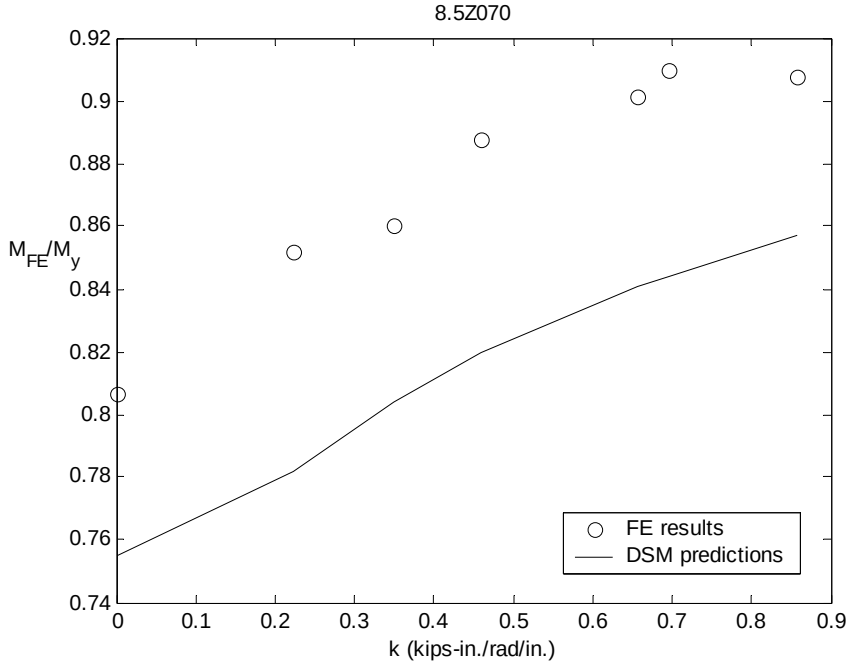

Figure 8.18 Strength of 8.5Z070 section with varied restraints on flange

Figure 8.18 illustrates the bending strength of the 8.5Z070 section with respect to the varied rotational stiffness k provided by the panel. The section's strength increases (with some scatter) when the panel becomes stiffer until the rotational stiffness reaches 0.64 kip-in./rad/in. Above this k, the bending strength no longer increases although the rotational stiffness continuously gets larger. Without the panel, or with relatively small panel restraint, distortional buckling controls the failure; and stiffer rotational restraint on flange will increase the ultimate strength. On the other hand, the rotational stiffness does

not change the ultimate strength in local buckling, thus when the restraint on the flanges is large enough and over a certain level (full restraint), the local buckling strength or yield strength will be less than the distortional buckling strength, and thus control the failure. When one designs an 8.5 in. deep, 2.5 in. wide, and 0.070 in. thick Z-section with attached panels, the panel system is required to provide an equivalent rotational stiffness of 0.64 kip-in./rad/in. to restrict the distortional buckling failure. Figure 8.18 also indicates that the modified Direct Strength Method (which employs the elastic buckling moments including restraint effects) provides conservative and reasonable predictions for the distortional buckling strength of the analyzed Z section with varied flange restraint, and DSM captures the trend as well.

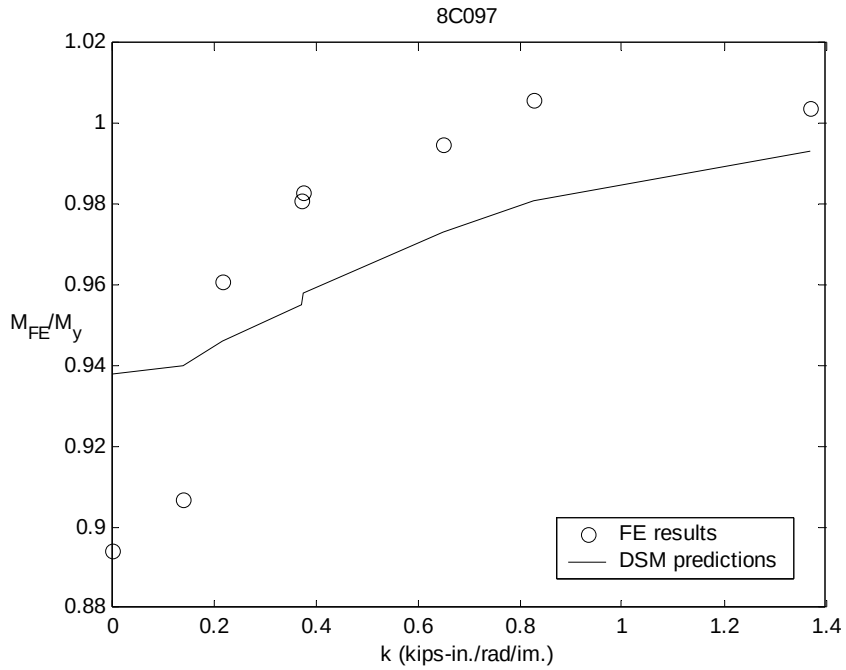

Figure 8.19 Strength of 8C097 section with varied restraints on flange

Figure 8.19 shows the rotational restraint influence on the 8C097 C-section. Similar to the 8.5Z070 Z-section, the bending capacity of 8C097 increases when the rotational restraint becomes stiffer. When the rotational stiffness is larger than 0.6 kip-in./rad/in.,

the bending capacity no longer increases and instead keeps the same value, which is equal to the yield moment of the section. When the rotational restraint is large enough, the failure changes from distortional buckling to material yielding. Since 8C097 has a much higher elastic local buckling moment than yield moment, local buckling is not expected to control the failure. Figure 8.19 also indicates that the Direct Strength Method is able to include the rotational restraint effect in the determination of ultimate strength of cold-formed steel beams. When the designer calculates the bending capacity of the analyzed C-section with flange restraint, distortional buckling strength needs to be checked if the panel provides an equivalent rotational stiffness less than 0.6 kip-in./rad/in.

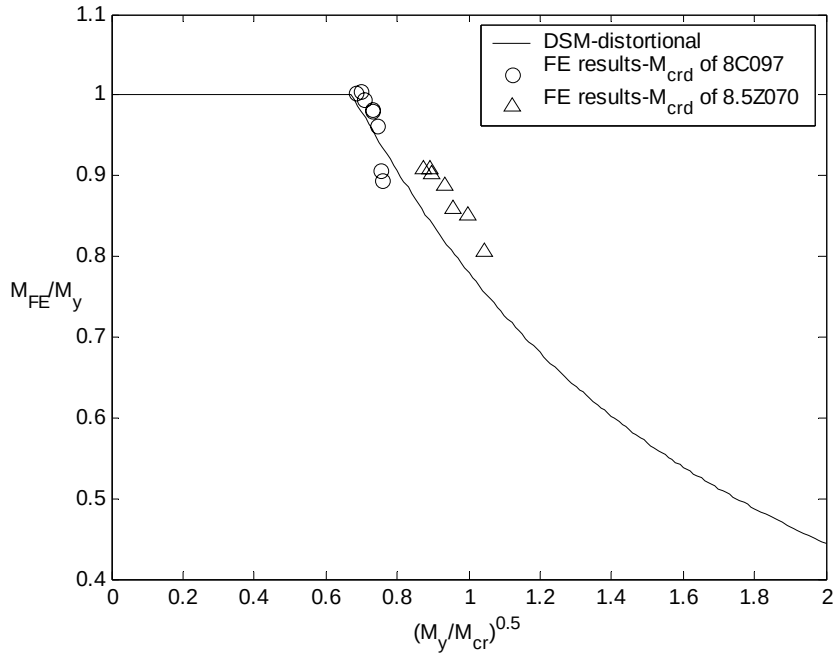

Figure 8.20 FE results vs. modified DSM predictions

Figure 8.20 illustrates a comparison of finite element results with the strength predictions by the modified Direct Strength Method for restrained distortional buckling. In the modified Direct Strength Method, the elastic buckling moment of the section with

rotational restraint is used. The results demonstrate that the predicted ultimate strength of analyzed C and Z-sections with varied flange restraint by the modified Direct Strength Method has good agreement with the results by finite element analysis, and in general the prediction is conservative and reasonable. Similar analyses on a large number of cold-formed steel beams are planned for future work (Chapter 10). Best current practice for considering the partial flange restraint effect on the distortional buckling strength is to use the exact elastic buckling moment of the section-panel system in the DSM formulae.

8.4 Conclusions

The effect of partial flange restraint on both the elastic critical moment and the ultimate strength of distortional buckling of cold-formed steel C and Z-sections was analyzed herein by the finite strip method (CUFSM) and finite element method (ABAQUS). The addition of a single rotational spring to the pure section finite strip analysis (CUFSM) was proposed for determining the elastic distortional buckling moment of the section-panel system. The simplified model was verified by finite element analysis in which the panel and fastener details are considered. It was found that the rotational restraint does not change the elastic local buckling moment of C or Z-sections, but increases the elastic distortional buckling moment. A modified closed-form solution was proposed to determine the elastic distortional buckling moment of section-panel systems, and the method works best for the sections with relatively small rotational restraint. For sections with large rotational restraint the proposed closed-form solution gives slightly unconservative results for elastic distortional buckling moment of the section-panel system.

A nonlinear finite element model in ABAQUS was employed to study the panel restraint effect on the distortional buckling strength of C and Z-sections. An 8.5Z070 Z section-panel system and an 8C097 C section-panel system were analyzed. The results show that the varied panel restraint does not change the local buckling strength, but influences the distortional buckling strength significantly, and the effect could be considered in design. A modified Direct Strength Method provides good predictions for the distortional buckling strength of the sections with partial restraints. In the modified DSM, the appropriate elastic distortional buckling moment of sections with panel restraint is used. The appropriate elastic buckling moment could be determined by a complete finite element model, or the proposed simple numerical model in which an equivalent rotational stiffness is used to simulate the panel fastener configuration.

Chapter 9

Design of Cold-Formed Steel Beams in Distortional Buckling Failure

9.1 Introduction

The buckling tests described herein (Chapters 2 and 3) and recent findings by other researchers reveal that the conventional design Specifications, including AISI (1996), CSA S136 (1994), and the main body of NAS (2001), do not fully account for distortional buckling and give unconservative strength predictions for common C and Z-sections which are braced against lateral-torsional buckling, but do not fully restrict the compression flange. Further, it is found that the Direct Strength Method is an efficient and reliable alternative to current design practice, particularly for distortional buckling where it provides an accurate strength prediction. In 2003, the Direct Strength Method was approved by the American Iron and Steel Institute Committee on Specifications and was documented as Appendix 1 of the North American Specification in January 2004.

Research summarized in Chapters 7 and 8 has demonstrated that both the moment gradient and partial restraint on the compression flange can have a strong influence on the distortional buckling strength of cold-formed steel beams, and these effects could be considered in design. In this chapter, draft design provisions are proposed to allow the designer to calculate the bending capacity of cold-formed steel beams under moment gradients and/or partial restraints. Simple closed-form solutions will be presented for this purpose.

9.2 Elastic Distortional Buckling of Beams under Uniform Moment with Unrestrained Flanges

9.2.1 Numerical Solutions

The Direct Strength Method employs strength curves for the entire section to predict the load carrying capacity. The strength curves were initiated from the Winter's curve and have been modified by a number of experimental results on cold-formed steel structural members. The current provisions of DSM for the distortional buckling of beams are presented below.

The nominal flexural strength, M_{nd}, for distortional buckling is

$$\text{for } \lambda_d \le 0.673 \qquad M_{nd} = M_y \tag{9.1}$$

$$\text{for } \lambda_d > 0.673 \qquad M_{nd} = \left(1 - 0.22\left(\frac{M_{crd}}{M_y}\right)^{0.5}\right)\left(\frac{M_{crd}}{M_y}\right)^{0.5} M_y \tag{9.2}$$

where $\lambda_d = \sqrt{M_y / M_{crd}}$; M_{crd} = critical elastic distortional buckling moment.

Therefore the elastic distortional buckling moment of cold-formed steel members is required for Direct Strength Method and it can be obtained by numerical methods such as finite element analysis (ABAQUS, ANSYS, …) or finite strip analysis (CUFSM, THINWALL, …). The elastic buckling analysis by ABAQUS and CUFSM was detailed in Chapter 5, Section 5.2.

9.2.2 Analytical Model for Distortional Buckling of Cold-Formed Steel Members

For design purposes, closed-form solutions for elastic buckling moment are often desired.

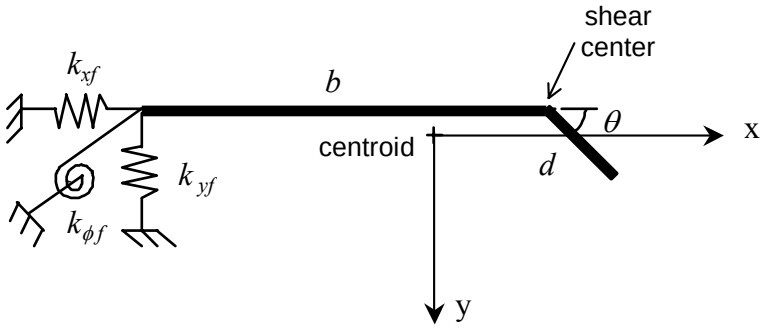

Figure 9.1 Analytical model for flange

Since distortional buckling mainly involves the rotation of the flange, the distortional buckling of an entire section can be obtained by considering the lateral-torsional buckling of the compression flange. As shown in Figure 9.1, the flange is modeled as an undistorted column with springs along one edge. The three springs represent the effect of the web. By considering equilibrium of forces in the x and y directions and equilibrium of moments about the shear center axis, the governing differential equations are:

$$EI_{yf}\frac{d^4u}{dz^4}+EI_{xyf}\frac{d^4v}{dz^4}+P\left(\frac{d^2u}{dz^2}+y_o\frac{d^2\phi}{dz^2}\right)+k_{xf}\left(u+\left(y_o-h_y\right)\phi\right)=0 \tag{9.3}$$

$$EI_{xf}\frac{d^4v}{dz^4}+EI_{xyf}\frac{d^4u}{dz^4}+P\left(\frac{d^2v}{dz^2}-x_o\frac{d^2\phi}{dz^2}\right)+k_{yf}\left(v-\left(x_o-h_x\right)\phi\right)=0 \tag{9.4}$$

$$\begin{aligned}&EC_{wf}\frac{d^4\phi}{dz^4}-\left(GJ_f-\frac{I_{of}}{A_f}P\right)\frac{d^2\phi}{dz^2}-P\left(x_o\frac{d^2v}{dz^2}-y_o\frac{d^2u}{dz^2}\right)\\&+k_{xf}\left(u+\left(y_o-h_y\right)\phi\right)\left(y_o-h_y\right)-k_{yf}\left(v-\left(x_o-h_x\right)\phi\right)\left(x_o-h_x\right)+k_{\phi f}\phi=0\,.\end{aligned} \tag{9.5}$$

where I_{xf}, I_{yf}, I_{xyf}, I_{of}, C_{wf}, J_f and A_f are section properties of the flange, k_{xf}, k_{yf}, and $k_{\phi f}$ are the springs' stiffness, x_o and y_o are the distances from the centroid to the shear center, and h_x and h_y are the distances from the centroid to the springs.

The flange model has been applied successfully by Lau and Hancock (1987) for compression members, Hancock (1995) for flexural members, Schafer and Peköz (1999) for flexural members, and Schafer (2001) for compression members. The work by Schafer and Peköz (1999) proposed an explicit treatment of the role of the elastic and geometric rotational stiffness at the web-flange junction and the method can account for the cases where the buckling is initiated by web instability. The elastic distortional buckling solutions of Schafer and Peköz (1999) are summarized here.

The elastic distortional buckling stress (f_d) is:

$$f_d=\frac{k_{\phi fe}+k_{\phi we}}{\tilde{k}_{\phi fg}+\tilde{k}_{\phi wg}} \tag{9.6}$$

where the flange rotational stiffness is:

$$k_{\phi fe} = \left(\frac{\pi}{L}\right)^4 \left(EI_{xf}\left(x_o - h_x\right)^2 + EC_{wf} - E\frac{I_{xyf}^2}{I_{yf}}\left(x_o - h_x\right)^2 \right) + \left(\frac{\pi}{L}\right)^2 GJ_f \qquad (9.7)$$

$$\widetilde{k}_{\phi fg} = \left(\frac{\pi}{L}\right)^2 \left[A_f \left(\left(x_o - h_x\right)^2 \left(\frac{I_{xyf}}{I_{yf}}\right)^2 - 2y_o\left(x_o - h_x\right)\left(\frac{I_{xyf}}{I_{yf}}\right) + h_x^2 + y_o^2 \right) + I_{xf} + I_{yf} \right] \qquad (9.8)$$

and the web rotational stiffness is:

$$k_{\phi we} = \frac{Et^3}{12\left(1-\nu^2\right)} \left(\frac{3}{h} + \left(\frac{\pi}{L}\right)^2 \frac{19h}{60} + \left(\frac{\pi}{L}\right)^4 \frac{h^3}{240} \right) \qquad (9.9)$$

$$\widetilde{k}_{\phi wg} = \frac{ht\pi^2}{13440} \left(\frac{\left(45360\left(1-\xi_{web}\right)+62160\right)\left(\frac{L}{h}\right)^2 + 448\pi^2 + \left(\frac{h}{L}\right)^2 \left(53+3\left(1-\xi_{web}\right)\right)\pi^4}{\pi^4 + 28\pi^2\left(\frac{L}{h}\right)^2 + 420\left(\frac{L}{h}\right)^4} \right) \qquad (9.10)$$

L in Equations 9.9 and 9.10 is defined as the minimum of the critical distortional buckling length L_{cr}, and the distance between restraints which restrict distortional buckling L_m. The critical buckling length L_{cr} can be determined by minimizing the elastic buckling stress f_d with respect to the L. The general solution for L_{cr} is:

$$L_{cr} = \left(\frac{4\pi^4 h\left(1-\nu^2\right)}{t^3} \left(I_{xf}\left(x_o - h_x\right)^2 + C_{wf} - \frac{I_{xyf}^2}{I_{yf}}\left(x_o - h_x\right)^2 \right) + \frac{\pi^4 h^4}{720} \right)^{1/4} \qquad (9.11)$$

The simplified expressions for the section properties of simple C or Z-sections can be found in Table 9.1.

Table 9.1 Geometric flange properties for C and Z-sections (Schafer 1997)

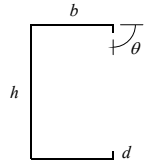	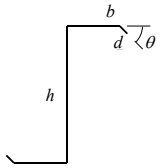
$A_f = (b+d)t$	$A_f = (b+d)t$
$J_f = \frac{1}{3}bt^3 + \frac{1}{3}dt^3$	$J_f = \frac{1}{3}bt^3 + \frac{1}{3}dt^3$
$I_{xf} = \frac{t\left(t^2b^2 + 4bd^3 + t^2bd + d^4\right)}{12(b+d)}$	$I_{xf} = \frac{t\left(t^2b^2 + 4bd^3 - 4bd^3\cos^2(\theta) + t^2bd + d^4 - d^4\cos^2(\theta)\right)}{12(b+d)}$
$I_{yf} = \frac{t\left(b^4 + 4db^3\right)}{12(b+d)}$	$I_{yf} = \frac{t\left(b^4 + 4db^3 + 6d^2b^2\cos(\theta) + 4d^3b\cos^2(\theta) + d^4\cos^2(\theta)\right)}{12(b+d)}$
$I_{xyf} = \frac{tb^2d^2}{4(b+d)}$	$I_{xyf} = \frac{tbd^2\sin(\theta)(b + d\cos(\theta))}{4(b+d)}$
$I_{of} = \frac{1}{3}tb^3 + \frac{1}{12}bt^3 + \frac{1}{3}td^3$	$I_{of} = \frac{1}{3}tb^3 + \frac{1}{12}bt^3 + \frac{1}{3}td^3$
$C_{wf} = 0$	$C_{wf} = 0$
$x_o = \frac{b^2}{2(b+d)}$	$x_o = \frac{b^2 - d^2\cos(\theta)}{2(b+d)}$
$h_y = y_o = \frac{-d^2}{2(b+d)}$	$h_y = y_o = \frac{-d^2\sin(\theta)}{2(b+d)}$
$h_x = \frac{-\left(b^2 + 2db\right)}{2(b+d)}$	$h_x = \frac{-\left(b^2 + 2db + d^2\cos(\theta)\right)}{2(b+d)}$
$b = x_o - h_x$	$b = x_o - h_x$

9.2.2 Simplified Expressions for the Closed-Form Solutions of Elastic Distortional Buckling

The closed-form solutions for the buckling stress f_d and critical buckling length L_{cr} were previously proposed and verified, but the expressions are still complicated. Therefore, simple empirical expressions are proposed herein, applicable for C and Z-sections with simple lip edge stiffeners within the following dimensional limits:

(a) $50 \leq h_o/t \leq 200$

(b) $25 \leq b_o/t \leq 100$

(c) $6.25 < D/t \leq 50$

(d) $45 \text{ deg.} \leq \theta < 90 \text{ deg.}$

(e) $2 \leq h_o/b_o \leq 8$

(f) $0.04 \leq D\sin(\theta)/b \leq 0.5$

where:

h_o = out-to-out dimension of web

b_o = out-to-out dimension of flange

D = as defined in Figure 9.2

t = base steel thickness

θ = as defined in Figure 9.2

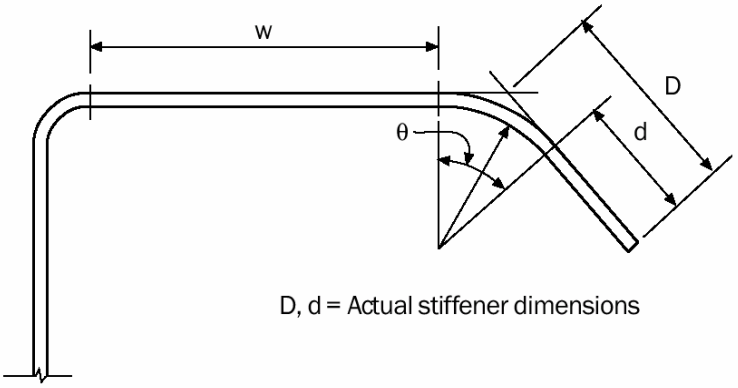

Figure 9.2 Element with simple lip edge stiffener

The proposed simple expressions are:

$$f_d = \alpha k_d \frac{\pi^2 E}{12(1-\nu^2)}\left(\frac{t}{b_o}\right)^2 \tag{9.12}$$

$$k_d = 0.5 \le 0.6\left(\frac{b_o D \sin\theta}{h_o t}\right)^{0.7} \le 8.0 \tag{9.13}$$

where α accounts for bracing as follow:

$L_m \ge L_{cr}$

$$\alpha = 1 \tag{9.14}$$

$L_m < L_{cr}$

$$\alpha = \left(\frac{L_m}{L_{cr}}\right)^{\ln\left(\frac{L_m}{L_{cr}}\right)} \tag{9.15}$$

L_m= Distance between restraints which restrict distortional buckling

L_{cr} = critical distortional buckling wavelength

$$L_{cr} = 1.2h_o\left(\frac{b_o D \sin\theta}{h_o t}\right)^{0.6} \le 10h_o \tag{9.16}$$

Efforts have been made to verify these simplified provisions by an extensive parametric study using a total of 7251 geometries of C and Z-sections. Figure 9.3 illustrates the simple expression (Equation 9.13) vs. the closed-form solution (based on Equation 9.6) for k_d (it is assumed that $L_m > L_{cr}$). The result indicates the simple expression is a lower bound approximation of the closed-form solution. Figure 9.4 illustrates the parametric study on the critical buckling length L_{cr}, and it is assumed that $L_m > L_{cr}$. It can be seen that the simple expression gives good agreement with the closed-form solution, and the approximation is conservative.

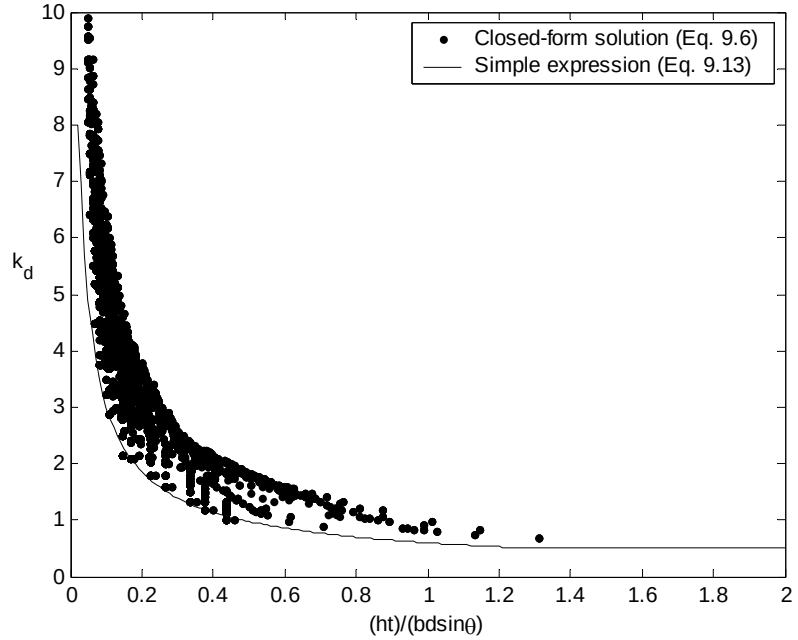

Figure 9.3 Development of simple expression for distortional buckling k_d of C and Z-section based on closed-form solution

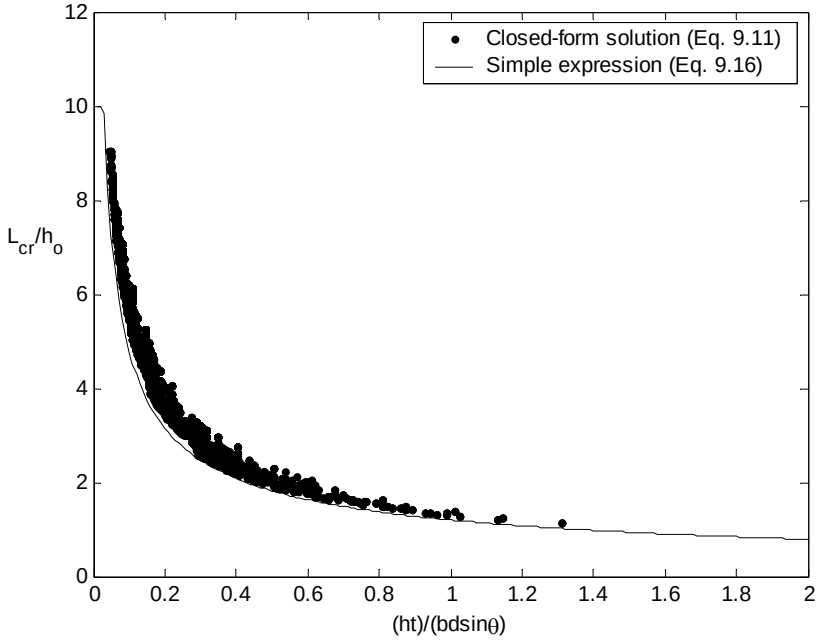

Figure 9.4 Development of simple expression for critical wavelength L_{cr} based on parametric study of C and Z-sections

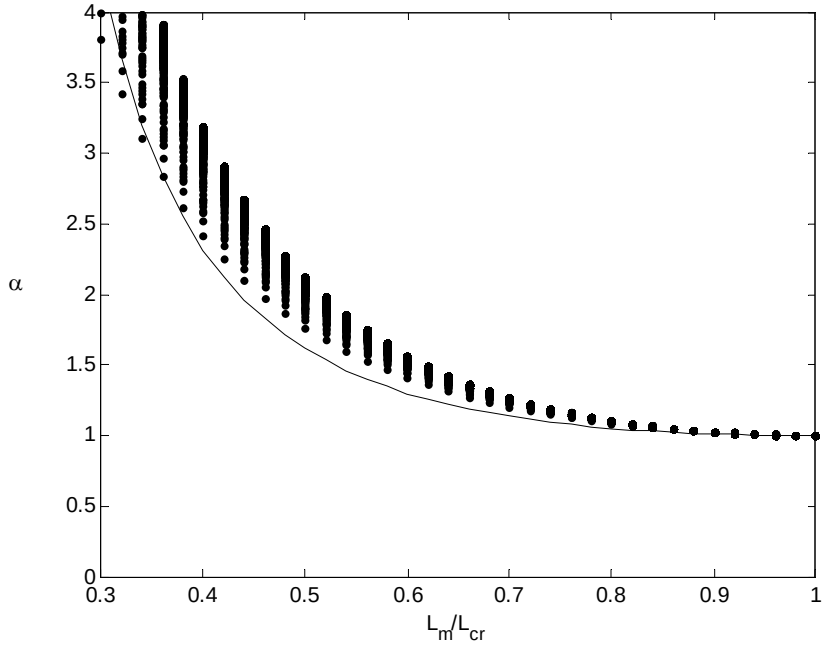

Figure 9.5 Development of simple expression for increase in f_d for bracing at length shorter than the critical wavelength, based on parametric study of C and Z-sections

Figure 9.5 shows the parametric study for the increase in f_d due to a shorter unrestricted length (L_m) than the critical distortional buckling wavelength (L_{cr}). The simple expression provides a conservative approximation of the closed-form solution for the factor α. Table 9.2 gives a summary of the simple expressions vs. closed-form solution. On average, the simple expressions are conservative in the prediction of elastic distortional buckling moment.

Table 9.2 Summary of simple expression to closed-form solution ratios

	Simple expression to closed-form solution		
	f_d	L_{cr}	α
Average	1.55	1.21	1.17
Standard deviation	0.27	0.08	0.13

9.2.2.2 Performance of Hand Solution against Experimental Results

Figure 9.6 illustrates the comparison of the Direct Strength Method predictions with three different methods for the elastic distortional buckling moment (M_{crd}): finite strip method (CUFSM), closed-form solution (Equation 9.6), and the simplified expression (Equation 9.12). The analyzed C and Z-sections include the tested specimens in the Phase 2 tests (Chapter 3) and the sections for the extended finite element analyses (Chapter 5).

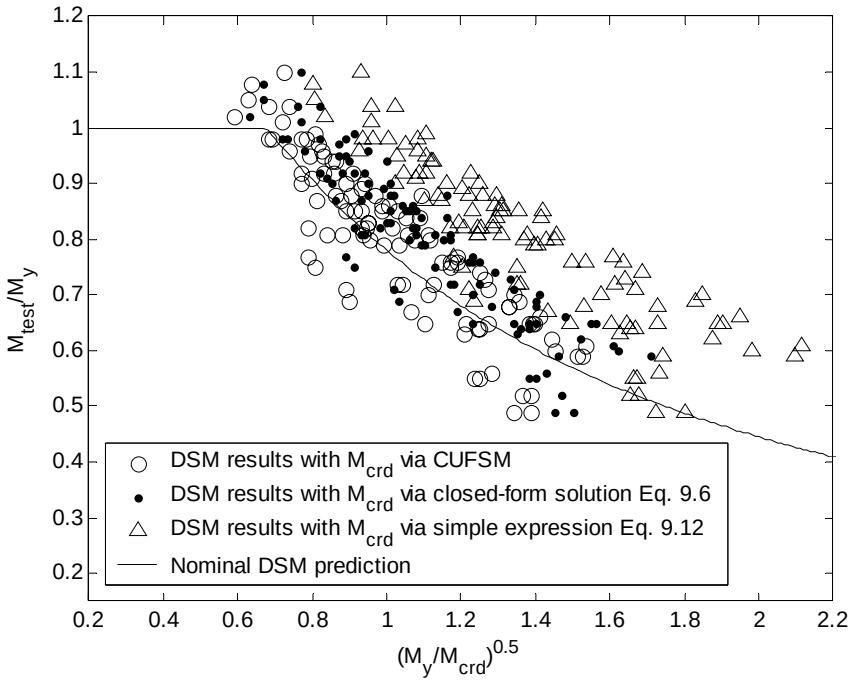

Figure 9.6 Comparison of DSM predictions with different M_{crd}

Figure 9.6 indicates that the DSM predictions using the closed-form solution for elastic buckling moment (M_{crd}) are close to the results by DSM using CUFSM for M_{crd}, but slightly more conservative. The DSM predictions with the simplified expression for M_{crd} are much more conservative than the other two methods. Table 9.3 summarizes the statistical results for all three predictions. All methods provide conservative predictions

compared with the test results and the finite element results. Both the finite strip method and closed-form solution work well for the distortional buckling strength and thus are recommended. The proposed simple expression is much more efficient, however an average 26% conservative prediction is observed in this research, as such it is useful primarily only as a first design check.

Table 9.3 Summary of test-to-predicted ratio for DSM

	Test to DSM prediction ratio		
	M_{crd} via CUFSM	M_{crd} via closed-form solution	M_{crd} via simple expression
Average	1.03	1.08	1.26
Standard deviation	0.07	0.09	0.11

9.3 Design Provisions for the Effects of Moment Gradient and Partial Restraint.

9.3.1 Design Provisions for Moment Gradient Effect

Research summarized in Chapter 7 demonstrates that moment gradient has a significant influence on the distortional buckling of cold-formed steel beams. Beams under a moment gradient have higher bending capacity than the same beams under constant moment. The effect could be considered in design. The research also indicates that the Direct Strength Method still works well for the beams subjected to a moment gradient if the elastic distortional buckling under the moment gradient is calculated properly.

The elastic distortional buckling moment of beams under a moment gradient can be determined by finite element analysis, such as ABAQUS or ANSYS software. However,

hand solutions are desired for design purposes. In Chapter 7, an empirical equation (Equation 7.2) accounts for the moment gradient, and is based on a parametric study of C and Z-sections. Therefore, the closed-form solution (Equation 9.6) as well as the simple expression (Equation 9.16) can be modified by multiplying by a factor β to take into account the moment gradient effect. The modified formulae are listed below: Equation 9.17 for closed-form solution, and Equation 9.18 for the simplified expression.

$$f_d = \beta \frac{k_{\phi fe} + k_{\phi we}}{\tilde{k}_{\phi fg} + \tilde{k}_{\phi wg}} \tag{9.17}$$

$$f_d = \alpha\beta k_d \frac{\pi^2 E}{12(1-\nu^2)}\left(\frac{t}{b_o}\right)^2 \tag{9.18}$$

$$\text{where } \beta = 1.0 \le 1 + 0.4(L_d/L_m)^{0.7}(1 - M_1/M_2)^{0.7} \le 1.3 \tag{9.19}$$

$|M_2|>|M_1|$;

M_1/M_2 is positive for single curvature;

M_2 and M_1 are the largest moments at the distance between restraints which restrict distortional buckling.

9.3.2 Design Provisions for Effect of Partial Restraint

Research summarized in Chapter 8 indicates that the partial restraint on compression flanges has significant influence on the ultimate strength as well as the buckling mode of cold-formed C and Z-sections which are laterally braced to restrict lateral-torsional buckling. The effect of partial restraint on the ultimate distortional buckling strength could be considered in the Direct Strength Method by using an appropriate elastic distortional buckling moment in which the partial restraint is considered.

The appropriate elastic distortional buckling moment can be obtained by a complete finite element method (Chapter 8, Section 8.2). A simple numerical model is proposed in Chapter 8 to calculate the elastic distortional buckling moment of sections with partial restraint on the compression flanges. The simple model adopts a rotational spring to represent the flange restraint and the finite strip method works well for this simple model. A hand solution is also proposed in Chapter 8 for the elastic distortional buckling subjected to partial restraint. The closed-form solution for distortional buckling could be modified accordingly, as expressed in Equation 9.20.

$$f_d = \beta \frac{k_{\phi fe} + k_{\phi we} + k_p}{\tilde{k}_{\phi fg} + \tilde{k}_{\phi wg}} \tag{9.20}$$

where k_p is the elastic rotational stiffness provided by the panel.

However, the results of Chapter 8 indicate the modified closed-form solution works best only when the distortional buckling moment is lower than the local buckling moment. For sections with large rotational stiffness, the modified closed-form solution may be somewhat unconservative, therefore the finite strip method is recommended for such cases.

9.4 Conclusions

The previously derived closed-form solution and the newly proposed simplified expressions for the elastic distortional buckling moment of cold-formed steel C and Z-sections in bending were presented in this chapter. An extensive parametric study was conducted to develop and verify simplified expressions for the buckling coefficient, k_d,

critical buckling length, L_{cr}, and factor, α, which accounts for the increase in buckling moment caused by unbraced lengths shorter than the critical half-wavelength. The proposed simplified expressions give conservative approximations to the closed-form solution and are expected to be useful in preliminary design.

The predictions of the Direct Strength Method with three different methods for the elastic buckling moment (M_{crd}) are compared with both the distortional buckling tests (Chapter 3) and extended finite element analyses (Chapter 5). It is shown that DSM results with M_{crd} via both CUFSM and the closed-formed solution have good agreement with the test results. DSM with the simplified expressions for M_{crd} provide a conservative prediction of the ultimate distortional buckling strength for the analyzed C and Z-sections.

The effect of moment gradient and partial restraint on distortional buckling are discussed herein. The Direct Strength Method allows the designer to take those effects into account by using an appropriate elastic buckling moment. A simple empirical equation is proposed for the closed-form solution to account for the moment gradient effect. For the partial restraint effect, a closed-form solution is also proposed for design proposes. A draft design ballot for consideration by the AISI Committee on Specification is presented in Appendix B.

Chapter 10

Summary and Recommendations

10.1 Summary

This dissertation presents a comprehensive set of research efforts including experimental investigations, finite element analyses, and the development of design provisions, with a concentration on distortional buckling of cold-formed steel (CFS) structural members in bending.

Two series of full-scale, four-point bending tests are conducted to explore the post-buckling behavior of CFS beams. In the first series of tests, also called the local buckling tests, two C or Z-sections are paired together by four steel tubes and fully braced to ensure that the beams fail in the local buckling mode. Five existing design specifications AISI (1996), CSA S136 (1994), AS/NAZ (1996), EN1993 (2002), NAS (2001) and the Direct Strength Method (DSM 2004) are analyzed by the experimental results. It is shown that all the design methods give good agreement with the local buckling test results, but the AISI (1996) predictions are found equal to or systemically higher than the

predictions by CSA S136 (1994). Among the considered methods, DSM provides the best test-to-predicted ratio.

In the second series of tests, named the distortional buckling tests, the same industry standard C and Z-sections are used. The testing setup is kept the same, but the through-fastened panel is removed from the compression flanges in the middle third of the beam, this allows distortional buckling (and local buckling) to occur while lateral-torsional buckling remains restricted. The distortional buckling mechanism is observed for all the tested Z beams and most C beams, while local buckling and local-distortional mixed buckling mechanisms are observed for some C beams. The tests demonstrate a significant loss in the ultimate strength when compared with the results from the local buckling tests of the same members. The predictions by AISI (1996), CSA S136 (1994) and NAS (2001) are unconservative for distortional buckling failures. On the other hand, distortional buckling predictions by DSM and AS/NZS 4600 have good agreement, while the test results of Eurocode EN1993 is, on average, 4% unconservative.

Based on the bending tests, finite element modeling is performed in ABAQUS. The shell element S4R is selected for the section, panel and tube; and solid element C3D8 for the loading beam. Material nonlinearity and geometric imperfections are considered in the FE modeling. The geometric imperfection is obtained by the summation of local and distortional buckling shapes with magnitudes determined according to observed statistical cumulative distribution function (CDF) values (Schafer and Peköz 1998b). The FE model is verified by comparing the experiment results with two FE analyses; one with a 25% CDF and second with a 75% CDF imperfection magnitude. The comparisons show that the bending strengths of the tested beams are well bounded by the two FE analyses, and

the average results of two simulations have an expected 100% of the real values for the local buckling failures with a standard deviation of 6%; and 102% for the distortional buckling failures with a standard deviation of 8%. The verified FE analysis with 50% CDF geometric imperfections is extended to study a number of C and Z-sections which are not examined in the two series of physical tests.

Since distortional buckling occurs at wavelengths intermediate to local and lateral-torsional buckling, moment gradient may have an influence on the buckling behavior. Further, it has been found that the behavior of the compression flange generally characterizes the distortional buckling of sections. Moment gradient on the section creates stress gradient on the flange, therefore research is conducted focusing on the stress gradient effect on the buckling of thin plates. A numerical method based on the energy method is developed to determine the elastic buckling stress of both stiffened and unstiffened thin plates with elastic rotational restraint along one longitudinal edge. The buckling coefficient, k, values of the stiffened and unstiffened elements under a stress gradient are given. The results indicate that stress gradient increases the buckling stress at the maximum loaded edge of plates. For stiffened elements, thin plates with four edges simply supported or fixed, the influence is limited. Thus, the moment gradient has little effect on the local buckling of beams consisting of stiffened elements. On the other hand, the stress gradient has significant influence on unstiffened elements: thin plates with three simply supported or fixed longitudinal edges and one free longitudinal edge. Thus, moment gradient may have a significant effect on beams with unstiffened elements. A nonlinear finite element model is developed to study the post-buckling/ultimate strength of thin plates under stress gradients. Consistent with the findings for the elastic buckling

behavior; the stress gradient has limited influence on the strength of the stiffened elements, but has great influence on the unstiffened elements. It is also found that the strength prediction by Winter's equation works well for the thin plates under a stress gradient if the elastic buckling stress considers the stress gradient effects. This is the case despite the fact that the observed stress distributions are not consistent with typical effective width assumptions. The elastic buckling coefficients for the stress gradient cases are summarized in this thesis.

The effect of stress gradient on unstiffened elements leads to a study of the moment gradient influence on the distortional buckling of cold-formed steel beams. Finite element analysis by ABAQUS is utilized to explore the elastic buckling as well as the post-buckling behavior of cold-formed steel C and Z-sections in bending. The results indicate that moment gradient increases the distortional buckling capacity significantly and the Direct Strength Method gives conservative but reasonable strength predictions for distortional buckling failures of beams subjected to moment gradients. For the method to not be overly conservative, the moment gradient should be considered in the calculation of the elastic buckling moment. An empirical equation to determine the elastic buckling moments, involving moment gradient effects, is proposed by a parametric study.

The partial compression flange restraint effect on the distortional buckling of beams is studied by both tests and finite element analysis. Three tests on cold-formed steel Z beams with varied panel fastener details are conducted in the Phase 1 tests. The ultimate strength of cold-formed steel beams is sensitive to the restraint of the compression flange. Finite element analyses are performed to investigate the partial restraint influence to both elastic buckling and post-buckling behavior of section-panel systems with a focus on

distortional buckling. The results indicate that partial restraint increases the distortional buckling moment, but has limited influence on local buckling. The Direct Strength Method can predict the distortional buckling strength of sections with partial restraint if an appropriate elastic buckling moment is used. The calculation of the appropriate elastic buckling moment should consider the partial restraint effect, and it can be obtained by a complete finite element model or by a simplified numerical method as proposed in Chapter 8. A closed-form solution based on the simple method is proposed with a limit on its usage. The finite strip method, in general, works well for the simplified numerical method.

Chapter 9 provides support for draft design provisions to account for the effect of moment gradient as well as partial restraint, on the distortional buckling of cold-formed steel C and Z-sections in bending. Further, simplified expressions for the closed-form solution of elastic distortional buckling moment of commonly used C and Z-sections are developed and verified herein for design proposes.

Among other things, the results summarized in this dissertation demonstrate that the Direct Strength Method is a general design concept for the distortional buckling of cold-formed steel members. By employing the elastic buckling of the whole section, the Direct Strength Method can account for a variety of loading and boundary conditions, as well as the interaction between components and one section. These factors can have significant influence on the instability of cold-formed steel structures, and could be considered in design.

10.2 Recommendations for Future Research

Many problems remain unaddressed in the fields of behavior, computational modeling, and design of thin-walled, cold-formed steel structures. Some subjects could be studied immediately and most have promising outcomes. Those topics include:

- Experimental investigation on the moment gradient influence is worth performing. The finite element simulations in this dissertation have shown a significant effect on distortional buckling due to the moment gradient, and design provisions to account for this effect are proposed. A series of flexural tests are necessary to examine these design provisions. The tests can employ the same setup of the distortional buckling tests described in Chapter 3, but the load is expected to be placed at one 1/3 points so that a moment gradient (r = 0.5) could be achieved at the center region of the beam.

- The moment gradient effect caused by uneven end moments has been studied herein. However the moment gradient effect by distributed loads and other loading situations is also worthy of further research. In those cases the moment gradient is no longer linear, and the maximum moment may occur inside the length of beams, therefore the end moments and the maximum inside moment are expected to be included in the closed-form solutions. Extensive finite element analysis and experiments are desired to investigate this subject.

- Experimental investigation on the partial restraint influence is in need. The partial restraint situation commonly exists in practice. The design recommendation herein accounts for this effect based on finite element simulations alone. Tests are

necessary to verify the proposed method. In fact, a small series of tests focusing on the partial restraint has been conducted in the local buckling tests to determine the restraint configuration. Similar tests could be performed on a large variety of cold-formed steel C and Z-sections. Partial restraints can be achieved practically by changing the fastener configurations and/or changing the panel thickness.

- The elastic buckling moments of the section-panel system are required in the proposed design method, a numerical method for calculating the elastic buckling is proposed in this dissertation. However, extensive finite element analysis is desired to study the standard bracing systems - then the suggested rotational spring stiffness for the practical bracing configurations can be given for designer.

- Distortional buckling of cold-formed steel sections in bending is studied herein, research on distortional buckling of cold-formed steel section in compression is in great need as well. Similar to the work for beams, tests, finite element analyses and design provision proposal on cold-formed steel columns could be performed in the near future. Sections with intermediate stiffeners in the web are of particular interest since they are more prone to distortional buckling.

More and more complicated cross-section geometry, the interaction between buckling and yielding, and significant strength sensitivity to imperfections make the full understating of buckling behavior of thin-walled, cold-formed steel structures a great challenge to researchers. There are still numerous difficult and interesting topics that need to be explored, the author would like to continue on an enjoyable journey of research in the field of cold-formed steel structures.

References

ABAQUS (2001). ABAQUS Version 6.2., ABAQUS, Inc. Pawtucket, RI, USA. (www.abaqus.com)

AISI (1946). "Specification for the Design of Light Gauge Steel Structural Members 1946", American Iron and Steel Institute. Washington, DC, USA.

AISI (1996). "Specification for the Design of Cold-Formed Steel Structural Members. 1996", American Iron and Steel Institute. Washington, DC, USA.

AISI (2001). "AISI Standard for Cold-formed Steel Framing", American Iron and Steel Institute. Washington, DC, USA.

AS/NZS 4600 (1996). "AS/NZS 4600: 1996 Cold-Formed Steel Structures Standards",Australia and the Australian Institute of Steel Construction.

ASTM (2000). "E8-00, Standard Test Methods for Tension Testing of Metallic Material", American Society for Testing and Materials. Pennsylvania, USA.

Bambach, M. R., Rasmussen, J. R. (2002). "Effective Widths of Unstiffened Elements Under Combined Compression and Bending", *Proceedings of the 16th International Specialty Conference on Cold-Formed Steel Structures*, Orlando, FL, USA.

Cheung, Y.K. (1997). "Finite Strip Method in Structural Analysis", Pergamon Press, New York, USA.

Crisfield, M.A. (1981). "A Fast Incremental/Iteration Solution Procedure that Handles `Snap-Through´", *Computers and Structures*, vol.13, pp. 55–62, 1981.

CSA S136 (1994). "Cold-Formed Steel Structural Members S136-94", Canadian Standards Association. Rexdale, Ontario, Canada.

CUFSM (2001). CUFSM Version 2.5, by Ben Schafer, Department of Civil Engineering, Johns Hopkins University. http://www.ce.jhu.edu/bschafer/cufsm/

Desmond T.P., Peköz, T. and Winter, G. (1981). "Edge Stiffeners for Thin-Walled Members", *Journal of the Structural Division*, ASCE, February 1981.

DSM (2004). "Appendix 1 of the North American Specification for the Design of Cold-formed Steel Structural Members", American Iron and Steel Institute. Washington, DC, USA.

Elhouar, S., Murray, T.M. (1985). "Adequacy of Proposed AISI Effective Width Specification Provisions for Z- and C-Purlin Design", *Fears Structural Engineering Laboratory,* FSEL/MBMA 85-04, University of Oklahoma, Norman, Oklahoma, USA.

EN1993 (2002). "European Standard EN1993-1-3. Eurocode 3: Design of steel structure", European Committee for Standardization.

Ellifritt, D. S., Glover, R.L., and Hren, J.D. (1997). "Distortional Buckling of Channels and Zees Not Attached to Sheathing", Report for the American Iron and Steel Institute.

Ellifritt, D. S., Glover, R.L., and Hren, J.D. (1998). "A Simplified Model for Distortional Buckling of Channels and Zees in Flexure", *Proceedings of the 14th International Specialty Conference on Cold-Formed Steel Structures*, St. Louis MO., October 15-16.

Elhajj, N. (2001). "Designing Homes Using Cold-Formed Steel Framing", NAHB Research Center, Upper Marlboro, MD, USA.

Hancock, G.J., Rogers, C.A., Schuster, R.M. (1996). "Comparison of the Distortional Buckling Method for Flexural Members with Tests", *Proceedings of the 16th International Specialty Conference on Cold-Formed Steel Structures*, 125-140, St. Louis, MO, USA.

Hancock, G.J. (1977). "Local, Distortional and Lateral Buckling of I-Beams", *Research Report*, School of Civil Engineering, University of Sydney. Australia, R312.

Hancock, G.J. (1978). "Local, Distortional and Lateral Buckling of I-Beams", *Journal of the Structural Division*, ASCE. 104(11).

Hancock, G.J. (1994). "Design of Cold-Formed Steel Structures (To Australian Standard AS 1538-1988)", 2nd Edition, Australian Institute of Steel Construction, North Sydney, Australia.

Hancock, G.J. (1995). "Design for Distortional Buckling of Flexural Members", *Proceedings of the Third International Conference on Steel and Aluminum Structures*, Istanbul, Turkey.

Hancock, G.J., Rogers, C.A., Schuster, R.M. (1996). "Comparison of the Distortional Buckling Method for Flexural Members with Tests", *Proceedings of the 13th*

International Specialty Conference on Cold-Formed Steel Structures, 125-140, St. Louis, MO.

Kalyanaraman, V., Peköz, T., and Winter, G. (1972). "Performance of Unstiffened Compression Elements", *Department of Structural Engineering Report*, Cornell University, NY, USA.

Kalyanaraman, V., Peköz, T., and Winter, G. (1977). "Unstiffened Compression Elements", *Journal of the Structural Division*, ASCE, vol. 103, Sept. 1977.

Kalyanaraman, V., Peköz, T. (1978). "Analytical Study of Unstiffened Element", *Journal of the Structural Division*, ASCE, vol. 104, Sept. 1978.

Lau, S.C.W., Hancock, G.J. (1987). "Distortional Buckling Formulas for Channel Columns", *Journal of Structural Engineering*, ASCE, 113(5), 1987.

Libove, C., Ferdman, S., Reusch, J. (1949). "Elastic Buckling of A Simply Supported Plate under A Compressive Stress that Varies Linearly in the Direction of Loading", *NACA Technical Notet,* No. 1891. National Advisory Committee for Aeronautics, Washington, 1949.

Lundquist, E., Stowell, E. (1942a). "Critical Compressive Stress for Flat Rectangular Plates Supported along All Edges and Elastically Restrained against Rotation along the Unloaded Edges", *NACA Report* No. 733, NACA Langley Memorial Aeronautical Laboratory (Langley Field, Va, United States), 11 pp., 1942.

Lundquist E., Stowell E. (1942b). "Critical Compressive Stress for Outstanding Flanges", *NACA Report No. 734,* National Advisory Committee for Aeronautics, Washington, 1942.

MATLAB (2001). MATLAB v6.0 for Windows, the Mathworks, Inc.

Moreyra, M.E. (1993). "The Behavior of Cold-Formed Lipped Channels under Bending", M.S. Thesis, Cornell University, Ithaca, New York, USA.

NAS (2001). "North American Specification for the Design of Cold-Formed Steel Structural Members", American Iron and Steel Institute, Washington, DC, USA

Peköz, T. (1986). "Development of a Unified Approach to the Design of Cold-Formed Steel Members", *Proceedings of the 8th International Specialty Conference on Cold-Formed Steel Structures*, University of Missouri-Rolla, November 11-12, 1986

Rogers, C.A., Schuster, R.M. (1995). "Interaction Buckling of Flange, Edge Stiffener and Web of C-Sections in Bending", *Research Into Cold Formed Steel*, Final Report of CSSBI/IRAP Project, Department of Civil Engineering, University of Waterloo, Waterloo, Ontario, Canada.

Rogers, C.A., Schuster, R.M. (1997). "Flange/web distortional buckling of cold-formed steel sections in bending", *Thin-Walled Structures,* Vol. 27, No. 1, 13-29, 1997.

Powell,G., Simons, J. (1981). "Improved Iterative Strategy for Nonlinear Structures", *International Journal for Numerical Methods in Engineering*, vol.17, pp. 1455–1467, 1981.

Ramm, E. (1981). "Strategies for Tracing the Nonlinear Response Near Limit Points", *Nonlinear Finite Element Analysis in Structural Mechanics*, Edited by E. Wunderlich, E. Stein, and K. J. Bathe, Springer-Verlag, Berlin, Germany.

Schafer, B.W. (1997). "Cold-Formed Steel Behavior and Design: Analytical and Numerical Modeling of Elements and Members with Longitudinal Stiffeners", Ph.D. Dissertation, Cornell University, Ithaca, NY, USA.

Schafer, B.W., Peköz, T. (1998a). "Direct Strength Prediction of Cold-Formed Steel Members using Numerical Elastic Buckling Solutions", *Proceedings of the 14th International Specialty Conference on Cold-Formed Steel Structures*, St. Louis, MO, UAS.

Schafer, B.W., Peköz, T. (1998b). "Computational Modeling of Cold-Formed Steel: Characterizing Geometric Imperfections and Residual Stresses", Elsevier, *Journal of Constructional Steel Research.* 47 (3) 193-210.

Schafer, B.W., Peköz, T. (1999). "Laterally Braced Cold-Formed Steel Flexural Members with Edge Stiffened Flanges", *Journal of Structural Engineering,* ASCE, 125(2) 118-127, 1999.

Schafer, B.W. (2001). "Thin-Walled Column Design Considering Local, Distortional and Euler Buckling", *Proceedings of Annual Technical Session and Meeting, Structural Stability Research Council*, May 8–12, 2001. Ft. Lauderdale, FL, USA.

Schafer, B.W. (2002). "Local, Distortional, and Euler Buckling in Thin-walled Columns". *Journal of Structural Engineering*., ASCE, 128(3) 289-299, 2002.

Schafer, B.W., Trestain, T. (2002). "Interim Design Rules for Flexure in Cold-Formed Steel Webs", *Proceedings of the 16th International Specialty Conference on Cold-Formed Steel Structure*s, Orlando, FL, USA.

Schuster, R.M. (1992). "Testing of Perforated C-Stud Sections in Bending", *Report for the Canadian Sheet Steel Building Institute*, University of Waterloo, Waterloo Ontario.

Shan, M., LaBoube, R.A., Yu, W. (1994). "Behavior of Web Elements with Openings Subjected to Bending, Shear and the Combination of Bending and Shear", *Civil Engineering Study Structural Series*, 94-2, Department of Civil Engineering, University of Missouri-Rolla, Rolla, Missouri.

Timoshenko, S.P., Gere, J.M. (1961). "Theory of Elastic Stability", Second Edition, McGrqw-Hill Book Co., 1961.

Von Karman, T., Sechler, E. E., and Donnell, L. H. (1932). "The Strength of Thin Plates in Compression", *Transactions*, ASME, vol. 54, APM 5405

Willis, C.T., Wallace, B. (1990). "Behavior of Cold-Formed Steel Purlins under Gravity Loading", *Journal of Structural Engineering*, ASCE, 116(8).

Winter, G., (1947) "Strength of Thin Steel Compression Flanges", *Transactions of ASCE*, Paper No. 2305, Trans., 112, 1.

Yu, C., Schafer, B.W. (2002). "Local Buckling Tests on Cold-Formed Steel Beams", *Proceedings of the 16th International Specialty Conference on Cold-Formed Steel Structures*, Orlando, FL, USA

Yu, C., Schafer, B.W. (2003a). "Local buckling Test on Cold-Formed Steel Beams", *Journal of Structural Engineering,* ASCE 129 (12) 1596-1606.

Yu, C., Schafer, B.W. (2003b). "Analysis and Testing of Cold-Formed Steel Beams", Advances in Structures: Steel, Concrete, Composite and Aluminum - ASSCCA'03, Sydney, Australia.

Yu, C., Schafer, B.W. (2004a). "Distortional Buckling Tests on Cold-Formed Steel Beams", *Proceedings of the 17th International Specialty Conference on Cold-Formed Steel Structures*, Orlando, FL, USA.

Yu, C., Schafer, B.W. (2004b). "Stress Gradient Effect on the Buckling of Thin Plates", *Proceedings of the 17th International Specialty Conference on Cold-Formed Steel Structures*, Orlando, FL, USA.

Yu, W.W. (2001). "Cold-Formed Steel Design", Third Edition, John Wiley & Sons, Inc., New York, NY, USA.

Appendix A

Experimental Data

Local Buckling Test 8.5Z120-3E2W (panel fastener type C)

Specimen	h (in.)	b_c (in.)	d_c (in.)	θ_c (deg.)	b_t (in.)	d_t (in.)	θ_t (deg.)	r_{hc} (in.)	r_{dc} (in.)	r_{ht} (in.)	r_{dt} (in.)	t (in.)	f_y (ksi)	f_u (ksi)	M_{test} (kips-in.)
8.5Z120-3	8.44	2.58	0.96	47.2	2.46	0.99	48.9	0.36	0.36	0.35	0.35	0.1183	61.3	84.27	280
8.5Z120-2	8.47	2.59	0.96	47.8	2.46	1.00	48.9	0.36	0.36	0.34	0.34	0.1180	60.1	82.56	280

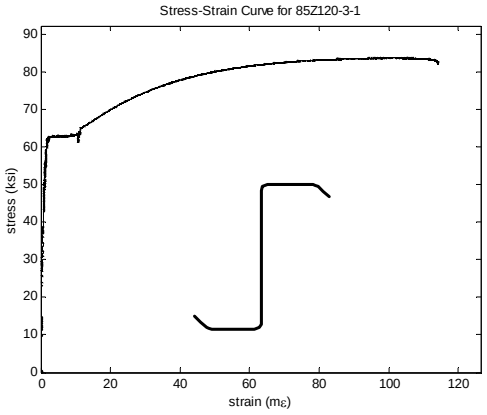

(a)

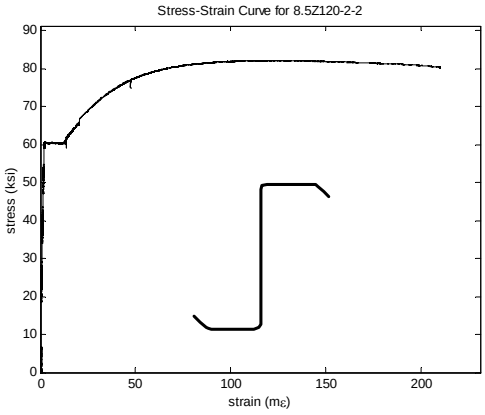

(b)

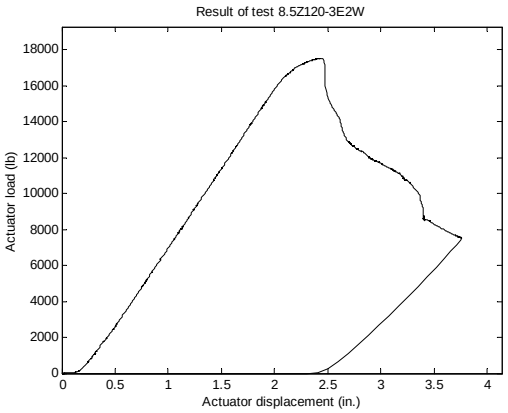

(c)

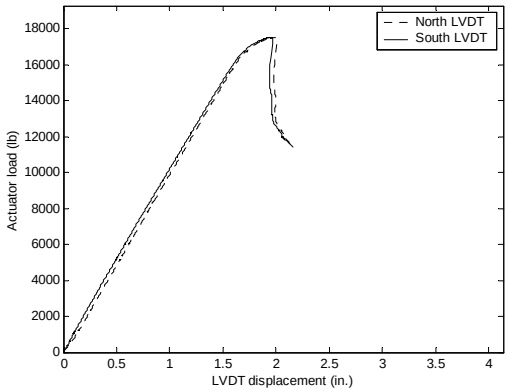

(d)

(e)

(f)

(a) material stress vs. strain of 8.5Z120-3; (b) material stress vs. strain of 8.5Z120-2; (c) actuator load vs. displacement; (d) actuator load vs. displacements of LVDTs; (e, f) pictures of collapse mechanism.

Local Buckling Test 8.5Z105-2E1W (panel fastener type C)

Specimen	h (in.)	b_c (in.)	d_c (in.)	θ_c (deg.)	b_t (in.)	d_t (in.)	θ_t (deg.)	r_{hc} (in.)	r_{dc} (in.)	r_{ht} (in.)	r_{dt} (in.)	t (in.)	f_y (ksi)	f_u (ksi)	M_{test} (kips-in.)
8.5Z105-2	8.48	2.66	0.95	50.5	2.36	0.95	48.7	0.32	0.32	0.34	0.34	0.1040	68.8	91.3	268
8.5Z105-1	8.42	2.69	0.97	50.7	2.36	0.91	48.7	0.31	0.31	0.34	0.34	0.1050	66.8	89.1	268

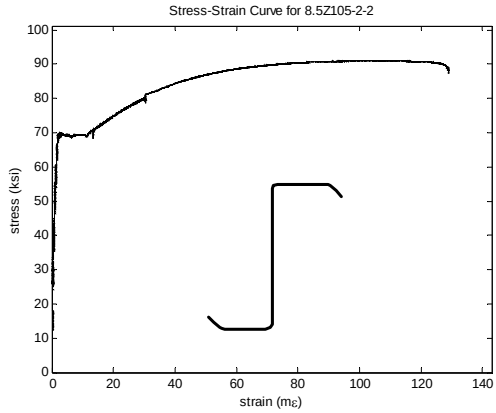

(a)

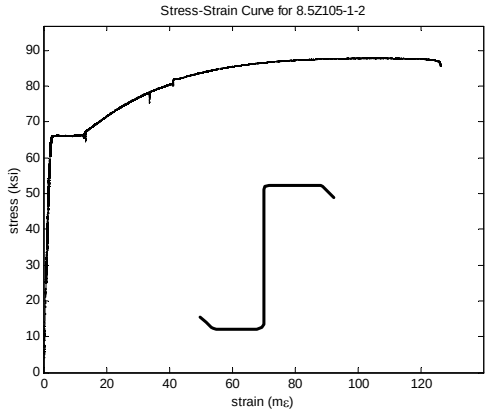

(b)

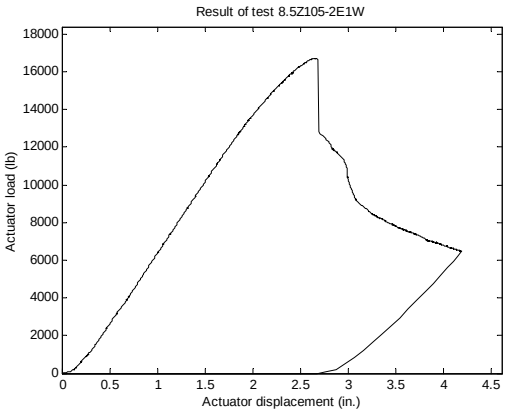

(c)

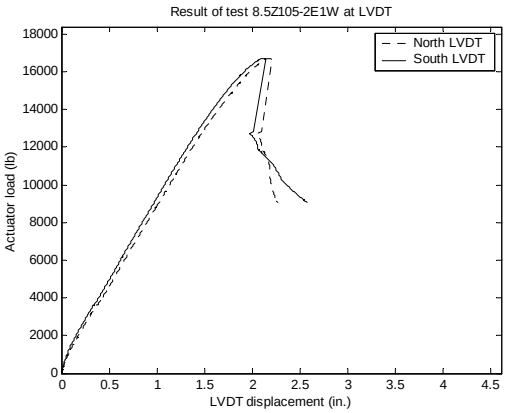

(d)

(e)

(f)

(a) material stress vs. strain of 8.5Z105-2; (b) material stress vs. strain of 8.5Z105-1; (c) actuator load vs. displacement; (d) actuator load vs. displacements of LVDTs; (e, f) pictures of collapse mechanism.

Local Buckling Test 8.5Z092-4E2W (panel fastener type C)

Specimen	h (in.)	b_c (in.)	d_c (in.)	θ_c (deg.)	b_t (in.)	d_t (in.)	θ_t (deg.)	r_{hc} (in.)	r_{dc} (in.)	r_{ht} (in.)	r_{dt} (in.)	t (in.)	f_y (ksi)	f_u (ksi)	M_{test} (kips-in.)
8.5Z092-4	8.41	2.61	0.93	53.0	2.41	0.96	50.8	0.29	0.29	0.31	0.31	0.0900	57.3	91.3	181
8.5Z092-2	8.43	2.61	0.92	51.8	2.40	0.95	50.4	0.28	0.28	0.31	0.31	0.0887	57.0	89.1	181

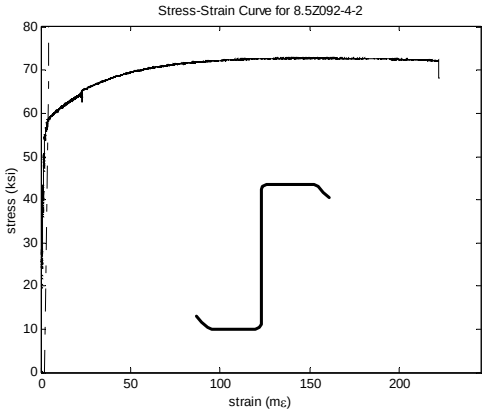

(a)

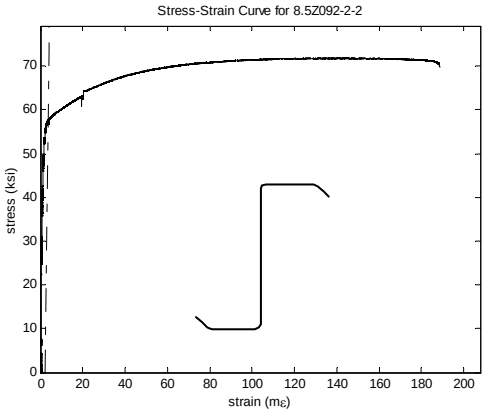

(b)

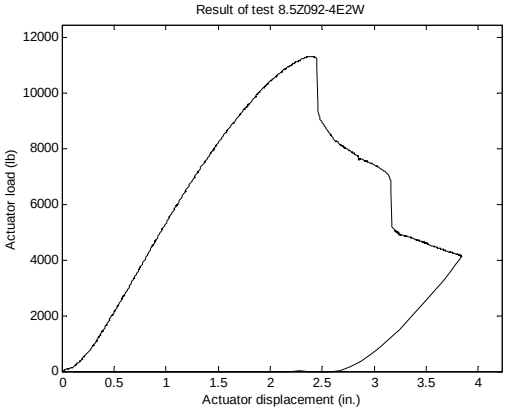

(c)

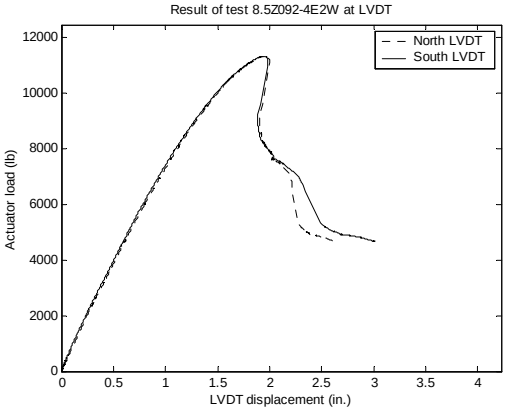

(d)

(e)

(f)

(a) material stress vs. strain of 8.5Z092-4; (b) material stress vs. strain of 8.5Z092-2; (c) actuator load vs. displacement; (d) actuator load vs. displacements of LVDTs; (e, f) pictures of collapse mechanism.

Local Buckling Test 8.5Z082-1E2W (panel fastener type C)

Specimen	h (in.)	b_c (in.)	d_c (in.)	θ_c (deg.)	b_t (in.)	d_t (in.)	θ_t (deg.)	r_{hc} (in.)	r_{dc} (in.)	r_{ht} (in.)	r_{dt} (in.)	t (in.)	f_y (ksi)	f_u (ksi)	M_{test} (kips-in.)
8.5Z082-1	8.46	2.50	0.95	49.0	2.36	0.97	50.3	0.28	0.28	0.30	0.30	0.0801	58.4	74.0	162
8.5Z082-2	8.45	2.51	0.95	47.9	2.40	0.95	52.4	0.28	0.28	0.30	0.30	0.0804	58.1	74.0	162

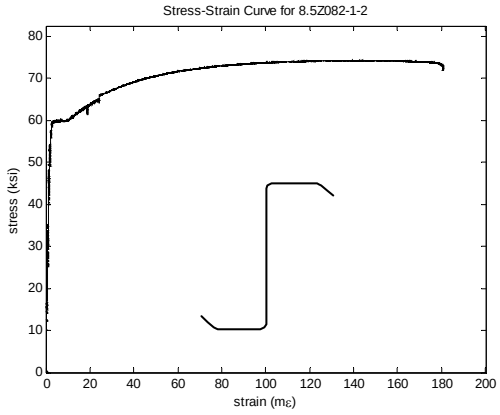

(a)

(b)

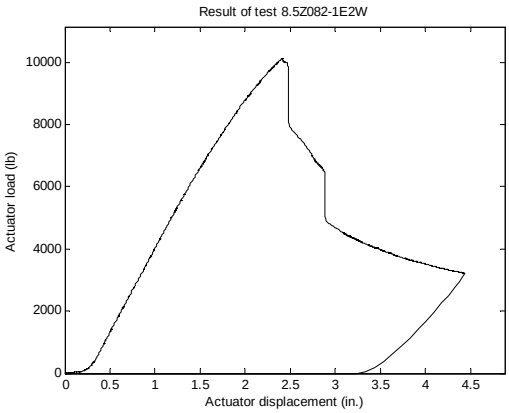

(c)

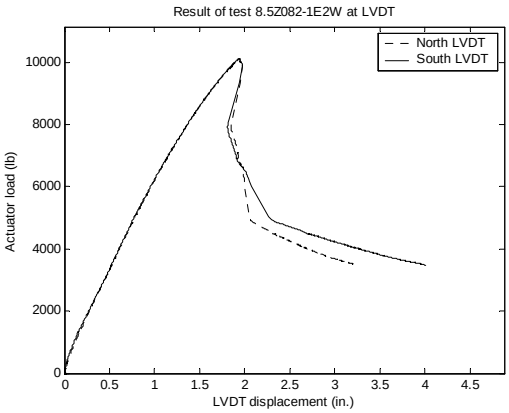

(d)

(e)

(f)

(a) material stress vs. strain of 8.5Z082-1; (b) material stress vs. strain of 8.5Z082-2; (c) actuator load vs. displacement; (d) actuator load vs. displacements of LVDTs; (e, f) pictures of collapse mechanism.

Local Buckling Test 8.5Z073-6E5W (panel fastener type A)

Specimen	h (in.)	b_c (in.)	d_c (in.)	θ_c (deg.)	b_t (in.)	d_t (in.)	θ_t (deg.)	r_{hc} (in.)	r_{dc} (in.)	r_{ht} (in.)	r_{dt} (in.)	t (in.)	f_y (ksi)	f_u (ksi)	M_{test} (kips-in.)
8.5Z073-6	8.50	2.52	0.92	49.6	2.40	0.94	50.9	0.28	0.28	0.30	0.30	0.0720	54.0	74.0	121
8.5Z073-5	8.50	2.52	0.92	49.6	2.40	0.94	50.9	0.28	0.28	0.30	0.30	0.0727	55.6	72.6	121

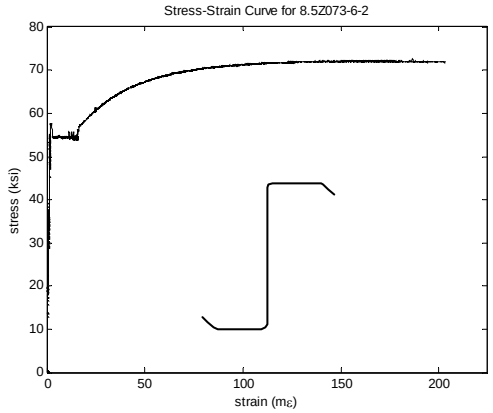

(a)

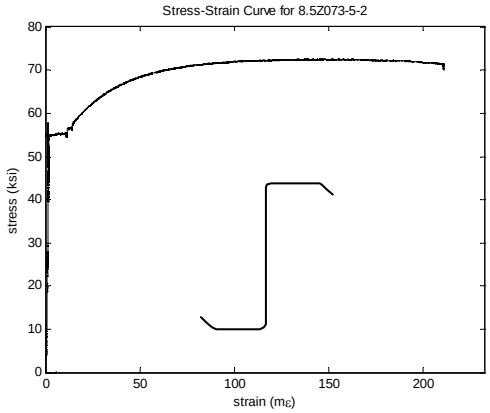

(b)

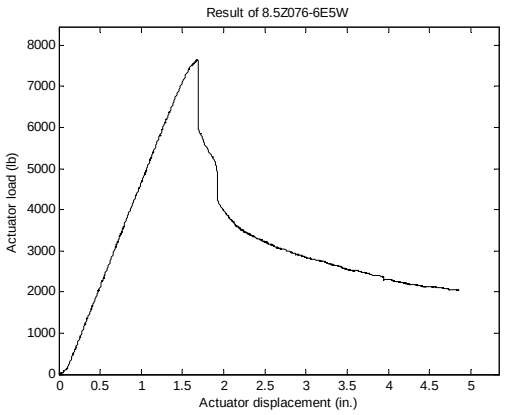

(c)

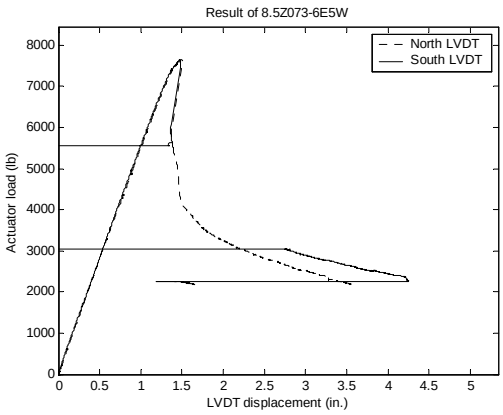

(d)

(e)

(f)

(a) material stress vs. strain of 8.5Z073-6; (b) material stress vs. strain of 8.5Z073-5; (c) actuator load vs. displacement; (d) actuator load vs. displacements of LVDTs; (e, f) pictures of collapse mechanism.

Local Buckling Test 8.5Z073-4E3W (panel fastener type C)

Specimen	h (in.)	b_c (in.)	d_c (in.)	θ_c (deg.)	b_t (in.)	d_t (in.)	θ_t (deg.)	r_{hc} (in.)	r_{dc} (in.)	r_{ht} (in.)	r_{dt} (in.)	t (in.)	f_y (ksi)	f_u (ksi)	M_{test} (kips-in.)
8.5Z073-4	8.51	2.53	0.93	49.6	2.41	0.92	50.3	0.28	0.28	0.29	0.29	0.0715	56.1	74.7	134
8.5Z073-3	8.50	2.53	0.91	50.1	2.38	0.96	51.0	0.28	0.28	0.30	0.30	0.0720	55.6	74.3	134

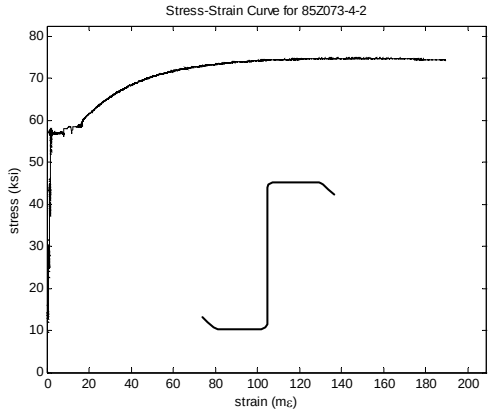

(a)

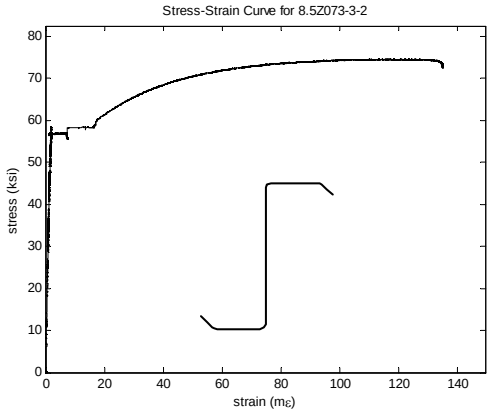

(b)

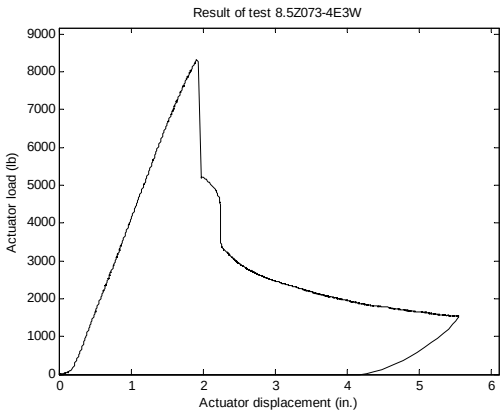

(c)

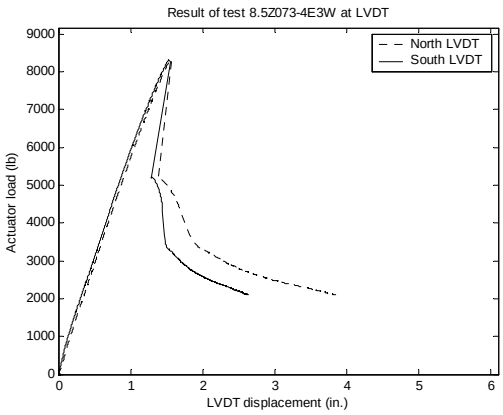

(d)

(e)

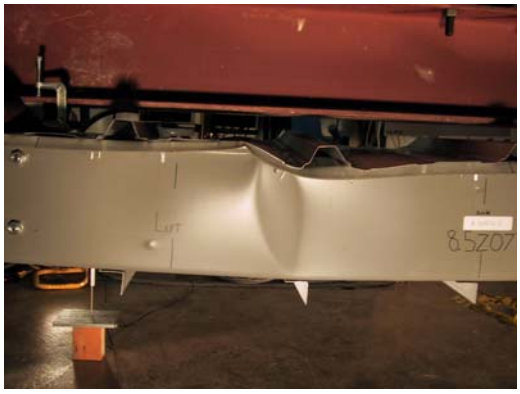

(f)

(a) material stress vs. strain of 8.5Z073-4; (b) material stress vs. strain of 8.5Z073-3; (c) actuator load vs. displacement; (d) actuator load vs. displacements of LVDTs; (e, f) pictures of collapse mechanism.

Local Buckling Test 8.5Z073-1E2W (panel fastener type B)

Specimen	h (in.)	b_c (in.)	d_c (in.)	θ_c (deg.)	b_t (in.)	d_t (in.)	θ_t (deg.)	r_{hc} (in.)	r_{dc} (in.)	r_{ht} (in.)	r_{dt} (in.)	t (in.)	f_y (ksi)	f_u (ksi)	M_{test} (kips-in.)
8.5Z073-1	8.49	2.50	0.92	48.4	2.41	0.95	51.2	0.28	0.28	0.30	0.30	0.0720	54.8	74.1	123
8.5Z073-2	8.50	2.54	0.93	50.2	2.41	0.92	51.0	0.28	0.28	0.30	0.30	0.0715	55.7	73.2	123

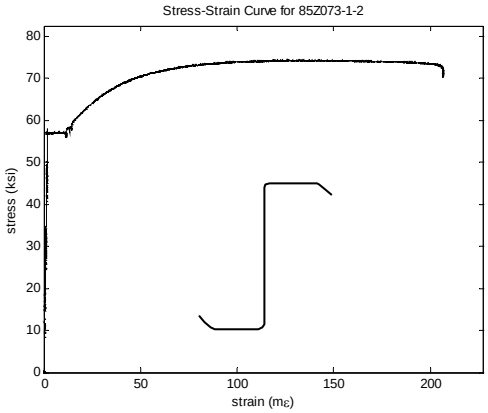

(a)

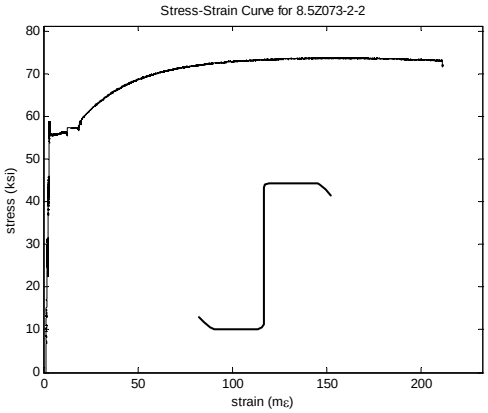

(b)

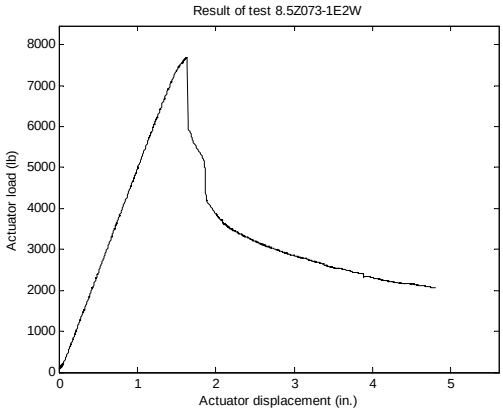

(c)

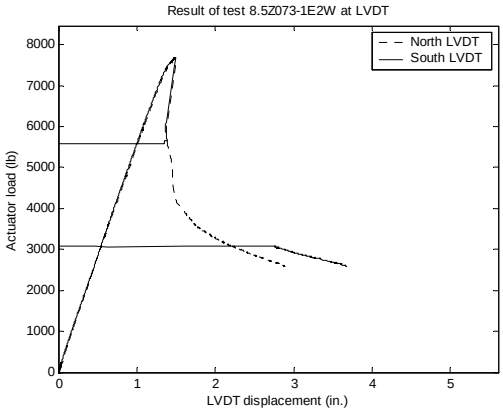

(d)

(e)

(f)

(a) material stress vs. strain of 8.5Z073-1; (b) material stress vs. strain of 8.5Z073-2; (c) actuator load vs. displacement; (d) actuator load vs. displacements of LVDTs; (e, f) pictures of collapse mechanism.

Local Buckling Test 8.5Z065-3E1W (panel fastener type B)

Specimen	h (in.)	b_c (in.)	d_c (in.)	θ_c (deg.)	b_t (in.)	d_t (in.)	θ_t (deg.)	r_{hc} (in.)	r_{dc} (in.)	r_{ht} (in.)	r_{dt} (in.)	t (in.)	f_y (ksi)	f_u (ksi)	M_{test} (kips-in.)
8.5Z065-3	8.47	2.42	0.83	47.3	2.43	0.79	47.3	0.27	0.27	0.28	0.28	0.0640	53.5	68.9	96
8.5Z065-1	8.47	2.44	0.76	47.4	2.43	0.84	47.1	0.28	0.28	0.27	0.27	0.0640	53.1	68.6	96

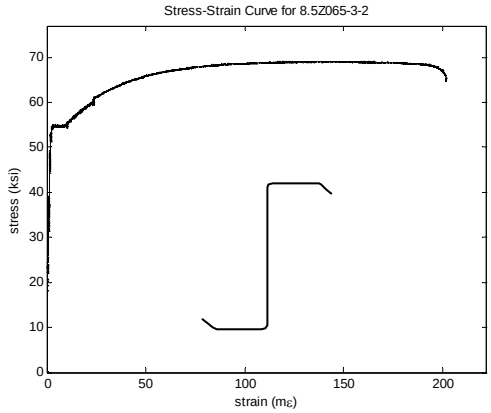

(a)

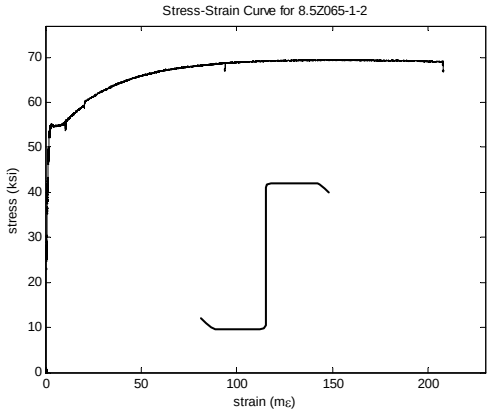

(b)

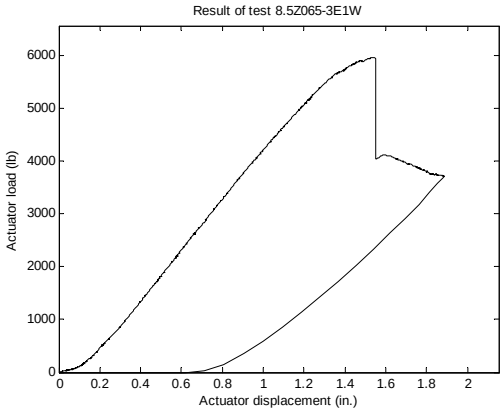

(c)

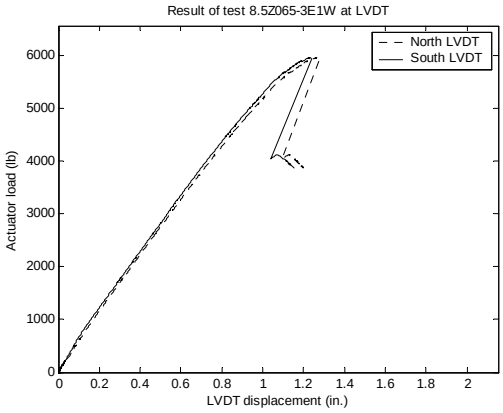

(d)

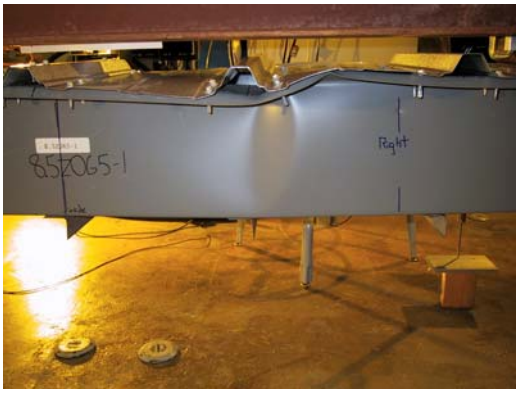

(e)

(f)

(a) material stress vs. strain of 8.5Z065-3; (b) material stress vs. strain of 8.5Z065-1; (c) actuator load vs. displacement; (d) actuator load vs. displacements of LVDTs; (e, f) pictures of collapse mechanism.

Local Buckling Test 8.5Z059-4E3W (panel fastener type C)

Specimen	h (in.)	b_c (in.)	d_c (in.)	θ_c (deg.)	b_t (in.)	d_t (in.)	θ_t (deg.)	r_{hc} (in.)	r_{dc} (in.)	r_{ht} (in.)	r_{dt} (in.)	t (in.)	f_y (ksi)	f_u (ksi)	M_{test} (kips-in.)
8.5Z059-4	8.50	2.50	0.77	50.9	2.35	0.72	48.9	0.28	0.28	0.28	0.28	0.0590	58.6	80.9	100
8.5Z059-3	8.50	2.44	0.78	50.2	2.22	0.69	50.4	0.28	0.28	0.28	0.28	0.0595	58.5	81.0	100

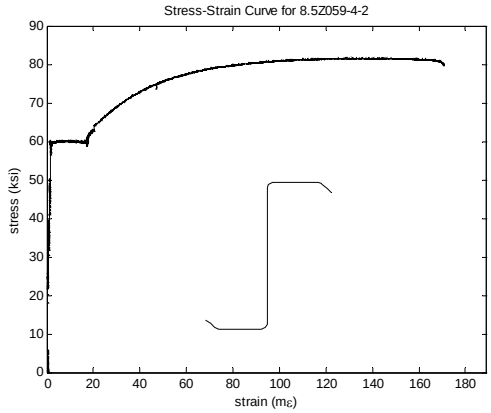

(a)

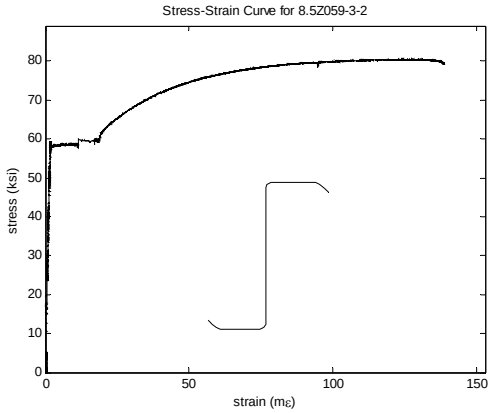

(b)

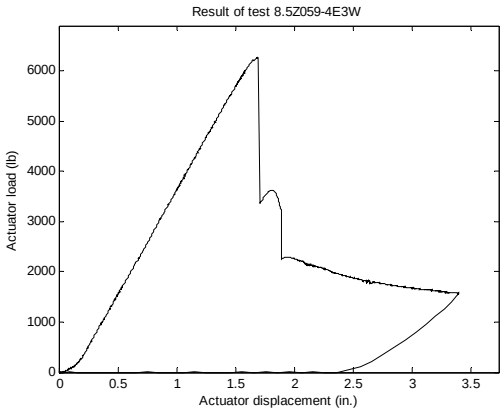

(c)

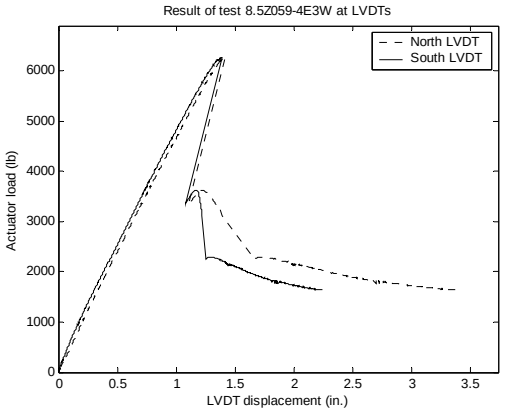

(d)

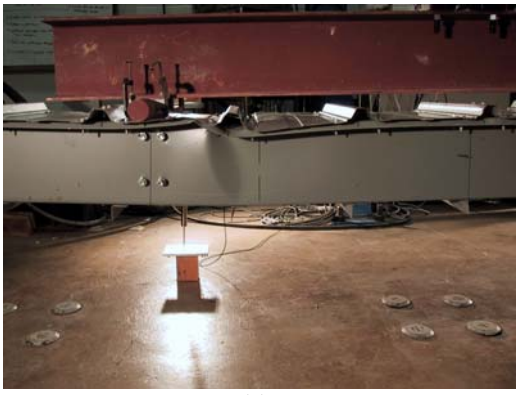

(e)

(f)

(a) material stress vs. strain of 8.5Z059-4; (b) material stress vs. strain of 8.5Z059-3; (c) actuator load vs. displacement; (d) actuator load vs. displacements of LVDTs; (e, f) pictures of collapse mechanism.

Local Buckling Test 8.5Z059-2E1W (panel fastener type D)

Specimen	h (in.)	b_c (in.)	d_c (in.)	θ_c (deg.)	b_t (in.)	d_t (in.)	θ_t (deg.)	r_{hc} (in.)	r_{dc} (in.)	r_{ht} (in.)	r_{dt} (in.)	t (in.)	f_y (ksi)	f_u (ksi)	M_{test} (kips-in.)
8.5Z059-2	8.49	2.51	0.78	50.6	2.33	0.70	50.2	0.28	0.28	0.28	0.28	0.0590	59.1	80.8	99
8.5Z059-1	8.50	2.51	0.78	51.2	2.33	0.71	49.4	0.28	0.28	0.28	0.28	0.0590	58.9	80.6	99

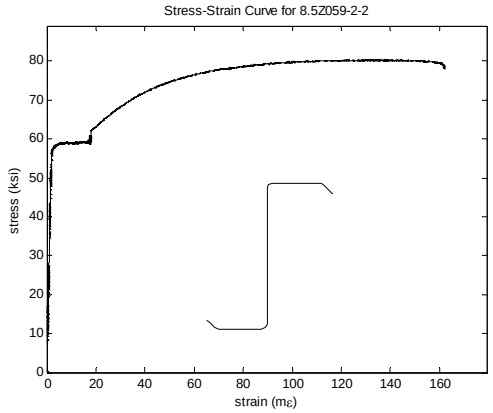

(a)

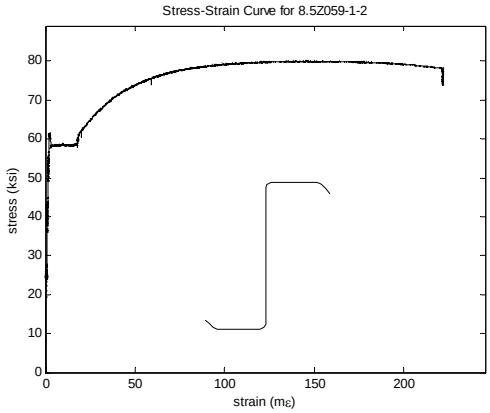

(b)

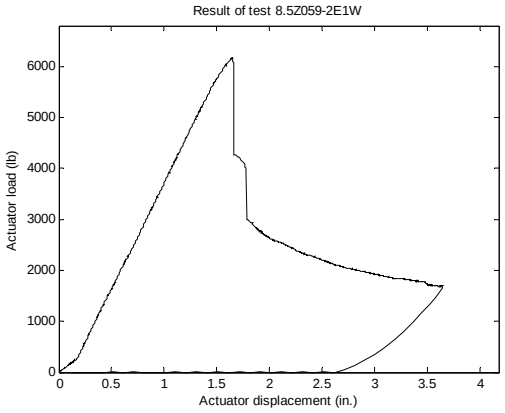

(c)

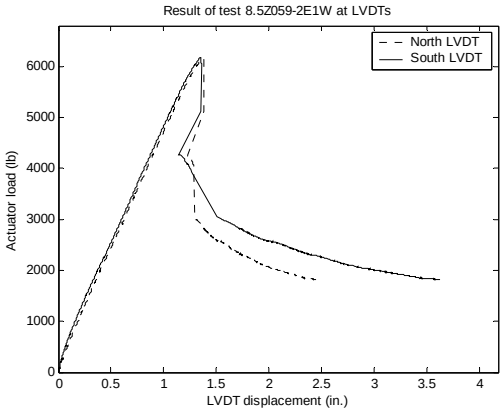

(d)

(e)

(f)

(a) material stress vs. strain of 8.5Z059-2; (b) material stress vs. strain of 8.5Z059-1; (c) actuator load vs. displacement; (d) actuator load vs. displacements of LVDTs; (e, f) pictures of collapse mechanism.

Local Buckling Test 11.5Z092-1E2W (panel fastener type C)

Specimen	h (in.)	b_c (in.)	d_c (in.)	θ_c (deg.)	b_t (in.)	d_t (in.)	θ_t (deg.)	r_{hc} (in.)	r_{dc} (in.)	r_{ht} (in.)	r_{dt} (in.)	t (in.)	f_y (ksi)	f_u (ksi)	M_{test} (kips-in.)
11.5Z092-1	11.41	3.33	0.96	50.1	3.51	0.96	49.5	0.25	0.27	0.27	0.27	0.1027	61.0	78.5	352
11.5Z092-2	11.34	3.33	0.98	48.3	3.54	0.89	48.1	0.28	0.27	0.28	0.28	0.1033	60.4	78.0	352

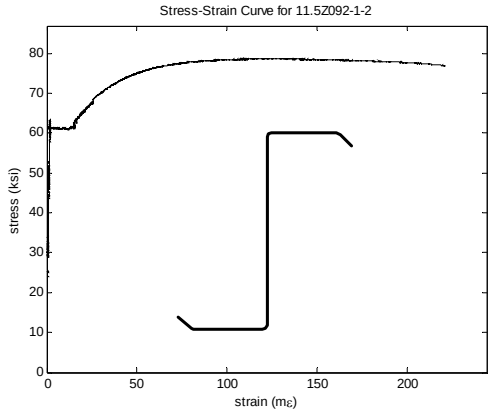

(a)

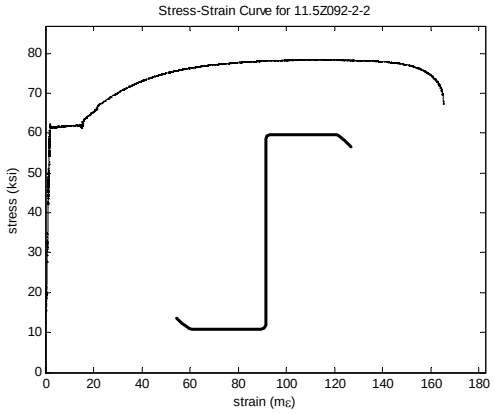

(b)

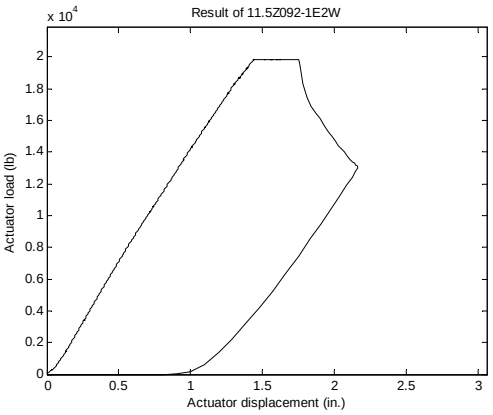

(c)

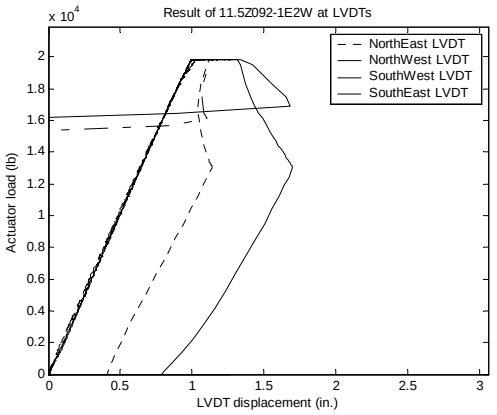

(d)

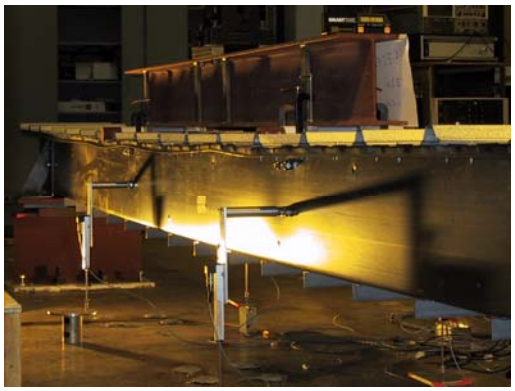

(e)

(f)

(a) material stress vs. strain of 11.5Z092-1; (b) material stress vs. strain of 11.5Z092-2;
(c) actuator load vs. displacement; (d) actuator load vs. displacements of LVDTs;
(e, f) pictures of collapse mechanism.

Local Buckling Test 11.5Z082-2E1W (panel fastener type C)

Specimen	h (in.)	b_c (in.)	d_c (in.)	θ_c (deg.)	b_t (in.)	d_t (in.)	θ_t (deg.)	r_{hc} (in.)	r_{dc} (in.)	r_{ht} (in.)	r_{dt} (in.)	t (in.)	f_y (ksi)	f_u (ksi)	M_{test} (kips-in.)
11.5Z082-2	11.45	3.50	0.88	50.3	3.45	0.87	52.2	0.31	0.31	0.35	0.35	0.0837	61.5	78.0	274
11.5Z082-1	11.47	3.49	0.90	50.6	3.43	0.88	51.0	0.32	0.32	0.35	0.35	0.0839	60.4	79.9	274

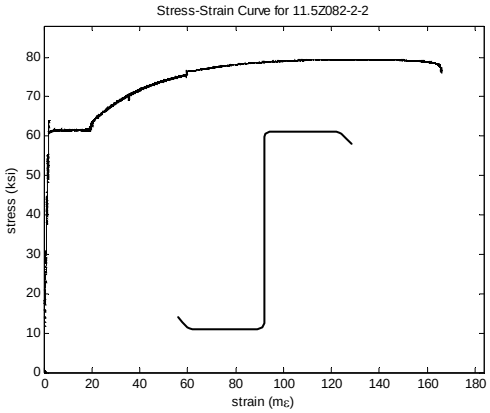

(a)

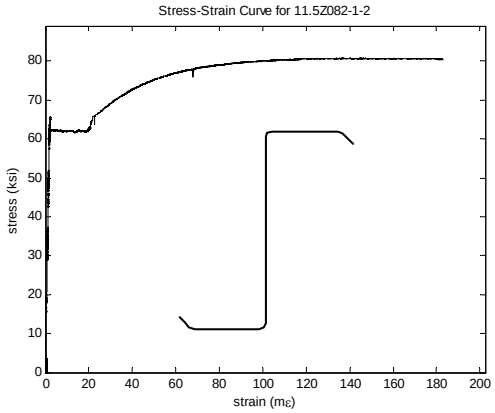

(b)

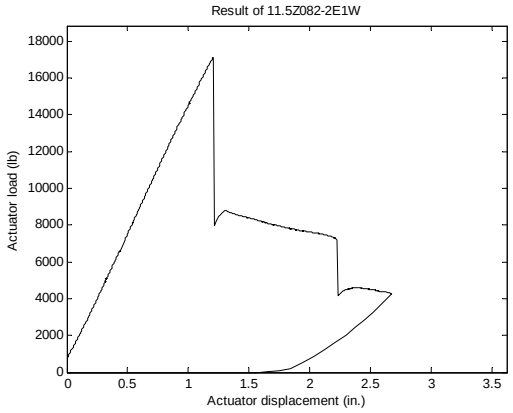

(c)

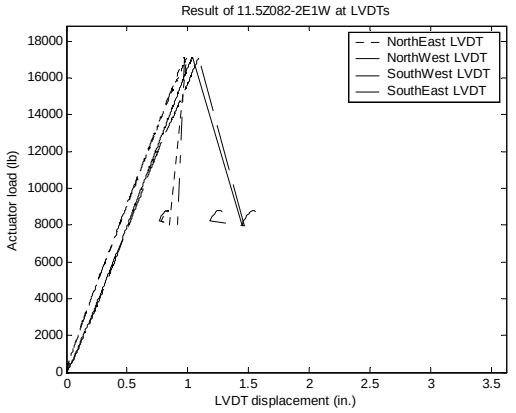

(d)

(e)

(f)

(a) material stress vs. strain of 11.5Z082-2; (b) material stress vs. strain of 11.5Z082-1;
(c) actuator load vs. displacement; (d) actuator load vs. displacements of LVDTs;
(e, f) pictures of collapse mechanism.

Local Buckling Test 11.5Z073-2E1W (panel fastener type C)

Specimen	h (in.)	b_c (in.)	d_c (in.)	θ_c (deg.)	b_t (in.)	d_t (in.)	θ_t (deg.)	r_{hc} (in.)	r_{dc} (in.)	r_{ht} (in.)	r_{dt} (in.)	t (in.)	f_y (ksi)	f_u (ksi)	M_{test} (kips-in.)
11.5Z073-2	11.39	3.51	0.87	46.0	3.35	0.83	44.8	0.27	0.28	0.27	0.28	0.0709	65.4	82.8	194
11.5Z073-1	11.35	3.52	0.95	45.4	3.40	0.90	44.2	0.27	0.11	0.27	0.07	0.0695	66.8	84.6	194

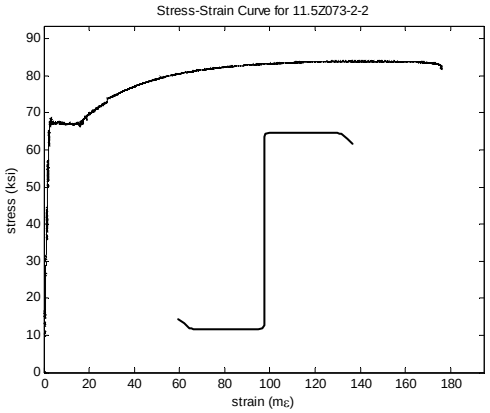

(a)

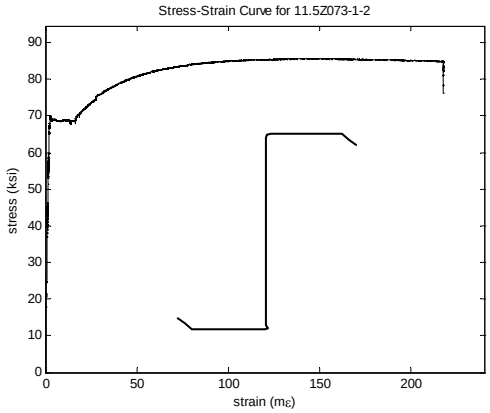

(b)

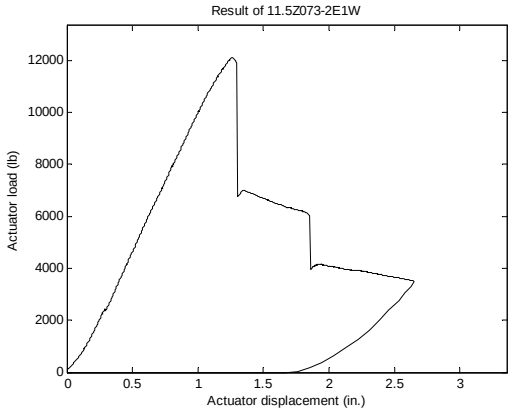

(c)

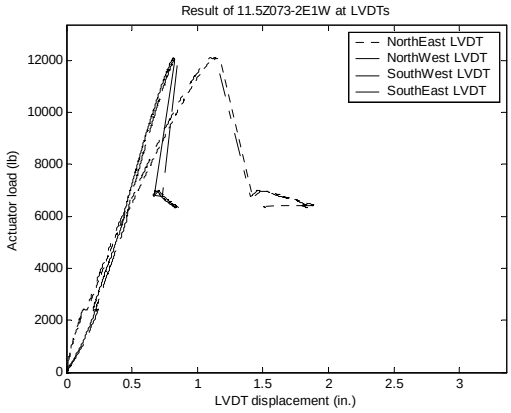

(d)

(e)

(f)

(a) material stress vs. strain of 11.5Z073-2; (b) material stress vs. strain of 11.5Z073-1;
(c) actuator load vs. displacement; (d) actuator load vs. displacements of LVDTs;
(e, f) pictures of collapse mechanism.

Local Buckling Test 8C097-2E3W (panel fastener type C)

Specimen	h (in.)	b_c (in.)	d_c (in.)	θ_c (deg.)	b_t (in.)	d_t (in.)	θ_t (deg.)	r_{hc} (in.)	r_{dc} (in.)	r_{ht} (in.)	r_{dt} (in.)	t (in.)	f_y (ksi)	f_u (ksi)	M_{test} (kips-in.)
8C097-2	8.04	2.12	0.57	85.6	2.08	0.52	85.7	0.30	0.28	0.28	0.30	0.0980	59.9	76.7	172
8C097-3	8.03	2.09	0.56	84.0	2.08	0.54	88.2	0.30	0.28	0.28	0.29	0.0940	59.6	76.1	172

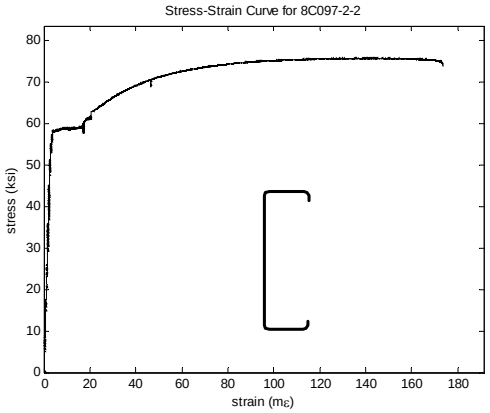

(a)

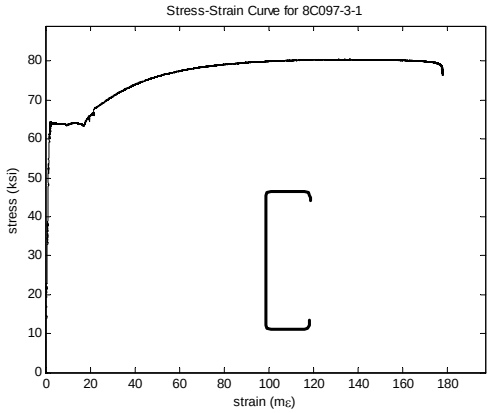

(b)

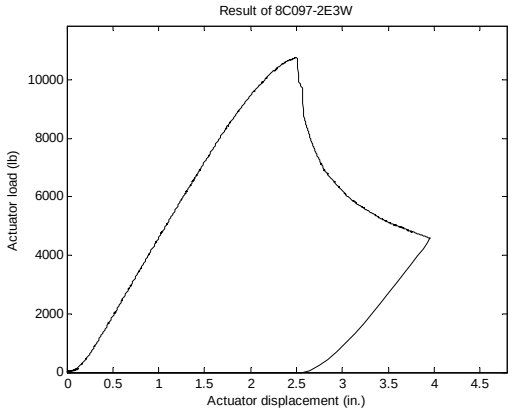

(c)

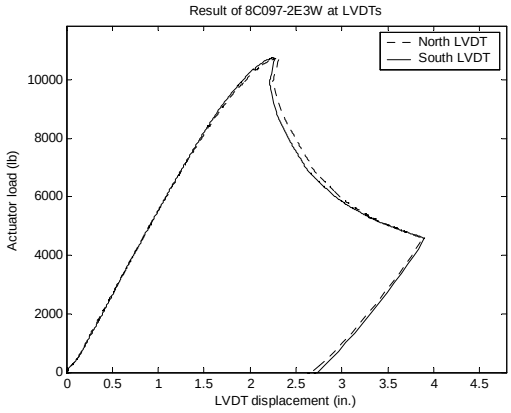

(d)

(e)

(f)

(a) material stress vs. strain of 8C097-2; (b) material stress vs. strain of 8C097-3; (c) actuator load vs. displacement; (d) actuator load vs. displacements of LVDTs; (e, f) pictures of collapse mechanism.

Local Buckling Test 8C068-4E5W (panel fastener type C)

Specimen	h (in.)	b_c (in.)	d_c (in.)	θ_c (deg.)	b_t (in.)	d_t (in.)	θ_t (deg.)	r_{hc} (in.)	r_{dc} (in.)	r_{ht} (in.)	r_{dt} (in.)	t (in.)	f_y (ksi)	f_u (ksi)	M_{test} (kips-in.)
8C068-5	8.03	2.03	0.52	83.2	2.04	0.53	87.0	0.28	0.25	0.24	0.24	0.0750	48.6	76.7	104
8C068-4	8.01	2.05	0.52	84.0	2.04	0.54	87.6	0.27	0.26	0.24	0.27	0.0770	53.1	76.1	104

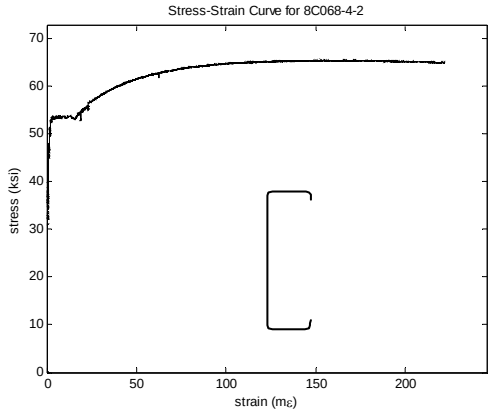

(a)

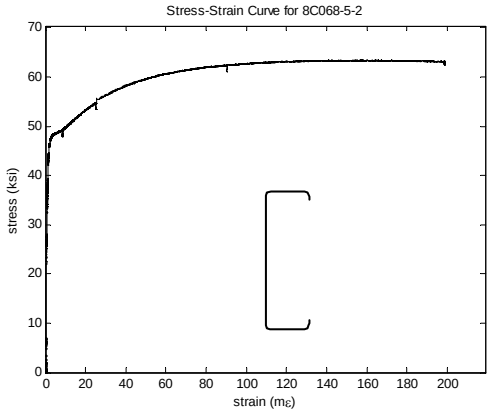

(b)

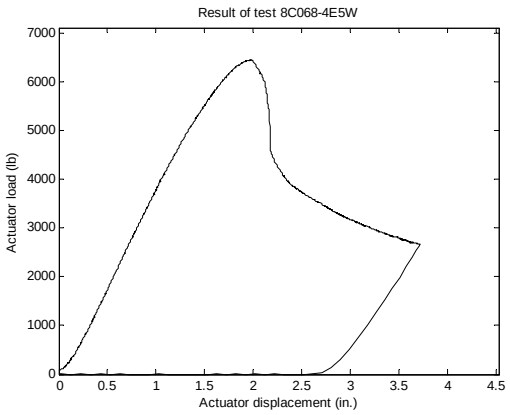

(c)

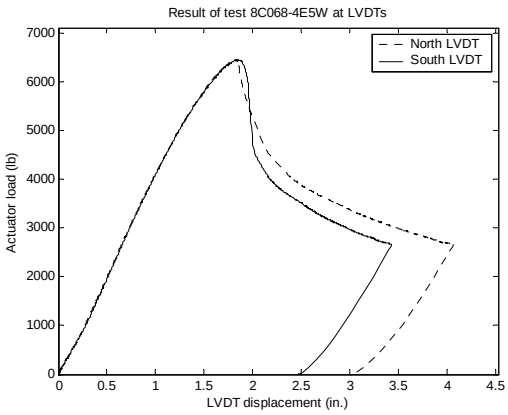

(d)

(e)

(f)

(a) material stress vs. strain of 8C068-4; (b) material stress vs. strain of 8C068-5; (c) actuator load vs. displacement; (d) actuator load vs. displacements of LVDTs; (e, f) pictures of collapse mechanism.

Local Buckling Test 8C068-1E2W (panel fastener type C)

Specimen	h (in.)	b_c (in.)	d_c (in.)	θ_c (deg.)	b_t (in.)	d_t (in.)	θ_t (deg.)	r_{hc} (in.)	r_{dc} (in.)	r_{ht} (in.)	r_{dt} (in.)	t (in.)	f_y (ksi)	f_u (ksi)	M_{test} (kips-in.)
8C068-2	8.02	2.04	0.52	83.4	2.04	0.53	87.6	0.28	0.25	0.24	0.26	0.0758	51.7	66.0	98
8C068-1	8.03	2.03	0.53	83.1	2.05	0.53	88.1	0.30	0.26	0.25	0.26	0.0754	51.4	65.3	98

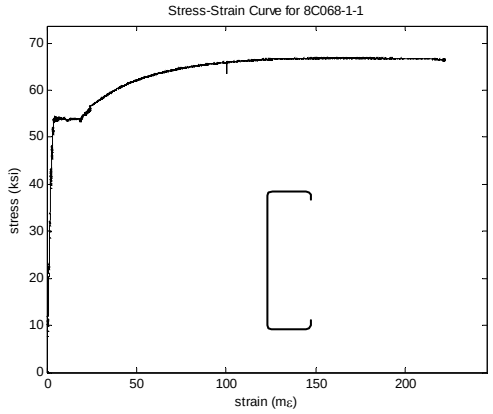

(a)

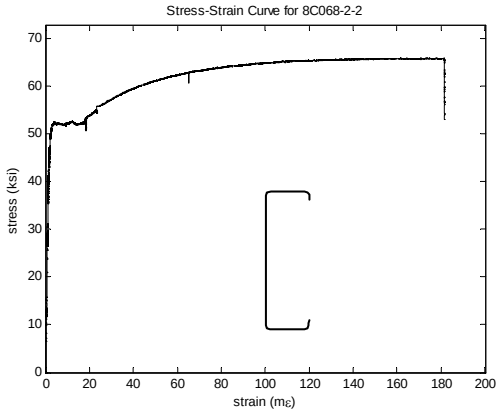

(b)

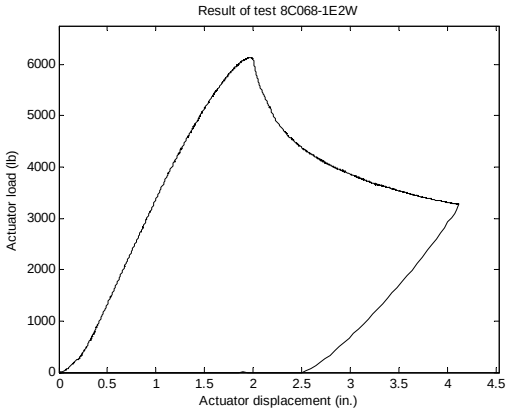

(c)

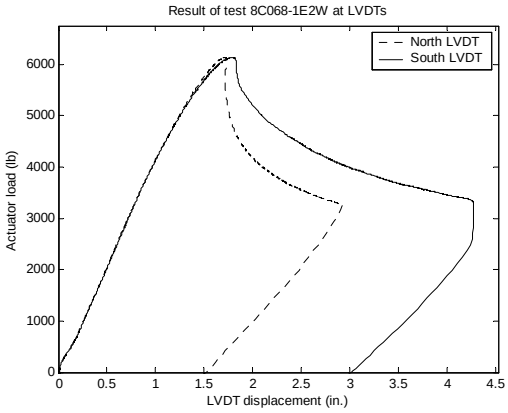

(d)

(e)

(f)

(a) material stress vs. strain of 8C068-1; (b) material stress vs. strain of 8C068-2; (c) actuator load vs. displacement; (d) actuator load vs. displacements of LVDTs; (e, f) pictures of collapse mechanism.

Local Buckling Test 8C054-1E8W (panel fastener type C)

Specimen	h (in.)	b_c (in.)	d_c (in.)	θ_c (deg.)	b_t (in.)	d_t (in.)	θ_t (deg.)	r_{hc} (in.)	r_{dc} (in.)	r_{ht} (in.)	r_{dt} (in.)	t (in.)	f_y (ksi)	f_u (ksi)	M_{test} (kips-in.)
8C054-1	8.00	2.04	0.52	88.9	2.07	0.50	84.7	0.22	0.23	0.23	0.23	0.0550	40.0	52.1	56
8C054-8	8.08	2.02	0.58	88.1	1.96	0.48	82.3	0.22	0.20	0.22	0.23	0.0540	40.3	52.8	56

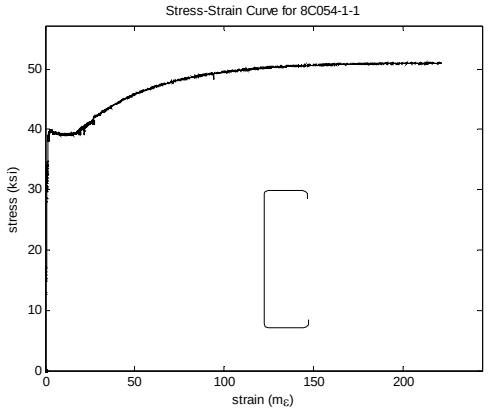

(a)

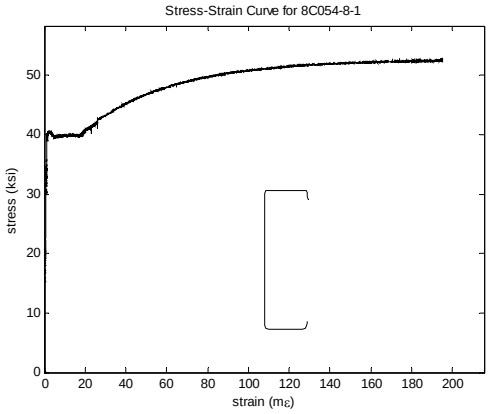

(b)

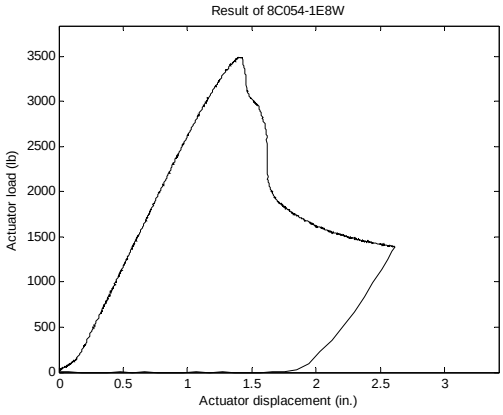

(c)

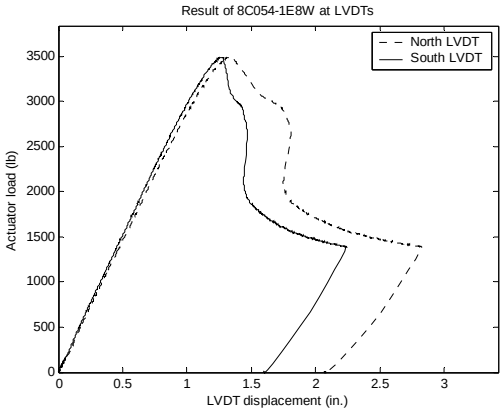

(d)

(e)

(f)

(a) material stress vs. strain of 8C054-1; (b) material stress vs. strain of 8C054-8; (c) actuator load vs. displacement; (d) actuator load vs. displacements of LVDTs; (e, f) pictures of collapse mechanism.

Local Buckling Test 8C043-5E6W (panel fastener type C)

Specimen	h (in.)	b_c (in.)	d_c (in.)	θ_c (deg.)	b_t (in.)	d_t (in.)	θ_t (deg.)	r_{hc} (in.)	r_{dc} (in.)	r_{ht} (in.)	r_{dt} (in.)	t (in.)	f_y (ksi)	f_u (ksi)	M_{test} (kips-in.)
8C043-5	8.04	2.02	0.53	88.8	1.98	0.53	87.3	0.18	0.20	0.21	0.20	0.0496	44.9	61.0	51
8C043-6	8.06	2.01	0.53	88.9	2.00	0.46	87.0	0.19	0.20	0.22	0.20	0.0490	45.0	60.8	51

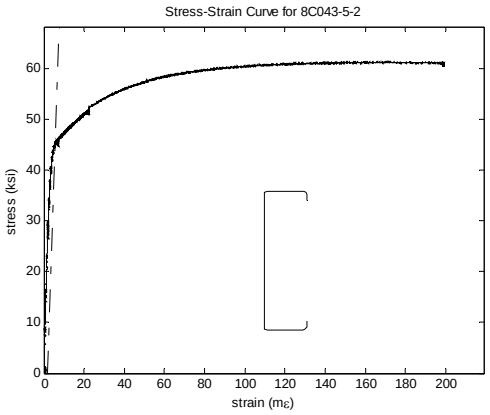

(a)

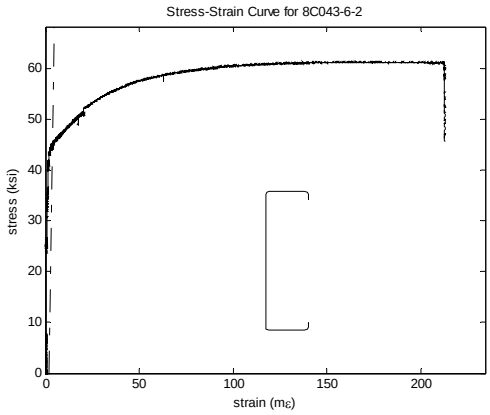

(b)

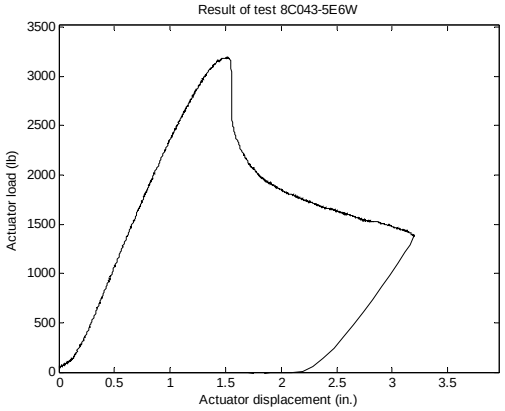

(c)

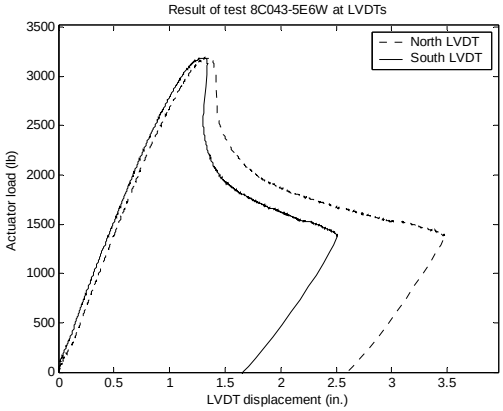

(d)

(e)

(f)

(a) material stress vs. strain of 8C043-5; (b) material stress vs. strain of 8C043-6; (c) actuator load vs. displacement; (d) actuator load vs. displacements of LVDTs; (e, f) pictures of collapse mechanism.

Local Buckling Test 8C043-3E1W (panel fastener type C)

Specimen	h (in.)	b_c (in.)	d_c (in.)	θ_c (deg.)	b_t (in.)	d_t (in.)	θ_t (deg.)	r_{hc} (in.)	r_{dc} (in.)	r_{ht} (in.)	r_{dt} (in.)	t (in.)	f_y (ksi)	f_u (ksi)	M_{test} (kips-in.)
8C043-3	8.04	2.02	0.54	89.3	2.01	0.53	87.5	0.19	0.19	0.19	0.19	0.0474	46.0	61.5	48
8C043-1	8.03	2.02	0.54	89.0	1.98	0.54	85.8	0.19	0.19	0.29	0.19	0.0476	45.7	61.3	48

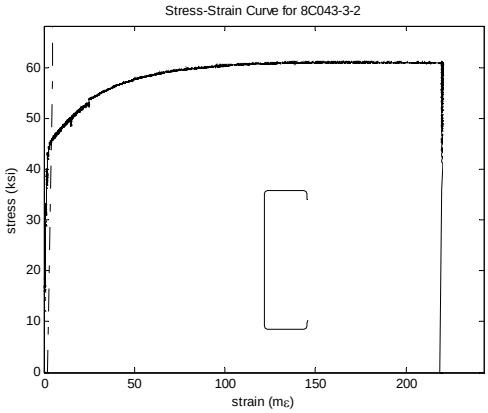

(a)

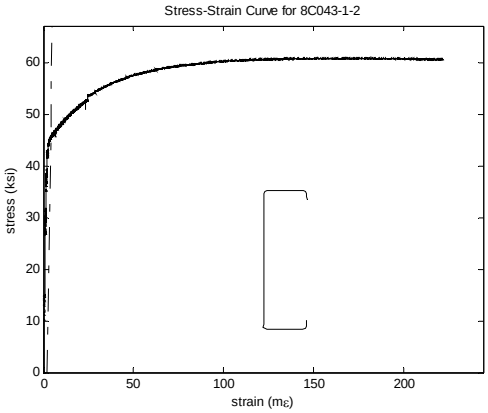

(b)

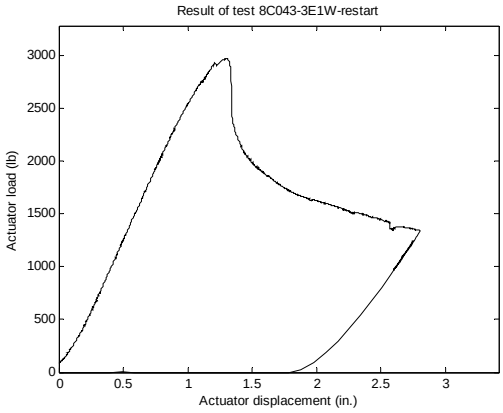

(c)

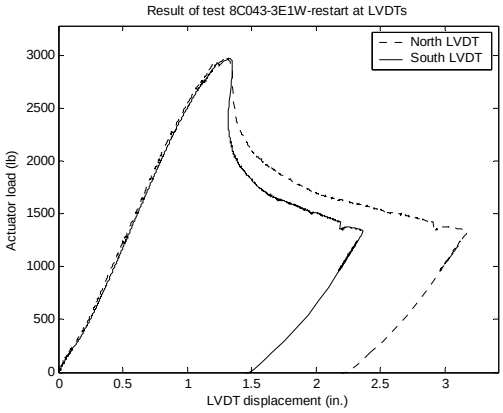

(d)

(e)

(f)

(a) material stress vs. strain of 8C043-3; (b) material stress vs. strain of 8C043-1; (c) actuator load vs. displacement; (d) actuator load vs. displacements of LVDTs; (e, f) pictures of collapse mechanism.

Local Buckling Test 12C068-9E5W (panel fastener type C)

Specimen	h (in.)	b_c (in.)	d_c (in.)	θ_c (deg.)	b_t (in.)	d_t (in.)	θ_t (deg.)	r_{hc} (in.)	r_{dc} (in.)	r_{ht} (in.)	r_{dt} (in.)	t (in.)	f_y (ksi)	f_u (ksi)	M_{test} (kips-in.)
12C068-9	12.02	1.92	0.53	82.0	2.00	0.55	85.3	0.28	0.27	0.30	0.28	0.0652	35.1	58.5	104
12C068-5	12.00	1.79	0.55	85.9	2.06	0.53	94.8	0.27	0.27	0.22	0.27	0.0654	35.0	58.6	104

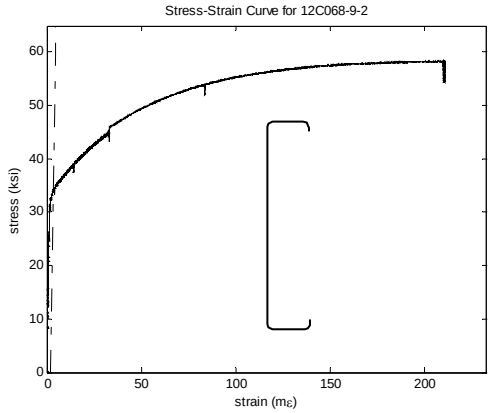

(a)

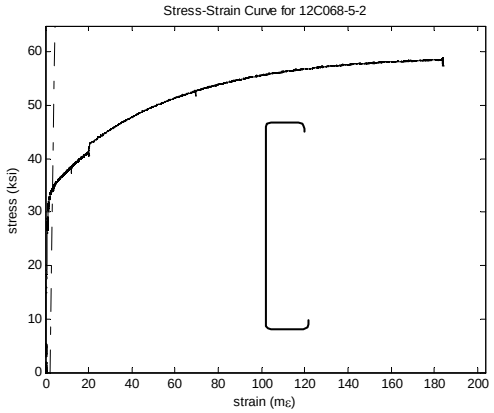

(b)

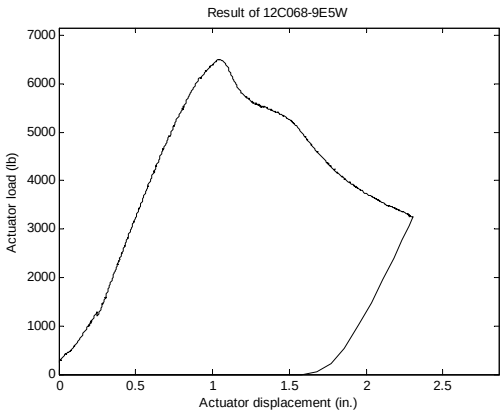

(c)

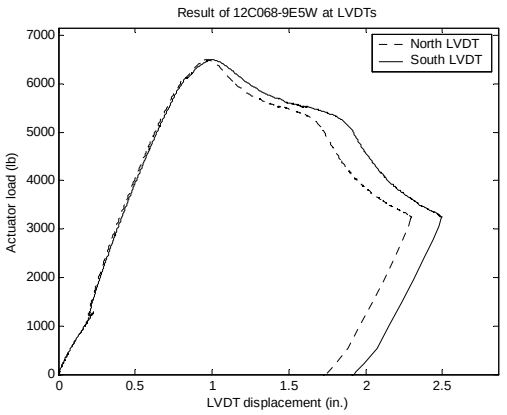

(d)

(e)

(f)

(a) material stress vs. strain of 12C068-9; (b) material stress vs. strain of 12C068-5; (c) actuator load vs. displacement; (d) actuator load vs. displacements of LVDTs; (e, f) pictures of collapse mechanism.

Local Buckling Test 12C068-3E4W (panel fastener type C)

Specimen	h (in.)	b_c (in.)	d_c (in.)	θ_c (deg.)	b_t (in.)	d_t (in.)	θ_t (deg.)	r_{hc} (in.)	r_{dc} (in.)	r_{ht} (in.)	r_{dt} (in.)	t (in.)	f_y (ksi)	f_u (ksi)	M_{test} (kips-in.)
12C068-3	11.97	1.96	0.59	82.5	1.99	0.56	77.4	0.26	0.27	0.27	0.27	0.0671	56.6	74.9	137
12C068-4	12.02	2.01	0.52	80.6	2.00	0.52	83.3	0.26	0.27	0.26	0.27	0.0670	57.3	75.9	137

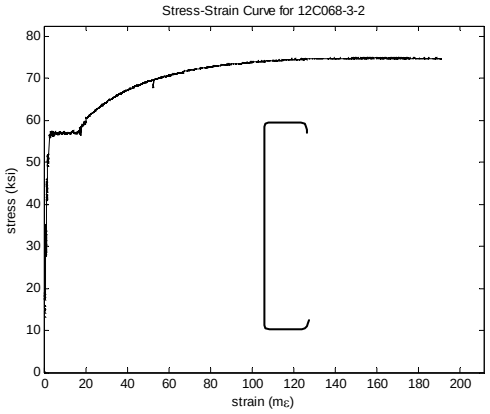

(a)

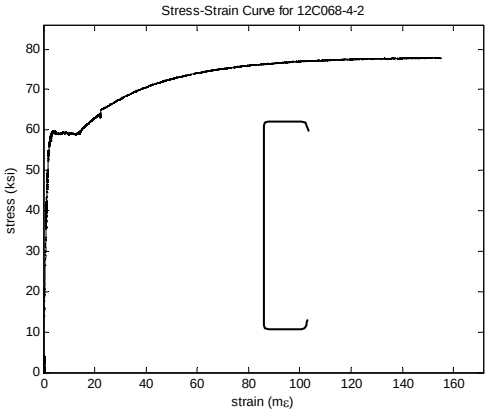

(b)

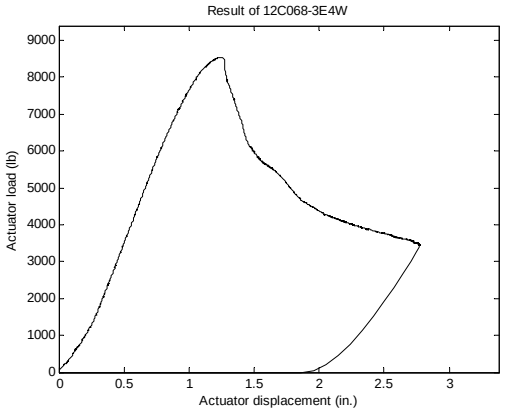

(c)

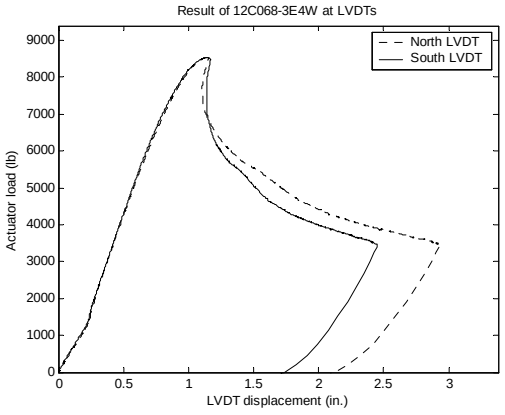

(d)

(e)

(f)

(a) material stress vs. strain of 12C068-3; (b) material stress vs. strain of 12C068-4; (c) actuator load vs. displacement; (d) actuator load vs. displacements of LVDTs; (e, f) pictures of collapse mechanism.

Local Buckling Test 10C068-2E1W (panel fastener type C)

Specimen	h (in.)	b_c (in.)	d_c (in.)	θ_c (deg.)	b_t (in.)	d_t (in.)	θ_t (deg.)	r_{hc} (in.)	r_{dc} (in.)	r_{ht} (in.)	r_{dt} (in.)	t (in.)	f_y (ksi)	f_u (ksi)	M_{test} (kips-in.)
10C068-2	10.08	1.93	0.50	83.2	1.98	0.52	83.3	0.27	0.25	0.27	0.25	0.0572	33.6	57.3	70
10C068-1	10.03	2.04	0.55	80.7	1.97	0.54	81.9	0.27	0.26	0.28	0.25	0.0573	34.2	56.9	70

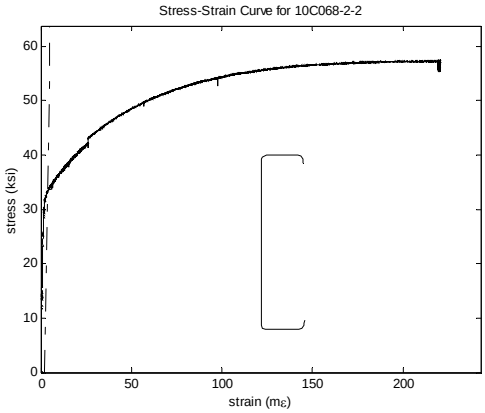

(a)

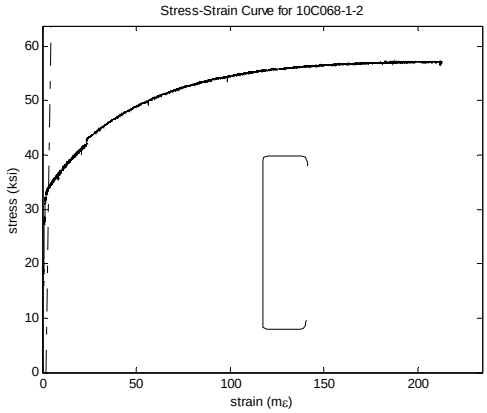

(b)

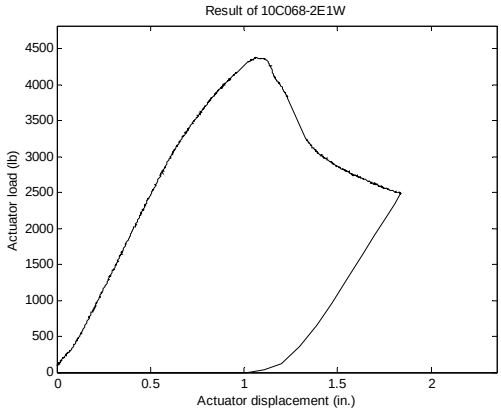

(c)

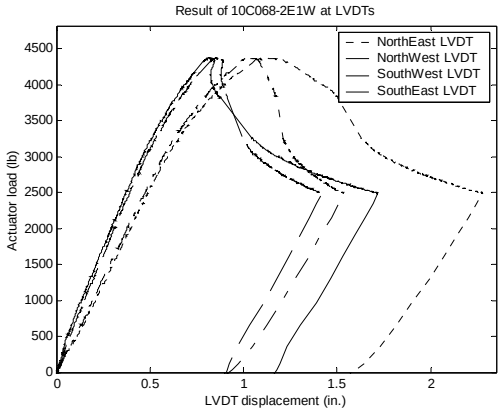

(d)

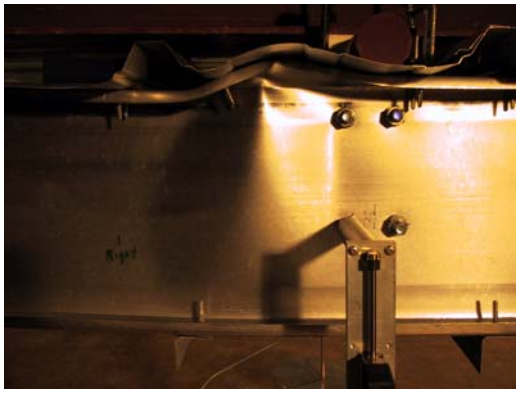

(e)

(f)

(a) material stress vs. strain of 10C068-2; (b) material stress vs. strain of 10C068-1; (c) actuator load vs. displacement; (d) actuator load vs. displacements of LVDTs; (e, f) pictures of collapse mechanism.

Local Buckling Test 6C054-2E1W (panel fastener type C)

Specimen	h (in.)	b_c (in.)	d_c (in.)	θ_c (deg.)	b_t (in.)	d_t (in.)	θ_t (deg.)	r_{hc} (in.)	r_{dc} (in.)	r_{ht} (in.)	r_{dt} (in.)	t (in.)	f_y (ksi)	f_u (ksi)	M_{test} (kips-in.)
6C054-2	6.04	2.00	0.56	85.7	2.00	0.52	90.0	0.21	0.24	0.26	0.25	0.0616	36.1	50.3	45
6C054-1	6.03	2.01	0.56	86.5	2.05	0.52	90.5	0.22	0.25	0.25	0.24	0.0616	37.0	50.0	45

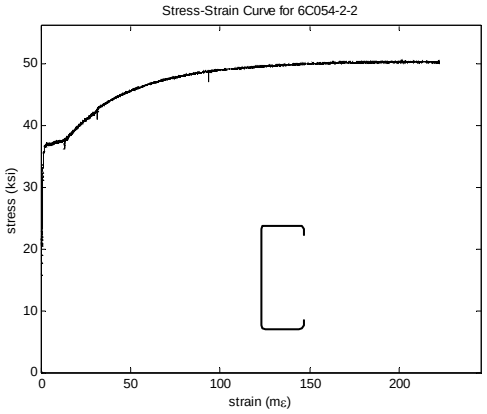

(a)

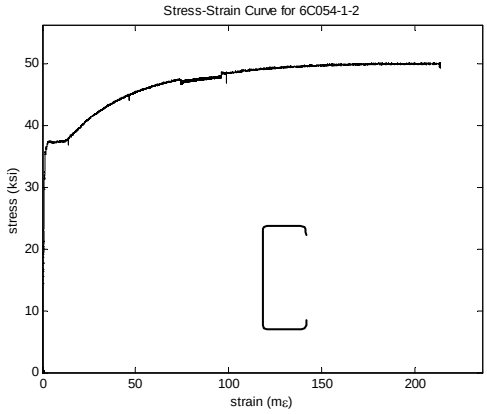

(b)

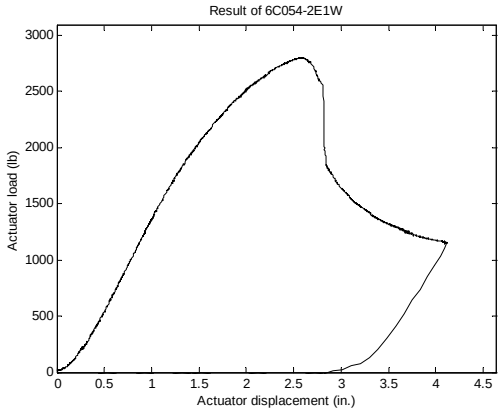

(c)

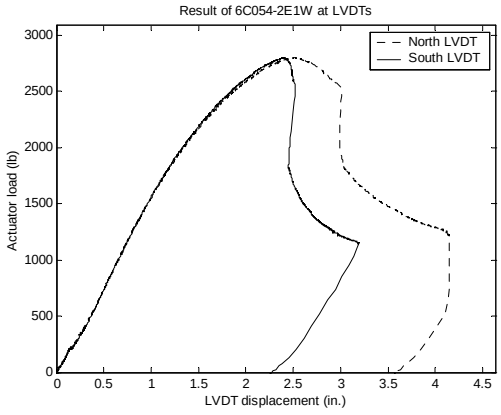

(d)

(e)

(f)

(a) material stress vs. strain of 6C054-2; (b) material stress vs. strain of 6C054-1; (c) actuator load vs. displacement; (d) actuator load vs. displacements of LVDTs; (e, f) pictures of collapse mechanism.

Local Buckling Test 4C054-1E2W (panel fastener type D)

Specimen	h (in.)	b_c (in.)	d_c (in.)	θ_c (deg.)	b_t (in.)	d_t (in.)	θ_t (deg.)	r_{hc} (in.)	r_{dc} (in.)	r_{ht} (in.)	r_{dt} (in.)	t (in.)	f_y (ksi)	f_u (ksi)	M_{test} (kips-in.)
4C054-1	3.95	1.99	0.55	79.2	2.02	0.55	77.4	0.24	0.24	0.23	0.24	0.0551	45.0	55.5	28
4C054-2	3.96	1.95	0.50	74.2	1.96	0.55	74.8	0.22	0.27	0.25	0.25	0.0561	44.7	54.5	28

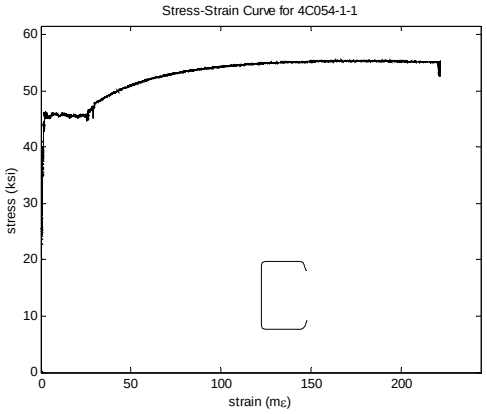

(a)

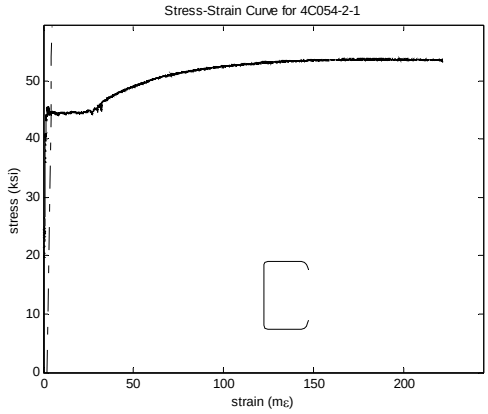

(b)

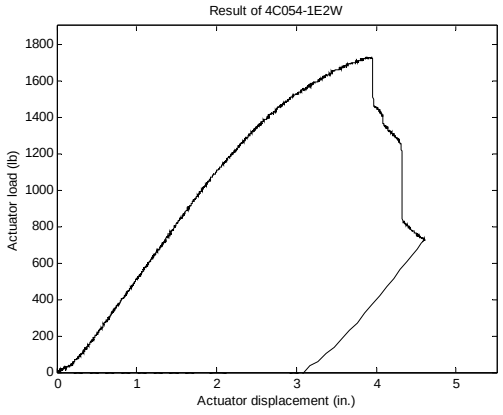

(c)

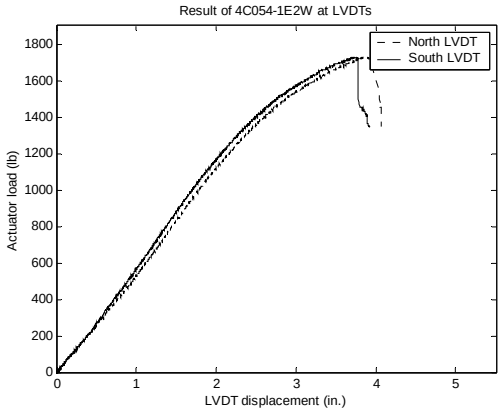

(d)

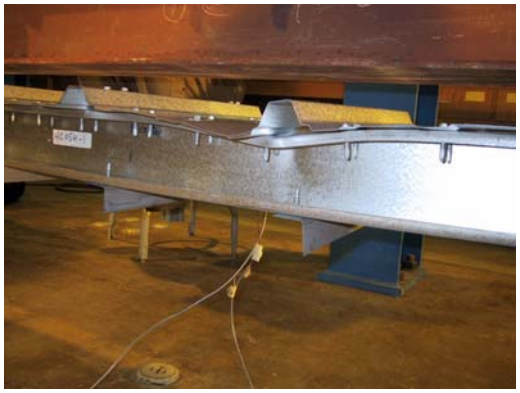

(e)

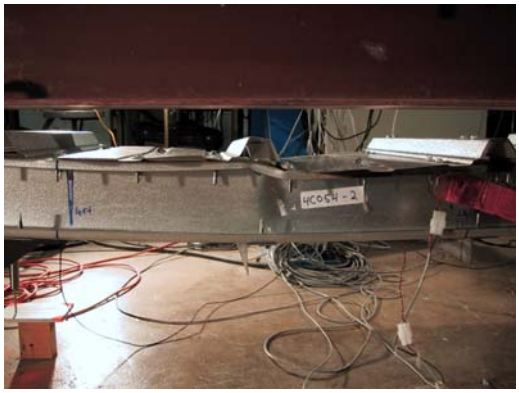

(f)

(a) material stress vs. strain of 4C054-1; (b) material stress vs. strain of 4C054-2; (c) actuator load vs. displacement; (d) actuator load vs. displacements of LVDTs; (e, f) pictures of collapse mechanism.

Local Buckling Test 3.62C054-1E2W (panel fastener type D)

Specimen	h (in.)	b_c (in.)	d_c (in.)	θ_c (deg.)	b_t (in.)	d_t (in.)	θ_t (deg.)	r_{hc} (in.)	r_{dc} (in.)	r_{ht} (in.)	r_{dt} (in.)	t (in.)	f_y (ksi)	f_u (ksi)	M_{test} (kips-in.)
3.62C054-1	3.65	1.97	0.49	77.1	2.00	0.42	88.1	0.23	0.26	0.26	0.25	0.0555	32.8	55.5	20
3.62C054-2	3.67	1.99	0.51	79.8	1.97	0.44	79.8	0.24	0.25	0.26	0.26	0.0554	32.0	54.5	20

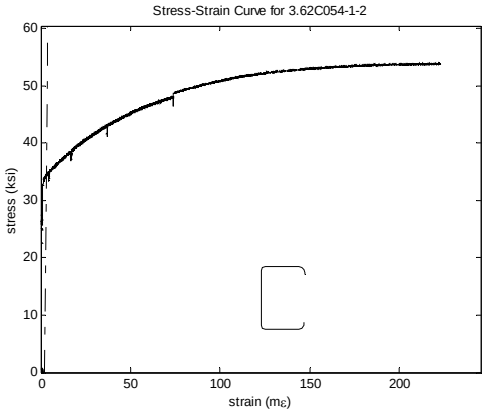

(a)

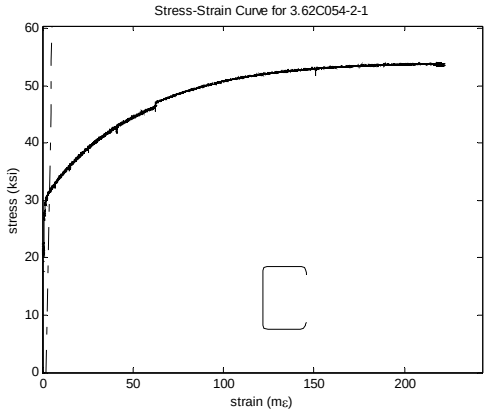

(b)

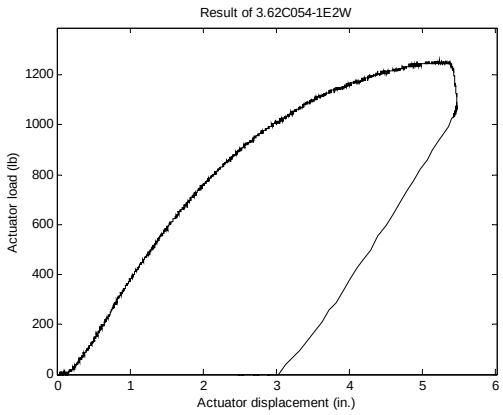

(c)

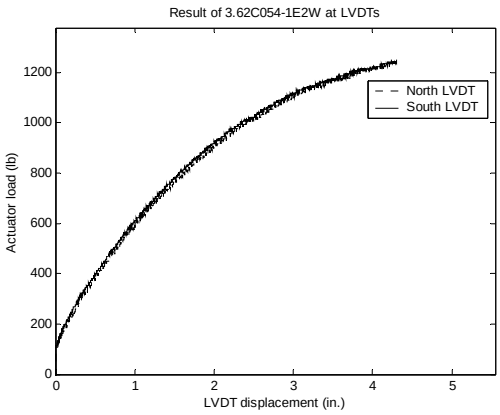

(d)

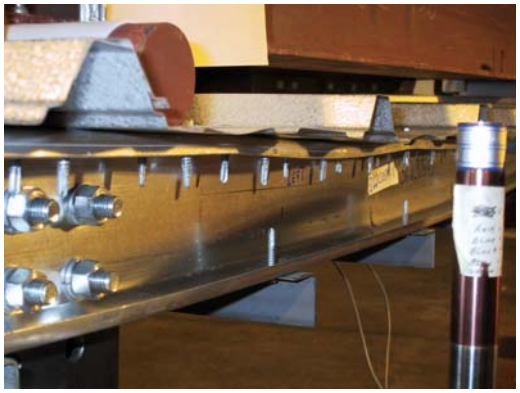

(e)

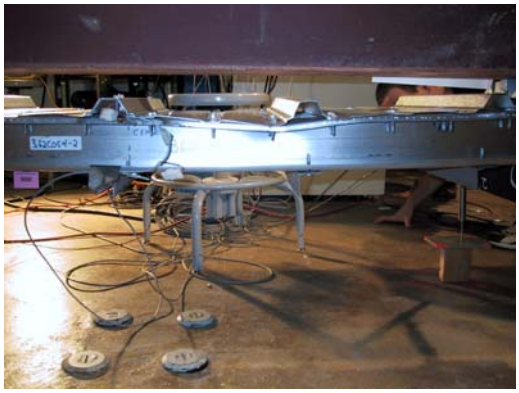

(f)

(a) material stress vs. strain of 3.62C054-1; (b) material stress vs. strain of 3.62C054-2;
(c) actuator load vs. displacement; (d) actuator load vs. displacements of LVDTs;
(e, f) pictures of collapse mechanism.

Distortional Buckling Test D8.5Z120-4E1W

Specimen	h (in.)	b_c (in.)	d_c (in.)	θ_c (deg.)	b_t (in.)	d_t (in.)	θ_t (deg.)	r_{hc} (in.)	r_{dc} (in.)	r_{ht} (in.)	r_{dt} (in.)	t (in.)	f_y (ksi)	f_u (ksi)	M_{test} (kips-in.)
D8.5Z120-4	8.44	2.63	0.93	54.20	2.47	1.00	50.20	0.34	0.34	0.34	0.34	0.1181	61.4	83.1	254
D8.5Z120-1	8.43	2.65	0.94	48.10	2.52	0.99	52.10	0.36	0.36	0.35	0.35	0.1181	61.9	83.3	254

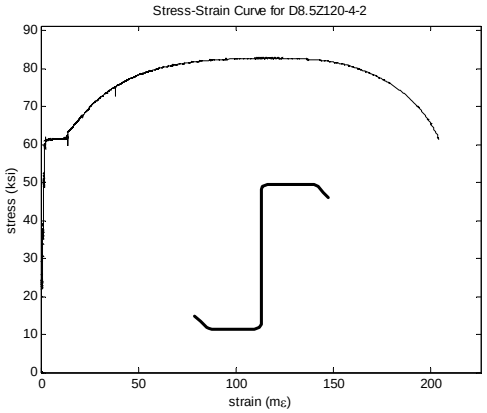

(a)

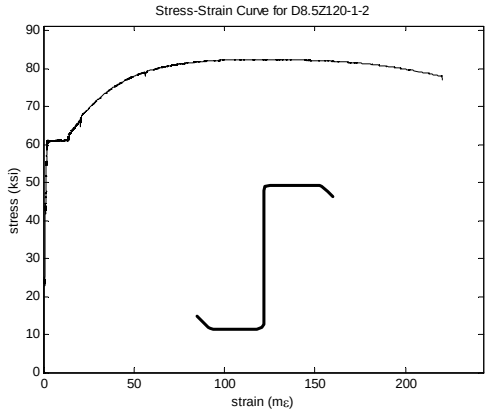

(b)

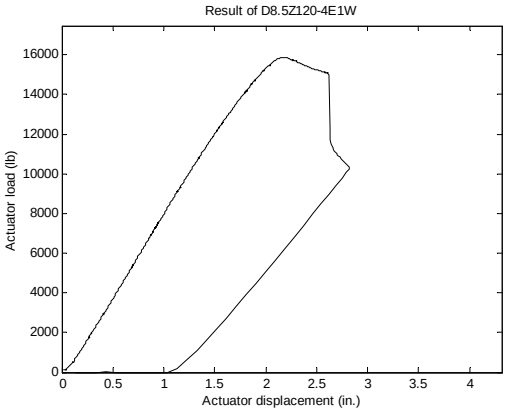

(c)

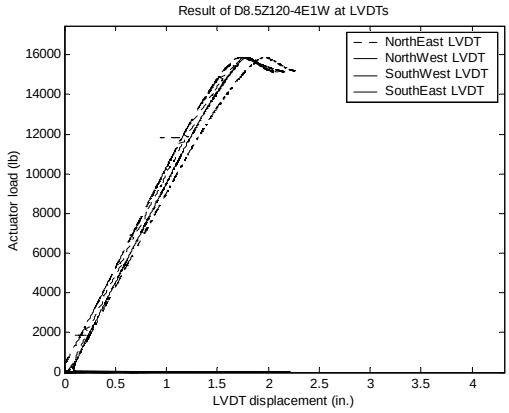

(d)

(e)

(f)

(a) material stress vs. strain of D8.5Z120-4; (b) material stress vs. strain of D8.5Z120-1;
(c) actuator load vs. displacement; (d) actuator load vs. displacements of LVDTs;
(e, f) pictures of collapse mechanism.

Distortional Buckling Test D8.5Z115-1E2W

Specimen	h (in.)	b_c (in.)	d_c (in.)	θ_c (deg.)	b_t (in.)	d_t (in.)	θ_t (deg.)	r_{hc} (in.)	r_{dc} (in.)	r_{ht} (in.)	r_{dt} (in.)	t (in.)	f_y (ksi)	f_u (ksi)	M_{test} (kips-in.)
D8.5Z115-2	8.54	2.56	0.91	49.00	2.40	0.89	48.30	0.35	0.35	0.37	0.37	0.1171	64.1	83.9	237
D8.5Z115-1	8.50	2.66	0.82	48.33	2.47	0.87	48.30	0.37	0.37	0.39	0.39	0.1166	65.8	84.7	237

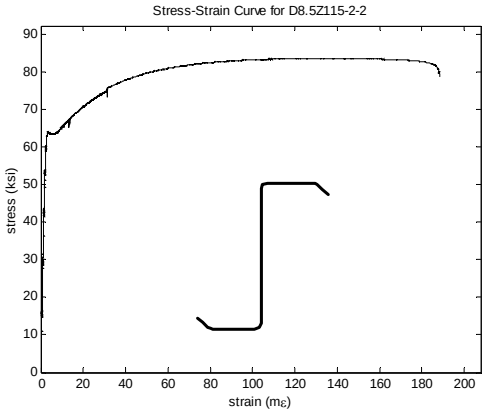

(a)

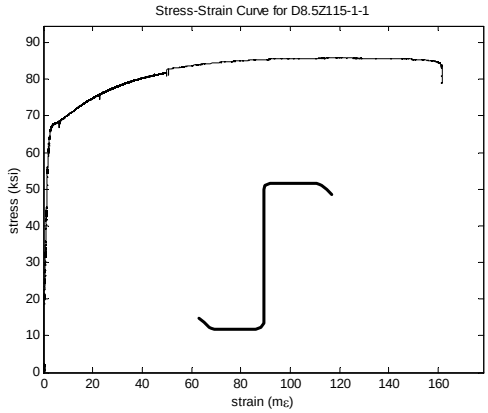

(b)

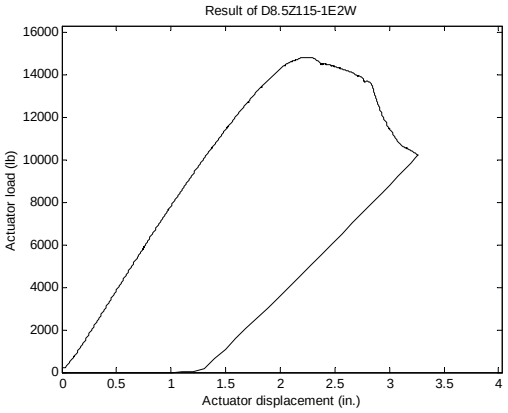

(c)

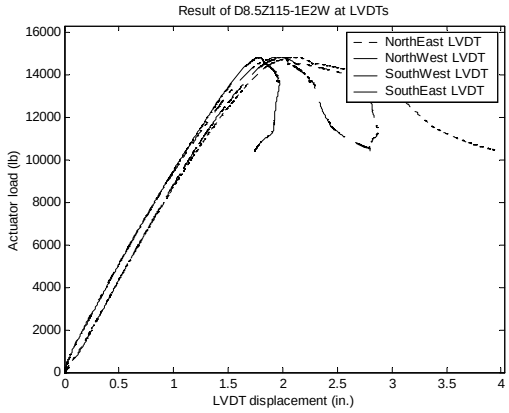

(d)

(e)

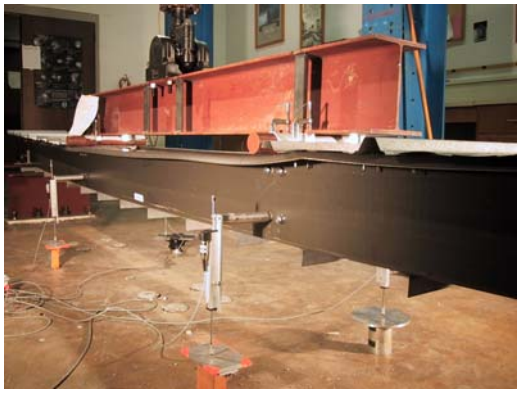

(f)

(a) material stress vs. strain of D8.5Z115-2; (b) material stress vs. strain of D8.5Z115-1;
(c) actuator load vs. displacement; (d) actuator load vs. displacements of LVDTs;
(e, f) pictures of collapse mechanism.

Distortional Buckling Test D8.5Z092-3E1W

Specimen	h (in.)	b_c (in.)	d_c (in.)	θ_c (deg.)	b_t (in.)	d_t (in.)	θ_t (deg.)	r_{hc} (in.)	r_{dc} (in.)	r_{ht} (in.)	r_{dt} (in.)	t (in.)	f_y (ksi)	f_u (ksi)	M_{test} (kips-in.)
D8.5Z092-3	8.40	2.58	0.95	51.90	2.41	0.94	51.60	0.29	0.29	0.31	0.31	0.0893	57.6	72.1	153
D8.5Z092-1	8.42	2.59	0.93	52.40	2.39	0.95	50.90	0.28	0.28	0.31	0.31	0.0897	57.8	72.6	153

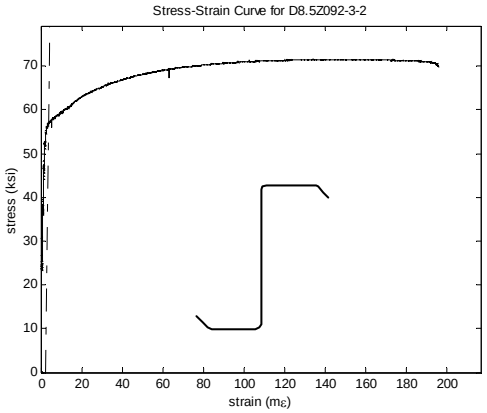

(a)

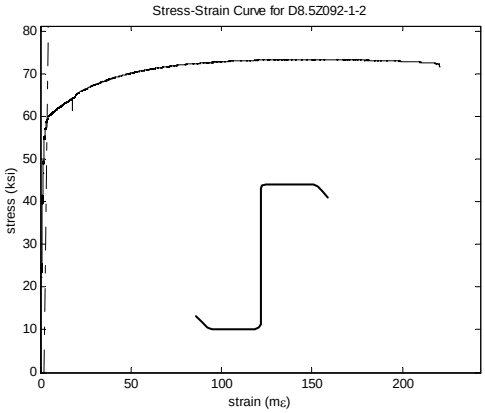

(b)

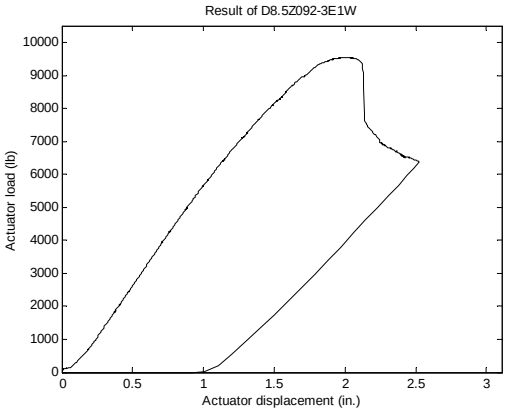

(c)

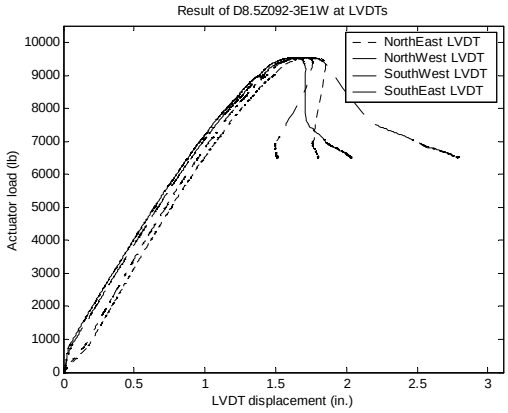

(d)

(e)

(f)

(a) material stress vs. strain of D8.5Z092-3; (b) material stress vs. strain of D8.5Z092-1;
(c) actuator load vs. displacement; (d) actuator load vs. displacements of LVDTs;
(e, f) pictures of collapse mechanism.

Distortional Buckling Test D8.5Z082-4E3W

Specimen	h (in.)	b_c (in.)	d_c (in.)	θ_c (deg.)	b_t (in.)	d_t (in.)	θ_t (deg.)	r_{hc} (in.)	r_{dc} (in.)	r_{ht} (in.)	r_{dt} (in.)	t (in.)	f_y (ksi)	f_u (ksi)	M_{test} (kips-in.)
D8.5Z082-4	8.48	2.52	0.94	48.50	2.39	0.97	51.30	0.28	0.28	0.30	0.30	0.0810	59.21	74.0	127
D8.5Z082-3	8.50	2.53	0.94	49.90	2.37	0.96	49.50	0.28	0.28	0.30	0.30	0.0810	58.99	73.8	127

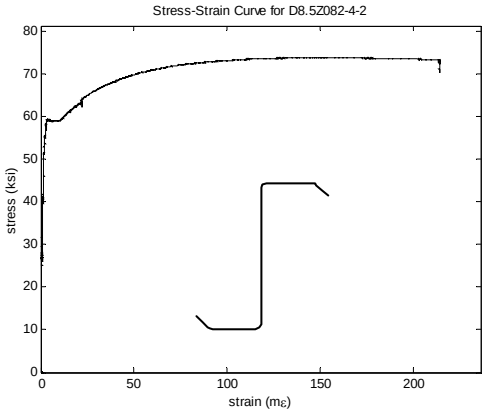

(a)

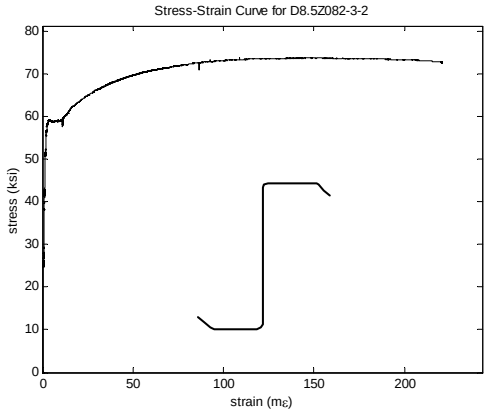

(b)

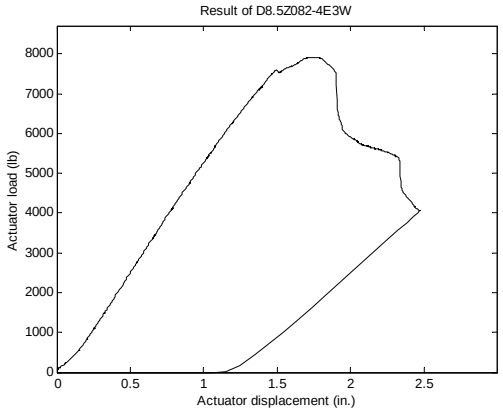

(c)

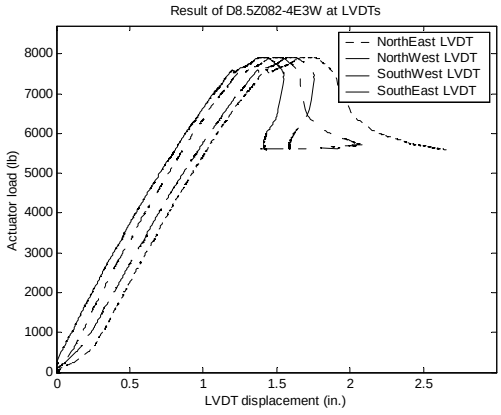

(d)

(e)

(f)

(a) material stress vs. strain of D8.5Z082-4; (b) material stress vs. strain of D8.5Z082-3;
(c) actuator load vs. displacement; (d) actuator load vs. displacements of LVDTs;
(e, f) pictures of collapse mechanism.

Distortional Buckling Test D8.5Z065-7E6W

Specimen	h (in.)	b_c (in.)	d_c (in.)	θ_c (deg.)	b_t (in.)	d_t (in.)	θ_t (deg.)	r_{hc} (in.)	r_{dc} (in.)	r_{ht} (in.)	r_{dt} (in.)	t (in.)	f_y (ksi)	f_u (ksi)	M_{test} (kips-in.)
D8.5Z065-7	8.48	2.47	0.83	50.00	2.47	0.82	49.33	0.32	0.32	0.33	0.33	0.0642	62.36	83.5	93
D8.5Z065-6	8.52	2.48	0.87	53.00	2.43	0.83	48.33	0.32	0.32	0.34	0.34	0.0645	63.34	83.4	93

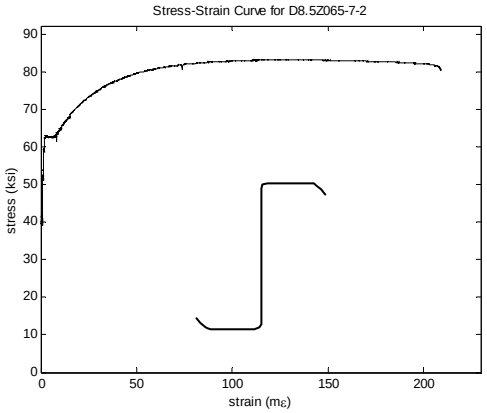

(a)

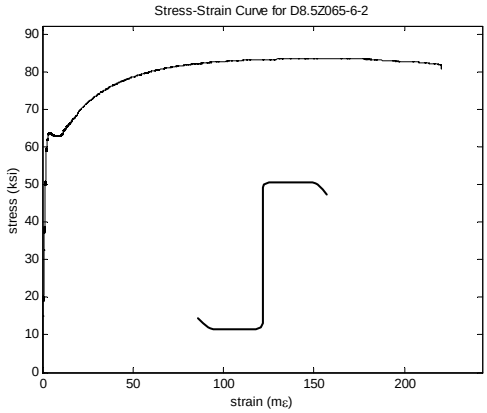

(b)

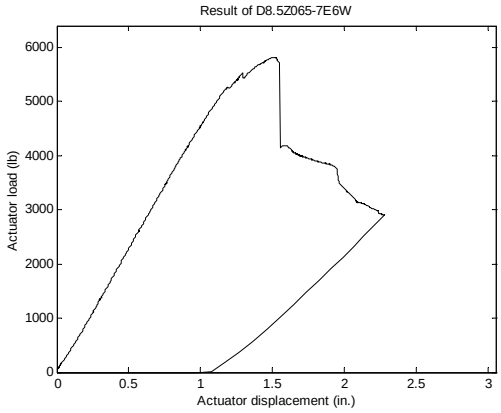

(c)

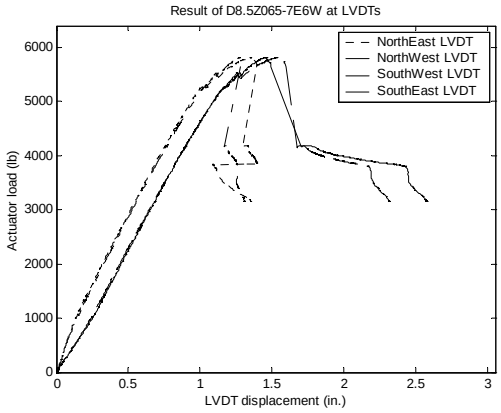

(d)

(e)

(f)

(a) material stress vs. strain of D8.5Z065-7; (b) material stress vs. strain of D8.5Z065-6;
(c) actuator load vs. displacement; (d) actuator load vs. displacements of LVDTs;
(e, f) pictures of collapse mechanism.

Distortional Buckling Test D8.5Z065-4E5W

Specimen	h (in.)	b_c (in.)	d_c (in.)	θ_c (deg.)	b_t (in.)	d_t (in.)	θ_t (deg.)	r_{hc} (in.)	r_{dc} (in.)	r_{ht} (in.)	r_{dt} (in.)	t (in.)	f_y (ksi)	f_u (ksi)	M_{test} (kips-in.)
D8.5Z065-5	8.50	2.36	0.67	51.33	2.52	0.90	47.17	0.27	0.27	0.28	0.28	0.0645	62.79	83.2	80
D8.5Z065-4	8.40	2.40	0.81	47.33	2.25	0.65	51.17	0.30	0.30	0.27	0.27	0.0619	58.26	78.4	80

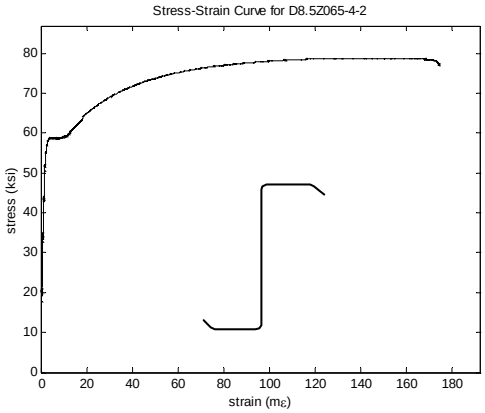

(a)

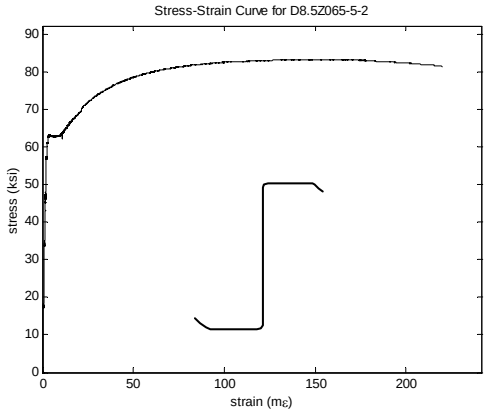

(b)

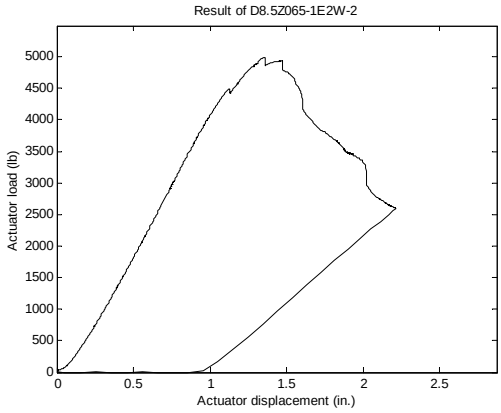

(c)

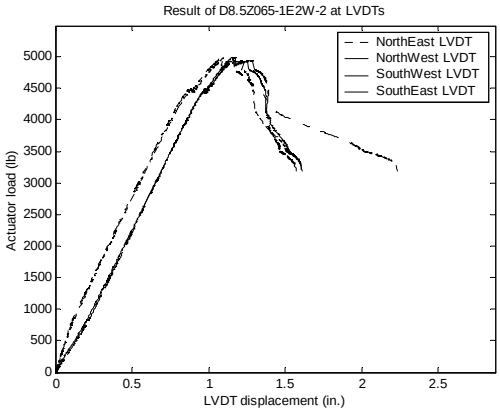

(d)

(e)

(f)

(a) material stress vs. strain of D8.5Z065-7; (b) material stress vs. strain of D8.5Z065-6;
(c) actuator load vs. displacement; (d) actuator load vs. displacements of LVDTs;
(e, f) pictures of collapse mechanism.

Distortional Buckling Test D8.5Z059-6E5W

Specimen	h (in.)	b_c (in.)	d_c (in.)	θ_c (deg.)	b_t (in.)	d_t (in.)	θ_t (deg.)	r_{hc} (in.)	r_{dc} (in.)	r_{ht} (in.)	r_{dt} (in.)	t (in.)	f_y (ksi)	f_u (ksi)	M_{test} (kips-in.)
D8.5Z059-6	8.44	2.42	0.77	50.40	2.39	0.86	48.00	0.32	0.32	0.30	0.30	0.0618	58.54	79.1	71
D8.5Z059-5	8.50	2.42	0.80	48.30	2.40	0.76	48.33	0.30	0.30	0.32	0.32	0.0615	59.05	79.4	71

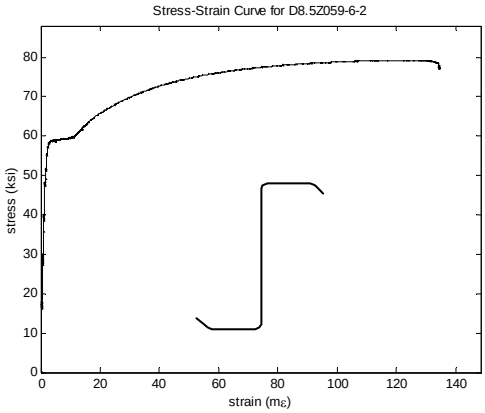

(a)

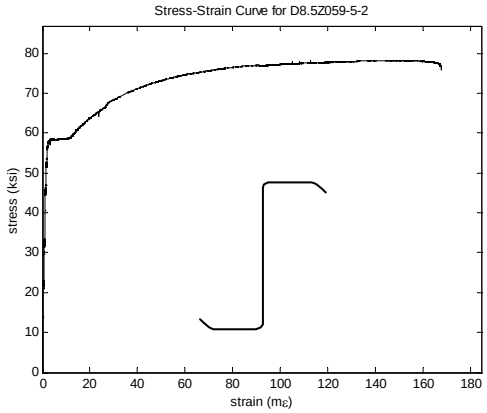

(b)

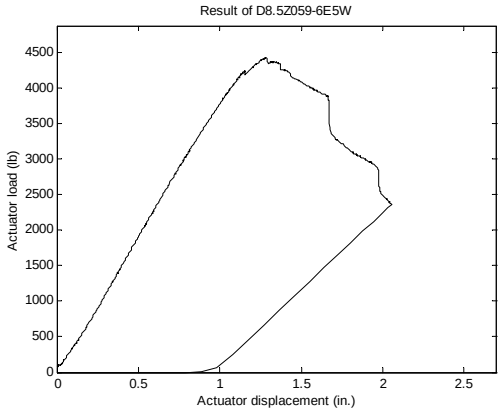

(c)

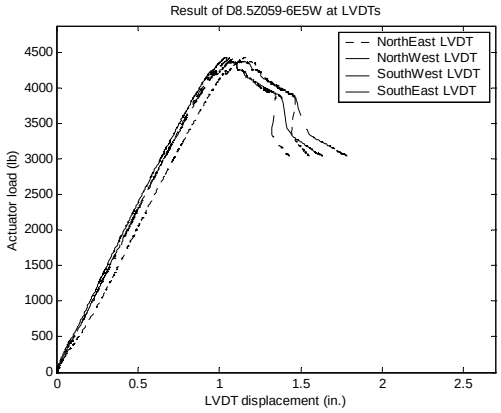

(d)

(e)

(f)

(a) material stress vs. strain of D8.5Z059-6; (b) material stress vs. strain of D8.5Z059-5;
(c) actuator load vs. displacement; (d) actuator load vs. displacements of LVDTs;
(e, f) pictures of collapse mechanism.

Distortional Buckling Test D11.5Z092-3E4W

Specimen	h (in.)	b_c (in.)	d_c (in.)	θ_c (deg.)	b_t (in.)	d_t (in.)	θ_t (deg.)	r_{hc} (in.)	r_{dc} (in.)	r_{ht} (in.)	r_{dt} (in.)	t (in.)	f_y (ksi)	f_u (ksi)	M_{test} (kips-in.)
D11.5Z092-4	11.23	3.47	0.94	48.70	3.40	0.91	49.60	0.33	0.33	0.31	0.31	0.0887	69.89	89.9	262
D11.5Z092-3	11.25	3.43	0.89	49.29	3.46	0.87	49.50	0.33	0.33	0.32	0.32	0.0889	70.11	90.2	262

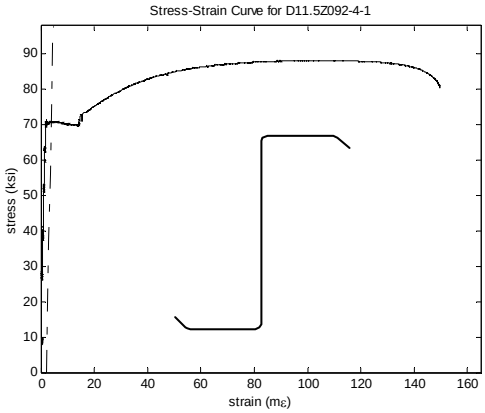

(a)

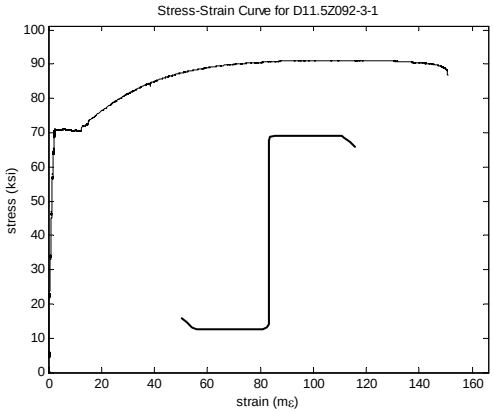

(b)

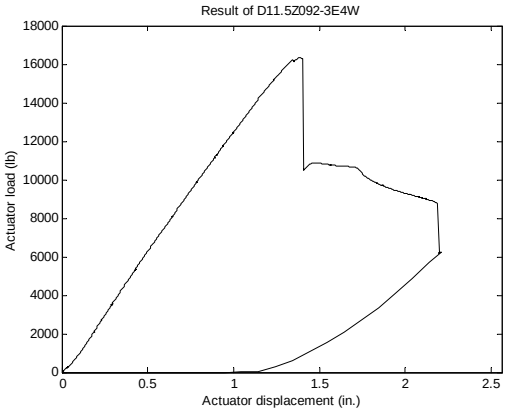

(c)

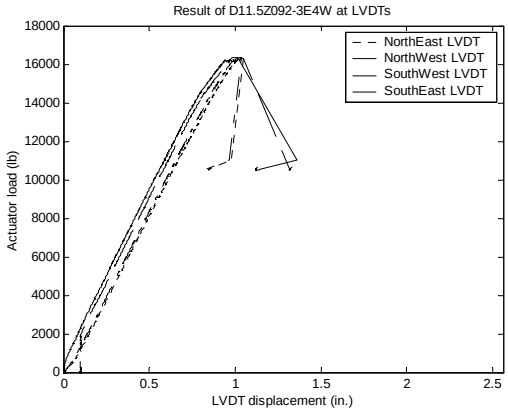

(d)

(e)

(f)

(a) material stress vs. strain of D11.5Z092-3; (b) material stress vs. strain of D11.5Z092-4;
(c) actuator load vs. displacement; (d) actuator load vs. displacements of LVDTs;
(e, f) pictures of collapse mechanism.

Distortional Buckling Test D11.5Z082-3E4W

Specimen	h (in.)	b_c (in.)	d_c (in.)	θ_c (deg.)	b_t (in.)	d_t (in.)	θ_t (deg.)	r_{hc} (in.)	r_{dc} (in.)	r_{ht} (in.)	r_{dt} (in.)	t (in.)	f_y (ksi)	f_u (ksi)	M_{test} (kips-in.)
D11.5Z082-4	11.40	3.41	0.88	48.40	3.40	0.86	49.90	0.30	0.30	0.32	0.32	0.0812	73.65	93.2	233
D11.5Z082-3	11.33	3.41	0.94	50.20	3.42	0.93	50.97	0.31	0.31	0.31	0.31	0.0818	71.80	92.0	233

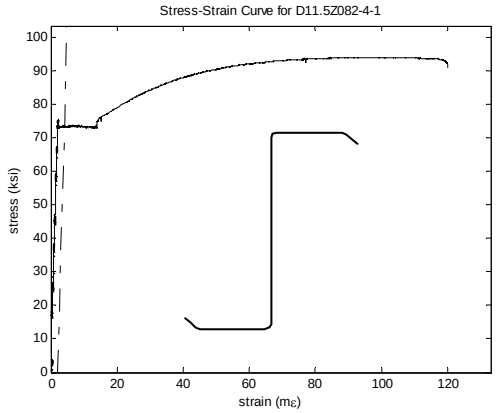

(a)

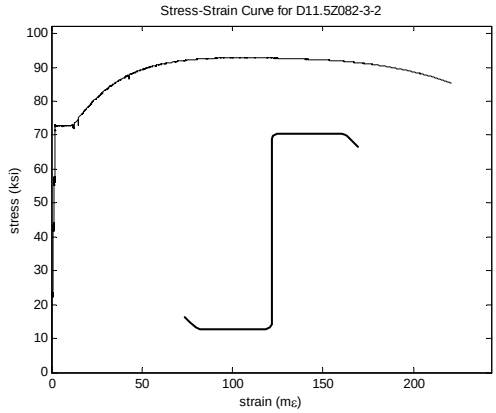

(b)

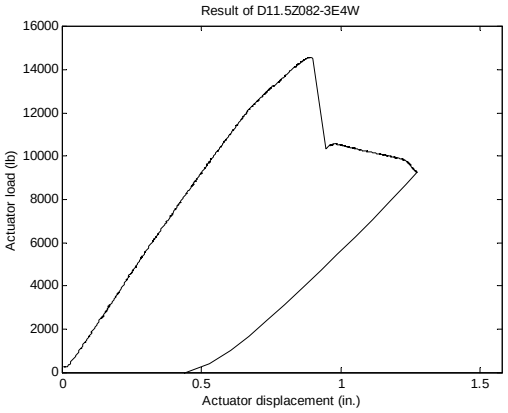

(c)

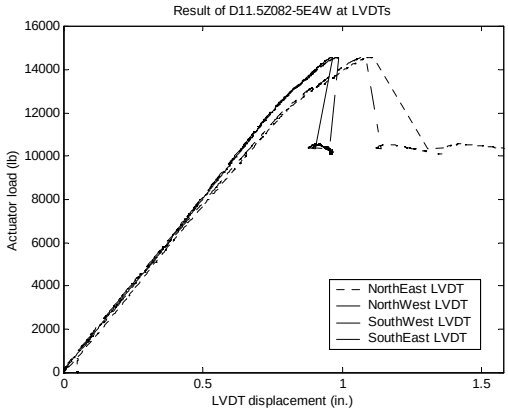

(d)

(e)

(f)

(a) material stress vs. strain of D11.5Z082-3; (b) material stress vs. strain of D11.5Z082-4;
(c) actuator load vs. displacement; (d) actuator load vs. displacements of LVDTs;
(e, f) pictures of collapse mechanism.

Distortional Buckling Test D8C097-7E6W

Specimen	h (in.)	b_c (in.)	d_c (in.)	θ_c (deg.)	b_t (in.)	d_t (in.)	θ_t (deg.)	r_{hc} (in.)	r_{dc} (in.)	r_{ht} (in.)	r_{dt} (in.)	t (in.)	f_y (ksi)	f_u (ksi)	M_{test} (kips-in.)
D8C097-7	8.13	2.15	0.65	80.75	2.13	0.62	80.00	0.27	0.29	0.27	0.30	0.1001	85.18	90.8	204
D8C097-6	8.15	2.09	0.64	81.00	2.09	0.61	80.00	0.27	0.29	0.27	0.30	0.1005	85.27	91.8	204

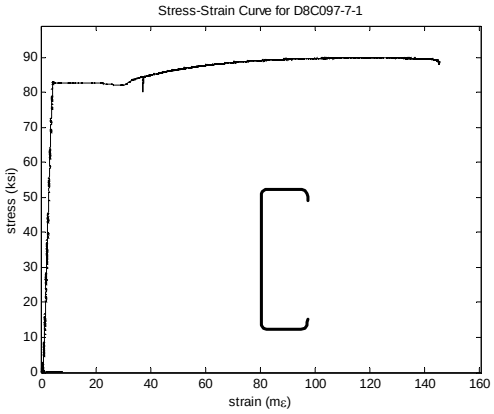

(a)

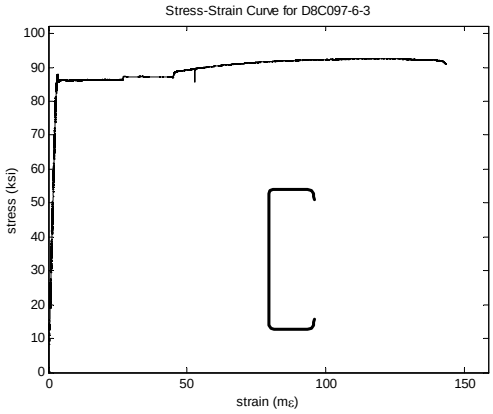

(b)

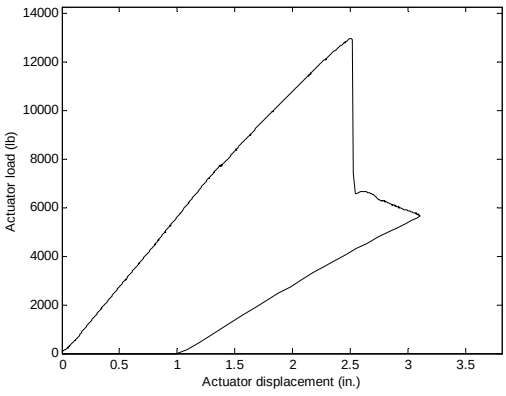

(c)

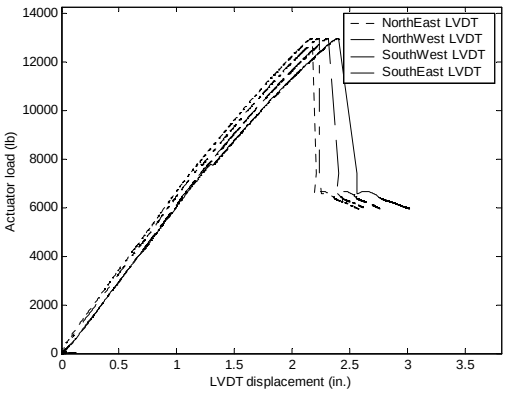

(d)

(e)

(f)

(a) material stress vs. strain of D8C097-7; (b) material stress vs. strain of D8C097-6; (c) actuator load vs. displacement; (d) actuator load vs. displacements of LVDTs; (e, f) pictures of collapse mechanism.

Distortional Buckling Test D8C097-5E4W

Specimen	h (in.)	b_c (in.)	d_c (in.)	θ_c (deg.)	b_t (in.)	d_t (in.)	θ_t (deg.)	r_{hc} (in.)	r_{dc} (in.)	r_{ht} (in.)	r_{dt} (in.)	t (in.)	f_y (ksi)	f_u (ksi)	M_{test} (kips-in.)
D8C097-5	8.06	2.00	0.66	86.70	1.99	0.67	83.00	0.28	0.30	0.28	0.28	0.0998	83.73	90.7	166
D8C097-4	8.06	2.03	0.67	83.00	2.00	0.68	83.00	0.27	0.28	0.27	0.28	0.0998	84.16	91.1	166

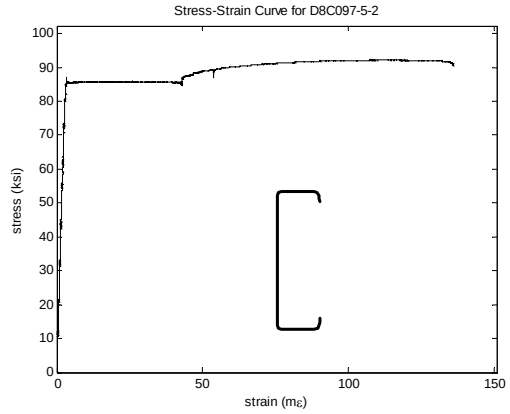

(a)

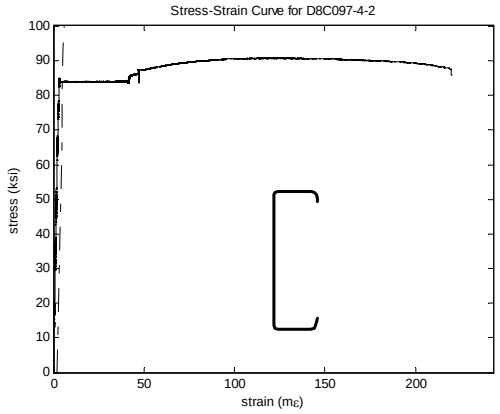

(b)

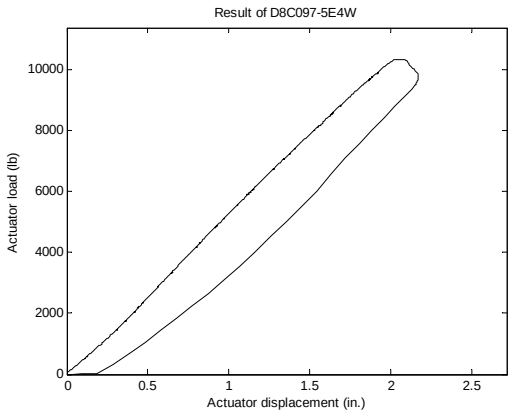

(c)

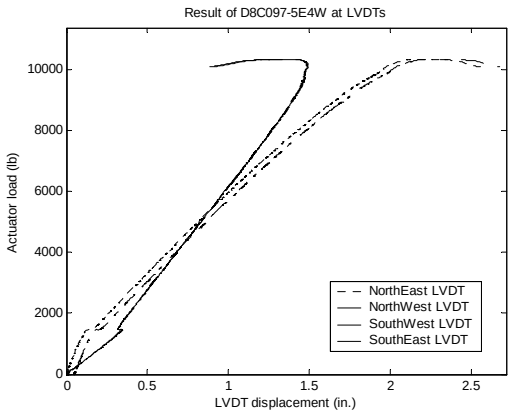

(d)

(e)

(f)

(a) material stress vs. strain of D8C097-5; (b) material stress vs. strain of D8C097-4; (c) actuator load vs. displacement; (d) actuator load vs. displacements of LVDTs; (e, f) pictures of collapse mechanism.

Distortional Buckling Test D8C085-2E1W

Specimen	h (in.)	b_c (in.)	d_c (in.)	θ_c (deg.)	b_t (in.)	d_t (in.)	θ_t (deg.)	r_{hc} (in.)	r_{dc} (in.)	r_{ht} (in.)	r_{dt} (in.)	t (in.)	f_y (ksi)	f_u (ksi)	M_{test} (kips-in.)
D8C085-2	8.06	1.98	0.63	86.00	1.96	0.68	86.60	0.22	0.22	0.23	0.22	0.0825	52.80	65.8	166
D8C085-1	8.06	1.98	0.62	88.60	1.96	0.68	89.00	0.22	0.19	0.23	0.19	0.0848	51.85	64.2	166

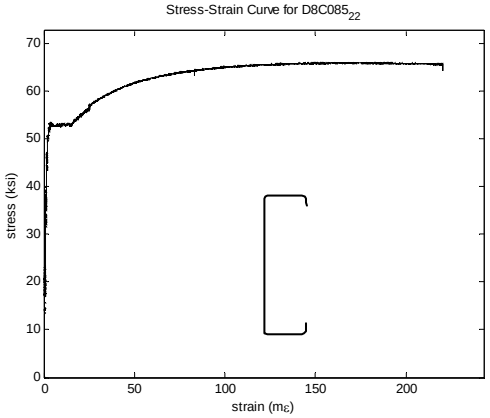

(a)

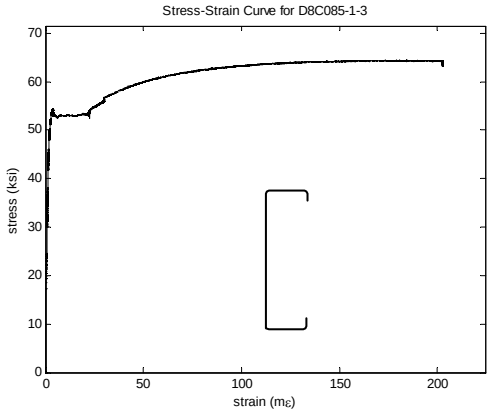

(b)

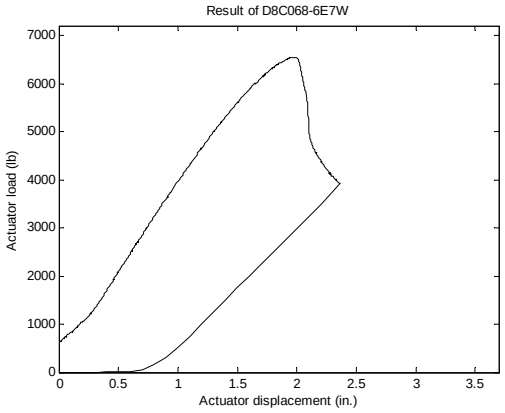

(c)

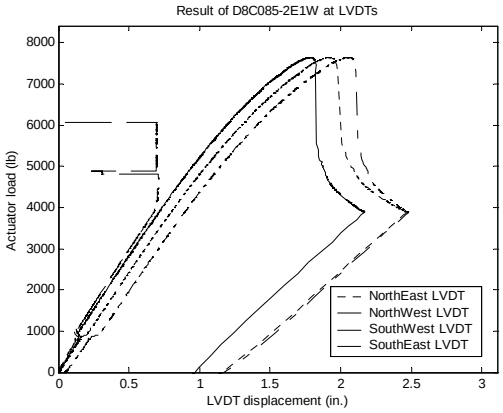

(d)

(e)

(f)

(a) material stress vs. strain of D8C085-2; (b) material stress vs. strain of D8C085-1; (c) actuator load vs. displacement; (d) actuator load vs. displacements of LVDTs; (e, f) pictures of collapse mechanism.

Distortional Buckling Test D8C068-6E7W

Specimen	h (in.)	b_c (in.)	d_c (in.)	θ_c (deg.)	b_t (in.)	d_t (in.)	θ_t (deg.)	r_{hc} (in.)	r_{dc} (in.)	r_{ht} (in.)	r_{dt} (in.)	t (in.)	f_y (ksi)	f_u (ksi)	M_{test} (kips-in.)
D8C068-6	7.94	1.91	0.66	80.00	1.97	0.64	77.80	0.16	0.16	0.16	0.16	0.0708	78.94	80.9	105
D8C068-7	7.94	1.97	0.64	76.50	1.95	0.67	77.50	0.16	0.16	0.16	0.16	0.0708	79.87	80.8	105

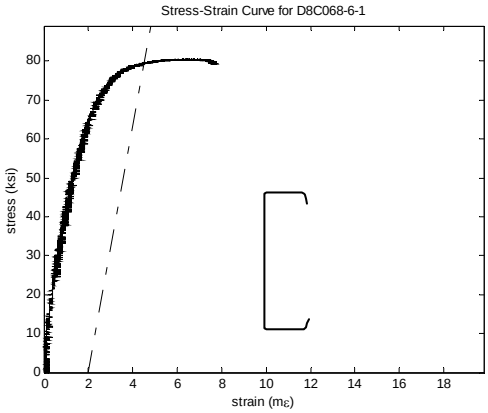

(a)

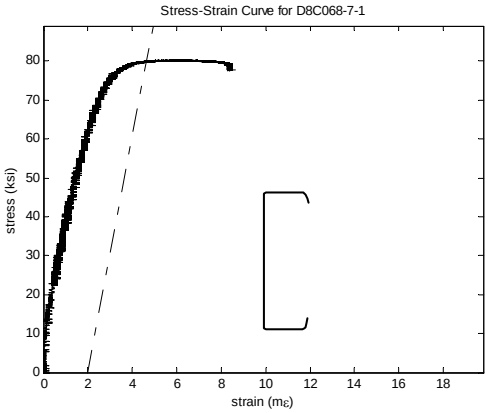

(b)

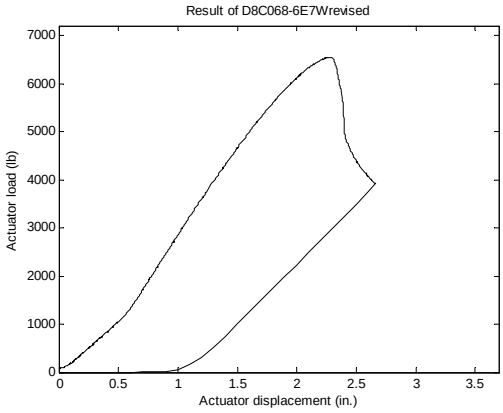

(c)

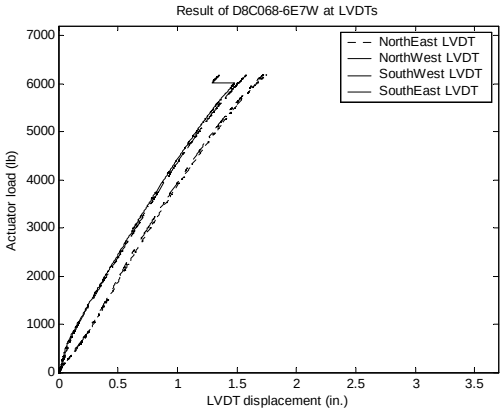

(d)

(e)

(f)

(a) material stress vs. strain of D8C085-2; (b) material stress vs. strain of D8C085-1; (c) actuator load vs. displacement; (d) actuator load vs. displacements of LVDTs; (e, f) pictures of collapse mechanism.

Distortional Buckling Test D8C054-7E6W

Specimen	h (in.)	b_c (in.)	d_c (in.)	θ_c (deg.)	b_t (in.)	d_t (in.)	θ_t (deg.)	r_{hc} (in.)	r_{dc} (in.)	r_{ht} (in.)	r_{dt} (in.)	t (in.)	f_y (ksi)	f_u (ksi)	M_{test} (kips-in.)
D8C054-7	8.01	2.04	0.53	83.40	2.03	0.57	88.70	0.24	0.23	0.21	0.23	0.0528	40.81	52.5	49
D8C054-6	8.00	2.05	0.59	89.40	2.04	0.56	83.30	0.22	0.23	0.23	0.24	0.0520	40.68	50.9	49

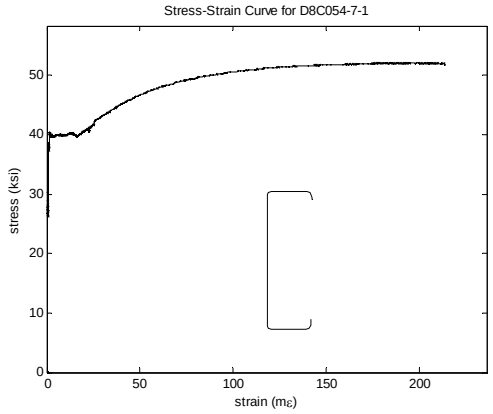

(a)

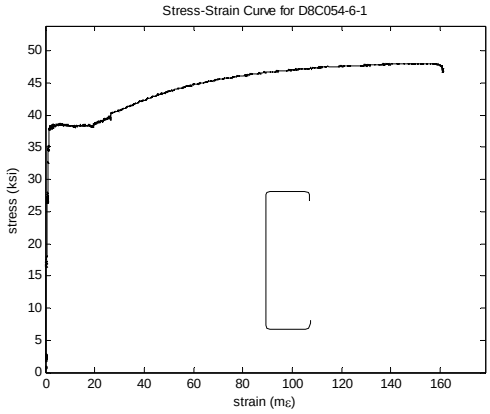

(b)

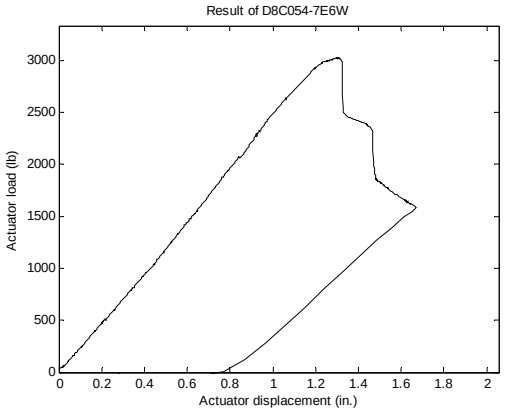

(c)

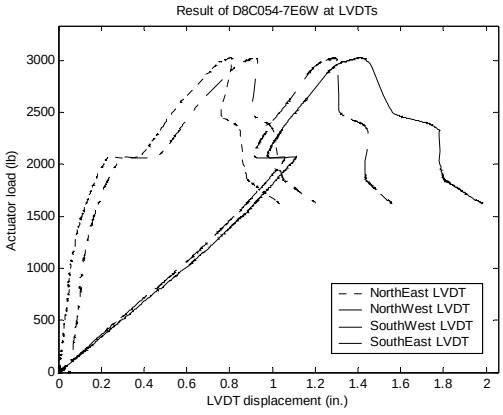

(d)

(e)

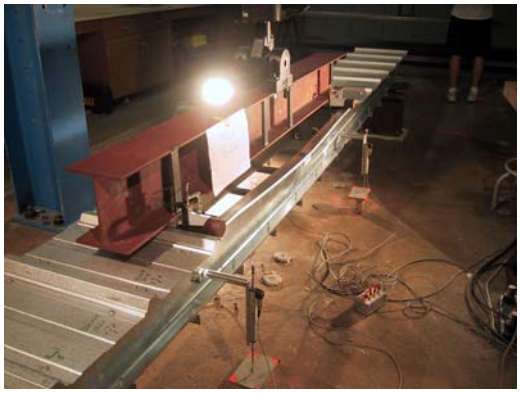

(f)

(a) material stress vs. strain of D8C054-7; (b) material stress vs. strain of D8C054-6; (c) actuator load vs. displacement; (d) actuator load vs. displacements of LVDTs; (e, f) pictures of collapse mechanism.

Distortional Buckling Test D8C045-1E2W

Specimen	h (in.)	b_c (in.)	d_c (in.)	θ_c (deg.)	b_t (in.)	d_t (in.)	θ_t (deg.)	r_{hc} (in.)	r_{dc} (in.)	r_{ht} (in.)	r_{dt} (in.)	t (in.)	f_y (ksi)	f_u (ksi)	M_{test} (kips-in.)
D8C045-1	8.18	1.95	0.67	89.00	1.92	0.66	87.60	0.28	0.19	0.22	0.20	0.0348	21.38	42.7	17
D8C045-2	8.14	1.94	0.69	88.80	1.92	0.69	88.30	0.28	0.20	0.23	0.20	0.0348	21.04	42.6	17

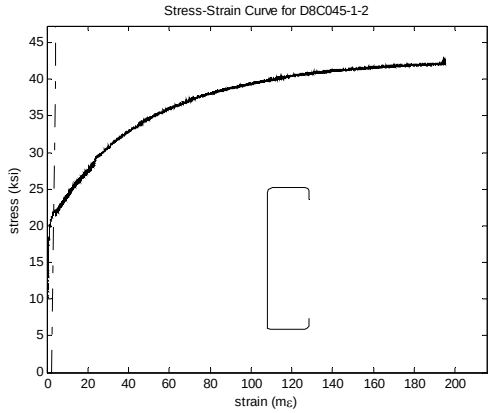

(a)

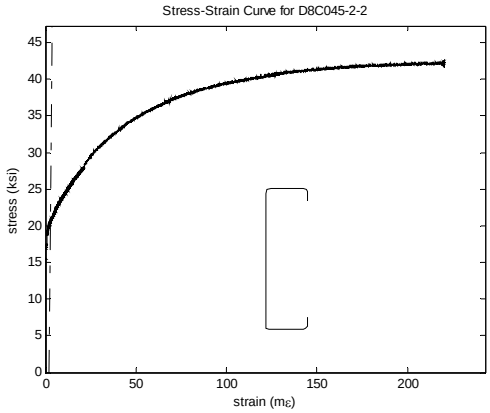

(b)

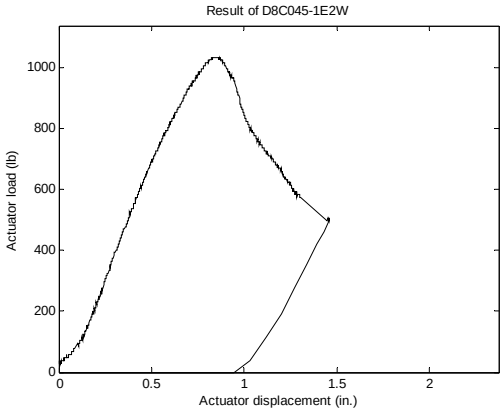

(c)

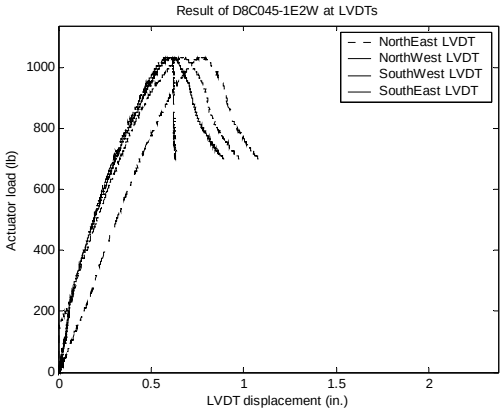

(d)

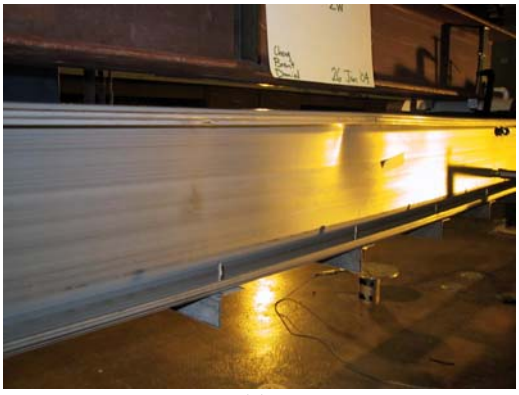

(e)

(f)

(a) material stress vs. strain of D8C045-1; (b) material stress vs. strain of D8C045-2; (c) actuator load vs. displacement; (d) actuator load vs. displacements of LVDTs; (e, f) pictures of collapse mechanism.

Distortional Buckling Test D8C043-4E2W

Specimen	h (in.)	b_c (in.)	d_c (in.)	θ_c (deg.)	b_t (in.)	d_t (in.)	θ_t (deg.)	r_{hc} (in.)	r_{dc} (in.)	r_{ht} (in.)	r_{dt} (in.)	t (in.)	f_y (ksi)	f_u (ksi)	M_{test} (kips-in.)
D8C043-4	8.02	2.01	0.53	87.30	2.01	0.53	88.80	0.17	0.18	0.17	0.20	0.0459	45.44	61.0	43
D8C043-2	8.03	1.99	0.52	88.93	1.98	0.54	87.70	0.18	0.19	0.20	0.19	0.0472	45.47	61.0	43

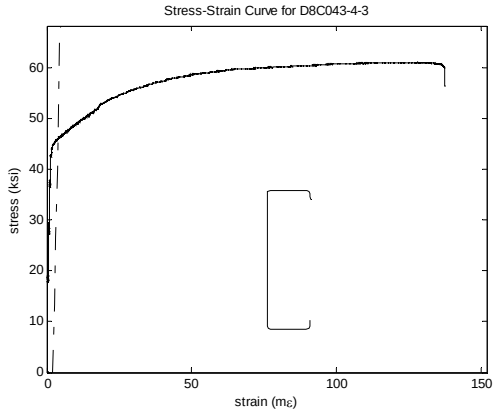

(a)

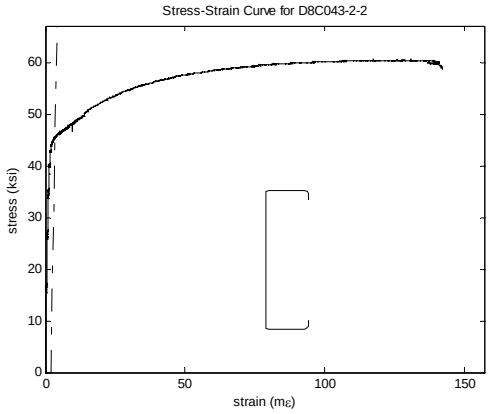

(b)

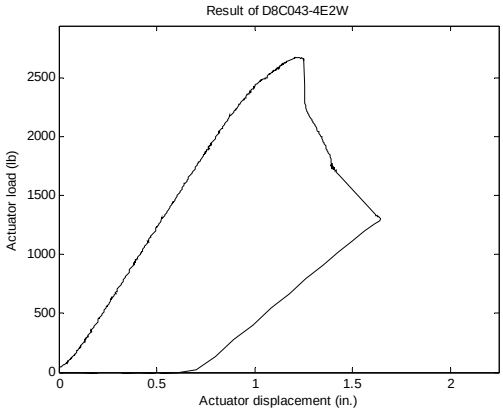

(c)

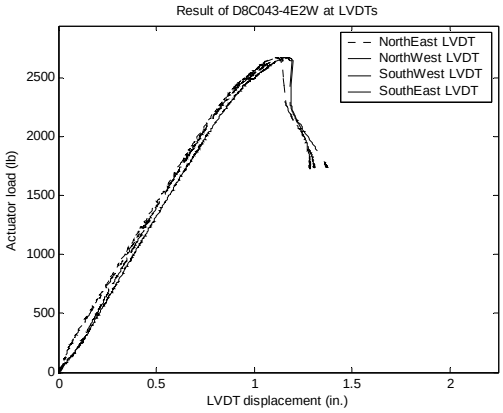

(d)

(e)

(f)

(a) material stress vs. strain of D8C043-4; (b) material stress vs. strain of D8C043-2; (c) actuator load vs. displacement; (d) actuator load vs. displacements of LVDTs; (e, f) pictures of collapse mechanism.

Distortional Buckling Test D8C033-1E2W

Specimen	h (in.)	b_c (in.)	d_c (in.)	θ_c (deg.)	b_t (in.)	d_t (in.)	θ_t (deg.)	r_{hc} (in.)	r_{dc} (in.)	r_{ht} (in.)	r_{dt} (in.)	t (in.)	f_y (ksi)	f_u (ksi)	M_{test} (kips-in.)
D8C033-2	8.15	1.99	0.68	87.10	1.91	0.63	85.80	0.17	0.30	0.20	0.30	0.0337	20.47	41.9	16
D8C033-1	8.08	2.00	0.61	86.00	1.96	0.77	88.00	0.21	0.26	0.18	0.28	0.0339	20.35	42.2	16

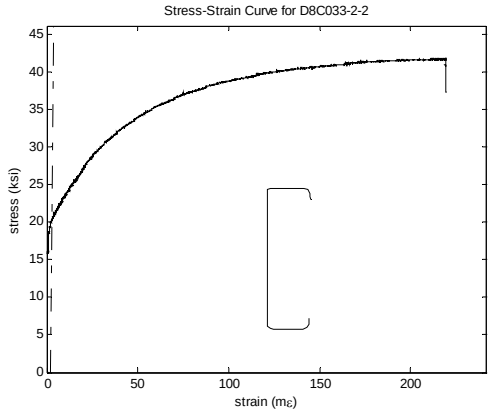

(a)

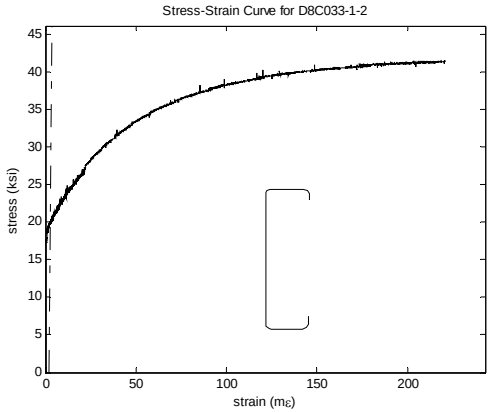

(b)

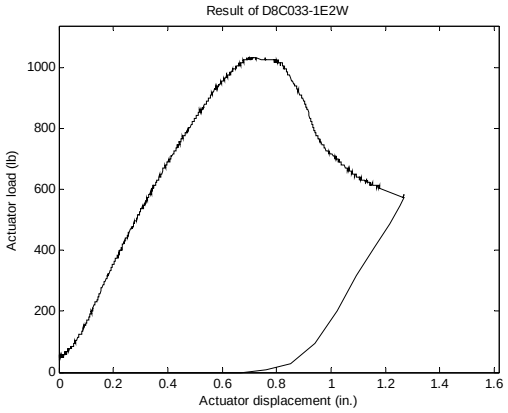

(c)

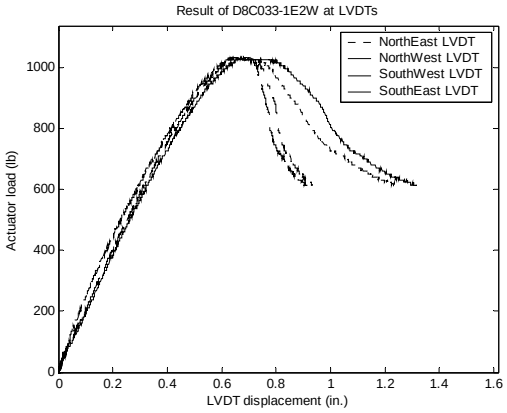

(d)

(e)

(f)

(a) material stress vs. strain of D8C033-2; (b) material stress vs. strain of D8C033-1; (c) actuator load vs. displacement; (d) actuator load vs. displacements of LVDTs; (e, f) pictures of collapse mechanism.

Distortional Buckling Test D12C068-10E11W

Specimen	h (in.)	b_c (in.)	d_c (in.)	θ_c (deg.)	b_t (in.)	d_t (in.)	θ_t (deg.)	r_{hc} (in.)	r_{dc} (in.)	r_{ht} (in.)	r_{dt} (in.)	t (in.)	f_y (ksi)	f_u (ksi)	M_{test} (kips-in.)
D12C068-11	12.03	2.03	0.51	81.97	2.00	0.53	85.33	0.22	0.22	0.24	0.23	0.0645	32.90	56.9	95
D12C068-10	12.05	2.02	0.54	85.87	1.98	0.51	94.80	0.24	0.24	0.27	0.23	0.0648	34.70	56.7	95

(a)

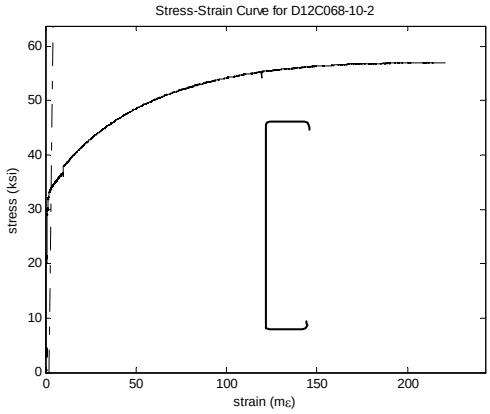

(b)

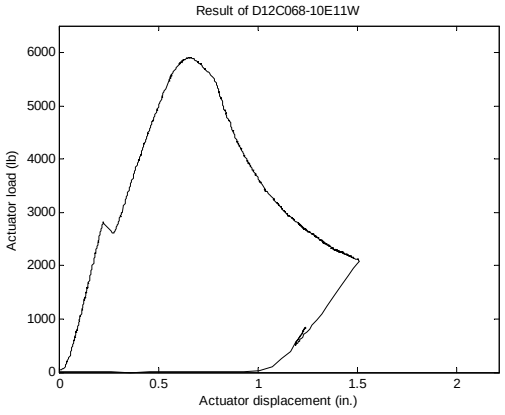

(c)

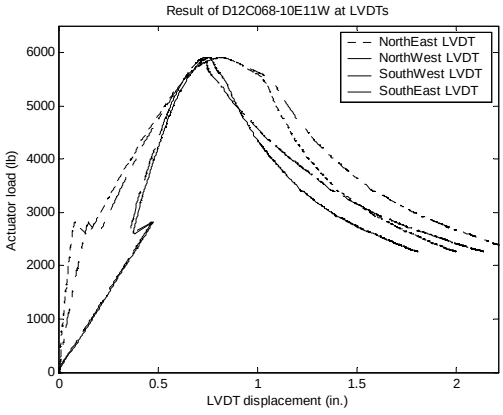

(d)

(e)

(f)

(a) material stress vs. strain of D12C068-10; (b) material stress vs. strain of D12C068-11;
(c) actuator load vs. displacement; (d) actuator load vs. displacements of LVDTs;
(e, f) pictures of collapse mechanism.

Distortional Buckling Test D12C068-1E2W

Specimen	h (in.)	b_c (in.)	d_c (in.)	θ_c (deg.)	b_t (in.)	d_t (in.)	θ_t (deg.)	r_{hc} (in.)	r_{dc} (in.)	r_{ht} (in.)	r_{dt} (in.)	t (in.)	f_y (ksi)	f_u (ksi)	M_{test} (kips-in.)
D12C068-2	11.92	2.05	0.52	82.47	2.03	0.59	77.37	0.26	0.24	0.25	0.24	0.0664	56.31	73.7	99
D12C068-1	11.97	2.12	0.52	80.60	2.00	0.56	83.30	0.25	0.25	0.26	0.26	0.0668	55.86	73.6	99

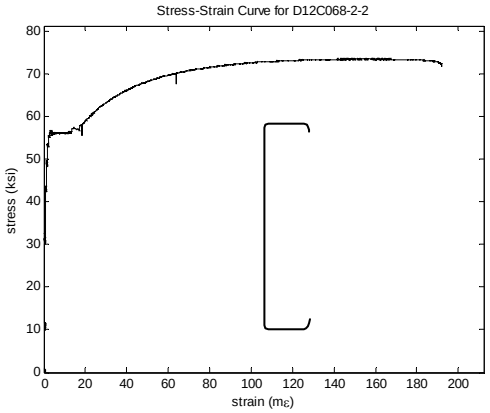

(a)

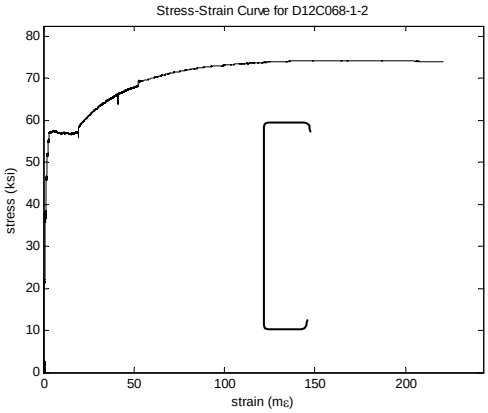

(b)

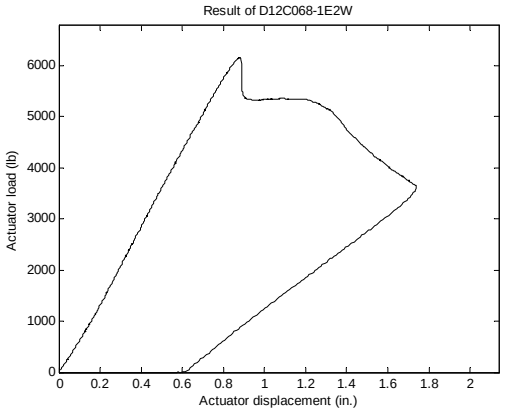

(c)

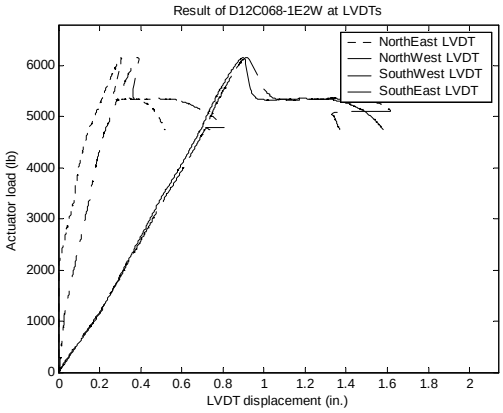

(d)

(e)

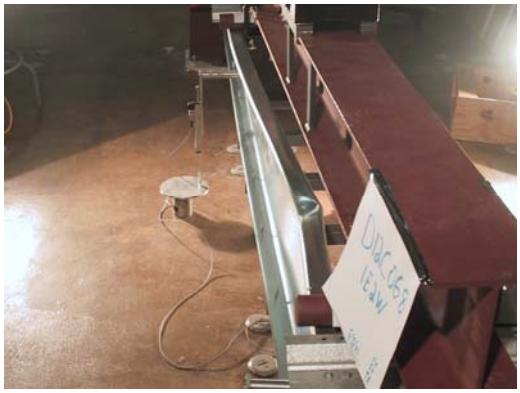

(f)

(a) material stress vs. strain of D12C068-2; (b) material stress vs. strain of D12C068-1;
(c) actuator load vs. displacement; (d) actuator load vs. displacements of LVDTs;
(e, f) pictures of collapse mechanism.

Distortional Buckling Test D10C068-4E3W

Specimen	h (in.)	b_c (in.)	d_c (in.)	θ_c (deg.)	b_t (in.)	d_t (in.)	θ_t (deg.)	r_{hc} (in.)	r_{dc} (in.)	r_{ht} (in.)	r_{dt} (in.)	t (in.)	f_y (ksi)	f_u (ksi)	M_{test} (kips-in.)
D10C068-4	10.08	2.00	0.48	83.23	2.08	0.53	83.30	0.26	0.21	0.23	0.23	0.0626	22.01	40.3	51
D10C068-3	10.10	2.07	0.53	80.70	2.08	0.52	81.85	0.24	0.23	0.23	0.22	0.0634	22.54	40.9	51

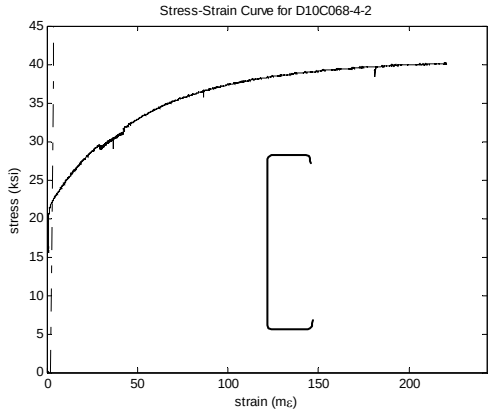

(a)

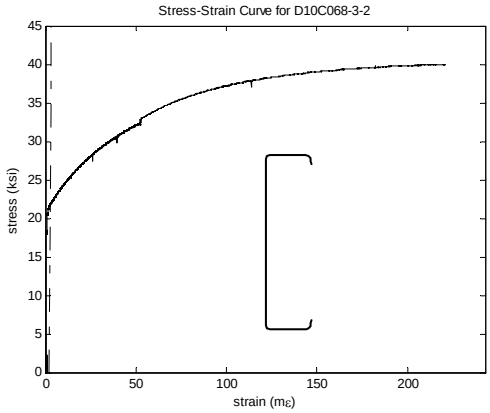

(b)

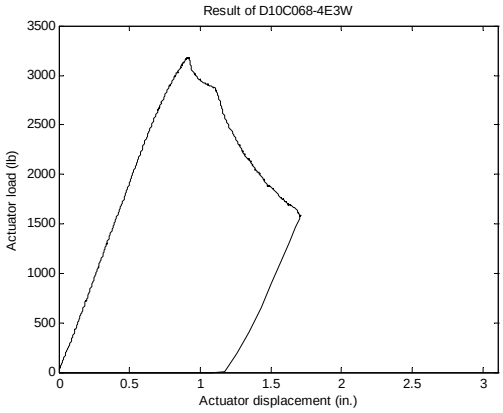

(c)

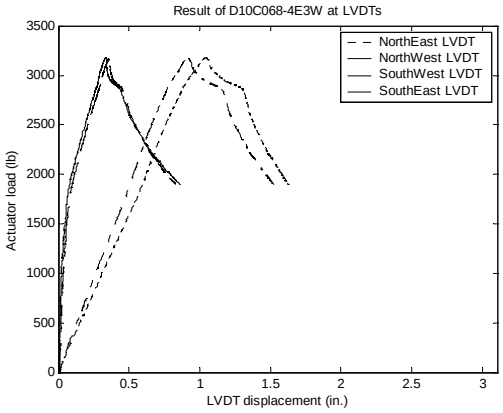

(d)

(e)

(f)

(a) material stress vs. strain of D10C068-4; (b) material stress vs. strain of D10C068-3;
(c) actuator load vs. displacement; (d) actuator load vs. displacements of LVDTs;
(e, f) pictures of collapse mechanism.

Distortional Buckling Test D10C056-3E4W

Specimen	h (in.)	b_c (in.)	d_c (in.)	θ_c (deg.)	b_t (in.)	d_t (in.)	θ_t (deg.)	r_{hc} (in.)	r_{dc} (in.)	r_{ht} (in.)	r_{dt} (in.)	t (in.)	f_y (ksi)	f_u (ksi)	M_{test} (kips-in.)
D10C056-3	9.99	1.97	0.66	88.00	1.95	0.63	89.00	0.13	0.16	0.13	0.13	0.0569	77.28	80.4	85
D10C056-4	10.00	1.94	0.72	88.60	1.92	0.66	87.70	0.13	0.16	0.13	0.18	0.0569	76.93	81.6	85

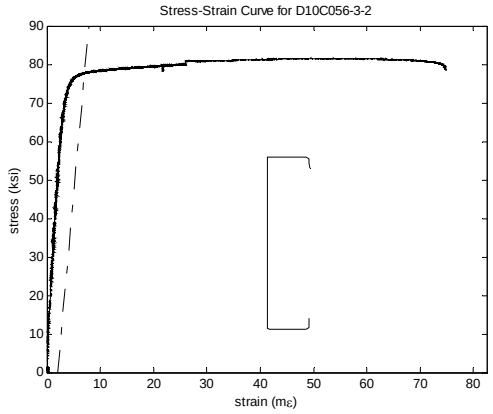

(a)

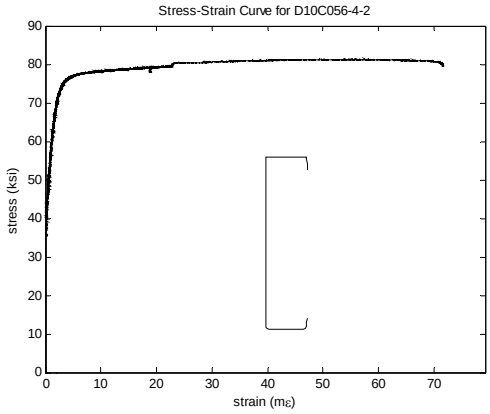

(b)

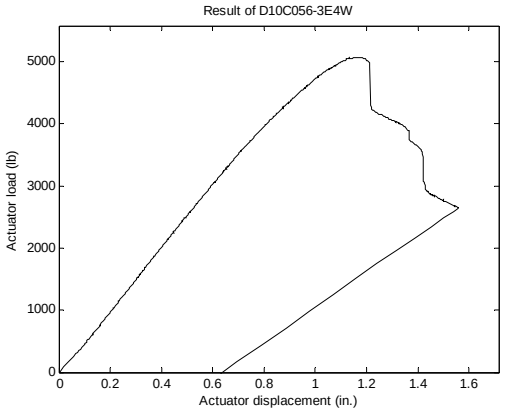

(c)

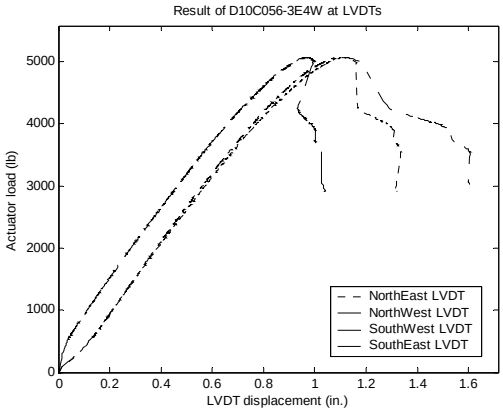

(d)

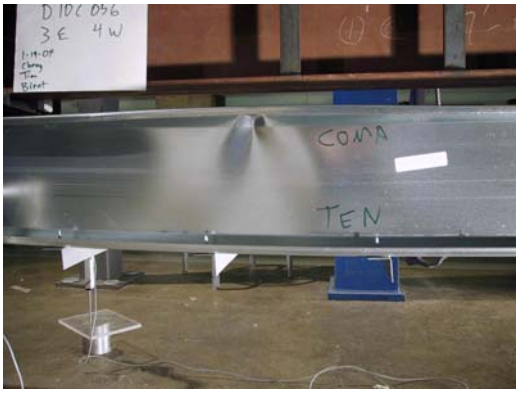

(e)

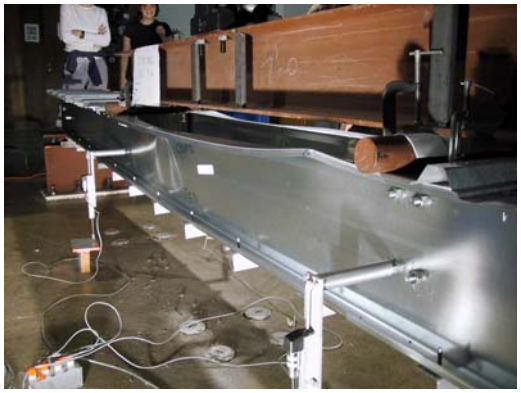

(f)

(a) material stress vs. strain of D10C056-3; (b) material stress vs. strain of D10C056-4;
(c) actuator load vs. displacement; (d) actuator load vs. displacements of LVDTs;
(e, f) pictures of collapse mechanism.

Distortional Buckling Test D10C048-1E2W

Specimen	h (in.)	b_c (in.)	d_c (in.)	θ_c (deg.)	b_t (in.)	d_t (in.)	θ_t (deg.)	r_{hc} (in.)	r_{dc} (in.)	r_{ht} (in.)	r_{dt} (in.)	t (in.)	f_y (ksi)	f_u (ksi)	M_{test} (kips-in.)
D10C048-1	9.94	2.06	0.62	86.10	1.94	0.63	79.60	0.20	0.19	0.20	0.19	0.0478	51.08	58.5	62
D10C048-2	9.94	2.02	0.63	85.70	1.95	0.63	83.70	0.18	0.19	0.19	0.20	0.0486	50.62	57.8	62

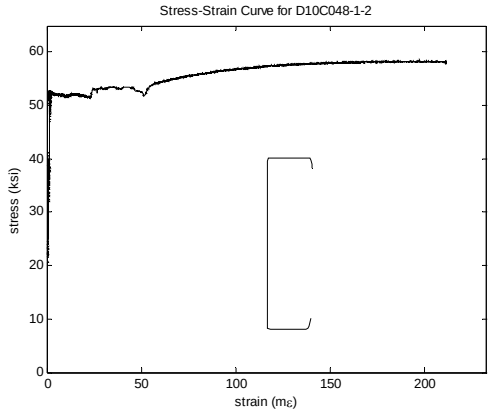

(a)

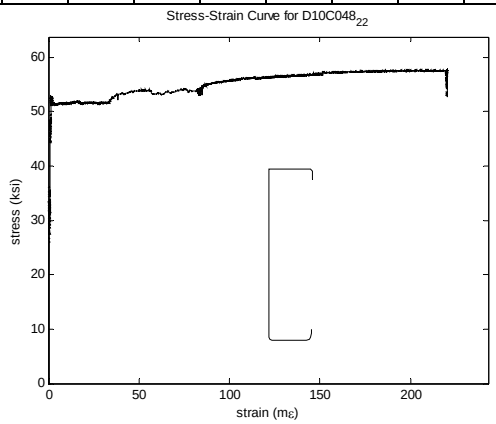

(b)

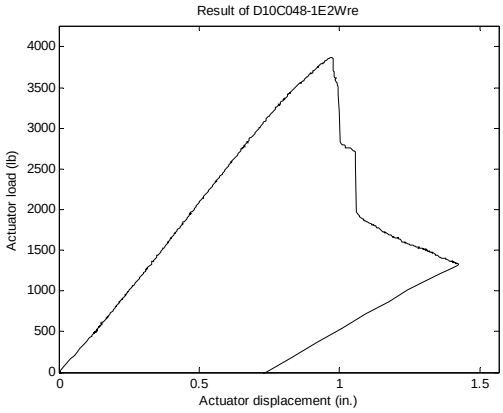

(c)

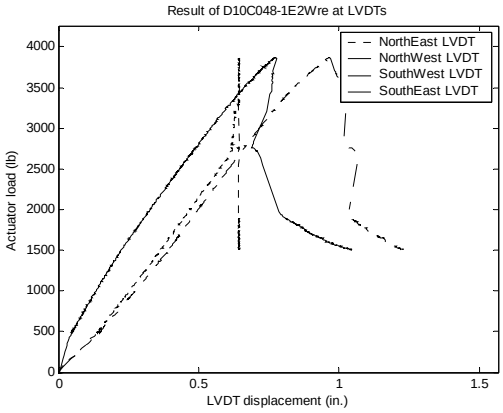

(d)

(e)

(f)

(a) material stress vs. strain of D10C048-1; (b) material stress vs. strain of D10C048-2;
(c) actuator load vs. displacement; (d) actuator load vs. displacements of LVDTs;
(e, f) pictures of collapse mechanism.

Distortional Buckling Test D6C063-2E1W

Specimen	h (in.)	b_c (in.)	d_c (in.)	θ_c (deg.)	b_t (in.)	d_t (in.)	θ_t (deg.)	r_{hc} (in.)	r_{dc} (in.)	r_{ht} (in.)	r_{dt} (in.)	t (in.)	f_y (ksi)	f_u (ksi)	M_{test} (kips-in.)
D6C063-2	5.99	1.99	0.63	88.74	1.97	0.63	87.30	0.19	0.17	0.19	0.22	0.0578	55.94	66.8	52
D6C063-1	5.99	1.99	0.62	87.03	1.97	0.63	86.13	0.22	0.17	0.22	0.17	0.0559	57.82	69.5	52

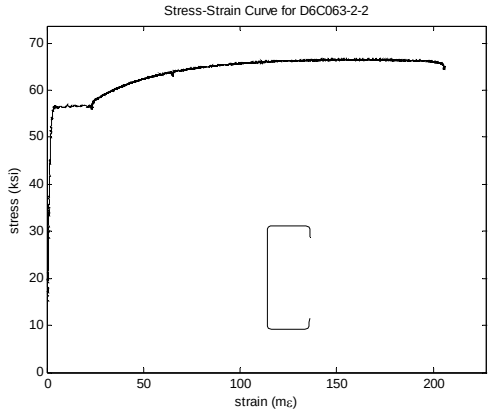

(a)

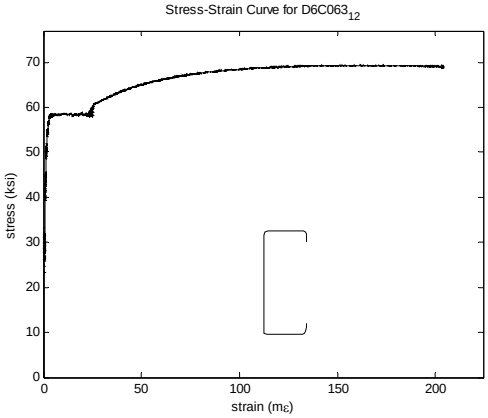

(b)

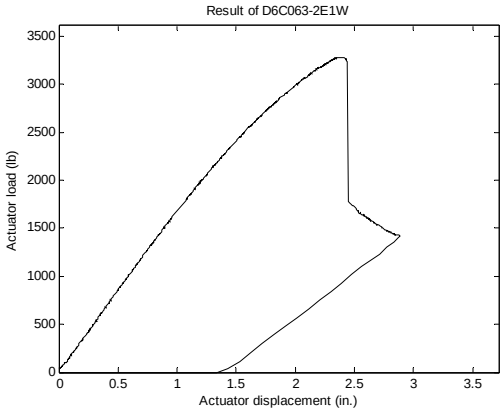

(c)

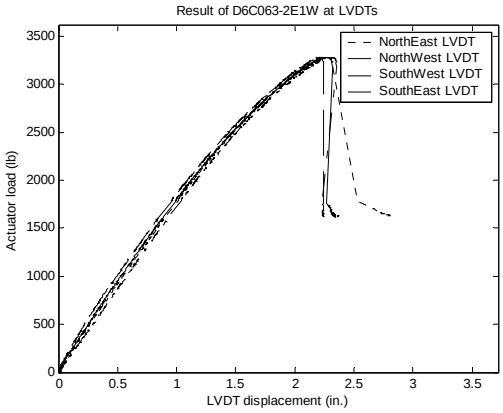

(d)

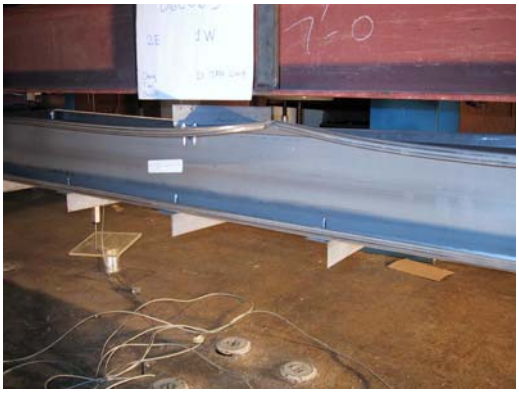

(e)

(f)

(a) material stress vs. strain of D6C063-2; (b) material stress vs. strain of D6C063-1; (c) actuator load vs. displacement; (d) actuator load vs. displacements of LVDTs; (e, f) pictures of collapse mechanism.

Distortional Buckling Test D3.62C054-3E4W

Specimen	h (in.)	b_c (in.)	d_c (in.)	θ_c (deg.)	b_t (in.)	d_t (in.)	θ_t (deg.)	r_{hc} (in.)	r_{dc} (in.)	r_{ht} (in.)	r_{dt} (in.)	t (in.)	f_y (ksi)	f_u (ksi)	M_{test} (kips-in.)
D3.62C054-4	3.73	1.88	0.41	87.00	1.87	0.43	89.00	0.26	0.24	0.27	0.27	0.0555	32.11	53.6	52
D3.62C054-3	3.72	1.89	0.35	88.00	1.86	0.36	88.00	0.24	0.28	0.26	0.26	0.0556	32.91	53.3	52

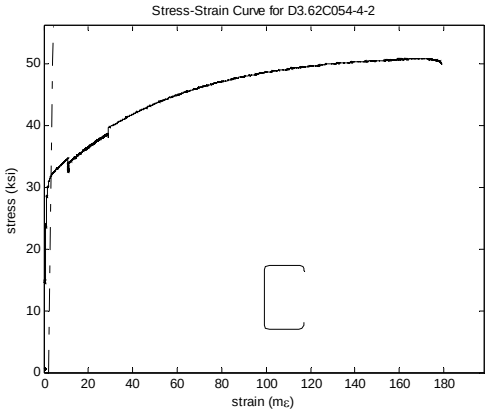

(a)

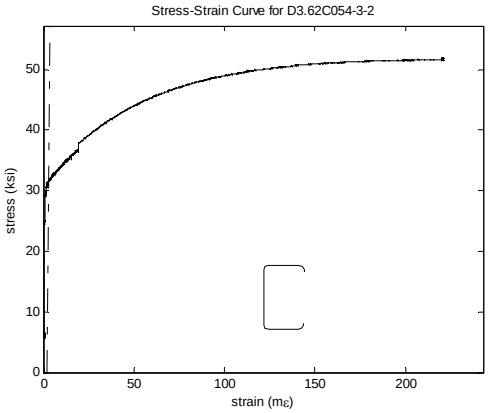

(b)

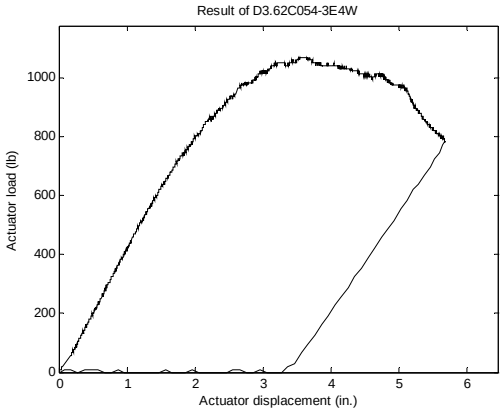

(c)

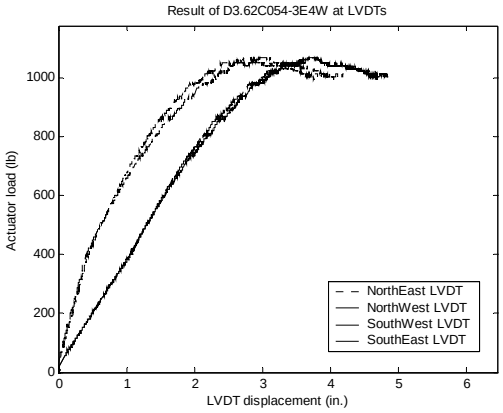

(d)

(e)

(f)

(a) material stress vs. strain of D3.62C054-4; (b) material stress vs. strain of D3.62C054-3;
(c) actuator load vs. displacement; (d) actuator load vs. displacements of LVDTs;
(e, f) pictures of collapse mechanism.

Appendix B

Draft Design Provisions for Distortional Buckling of Cold-Formed Steel Beams

By Benjamin W. Schafer, Cheng Yu

Note:
The author of this dissertation is only a secondary contributor to the work presented in Appendix B. However, it was decided to include this document to supplement the reader's knowledge and comprehension of topics covered in the dissertation. The draft design provisions in Appendix B are being submitted to the AISI Committee on Specifications for review.

C3 Flexural Members

C3.1 Bending

The nominal flexural strength [moment resistance], M_n, shall be the smallest of the values calculated according to Sections C3.1.1, C3.1.2, C3.1.3, C3.1.4, ~~and~~ C3.1.5, <u>and C3.1.6</u> where applicable.

[The following is entirely new]

C3.1.6 Distortional Buckling Strength [Resistance]

The provisions of this section apply to I-, Z-, C-, and other open cross-section members which employ compression flanges with edge stiffeners. The nominal flexural strength [moment resistance] shall be calculated as follows:

USA and Mexico		Canada
Ω_b (ASD)	ϕ_b (LRFD)	ϕ_b (LSD)
1.67	0.90	0.85

for $\lambda_d \leq 0.673$

$$M_n = M_y \qquad (Eq.\ 3.1.6\text{-}1)$$

for $\lambda_d > 0.673$

$$M_n = \left(1 - 0.22\left(\frac{M_{crd}}{M_y}\right)^{0.5}\right)\left(\frac{M_{crd}}{M_y}\right)^{0.5} M_y \qquad (Eq.\ 3.1.6\text{-}2)$$

where $\lambda_d = \sqrt{M_y / M_{crd}}$ (*Eq.* 3.1.6-3)

$M_{crd} = S_{fc}F_d$ (*Eq.* 3.1.6-4)

$M_y = S_fF_y$ (*Eq.* 3.1.6-5)

S_f is referenced to the extreme fiber in first yield

S_{fc} is referenced to the extreme compression fiber

F_d is the elastic distortional buckling stress calculated according to either (a), (b) or (c)

(a) For C and Z sections with simple lip edge stiffeners

These provisions shall be applicable for C- and Z-sections with simple lip edge stiffeners within the following dimensional limits:

(1) $50 \leq h_o/t \leq 200$

(2) $25 \leq b_o/t \leq 100$

(3) $6.25 < D/t \leq 50$

(4) 45 deg. $\leq \theta <$ 90 deg.

(5) $2 \leq h_o/b_o \leq 8$

(6) $0.04 \leq D\sin(\theta)/b \leq 0.5$

where:

h_o = as defined in Figure B2.3-2

b_o = as defined in Figure B2.3-2

D = as defined in Figure B4-2

t = base steel thickness

θ = as defined in Figure B4-2

$$F_d = \alpha\beta k_d \frac{\pi^2 E}{12(1-v^2)}\left(\frac{t}{b_o}\right)^2 \qquad (Eq.\ C3.1.6\text{-}6)$$

$$k_d = 0.5 \leq 0.6\left(\frac{b_o D\sin\theta}{h_o t}\right)^{0.7} \leq 8.0 \qquad (Eq.\ C3.1.6\text{-}7)$$

α, accounts for bracing as follows:

$L_m \geq L_{cr}$

$$\alpha = 1 \qquad (Eq.\ C3.1.6\text{-}8)$$

$L_m < L_{cr}$

$$\alpha = \left(\frac{L_m}{L_{cr}}\right)^{\ln\left(\frac{L_m}{L_{cr}}\right)} \qquad (Eq.\ C3.1.6\text{-}9)$$

$$L_{cr} = 1.2h_o\left(\frac{b_o D\sin\theta}{h_o t}\right)^{0.6} \leq 10h_o \qquad (Eq.\ C3.1.6\text{-}10)$$

L_m=Distance between restraints which restrict distortional buckling

β, accounts for moment gradient as follows:

$$\beta = 1.0 \leq 1 + 0.4(L_{cr}/L_m)^{0.7}(1 - M_1/M_2)^{0.7} \leq 1.3 \qquad (Eq.\ C3.1.6\text{-}11)$$

$|M_2| > |M_1|$, single curvature is positive

where, M_2 and M_1 are the end moments a distance L_m apart

(b) For C and Z sections with simple lip stiffeners and <u>any</u> open section with a single web and single edge stiffened compression flange, including complex edge stiffeners

$$F_d = \beta \frac{k_{\phi fe} + k_{\phi we}}{\tilde{k}_{\phi fg} + \tilde{k}_{\phi wg}} \qquad \text{(Eq. C3.1.6-12)}$$

L = minimum of L_{cr} and L_m

where, critical length is:

$$L_{cr} = \left(\frac{4\pi^4 h\left(1-\nu^2\right)}{t^3} \left(I_{xf}\left(x_o - h_x\right)^2 + C_{wf} - \frac{I_{xyf}^2}{I_{yf}}\left(x_o - h_x\right)^2 \right) + \frac{\pi^4 h^4}{720} \right)^{1/4} \qquad \text{(Eq. C3.1.6-13)}$$

flange rotational stiffness is:

$$k_{\phi fe} = \left(\frac{\pi}{L}\right)^4 \left(EI_{xf}\left(x_o - h_x\right)^2 + EC_{wf} - E\frac{I_{xyf}^2}{I_{yf}}\left(x_o - h_x\right)^2 \right) + \left(\frac{\pi}{L}\right)^2 GJ_f \qquad \text{(Eq. C3.1.6-14)}$$

$$\tilde{k}_{\phi fg} = \left(\frac{\pi}{L}\right)^2 \left[A_f \left(\left(x_o - h_x\right)^2 \left(\frac{I_{xyf}}{I_{yf}}\right)^2 - 2y_o\left(x_o - h_x\right)\left(\frac{I_{xyf}}{I_{yf}}\right) + h_x^2 + y_o^2 \right) + I_{xf} + I_{yf} \right] \qquad \text{(Eq. C3.1.6-15)}$$

web rotational stiffness is:

$$k_{\phi we} = \frac{Et^3}{12\left(1-\nu^2\right)} \left(\frac{3}{h} + \left(\frac{\pi}{L}\right)^2 \frac{19h}{60} + \left(\frac{\pi}{L}\right)^4 \frac{h^3}{240} \right) \qquad \text{(Eq. C3.1.6-16)}$$

$$\tilde{k}_{\phi wg} = \frac{ht\pi^2}{13440} \left(\frac{\left(45360\left(1-\xi_{web}\right)+62160\right)\left(\frac{L}{h}\right)^2 + 448\pi^2 + \left(\frac{h}{L}\right)^2 \left(53 + 3\left(1-\xi_{web}\right)\right)\pi^4}{\pi^4 + 28\pi^2\left(\frac{L}{h}\right)^2 + 420\left(\frac{L}{h}\right)^4} \right) \qquad \text{(Eq. C3.1.6-17)}$$

β, accounts for moment gradient as follows:

$$\beta = 1.0 \le 1 + 0.4\left(L_{cr}/L_m\right)^{0.7}\left(1 - M_1/M_2\right)^{0.7} \le 1.3 \qquad \text{(Eq. C3.1.6-18)}$$

$|M_2| > |M_1|$, single curvature is positive

where, M_2 and M_1 are the end moments a distance L_m apart

and:

L_m =Distance between restraints which restrict distortional buckling

h =web depth (h_o)

ξ_{web} =$(f_1 - f_2)/f_1$ = stress gradient in the web, where f_1 and f_2 are the stresses at the opposite ends of the web, $f_1 > f_2$, compression positive, tension negative,

calculated on the basis of the gross section, (e.g., pure symmetrical bending, f_1=-f_2, ξ_{web} = 2)

A_f, I_{xf}, I_{yf}, I_{xyf}, C_{wf}, J_f, x_o, and h_x, are properties of the compression flange (flange and edge stiffener) about x, y axes, where the x, y axes are located at the centroid of the flange, with the x-axis measured positive to the right from the centroid, and the y-axis positive down from the centroid. For a flange with a simple lip stiffener (i.e, the flange of a typical C or Z) appropriate expressions (without considering the effects of corner radius) are in the commentary.

A_f =cross-sectional area of the flange

I_{xf} =x-axis moment of inertia of the flange

I_{yf} =y-axis moment of inertia of the flange

I_{xyf} =product of the moment of inertia of the flange

C_{wf} =warping torsion constant of the flange

J_f =St. Venant torsion constant of the flange

x_o =x distance from the flange/web junction to the centroid of the flange

h_x =x distance from the centroid of the flange to the shear center of the flange

(c) rational elastic buckling analysis

A rational elastic buckling analysis may be used in lieu of the expressions of C3.1.6(a) or (b).

COMMENTARY

[The following is entirely new]

C3.1.6 Distortional Buckling Strength [Resistance]

Distortional buckling is an instability that may occur in members with edge stiffened flanges, such as lipped C- and Z-sections. As shown in Fig. C-C3.1.6-1, this buckling mode is characterized by instability of the entire flange, as the flange and edge stiffener buckle together. Further, the length of the buckling wave in the distortional mode is (1) considerably longer than conventional local buckling, and (2) noticeably shorter than lateral-torsional buckling of the entire beam. In some situations, particularly when the compression flange is unrestrained over several feet, but discrete bracing is still provided to partially restrict lateral-torsional buckling, distortional buckling may be the dominant failure mode.

The provisions of section B4.2 based primarily on the work of Desmond, Peköz, and Winter (1981) partially account for distortional buckling, but research has shown that when distortional buckling is unrestrained a separate limit state check is required (Ellifritt, Sputo, and Haynes 1992, Hancock, Rogers, and Schuster 1996, Kavanagh and Ellifritt 1994, Schafer and Peköz 1999, Yu and Schafer 2004). An example of test results in bending is shown in Fig. C-C3.1.6-2 (Yu and Schafer 2004). In the figure, the applied vertical load is designated as P and the results are shown for nominally identical specimens, failing in both local and distortional buckling. As the compression flange restraint is removed, failures are observed to change from local buckling to distortional buckling, as characterized by both the shape and length of the buckling modes (Fig. C-C3.1.6-1). While stiffness is not affected, ultimate strength is, the reduction in ultimate strength from local to distortional buckling is commonly on the order of 15%.

Determination of the ultimate strength in distortional buckling was completed by testing. Results of one such study (Yu and Schafer 2004) are shown in Fig. C-C3.1.6-3. By restricting lateral-torsional buckling, and examining specimens which failed in distortional buckling before local buckling, *Eq*. C3.1.6-2 was validated. The strength prediction of *Eq*. C3.1.6-2 is the same as that used for distortional buckling of beams in the Direct Strength Method of Appendix 1 of the *Specification*. In addition, the Australian/New Zealand Specification (AS/NZS 4600:1996) has used this equation successfully since 1996. Additional explanation of these expressions, including calibration of the safety and resistance factors are provided in the commentary to Appendix 1.

The primary difficulty in efficiently calculating the strength in distortional buckling is quickly estimating the elastic distortional buckling stress, F_d. Recognizing the complexity of this calculation this section provides three alternatives: C3.1.6-(a) a conservative, approximate, hand method for C- and Z-sections with lip stiffeners, (b) a general purpose hand method for any open section with edge stiffeners, and (c) the option to use rational elastic buckling analysis (computer models) such as that discussed in detail in the commentary to Appendix 1 of the *Specification.*

Distortional buckling is unlikely to control the strength if (a) unbraced lengths are long and lateral-torsional buckling strength limits the capacity, or (b) adequate restraint is provided to the compression flange. At this time requirements for providing adequate supplemental restraint (from decking, sheathing, etc.) to restrict distortional buckling are not general enough in nature to be useful in design. If fully engaged standard corrugated panels have been shown to provide adequate restraint, but the fastener details employed are unconventional (Yu and Schafer 2004, Yu 2005). However, two phenomena which do positively influence the distortional buckling capacity have been included in the design process: (1) bracing in the compression flange that is at a length shorter than the natural buckling length of distortional buckling, and (2) the stabilizing influence of moment gradient on the beam.

A significant boost in the distortional buckling moment (or equivalently stress, F_d) occurs when the unbraced length, L_m, is shorter than the natural buckling length for distortional buckling, L_{cr}. The increase, α of *Eq*. C3.1.6-9, has been quantified by application of the theoretical model of section C3.1.6(b), as developed by Schafer and Peköz (1999) and detailed in Yu (2005). The expression for α was arrived at by examination of a wide class of C- and Z-sections meeting the geometric limits given in C3.1.6(a) as summarized in Fig. C-C3.1.6-4. A lowerbound to the results was selected, but the increases in the elastic buckling stress can be significant on design.

The presence of moment gradient can also increase the distortional buckling moment (or equivalently stress, F_d). However, this increase is lessened if the moment gradient occurs over a longer length. Thus, in determining the influence of moment gradient (β) the ratio of the end moments, M_1/M_2, and the ratio of the natural distortional buckling length to the unbraced length, L_{cr}/L_m, must both be accounted for. Yu (2005) performed elastic buckling analysis with shell finite element models of C- and Z-sections under different moment gradients to examine this problem. The study covered C- and Z-members with simple lip edge stiffeners within the following dimensional limits:

(1) $60 \leq h_o/t \leq 160$
(2) $25 \leq b_o/t \leq 45$
(3) $6.25 < D/t \leq 20$
(4) $45 \text{ deg.} \leq \theta < 90 \text{ deg.}$
(5) $2 \leq h_o/b_o \leq 5$
(6) $0.2 \leq D\sin(\theta)/b \leq 0.3$

For a moment gradient where $M_1=0$, $M_2=M$, and thus the ratio, $r = M_1/M_2 = 0$, Fig. C-C3.1.6-5 demonstrates the increase in the elastic distortional buckling moment (stress) as a function of the unbraced length, L_m. If the unbraced length is long enough (L_m/L_{cr} large enough) the moment gradient will not be sharp enough to retard distortional buckling, and no increase will occur ($\beta=1$). Significant scatter exists in the results, in this case a lowerbound prediction (*Eq*. C3.1.6-11) for the increase was selected.

Fig. C-C3.1.6-6 demonstrates that all cases of linear moment gradient can be considered as a special case of $r = 0$ moment gradient ($M_1=0$, $M_2=M$) occurring at an equivalent length. Thus, the distance from an inflection point to the maximum moment is adequate

for determining the influence of moment gradient on elastic distortional buckling. The developed equation for β reflects this finding.

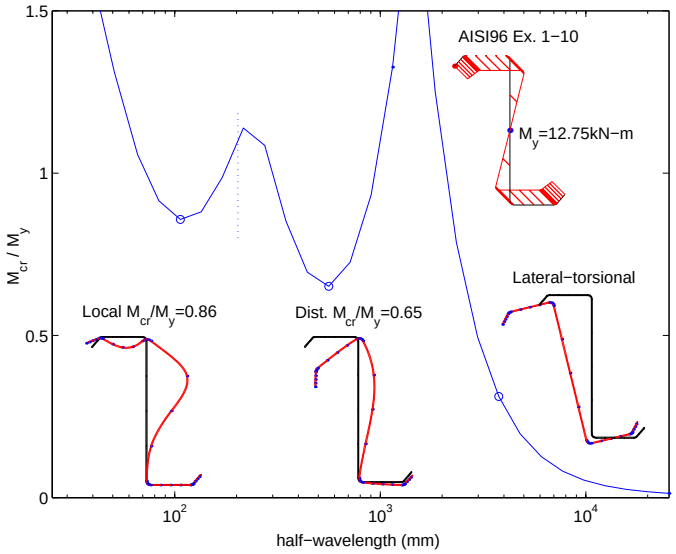

Figure C-C3.1.6-1 Rational elastic buckling analysis

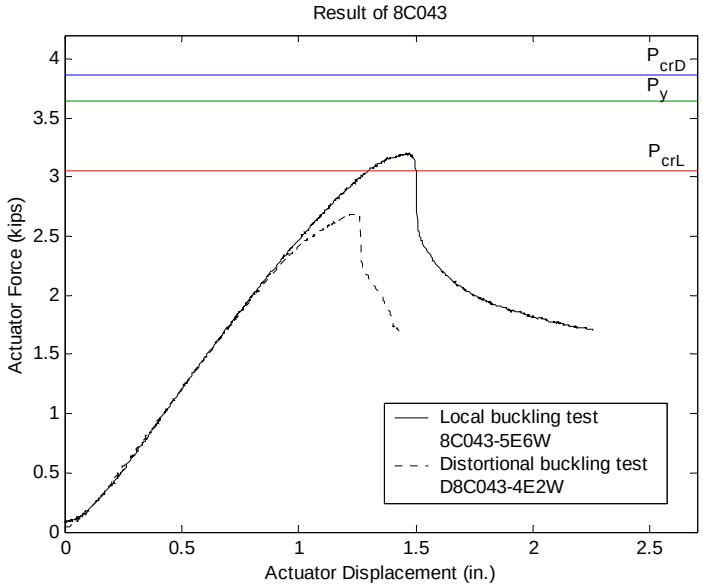

Figure C-C3.1.6-2 Difference in ultimate response for nominally identical C-sections with and without bracing to restrict distortional buckling (Yu and Schafer 2004)

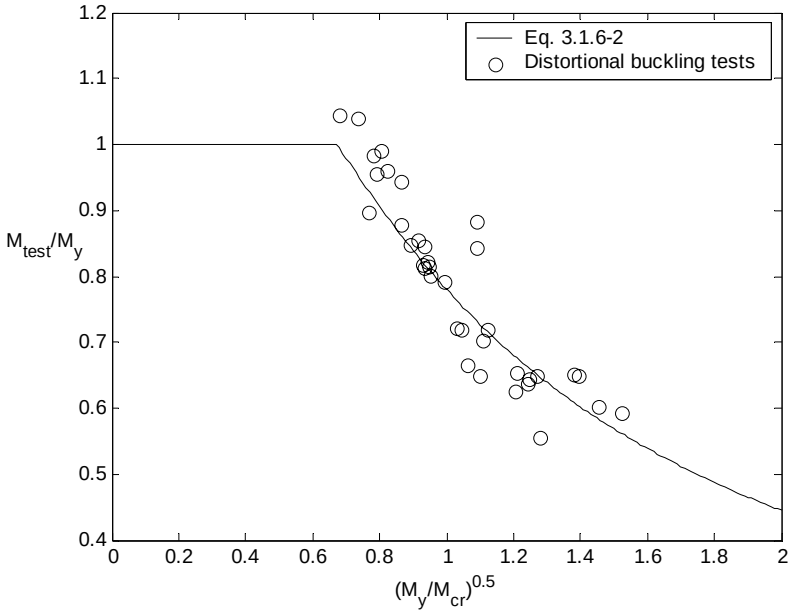

Figure C-C3.1.6-3 Performance of distortional buckling prediction with test data on common C- and Z-sections in bending (Yu and Schafer 2004)

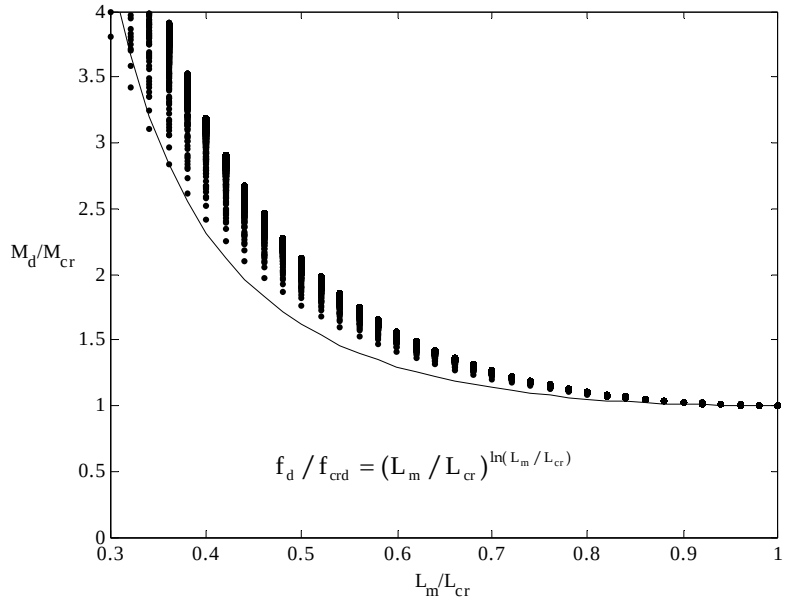

Figure C-C3.1.6-4 Development of expressions for increase in F_d for unbraced lengths, L_m, shorter than the natural distortional buckling length, L_{cr} (Yu 2005)

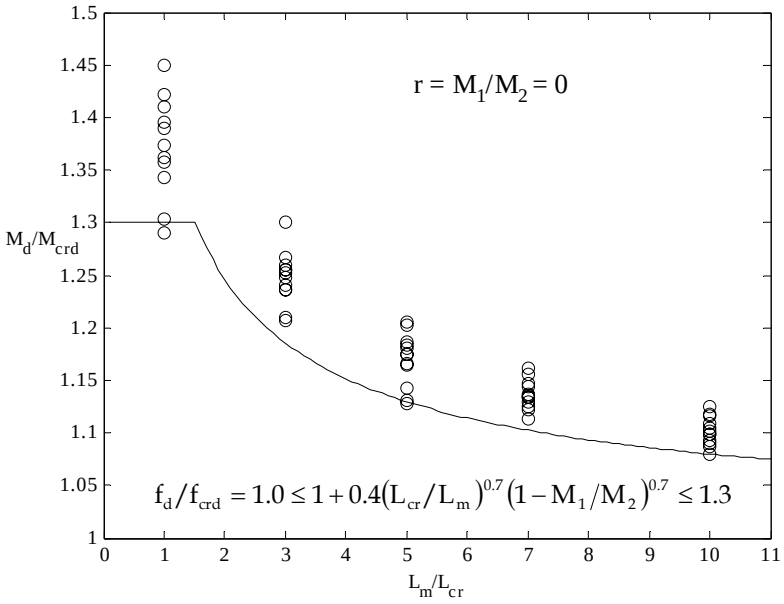

Figure C-C3.1.6-5 Development of expressions for increase in F_d for moment gradient effect (Yu 2005)

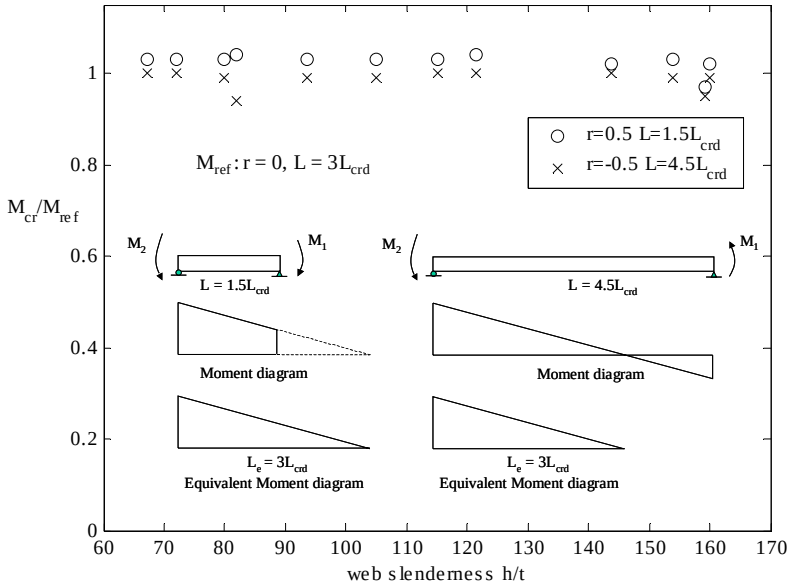

Figure C-C3.1.6-6 Development of expressions for increase in F_d for moment gradient effect (Yu 2005)

C3.1.6(a) For C and Z sections with simple lip edge stiffeners

The provisions of C3.1.6(a) provide a conservative approximation to the distortional buckling length, L_{cr}, and stress, F_d, for C- and Z-sections with simple lip stiffeners bent about an axis perpendicular to the web. The expressions were specifically derived as a conservative simplification to those provided in section C3.1.6(b) and (c). For sections within the geometric limits given in C3.1.6(a) Figures C-C3.1.6(a)-1 and -2 demonstrate the adequacy of the approximate provisions.

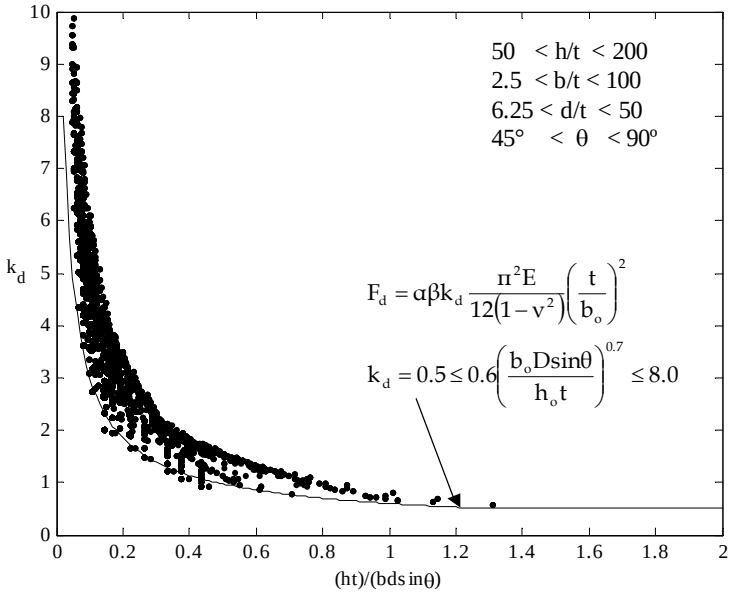

Figure C-C3.1.6(a)-1 Approximate expression for distortional buckling of C- and Z-sections based on finite strip analysis parametric study inside geometric limits of C3.1.6(a) (Yu 2005)

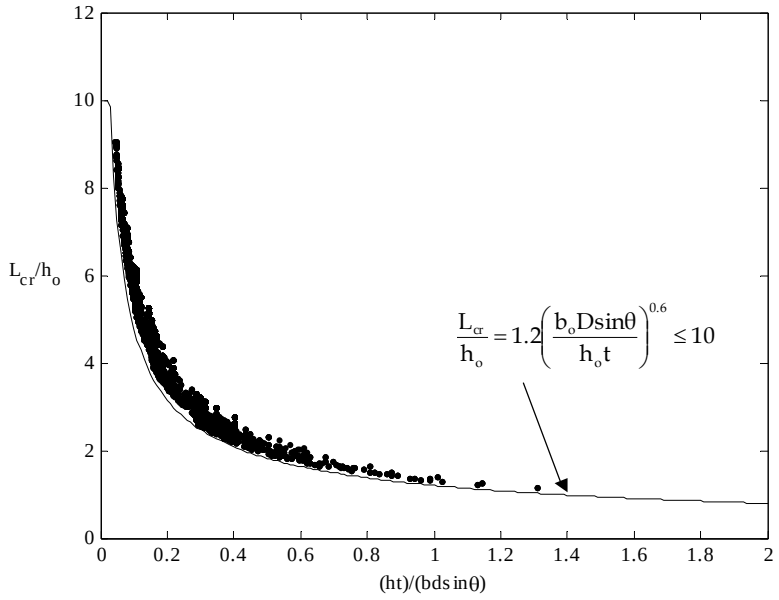

Figure C-C3.1.6(a)-2 Approximate expression for critical buckling length of C- and Z-sections based on finite strip analysis parametric study inside geometric limits of C3.1.6(a) (Yu 2005)

C3.1.6(b) For C and Z sections with simple lip stiffeners and any open section with a single web and single edge stiffened compression flange, including complex edge stiffeners

The provisions of C3.1.6(b) provide a general method for calculation of the distortional buckling stress, F_d, for any open section with an edge stiffened compression flange, including complex edge stiffeners. The provisions of C3.1.6(b) also provide a more refined answer for any C- and Z-section including those meeting the criteria of C3.1.6(a). The expressions employed here are derived in Schafer and Peköz (1999) and verified for complex stiffeners in Schafer et al. (2004).

Since the provided expressions can be complicated, solutions for C- and Z- sections based on centerline dimensions are provided in Figure C3.1.6(b)-1

$$A_f = (b+d)t \qquad A_f = (b+d)t$$

$$J_f = \tfrac{1}{3}bt^3 + \tfrac{1}{3}dt^3 \qquad J_f = \tfrac{1}{3}bt^3 + \tfrac{1}{3}dt^3$$

$$I_{xf} = \frac{t\left(t^2b^2 + 4bd^3 + t^2bd + d^4\right)}{12(b+d)} \qquad I_{xf} = \frac{t\left(t^2b^2 + 4bd^3 - 4bd^3\cos^2(\theta) + t^2bd + d^4 - d^4\cos^2(\theta)\right)}{12(b+d)}$$

$$I_{yf} = \frac{t\left(b^4 + 4db^3\right)}{12(b+d)} \qquad I_{yf} = \frac{t\left(b^4 + 4db^3 + 6d^2b^2\cos(\theta) + 4d^3b\cos^2(\theta) + d^4\cos^2(\theta)\right)}{12(b+d)}$$

$$I_{xyf} = \frac{tb^2d^2}{4(b+d)} \qquad I_{xyf} = \frac{tbd^2\sin(\theta)(b+d\cos(\theta))}{4(b+d)}$$

$$C_{wf} = 0 \qquad C_{wf} = 0$$

$$x_o = \frac{b^2}{2(b+d)} \qquad x_o = \frac{b^2 - d^2\cos(\theta)}{2(b+d)}$$

$$h_x = \frac{-\left(b^2 + 2db\right)}{2(b+d)} \qquad h_x = \frac{-\left(b^2 + 2db + d^2\cos(\theta)\right)}{2(b+d)}$$

$$h_y = y_o = \frac{-d^2}{2(b+d)} \qquad h_y = y_o = \frac{-d^2\sin(\theta)}{2(b+d)}$$

Figure C3.1.6(b)-1 Geometric flange properties for C- and Z-sections

C3.1.6(c) Rational elastic buckling analysis

Rational elastic buckling analysis consists of any numerical method following the principles of mechanics to arrive at an accurate prediction of the elastic distortional buckling stress (moment). Complete details are provided in section 1.1.2 of the commentary to Appendix 1 of the *Specification.*

REFERENCES

Already in the reference list…

Desmond, Peköz, and Winter (1981)
Ellifritt, Sputo, and Haynes (1992)
Hancock, Rogers, and Schuster (1996)
Kavanagh, and Ellifritt (1994)
Schafer, and Peköz (1999).

New references

AS/NZS (1996). AS/NZS 4600: 1996 Cold-Formed Steel Structures. Standards Australia and the Australian Institute of Steel Construction.

Schafer, B.W., Sarawit, A., Peköz, T. (2004). "Complex edge stiffeners for thin-walled members." ASCE, *Journal of Structural Engineering* (Submitted).

Yu, C. (2005). "Distortional Buckling of Cold-Formed Steel Members in Bending." Ph.D. Thesis, Johns Hopkins University, Baltimore, MD.

Yu, C., Schafer, B.W. (2004). "Distortional Buckling Tests on Cold-Formed Steel Beams." 17th International Specialty Conference on Cold-Formed Steel Structures, Orlando, FL.

DESIGN EXAMPLE

Example 1

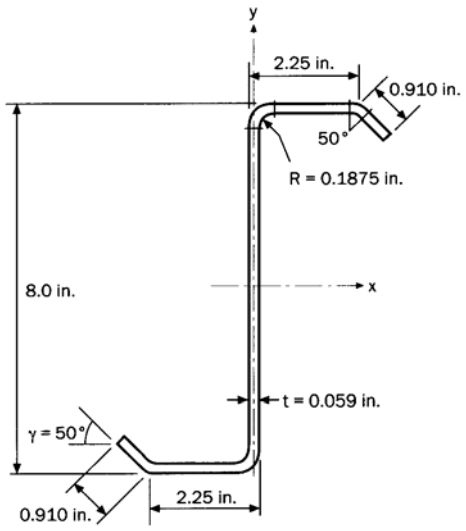

Given:

1. Steel: F_y = 55 ksi
2. Section: 8Z2.25x059 as shown above
3. End moment ratio M_1/M_2 = 0.5
4. Unbraced length L_m = 50 in.

Required:

1. Nominal distortional buckling strength

Method (a) according to C3.1.6-(a)

$$L_{cr} = 1.2\,h_o\left(\frac{b_o D\sin\theta}{h_o t}\right)^{0.6} = (1.2)(8)\left(\frac{(2.25)(0.910)\sin(50°)}{(8)(0.059)}\right)^{0.6} = 19.73 \text{ in.} \le 80 \text{ in.}$$

(Eq. C3.1.6-10)

since $L_m \geq L_{cr}$, $\alpha = 1$ (Eq. C3.1.6-8)

$$k_d = 0.6\left(\frac{b_o D\sin\theta}{h_o t}\right)^{0.7} = 0.6\left(\frac{(2.25)(0.91)\sin(50°)}{(8)(0.059)}\right)^{0.7} = 1.39;\ 0.5 \le 1.39 \le 8.0$$

(Eq. C3.1.6-7)

$$\beta = 1 + 0.4\left(L_{cr}/L_m\right)^{0.7}\left(1 - M_1/M_2\right)^{0.7} = 1 + (0.4)(19.73/50)^{0.7}(1-0.5)^{0.7} = 1.13 \le 1.3$$

(Eq. C3.1.6-11)

$$F_d = \alpha\beta k_d \frac{\pi^2 E}{12\left(1-\nu^2\right)}\left(\frac{t}{b_o}\right)^2 = (1)(1.13)(1.39)\frac{\pi^2(29500)}{(12)(1-0.3^2)}\left(\frac{0.059}{2.25}\right)^2 = 28.80 \text{ ksi}$$

(Eq. C3.1.6-6)

$M_{crd} = S_{fc}F_d = (1.94)(28.80) = 55.87$ kip-in. (Eq. C3.1.6-4)

$M_y = S_f F_y = (1.94)(55) = 106.70$ kip-in. (Eq. C3.1.6-5)

$$\lambda_d = \sqrt{M_y/M_{crd}} = \sqrt{106.70/55.87} = 1.38 > 0.673$$ (Eq. C3.1.6-3)

$$M_n = \left(1 - 0.22\left(\frac{M_{crd}}{M_y}\right)^{0.5}\right)\left(\frac{M_{crd}}{M_y}\right)^{0.5} M_y$$

$$= \left(1 - 0.22\left(\frac{55.87}{106.70}\right)^{0.5}\right)\left(\frac{55.87}{106.70}\right)^{0.5} 106.70 = 64.9 \text{ kip-in.}$$ (Eq. C3.1.6-2)

Method (b) according to C3.1.6-(b)

The centerline dimensions are h = 7.94 in., b = 2.21 in., d = 0.896 in., t = 0.059 in., θ = 50 .

$$A_f = (b+d)t = (2.21+0.896)(0.059) = 0.183 \text{ in.}^2$$ (Fig. C3.1.6(b)-1)

$$I_{xf} = \frac{t\left(t^2b^2 + 4bd^3 - 4bd^3\cos^2(\theta) + t^2bd + d^4 - d^4\cos^2(\theta)\right)}{12(b+d)} =$$

$$\frac{(0.059)\left((0.059)^2(2.21)^2 + (4)(2.21)(0.896)^3 - (4)(2.21)(0.896)^3\cos^2(50°) + (0.059)^2(2.21)(0.896) + (0.896)^4 - (0.896)^4\cos^2(50°)\right)}{(12)(2.21+0.896)}$$

$= 0.0065 \text{ in.}^4$ (Fig. C3.1.6(b)-1)

$$x_o = \frac{b^2 - d^2\cos(\theta)}{2(b+d)} = \frac{(2.21)^2 - (0.896)^2\cos(50°)}{(2)(2.21+0.896)} = 0.702 \text{ in.}$$ (Fig. C3.1.6(b)-1)

$$h_x = \frac{-\left(b^2 + 2db + d^2\cos(\theta)\right)}{2(b+d)} = \frac{-\left((2.21)^2 + (2)(0.896)(2.21) + (0.896)^2\cos(50°)\right)}{(2)(2.21+0.896)}$$

$= -1.505 \text{ in.}$ (Fig. C3.1.6(b)-1)

$$h_y = y_o = \frac{-d^2\sin(\theta)}{2(b+d)} = \frac{-(0.896)^2\sin(50°)}{(2)(2.21+0.896)} = -0.992 \text{ in.}$$ (Fig. C3.1.6(b)-1)

$C_{wf} = 0$ (Fig. C3.1.6(b)-1)

$$I_{xyf} = \frac{tbd^2\sin(\theta)(b + d\cos(\theta))}{4(b+d)} = \frac{(0.059)(2.21)(0.896)^2\sin(50°)(2.21 + 0.896\cos(50°))}{(4)(2.21+0.896)}$$

$= 0.018$ (Fig. C3.1.6(b)-1)

$$I_{yf} = \frac{t\left(b^4 + 4db^3 + 6d^2b^2\cos(\theta) + 4d^3b\cos^2(\theta) + d^4\cos^2(\theta)\right)}{12(b+d)} =$$

$$\frac{(0.059)\left((2.21)^4 + 4(0.896)(2.21)^3 + (6)(0.896)^2(2.21)^2\cos(50°) + (4)(0.896)^3(2.21)\cos^2(50°) + (0.896)^4\cos^2(50°)\right)}{(12)(2.21+0.896)}$$

$= 0.127 \text{ in.}^4$ (Fig. C3.1.6(b)-1)

$$J_f = \tfrac{1}{3}bt^3 + \tfrac{1}{3}dt^3 = \tfrac{1}{3}(2.21)(0.059)^3 + \tfrac{1}{3}(0.896)(0.059)^3 = 0.000212 \text{ in.}^4$$ (Fig. C3.1.6(b)-1)

$$L_{cr} = \left(\frac{4\pi^4h(1-\nu^2)}{t^3}\left(I_{xf}(x_o - h_x)^2 + C_{wf} - \frac{I_{xyf}^2}{I_{yf}}(x_o - h_x)^2\right) + \frac{\pi^4h^4}{720}\right)^{1/4} =$$

$$\left(\frac{4\pi^4(7.94)\left(1-0.3^2\right)}{0.059^3}\left((0.0065)(0.702-(-1.505))^2+0-\frac{(0.018)^2}{0.127}(0.702-(-1.505))^2\right)+\frac{\pi^4(7.94)^4}{720}\right)^{1/4}$$

= 22.76 in. (Eq. C3.1.6-13)

L=minimum of L_{cr} and L_m = 22.76 in.

$$k_{\phi fe}=\left(\frac{\pi}{L}\right)^4\left(EI_{xf}\left(x_o-h_x\right)^2+EC_{wf}-E\frac{I_{xyf}^2}{I_{yf}}\left(x_o-h_x\right)^2\right)+\left(\frac{\pi}{L}\right)^2 GJ_f =$$

$$\left(\frac{\pi}{22.76}\right)^4\left((29500)(0.0065)(0.702-(-1.505))^2+0-(29500)\frac{(0.018)^2}{0.127}(0.702-(-1.505))^2\right)+\left(\frac{\pi}{22.76}\right)^2(11346)(0.000212)$$

= 0.255 (Eq. C3.1.6-14)

$$\tilde{k}_{\phi fg}=\left(\frac{\pi}{L}\right)^2\left[A_f\left(\left(x_o-h_x\right)^2\left(\frac{I_{xyf}}{I_{yf}}\right)^2-2y_o\left(x_o-h_x\right)\left(\frac{I_{xyf}}{I_{yf}}\right)+h_x^2+y_o^2\right)+I_{xf}+I_{yf}\right]=$$

$$\left(\frac{\pi}{22.76}\right)^2\left[0.183\left((0.702-(-1.505))^2\left(\frac{0.018}{0.127}\right)^2-(2)(-0.992)(0.702-(-1.505))\left(\frac{0.018}{0.127}\right)+(-1.505)^2+(-0.992)^2\right)+0.0065+0.127\right]$$

= 0.011 (Eq. C3.1.6-15)

$$k_{\phi we}=\frac{Et^3}{12\left(1-\nu^2\right)}\left(\frac{3}{h}+\left(\frac{\pi}{L}\right)^2\frac{19h}{60}+\left(\frac{\pi}{L}\right)^4\frac{h^3}{240}\right)=$$

$$\frac{(29500)(0.059)^3}{(12)\left(1-(0.3)^2\right)}\left(\frac{3}{7.94}+\left(\frac{\pi}{22.76}\right)^2\frac{(19)(7.94)}{60}+\left(\frac{\pi}{22.76}\right)^4\frac{(7.94)^3}{240}\right)=0.237$$

(Eq. C3.1.6-16)

$$\tilde{k}_{\phi wg}=\frac{ht\pi^2}{13440}\left(\frac{\left(45360\left(1-\xi_{web}\right)+62160\right)\left(\frac{L}{h}\right)^2+448\pi^2+\left(\frac{h}{L}\right)^2\left(53+3\left(1-\xi_{web}\right)\right)\pi^4}{\pi^4+28\pi^2\left(\frac{L}{h}\right)^2+420\left(\frac{L}{h}\right)^4}\right)=$$

$$\frac{(7.94)(0.059)\pi^2}{13440}\left(\frac{(45360(1-2)+62160)\left(\frac{22.76}{7.94}\right)^2+(448)\pi^2+\left(\frac{7.94}{22.76}\right)^2(53+(3)(1-2))\pi^4}{\pi^4+(28)\pi^2\left(\frac{22.76}{7.94}\right)^2+420\left(\frac{22.76}{7.94}\right)^4}\right)$$

= 0.0016 (Eq. C3.1.6-17)

$$\beta=1+0.4\left(L_{cr}/L_m\right)^{0.7}\left(1-M_1/M_2\right)^{0.7}=1+(0.4)(22.76/50)^{0.7}(1-0.5)^{0.7}=1.14\le 1.3$$

(Eq. C3.1.6-18)

$$F_d=\beta\frac{k_{\phi fe}+k_{\phi we}}{\tilde{k}_{\phi fg}+\tilde{k}_{\phi wg}}=1.14\frac{0.255+0.237}{0.011+0.0016}=44.51\text{ ksi}$$ (Eq. C3.1.6-12)

$M_{crd} = S_{fc}F_d = (1.94)(44.51) = 86.35$ kip-in. (Eq. C3.1.6-4)

$M_y = S_fF_y = (1.94)(55) = 106.70$ kip-in. (Eq. C3.1.6-5)

$\lambda_d = \sqrt{M_y / M_{crd}} = \sqrt{106.70/86.35} = 1.11 > 0.673$ (Eq. C3.1.6-3)

$$M_n = \left(1 - 0.22\left(\frac{M_{crd}}{M_y}\right)^{0.5}\right)\left(\frac{M_{crd}}{M_y}\right)^{0.5} M_y$$

$$= \left(1 - 0.22\left(\frac{86.35}{106.70}\right)^{0.5}\right)\left(\frac{86.35}{106.70}\right)^{0.5} 106.70 = 77.0 \text{ kip-in.}$$ (Eq. C3.1.6-2)

Method (c) according to C3.1.6-(c)

L_{cr} and M'_{crd} (for constant moment) are obtained from finite strip analysis by CUFSM:

L_{cr} = 23 in.

M'_{crd} = 83.16 kip-in.

since $L_m \geq L_{cr}$, $\alpha = 1$ (Eq. C3.1.6-8)

$$\beta = 1 + 0.4\left(L_{cr}/L_m\right)^{0.7}\left(1 - M_1/M_2\right)^{0.7} = 1 + (0.4)(23/50)^{0.7}(1-0.5)^{0.7} = 1.14 \leq 1.3$$ (Eq. C3.1.6-11)

$M_{crd} = \alpha\beta M'_{crd} = (1)(1.14)(83.16) = 94.80$ kip-in.

$M_y = S_f F_y = (1.94)(55) = 106.70$ kip-in. (Eq. C3.1.6-5)

$\lambda_d = \sqrt{M_y/M_{crd}} = \sqrt{106.70/94.80} = 1.06 > 0.673$ (Eq. C3.1.6-3)

$$M_n = \left(1 - 0.22\left(\frac{M_{crd}}{M_y}\right)^{0.5}\right)\left(\frac{M_{crd}}{M_y}\right)^{0.5} M_y$$

$$= \left(1 - 0.22\left(\frac{94.80}{106.70}\right)^{0.5}\right)\left(\frac{94.80}{106.70}\right)^{0.5} 106.70 = 79.7 \text{ kip-in.}$$ (Eq. C3.1.6-2)

Example 2

Given:

1. Steel: F_y = 55 ksi
2. Section: 8Z2.25x059 same as Example1
3. End moment ratio M_1/M_2 = 0.5
4. Unbraced length **L_m = 10 in (changed from example 1)**.

Required:

1. Nominal distortional buckling strength

Method (a) according to C3.1.6-(a)

$$L_{cr} = 1.2\,h_o\left(\frac{b_o D\sin\theta}{h_o t}\right)^{0.6} = 19.73 \text{ in.}$$

since $L_m < L_{cr}$, $\alpha = \left(\frac{L_m}{L_{cr}}\right)^{\ln\left(\frac{L_m}{L_{cr}}\right)} = \left(\frac{10}{19.73}\right)^{\ln\left(\frac{10}{19.73}\right)} = 1.59$ (Eq. C3.1.6-9)

$$k_d = 0.6\left(\frac{b_o D\sin\theta}{h_o t}\right)^{0.7} = 1.39$$

$$\beta = 1 + 0.4\left(L_{cr}/L_m\right)^{0.7}\left(1 - M_1/M_2\right)^{0.7} = 1 + (0.4)(19.73/10)^{0.7}(1-0.5)^{0.7} = 1.40 > 1.3,$$

therefore β = 1.3

$$F_d = \alpha\beta k_d \frac{\pi^2 E}{12\left(1-\nu^2\right)}\left(\frac{t}{b_o}\right)^2 = (1.59)(1.3)(1.39)\frac{\pi^2(29500)}{(12)(1-0.3^2)}\left(\frac{0.059}{2.25}\right)^2 = 52.67 \text{ ksi}$$

$M_{crd} = S_{fc}F_d = (1.94)(52.67) = 102.18$ kip-in.

$M_y = S_f F_y = (1.94)(55) = 106.70$ kip-in.

$$\lambda_d = \sqrt{M_y/M_{crd}} = \sqrt{106.70/102.18} = 1.022 > 0.673$$

$$M_n = \left(1 - 0.22\left(\frac{M_{crd}}{M_y}\right)^{0.5}\right)\left(\frac{M_{crd}}{M_y}\right)^{0.5} M_y$$

$$= \left(1 - 0.22\left(\frac{102.18}{106.70}\right)^{0.5}\right)\left(\frac{102.18}{106.70}\right)^{0.5} 106.70 = 81.9 \text{ kip-in.}$$

Method (b) according to C3.1.6-(b)

The centerline dimensions are h = 7.94 in., b = 2.21 in., d = 0.896 in., t = 0.059 in., θ = 50 .

$$A_f = (b+d)t = (2.21+0.896)(0.059) = 0.183 \text{ in.}^2$$

$$I_{xf} = \frac{t\left(t^2b^2 + 4bd^3 - 4bd^3\cos^2(\theta) + t^2bd + d^4 - d^4\cos^2(\theta)\right)}{12(b+d)} = 0.0065 \text{ in.}^4$$

$$x_o = \frac{b^2 - d^2\cos(\theta)}{2(b+d)} = 0.702 \text{ in.}$$

$$h_x = \frac{-\left(b^2 + 2db + d^2\cos(\theta)\right)}{2(b+d)} = -1.505 \text{ in.}$$

$$h_y = y_o = \frac{-d^2\sin(\theta)}{2(b+d)} = -0.992 \text{ in.}$$

$C_{wf} = 0$

$$I_{xyf} = \frac{tbd^2\sin(\theta)(b + d\cos(\theta))}{4(b+d)} = 0.018 \text{ in.}^4$$

$$I_{yf} = \frac{t\left(b^4 + 4db^3 + 6d^2b^2\cos(\theta) + 4d^3b\cos^2(\theta) + d^4\cos^2(\theta)\right)}{12(b+d)} = 0.127 \text{ in.}^4$$

$$J_f = \tfrac{1}{3}bt^3 + \tfrac{1}{3}dt^3 = 0.000212 \text{ in.}^4$$

$$L_{cr} = \left(\frac{4\pi^4 h\left(1-\nu^2\right)}{t^3}\left(I_{xf}\left(x_o - h_x\right)^2 + C_{wf} - \frac{I_{xyf}^2}{I_{yf}}\left(x_o - h_x\right)^2\right) + \frac{\pi^4 h^4}{720}\right)^{1/4} = 22.76 \text{ in.}$$

L=minimum of L_{cr} and L_m = 10 in.

$$k_{\phi fe} = \left(\frac{\pi}{L}\right)^4\left(EI_{xf}\left(x_o - h_x\right)^2 + EC_{wf} - E\frac{I_{xyf}^2}{I_{yf}}\left(x_o - h_x\right)^2\right) + \left(\frac{\pi}{L}\right)^2 GJ_f =$$

$$\left(\frac{\pi}{10}\right)^4\left((29500)(0.0065)(0.702-(-1.505))^2 + 0 - (29500)\frac{(0.018)^2}{0.127}(0.702-(-1.505))^2\right) + \left(\frac{\pi}{10}\right)^2(11346)(0.000212)$$

= 5.846

$$\tilde{k}_{\phi fg} = \left(\frac{\pi}{L}\right)^2\left[A_f\left((x_o - h_x)^2\left(\frac{I_{xyf}}{I_{yf}}\right)^2 - 2y_o(x_o - h_x)\left(\frac{I_{xyf}}{I_{yf}}\right) + h_x^2 + y_o^2\right) + I_{xf} + I_{yf}\right] =$$

$$\left(\frac{\pi}{10}\right)^2\left[0.183\left((0.702-(-1.505))^2\left(\frac{0.018}{0.127}\right)^2 - (2)(-0.992)(0.702-(-1.505))\left(\frac{0.018}{0.127}\right) + (-1.505)^2 + (-0.992)^2\right) + 0.0065 + 0.127\right]$$

$= 0.0572$

$$k_{\phi we} = \frac{Et^3}{12(1-\nu^2)}\left(\frac{3}{h} + \left(\frac{\pi}{L}\right)^2\frac{19h}{60} + \left(\frac{\pi}{L}\right)^4\frac{h^3}{240}\right)$$

$$= \frac{(29500)(0.059)^3}{(12)(1-(0.3)^2)}\left(\frac{3}{7.94} + \left(\frac{\pi}{10}\right)^2\frac{(19)(7.94)}{60} + \left(\frac{\pi}{10}\right)^4\frac{(7.94)^3}{240}\right) = 0.359$$

$$\tilde{k}_{\phi wg} = \frac{ht\pi^2}{13440}\left(\frac{(45360(1-\xi_{web}) + 62160)\left(\frac{L}{h}\right)^2 + 448\pi^2 + \left(\frac{h}{L}\right)^2(53 + 3(1-\xi_{web}))\pi^4}{\pi^4 + 28\pi^2\left(\frac{L}{h}\right)^2 + 420\left(\frac{L}{h}\right)^4}\right) =$$

$$\frac{(7.94)(0.059)\pi^2}{13440}\left(\frac{(45360(1-2) + 62160)\left(\frac{10}{7.94}\right)^2 + (448)\pi^2 + \left(\frac{7.94}{10}\right)^2(53 + (3)(1-2))\pi^4}{\pi^4 + (28)\pi^2\left(\frac{10}{7.94}\right)^2 + 420\left(\frac{10}{7.94}\right)^4}\right)$$

$= 0.0074$

$\beta = 1 + 0.4(L_{cr}/L_m)^{0.7}(1 - M_1/M_2)^{0.7} = 1 + (0.4)(22.76/10)^{0.7}(1-0.5)^{0.7} = 1.44 > 1.3,$

therefore $\beta = 1.3$

$$F_d = \beta\frac{k_{\phi fe} + k_{\phi we}}{\tilde{k}_{\phi fg} + \tilde{k}_{\phi wg}} = 1.3\frac{5.846 + 0.359}{0.0572 + 0.0074} = 124.87 \text{ ksi}$$

$M_{crd} = S_{fc}F_d = (1.94)(124.87) = 242.25$ kip-in.

$M_y = S_fF_y = (1.94)(55) = 106.70$ kip-in.

$\lambda_d = \sqrt{M_y/M_{crd}} = \sqrt{106.70/242.25} = 0.664 \le 0.673$

$M_n = M_y = 106.7$ kip-in.

Method (c) according to C3.1.6-(c)

L_{cr} and M'_{crd} (for constant moment) are obtained form finite strip analysis by CUFSM:

L_{cr} = 23 in.

M'_{crd} = 83.16 kip-in.

since $L_m < L_{cr}$, $\alpha = \left(\frac{L_m}{L_{cr}}\right)^{\ln\left(\frac{L_m}{L_{cr}}\right)} = \left(\frac{10}{23}\right)^{\ln\left(\frac{10}{23}\right)} = 2.0$

(It is possible to perform this correction in the analysis, in some cases, here the simplified equation for α is employed.)

$\beta = 1 + 0.4(L_{cr}/L_m)^{0.7}(1 - M_1/M_2)^{0.7} = 1 + (0.4)(23/10)^{0.7}(1 - 0.5)^{0.7} = 1.44 > 1.3,$

therefore $\beta = 1.3$

$M_{crd} = \alpha\beta M'_{crd} = (2.0)(1.3)(83.16) = 216.22$ kip-in.

$M_y = S_f F_y = (1.94)(55) = 106.70$ kip-in.

$\lambda_d = \sqrt{M_y/M_{crd}} = \sqrt{106.70/216.22} = 0.703 > 0.673$

$$M_n = \left(1 - 0.22\left(\frac{M_{crd}}{M_y}\right)^{0.5}\right)\left(\frac{M_{crd}}{M_y}\right)^{0.5} M_y$$

$$= \left(1 - 0.22\left(\frac{216.22}{106.70}\right)^{0.5}\right)\left(\frac{216.22}{106.70}\right)^{0.5} 106.70 = 104.3 \text{ kip-in.}$$

Summary of predictions of distortional buckling strength

	Example 1	Example2
Method (a)	64.9 kip-in.	81.9 kip-in.
Method (b)	77.0 kip-in.	106.7 kip-in.
Method (c)	79.7 kip-in.	104.3 kip-in.

Local buckling strength is 98.5 kip-in. from the Example I-10 in the AISI Cold-Formed Steel Design Manual (2002 edition).

Vita

The author was born in Beijing, China, on May 15, 1974. In June of 1993, the author graduated from the No. Four High School in Beijing, China. Subsequently, the author enrolled at the Tsinghua University, Beijing, China, where he earned a Bachelor of Science degree in Structural Engineering in June 1998.

In 2000 the author entered graduate studies in Structural Engineering at Johns Hopkins University, Baltimore, Maryland under the guidance of Professor Benjamin W. Schafer. In 2004, the author was awarded the degree of Master of Science in Structural Engineering from Johns Hopkins University. The author continued his studies under Professor Schafer for his Ph.D.